

STATE OF CALIFORNIA • DEPARTMENT OF TRANSPORTATION  
**TECHNICAL REPORT DOCUMENTATION PAGE**  
 TR0003 (REV 10/98)

**ADA Notice**  
 For individuals with sensory disabilities, this document is available in alternate formats. For information call (916) 654-6410 or TDD (916) 654-3880 or write Records and Forms Management, 1120 N Street, MS-89, Sacramento, CA 95814.

1. Report Number <b>CA13-2349</b>	2. Government Accession Number	3. Recipient's Catalog Number
4. Title and Subtitle <b>The Effect of Live Load on the Seismic Response of Bridges</b>		5. Report Date <b>May 2013</b>
		6. Performing Organization Code
7. Authors <b>Hartanto Wibowo, Danielle M. Sanford, Ian G. Buckle, and David H. Sanders</b>		8. Performing Organization Report Number <b>CCEER 13-10</b>
9. Performing Organization Name and Address <b>Center for Civil Engineering Earthquake Research Department of Civil and Environmental Engineering University of Nevada, Reno, MS 258, Reno, NV 89557</b>		10. Work Unit Number
		11. Contract or Grant Number <b>59A0695</b>
12. Sponsoring Agency and Address <b>California Department of Transportation Division of Research and Innovation, MS-83 P.O. Box 942873 Sacramento, CA 94273-0001.</b>		13. Type of Report and Period Covered
		14. Sponsoring Agency Code
15. Supplementary Notes		
16. Abstract <p>With increasing congestion in major cities the occurrence of the design earthquake at the same time as the design live load is crossing a bridge is now more likely than in the past. But little is known about the effect of live load on seismic response and this report describes an experimental and analytical project that investigates this behavior. The experimental work included shake table testing of a 0.4-scale model of a three-span, horizontally curved, steel girder bridge loaded with a series of representative trucks. The model spanned four shake tables each synchronously excited with scaled ground motions from the 1994 Northridge earthquake. Observations from the experimental work showed the presence of the live load had a beneficial effect on performance of this bridge, but this effect diminished with increasing amplitude of shaking. Parameters used to measure performance included column displacement, abutment shear force, and degree of concrete spalling in the plastic hinge zones. Results obtained from a SAP2000 analysis of a nonlinear finite element model of the bridge and trucks confirmed this behavior, that live load reduces the dynamic response of the bridge. The most likely explanation for this phenomenon is that the trucks act as a set of nonlinear tuned mass dampers, which are known to be effective at controlling wind vibrations in buildings. Preliminary parameter studies have also been conducted and show the above beneficial effect is generally true for other earthquake ground motions, and vehicles with different dynamic properties. Exceptions exist, but adverse effects are usually within 10% of the no-live load case.</p>		
17. Key Words <b>seismic response, bridges, live load, shake table experiments, finite element modeling, parameter studies</b>	18. Distribution Statement <b>No restriction. This Document is available to the public through the Center for Civil Engineering Earthquake Research, University of Nevada, Reno, NV, 89557.</b>	
19. Security Classification (of this Report) <b>Unclassified</b>	20. Number of Pages <b>422</b>	21. Cost of Report Charged

## **DISCLAIMER STATEMENT**

This document is disseminated in the interest of information exchange. The contents of this report reflect the views of the authors who are responsible for the facts and accuracy of the data presented herein. The contents do not necessarily reflect the official views or policies of the State of California or the Federal Highway Administration. This publication does not constitute a standard, specification or regulation. This report does not constitute an endorsement by the Department of any product described herein.

For individuals with sensory disabilities, this document is available in Braille, large print, audiocassette, or compact disk. To obtain a copy of this document in one of these alternate formats, please contact: the Division of Research and Innovation, MS-83, California Department of Transportation, P.O. Box 942873, Sacramento, CA 94273-0001.

Report No. CCEER 13-10

**THE EFFECT OF LIVE LOAD ON THE  
SEISMIC RESPONSE OF BRIDGES**

Hartanto Wibowo  
Danielle M. Sanford  
Ian G. Buckle  
David H. Sanders

A report to the California Department of Transportation  
Contract No. 59A0695

---

**Center for Civil Engineering Earthquake Research**

University of Nevada, Reno  
Department of Civil and Environmental Engineering, MS258  
1664 N. Virginia St.  
Reno, NV 89557

May 2013

## ACKNOWLEDGMENTS

This project was principally funded by California Department of Transportation (Caltrans) under contract number 59A0695. The Caltrans Program Manager was Dr. Allaoua Kartoum. The experimental work undertaken in this study was part of a larger project on the seismic behavior of curved bridges funded by the Federal Highway Administration (FHWA) under contract number DTFH61-C-00031. The FHWA Contract Technical Representative was Dr. Wen-huei (Phillip) Yen. The authors therefore wish to acknowledge both Caltrans and FHWA and their respective program managers for their sponsorship and oversight of this project.

In particular the authors acknowledge FHWA for the construction and instrumentation of the model as well as the following graduate students who worked on various phases of this project: Nathan Harrison, Ebrahim Hormozaki, Michael Levi, Eric Monzon, Ahmad Saad, Chunli Wei, and Joseph Wieser. In addition, valuable faculty support was provided by Dr. Ahmad Itani and Dr. Gökhan Pekcan. The authors would also like to express their gratitude to Dr. Koji Kinoshita (Visiting Professor), Dr. Arash Esmaili Zaghi (Post-doctoral Scholar), and Moustafa Al-Ani (Visiting Researcher) for their contribution to this project. Furthermore, the experimental work would not have been possible without the skill and dedication of the laboratory staff including Kelly Doyle, Dr. Sherif Elfass, Dr. Patrick Laplace, Robert Nelson, Mark Lattin, Chad Lyttle, Todd Lyttle, Paul Lucas, as well as student workers including Kevin Boles and Joel Heidema.

Finally, the authors acknowledge the National Science Foundation for the use of the NEES Shake Table Array at the University of Nevada, Reno under a Shared-Use Agreement with NEEScomm at Purdue University.

# TABLE OF CONTENTS

Acknowledgements, iv

Table of Contents, 1

Abstract, 5

Chapter 1 Introduction, 6

- 1.1. General, 6
- 1.2. Background, 6
- 1.3. Problem Statement, 7
- 1.4. Scope of Study, 7
- 1.5. Organization of Report, 8
- 1.6. Summary, 8

Chapter 2 Literature Review, 10

- 2.1. General, 10
- 2.2. Previous Studies of the Impact Effects of Live Load on Bridges, 10
- 2.3. Previous Studies of Live Load Effects on the Seismic Response of Bridges, 14
  - 2.3.1. Live Load Effects on the Seismic Response of Highway Bridges, 14
  - 2.3.2. Live Load Effects on the Seismic Response of Railway Bridges, 16
- 2.4. Previous Studies on the Effects of Multiple Tuned-Mass Dampers and Nonlinear Energy Sinks on Structure Response, 17
- 2.5. Vehicle Models, 18
  - 2.5.1. Single Degree-of-Freedom Vehicle Models, 19
  - 2.5.2. Multiple Degree-of-Freedom Vehicle Models, 19
- 2.6. Summary, 21

Chapter 3 Vehicle Selection and Characterization, 28

- 3.1. General, 28
- 3.2. Vehicle Selection, 28
  - 3.2.1. Background and Rationale, 28
  - 3.2.2. Basic Vehicle Data, 29
- 3.3. Single Truck Experiment Setup, 29
  - 3.3.1. Outrigger Beam Design, 29
  - 3.3.2. Experiment Configuration, 30
  - 3.3.3. Experiment Logistics, 30
  - 3.3.4. Experiment Protocol, 30
  - 3.3.5. Instrumentation Plan, 31

- 3.4. Numerical Models, 31
  - 3.4.1. Single-Axle Model, 32
  - 3.4.2. Two-Axle Model, 32
- 3.5. Truck Properties in Vertical Direction, 33
  - 3.5.1. Application of Snap Test Data to Determine Truck Properties, 33
  - 3.5.2. Truck Vertical Properties without Tires, 35
    - 3.5.2.1. Empty Truck, 35
    - 3.5.2.2. Fully-Laden Truck, 35
  - 3.5.3. Truck Vertical Properties with Tires, 35
- 3.6. Truck Properties in Longitudinal and Transverse Directions, 36
  - 3.6.1. Truck Properties in Transverse Direction, 37
  - 3.6.2. Truck Properties in Longitudinal Direction, 37
- 3.7. Vehicle Response during Earthquake Excitation, 37
  - 3.7.1. Observed Vehicle Response, 37
    - 3.7.1.1. Vertical Direction, 38
    - 3.7.1.2. Transverse and Longitudinal Directions, 38
    - 3.7.1.3. Empty and Fully-Laden Trucks, 39
  - 3.7.2. Comparison of Numerical Model and Observed Responses, 39
- 3.8. Modal Properties of Truck, 40
- 3.9. Summary, 40

#### Chapter 4 Bridge Model and Experiment Setup, 61

- 4.1. General, 61
- 4.2. Prototype Bridge and Scaling Requirements, 61
  - 4.2.1. Prototype Bridge Selection, 61
  - 4.2.2. Seismic Hazard, 61
  - 4.2.3. Scaling and Similitude Requirements, 62
- 4.3. Model Substructure Design and Instrumentation Plan, 63
  - 4.3.1. Column, 63
  - 4.3.2. Footing, 63
  - 4.3.3. Bent Cap, 63
  - 4.3.4. Additional Substructure Mass, 64
  - 4.3.5. Instrumentation Plan, 64
- 4.4. Model Superstructure Design and Instrumentation Plan, 65
  - 4.4.1. Girders, 66
  - 4.4.2. Deck Slab, 66
  - 4.4.3. Cross Frames, 67
  - 4.4.4. Shear Keys, 67
  - 4.4.5. Additional Superstructure Mass, 68
  - 4.4.6. Instrumentation Plan, 68
- 4.5. Model Construction, 69
- 4.6. Live Load Vehicle, 69
  - 4.6.1. Vehicle Placement, 70
  - 4.6.2. Vehicle Instrumentation, 70
- 4.7. Ground Motion and Test Matrix, 71

- 4.7.1. Ground Motion, 71
- 4.7.2. Test Matrix, 72
- 4.8. Summary, 72

## Chapter 5. Experimental Results, 117

- 5.1. General, 117
- 5.2. Material Properties, 121
  - 5.2.1. Concrete, 117
  - 5.2.2. Steel Reinforcement, 117
  - 5.2.3. Section Analysis, 118
- 5.3. Shake Table Performance, 118
- 5.4. Bridge Dynamic Properties, 118
  - 5.4.1. System Frequency, 119
  - 5.4.2. System Damping, 119
- 5.5. Bridge Displacement, 120
- 5.6. Bridge Acceleration, 121
- 5.7. Bridge Forces and Moments, 121
  - 5.7.1. Force and Moment Histories from Load Cells, 121
  - 5.7.2. Calculation of Force and Moment at Bottom of the Bent, 122
  - 5.7.3. Force vs. Displacement and Moment vs. Curvature Relationships, 124
- 5.8. Column Damage, 126
  - 5.8.1. Cracking and Spalling, 126
  - 5.8.2. Reinforcement Yield Strain, 127
  - 5.8.3. Post-Experiment Torsional Stiffness, 127
- 5.9. Shear Key Performance, 128
- 5.10. Discussion, 128
- 5.11. Summary, 128

## Chapter 6. Analysis Results and Validation of Numerical Model, 345

- 6.1. General, 345
- 6.2. Bridge Model and Input Motion, 345
  - 6.2.1. Model Development, 345
  - 6.2.2. Input Motion for Nonlinear Response History Analysis, 348
- 6.3. Vehicle Model, 348
  - 6.3.1. Model Development, 348
  - 6.3.2. Vehicle Properties, 348
- 6.4. Refinements to Analytical Model, 345
- 6.5. Structural Response and Comparison with Experimental Results, 349
  - 6.5.1. Displacement, 349
  - 6.5.2. Acceleration, 349
  - 6.5.3. Forces and Moments, 350
- 6.6. Analysis of Bridge Model With and Without Live Load, 350
- 6.7. Discussion, 350

6.7. Summary, 350

Chapter 7. Preliminary Parameter Study, 371

- 7.1. General, 371
- 7.2. Parameters of Interest, 371
  - 7.2.1. Live Load to Bridge Mass Ratio and Live Load Period, 371
  - 7.2.2. Earthquake Ground Motion, 372
  - 7.2.3. Number of Vehicles, 372
- 7.3. Numerical Models, 372
  - 7.3.1. Stick Model, 372
  - 7.3.2. Finite Element Model, 372
- 7.4. Parameter Study Results, 373
  - 7.4.1. Effect of Live Load-to-Structure Mass Ratio, Vehicle Period, Damping and Ground Motion, 373
  - 7.4.2. Effect of Earthquake Ground Motion, 373
  - 7.4.3. Effect of Number of Vehicles and Placement, 374
- 7.5. Discussion, 375
- 7.6. Summary, 375

Chapter 8 Observations and Recommendations, 391

- 8.1. Observations, 391
- 8.2. Recommendations / Future Work, 392

References, 393

Appendix A Basic Theory for Tuned Mass Dampers (TMD) and Multiple Tuned Mass Dampers (MTMD), 405

- A.1 General, 405
- A.2 Undamped Structure and Undamped Tuned Mass Damper, 405
- A.3 Undamped Structure and Damped Tuned Mass Damper, 407
- A.4 Damped Structure and Damped Tuned Mass Damper, 409
- A.5 Multiple Degree-of-Freedom System with Tuned Mass Damper, 410
- A.6 System with Multiple Tuned Mass Dampers, 414
- A.7 Summary, 414

## ABSTRACT

With increasing congestion in major cities the occurrence of the design earthquake at the same time as the design live load is crossing a bridge is now more likely than in the past. But little is known about the effect of live load on seismic response and this report describes an experimental and analytical project that investigates this behavior. The experimental work included shake table testing of a 0.4-scale model of a three-span, horizontally curved, steel girder bridge loaded with a series of representative trucks. The model spanned four shake tables each synchronously excited with scaled ground motions from the 1994 Northridge earthquake. Observations from the experimental work show the presence of the live load had a beneficial effect on performance of this bridge, but this effect diminished with increasing amplitude of shaking. Parameters used to measure performance included column displacement, abutment shear force, and degree of concrete spalling in the plastic hinge zones. Results obtained from a SAP2000 analysis of a nonlinear finite element model of the bridge and trucks confirm this behavior, that live load reduces the dynamic response of the bridge. The most likely explanation for this phenomenon is that the trucks act as a set of nonlinear tuned mass dampers, which are known to be effective at controlling wind vibrations in buildings. Preliminary parameter studies have also been conducted and show the above beneficial effect is generally true for other earthquake ground motions, and vehicles with different dynamic properties. Exceptions exist, but adverse effects are usually within 10% of the no-live load case.

# CHAPTER 1. INTRODUCTION,

## 1.6. General

An experimental and analytical study on the effect of live load on the seismic response of ordinary bridges has been conducted. The experimental study featured a series of shake table tests on a large-scale model of a 3-span bridge loaded with six representative trucks. The experiment was used to gain insight into the effect of trucks on seismic response and to validate a computer model of the bridge-vehicle system. This report presents the findings from the study and shows that live load changes the behavior of bridge during an earthquake and, in this case, in a beneficial way.

## 1.2. Background

Dynamic interaction between vehicles and bridges has long been studied, but mainly in regard to the impact effect of live load due to surface roughness and vehicle speed and not the dynamic effect of sprung live load on seismic behavior. Consequently the effect of vehicle-bridge interaction on the seismic response is not well understood.

Bridge design specifications have few requirements concerning the inclusion of live load in the seismic design of bridges for perhaps two reasons. The likelihood of the full design live load occurring at the same time as the design earthquake is judged to be negligible, and adverse behavior due to live load in an earthquake has not been observed in practice. But traffic congestion has become a common situation in major cities and the occurrence of significant live load at the time of a major earthquake is much more likely than previously thought possible. It is clear that live load not only provides additional gravity load but also dynamic force effects due to its sprung nature. However, the significance of these effects on the seismic response of a bridge is not very obvious.

The live load project described in this report was undertaken to investigate this question. It was able to take advantage of a separate study being conducted on the seismic response of curved bridges at the University of Nevada, Reno. Funded by the Federal Highway Administration (FHWA), this study involved a series of shake table experiments on a 0.4-scale model of three-span steel girder bridge with a high degree of horizontal curvature, as shown in Figure 1.2.1. This series included a conventional bridge with and without abutment pounding, and an isolated bridge with full, hybrid, and rocking isolation systems, as shown in Table 1.2.1.

For the purpose of the live load project described in this report six trucks were placed on the conventional bridge and performance compared with the no-live load case. Experimental studies on curved bridges have been done previously with either static testing (Clarke, 1966; Culver and Christiano, 1969) or dynamic testing (Williams and Godden, 1979; Kawashima and Penzien, 1979). However, those studies were done at a

much smaller scale than in this project and none studied the effect of live load on response.

In addition to the above experimental study, an analytical model was also developed. Once it was calibrated against the experimental results, the model was used to conduct a limited parameter study to determine if the observations found in the experimental phase extend to bridges and trucks of different mass and frequency ratios.

### **1.3. Problem Statement**

The main objective of this study was to investigate and obtain insight into the effect of bridge-vehicle interaction during earthquake excitation. As noted above, the study consists of both experimental and analytical investigations with the following objectives:

- Determine the effect of live load (beneficial or adverse) on the seismic response of ordinary bridge structures
- Determine the limitations of live load effects (beneficial or adverse)
- Investigate ways to simplify the mechanics of bridge-vehicle interaction during earthquake excitation so that methods can be developed for preliminary design of bridges with live load
- Determine if live load can be conveniently modeled in commonly available structural analysis software packages, and
- Make recommendations about the inclusion of live load in the seismic design of bridges.

### **1.4. Scope of Study**

To achieve the objectives in the problem statement, a scope of study was devised comprising five tasks as follows:

Task 1. Literature Survey and Review of Field Data (Chapter 2)

Task 2. Experimental Studies (Chapters 3, 4, and 5)

- Single truck characterization and modifications to 6DOF shake table
- Replace damaged columns from previous experiment with no trucks
- Shake table experiments with trucks on bridge

Task 3. Analytical Studies (Chapter 6)

- Develop 3D Finite element model of bridge and trucks
- Verify model against experimental data
- Develop simplified models for parameter studies

Task 4. Preliminary Parameter Studies (Chapter 7)

- Select parameters
- Analyze bridges for inertial effects of sprung live load

Task 5. Reporting

## **1.5. Organization of Report**

This report comprises of eight chapters. Chapter one is an introduction to the project including the background, problem statement, and scope of the study. Chapter two provides an extensive literature review on the topic of live load effects on bridges with some discussion on tuned-mass-damper effects on structures. Chapter three describes the selection, characterization, and dynamic properties of the truck used in the experimental studies. Chapter four presents the experimental setup for the shake table study of a horizontally curved bridge model loaded with six test vehicles. Chapter five discusses the results obtained from the experimental study. Chapter six describes the numerical model and the results obtained from the analytical study. Chapter seven summarizes the results from the parameter study and chapter eight presents conclusions and recommendations.

## **1.6. Summary**

An overview of the background, problem statement, and scope of this study has been presented in this chapter. This is an exploratory study to determine the effect of live load on the seismic response of bridges using both experimental and analytical methods. Of note is the large-scale (i.e., 0.4-scale) used for the experimental models.

**Table 1.2.1. Horizontally Curved Bridge Experiment Matrix**

No.	Experiment Focus	Superstructure Type	Substructure Type	Yield Columns ?	Bearing Type	Abutment Pounding?
1	Conventional	Elastic Cross-frames	24" Column (Set A)	Yes	Steel	No
2	Live Load	Elastic Cross-frames	24" Column (Set B)	Yes	Steel	No
3	Full Isolation	Elastic Cross-frames	24" Column (Set C)	No	LRB Isolators	No
4	Hybrid Isolation	Ductile End Cross-frames	24" Column (Set C)	Yes	LRB Isolators at Abutments	No
5	Abutment Pounding	Elastic Cross-frames	24" Column (Set D)	Yes	Steel	Yes
6	Rocking Footing	Elastic Cross-frames	16" Column (Rocking)	Yes	Steel	No

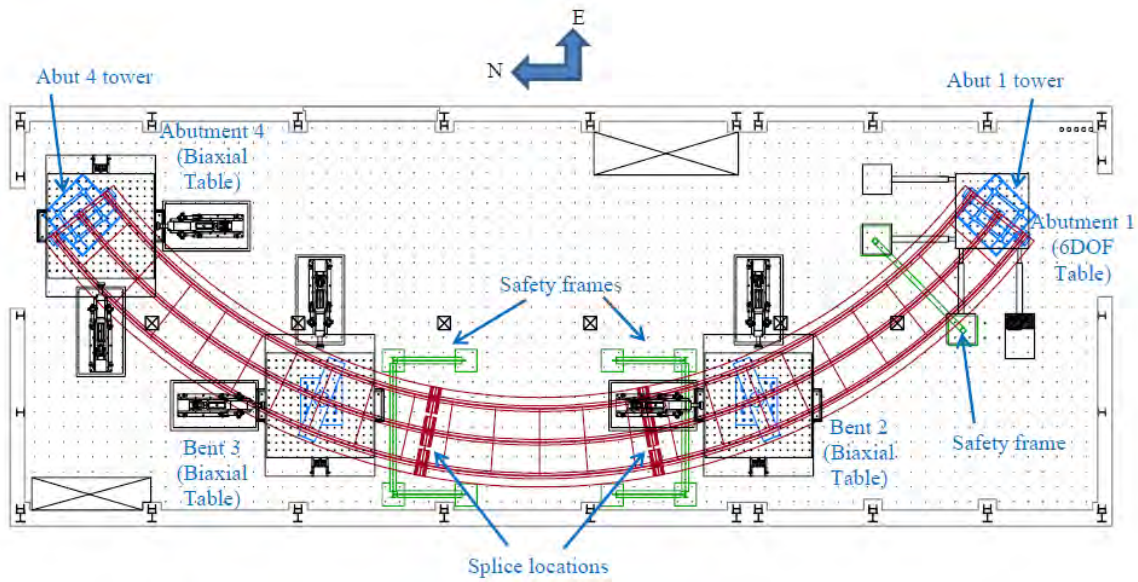


**Figure 1.2.1. Plan of Horizontally Curved Bridge Model in Laboratory**

## CHAPTER 2. LITERATURE REVIEW

### 2.1. General

Most seismic design procedures for earthquake-resistant bridges do not include the effect of live load for two primary reasons. First, it is unclear, what fraction of the full design live load will be on the bridge during the design earthquake, and second, it is believed the seismic response of a bridge is dominated by the dead load of the bridge, and the self-weight and inertial effects of the live load are negligible in comparison. However, with increasing congestion the likelihood of significant live load being on a bridge during the design earthquake is much more likely today than perhaps a decade ago. As a consequence some bridge design specifications (e.g., AASHTO, 2012; Caltrans, 2011) now require a fraction of the live load self-weight to be included in seismic analyses.

On the other hand, no current design specification is believed to require the inclusion of the inertial effects of live load in a seismic analysis, possibly because they are believed negligible. However, there is not a lot of evidence in the literature to confirm this assumption. In fact, it appears very little research has been conducted on the dynamic effect of live load on a bridge during an earthquake whereas there is a considerable body of work done on dynamic load allowance – the increase in wheel load due to the impact effect of moving vehicles on bridge decks. Nevertheless this work is of interest to the earthquake problem since the vehicle-bridge models used for the work on dynamic load allowance are applicable to studies on the effect of live load on seismic response. Previous work in both areas is therefore reviewed in the following sections.

### 2.2. Previous Studies of the Impact Effects of Live Load on Bridges

This section summarizes previous studies on the effect of live load on the vibration of bridges, particularly the impact effect due to moving vehicles on the bridge. Findings about these effects and identification of significant parameters are the main focus of the discussion. In addition, review of various analytical methods that have been used to study this phenomenon, as well as some previous experimental studies, are also presented.

The simplest approach to study vehicle-structure interaction on the vibration of a bridge is to model the vehicle as force instead of unsprung or sprung mass. One of the earliest research efforts on vehicle-structure interaction by Ayre *et al.* (1950) investigated the effect of a moving a constant force along a slender beam using experimental and theoretical methods. It was found that the maximum response of the beam was dependent on the ratio of the forcing frequency to the structure's frequency and the absolute maximum was found to occur a little below the resonance frequency. Similar observations were reported in a continuation study by Ayre and Jacobsen (1950) using a moving alternating force. Later Ayre *et al.* (1952) included the inertia term due to the

vehicle mass to the study and concluded that the inertia term increases the structural response in higher modes vibrations. This conclusion was corroborated by Gesund and Young (1961). However, these studies did not include the effect of damping in the structure. Furthermore, a study by Licari and Wilson (1962) pointed out that the problem of vibration of a beam with a series of moving masses cannot be simplified by superimposing the response of several single masses. A theoretical solution of the vibration of beam with moving masses has since been developed by Cifuentes (1989).

A study by Klasztorny and Langer (1990) analyzed the dynamic stability and steady-state vibrations of a simply-supported beam bridge with periodic unlimited sprung and unsprung moving masses. The vehicles were modeled as inertial concentrated loads along the length of the bridge at regular intervals. The results showed that the sprung masses tended to stabilize the response of the bridge, especially within its resonance zones.

In another study of the dynamic response of simply supported bridges under moving load, Humar and Kashif (1993) describe the complexity of the dynamic behavior and its dependence on many variables such as the ratio of the bridge-to-vehicle frequency, the ratio of bridge-to-vehicle weight, and the ratio of bridge period to the traversing time. This study found that the maximum dynamic effect of the moving load does not occur at resonance. Also, the pitching mode of the vehicle does not affect the bridge response. A more recent study by Kim and Kawatani (2001) showed that bridge response and dynamic wheel load are strongly influenced by the forced vibration due to the vehicle's bounce mode.

As computational methods became more user friendly, researchers have moved towards developing numerical methods to obtain insights into dynamic vehicle-structure interaction. Some researchers worked in the area of developing analytical methods for solving dynamic vehicle-structure interaction (Ngo, 1978; Sridharan and Malik, 1979; Hawk and Ghali, 1981; Wu and Dai, 1987; Green and Cebon, 1994, 1997; Yener and Chompooming, 1994; Yang and Lin, 1995; Yang and Fonder, 1996; Tan *et al.*, 1998; Zeng and Bert, 2001; Pan and Li, 2002; Nassif *et al.*, 2003; Xiang and Zhao, 2005; Xiang *et al.*, 2007; Lin, 2012; Neves *et al.*, 2012).

Ngo (1978) used both an open grid and a finite strip method to model response of single- and multi-span bridges subject to moving trucks. These vehicles were represented by 3-dimensional models that permitted coupling between the vertical, pitching, and rolling modes of vibration. This study of vehicle-induced vibration concluded that the effects of speed, lane traveled, and surface conditions were obscured by the more important effect of initial amplitude and phase of truck vibration. When comparing the effect of vehicle-induced response on straight and curved bridges, it was shown that the effect of horizontal curvature was to couple the translational and torsional responses, which led to lower translational frequencies and higher torsional frequencies compared to a straight bridge. Thus, the effect of vehicle load, which was dominated by the translational mode, was expected to be higher for a horizontally curved bridge.

Sridharan and Malik (1979) formulated the vehicle-structure interaction problem for a multi-span continuous beam using finite element method (FEM) and obtained a

solution using Wilson's  $\theta$  method. An analytical method to solve the coupled equations of bridge-vehicle interaction problems including road roughness and vehicle speed was developed by Green and Cebon (1994, 1997). The method involved a convolution integral in the frequency domain using a fast Fourier transformation and was extended by an iterative procedure to incorporate the dynamic interaction between the bridge and the vehicle. One of their conclusions was that bridge-vehicle interaction can be ignored when the ratio of the lowest vehicle natural frequency to the first bridge natural frequency is less than 0.5 (Green and Cebon, 1997). This method was then modified by Zeng and Bert (2001), who eliminated the convolution integral to make the method faster. Yener and Chompooming (1994) used a spatial discretization procedure (Newmark's method) to reduce the complexity of the partial differential equation to an ordinary differential equation. The nonlinearity problem was then solved by a multi predictor-corrector scheme. This study concluded that vehicle characteristics, stiffness of the bridge superstructure, traffic conditions, and roadway irregularities play an important role in bridge dynamic response.

Yang and Fonder (1996) also proposed an iterative numerical solution for solving bridge-vehicle interaction problems. The method was shown to be satisfactory for vehicles on continuous beams. Similarly, Xiang and Zhao (2005) and Xiang *et al.* (2007) used the transfer matrix method to solve the partial differential equation of beam vibration after adopting Newmark's method to reduce the problem to an ordinary differential equation. Wu and Dai (1987) also studied the dynamic response of multi-span beams subject to moving loads using the transfer matrix method. The study concluded that beam response to a series of moving loads can be approximated by the vector sum of the response due to the individual moving load. However, the trend of the dynamic response induced by a series of moving loads is different than the response induced by a single moving load. This study was corroborated by Lin (2012) and Neves *et al.* (2012) who also developed analytical approaches for the problem.

Yang and Lin (1995) used a dynamic condensation method to reduce the number of degrees-of-freedom in their matrix-based solutions, i.e., all degrees-of-freedom associated with the vehicle bodies were condensed out at the element level. Impact factors were then developed for vehicles moving over simple and continuous beams (Yang *et al.*, 1995). Pan and Li (2002) developed a dynamic vehicle element method to solve the transient response of dynamic vehicle-structure interaction caused by road roughness in the time domain. This method considered the vehicle as a moving part of the entire system. A simplified decoupled dynamic nodal loading method to generate a time series of concentrated nodal loads representing the vehicle reaction force on the structure was also proposed. It was shown that the displacement, velocity, and acceleration responses are almost linearly proportional to the vehicle speed and the vehicle-structure mass ratio. Tan *et al.* (1998) utilized a two-dimensional grillage model to idealize the bridge superstructure and the vehicle was modeled as a seven degree-of-freedom system. This study concluded that the vehicle speed had the most effect on the response of the bridge. Similarly, Nassif *et al.* (2003) used a finite element three-dimensional grillage model in their study to develop dynamic load factors for bridges.

Other researchers have also studied the dynamic interaction of a bridge and vehicle caused by road roughness (Rösler, 1994; Baumgaertner, 1998; Szöke and Györgyi, 2002; Bruni *et al.*, 2003). These studies showed that internal forces can increase significantly due to impact caused by vehicle excitation. A study by Chatterjee *et al.* (1994) on vehicle-bridge interaction due to road roughness concluded that for a smooth road, modeling the vehicle as sprung or unsprung mass does not make any significant difference to the bridge response but on the contrary, it makes a significant difference when the road profile has random irregularities. In addition, the study also showed that the speed of the vehicle was an important parameter: the higher the speed the higher the dynamic amplification factor. Earlier studies by Gupta and Traill-Nash (1980) and Mulcahy (1983) included the effect of braking forces, in addition to road roughness, and showed that these forces amplifies the dynamic response of the bridge. The effect of road roughness profile, boundary conditions, suspension type, multiple presence, and vehicle speed were also observed by Nassif and Liu (2004). It was concluded that truck suspension properties have significant effects on the dynamic behavior of the bridge.

Au *et al.* (2001) reviewed several studies on the dynamic analysis of moving vehicles on railway, girder, slab, cable-stayed, and suspension bridges. Based on this review, important parameters affecting the dynamic vehicle-bridge interaction due to moving vehicle were identified including the natural frequencies of the bridge, vehicle properties, vehicle velocity and moving path, number of vehicles and their relative positions on the bridge, road profile or surface roughness, and damping of the bridge and vehicle.

Law and Zhu (2004) studied the effects of a moving vehicle on the response of damaged concrete bridges. An experimental study was also carried out using a simulated vehicle on a simply supported concrete T-beam. It was found that the deflection increases in the damaged bridge, and surface roughness had less effect on the response.

For suspension bridges, Bryja and Śniady (1998) investigated the vibration of a single span suspension bridge due to a random stream of moving vehicles. The results showed that the effect of the vehicles' springing and the inertial forces were both negligible. Yau and Frýba (2007) analyzed a suspension bridge under moving loads and vertical seismic ground acceleration and showed that the resonance effect caused by the moving load could be very significant. Also, the moving load could excite the bridge in the higher mode, especially for long-span bridges.

Several researchers have also studied train-bridge interactions (Aida *et al.*, 1990; Wakui *et al.*, 1994; Yau *et al.*, 2001; Kim and Kawatani, 2006; Majka and Hartnett, 2008; Liu *et al.*, 2009). Aida *et al.* (1990) studied the effect of train load on the stability of a Shinkansen viaduct in Japan. The results showed that damping tends to stabilize the response of the bridge. Wakui *et al.* (1994) showed that nonlinear modal analysis could be developed as a numerical method to solve large-scale train-structure interaction problems.

Yau *et al.* (2001) studied the dynamic response of bridges with elastic bearings due to train moving loads and developed an envelope impact formula for the bridge. Majka and Hartnett (2008) identified various parameters that affect dynamic train-bridge

interaction such as the speed of the train, train-to-bridge frequency, mass and span ratios, and bridge damping. Furthermore, the results of their study show that train damping has negligible influence on the bridge response and that dynamic amplification is found to be significant for a train with short and regularly spaced axles traveling at its critical speed. In agreement with these findings, Liu *et al.* (2009) also showed that dynamic train-bridge interaction is more apparent if the ratio of the mass of the vehicle to the bridge is large.

Some researchers have studied the dynamic bridge-vehicle interaction on curved bridges. Mermetas (1998) analyzed a four degree-of-freedom vehicle on a simply supported curved beam using multi predictor-corrector procedure with Newmark's method. It was found that the mid-span deflection increased as the speed and the radius of the curved bridge increase. Senthilvasan *et al.* (1997) used a seven degree-of-freedom two-axle vehicle model on curved box girder bridges in their analyses utilizing spline finite strip method. The results showed that if the ratio of the mass of the vehicle to the mass of the bridge is less than 35%, the vehicle can be treated as moving load rather than moving mass.

### **2.3. Previous Studies of Live Load Effects on the Seismic Response of Bridges**

Only a few studies have been reported in the literature concerning the effect of dynamic vehicle-bridge interaction on the seismic response of bridges. It appears that both highway and railway bridges have been investigated. Some of the results of these studies suggest that live load has an adverse effect on structure response and some suggest the opposite, that live load has a beneficial effect. The reason for this contradiction is not clear.

#### **2.3.1. Live Load Effects on Seismic Response of Highway Bridges**

A vibration test is reported by Sugiyama *et al.* (1990) on an existing steel girder bridge with and without trucks in the longitudinal and transverse directions to verify the results from a simple numerical model. In this test, two large trucks were parked facing the same direction on a portion of an existing off ramp whose girders were vibrated using an electro-hydraulic exciter. The bridge was tested with the vehicles empty and loaded to various capacities. The results showed that the dynamic effect of the vehicles was more dominant in the transverse direction and that they tended to reduce the response of the bridge. The authors also observed that as the exciting force level increased, the effects of nonlinearity became more apparent since the dynamic characteristics of the vehicles themselves were nonlinear. These results are corroborated by Kameda *et al.* (1992) who used a five degree-of-freedom model in their study. These authors state that the vehicles tended to increase the bridge response when the vehicles were in-phase with the bridge and decrease the response when they were out-of-phase. Furthermore, the authors also concluded that the ratio of the fundamental frequency of the bridge to the vehicle plays an important role in the response of the bridge. Moreover, Kameda *et al.* (1999) also

concluded that live load gives beneficial effect when the period of the vehicle is greater than the period of the bridge and that the effect of live load is more pronounced when the bridge is still in its elastic stage.

Kawatani *et al.* (2007) have analytically investigated the seismic response of a steel plate girder bridge under vehicle loading during earthquake excitation. The vehicles were modeled with twelve degrees-of-freedom that included sway, yaw, bounce, pitch, and roll degrees-of-freedom. The observations from the numerical analyses showed that heavy vehicles can reduce the seismic response of bridges under a ground motion with low frequency characteristics, but that these vehicles have the opposite effect and slightly amplify the seismic response of the bridge, under high frequency ground motions.

Kawashima *et al.* (1994) and Otsuka *et al.* (1999) have performed two studies to determine the effect of live load on seismic response. A two-span simply supported girder bridge was studied with a mix of ordinary cars, modeled as additional dead load mass, and large trucks, each modeled with five degree-of-freedom. The bridge was analyzed in the transverse direction because it was expected deck response would be significantly affected in this direction by the rolling of the large trucks. The studies found that the displacement response of the girders increased by 10% when live load was included. The ductility demand at the bottom of the column also increased by 10% when live load was on the bridge. The study concluded that this was not enough of an effect to be significant and safety factors could be modified to take this effect into account during design if they are not already sufficient. It was also concluded that the increase in response was due to the increase of weight. However, the effect of the large trucks was not just to increase the dead weight, but they also behaved as a mass damper.

Scott (2010) has developed a simplified modeling approach for dynamic analysis of combined live and seismic load. Using this approach, it was shown that for short-span bridges, the displacement response is mainly due to the fundamental bridge mode. In addition, for long-span bridges, vehicle speed has only a small influence on the displacement and acceleration responses of the bridge.

A recent study on the effects of live load on a highway bridge under moderate earthquake in the horizontal and vertical directions has been reported by Kim *et al.* (2011). This study concluded that the seismic response of the bridge is amplified when the vehicle is considered as merely additional gravity load or mass, and the amplification is dependent on the relationship between the fundamental frequency of the bridge and the response spectra of the ground motion. However, when the vehicle is considered as dynamic or mass-spring-damper system, which is a more realistic assumption, the dynamic effect of the vehicle is greater than simply additional gravity load, and thus it reduces the seismic response. In addition, the study also showed that the effect of a moving vehicle, compared to a stationary vehicle, is negligible. It is noted that a study by Sen *et al.* (2012) showed that the effect of surface irregularities is not significant in vehicle-bridge interaction during an earthquake.

A full finite element model to represent vehicle-bridge interaction was developed using LS-DYNA by Kwasniewski *et al.* (2006a). This model can be used for three-dimensional representation of a bridge and vehicle, including pneumatic tires, rotating

wheels, and nonlinear suspension. However, this degree of modeling rigor is computationally intensive and time consuming to execute. It is also limited by the accuracy to which the stiffness and damping properties of the elements are known.

Some studies have focused on the effects of live load combined with vertical ground excitation. Kožar (2009) compared the forces in a bridge due to moving loads and vertical earthquake ground motion and showed that the actions induced by the moving loads have greater effect than the earthquake if the mass of the bridge is relatively small compared to the vehicle mass. A more recent study on a long-span suspension bridge under moving vehicle loads and vertical earthquake ground motions by Liu *et al.* (2011) indicated that the interaction of the moving vehicles and seismic loads can significantly amplify the response of the bridge especially in the vicinity of the end supports.

### **2.3.2. Live Load Effects on Seismic Response of Railway Bridges**

Dynamic interaction between a train and a bridge under earthquake excitation has been studied by several researchers. Han *et al.* (2003) investigated the effects of a running train and an earthquake in the lateral and vertical directions, on a cable-stayed bridge, and concluded that the earthquake significantly increases the bridge response. Another study by Frýba and Yau (2009) also found that the low frequencies of long-span bridges are separated from the higher frequencies excited by earthquakes and quickly moving trains. In addition to this observation, the authors also showed that the interaction between the moving and earthquake loads could amplify the response of long-span suspension bridges near the supports. Zhang *et al.* (2010) have investigated non-stationary random responses of three-dimensional train-bridge systems subjected to earthquake motions in the lateral direction, and found similar results, that earthquake motion has a big influence on bridge response. In addition, earthquake intensity, site type or soil condition, and train speed also influence bridge response, but to different degrees.

Xia *et al.* (2006) studied the effects of moving trains on a continuous bridge subjected to multiple support excitations and showed that the propagating velocity of the seismic wave plays an important role in the dynamic response of a train-bridge system. Furthermore, Yan *et al.* (2009) have done a similar study on the effects of moving vehicles, modeled as oscillators, on a suspension bridge under multiple support excitations. It is shown that the vehicle passage frequency can have a resonance effect in the response of the bridge. However, if the passage speed is in resonance with the frequency of the first symmetric mode of the bridge, the vehicle passage may suppress response leading to a beneficial effect.

Kim and Kawatani (2006) examined the seismic response of a bridge subjected to a moderate earthquake in conjunction with a moving train load and found that the train acts as a damper and tends to reduce the seismic response under a particular earthquake. He *et al.* (2011) has also studied the effect of a moving train on a Shinkansen viaduct in Japan under moderate earthquake. The study concluded that with the moving train, the seismic response of the bridge is very complex and dependent on the dynamic properties of the bridge and the characteristics of the ground motions. The analytical results showed

that the train can act as a damper for the bridge. Also, considering the train as only additional load or mass can either overestimate or underestimate the bridge response. Furthermore a study by Sungil and Jongwon (2012) on the Young-jong Grand Bridge, which is a suspension bridge, showed that the deflection of the bridge due to surface irregularities, could be less than or greater than the maximum deflection when the earthquake was present, depending on the speed of the passing train. The ratio of the mass of the train to the mass of bridge also played an important role determining whether the live load reduced or increased the demand in the structure. Tokunaga and Sogabe (2012) showed that for a low mass ratio, the live load tended to give a beneficial effect and the opposite effect was found for a higher mass ratio.

## **2.4. Previous Studies on the Effects of Multiple Tuned Mass Dampers and Nonlinear Energy Sinks on Structure Response**

The behavior of a group of vehicles on a bridge can be likened to that of a set of tuned mass dampers on the bridge, and this observation offers a potential explanation for the observed effect of live load on seismic response. This section therefore reviews previous studies on multiple tuned mass dampers (MTMD) and a similar but more sophisticated device, the nonlinear energy sink (NLES).

One of the earliest publications on MTMDs by Xu and Igusa (1992) discussed the effect of having multiple sub-oscillators (i.e., MTMDs) on the main oscillator (i.e., structure). The results showed that a MTMD can reduce the response of a structure subjected to harmonic excitation and they were more effective than single tuned-mass dampers (TMD) at lower damping values. It was also found that the reduction of the structure's response could be explained by equivalent damping in the MTMD system. Yamaguchi and Harnpornchai (1993) also note that an MTMD can be optimized to minimize a structure's response to harmonic excitation, and can be designed for a wider frequency range than a TMD, which makes an MTMD more robust than a TMD. These findings were corroborated by Abé and Fujino (1994), who also found that an MTMD system is efficient when at least one of the oscillators is highly coupled with any structural mode. A study by Jangid (1995) also concluded that an MTMD is more robust than a TMD. This study also found that the effectiveness of an MTMD system is higher when the mass ratio is in the range of 2% to 3% and the effectiveness is lower for low frequency excitation when the ratio is less than one. Furthermore, a study by Li and Liu (2002) showed that there is a limit to the number of dampers in an MTMD system that should be used, above which there is no gain in efficiency. For a building, this number is about 20.

Clark (1988) developed a simple model to show that an MTMD can be used to reduce seismic response in a building. A study of an MTMD system subjected to wind and earthquake loadings has been carried out by Kareem and Kline (1995). This study found similar results as in previous studies for harmonic loading, that an MTMD is more effective and robust than a TMD, and that there exists an optimal MTMD design for a given frequency range of the system. Chen and Wu (2001) compared a structure with an MTMD and a TMD subjected to 13 different earthquake records and concluded that the

MTMD system performed better than the TMD at reducing the acceleration response of the structure. But the MTMD system was less effective at reducing the displacement response.

Park and Reed (2001) found that a uniformly distributed MTMD system was more effective at reducing the response of a structure and more robust to mistuning compared to a TMD system, when the structure is subjected to harmonic excitation. Also, the MTMD system was more reliable should an individual damper fail. On the other hand, this study showed that the MTMD system, as well as the TMD system, is less effective when it is subjected to earthquake excitations. However, the conditions when this is the case are still unclear.

Similar observations are found in the studies by Lewandowski and Grzymilawska (2009), Zuo (2009), and Shooshtari and Mortezaie (2012). Rana (1996) showed that an MTMD system is not as effective at reducing response when the earthquake excites a mode that is not one of the tuned modes. Several other studies have also showed that an MTMD can be used for reducing the translational and torsional response of structures (Li and Qu, 2006) and also for buffeting control of bridges (Gu *et al.*, 2001).

As noted above by Park and Reed (2001), a TMD system is only effective for a small frequency range. This observation is further discussed in a recent study by Lee *et al.* (2012) using structures modeled as single degree-of-freedom (SDOF) systems. It is shown that the effectiveness of the TMD depended on the mass ratio and the TMD was more effective for more flexible structures. The study also showed that the effectiveness of the TMD decreased as the seismic excitation level increased, i.e., as the structure became nonlinear. And in some cases the TMD adversely affected the structure's response. It is not known to what extent these findings extend to multi-degree of freedom systems.

A nonlinear energy sink (NLES) is very similar to a TMD except that the stiffness of the damper is nonlinear. The performance of the device is therefore load dependent, but if tuned correctly can dissipate energy more efficiently than a TMD and exhibit a wider effective frequency range. These devices have been shown to reduce demand in structures subjected to seismic loading (Wierschem *et al.*, 2011, 2012) more effectively than MTMDs. It is noted that the nonlinear nature of a truck suspension system can be likened to an NLES, with consequential implications for seismic response.

Appendix A summarizes the theory of undamped and damped TMDs and MTMDs for undamped and damped structures.

## **2.5. Vehicle Models**

Various vehicle models have been used by researchers to study vehicle-bridge interaction as noted in previous section. The models range from simple single degree-of-freedom (SDOF) systems to more sophisticated models involving multiple degree-of-freedom (MDOF) systems as described below.

### 2.5.1. Single Degree-of-Freedom Vehicle Models

A SDOF vehicle model can be used for simple analyses of structure-vehicle interaction as shown by Kłasztorny and Langer, 1990; Yang and Yau, 1997; Bryja and Śniady, 1998; Lin, 2006). Bryja and Śniady (1998) modeled the vehicle as a set of viscoelastic oscillators with a vertical degree-of-freedom as shown in Figure 2.5.1(a). This model was used to analyze a suspension bridge under inertial sprung moving load. A similar model was also used by Kłasztorny and Langer (1990) as shown in Figure 2.5.1(b). Although this type of model is able to simulate the dynamic effect of vibration induced by surface or road roughness (Yang and Yau, 1997; Lin, 2006), it is less suitable for the analysis of dynamic vehicle-bridge interaction during an earthquake.

### 2.5.2. Multiple Degree-of-Freedom Vehicle Models

The vehicle model by Ngo (1978) is a set of one or more three-dimensional bodies, each one representing a section of the vehicle with a rigid chassis, as depicted in Figure 2.5.2. If there is more than one body, they are interconnected such that there is continuity of vertical displacement at the point of connection. The vehicle body is supported by wheel mechanisms that consist of a tire spring and a suspension spring in series, a frictional damper in parallel with the suspension spring, and a viscous damper in parallel with both springs.

Yang *et al.* (1999) developed a three degree-of-freedom two-axle vehicle model to account for pitching in the vehicle motion as shown in Figure 2.5.3(a). This model consisted of a sprung mass with a spring and damper in the suspension level, and an unsprung mass at the wheel level. A similar model was developed by Lou (2005). In addition, Lou (2005) utilized a simpler one-axle vehicle model as shown in Figure 2.5.3(b), which is similar to the model in Figure 2.5.1 but the degree-of-freedom is in horizontal direction. This model is commonly used for dynamic vehicle-bridge interaction study. This latter model was also adopted by Scott (2010) in the study of combined live and seismic loads effects on bridges.

Wang *et al.* (1993) developed models of H20-44 and HS20-44 trucks for their work on the dynamic response of trucks due to road roughness. As shown in Figure 2.5.4, the models consist of three rigid masses: the truck body, front wheel/axle set, and rear wheel/axle set. The truck body has three degrees-of-freedom corresponding to the vertical displacement, pitch, and roll. Each wheel/axle set has two degrees-of-freedom corresponding to the vertical and roll directions. There are a total of seven degrees of freedom in the model as shown in Figure 2.5.4. A similar spring-damper configuration was also used in the study by Law and Zhu (2004).

Kameda *et al.* (1992) used a five degree-of-freedom vehicle model in their study of dynamic structure-vehicle interaction for seismic load evaluation on bridges. The vehicle model is shown in Figure 2.5.5. In this model, a set of rigid bodies is connected

by rotational and translational springs and dampers. The same model was also used by Kawashima *et al.* (1994) and Otsuka *et al.* (1999).

Kim *et al.* (2005) modeled a two-axle cargo truck and a three-axle dump truck for their analyses as shown in Figure 2.5.6. The two-axle truck model has seven degrees-of-freedom and the three-axle truck model has eight degrees-of-freedom. The vehicle body was considered to be rigid and supported by a set of linear springs and viscous dampers attached to each axle. These models allowed the capture of the bounce, hop, roll, tramp, pitch, and windup in the vehicle motion and gave results in good agreement with experimental field test data.

Huang *et al.* (1998) and Huang (2008) developed a three-dimensional non-linear model to simulate the AASHTO LRFD design truck. The model consisted of five sprung masses that represent the tractor, trailer, and three wheel/axle sets. It has a total of eleven degrees-of-freedom comprising six rotational and five translational modes as shown in Figure 2.5.7. The tire springs and dampers are assumed to be linear. Similar models have been used by Wang (1993), Shi and Cai (2009), Wyss *et al.* (2011), and Bojanowski and Kulak (2011).

In the study by Kawatani *et al.* (2007), the vehicle was represented by a discrete rigid body system with twelve degrees-of-freedom as shown in Figure 2.5.8. This model is similar to the one shown in Figure 2.5.6 previously used by the same research group (Kim *et al.*, 2005). This model can capture sway, yaw, bounce, pitch, and roll motions of the vehicle. The model was used to investigate the seismic response of a bridge under traffic loading, but the analysis was mainly focused on the vertical motion of the structure and the resulting impact forces, and the vehicle model was chosen accordingly. However, a more recent study by this same research group (Kim *et al.*, 2011) also utilized this vehicle model to study the response of a bridge with live load and seismic motions in the horizontal and vertical directions. The model was shown to provide good results.

In a study of truck suspensions to reduce bridge loading, Valášek *et al.* (2004) developed a nonlinear half-car model with four degrees-of-freedom as shown in Figure 2.5.9. In this model, the car body as well as the front and rear axles were considered as sprung masses. However, this model was utilized to analyze the suspension of the car itself rather than the response of the bridge. Rajapakse and Happawana (2004) incorporated the roll motion into their model. The truck-trailer model has six degrees-of-freedom as shown in Figure 2.5.10, consisting of a sprung mass (body), an unsprung mass (axle), and suspension systems.

A more sophisticated model to simulate the ride of a truck was used in a study by Simeon *et al.* (1994). The model has eleven degrees-of-freedom to obtain the response of the tires, chassis, engine, cabin, seat, and loading area as shown in Figure 2.5.11. A more recent study by Ibrahim (2004) also used a similar model with eleven degrees-of-freedom as shown in Figure 2.5.12. This model can capture the movement of the vehicle in the vertical, pitch, and roll directions. However, these two models are considered unnecessarily complex for implementation in the analysis of vehicle-bridge interaction, where the response of the driver or simulation of the ride is less important than the structure response.

## 2.6. Summary

Although various studies have been completed on vehicle-bridge interaction, most have focused on the impact effects of live load and very few have investigated the effect of live load on seismic response. In addition most of these studies have been analytical in nature and very few involved experimental work.

Conclusions that may be drawn regarding seismic response include: (1) a high ratio of vehicle-to-bridge weight strongly affects response to earthquake loading, (2) vehicle inertial effects may reduce bridge response during an earthquake in a manner similar to a tuned mass damper, but the benefit diminishes with increasing level of excitation, and (3) adverse effects are also possible but the effect is small (less than 10%). However, none of these conclusions appear to have been validated in the field or in large-scale laboratory experiments.

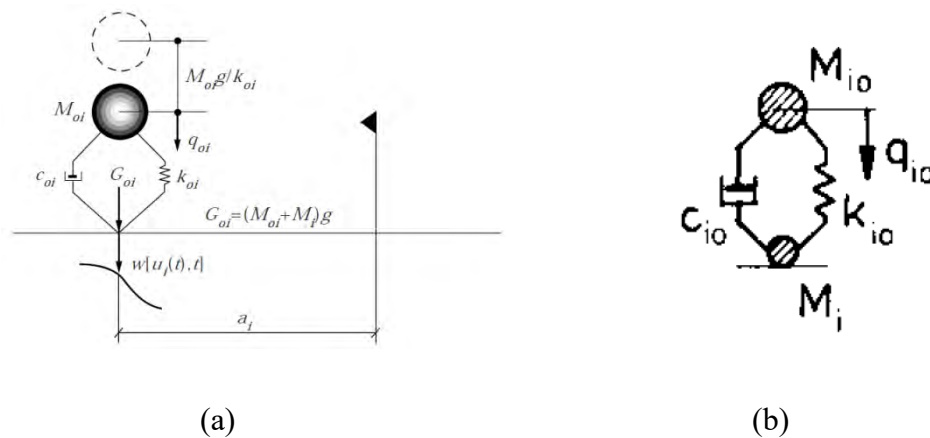


**Figure 2.5.1. Vehicle Models by (a) Bryja and Śniady (1998) and (b) Klasztorny and Langer (1990)**

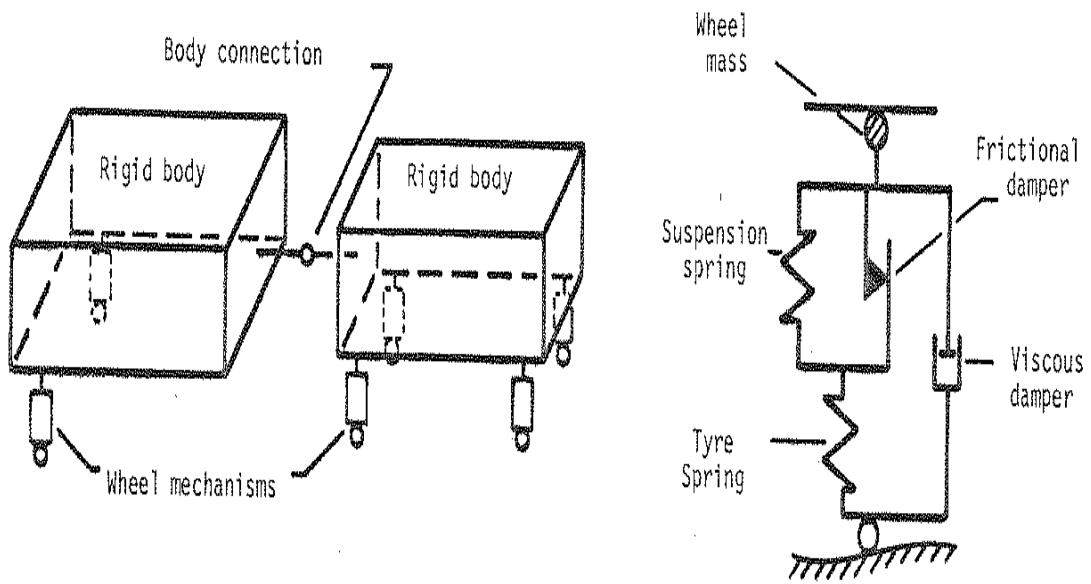


Figure 2.5.2. Vehicle Model and Wheel Mechanism (Ngo, 1978)

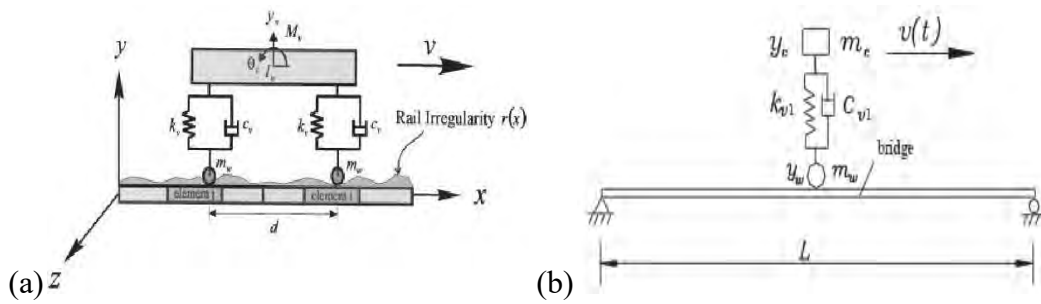
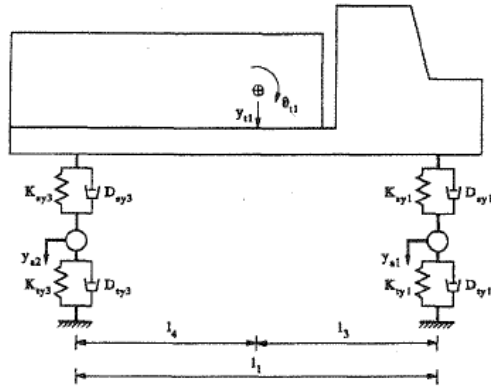
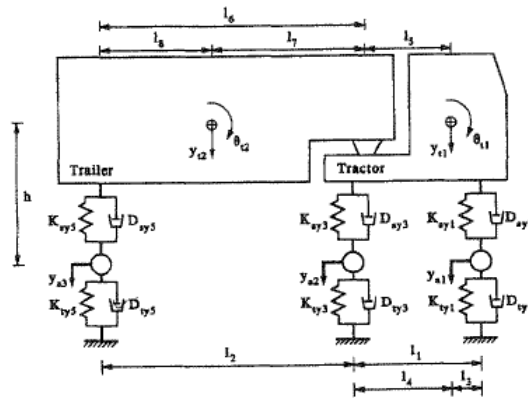


Figure 2.5.3. (a) Two-Axle Vehicle Model *et al.* (Yang, 1999) and (b) One-Axle Vehicle Model (Lou, 2005)



(a)



(b)

Figure 2.5.4. (a) H20-44 and (b) HS20-44 Vehicle Models (Wang *et al.*, 1993)

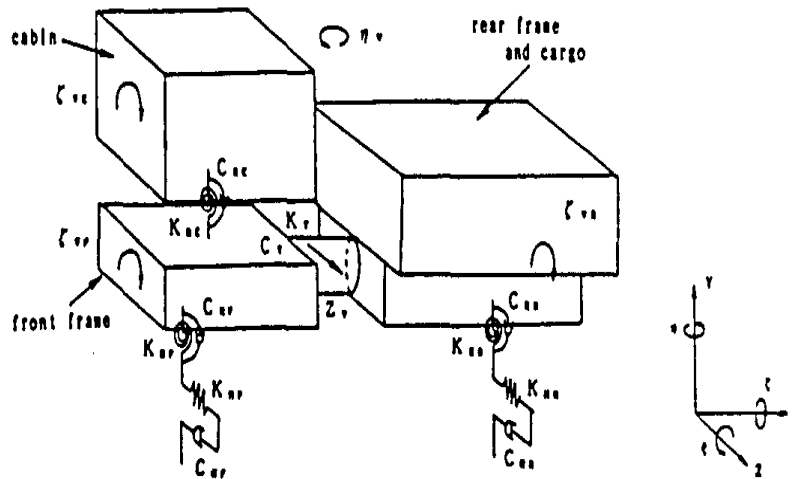
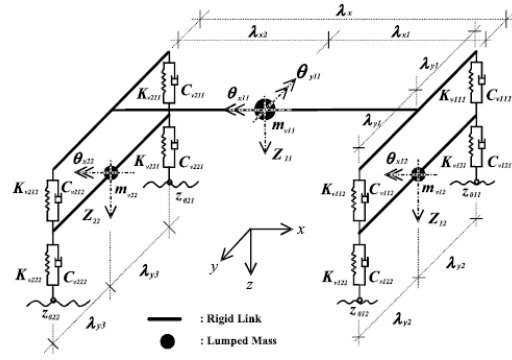
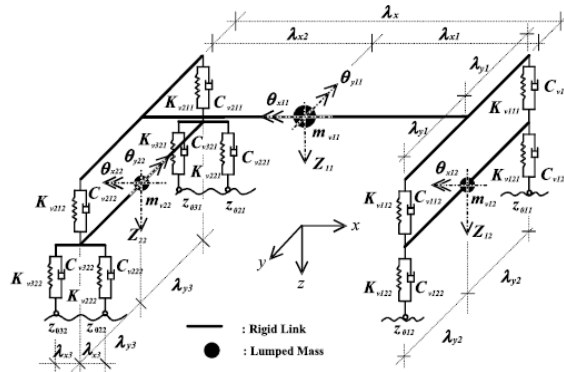


Figure 2.5.5. Vehicle Model by Kameda *et al.* (1992)



(a)



(b)

Figure 2.5.6. (a) Two-Axle and (b) Three-Axle Vehicle Models (Kim *et al.*, 2005)

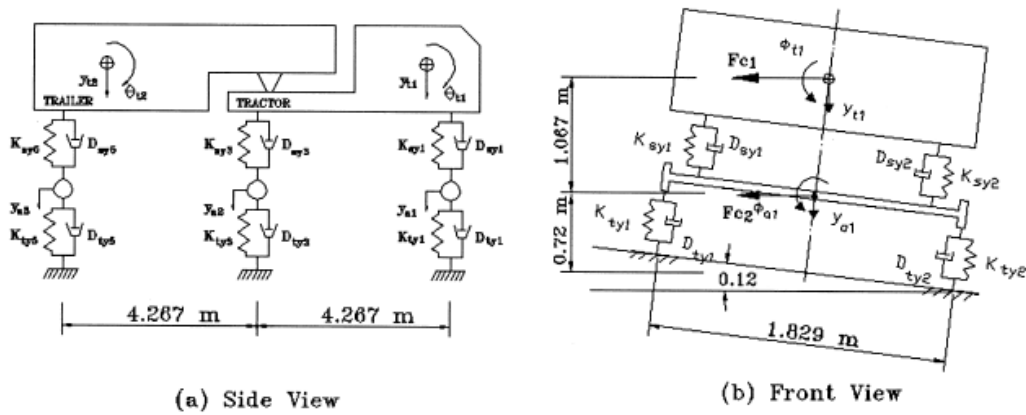


Figure 2.5.7. AASHTO HS20-44 Vehicle Model (Huang *et al.*, 1998; Huang, 2008)

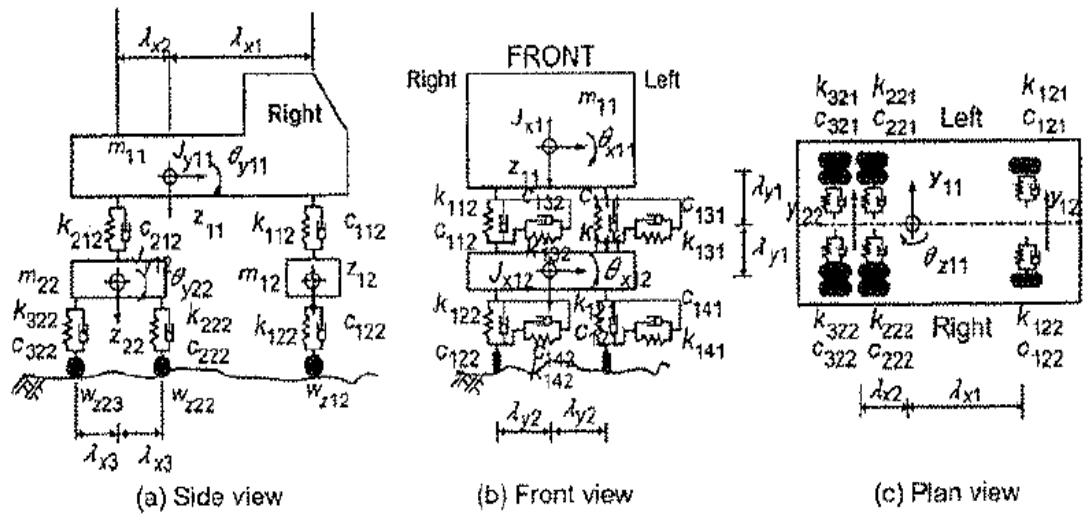


Figure 2.5.8. Vehicle Model by Kawatani *et al.* (2007) and Kim *et al.* (2011)

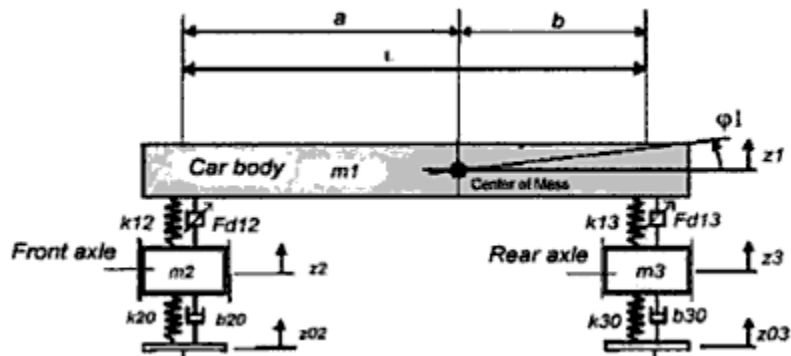


Figure 2.5.9. Vehicle Model by Valášek *et al.* (2004)

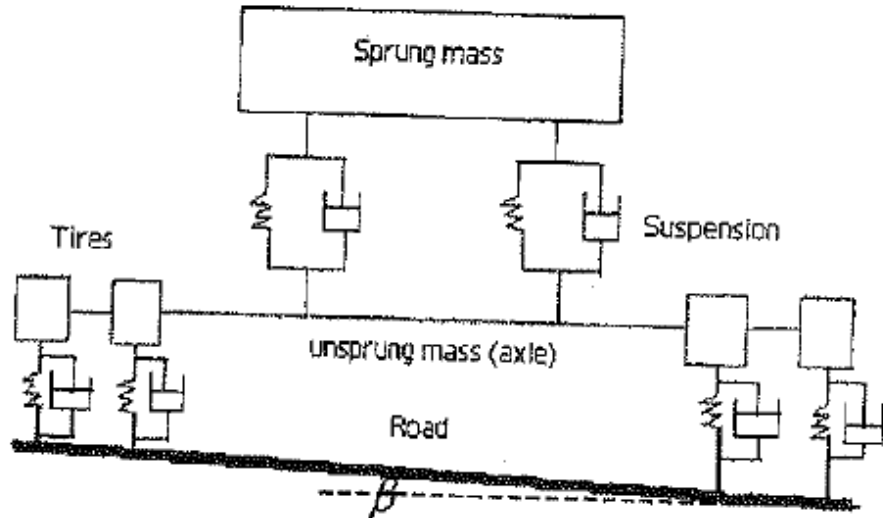


Figure 2.5.10. Vehicle Model by Rajapakse and Happawana (2004)

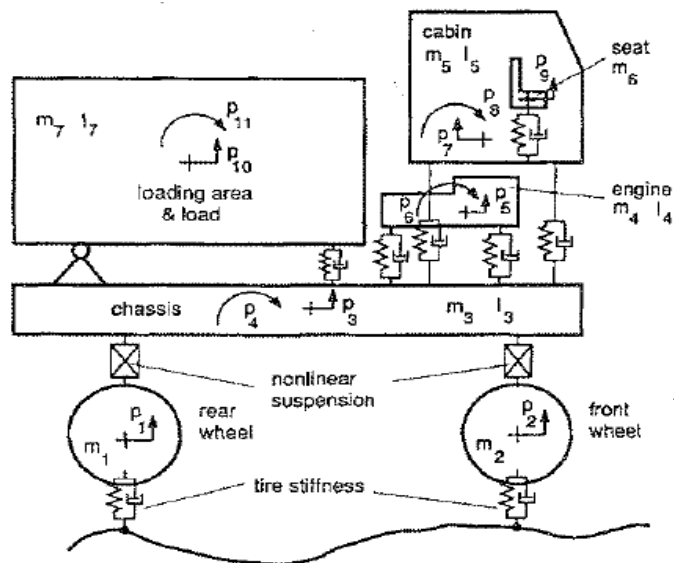


Figure 2.5.11. Vehicle Model by Simeon *et al.* (1994)

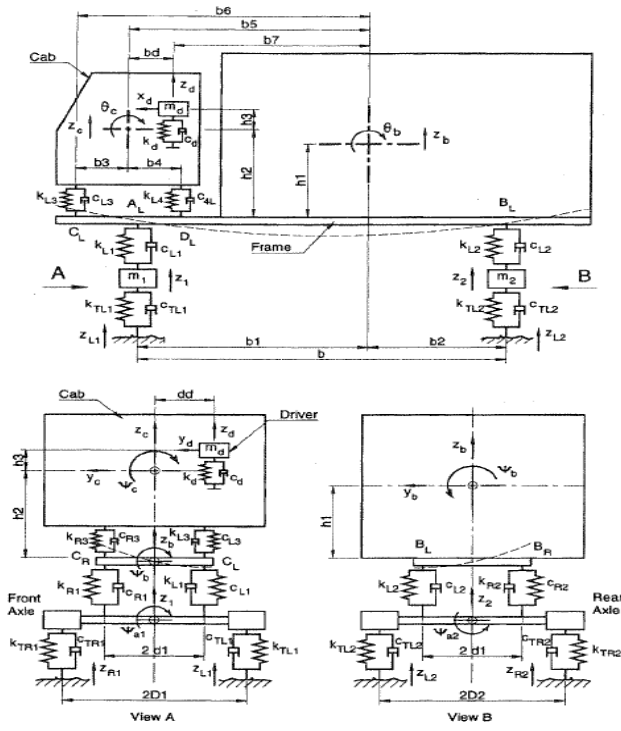


Figure 2.5.12. Vehicle Model by Ibrahim (2004)

## **CHAPTER 3. VEHICLE SELECTION AND CHARACTERIZATION**

### **3.1. General**

To study the dynamic interaction between a vehicle and bridge, the properties of both the truck and bridge must be known in as much detail as possible. This chapter first describes the selection of the test vehicle used in the shake table studies described in later chapters, and then the determination of the dynamic properties of the vehicle (mass, stiffness damping) used in modeling bridge-vehicle interaction. It will be seen that a shake table with six degrees-of-freedom was used to obtain the truck properties, rather than the more traditional approaches of mounting an eccentric mass shaker on the vehicle or driving the vehicle at various speeds across speed bumps to excite the vehicle in its several modes. Several numerical models were then developed to back-calculate the dynamic characteristics of the vehicle from the experimental data.

### **3.2. Vehicle Selection**

Selection of a representative vehicle was a challenging task. Care was taken to satisfy a number of constraints including a desired vehicle-to-bridge weight ratio, geometric scale effects, and budget.

#### **3.2.1. Background and Rationale**

The target vehicle used as a starting point for selection of the test vehicle was the H-20 truck (AASHTO, 2012), as shown in Figure 3.2.1. The H-20 truck is a two-axle vehicle weighing 40 k (8 k on the front axle and 32 k on the rear axle) with a 14 ft wheel base length. A two-axle vehicle was favored over a one with three or more axles due to the geometrical constraints. For a 2/5th-scale bridge model, the truck would ideally have a wheel base length of 5.6 ft, a width of 2.4 ft, and a weight of 6.4 k. Since such a vehicle was not readily available and would most likely have to be custom-built, the decision was made to ignore the similitude requirements and select a vehicle from commercially available trucks that had the closest match to the desired properties.

Previous studies have established that live load effects are maximized when the ratio of vehicle-to-bridge weight is high. A variety of vehicles were therefore examined, including commercial trucks and furniture-moving trucks, to find the heaviest vehicle for the shortest wheel base. The ideal vehicle was found to be the Ford F-550 truck. But since these trucks were only available on long term lease or purchase agreements and the decision was made to use F-250 trucks, which may be rented for short periods of time at reasonable rates. Budget considerations therefore led to the final selection of the F-250 as the test vehicle. It was delivered with a pre-fitted truck bed for additional payload.

Although the similitude requirements were not satisfied, the dynamic interaction effects of the chosen vehicle were believed to be similar to those of the target vehicle.

### **3.2.2. Basic Vehicle Data**

Basic data for the selected vehicle was obtained from the 2011 Ford Truck Source Book and are summarized in Table 3.2.1. The vehicle has an overall length of 247 in, an overall width of 68 in, a wheel base length of 156 in, and gross vehicle weight rating of 10 k. The weight of all six trucks (60 k) corresponds to approximately 19% of the weight of the bridge superstructure (320 k). A comparison of truck dimensions and weights compared to the scaled H-20 truck is given in Table 3.2.2. Dynamic properties of the truck are presented in subsequent sections.

## **3.3. Single Truck Experiment Setup**

As noted above, the vehicle tire and suspension properties were obtained from a sequence of shake table experiments in the Large-Scale Structures Laboratory. A six degree-of-freedom shake table was utilized to excite a specimen truck in each of the x-, y-, and z- directions in a controlled manner. After several logistical issues were resolved (described below), the test truck was lifted with cranes and placed on outrigger beams bolted to the table platen. The experiment setup and test protocol are presented in the following sections.

### **3.3.1. Outrigger Beam Design**

As previously mentioned, the F-250 truck has a wheel base length of 156 in (13 ft) and the six degree-of-freedom shake table measures 108 in (9 ft) in both directions. Two outrigger beams were therefore necessary to extend the table platen to support the truck. A W21x48 section was selected for each beam because it is the smallest rolled section with a web wide enough to support the truck tire when the beams are mounted on the table such that their webs are horizontal, i.e., loaded about their weak axis. The critical load case for the beam was a fully loaded truck balanced on the free end (unsupported portion) of the beam. Maximum allowable stress was taken at 50% of yield.

A series of holes was drilled through the beam webs to bolt the beams to the shake table. These holes were reinforced with pipe sections welded to the lower side of the web. Web stiffeners were also located where the beams pass over the edges of the table in case of extraordinary load concentrations due to impact effects during testing. Beam dimensions and details are shown in Figure 3.3.1.

### **3.3.2. Experiment Configuration**

The F-250 truck was tested with and without tires to determine the properties of the suspension system. Also, it was tested both empty and fully loaded with sand to determine the properties of the suspension for the two cases of loading. The combination of these cases gave a range of results to help identify the dynamic properties of the vehicle.

The suspension system of most trucks comprises two levels of springs and dampers. The first level is located between the axles and the ground where the tires provide significant flexibility and damping (for ease of discussion this is called the axle level). The second level is between the axles and the chassis where coils, leaf springs and shock absorbers provide flexibility and damping (for ease of discussion this is called the chassis level). As with many trucks, the rear springs of the F-250 truck are two-stage leaf springs with bilinear stiffness. To identify the contributions and properties of each level it was decided to test the truck in two configurations: first as a complete system and second with the tires removed. It was also tested both empty and fully-laden with 2.5 k of sand. Data from all four cases (with and without tires, with and without payload) were used to identify the properties of the numerical model of the truck.

### **3.3.3. Experiment Logistics**

An overhead crane and forklift were used to lift the truck onto the shake table using the lifting eyes at the front and back of the chassis as shown in Figures 3.3.2 and 3.3.3. When the truck was being tested with its tires, it was restrained from gross movements by loosely fitted chains that were threaded through the front-left and right-rear wheel rims just above the tire. The rims were protected by running the chain through a section of rubber hose. The chain was then bolted to the flanges of the outrigger beam. This restraining system is shown in Figure 3.3.4.

For the tests without tires, the wheels were removed and replaced with a set of second-hand rims. Angle brackets were welded to these rims and these brackets then bolted to the outrigger beams, providing effective restraining system for the rim (and axle) from any movement during testing, as shown in Figure 3.3.5.

As previously noted, sand was used to load the truck to its maximum rated capacity. Sand was chosen since the material was conveniently available and the loading/unloading process could be done in timely manner. Two large bags of sand were filled, weighed, and lifted into the bed of the truck as shown in Figure 3.3.6.

### **3.3.4. Experiment Protocol**

Table 3.3.1 presents the test protocol used to characterize the truck in each of four configurations: empty and loaded, with and without tires. As noted above, the purpose of these tests was to measure the dynamic response of the truck in each configuration from

which the stiffness and damping coefficients could be back-calculated for use in the numerical model. As seen in Table 3.3.1, this protocol included the following tests:

- Snap tests in the truck lateral (x- and y-) and vertical (z-) directions
- White noise tests in all three directions (30 s duration)
- Sine sweep tests (with frequencies ranging from 0.5 to 10 Hz) in all three directions
- Earthquake motion tests using the Sylmar record (1994 Northridge Earthquake)

With the exception of the earthquake motions, all tests were run at both low and high amplitudes of excitation. Different types of tests were carried out because it was not clear at the beginning which type of test would give the most reliable results for a MDOF specimen that likely has modal coupling due to non-classical damping, nonlinear springs and large displacements in some modes of vibration.

### **3.3.5. Instrumentation Plan**

The instrumentation for the truck was divided into two levels corresponding to the two layers of springs and dampers that make up the suspension system. The first level was the axle level, where the deformation is due to the tires alone and the second level was the chassis level, which the deformation is due to both the suspension system and the tires.

At the axle level, each of the tires had three accelerometers, for the x- (transverse), y- (longitudinal), and z- (vertical) directions, attached to the axle hub. In addition, a total of fourteen displacement transducers were used at this level: two in the z-direction for each tire, one in the y-direction for each tire, and three in the x-direction on the left side of the truck. Figure 3.3.7 shows the layout of the truck instrumentation at the axle level.

At the chassis level, three accelerometers were attached to the chassis above each wheel, in the x-, y, and z-directions. Fewer displacement measurement points were required on the chassis than at the axle level, since the chassis was expected to act as a rigid body. Eight displacement transducers were therefore used at the chassis level, four in the z-direction, two in the y-direction, and two in the x-direction. Figure 3.3.8 shows the layout of the truck instrumentation at the chassis level. Figure 3.3.4 also depicts a close-up view of the instrumentation cluster on the right-rear axle hub.

## **3.4. Numerical Models**

Two models were constructed of the truck using different levels of complexity: single-axle and two-axle models. For the single axle models, two models were developed, one for the front of the truck and another for the rear. Each single-axle model could be oriented in the transverse (x-), longitudinal (y-), and vertical (z-) directions depending on

the axis under consideration. In addition, each of these models was developed to accommodate the two configurations, with and without tires, to assist in identifying tire and suspension system properties. The two-axle model was a full 3-dimensional model (with x-, y-, and z- axes) and was used to analyze the properties in the two cases with and without tires. Figure 3.4.1 illustrates the family of models used to characterize the properties of the truck from the experimental data.

### **3.4.1. Single-Axle Model**

Two single-axle models were developed, one for the front and one for the rear of the truck. Each comprised an axle, a pair of tires (if included), a suspension system (coils in front, leaf springs in rear), and a tributary portion of the chassis weight and payload. As shown in Figure 3.4.2, each model was a 2 degree-of-freedom system and was analyzed independently of the other. A MATLAB routine was developed for this purpose to determine values for stiffness and damping from experimental test data.

The mass was separated into two levels: the axle level mass, which contains the weight of the axle and tires, and the chassis level mass, which contains the remainder of the truck's weight, including the payload for the fully-laden truck case. The weight of the empty truck carried by the front and rear axles for the model were taken from the 2011 Ford Truck Source Book. The loaded truck weight for the model was then calculated from the known empty truck weights plus a uniformly distributed load of 2,300 lb in the bed of the truck, which is the maximum allowable payload as determined from the specifications. The mass at the axle level was approximated by taking each the front and rear axle weights and adding the weight of the tires and rims. The final mass at the chassis level is the total empty (or loaded) truck weight subtracted by the weight from the axle level. The weight distributions used for the numerical model can be found in Table 3.4.1.

### **3.4.2. Two-Axle Model**

This 3-dimensional model was based on the model developed by Kim *et al.* (2005) and has individual elements for each spring and damper in the suspension and tire levels. The total number of degrees-of-freedom in this model is sixteen. For implementation in commercially-available structural analysis software such as SAP2000, these elements were modeled as linear link elements.

The chassis was modeled with seven nodes arranged in an "I" shape that were interconnected using body constraints so that various points on the chassis move in relation to each other. The front and rear axles were each also connected along their length with separate body constraints and the axles were linked to the chassis with an equal constraint for rotation about the x-axis (transversely). This allowed the truck model to pitch forward and backward but constrained the axle rotations to zero. This model was then used to analyze the same snap motions as the single-axle model in the z-direction, as well as other motions, in order to verify the results. Axle and chassis mass were calculated in the same manner as the single-axle models described in Section 3.4.1.

### 3.5. Truck Properties in Vertical Direction

Of the four different types of tests used to excite the truck listed above, data gathered from the white noise and sine sweep tests were inconclusive whereas the snap test results were found to be the most useful. Data from tests were therefore used to obtain the properties (stiffness and damping) of the suspension system and tires as discussed below.

#### 3.5.1. Application of Snap Test Data to Determine Truck Properties

In the snap tests, the table was “snapped” or “quick-released” from an initial position in up/down, left/right, or front/back directions several times incrementally from smaller to larger offsets to excite the truck in free vibration to higher amplitudes. The resulting history of truck displacement was used to back-calculate effective stiffness and damping properties in the direction the truck was snapped. However, the requirement of free vibration was not achievable since the table could not be released fast enough to allow unrestricted vibration. Therefore, the actual table motion was included in the derivation of the truck properties as noted below.

Each snap test run that resulted in at least one full cycle of truck movement was used in the model calibration. In the vertical direction, a full cycle of motion occurred when the truck displaced up, down, and back up again (or vice versa) and crossed the initial position of the truck twice after it started moving. This snap test run was assigned a letter value (A, B, C, *etc.*) and used to process data. During testing, it was observed that the motion of the truck damped out very quickly. Due to this high level of damping, the displacement history in the first cycle of motion was considered to be the most reliable and was used for the characterization of the truck’s properties. The values of time and displacement for the maximum chassis vertical displacement, the minimum chassis vertical displacement, and the horizontal axis crossing points (when the truck was back at its initial position), were used as input for the MATLAB routine.

As previously mentioned, although high performance actuators are used to drive the shake table, it was not possible to have an instantaneous release or snap in the table motion, and the finite time taken to achieve a snap of a specified value was included in the analysis of truck response. Figure 3.5.1 shows an example of table response to a snap of 0.34 in. It is seen that at 0.5 s, the table displacement is only about 75% of the target value. This ‘lag’ was included in the input motion to the analytical model as well as in the determination of truck response from measured data. This was particularly important in view of the heavy damping present in truck suspension systems. For example, Figure 3.5.2 shows the truck motion in this snap has damped out almost completely even though the table is still moving. Thus, the equation of motion for the SDOF system in this case becomes:

$$m\ddot{u} + c\dot{u} + ku = \square c\dot{u}_g \square ku_g \quad (3.5.1)$$

where:

$u_g$  = ground (table) displacement (in)

$\dot{u}_g$  = ground (table) velocity (in/s)

For analytical purposes, the table displacement history was approximated to be given by:

$$u_g = 2 \tan^{-1} \left[ \frac{-2h(t+1)}{t(t+2)(\pi+1)} \right] u_{go} \quad (3.5.2)$$

where:

$t$  = time (s)

$u_{go}$  = maximum table displacement or table offset (in)

$h$  = coefficient determined by curve fitting to experimental data

Figure 3.5.1 shows good agreement between experimental response and that given by Equation 3.5.2 for table displacement during snap B ( $u_{go} = 0.34$  in and  $h = 0.185$  in/sec). The values of  $u_{go}$  and  $h$  used in Equation 3.5.2, differ for each snap test. The single axle model was then subjected to this ground motion and the resulting chassis and axle displacement, relative to the table, were computed.

The MATLAB routine was utilized to sweep through combinations of values for the suspension stiffness and damping coefficient and the set of values with the best match for time and displacement in the first cycle of motion was determined.

A criterion of “best match” was determined by minimizing the error between the experimental and analytical displacements in three different ways: (1) SRSS method, (2) modified SRSS method, and (3) percent delta method. The SRSS method computed the error by comparing the square root of the sum of the squared differences between the experimental and numerical values. The modified SRSS method took the square root of the sum of the squared differences between the two time values for the x-axis crossing points and the sum of the squared difference between the displacement values for the maximum and minimum displacements of the truck chassis. This was done in order to focus on matching the maximum and minimum displacement values as closely as possible without considering the time at which they occurred. The time of the zero crossing points still gave the model some time boundaries to match. Since the displacement values are so small in comparison with the time values, the numerical model results from both the SRSS and modified SRSS methods give properties that favored matching the time values over the displacement values. To counter this, the percent delta method was also introduced. This involved taking the error between the

experiment and the numerical model as a percentage of the experimental values and summing the time and displacement errors.

### **3.5.2. Truck Vertical Properties without Tires**

The first model to be characterized was the truck without tires, both empty and loaded. This was the simplest model to be studied since it only involved one degree-of-freedom and allowed the suspension system to be isolated from the tires. The results from the two cases are given below.

#### **3.5.2.1. Empty Truck**

The empty truck without tires was snapped four times, Snaps A through D. Table 3.5.1 summarizes the results for the suspension system stiffness and equivalent viscous damping ratios for the front and rear of the truck determined using the three methods previously described. The properties obtained for each snap motion using these methods were averaged and the values from different snap motions averaged to obtain a final value for the suspension system stiffness and damping.

The values for the damping ratio for the front and rear axles are similar, which was expected in order to balance the ride of the truck. According to the 2011 Ford Truck Source Book, the stiffness values for the front suspension and the first stage of the rear leaf suspension are 0.469 k/in and 0.324 k/in, respectively. The final truck properties given in Table 3.5.1 (0.405 and 0.306 k/in resp.) differ from the Source Book properties by 13.7% for the front and 5.5% for the rear. The Source Book does not give damping ratios.

#### **3.5.2.2. Fully-Laden Truck**

The loaded truck without tires was snapped seven times, Snaps A through G. Table 3.5.2 summarizes the results for the suspension system stiffness and equivalent viscous damping ratios for the front and rear of the truck determined using the three methods previously described. The properties obtained for each snap motion using these methods were averaged and the values from different snap motions averaged to obtain a final value for the suspension system stiffness and damping.

The damping ratio increased with the added load but remained under 20% for both the front and rear, with a higher amount in the front. The 2011 Ford Truck Source Book gives values for the rear suspension system stiffness of 0.782 k/in for the second stage of the rear leaf spring, while the front remains as for the empty truck because it is a coil spring with a linear stiffness. The final truck properties given in Table 3.5.2 (0.459 and 0.718 k/in resp.) differ from the Source Book properties by 2.1% for the front and 8.1% for the rear. The Source Book does not give damping ratios.

### **3.5.3. Truck Vertical Properties with Tires**

Snap testing was not implemented in the experiment protocol until the second day of testing. As a result, the only case with tires for which the data is available is for the fully-laden truck case. In order to analyze the full truck with tires, the two degree-of-freedom single axle model was used. The suspension system properties for this model were taken from the case without tires (Section 3.3.2) and this model was used to find the vertical stiffness and damping coefficient values for the tires.

Data from six complete snap cycles for the fully-laden truck with tires were recorded. These are labeled Snaps A through F in Table 3.5.3 which summarizes the vertical stiffness determined from each case as well as the average value of 3.46 k/in from the results of all snap motion runs. The average values were used for the two-axle model analysis. The data for the tire stiffness obtained from the model was more varied than the suspension system results due to modeling the tire as a linear element when it most likely has a nonlinear but elastic stiffness.

The experimental data show two distinct maximum or minimum values in the first half cycle of the snap motion for the truck axles. The single-axle model was able to produce a double maximum or minimum, but the two values from the numerical model were not as pronounced as those in the experimental data. When the final averaged tire vertical stiffness value was used in the single-axle model, the model did not produce two distinct maximum or minimum values in the first half cycle of motion. However, the more rigorous two-axle model showed a double maximum or minimum value for the model in the vertical direction, but the second value was much smaller than the experimental data value in most cases. These are illustrated in Figure 3.5.3.

## **3.6. Truck Properties in Longitudinal and Transverse Directions**

The snap motion tests were also carried out in the transverse (x) and longitudinal (y) directions in addition to the vertical direction. The displacement data from the lateral snaps without tires show the truck suspension system to be very stiff in the transverse and longitudinal directions. This is to be expected since vehicle suspension systems are designed to be almost rigid in these directions to permit high speed cornering and rapid braking. Consequently the suspension system was taken to be infinitely stiff in the lateral directions compared to the vertical stiffness. Because the shock absorbers are mounted essentially on a vertical axis and very little damping was observed during testing, the damping of the truck suspension system was taken to be zero in these directions.

Since the suspension system was stiff in both lateral directions, any movement in the lateral directions during testing was caused by the tires compressing, stretching, or slipping. The two degree-of-freedom single-axle model did not produce stable results for stiffness in these directions, and the two-axle model was used instead to determine the tire stiffness properties. The same method for identifying the ‘best match’ by computing the error between the experiment and the model as previously discussed, was also used in the lateral directions (i.e., SRSS, modified SRSS, and percent difference methods).

### **3.6.1. Truck Properties in Transverse Direction**

The experimental snap data for the transverse (x) direction showed two distinct maxima or minima similar to the vertical axle experimental snap data. However, as opposed to the vertical case, the transverse double maximum or minimum values occurred within the second half-cycle of motion, and can be seen in both the axle and the chassis displacements on the front half of the truck, as shown in Figure 3.6.1. The two-axle model could recreate this same motion when snapped in the transverse direction, but only with very high values for the tire stiffness in that direction (values above 3.5 k/in). Higher stiffness values, however, led to lower maximum and minimum values than the experimental data and as a result, the stiffness values with the best fit curves to the experimental data were too low to create a double maximum or minimum. Final values for transverse (x) stiffness are given in Table 3.5.4.

### **3.6.2. Truck Properties in Longitudinal Direction**

Only three snap motion runs were available to determine truck properties in the longitudinal direction. Snaps in the longitudinal direction showed high displacements when compared with the displacements in the transverse and vertical directions. As a result, tire stiffness in the longitudinal direction was lower than corresponding values, which was not expected. This could be due to the tires slipping on the steel outrigger beams, which could be heard during testing. The truck also experienced residual displacement during the earthquake motions, which can be seen in Figure 3.6.2.

As with the vertical properties for the tires, the lateral stiffness values varied between snaps due to the nonlinearity of the tire stiffness. Final values for the longitudinal (y) stiffness are given in Table 3.5.5.

## **3.7. Vehicle Response during Earthquake Excitation**

As noted above, three (or four) levels of the Sylmar ground motion recorded during the 1994 Northridge Earthquake were used to excite the test truck. The 90° and the 360° components were applied in the longitudinal and transverse directions of the truck, respectively. No vertical component was applied. This is the same motion as that used for the bridge-vehicle experiment described in Chapter 4. Testing started at 25% of the recorded Sylmar motion and was increased in 25% increments to 75% Sylmar for the truck with tires, and 100% Sylmar for the truck without tires. The lower limit for the truck with tires was imposed to avoid the possibility of damaging the tires and rims.

### **3.7.1. Observed Vehicle Response**

Tables 3.7.1 and 3.7.2 give comparisons of the truck maxima and minima for accelerations and displacements against the table maxima and minima for the fully-laden

truck with tires. It is important to note that these maxima and minima do not necessarily occur for the truck and table at the same time, as can be seen in the plots of truck vs. table motion, an example of which is shown in Figure 3.7.1. The vehicle responses during earthquake excitations are discussed below.

#### 3.7.1.1. Vertical Direction

Truck-to-table ratios in the vertical direction have been omitted from the above tables because the vertical component of the table motion was zero. However, the truck vertical maxima and minima accelerations and displacements are shown in these tables since they are quite significant despite the absence of vertical table motion.

The accelerations at the rear of the empty truck are much larger than the accelerations at the front of the empty truck, both with and without tires. However, when the truck is loaded, the accelerations are much closer in value between the front and rear. This is due to a more equal weight distribution between the front and rear when the bed is loaded. The displacements of the truck in the vertical direction show greater values in the positive direction (when the truck moves up) than the negative direction (when the truck moves down) at the axle level. Bottoming-out (or maximum compression) of the suspension in the downward direction was not observed.

#### 3.7.1.2. Transverse and Longitudinal Directions

In the transverse (x) direction, the accelerations of the truck at the chassis level are smaller than the table accelerations when the truck is empty but greater than the table accelerations at the chassis level when the truck is full, both with and without tires.

The empty truck without tires had higher accelerations than the table in the longitudinal (y) direction and lower displacements than the table. However, when loaded, the truck without tires had accelerations very close to the table accelerations in the same direction. Loading the truck and compressing the rear leaf springs appear to stabilize the suspension system to a certain degree in the longitudinal direction of the truck. It is also possible that the earthquake motions excite a particular mode in the longitudinal direction when the truck is empty that would depend on the characteristics of the response spectrum for the Sylmar record. When tires are added to the system, there is little variation between the empty and loaded truck longitudinal accelerations or displacements maximum truck-to-table ratios. This indicates that the tires dominate system performance in the longitudinal direction.

Both lateral (longitudinal and transverse) directions show smaller displacements than the table when the truck has no tires, due to the rims being bolted to the steel beams and the very high stiffness of the suspension system in the lateral direction. However, once tires are added to the vehicle, the transverse (x) direction has displacement values greater than those of the table. The longitudinal (y) direction has greater displacement values than the table in one direction, but slightly lower displacement values than the table in the other direction. This could be due the truck sliding and reaching the boundaries of its restraints. The increased displacements in both directions show

flexibility in the lateral direction due to the tires that is not present when tires are removed and the stiff suspension system controls the truck motions.

### 3.7.1.3. Empty and Fully-Laden Trucks

Both the empty and fully-laden trucks show a greater truck-to-table acceleration ratios in the transverse (x) direction with tires than without. The front of the truck shows a large amplification in this direction, in most cases more than three times the ratio of the case without tires. This is most likely due to the front coil springs having more flexibility than the rear leaf springs and therefore adding to the truck's overall flexibility in the front. The longitudinal (y) direction shows a decrease in accelerations from the case without tires to the case with tires in all directions for the empty truck except the rear in the positive direction. This is due to the truck's ability to slide on its tires, decreasing the accelerations caused from the fixed base of the rims. The truck most likely slid to the end of the chain restraint in the positive direction, causing a higher value for these accelerations in certain cases. The full truck shows very similar acceleration ratios for both cases (with and without tires) in the longitudinal direction for the front, and a slight increase in the truck-to-table acceleration ratio in the rear with tires. This shows the added stiffness and stability of the truck system when loaded, as well as the added friction between the tires and table platen from the extra weight that prevents the truck from sliding as much as when it is empty.

The displacement ratios in the transverse (x) direction are all greater than one with tires and less than one without tires, for both the empty and fully-laden truck cases, showing the truck's ability to slide on its tires. The rear displacement ratio of the empty truck, with tires is less than one, indicating that the tire either hit the wall of the beam or engaged the chain restraint in that particular direction. The longitudinal (y) direction for both the empty and loaded truck with tires is less than one in the positive direction (when the truck moves forward) and greater than one in the negative direction, indicating the truck slid backwards for both scenarios. The empty truck without tires has a longitudinal displacement ratio close to 1.0, while the full truck without tires has very small displacement ratios in the longitudinal direction (approximately 0.03 to 0.1).

### 3.7.2. Comparison of Numerical Model and Observed Responses

Once the suspension system and tire properties had been identified for the truck model (as discussed in Sections 3.5 and 3.6), the two-axle model was used to calculate the theoretical response to the earthquake motions used in the single truck experiment for all four cases (empty with tires, empty without tires, fully-laden with tires, fully-laden without tires).

Comparisons of the maximum accelerations and displacements at the chassis level show that the numerical model is better at predicting the behavior of the fully-laden truck over the empty truck, both with and without tires. The model is slightly better at predicting the fully-laden truck chassis displacement than the empty truck chassis displacements with tires, but significantly better at predicting the fully-laden truck chassis

displacements than the empty truck chassis displacements without tires. The model is also able to more accurately predict the fully-laden truck chassis accelerations over the empty truck chassis accelerations for both with and without tires. However, the model is better at predicting the accelerations of the empty truck at the axle level over the accelerations of the fully-laden truck at the axle level.

The model is able to capture the accelerations of the chassis without tires better than with tires, for both the empty and loaded truck. It can also be seen that the model is better at matching the front displacements of the empty truck than the rear displacements of the empty truck, but there is no distinguishable difference in how close the front and rear of the full model are matched to the experimental data.

The truck without tires has a better correlation between the vertical (z) accelerations than the truck with tires for both the empty and fully-laden truck. It was also noted that the truck model with tires was able to match the experimental accelerations fairly closely in the rear longitudinal direction for both the empty and fully-laden cases. The model is not so effective at matching the transverse (x) acceleration data; it tends to overestimate the accelerations in that direction, possibly because the truck model is a simplified version that does not permit tire slippage on the table. The model has less error when predicting the maximum values for the axle displacements overall than the chassis displacements, for both the empty and fully-laden truck.

### **3.8. Modal Properties of Truck**

Summaries of the truck properties are given in Tables 3.8.1A and 3.8.1B for the empty and fully-laden cases, respectively. Applying these properties to the two-axle model, the modal properties of the vehicle can be calculated. Modal periods and mass participation factors are summarized in Table 3.8.2. Due to the flexibility and constraints of the truck's suspension and tires, the main modes of vibration of the truck are mostly rotational modes with small amounts of translational movement (except for the vertical mode where large vertical movements are seen). The corresponding mode shapes for the first 6 modes are shown in Figures 3.8.1 through 3.8.6.

The first mode is a pitching mode about the x-axis with some longitudinal translation. The second mode is mainly a vertical translation mode with some slight pitching. The third mode is a rolling mode about the y-axis with transverse translation. The fourth mode has longitudinal translation with some pitching, mainly at the axle level. The fifth mode is a yawing mode about the vertical centerline of the truck. Last, the sixth mode is a transverse mode with a very small amount of roll and yaw.

### **3.9. Summary**

Data from a series of shake table experiments on a single vehicle has been presented and used to characterize the dynamic properties of the subject vehicle (stiffness and damping). The vehicle, a Ford F-250, is used in the shake table studies of live load

effects on seismic response described in the next chapter. The methodology for deriving the properties of the vehicle has been described and the results presented. In addition, a numerical model of the vehicle that is to be used in the analytical study of live load effects on seismic response has been validated.

**Table 3.2.1. Ford F-250 Dimensions and Weights**

<b>Parameter</b>	<b>Value</b>
Overall Length (in)	247
Overall Width (in)	68
Overall Height (in)	80
Wheel Base Length (in)	156
Ground Clearance (in)	7.9
Curb Weight (k)	6.7
Gross Vehicle Weight Rating (k)	10.0
Maximum Allowable Payload (k)	2.3

**Table 3.2.2. Comparison of Fully-Laden Properties of H-20, scaled-H-20, and Ford F-250 Vehicles**

<b>Parameter</b>	<b>H-20</b>	<b>H-20 0.4-scale</b>	<b>F-250</b>
Gross Weight (k)	40.0	6.4	10.0
Wheelbase (in)	168	67.2	156
Width (in)	72	28.8	68

**Table 3.3.1. Experiment Protocol for Vehicle Characterization**

<b>Run</b>	<b>Test Type</b>	<b>Direction</b>	<b>Level</b>	<b>PGA</b>	<b>Other</b>
1	Snap	Y	-	-	-
2	Snap	X	-	-	-
3	Snap	Z	-	-	-
4	White Noise	Y	Low Amp.	0.025 g	30 s
5	White Noise	Y	High Amp.	0.050 g	30 s
6	White Noise	Z	Low Amp.	0.075 g	30 s
7	White Noise	Z	High Amp.	0.100 g	30 s
8	White Noise	X	Low Amp.	0.050 g	30 s
9	White Noise	X	High Amp.	0.075 g	30 s
10	Sine Sweep	Y	Low Amp.	0.025 g	0.5-10 Hz
11	Sine Sweep	Y	High Amp.	0.050 g	0.5-10 Hz
12	Sine Sweep	Z	Low Amp.	0.075 g	0.5-10 Hz
13	Sine Sweep	Z	High Amp.	0.100 g	0.5-10 Hz
14	Sine Sweep	X	Low Amp.	0.050 g	0.5-10 Hz
15	Sine Sweep	X	High Amp.	0.075 g	0.5-10 Hz
16	EQ: 25% Sylmar	-	-	-	-
17	EQ: 50% Sylmar	-	-	-	-
18	EQ: 75% Sylmar	-	-	-	-
19	EQ: 100% Sylmar*	-	-	-	-
20	White Noise	Y	High Amp.	0.050 g	30 s
21	White Noise	Z	High Amp.	0.100 g	30 s
22	White Noise	X	High Amp.	0.075 g	30 s

Note: \*Only for truck without tires.

**Table 3.4.1. Weight Distribution in Numerical Model**

	Empty Truck	Full Truck
Front Chassis Weight (k)	3.693	3.673
Front Axle Weight (k)	0.635	0.635
Total Front weight (k)	4.328	4.308
Rear Chassis Weight (k)	2.52	5.237
Rear Axle Weight (k)	0.455	0.455
Total Rear Weight (k)	2.975	5.692
Total Weight (k)	7.303	10.000

**Table 3.5.1. Empty Truck without Tires Vertical Snap Test Analysis Summary**

Average of	Front			Rear		
	k (k/in)	c (k.s/in)	$\zeta$ (%)	k (k/in)	c (k.s/in)	$\zeta$ (%)
All Snaps	0.405	0.017	10.7	0.306	0.014	11.8
Snap A	0.420	0.018	10.2	0.288	0.014	11.8
Snap B	0.398	0.020	11.5	0.287	0.016	12.8
Snap C	0.383	0.018	10.5	0.275	0.014	11.8
Snap D	0.417	0.013	10.7	0.375	0.011	10.7
SRSS Method	0.408	0.017	9.8	0.287	0.013	10.8
SRSSm Method	0.397	0.017	10.6	0.311	0.013	11.5
Avg $\Delta$ Method	0.409	0.019	11.8	0.321	0.015	13.1

Note: Values are for each suspension component.

**Table 3.5.2. Full Truck without Tires Vertical Snap Test Analysis Summary**

Average of	Front			Rear		
	k (k/in)	c (k.s/in)	$\zeta$ (%)	k (k/in)	c (k.s/in)	$\zeta$
All Snaps	0.459	0.037	17.5	0.718	0.041	13.9
Snap A	0.488	0.035	16.8	0.763	0.043	14.5
Snap B	0.482	0.030	14.7	0.713	0.038	13.0
Snap C	0.312	0.039	19.7	0.752	0.048	16.0
Snap D	0.500	0.035	16.7	0.678	0.032	11.3
Snap E	0.460	0.040	19.5	0.667	0.047	16.7
Snap F	0.495	0.038	18.0	0.688	0.035	12.2
Snap G	0.477	0.042	17.3	0.767	0.048	13.7
SRSS Method	0.494	0.041	19.4	0.711	0.039	13.4
SRSSm Method	0.434	0.031	15.6	0.696	0.039	13.4
Avg $\Delta$ Method	0.449	0.039	17.5	0.747	0.047	14.9

Note: Values are for each suspension system cot.

**Table 3.5.3. Fully-Laden Truck with Tires Vertical Snap Test Analysis Summary**

Average of	Front Tire			Rear Tire		
	k (k/in)	c (k.s/in)	$\zeta$ (%)	k (k/in)	c (k.s/in)	$\zeta$ (%)
All Snaps	3.137	0.000	0.0	3.781	0.000	0.0
Snap A	3.173	0.000	0.0	4.448	0.000	0.0
Snap B	3.153	0.000	0.0	4.525	0.000	0.0
Snap C	3.128	0.000	0.0	3.428	0.000	0.0
Snap D	3.255	0.000	0.0	2.867	0.000	0.0
Snap E	3.050	0.000	0.0	3.823	0.000	0.0
Snap F	3.060	0.000	0.0	3.597	0.000	0.0
SRSS Method	3.088	0.000	0.0	4.107	0.000	0.0
SRSSm Method	3.059	0.000	0.0	4.018	0.000	0.0
Avg $\Delta$ Method	3.263	0.000	0.0	3.160	0.000	0.0
Total Average	3.460	0.000	0.0	-	-	-

Note: Values are for each suspension component.

**Table 3.5.4. Transverse Snap Test Analysis Summary**

Average of	Front Tire Stiffness (k/in)			Rear Tire Stiffness (k/in)		
	$k_{SSRS}$	$k_{\% \Delta}$	$k_{SRSSm}$	$k_{SSRS}$	$k_{\% \Delta}$	$k_{SRSSm}$
Snap B	0.90	3.00	1.70	1.10	3.00	1.25
Snap C	0.90	2.25	1.75	0.80	1.90	1.90
Snap D	0.90	2.25	1.60	1.00	-	1.90
Snap E	0.90	1.60	1.60	1.20	3.10	2.30
Snap G	0.90	2.25	1.75	1.20	2.50	1.75
All Snaps	0.90	2.27	1.68	1.06	2.63	1.82
SRSS Method	0.98					
Avg $\Delta$ Method	2.45					
Avg SRSS Modified	1.75					
Total Average	1.73					

**Table 3.5.5. Longitudinal Snap Test Analysis Summary**

Average of	Front Tire Stiffness (k/in)		
	$k_{SSRS}$	$k_{\% \Delta}$	$k_{SRSSm}$
Snap A	0.50	0.60	0.60
Snap B	0.50	0.60	0.60
Snap C	0.50	0.50	0.60
All Snaps	0.50	0.57	0.60
Total Average	0.56		

**Table 3.7.1. Truck and Table Maximum Accelerations in Positive Direction for Fully-Laden Truck with Tires**

		25% Sylmar		50% Sylmar		75% Sylmar	
		Front	Rear	Front	Rear	Front	Rear
<b>Vertical</b>	Axle Acc. (g)	0.128	0.333	0.251	0.619	0.375	0.870
	Chassis Acc. (g)	0.027	0.143	0.052	0.286	0.075	0.428
<b>Transverse</b>	Axle Acc. (g)	0.466	0.012	0.824	0.023	1.210	0.035
	Chassis Acc. (g)	0.465	0.232	0.821	0.442	1.218	0.640
	Table Acc. (g)	0.115		0.240		0.355	
Max Truck/Table Ratio	Axle	4.041	0.103	3.429	0.097	3.412	0.099
	Chassis	4.037	2.009	3.415	1.840	3.436	1.804
<b>Longitudnl</b>	Axle Acc. (g)	0.234	0.465	0.433	0.821	0.611	1.218
	Chassis Acc. (g)	0.223	0.466	0.432	0.824	0.637	1.210
	Table Acc. (g)	0.222		0.420		0.636	
Max Truck/Table Ratio	Axle	1.054	2.094	1.029	1.953	0.961	1.916
	Chassis	1.005	2.096	1.029	1.961	1.001	1.903

Note: 1. Positive when truck moves upward or forward  
 2. Maxima do not necessarily occur at the same time

**Table 3.7.2. Truck and Table Maximum Displacements in Positive Direction for Fully-Laden Truck with Tires**

		25% Sylmar		50% Sylmar		75% Sylmar	
		Front	Rear	Front	Rear	Front	Rear
<b>Vertical</b>	Axle Disp. (in)	0.249	0.145	0.674	0.350	1.197	1.063
	Chassis Disp. (in)	0.922	0.754	1.644	1.075	2.146	1.384
<b>Transverse</b>	Axle Disp. (in)	0.548		1.181		1.921	
	Chassis Disp. (in)	0.456	0.379	0.995	0.707	1.432	1.434
	Table Disp. (in)	0.296		0.562		0.823	
Max Truck/Table Ratio	Axle	1.851		2.101		2.335	
	Chassis	1.541	1.280	1.770	1.258	1.741	1.744
<b>Longitudnl</b>	Axle Disp. (in)	1.176		2.010		4.030	
	Chassis Disp. (in)	1.399		2.319		4.240	
	Table Disp. (in)	1.692		3.377		5.028	
Max Truck/Table Ratio	Axle	0.695		0.595		0.801	
	Chassis	0.827		0.687		0.843	

Note: 1. Positive when truck moves upward or forward  
 2. Maxima do not necessarily occur at the same time

**Table 3.8.1. Summary of Vehicle Properties**

A. Empty Vehicle

		<b>Suspension Level</b>			<b>Tire Level</b>		
	Direction	Stiffness (k/in)	Damping Coefficient (k.s/in)	Damping Ratio (%)	Stiffness (k/in)	Damping Coefficient (k.s/in)	Damping Ratio (%)
Front	Vertical	0.405	0.017	13.63	3.48	0.000	0.00
	Transverse	1000	0.000	0.00	1.73	0.000	0.00
	Longitudinal	1000	0.000	0.00	0.56	0.000	0.00
Rear	Vertical	0.306	0.014	15.70	3.48	0.000	0.00
	Transverse	1000	0.000	0.00	1.73	0.000	0.00
	Longitudinal	1000	0.000	0.00	0.56	0.000	0.00

B. Fully-Laden Vehicle

		<b>Suspension Level</b>			<b>Tire Level</b>		
	Direction	Stiffness (k/in)	Damping Coefficient (k.s/in)	Damping Ratio (%)	Stiffness (k/in)	Damping Coefficient (k.s/in)	Damping Ratio (%)
Front	Vertical	0.459	0.037	25.92	3.48	0.000	0.00
	Transverse	1000	0.000	0.00	1.73	0.000	0.00
	Longitudinal	1000	0.000	0.00	0.56	0.000	0.00
Rear	Vertical	0.718	0.041	19.89	3.48	0.000	0.00
	Transverse	1000	0.000	0.00	1.73	0.000	0.00
	Longitudinal	1000	0.000	0.00	0.56	0.000	0.00

**Table 3.8.2. Vehicle Modal Periods and Mass Participation Factors from Numerical Model**

Mode	Period (s)	$U_x$	$U_y$	$U_z$	$\Sigma U_x$	$\Sigma U_y$	$\Sigma U_z$	$R_x$	$R_y$	$R_z$	$\Sigma R_x$	$\Sigma R_y$	$\Sigma R_z$
1	0.788	0	0.597	0.045	0	0.597	0.045	0.710	0.000	0.000	0.710	0.000	0.000
2	0.641	0	0.082	0.837	0	0.679	0.882	0.028	0.000	0.000	0.738	0.000	0.000
3	0.609	0.487	0	0	0.487	0.679	0.882	0.000	0.947	0.100	0.738	0.947	0.100
4	0.508	0	0.321	0.03	0.487	1	0.912	0.186	0.000	0.000	0.924	0.947	0.100
5	0.384	0.036	0	0	0.523	1	0.912	0.000	0.013	0.848	0.924	0.959	0.948
6	0.298	0.475	0	0	0.998	1	0.912	0.000	0.007	0.051	0.924	0.966	0.998
7	0.090	0	0	0.054	0.998	1	0.966	0.047	0	0	0.970	0.966	0.998
8	0.074	0	0	0.034	0.998	1	1	0.030	0	0	1	0.966	0.998
9	0.062	0.001	0	0	0.999	1	1	0	0.021	0.0009	1	0.987	0.999
10	0.051	0.001	0	0	1	1	1	0	0.013	0.0006	1	1	1
11	0.0017	0	0	0	1	1	1	0	0	0	1	1	1
12	0.0016	0	0	0	1	1	1	0	0	0	1	1	1
13	0.0015	0	0	0	1	1	1	0	0	0	1	1	1
14	0.0015	0	0	0	1	1	1	0	0	0	1	1	1
15	0.0013	0	0	0	1	1	1	0	0	0	1	1	1
16	0.0011	0	0	0	1	1	1	0	0	0	1	1	1

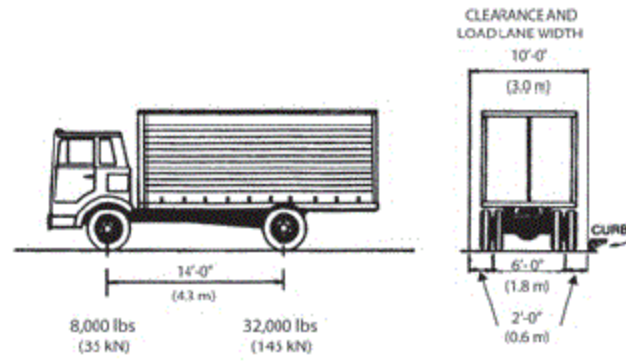


**Figure 3.2.1. AASHTO H-20 Truck (AASHTO, 2012)**



**Figure 3.2.2. Ford F-250**

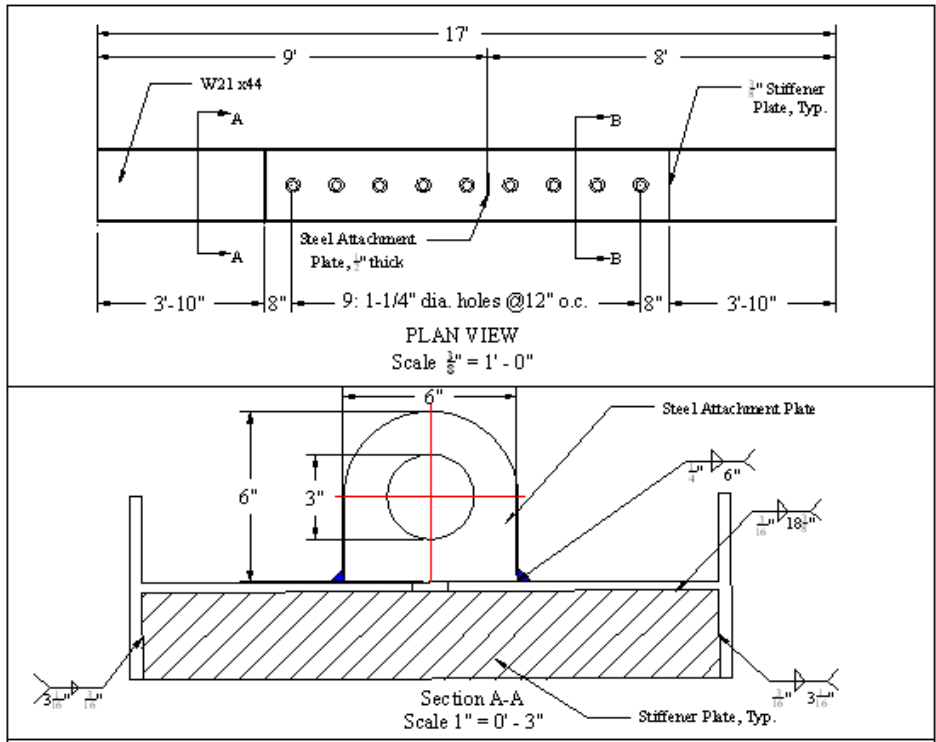


Figure 3.3.1. Outrigger Beam Details

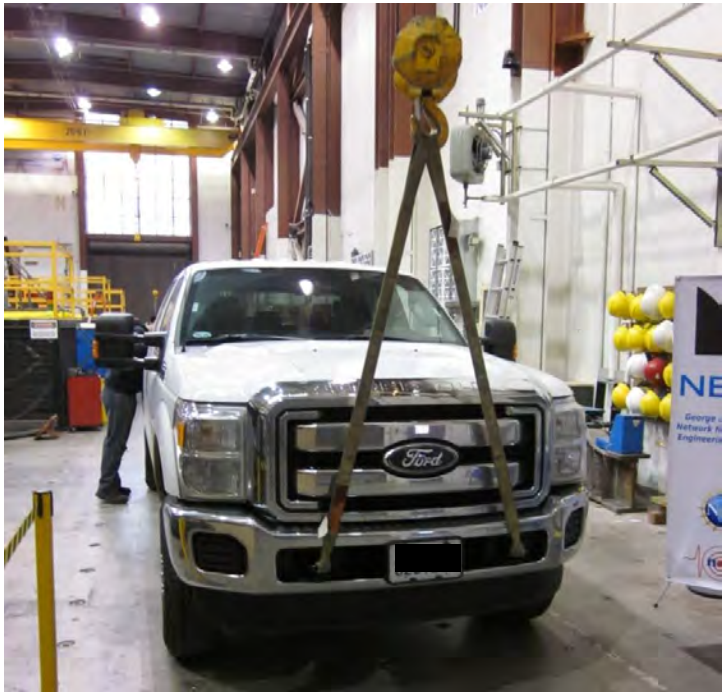


Figure 3.3.2. Lifting Truck at Front with Overhead Crane



**Figure 3.3.3. Truck Placement on Shake Table**



**Figure 3.3.4. Instrumentation of Rear Axle Note Restraint System for Truck with Tires**



**Figure 3.3.5. Restraint System for Truck without Tires**

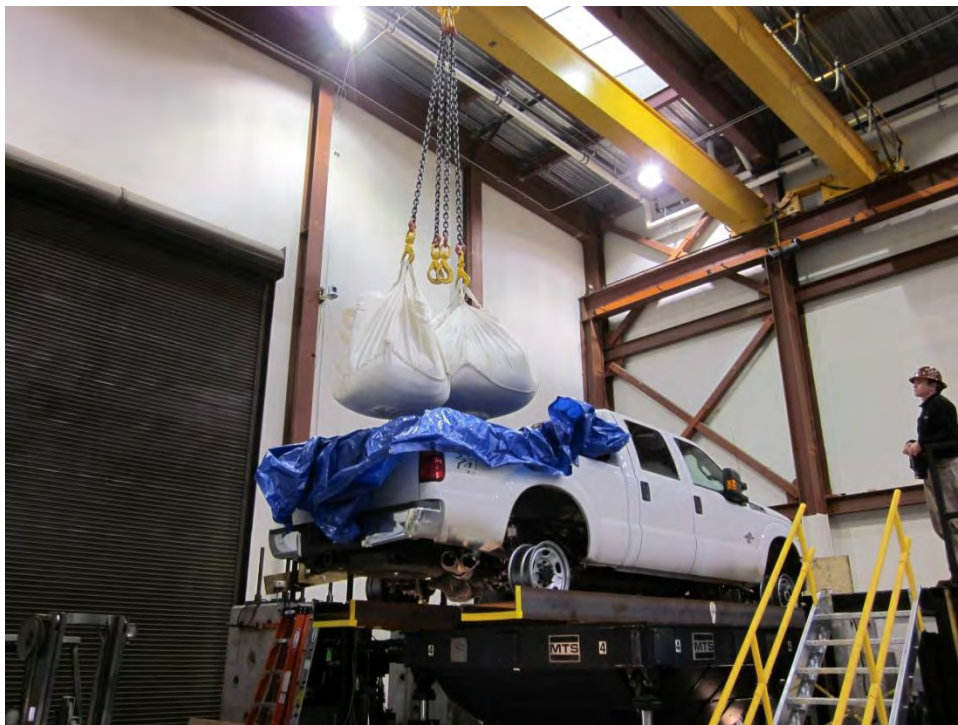


**Figure 3.3.6. Loading Payload**

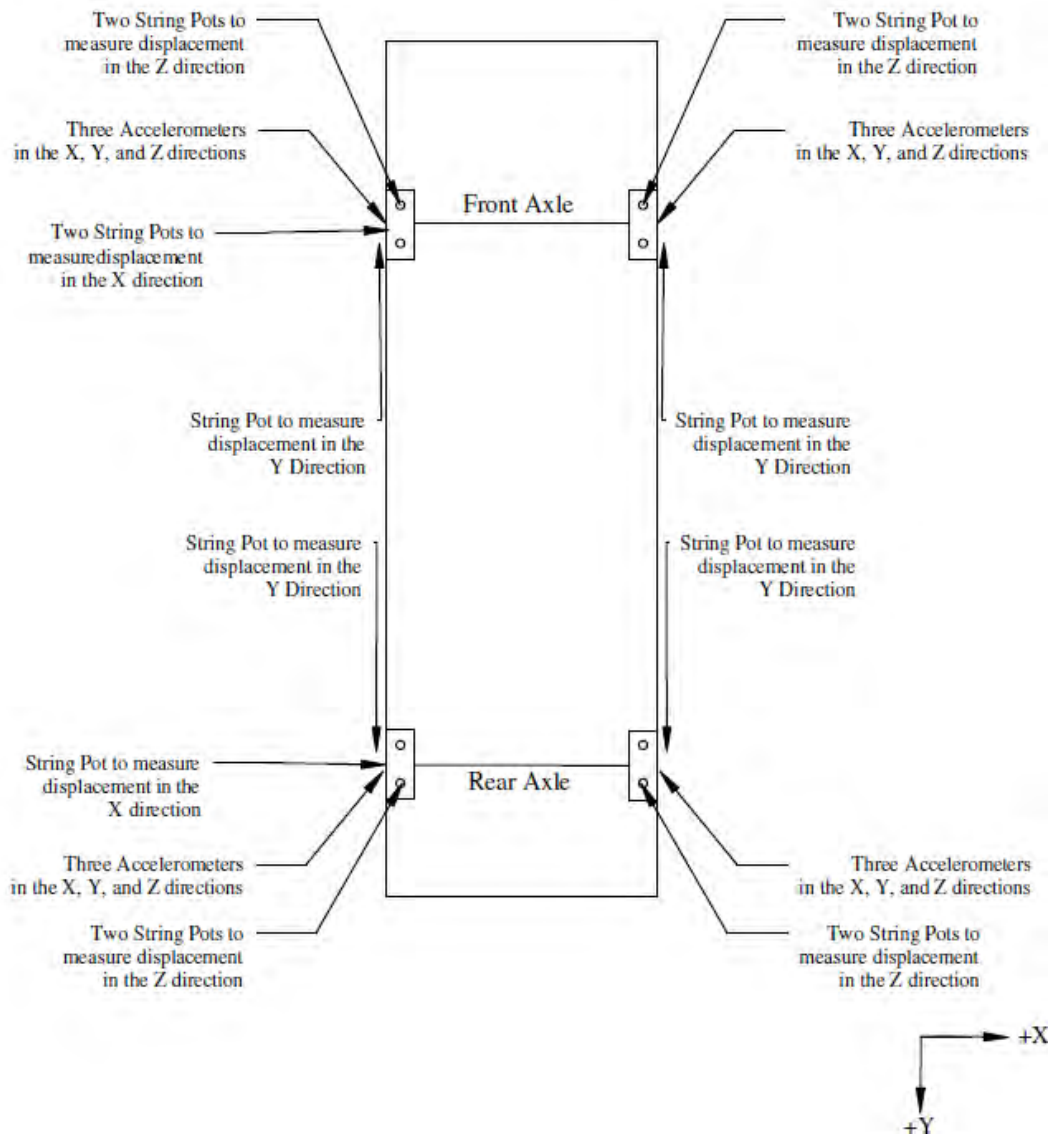


**Figure 3.3.7. Vehicle Instrumentation at the Axle Level**

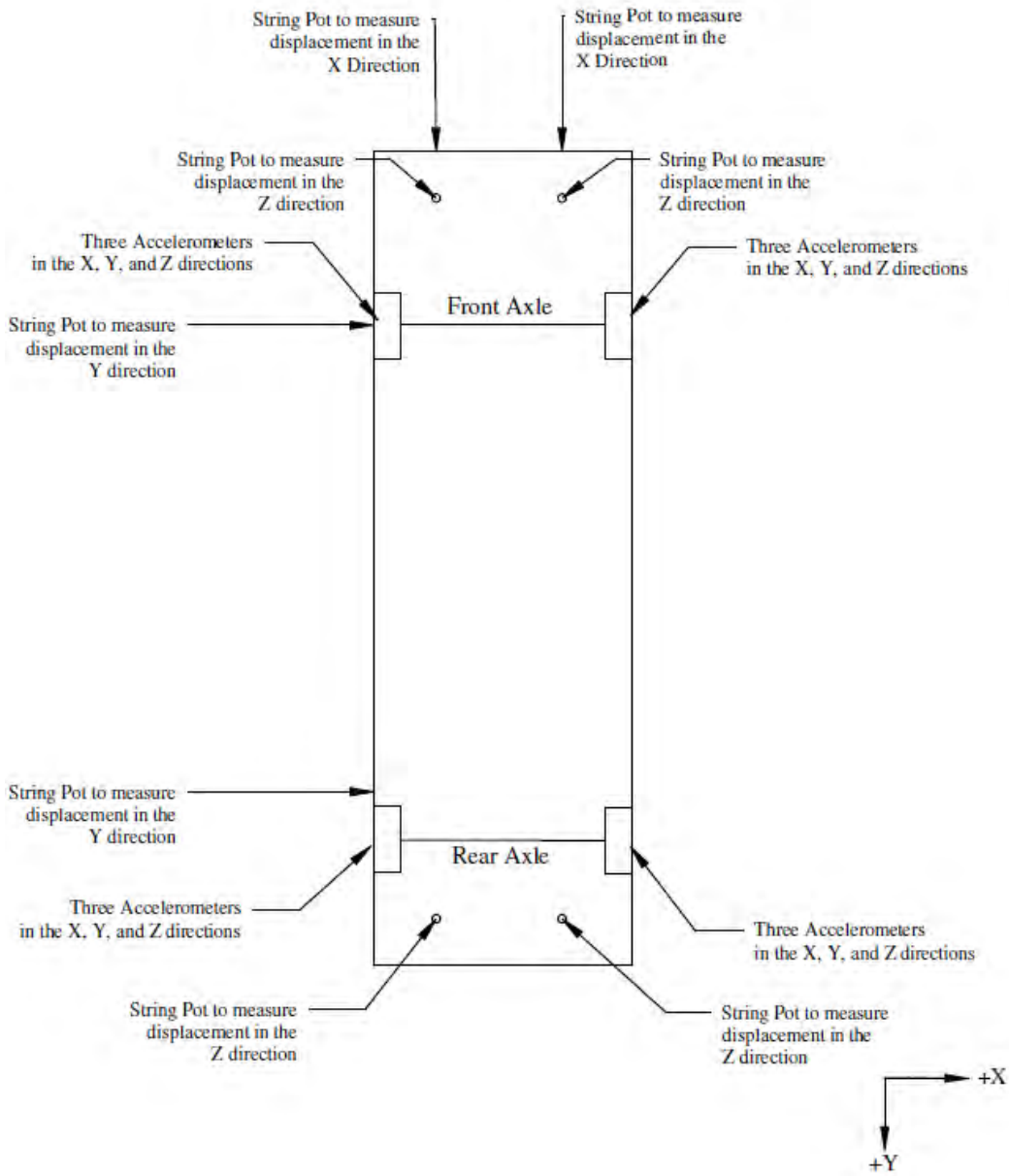


**Figure 3.3.8. Vehicle Instrumentation at the Chassis Level**

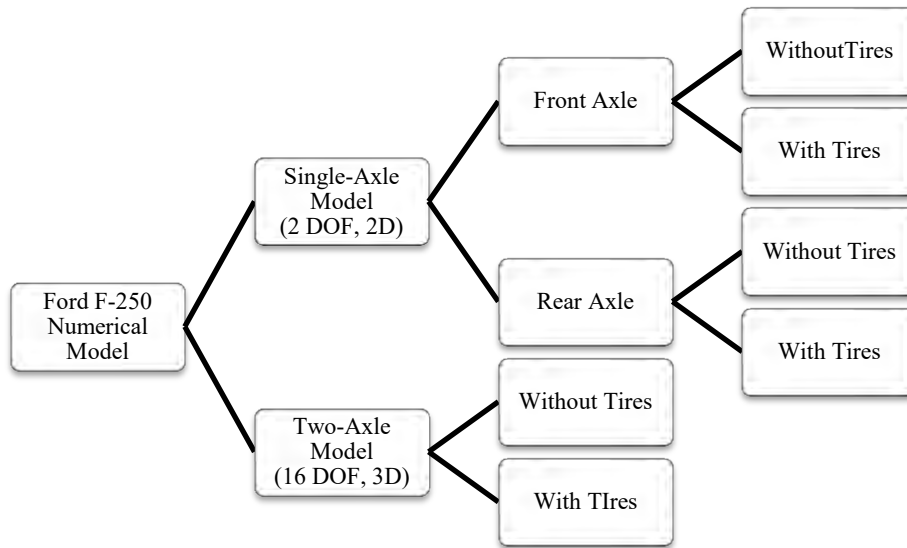


**Figure 3.4.1. Family of Numerical Models**

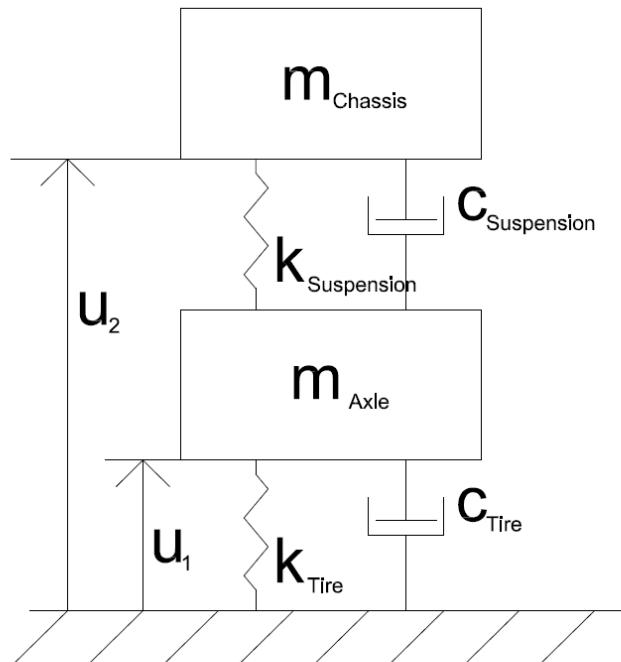


**Figure 3.4.2. Single-Axle Model**

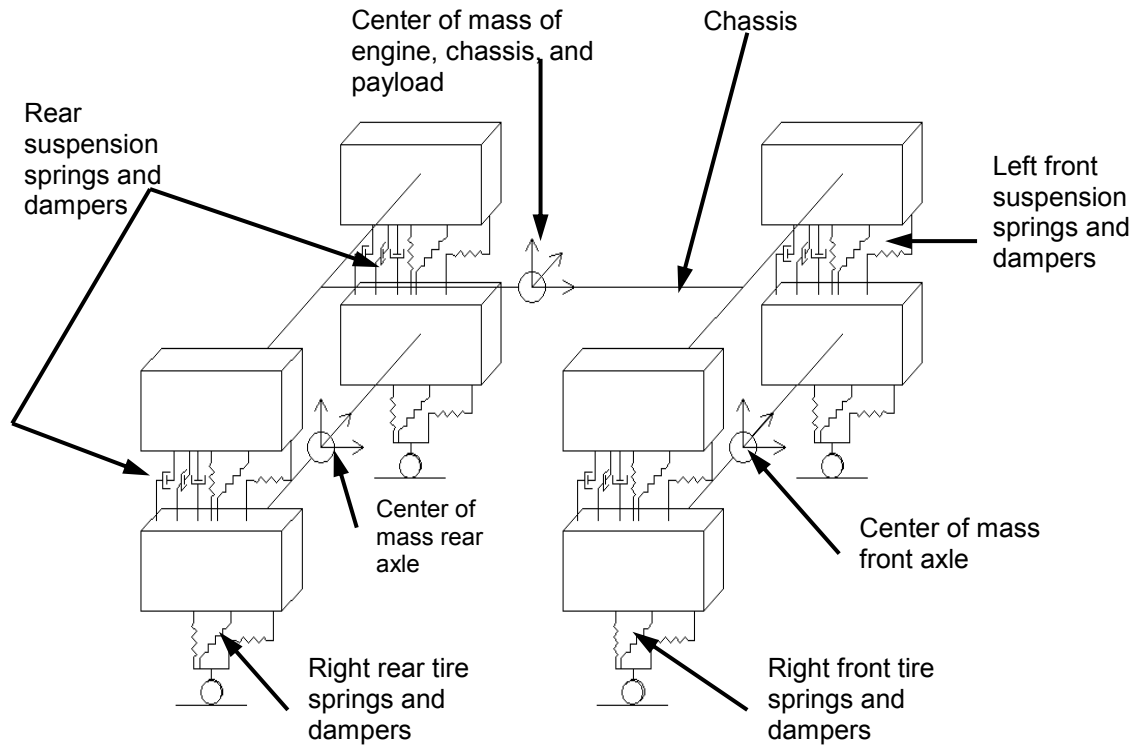


**Figure 3.4.3. Two-Axle Model**

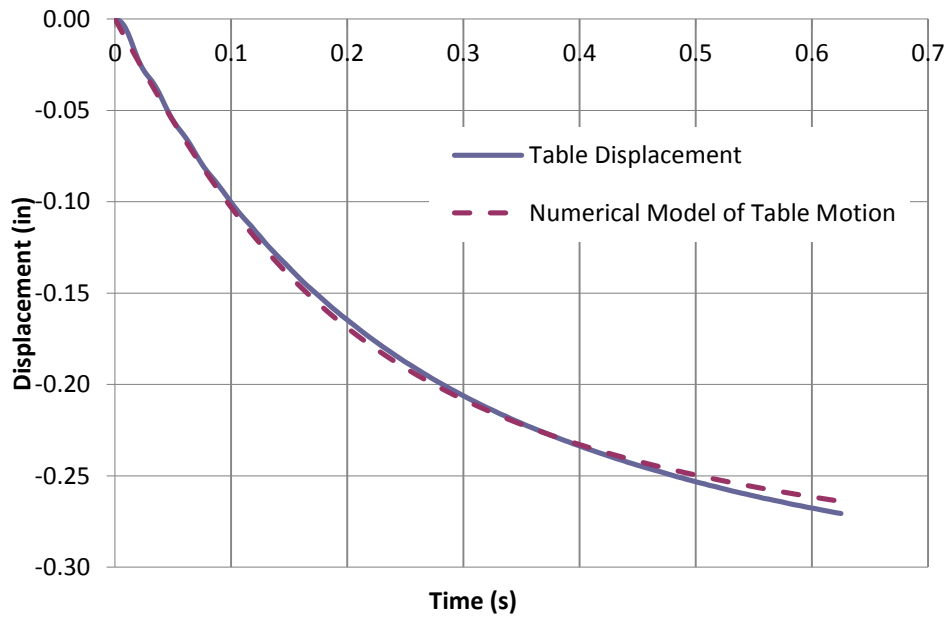


**Figure 3.5.1. Actual and Approximate Table Vertical Displacement Comparison for Full Truck with Tires Snap B Run**

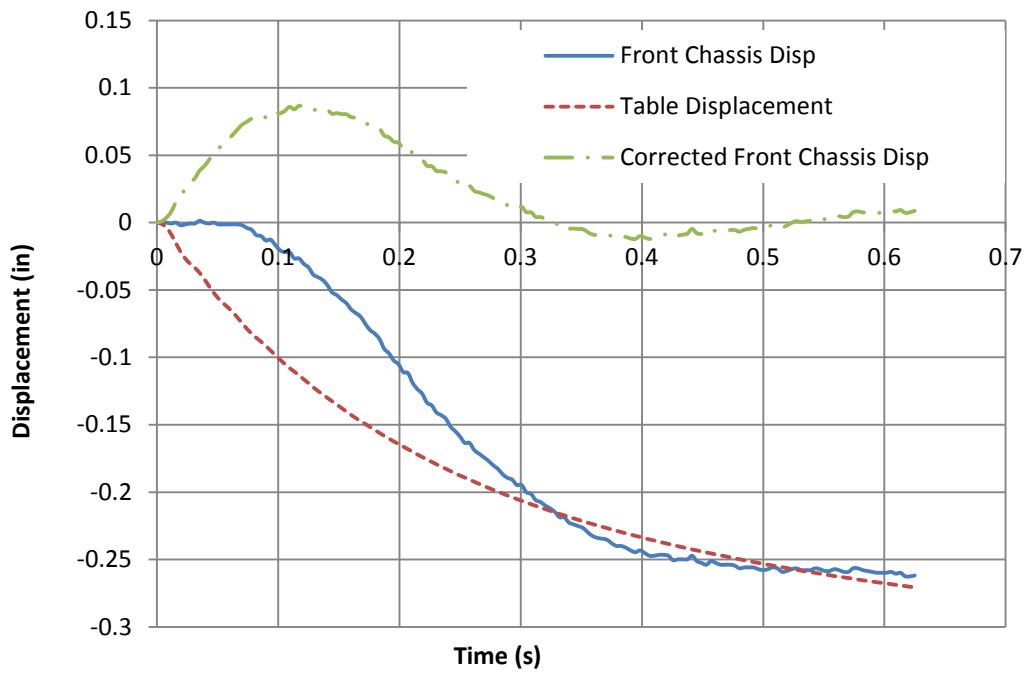


**Figure 3.5.2. Chassis and Table Vertical Displacements during Fully-Laden Truck with Tires Snap C Run**

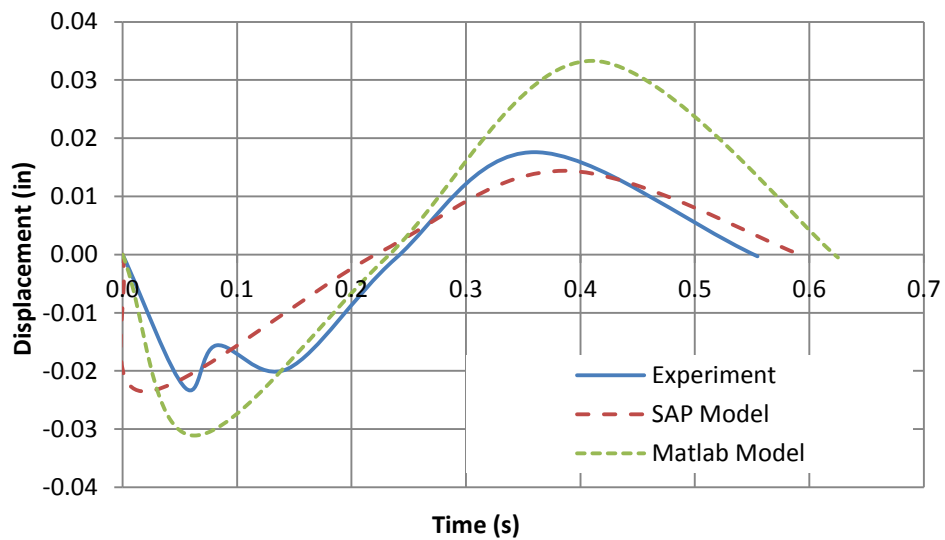


**Figure 3.5.3. Rear Axle Vertical Displacement during Vertical Snap of Fully-Laden Truck with Tires Snap C Run**

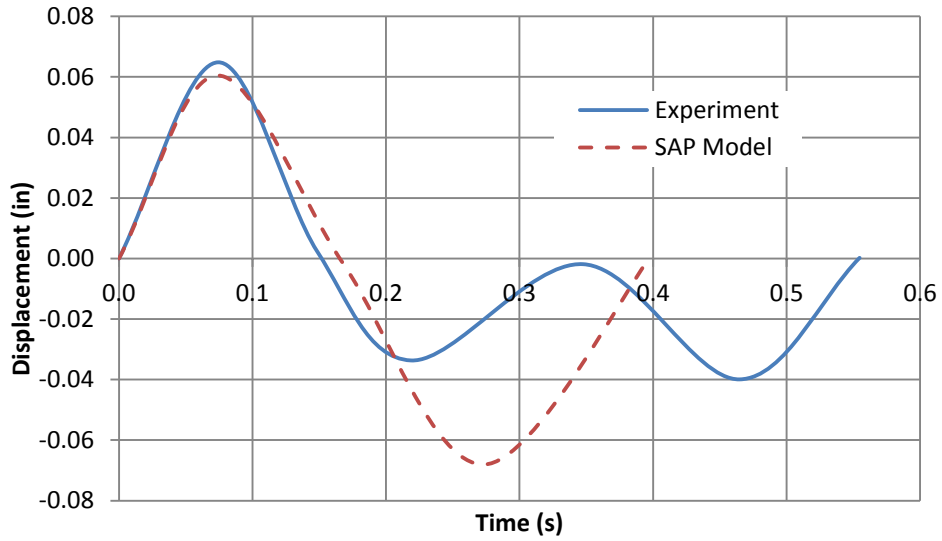


**Figure 3.6.1. Front Axle Transverse Displacement during Transverse Snap of Fully-Laden Truck with Tires Snap C Run**

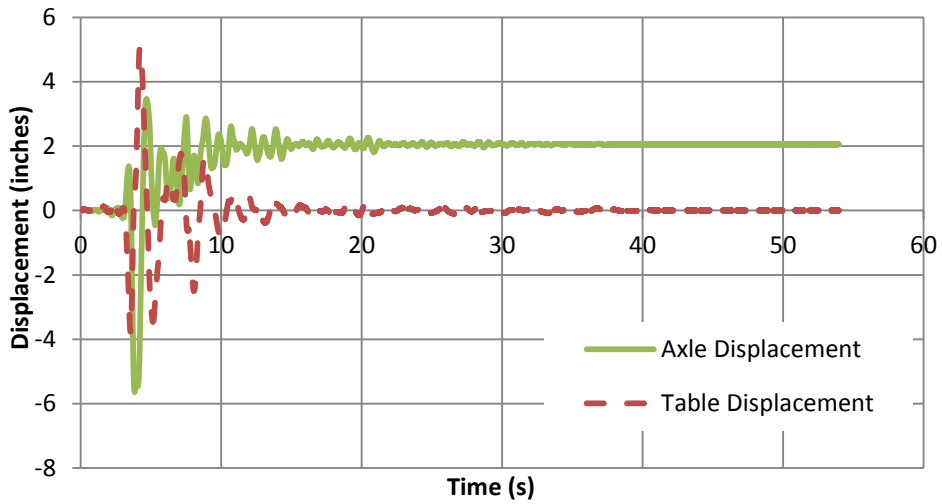


**Figure 3.6.2. Axle and Table Longitudinal Displacement during 75% Sylmar Run**

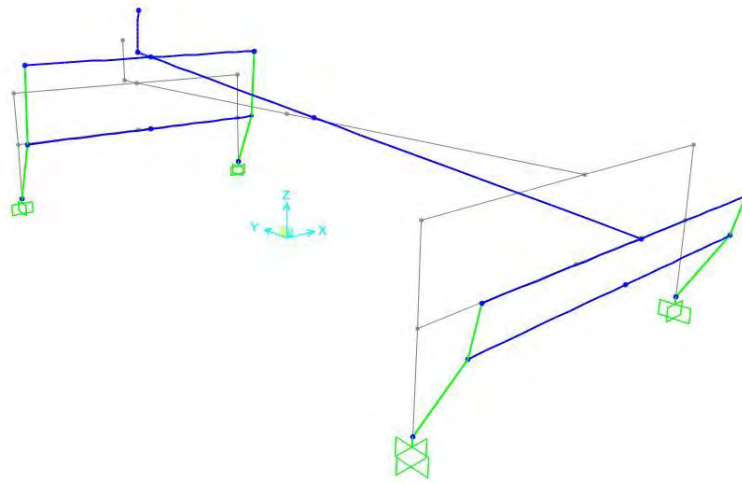


**Figure 3.8.1. First Mode Shape of the Vehicle Model ( $T_1 = 0.79$  s)**

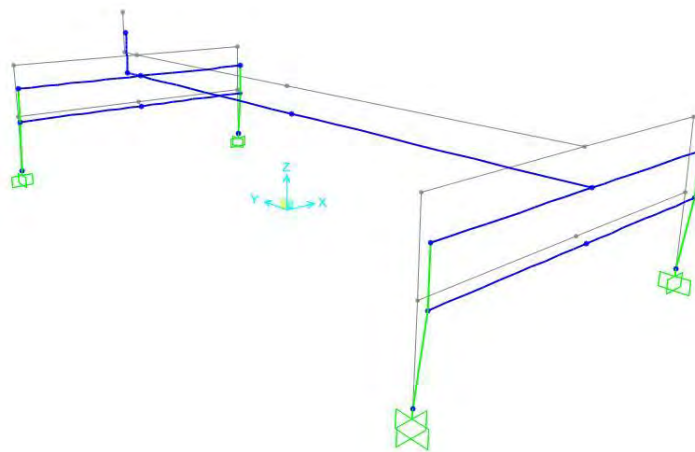


**Figure 3.8.2. Second Mode Shape of the Vehicle Model ( $T_2 = 0.64$  s)**

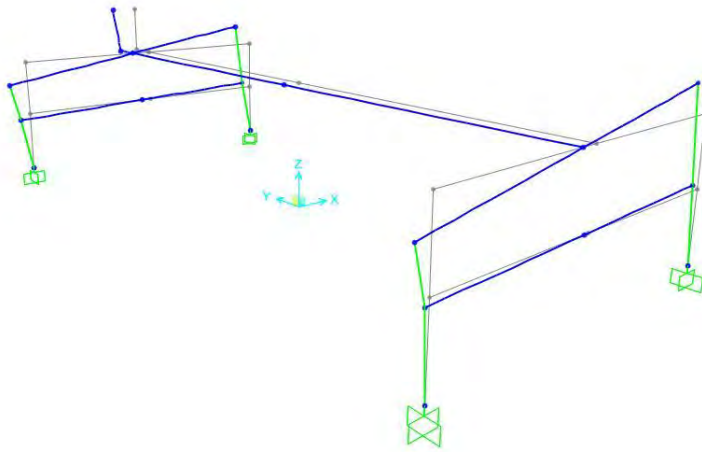


**Figure 3.8.3. Third Mode Shape of the Vehicle Model ( $T_3 = 0.61$  s)**

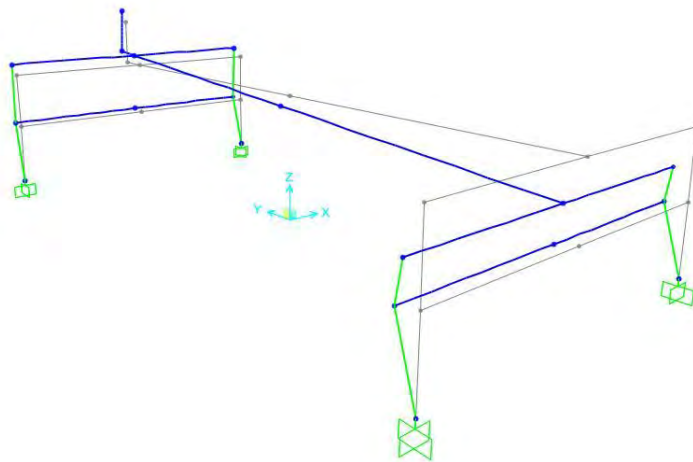


**Figure 3.8.4. Fourth Mode Shape of the Vehicle Model ( $T_4 = 0.51$  s)**

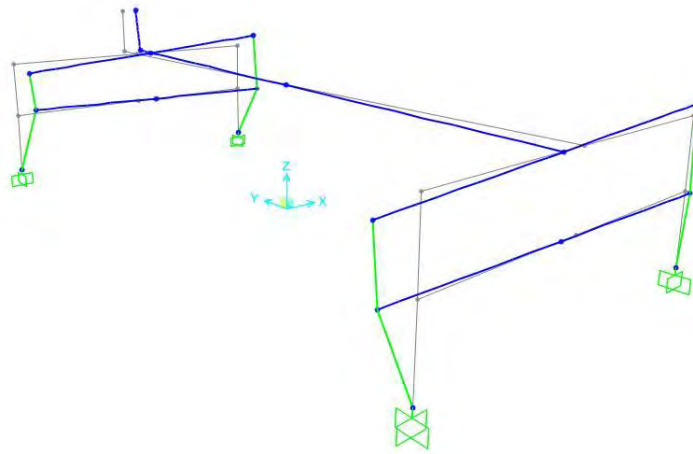


**Figure 3.8.5. Fifth Mode Shape of the Vehicle Model ( $T_5 = 0.38$  s)**

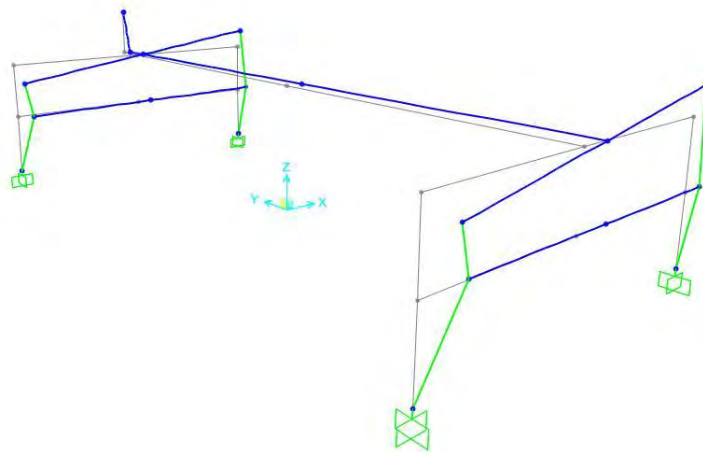


**Figure 3.8.6. Sixth Mode Shape of the Vehicle Model ( $T_6 = 0.30$  s)**

# CHAPTER 4. BRIDGE MODEL AND EXPERIMENT SETUP

## 4.1. General

The experimental task in this project was able to take advantage of a separate study being conducted on the seismic response of curved bridges at the University of Nevada Reno. Funded by the Federal Highway Administration (FHWA), this study involved a series of shake table experiments on a 2/5-scale model of 3-span steel girder bridge with a high degree of horizontal curvature. For the purpose of the live load project, six trucks were placed on the bridge and performance compared against the case without live load when subject to the same input motions. This chapter describes the design of the super- and sub-structure of the model, placement of vehicles, and the instrumentation plan for the model and vehicles. In addition the earthquake input motions and test protocol are described.

## 4.2. Prototype Bridge and Scaling Requirements

This section describes the selection of the prototype bridge as well as the choice of scale factors used in the experimental study. The similitude requirements, which link the scaled model to the prototype, are also presented herein.

### 4.2.1. Prototype Bridge Selection

The prototype bridge chosen for the FHWA curved bridge study was taken to have the same geometry as the bridge in Design Example 6 of the FHWA Seismic Design Examples (FHWA, 1996). The bridge in this design example is a three-span, reinforced concrete, cast-in-place concrete box girder. The total bridge length is 362.5 ft and the radius at centerline is 200 ft. The subtended angle at the center of curvature is  $104^\circ$ . The design was then modified for a steel girder superstructure for reasons discussed in Section 4.2.3.

### 4.2.2. Seismic Hazard

For the purposes of this project, the prototype bridge was assumed to be on a rock site (Site Class B) in Zone 3 for which the 1,000 year PGA was 0.472 g, the short period (0.2 s) spectral acceleration was 1.135 g and the long period (1.0 s) spectral acceleration was 0.41g. The AASHTO design spectrum for this site is shown in Figure 4.2.1.

### 4.2.3. Scaling and Similitude Requirements

The selection of the scale factor was constrained by the physical size of the laboratory and the payload capacity of the shake tables and overhead cranes. Although the laboratory area is 150 ft long by 50 ft wide, the maximum permissible length and width of the model was limited by the footprint that can be serviced by the overhead cranes. Furthermore the curvature of the model means that its radial width also affects the length and width of its own footprint which must fit inside the crane footprint. The net result of these geometric constraints led to a scale factor of 2/5 and the following dimensions for the model:

- overall length along the centerline = 145 ft, with 3 spans of 42, 61, and 42 ft
- radius = 80 ft
- width of superstructure along the radius = 12 ft

The shake tables in the Large-Scale Structures Laboratory have payload capacities at 1 g acceleration of 50 ton (100 k) each. The total capacity is therefore 400 k if all tables are uniformly loaded. However, even at 2/5-scale, the weight of the concrete box girder superstructure exceeds this capacity and rather than reduce the scale even further, it was decided to change the superstructure to a steel plate girder. Other reasons for making this change included:

- A steel plate girder on concrete columns is a more common form of bridge construction in the National Bridge Inventory than a concrete box girder.
- The non-integral connections over the piers allow for other experiments to be more easily conducted, such as full and hybrid isolation.
- A steel superstructure may be spliced at, say, third points making it easier to assemble and disassemble in the laboratory.

Dimensions of the prototype and scale model are shown in Table 4.2.2. The plan view of the model bridge in the laboratory is shown in Figure 4.2.2.

For the scale model to faithfully represent the prototype, it must satisfy the similitude laws for such models which in turn determine the scale factors for other parameters such as acceleration, velocity, stress, time, density, as summarized in Table 4.2.3. In models where damage is expected to occur, it is necessary to use the same material in the model as the prototype, which will mean the stress, modulus and density scale factors will be 1.0. Further, since gravity is the same for both the prototype and model (unless the model is in a centrifuge), the acceleration scale factor must also be 1.0. These constraints on the above scale factors mean that the inertia and self-weight forces are not scaled correctly and additional mass must be added to the model to correct this deficiency, particularly for models subject to dynamic loads. It may be shown that the added mass required is a function of the length scale factor and the mass of the model as indicated in Equation 4.2.2:

$$m_a = (S_L - 1)m_M \quad (4.2.2)$$

where:

$m_a$  = additional mass

$m_M$  = model mass

$S_L$  = scale factor for length

### **4.3. Model Substructure Design and Instrumentation Plan**

The substructure for this bridge is a single-column pier. The following sections describe the details of the column, footing and cap beam which were designed in accordance with the AASHTO LRFD Specifications (AASHTO, 2007) and AASHTO Seismic Guide Specifications (AASHTO, 2009). The calculation of the added mass to satisfy the similitude requirements and the instrumentation plan for the substructure level are also presented. Additional details are given by Levi (2011) and Harrison (2011).

#### **4.3.1. Column**

The column diameter in the prototype bridge is 60 in. With the scale factor of 0.4, the diameter of the model column is 24 in. Based on a parametric study done previously by Levi (2011), the longitudinal and lateral reinforcement ratios were chosen to be 1%, and the column therefore has 16, #5 longitudinal rebars and #3 spirals on a 2 in pitch. The column concrete clear cover is 0.75 in, and the spiral diameter is 22.125 in. Concrete strength was taken at 5.5 ksi and ASTM A706 steel was used for all reinforcing steel (Table 4.3.1).

With these properties determined, the capacity of the column section was checked in accordance with the AASHTO Seismic Guide Specifications (AASHTO, 2009), a moment-curvature analysis using XTRACT, and a nonlinear time history analysis using SAP 2000. Construction details for the substructure are shown in Figures 4.3.1 through 4.3.9.

#### **4.3.2. Footing**

Unlike for a typical bridge, the footing for this experiment was designed to be as rigid as possible. It was also designed to remain elastic under shears and moments transferred from the column and post-tensioned to the table platen to prevent uplift and sliding. Details are given by Levi (2011).

#### **4.3.3. Bent Cap**

Overall dimensions of the bent cap are shown in Figure 4.3.3. These dimensions were chosen to ensure sufficient elastic capacity for the maximum demand on the cap,

obtained from the results of a response history analysis for the maximum expected earthquake event (i.e., the earthquake expected to induce column failure in the system). For the purpose of design, this event was taken to be 300% of the design level earthquake. This analysis assumed that the bearings would have sufficient tension capacity to carry positive and negative moments applied to the joint region of the bent cap. The capacity for the section was determined following Section 5.8 of the AASHTO LRFD Specifications (AASHTO, 2007).

The capacity of the column/cap beam joint was checked to meet the requirements of the AASHTO Seismic Guide Specifications (AASHTO, 2009). These requirements included extending the spiral steel into the bent cap, adding vertical stirrups inside and outside the joint region, adding longitudinal steel to the top and bottom layers, providing horizontal side reinforcement, and horizontal J bars in the joint area. Additional vertical steel (16 of #5 J bars) was also provided in the joint region. The longitudinal and lateral reinforcement details for the bent cap are depicted in Figures 4.3.7 and 4.3.8.

#### **4.3.4. Additional Substructure Mass**

The additional mass required by Equation 4.2.2 to satisfy similitude requirements is shown in Table 4.3.2. It is noted that the required additional mass may also be calculated from the requirement the axial load ratios in prototype and model columns are the same. Both methods give the same result.

#### **4.3.5. Instrumentation Plan**

Instrumentation for the bridge included strain gauges, displacement transducers, accelerometers, load cells, and video recordings. Displacement transducers were either linear transducers or string pots.

Strain gauges were installed on the column longitudinal and transverse rebar as shown in Figures 4.3.10 and 4.3.11. These gauges were placed in the top and bottom plastic hinge zones of the columns primarily on the principal axes of the column (radial and tangential directions). Additional gauges were placed on the reinforcement between these axes to capture resultant effects and provide redundancy. Details are provided by Levi (2011).

Displacement transducers and string pots were used to measure curvature up the height of the column, and rotation and displacement of the bent cap. This was accomplished by embedding threaded rods into the column, attaching displacement transducers to the rods, and measuring the change in displacement between two adjacent rods, from which rotation and curvature could be calculated. Rods were placed on the principal axes of the column at 1 in, 4 in, 11.5 in, and 19 in from the top of the footing. Bond slip in the lower region of the column was determined by placing two transducers on the threaded rod 4 in above the footing; one measuring to the footing and the other to the threaded rod located 1 in above the footing. By taking the difference between these

two measurements, bond slip in the longitudinal reinforcement could be determined. At the top of the column, the same pattern was followed along the radial axis but was reduced in the tangential direction due to less expected damage in this direction, as shown in Figure 4.3.12.

Displacement transducers were attached to the bent cap at 5 locations to measure rotation about the radial axis in the steel bearings between the girders and bent cap, as depicted in Figure 4.3.13. To measure bent cap displacements and rotations, 8 string pots were placed on each bent cap in 6 locations in the x-, y-, and z- directions. For the x- and y-displacements, string pots were attached to the outer edge of the bent cap in the radial direction. These transducers were also used to determine the rotation of the column assuming the bent cap is a rigid body. For the vertical (z-) displacements of the column, 4 string pots were placed at the corners of the bottom face of the bent cap. These string pots were also used to determine the pitching of the bent cap. The layout of these instruments is shown in Figures 4.3.14 and 4.3.15.

Five-degree-of-freedom (5DOF) load cells were located under each girder at the each support, as shown in Figure 4.3.16. These load cells were oriented in the local coordinates at each support, i.e., in the radial and tangential direction, and used to measure the axial force, radial and tangential shears, as well as radial and tangential moments. Global displacements of the bridge were measured in the longitudinal (x-) and transverse (y-) displacements, using string pots at the abutments, bents, and the middle span of the bridge as shown in Figure 4.3.17. Three-component accelerometers were placed at three locations, along the deck, on the abutment towers, and on top of the bent caps, as shown in Figure 4.3.18.

Each instrument was named according to its type and location. For example, the instrument name for a string pot in the x- (longitudinal) direction on the inside of the north bent is SPX-NB-IC. The first three letters (SPX) identify the instrument as a string pot in the x-direction (longitudinal). The next two letters (NB) identify the substructure where the instrument is located as the north bent, and the last two letters (IC) indicate the location on the north bent as the side facing the inside of the curve. Another example is a strain gauge (SGB) on the north bent (NB) identified as follows: SGB-NB-LB-BH-T5. This gauge is on a longitudinal bar (LB) at the bottom of the hinge (BH) on bar number 5. A complete list of instrumentation for the model is given in Table 4.3.3.

#### **4.4. Model Superstructure Design and Instrumentation Plan**

As noted in Section 4.2.3, the superstructure for this bridge comprised steel plate girders, cross frames, and a composite concrete deck with the same curvature and number of girders lines as the prototype (i.e., three girder lines). This section presents a brief overview of the selection, design, and instrumentation of the superstructure.

#### 4.4.1. Girders

As just noted, the girders for the superstructure are steel plate I- girders. For ease of fabrication, girder dimensions were chosen to be identical to one another and of uniform section throughout their length. These dimensions were therefore based on the requirements for the outside girder, which carries the highest dead and live load of the three in the superstructure. Various load combination cases were used in the design according to AASHTO LRFD Specifications (AASHTO, 2007), i.e., Strength I, Extreme Event I, and Fatigue. Design was governed by the Strength I case.

Figure 4.4.1 shows typical cross-sections of the prototype and model bridge superstructures. The model has a subtended angle of  $104^\circ$ , a centerline radius of 80 feet and total centerline length of 145 ft. The girders are built-up sections with a 0.375 in x 26 in deep web, and two 0.625 in x 9 in wide flanges. Girder spacing is 54 in.

#### 4.4.2. Deck Slab

The equivalent strip method was used to determine live load moments and shear forces in the deck slab. The design positive and negative moments at interior panels were taken from AASHTO LRFD Specifications Table A4-1. The overhang negative moment was calculated by applying a 16 k wheel load (half of the 32-k design truck axle load) over the equivalent strip width. The required number of shear connectors was determined according to the Strength Limit States of AASHTO LRFD Specifications Article 6.10.10.4. This number was then checked against the requirements of the Fatigue Limit States of AASHTO LRFD Specifications Article 6.10.10.1.2. A summary of the shear connector design is given in Table 4.4.1.

The Strength I load combination case was used to determine the factored design positive and negative moments, which were then used to determine the transverse reinforcement in the slab. Spacing was checked against the limits in AASHTO LRFD Specifications Article 5.7.3.4. The slab thickness in the prototype bridge is 8.125 in., and the concrete strength is 4 ksi. In the model, the slab is 144 in wide (including 18 in overhangs) and 3.25 in thick with 0.75 in haunches. Bottom longitudinal reinforcement was determined according to AASHTO LRFD Specifications Article 9.7.3.2. Top longitudinal reinforcement was determined by shrinkage and temperature requirements, as given in AASHTO LRFD Specifications Article 5.10.8. In addition, in negative moment regions, the longitudinal reinforcement was checked against the minimum requirements of AASHTO LRFD Specifications Article 6.10.1.7. Table 4.4.2 summarizes the deck reinforcement.

The required number of shear connectors was determined according to the Strength limit states of AASHTO Article 6.10.10.4. This number was then checked against the requirements of the Fatigue limit state of AASHTO Article 6.10.10.1.2. Details are given by Monzon (2013).

#### 4.4.3. Cross-Frames

Each cross-frame is a chevron (V) brace configuration as shown in Figure 4.4.1. The top and bottom chords comprise double angles while the diagonal members are single angles. The compressive resistance was calculated according to the provisions of AASHTO LRFD Specifications Article 6.9.2. In a curved bridge, the cross frames are considered to be primary members and the slenderness ratio is therefore limited to 120 by the AASHTO LRFD Specifications Article 6.9.3. The tensile resistance was calculated according to AASHTO LRFD Specifications Article 6.8.2.

The cross-frames in the model are spaced at 6 ft centers along the span except those close to the abutments where the distance between the abutment cross-frame and first intermediate cross-frame is 5 ft – 4-1/2 in. This is because the abutment cross-frames are located 7-1/2 in from the end of the bridge to make them collinear with the bearing centerline. In the middle span of the bridge, the cross-frames are spaced at 6.5 ft. Intermediate cross-frame uses L2x2x1/4 angles for the diagonals and 2L1-1/4x1-1/4x1/4 angles for the top and bottom chords, respectively; cross-frames at the bents use single L2-1/2x2-1/2x5/16 angles for the diagonals and 2L1-1/4x1-1/4x1/4 angles for the top and bottom chords respectively. The size of diagonal members in the support cross-frames is larger than those at intermediate cross-frames because they resist larger forces, particularly under lateral loads. At the abutments, the top chord is also 2L1-1/4x1-1/4x1/4 angles and the diagonals are L2-1/2x2-1/2x5/16 angles, but the bottom chord comprises 2MC3x7.1 channels. As noted in Section 4.4.4, a shear key is mounted between the mid-point of this chord and the abutment seat below, and a heavier section is required for this member to transmit radial shear forces from the superstructure to the abutment through the key. The transverse stiffeners are 3/8 in by 4 in plates welded to the girder web and flanges. The stiffeners are spaced to coincide with the cross-frame locations and also serve as connecting elements between the cross-frames and girders. At the supports, the bearing stiffeners are 1/2 in by 4 in.

#### 4.4.4. Shear Keys

Shear keys were used to restrain the superstructure in the radial direction. These keys were designed to provide restraint for low-to-moderate seismic loads but fail under strong ground motions to limit the overturning moments on the shake tables below the abutments. (A similar approach is sometimes used by designers wishing to protect the piles below bridge abutments against damage during strong shaking.) To limit the overturning in this experiment the keys were designed to fail at a shear force equal to 25 k, which was expected to be reached during 75% of the design earthquake (DE).

Whereas the shear keys restrained radial movement of the superstructure (until fracture), they were designed to allow tangential displacements and teflon/stainless bearings were provided to accommodate this movement. Since tie-downs were not provided, the girders were also free to uplift, even while the shear keys were intact. Once the keys failed, the girders could move in any direction at the abutment.

Shown in Figures 4.4.2 through 4.4.4, the shear keys comprised four components: 1) stainless steel shear pin, 2) upper block (shaped as ‘dog-bone’) with hole to locate the upper half of the shear pin, 3) lower block with longitudinal slot, and 4) bushing which slides in the slot and holds the lower half of shear pin. As seen in Figure 4.4.5, the pin had a groove cut at mid-length and machined to a depth sufficient to cause failure at the required load (25 k). The reduced section of the upper block (‘dog bone’) was strain gaged and calibrated to allow measurement of the shear force transmitted through the device.

#### **4.4.5. Additional Superstructure Mass**

As shown in Table 4.3.2, the additional mass required to be placed on the model to satisfy similitude requirements was 184.71 k. However, the actual added weight was 191.57 k. The use of existing lead pallets and steel plate made it difficult to match the required weight exactly. Some added weight (24.18 k) was placed on top of the two bents, as mentioned in Section 4.3.4, and the rest (167.39 k) was mounted on the bridge deck. The added weight was uniformly distributed along the deck using a symmetrical pattern to minimize accidental torsion in the bridge, as shown in Figure 4.4.6.

#### **4.4.6. Instrumentation Plan**

As with the substructure, instrumentation was installed on the superstructure to capture global and local effects during experimental testing. This instrumentation included strain gauges, displacement transducers, and accelerometers.

For example, the sacrificial shear keys at the abutments were strain gauged and calibrated to give response histories of shear force in the keys up to and including rupture. Displacement transducers were placed across the splices in the plate girders in the middle span to monitor slippage and check for pounding in these splices. Transducers were also placed underneath the deck at the abutments in the inner and outer bays to measure the relative vertical movement (uplift) between the girders and the abutment seats. String pots and accelerometers were placed at the edges of the deck at various locations along its length to obtain the global movement of the superstructure, as shown previously in Figure 4.3.18. Displacement transducers were also installed in the support cross frames to measure the lateral drift and distortion of the cross-section under lateral load as shown in Figure 4.4.7.

Again, each instrument was named according to its type and location (Table 4.3.3). For example, the instrument name for an accelerometer in the x- (longitudinal) direction (ACX) at mid span (MS) of the top flange of the middle girder (MG) is ACX-MS-MG. Instrument SPY-NA-IE is a string pot in the y- (transverse) direction (SPY) located on the inner edge (IE) of the north abutment (NA).

## 4.5. Model Construction

Figures 4.5.1 to 4.5.7 show the various stages of construction and strain gauging of the single column bents for the model substructure. This work was done on a casting slab in the fabrication yard just outside the laboratory.

On the other hand the steel superstructure was constructed offsite in the shop of a local fabricator and trucked to the lab in three sections (2 x 51-ft sections and 1 x 31-ft section). Section lengths were optimized to satisfy truck flatbed constraints (weight and length), lab door clearances (width and height) and crane lifting capacity. Once each section had been lifted into position in the lab, they were mechanically spliced to provide full moment and shear continuity using a steel collars, web and flange plates and bolted connections.

Erection of the model involved six major steps:

1. Lift the abutment towers onto Tables 1 and 4, and the single column bents onto Tables 2 and 3 (Figure 4.5.8 and 4.5.9)
2. Adjust substructures for alignment and elevation of bearing seats and leveling plates
3. Install load cells and added mass on bent caps (Figure 4.5.10)
4. Move superstructure sections into lab and lift into place (Figures 4.5.11 to 4.5.13). Splice sections together to form a continuous 3-span superstructure
5. Install added mass on superstructure (Figure 4.5.14)
6. Install instrumentation (Figure 4.5.15)

As noted in Chapter 1, this model was used for several different experiments (in addition to the live load experiment reported herein). Since the bents were damaged in each experiment, they were replaced with a fresh set of columns before the next experiment. To do this the above process was reversed: remove instrumentation and added mass, unsplice the superstructure, take down each section, remove load cells and added mass on bents, remove damaged columns, replace with new set and repeat from Step 3.

## 4.6. Live Load Vehicle

As noted previously, to simulate the effect of live load on the bridge, six identical trucks were placed on the deck during the experiment. Chapter 3 describes the selection of these vehicles and determination of their properties. This section describes vehicle placement and instrumentation. It is noted that in these experiments the vehicles are stationary for logistical and safety reasons. Based on work by Kim *et al.* (2011), the consequences of this restriction are believed negligible.

#### **4.6.1. Vehicle Placement**

The vehicles were placed on the bridge deck at the locations shown in Figure 4.6.1. They were labeled TR1 through TR6 for Trucks 1 through 6 respectively, starting at the north end of the laboratory and progressing south. Although a symmetric arrangement was desired it was not always practical to do so in view of the added mass already bolted to the deck slab and the need to have sufficient clearance between the trucks and lead pallets front and back, and between the truck exhausts and steel plates underneath the chassis. As a consequence trucks TR2 and TR5 were slightly rotated about a vertical axis to avoid striking a lead pallet during pitching motions, but this was done as symmetrically as possible.

For the purpose of this experiment, the bridge was considered to have only one lane and the trucks were placed facing the same direction along the tangential axis of the bridge.

All six trucks were lifted into place using the two eye bolts at the front of the chassis and a spreader beam connected to the rear hitch as shown in Figures 4.6.2 and 4.6.3. Placement started with the two end trucks and worked towards the center. Figure 4.6.4 shows lifting one truck onto the bridge. Figures 4.6.5 and 4.6.6 show the bridge with the vehicles in place, viewed from the south and east respectively. The distortion in the latter view is due to the use of a fish-eye lens to obtain this wide-angle view.

The trucks were secured from gross movement by threading a slack chain through the rims of the left-front and right-rear wheels of each truck and bolting the chains to the bridge deck, as shown in Figure 4.6.7. Additional clearance was provided under each truck, by mounting each wheel on a 1½ in thick concrete pad epoxied to the bridge deck before placing the trucks.

Once the trucks were in their final positions they were loaded with two large bags of sand for a nominal payload of 2.3 k. This load varied slightly from truck-to-truck as shown in Table 4.6.1.

#### **4.6.2. Vehicle Instrumentation**

The trucks were instrumented with displacement transducers and accelerometers in a similar manner to the single truck test described in Chapter 3. Due to a limitation on the number of available instruments and data acquisition channels, not all trucks were instrumented to the same extent. Five trucks were lightly instrumented and one truck (TR3), near the midpoint of the bridge, was more densely instrumented. A total of 27 accelerometers were placed on all six trucks, of which 12 were placed on Truck 3. Of these 12, three were located on the chassis above each tire, in the x-, y- and z- directions (longitudinal, transverse and vertical respectively). The other five trucks had three accelerometers attached at the midpoint of the chassis of each truck, also in the x-, y- and z- directions (longitudinal, transverse and vertical respectively). The instrumentation layout for all six trucks is shown in Figures 4.6.8 and 4.6.9. Details for Truck TR3 are given in Figure 4.6.10.

String pots were placed on three of the six trucks to measure transverse and vertical movement. These three trucks included the two end trucks (TR1 and TR6) and one of the middle trucks (TR3), to capture a range of motions ranging from pitching to rolling. Trucks TR1 and TR6 had a total of five string pots installed: two in the vertical direction located at the front and rear of the chassis, and three in the horizontal direction located near the center of the chassis to enable the motion of the chassis to be triangulated in two lateral directions, as shown in Figure 4.6.11. Truck TR3 had a total of ten string pots installed, two in each lateral direction at the chassis level, four at the chassis level in the vertical direction (two in the front and two in the rear), and two at the axle level in the vertical direction (one in the front and one in the rear).

As with the instrumentation for the bridge, each truck instrument was named according to its type and location (Table 4.6.2). For example, the instrument name for an accelerometer in the y- (longitudinal) direction (ACC-Y) on Truck 1 (TR1) is TR1-ACC-Y. Instrument TR3-DISP-XS is a string pot (DISP) in the x-direction at south end (XS) of Truck 3 (TR3).

## **4.7. Ground Motion and Test Matrix**

Three of the four shake tables in the Large-Scale Structures Lab at UNR are biaxial tables, each with two translational degrees-of-freedom (longitudinal and transverse). The fourth table is a triaxial table with three translational degrees-of-freedom (longitudinal, transverse, and vertical) and three rotational degrees-of-freedom (pitch, yaw and roll). When operated synchronously with the biaxial tables, 4 of the 6 degrees-of-freedom in the triaxial table are suppressed (controlled to be zero). Since all four tables were used synchronously in this experiment and required to apply the same motion to all supports, only bidirectional earthquake motions (x- and y- directions) were used. No vertical component (z-direction) was applied. The selected motions and the test matrix are discussed in the following sections.

### **4.7.1. Ground Motion**

As noted in Section 4.2.1, the prototype bridge was designed for a Site Class B location in an AASHTO Seismic Zone 3 with a PGA of 0.47g,  $S_s = 1.14g$ , and  $S_1 = 0.41g$ . For the shake table study, the input ground motion was taken to be the Sylmar record from the 1994 Northridge Earthquake near Los Angeles, California, scaled to fit the AASHTO design spectrum given above. The method of scaling was based on equal spectral accelerations at 1.0 sec period (which is close to the fundamental period of the prototype bridge). This led to a scale factor of 0.475, which was applied to both the NS (North-South) and EW (East-West) components of the acceleration record from this station.

The accelerograms in the longitudinal (NS component) and transverse (EW component) directions are shown in Figure 4.7.1. To generate records for lower or higher

levels of excitation than the design level earthquake (DE), the accelerations at each time step were scaled accordingly.

It is important to note that the time axis of this record is scaled by a factor of 0.6325 ( $= 1/\sqrt{S_L} = 1/\sqrt{2.5} = \sqrt{0.4}$ ) to satisfy the similitude requirements given in Table 4.2.3. This means that the accelerograms used as excitation for the model have shorter duration and higher frequency content compared to the original unmodified accelerograms.

Before each run and after the last run, low amplitude white noise excitation was applied in the longitudinal and transverse directions of the bridge to characterize the dynamic properties of the bridge and changes in these properties with increasing levels of excitation. Based on the fundamental frequency of the bridge, the white noise frequency was selected to be in the range of 0 to 10 Hz.

#### **4.7.2. Test Matrix**

Based on the results of analytical modeling a set of input table motions was developed to give insight into bridge behavior for intensities ranging from very small to very large, where the upper limit was set by either the safety of the specimen or the capacity of the tables for extreme motions.

The test protocol therefore started at 10% of the design level earthquake (DE) to obtain the response of the bridge in the elastic state. The amplitude of the motion was then increased in increments to obtain response at 10, 20, 50, 75, and 100% of the DE followed by 150, 200, 250, 300, and 350% of the DE. Note that the DE is 0.475 of the Sylmar record (Section 4.7.1) and therefore 200% of the DE is about equal to the Sylmar ground motion. The complete test matrix is given in Table 4.7.1. Not all tests ran the full sequence, i.e., up to 350% DE. Some were terminated earlier for reasons of safety and/or protection of the shake tables or ancillary equipment.

#### **4.8. Summary**

The selection of the prototype bridge and design of the model has been presented in this chapter. The construction and instrumentation of the model has also been described, together with the selection, placement, and instrumentation of the vehicles. Finally, the selected ground motion has been described and the test matrix presented.

**Table 4.2.1. AASHTO Load Combinations and Load Factors (AASHTO, 2007)**

Load Combination Limit State	DC DD DW EH EV ES EL PS CR SH	LL IM CE BR PL LS	WA	WS	WL	FR	TU	TG	SE	Use One of These at a Time			
										EQ	IC	CI	CV
Strength I (unless noted)	$\gamma_p$	1.75	1.00	—	—	1.00	0.50/1.20	$\gamma_{TG}$	$\gamma_{SE}$	—	—	—	—
Strength II	$\gamma_p$	1.35	1.00	—	—	1.00	0.50/1.20	$\gamma_{TG}$	$\gamma_{SE}$	—	—	—	—
Strength III	$\gamma_p$	—	1.00	1.40	—	1.00	0.50/1.20	$\gamma_{TG}$	$\gamma_{SE}$	—	—	—	—
Strength IV	$\gamma_p$	—	1.00	—	—	1.00	0.50/1.20	—	—	—	—	—	—
Strength V	$\gamma_p$	1.35	1.00	0.40	1.0	1.00	0.50/1.20	$\gamma_{TG}$	$\gamma_{SE}$	—	—	—	—
Extreme Event I	$\gamma_p$	$\gamma_{EQ}$	1.00	—	—	1.00	—	—	—	1.00	—	—	—
Extreme Event II	$\gamma_p$	0.50	1.00	—	—	1.00	—	—	—	—	1.00	1.00	1.00
Service I	1.00	1.00	1.00	0.30	1.0	1.00	1.00/1.20	$\gamma_{TG}$	$\gamma_{SE}$	—	—	—	—
Service II	1.00	1.30	1.00	—	—	1.00	1.00/1.20	—	—	—	—	—	—
Service III	1.00	0.80	1.00	—	—	1.00	1.00/1.20	$\gamma_{TG}$	$\gamma_{SE}$	—	—	—	—
Service IV	1.00	—	1.00	0.70	—	1.00	1.00/1.20	—	1.0	—	—	—	—
Fatigue I—LL, IM & CE only	—	1.50	—	—	—	—	—	—	—	—	—	—	—
Fatigue I II— LL, IM & CE only	—	0.75	—	—	—	—	—	—	—	—	—	—	—

**Table 4.2.2. Bridge Geometry**

Parameter	Prototype	Model
Total Length	362'-6"	145'-0"
Span Lengths	105'-0", 152'-6", 105'-0"	42'-0", 61'-0", 42'-0"
Radius at Centerline	200'-0"	80'-0"
Subtended Angle	104° (1.8 rad)	104° (1.8 rad)
Total Width	30'-0"	12'-0"
Girder Spacing	11'-3"	4'-6"
Total Superstructure Depth	6'-6 $\frac{1}{8}$ "	2'-7 $\frac{1}{4}$ "
Column Height	19'-2"	7'-8"
Column Diameter	5'-0"	2'-0"

**Table 4.2.3. Scale Factors for Similitude Requirements**

<b>Parameter</b>	<b>Symbol</b>	<b>Scale Factor</b>	<b>Value Used in Experiment</b>
Length	L	$L_p/L_M = S_L$	2.5
Modulus of Elasticity	E	$S_E$	1
Mass Density	$\rho$	$S_\rho$	1
Area	A	$S_L^2$	6.25
Volume	V	$S_L^3$	15.625
Mass (bare model)	$m_b$	$S_\rho S_L^3$	15.625
Mass (model with added mass) <sup>1</sup>	m	$S_L^2$	6.25
Displacement	d	$S_L$	2.5
Velocity	v	$\sqrt{(S_a S_L)}$	1.581
Acceleration	a	$S_a$	1
Acceleration due to gravity	g	$S_g$	1
Weight (bare model)	$W_b$	$S_\rho S_L^3 S_g$	15.625
Weight (model with added mass) <sup>1</sup>	W	$S_L^2$	6.25
Force	F	$S_\sigma S_L^2$	6.25
Moment	M	$S_\sigma S_L^3$	15.625
Stress	$\sigma$	$S_\sigma$	1
Strain	$\epsilon$	$S_\epsilon$	1
Time	t	$\sqrt{(S_L / S_a)}$	1.581
Frequency	f	$\sqrt{(S_a / S_L)}$	0.6325

- Note: 1. Added mass =  $(S_a S_L - 1) m_b = 1.5 m_b$  in this experiment  
 2. Scale factors are expressed as prototype value / model value, e.g.  $S_L = L_p/L_M$ .  
 Can also be expressed by the inverse relationship, e.g.  $\lambda_L = L_M/L_p$ .

**Table 4.3.1. Properties of Steel Reinforcement (AASHTO, 2007)**

Property	Notation	Bar Size	ASTM A706
Specified Minimum Yield Stress (ksi)	$f_y$	#3 - #18	60
Expected Yield Stress (ksi)	$f_{ye}$	#3 - #18	68
Expected Tensile Strength (ksi)	$f_{ue}$	#3 - #18	95
Expected Yield Strain	$\epsilon_{ye}$	#3 - #18	0.0023
		#3 - #8	0.0150
		#9	0.0125
		#10 - #11	0.0115
		#14	0.0075
Onset of Strain Hardening	$\epsilon_{sh}$	#18	0.0050
		#4 - #10	0.090
		#11 - #18	0.060
		#4 - #10	0.120
Ultimate Tensile Strain	$\epsilon_{su}$	#11 - #18	0.090

**Table 4.3.2. Bridge Weight**

Prototype			
Superstructure	=	1670 k	(4.61 k/ft)
Bent Cap	=	220 k	(110 k/bent)
Column	=	112.9 k	(56.45 k/bent)
Total Prototype Weight	=	2002.9 k	
Model			
Superstructure	=	107 k	(0.74 k/ft)
Superstructure Added Weight	=	167.39 k	(Provided)
	=	160.53 k	(Required)
Bent Cap	=	12.24 k	(6.12 k/bent)
Column	=	7.22 k	(3.61 k/bent)
Substructure Added Weight	=	24.18 k	(12.09k/bent)
Total Model Weight	=	318.06 k	

**Table 4.3.3. Bridge Instrumentation List**

<b>Project Name Legend</b>			
<b>Instrument/Direction</b>		<b>Global Location</b>	
ACX	acc in x	NA	North Abut
ACY	acc in y	SA	South Abut
ACZ	acc in z	NB	North Bent
ACT	acc in tangential	SB	South Bent
ACR	acc in radial	NS	North Span
DTT	local disp in tangential	MS	Mid Span
DTZ	local disp in z	SS	South Span
DTC	local disp in cross frame	NC	North Splice Connection
SPX	global disp in x	SC	South Splice Connection
SPY	global disp in y		
SPZ	global disp in z		
SGB	strain gage bent		
SGX	strain gage cross frame		
BLC	Bearing Load Cell		
SLC	Shear Key Load Cell		
PLC	Pounding Load Cell		
<b>Local Location</b>		<b>Secondary Locations</b>	
IG	Inner Girder	WT	Wall Top
MG	Middle Girder	WB	Wall Bottom
OG	Outer Girder	AX	axial
IE	Inner Edge	VR	shear in radial
OE	Outer Edge	VT	shear in tangential
IB	Inner Bay	MR	moment about radial
OB	Outer Bay	MT	moment about tangential
LB	Longitudinal bar	TN	Top North Column
SB	Spiral Bar	TE	Top East Column
BS	Bond Slip	TS	Top South Column
LH	Low Hinge	TW	Top West Column
MH	Middle Hinge	BN	Bottom North Column
TH	Top Hinge	BE	Bottom East Column
IC	Inner Cap	BS	Bottom South Column
OC	Outer Cap	BW	Bottom West Column
AT	Abutment Tower	NC	North Cap
TB	Top of Bent Cap	SC	South Cap

**Table 4.6.1. Vehicle Payload**

<b>Truck Number</b>	<b>Added Weight (lb)</b>
1	2,285
2	2,305
3	2,315
4	2,530
5	2,300
6	2,310

**Table 4.6.2. Vehicle Instrumentation List**

<b>Instrumentation Type</b>	
SP	String Pot (Displacement transducer)
ACC	Accelerometer
<b>Direction</b>	
X	Transverse Direction of Truck (across the width)
Y	Longitudinal Direction of Truck (along the length)
Z	Vertical Direction of Truck
<b>Truck Numbering</b>	
TR1	Truck One
TR2	Truck Two
TR3	Truck Three
TR4	Truck Four
TR5	Truck Five
TR6	Truck Six

**Table 4.7.1. Experiment Test Protocol**

Run #	Earthquake Level	Input Motion					
		N-S			E-W		
		Ground Motion	Scale Factor	Target PGA (g)	Ground Motion	Scale Factor	Target PGA (g)
1w-x	White noise in x-direction						
1w-y	White noise in y-direction						
<b>1</b>	<b>10% Design Earthquake</b>	Syl360	0.0475	0.040	Syl090	0.0475	0.029
2w-x	White noise in x-direction						
2w-y	White noise in y-direction						
<b>2</b>	<b>20% Design Earthquake</b>	Syl360	0.095	0.080	Syl090	0.095	0.057
3w-x	White noise in x-direction						
3w-y	White noise in y-direction						
<b>3</b>	<b>50% Design Earthquake</b>	Syl360	0.2375	0.200	Syl090	0.2375	0.143
4w-x	White noise in x-direction						
4w-y	White noise in y-direction						
<b>4</b>	<b>75% Design Earthquake</b>	Syl360	0.35625	0.300	Syl090	0.35625	0.215
5w-x	White noise in x-direction						
5w-y	White noise in y-direction						
<b>5</b>	<b>100% Design Earthquake (DE)</b>	Syl360	0.475	0.400	Syl090	0.475	0.287
6w-x	White noise in x-direction						
6w-y	White noise in y-direction						
<b>6</b>	<b>150% Design Earthquake (MCE)</b>	Syl360	0.7125	0.601	Syl090	0.7125	0.430
7w-x	White noise in x-direction						
7w-y	White noise in y-direction						
<b>7</b>	<b>200% Design Earthquake</b>	Syl360	0.95	0.801	Syl090	0.95	0.574
8w-x	White noise in x-direction						
8w-y	White noise in y-direction						
<b>8</b>	<b>250% Design Earthquake</b>	Syl360	1.1875	1.001	Syl090	1.1875	0.717
9w-x	White noise in x-direction						
9w-y	White noise in y-direction						
<b>9</b>	<b>300% Design Earthquake</b>	Syl360	1.425	1.201	Syl090	1.425	0.861
10w-x	White noise in x-direction						
10w-y	White noise in y-direction						
<b>10</b>	<b>350% Design Earthquake</b>	Syl360	1.6625	1.401	Syl090	1.6625	1.005

Notes: 1.0 x Sylmar360 PGA = 0.843g  
1.0 x Sylmar090 PGA = 0.604 g  
Time scale factor = 0.6325

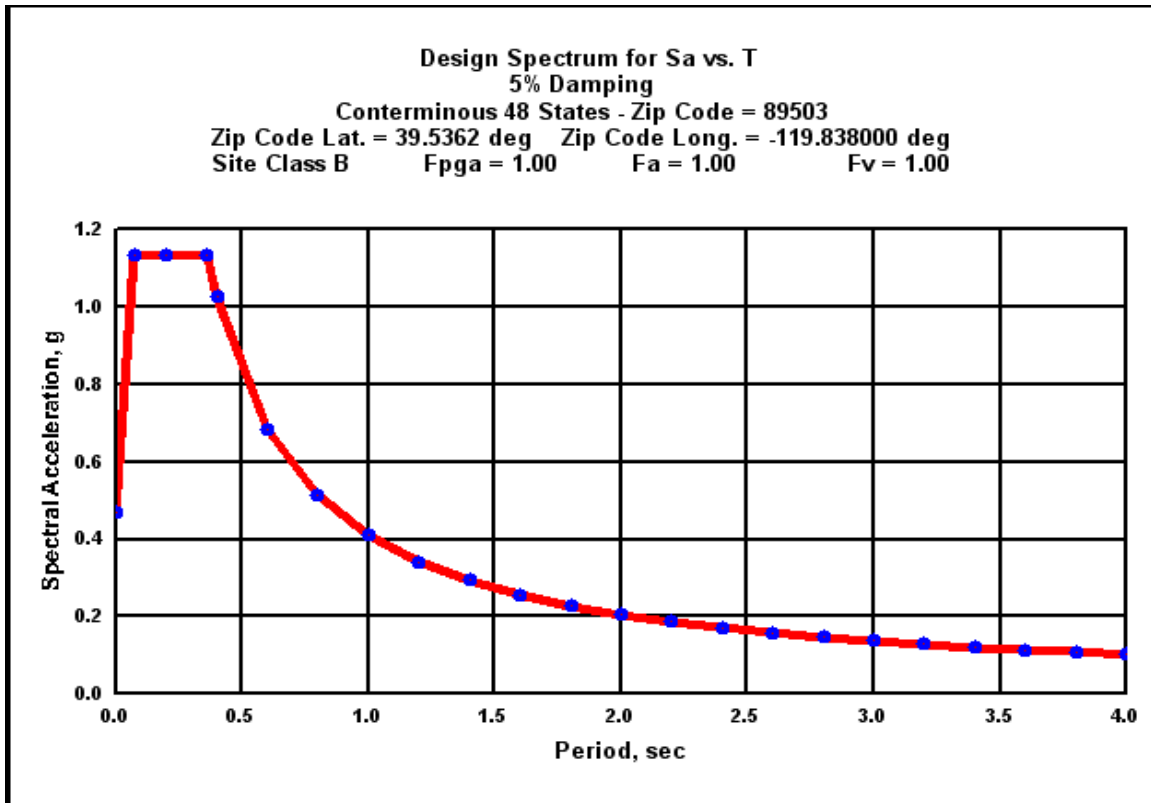


**Figure 4.2.1. Design Response Spectrum**

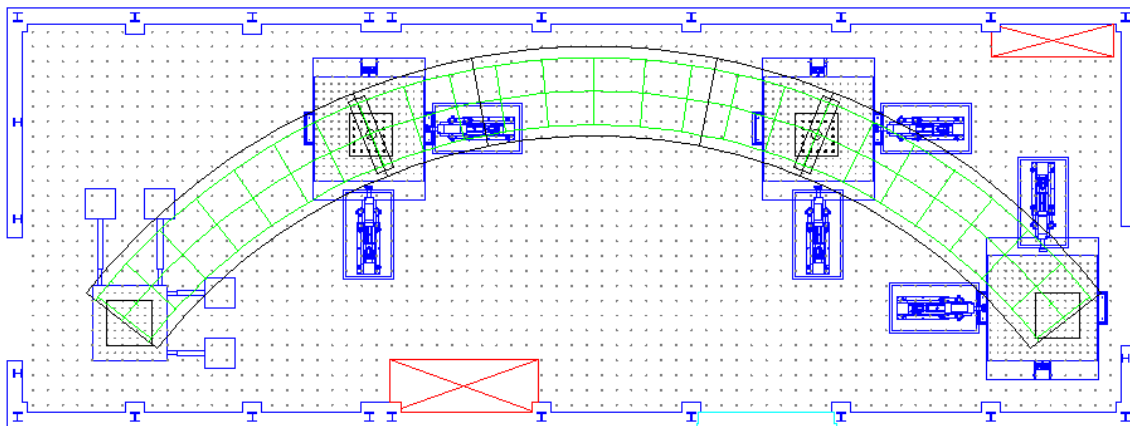


**Figure 4.2.2. Plan View of Bridge Model in the Laboratory**

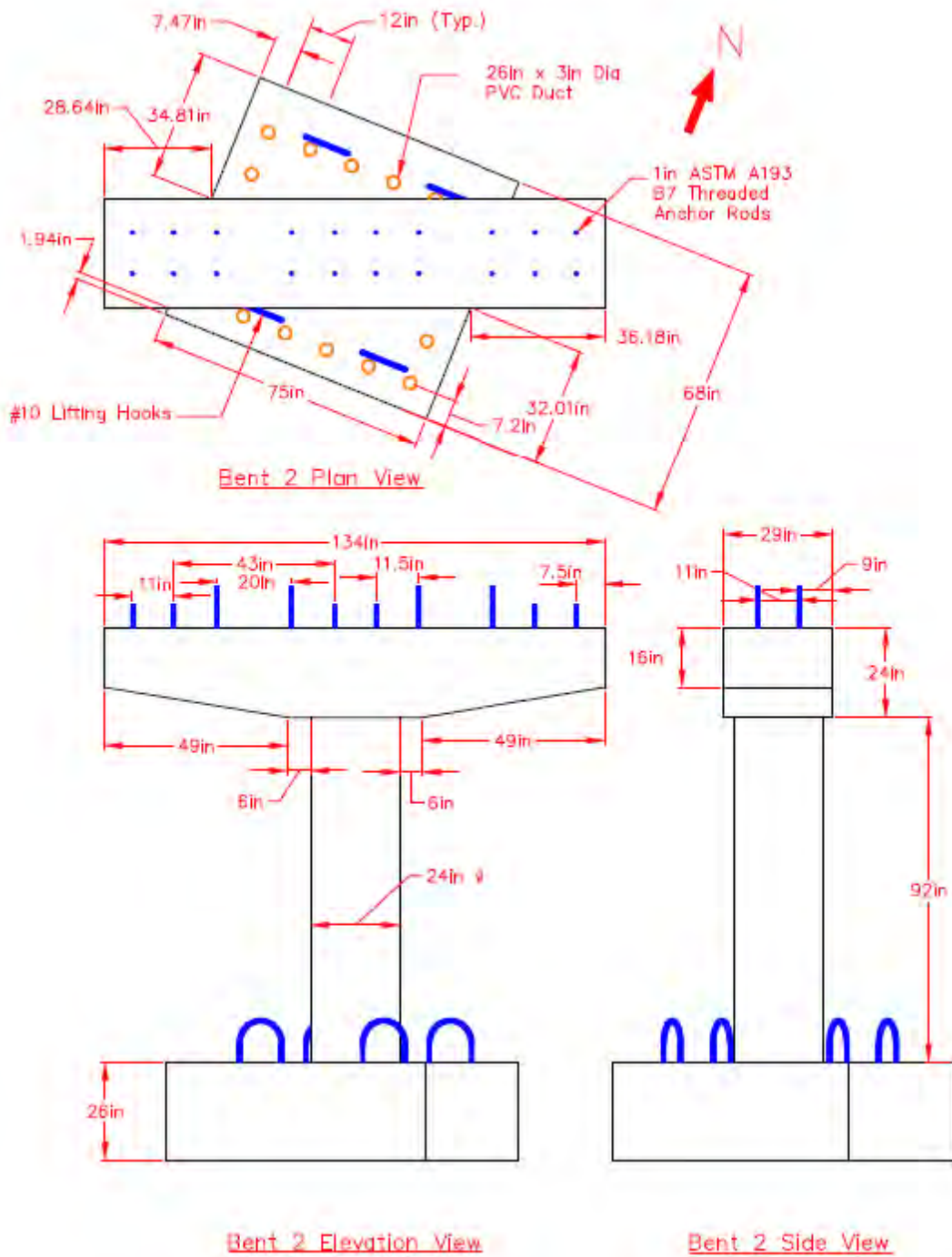


**Figure 4.3.1. Bent 2 Plan and Elevation Views**

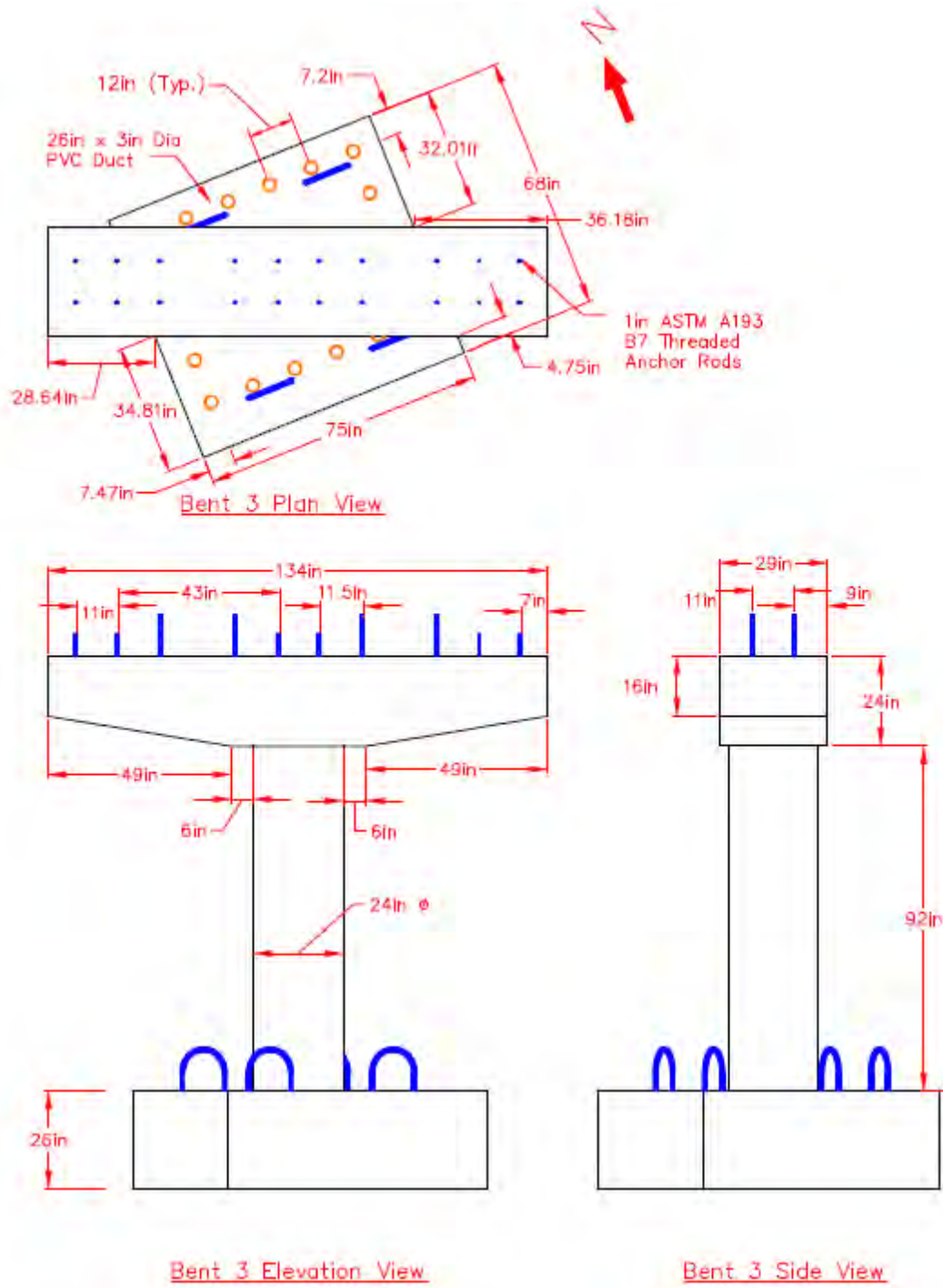


**Figure 4.3.2. Bent 3 Plan and Elevation Views**

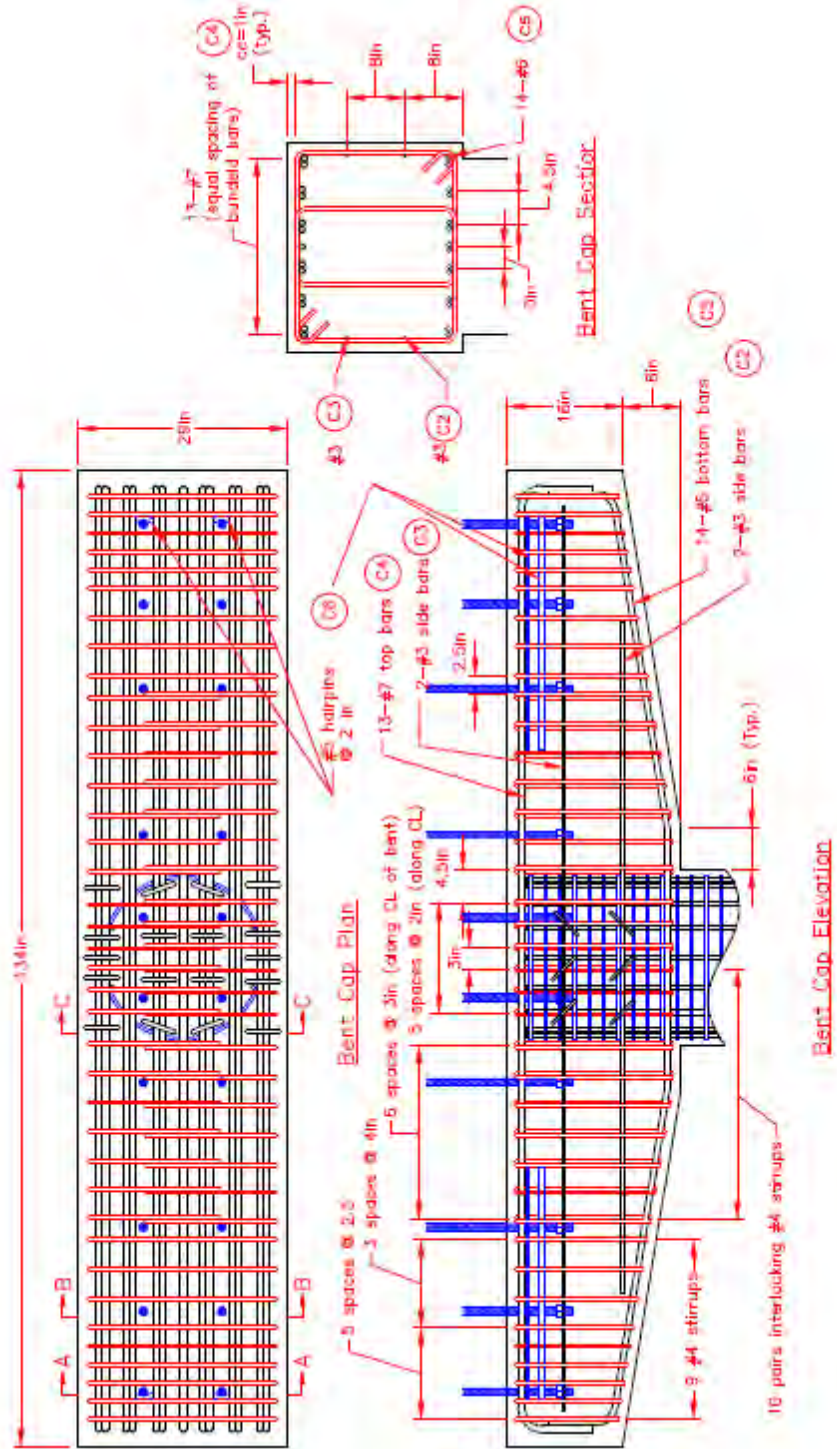


Figure 4.3.3. Typical Bent Cap Details

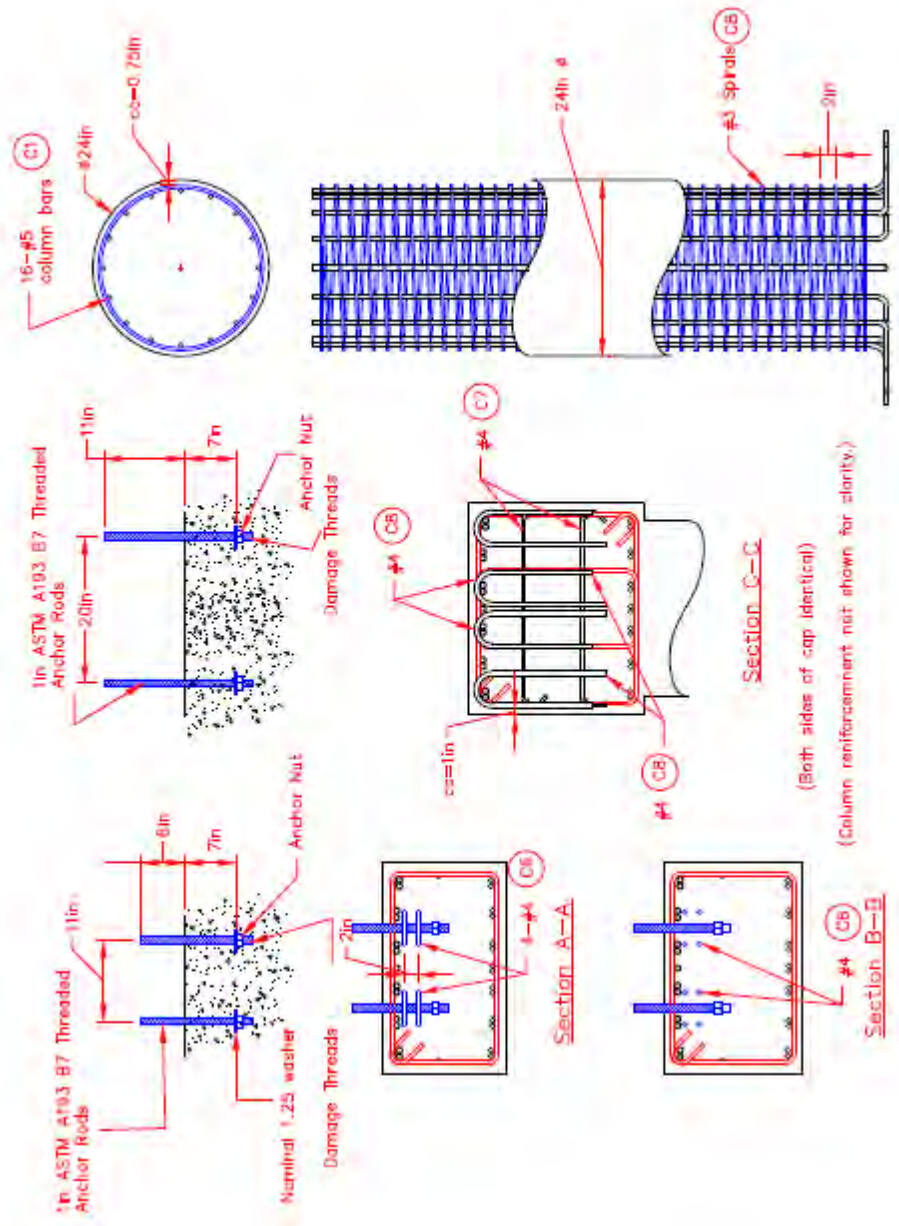


Figure 4.3.4. Bent Cap and Column Sections

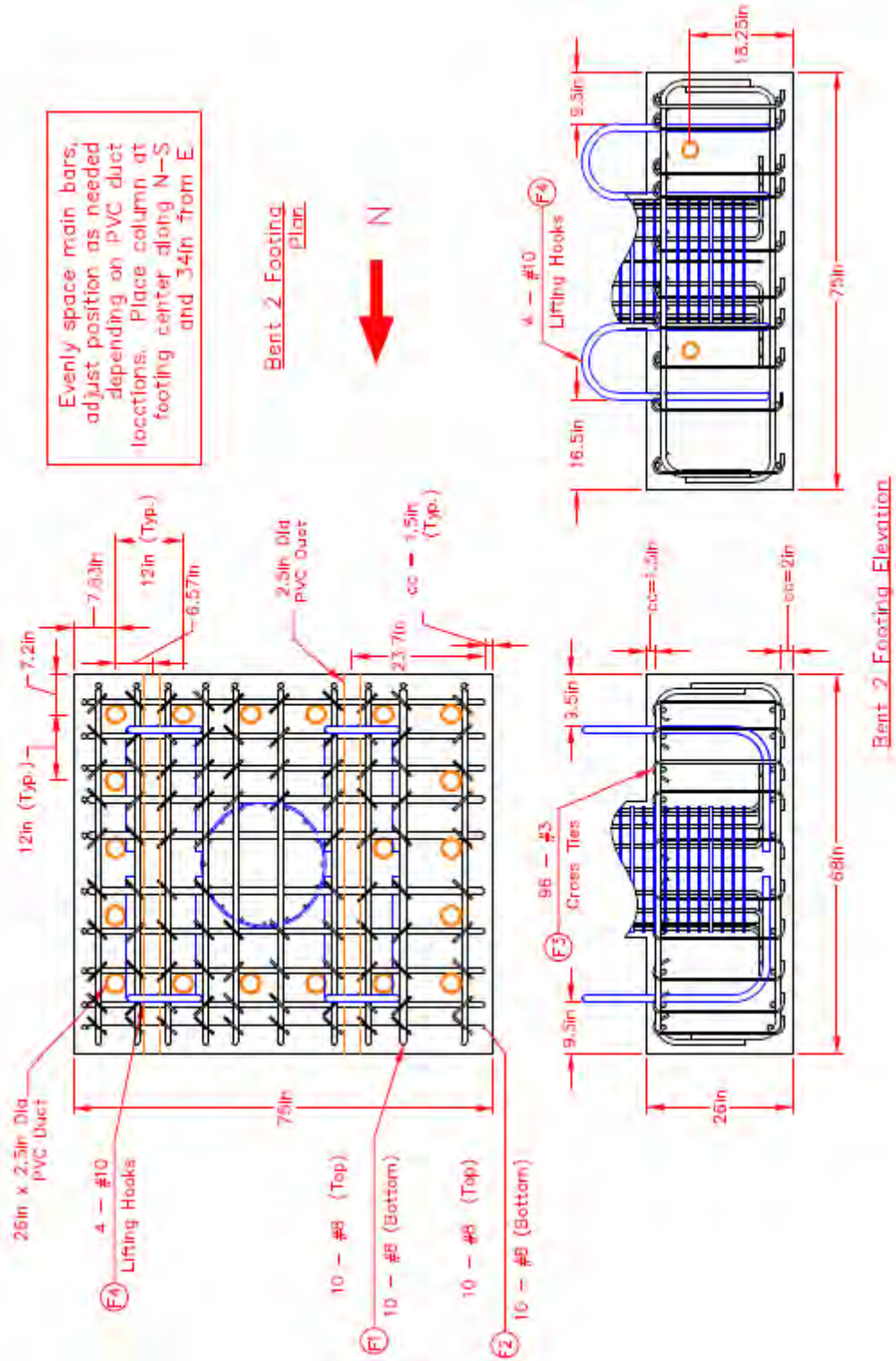


Figure 4.3.5. Bent 2 Footing Details

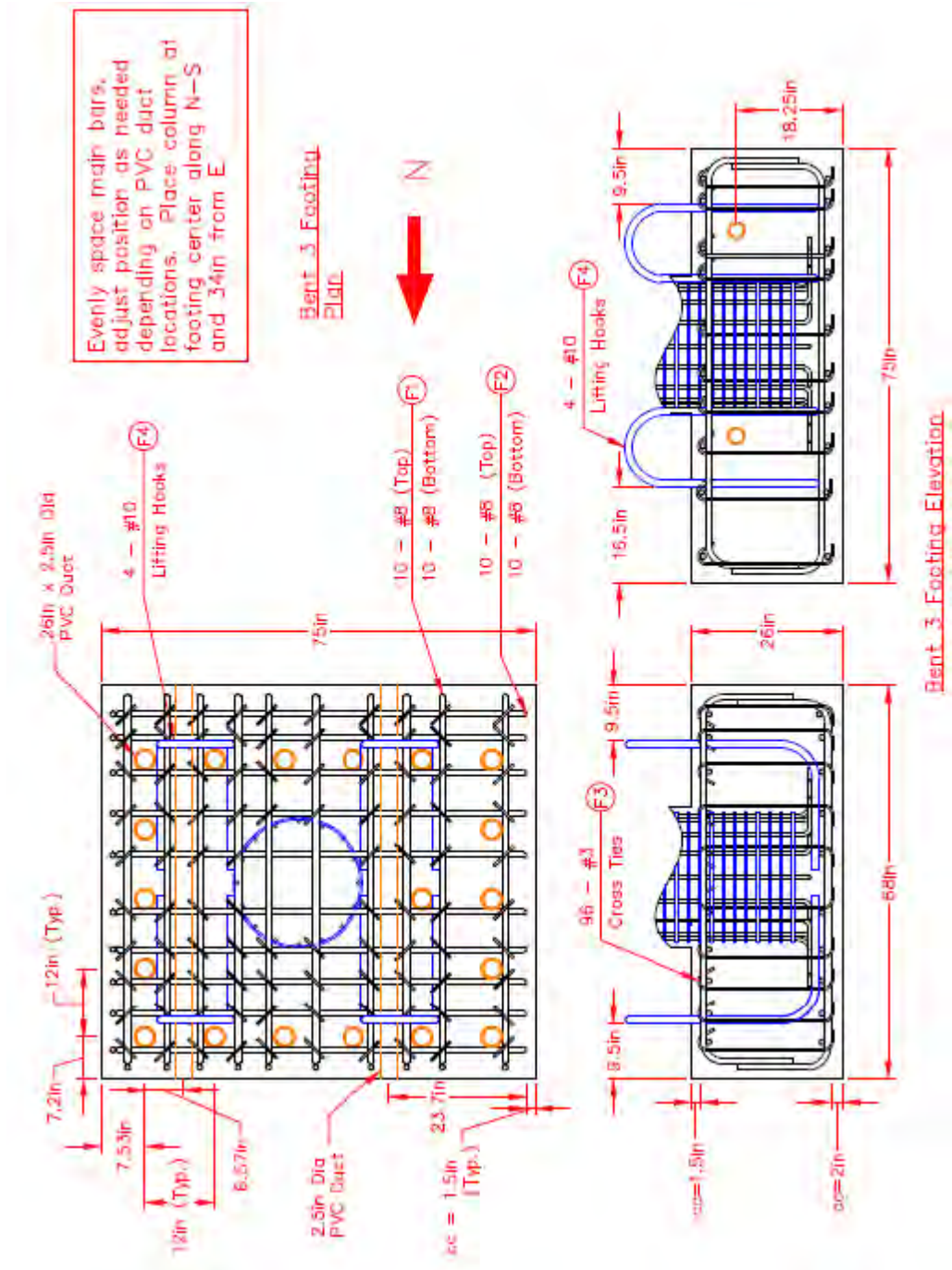


Figure 4.3.6. Bent 3 Footing Details

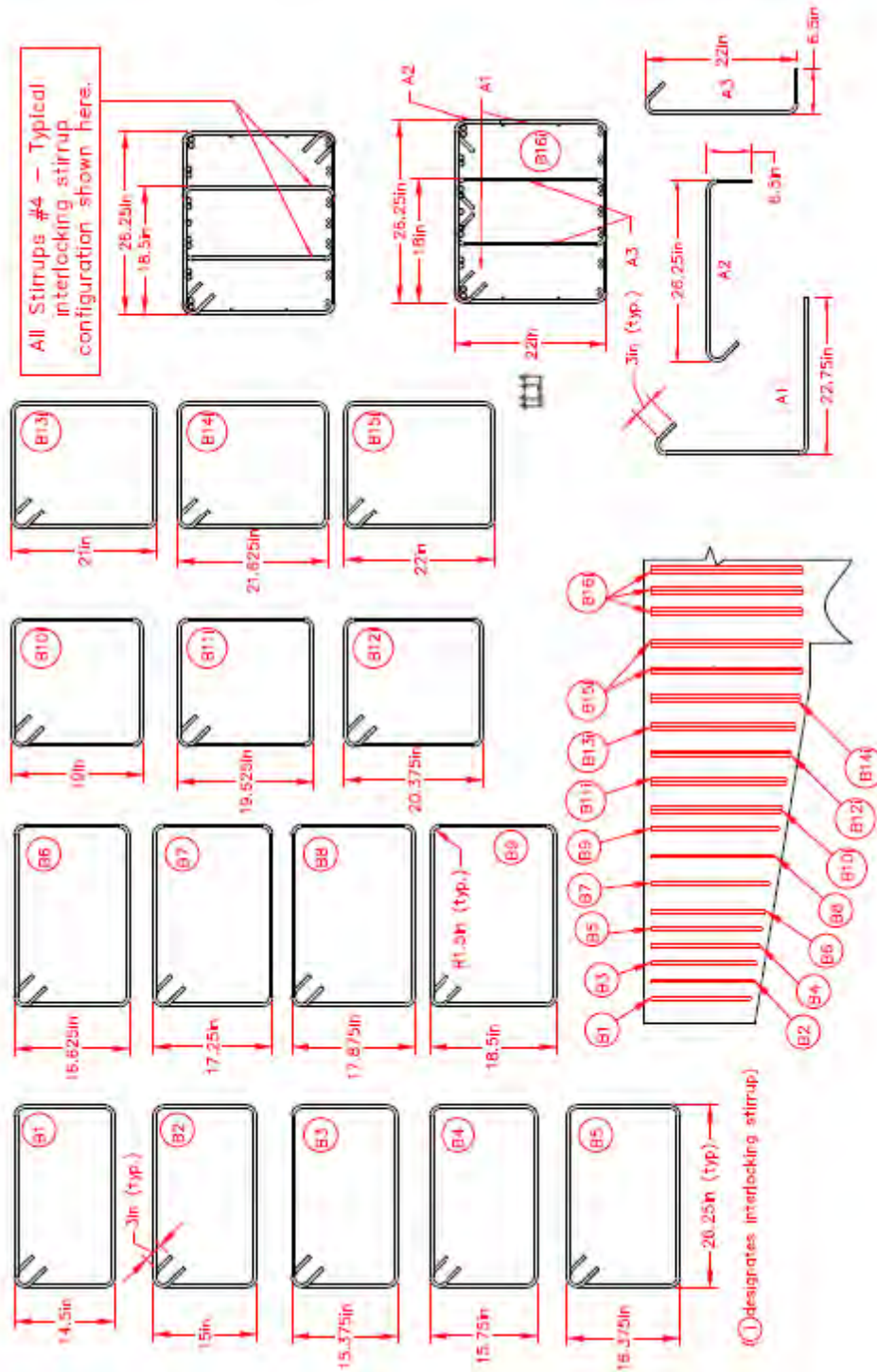
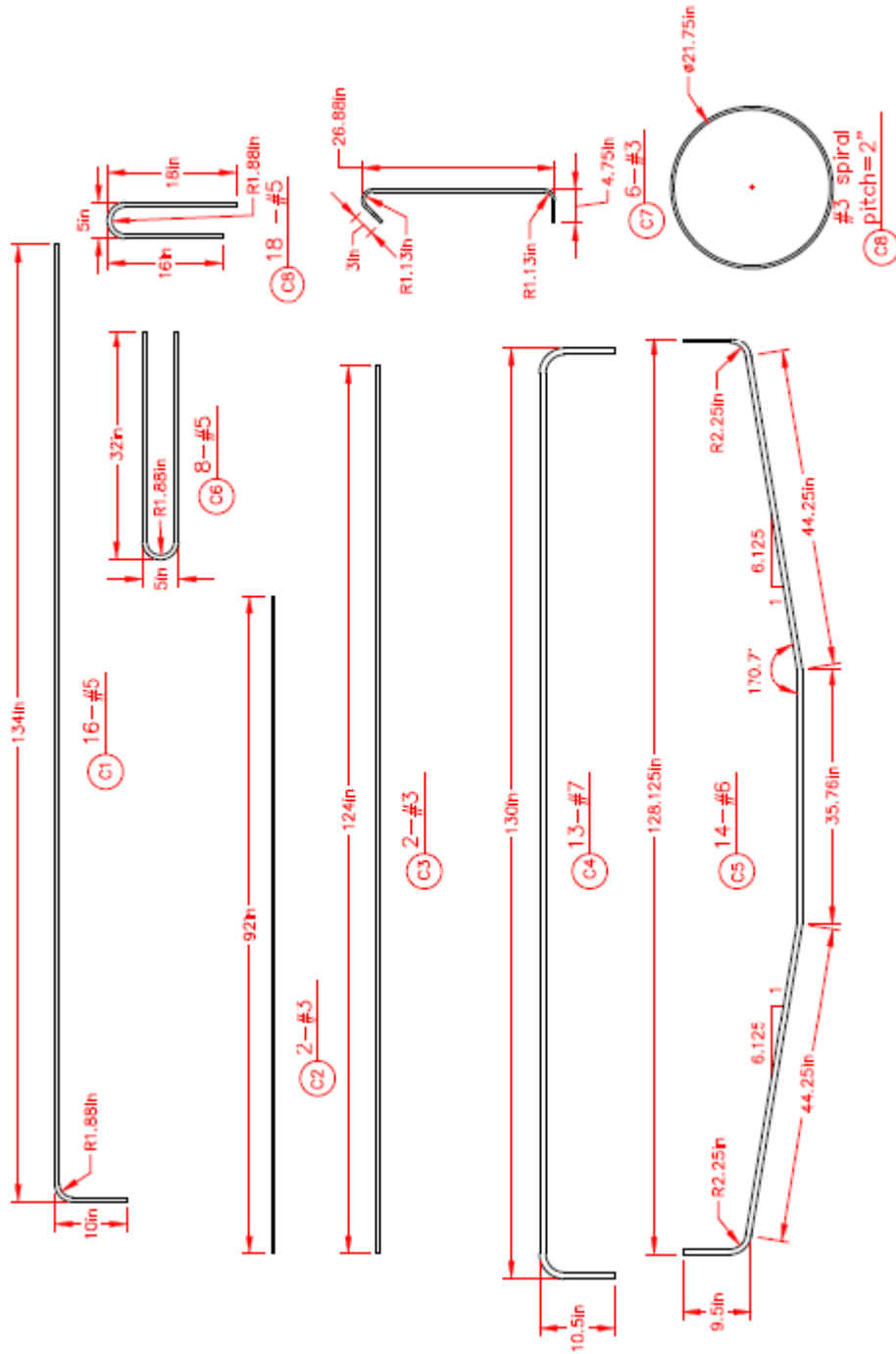
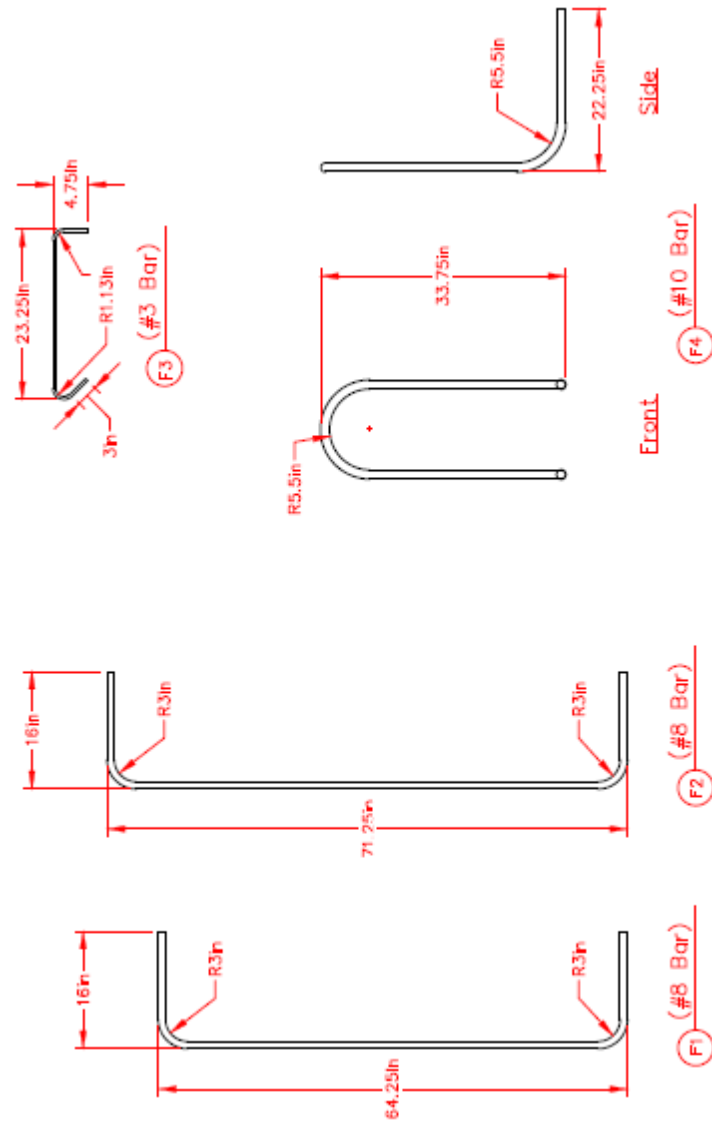


Figure 4.3.7. Bent Cap Stirrups



**Figure 4.3.8. Column and Bent Cap Reinforcement**



**Figure 4.3.9. Footing Reinforcement**

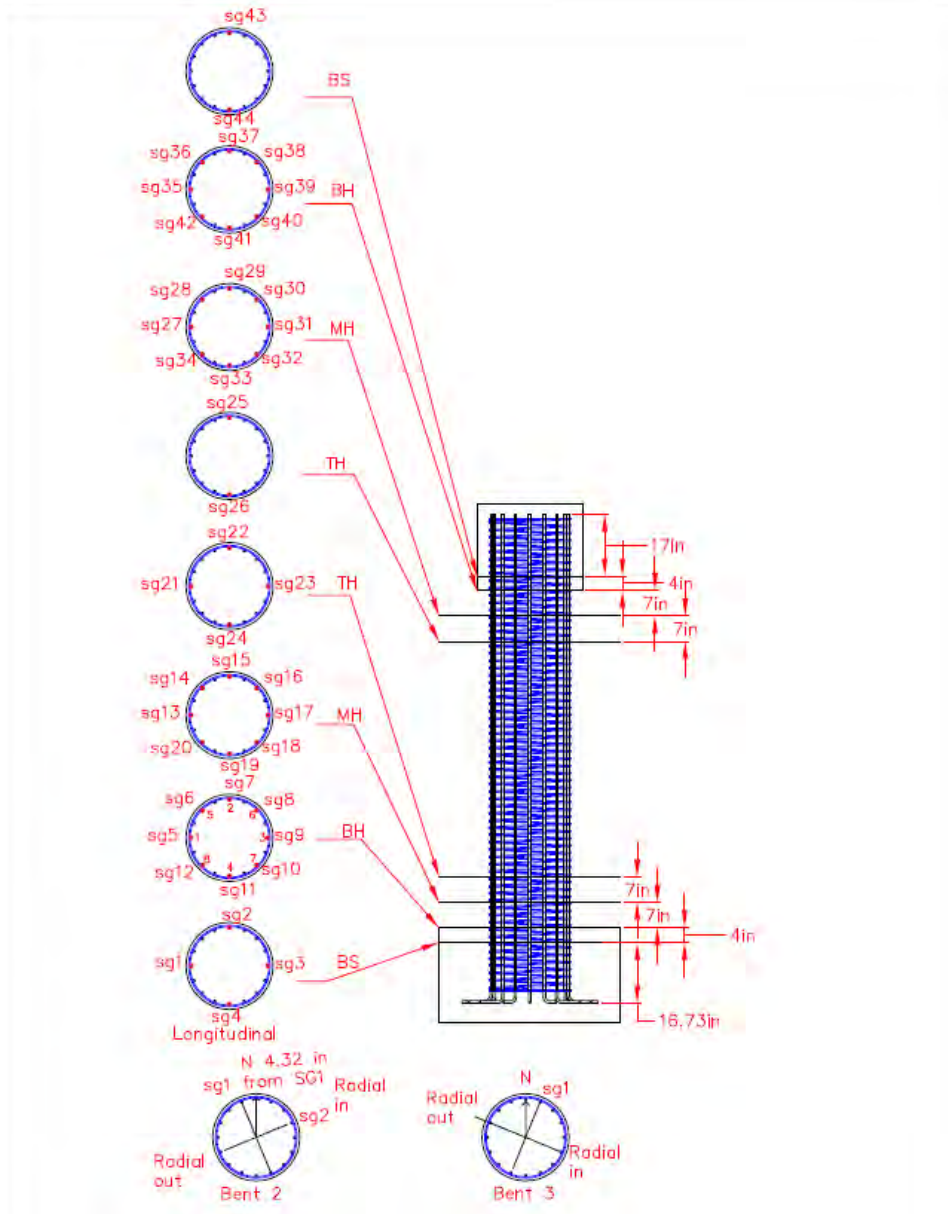


**Figure 4.3.10. Longitudinal Reinforcement Strain Gauge Layout**

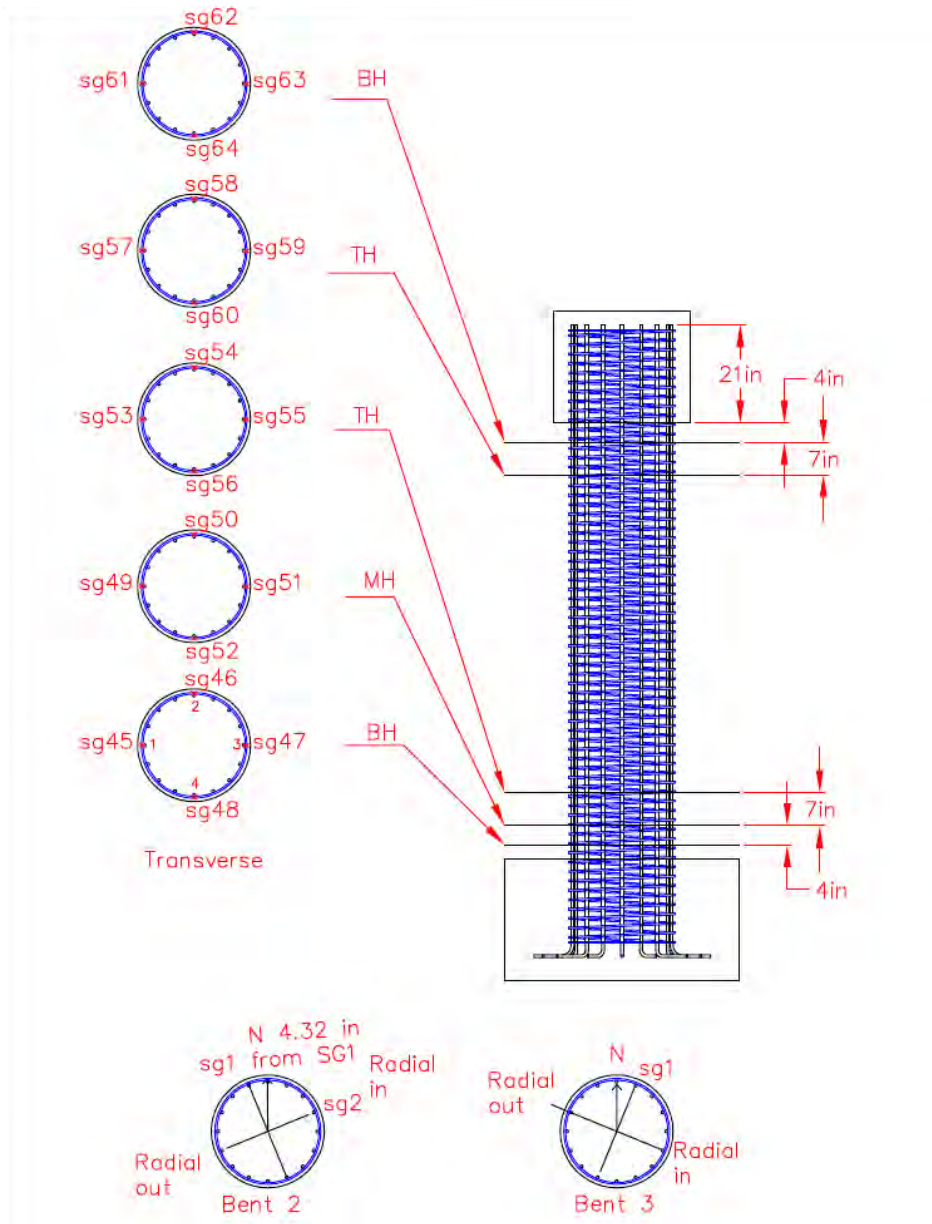


**Figure 4.3.11. Transverse Reinforcement Strain Gauge Layout**

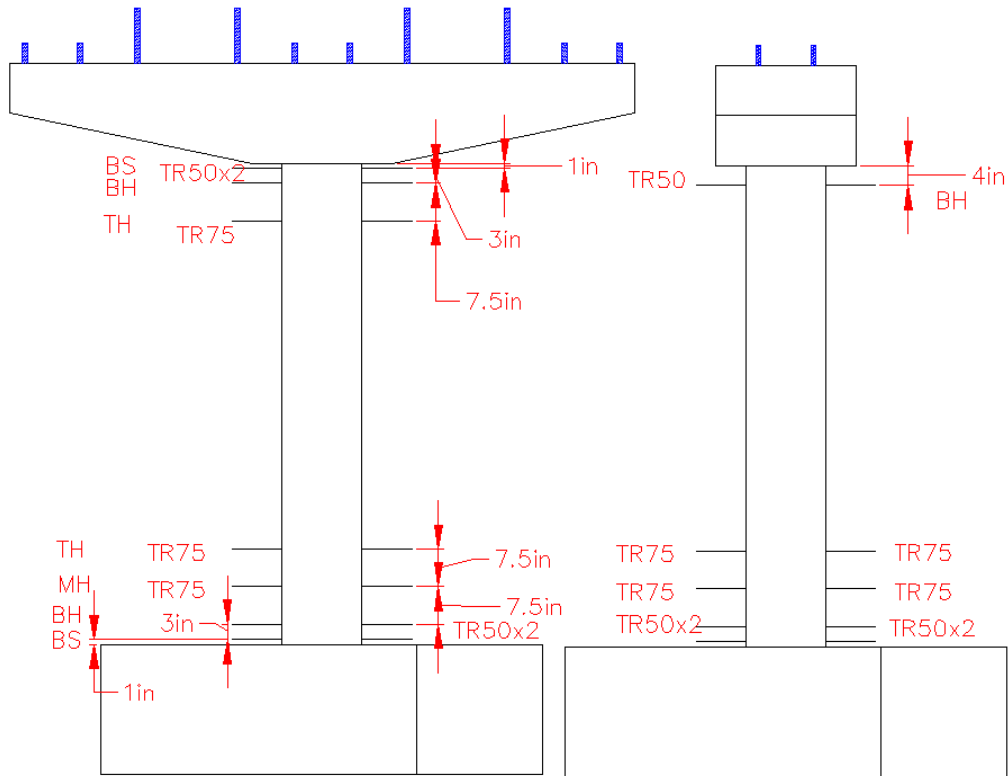


**Figure 4.3.12. Location of Displacement Transducers for Curvature Measurement in Potential Plastic Hinge Zones**

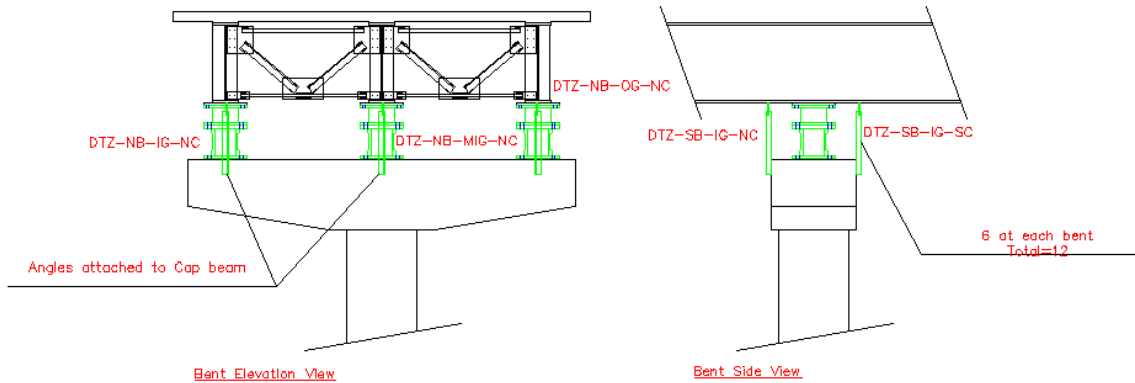


**Figure 4.3.13. Locations of Displacement Transducers for Bent Cap-to-Girder Rotation Measurement**

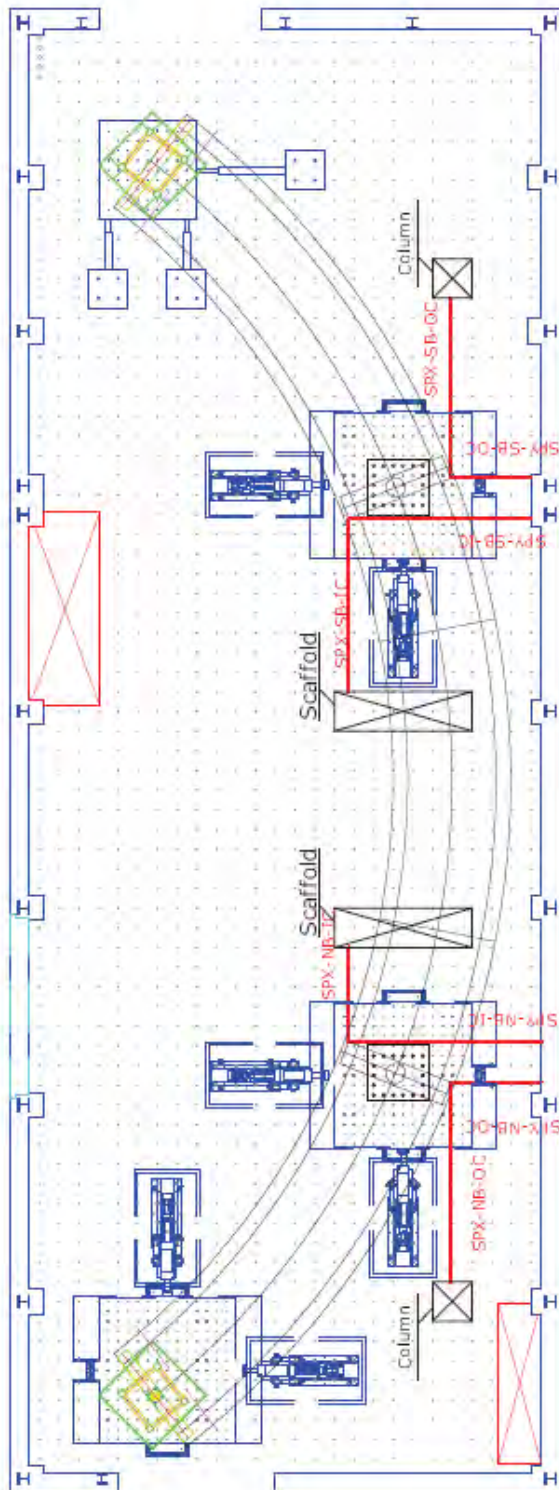


**Figure 4.3.14. Bent Cap Level String Pot Locations**

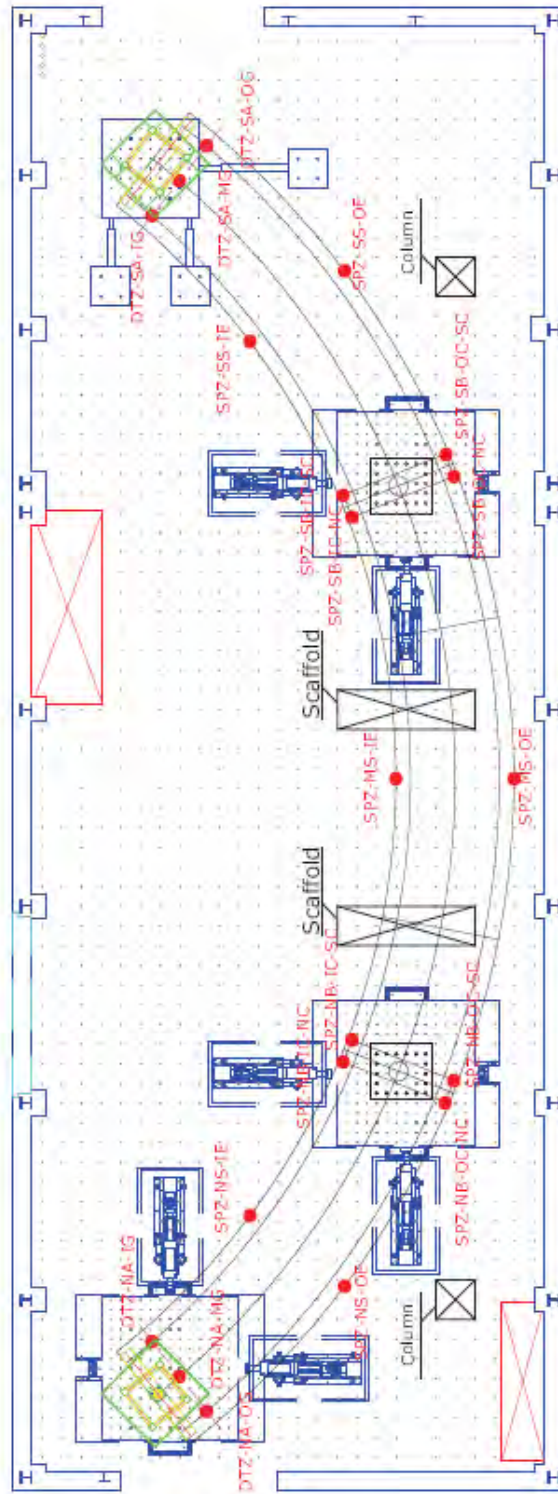


**Figure 4.3.15. Vertical String Pot Locations**

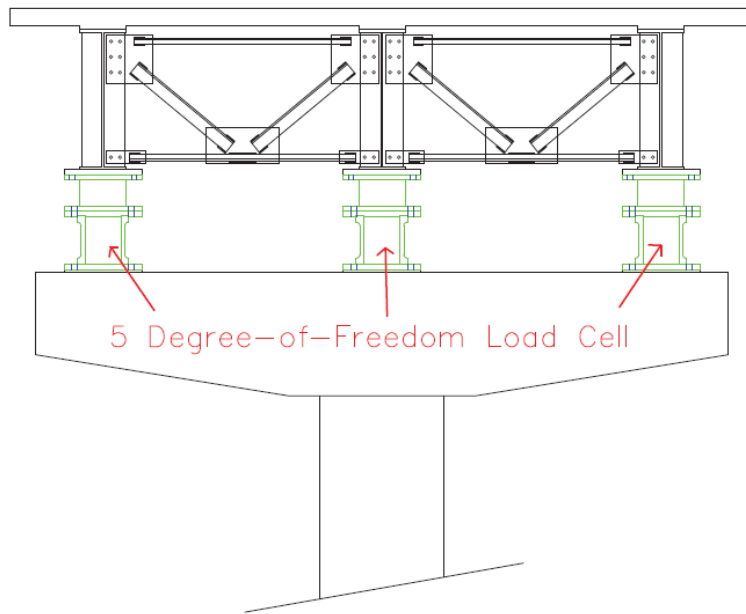


**Figure 4.3.16. 5-Degree-of-Freedom Load Cells Layout at Bent Cap**

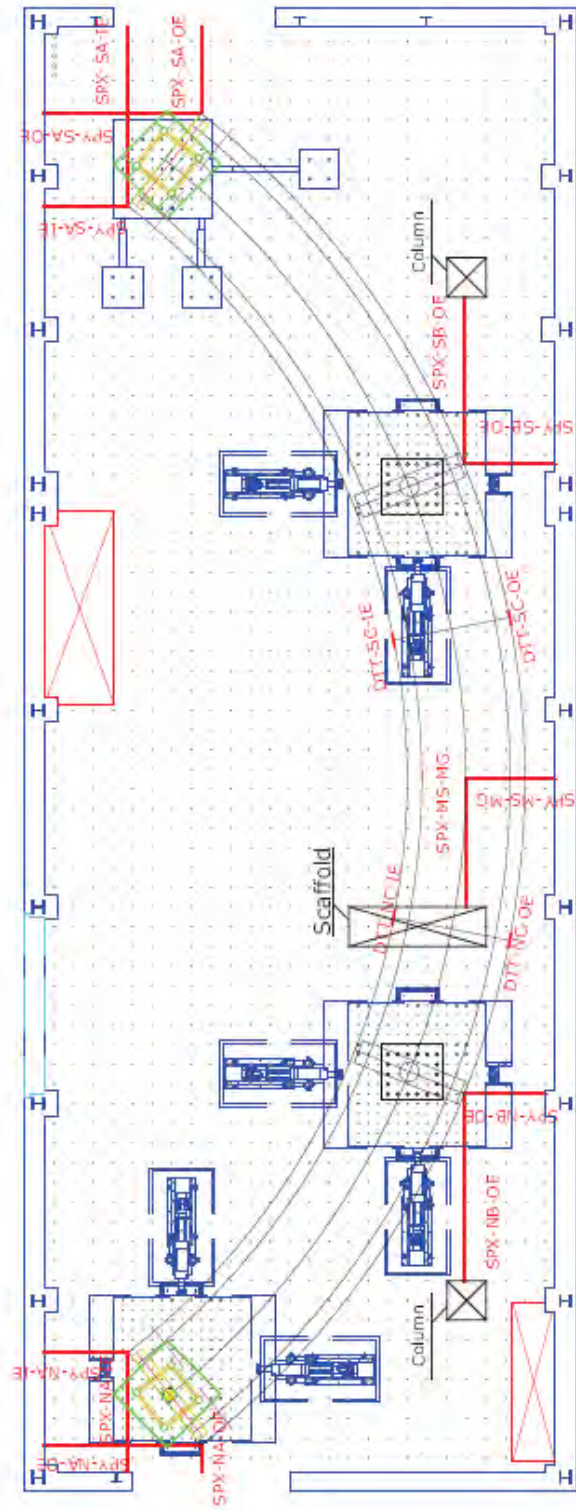
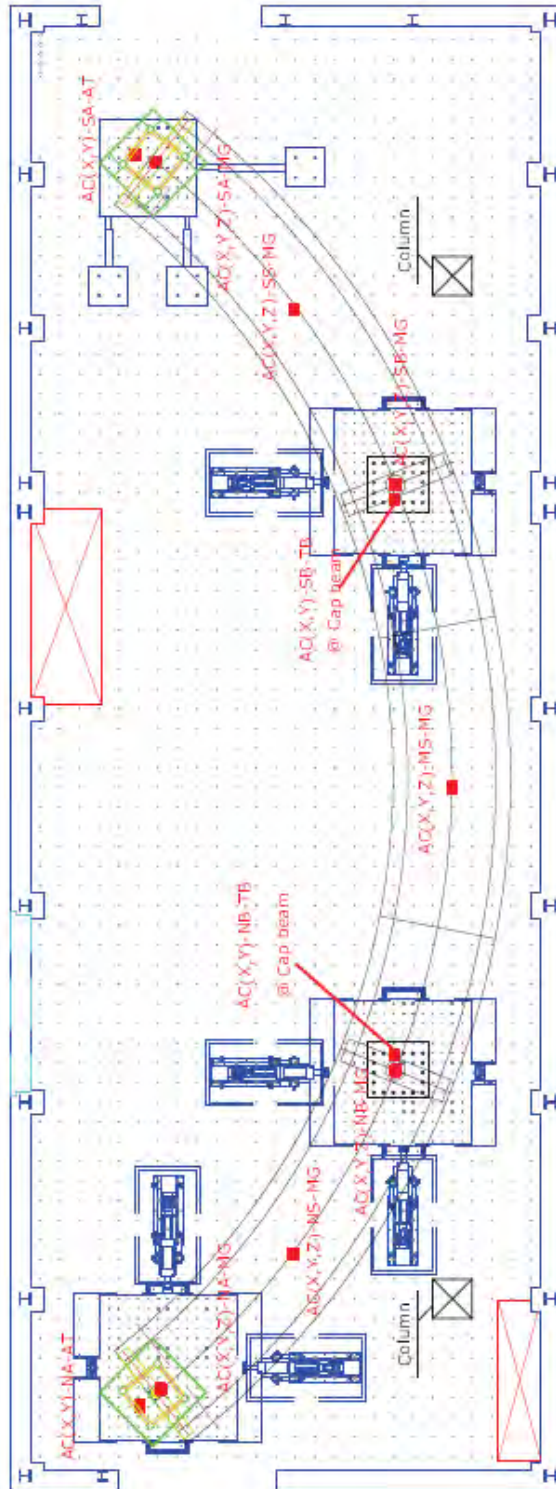
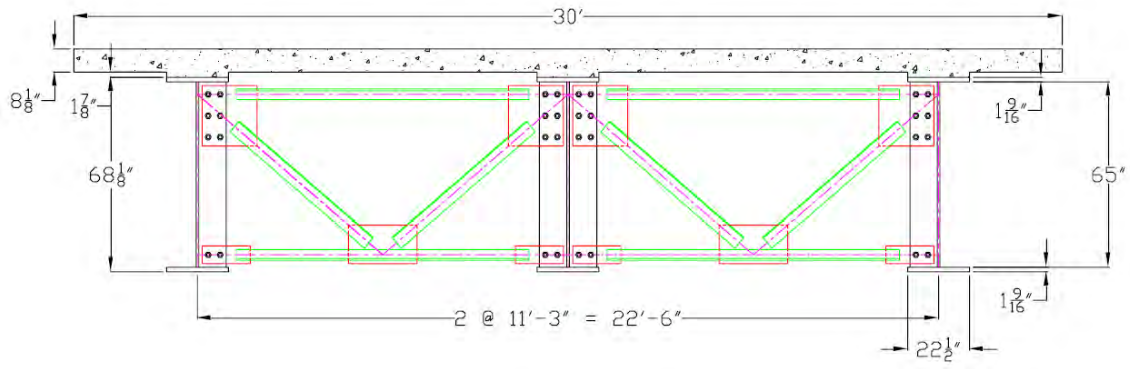


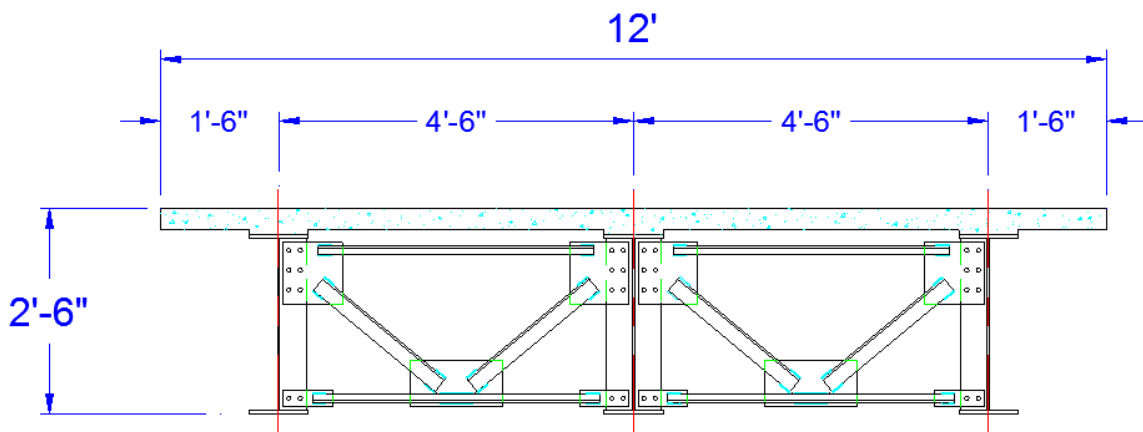
Figure 4.3.17. Deck Level String Pots



**Figure 4.3.18. Accelerometer Layout**



(a)



(b)

Figure 4.4.1. Typical Superstructure Cross-section for (a) Prototype and (b) Model

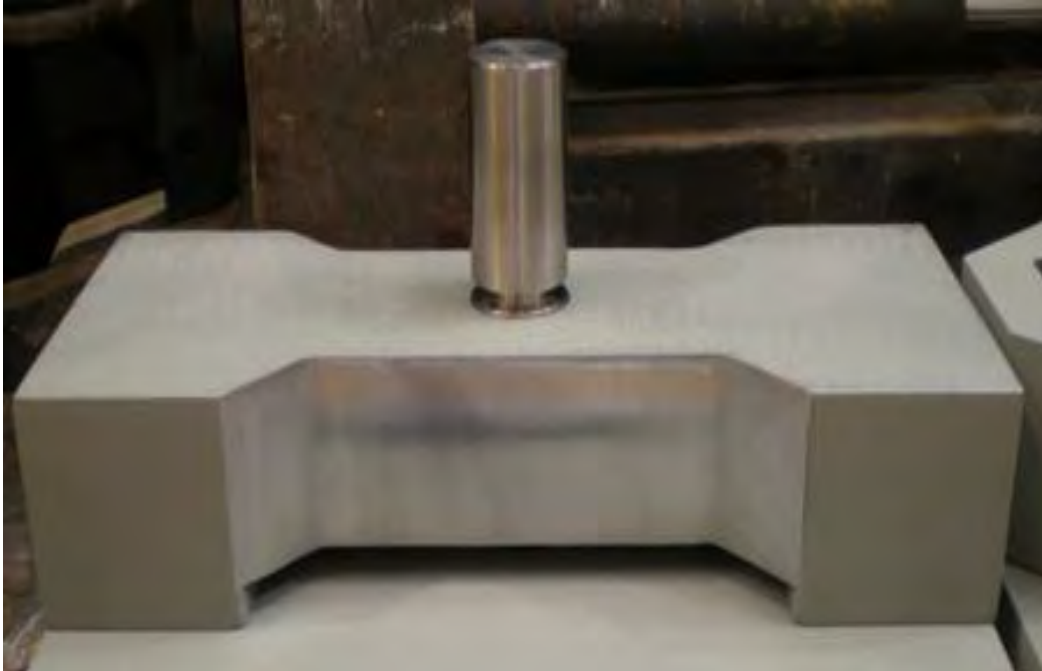


**Figure 4.4.2. Top Half of the Shear Key Assembly ('Dog Bone') and Shear Pin, Shown Upside Down Prior to Assembly**



**Figure 4.4.3. Bottom Half of the Shear Key Assembly Showing Pin in Bushing Located in Longitudinal Slot**



**Figure 4.4.4. Assembled Shear Key Installed Between Bottom Chord of Cross-Frame and Abutment Seat**



**Figure 4.4.5. Left: Plastic Shear Distortion in Shear Pin  
Right: Lower Half of Failed Shear Pin**

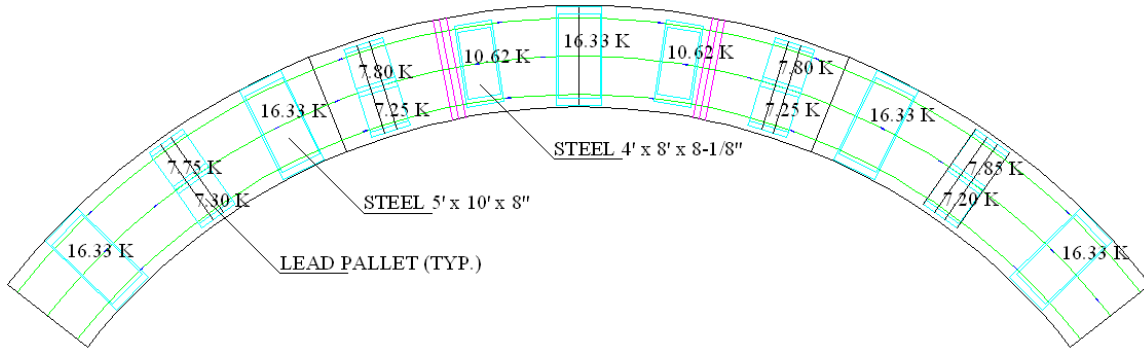


**Figure 4.4.6. Added Weight Layout on Bridge Deck**

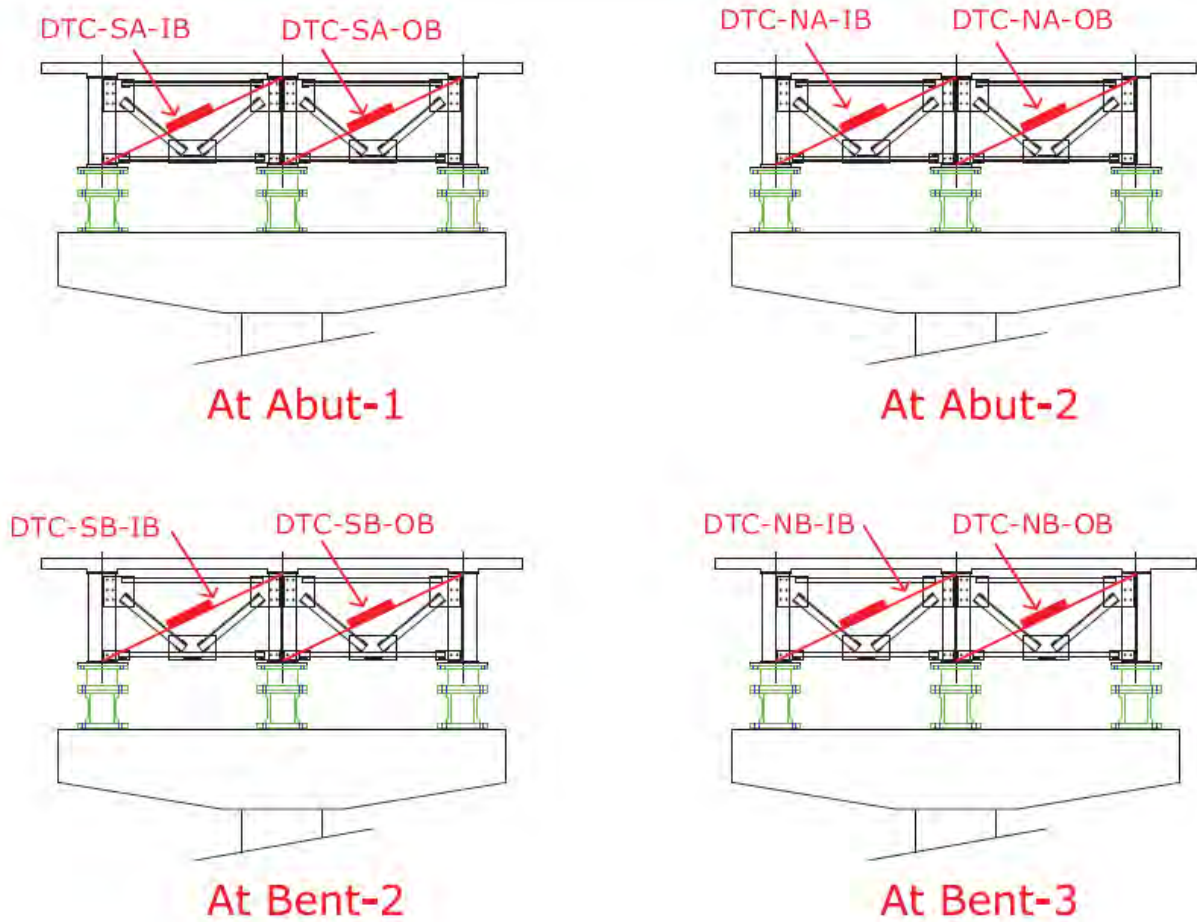


**Figure 4.4.7. Cross Frame Instrumentation**

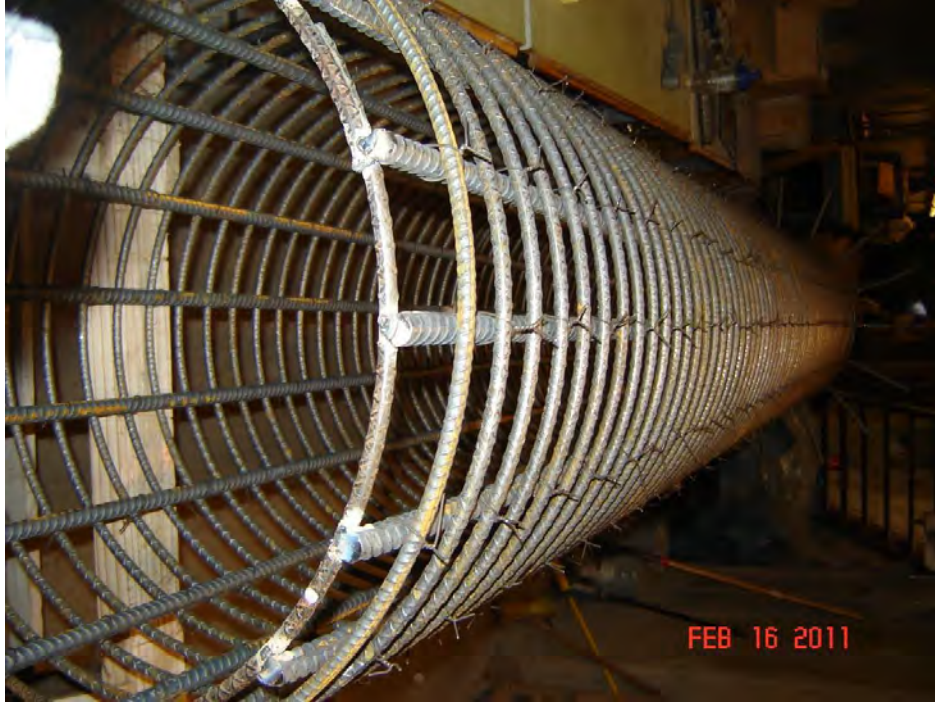


**Figure 4.5.1. Reinforcement Cage during Construction**



**Figure 4.5.2. Column Reinforcement Instrumented with Strain Gauges**



**Figure 4.5.3. Column Reinforcement Cage Placed in Footing Formwork**



**Figure 4.5.4. Cast Footing and Column Reinforcement Cage**



**Figure 4.5.5. Column Formwork and Bent Cap Reinforcement**



**Figure 4.5.6. Concrete Placement for Column and Bent Cap**



**Figure 4.5.7. Completed Single-Column Bents**



**Figure 4.5.8. Anchorage of Abutment Tower on North Shake Table**



**Figure 4.5.9. Single-Column Bent on Shake Table**



**Figure 4.5.10. Added Weight, Load Cells, and Bearings on a Bent Cap**



**Figure 4.5.11. Moving Superstructure Segment into the Laboratory**



**Figure 4.5.12. Placement of North Segment of Superstructure**



**Figure 4.5.13. North Segment of Superstructure in Place**



**Figure 4.5.14. Assembled Bridge Model**



**Figure 4.5.15. Added Weight on the Deck of Instrumented Bridge**

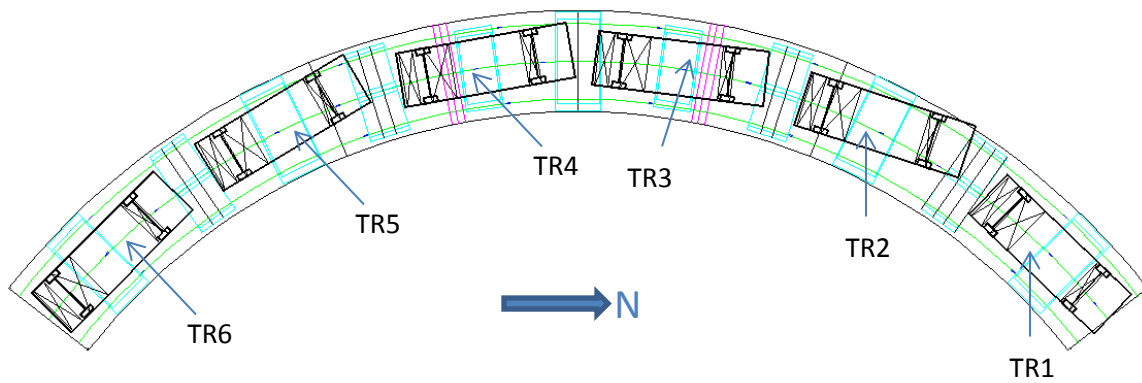


**Figure 4.6.1. Vehicle Layout on Bridge Deck**

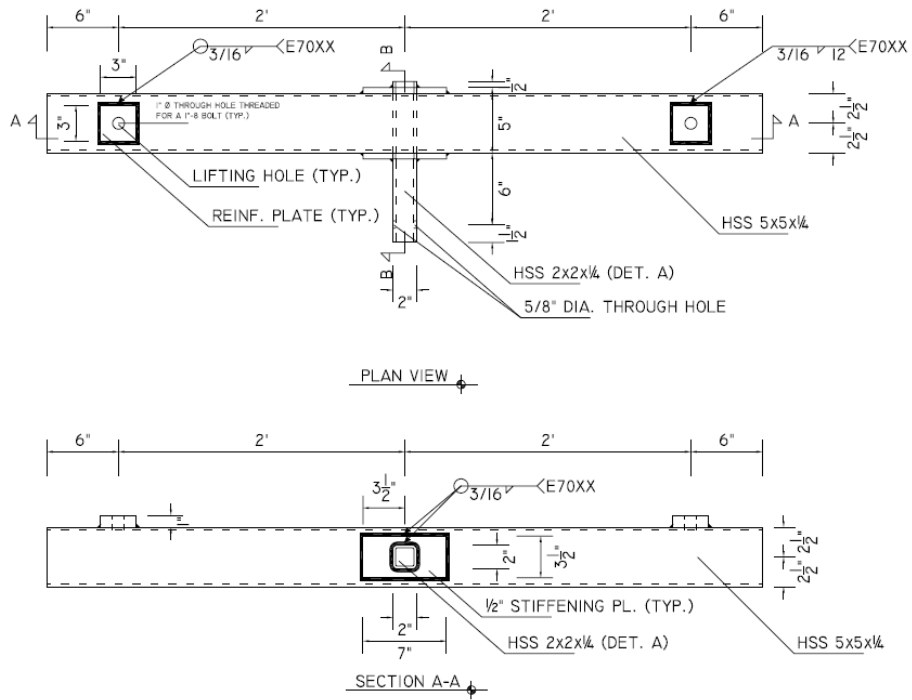


**Figure 4.6.2. Truck Lifting Beam Details**

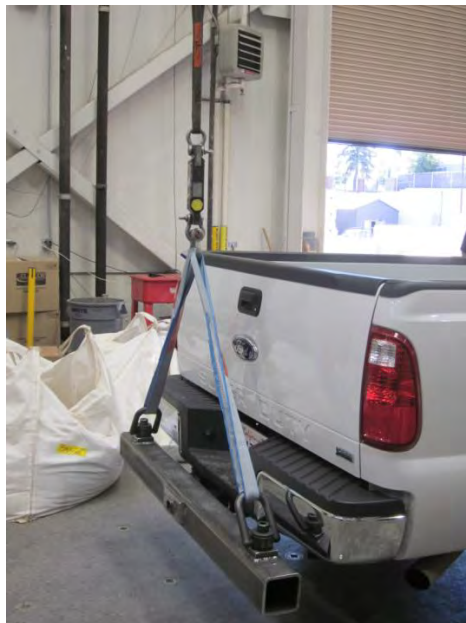


**Figure 4.6.3. Truck Lifting Beam Attached to the Truck Hitch**



**Figure 4.6.4. Lifting Truck with Overhead Cranes**



**Figure 4.6.5. Bridge with Vehicles from South End**



**Figure 4.6.6. Bridge with Vehicles from East (Wide-Angle View)**



**Figure 4.6.7. Wheel Restraint**

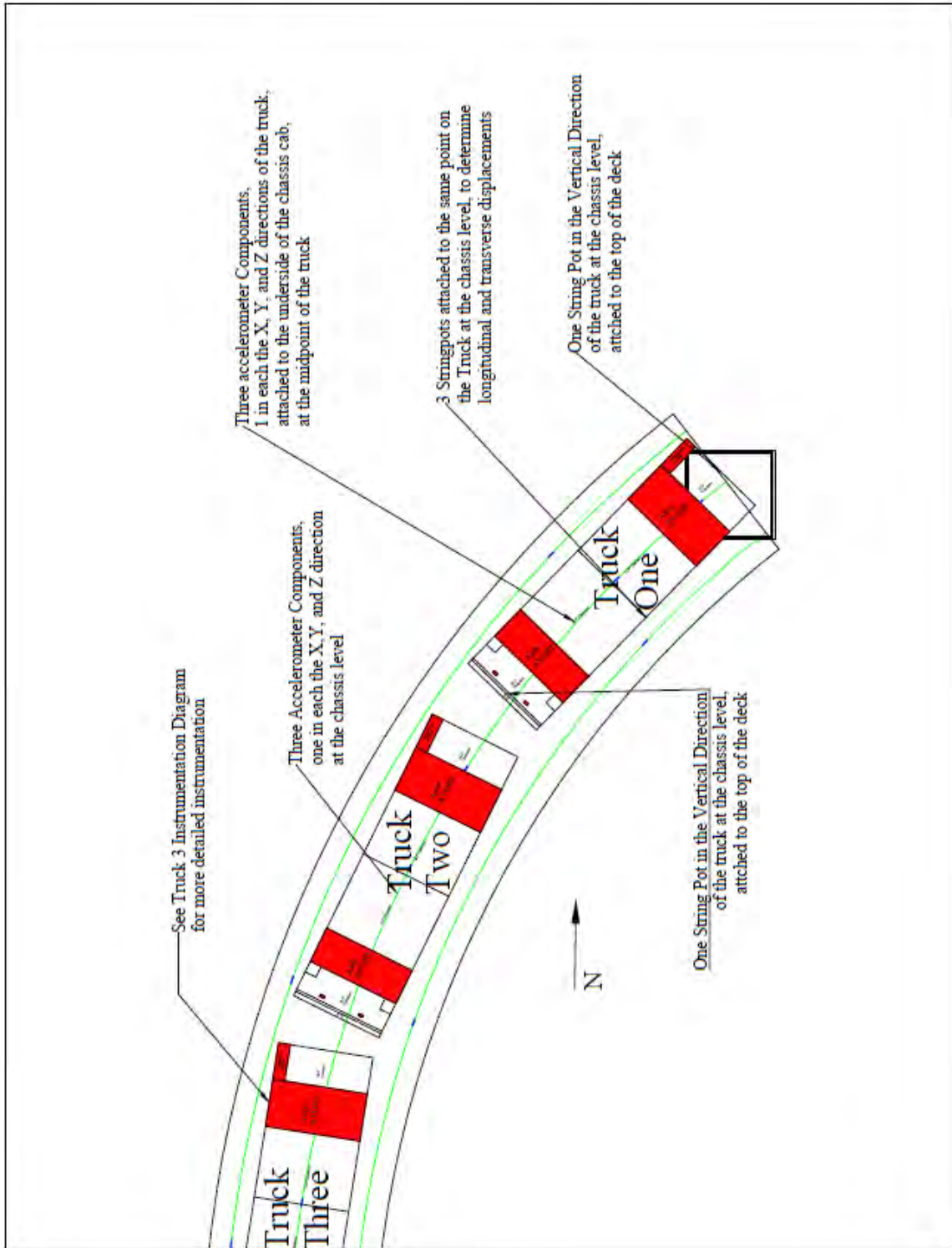


Figure 4.6.8. Instrumentation for TR1, TR2, and TR3

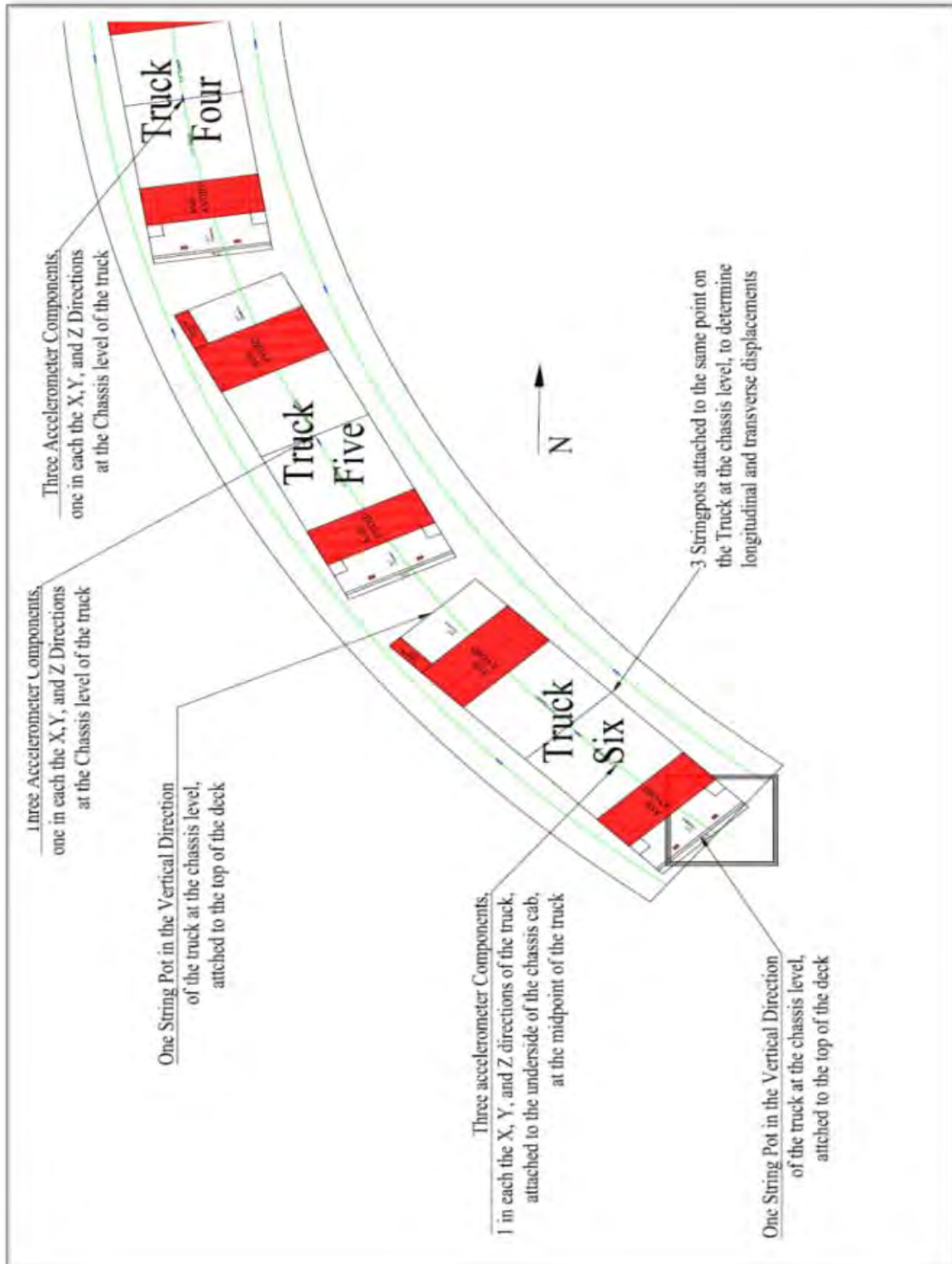
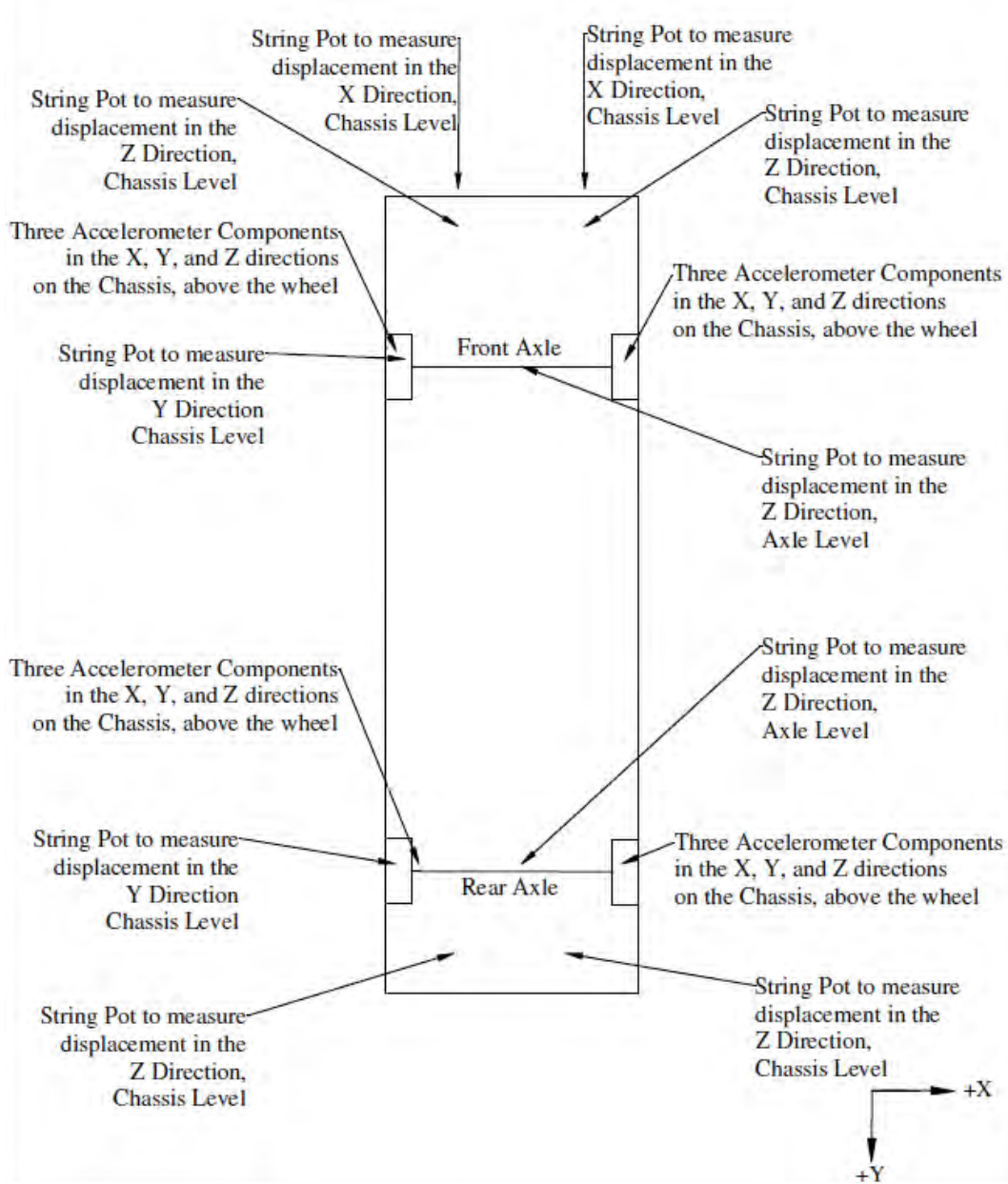


Figure 4.6.9. Instrumentation for TR4, TR5, and TR6



**Figure 4.6.10. TR3 Instrumentation Details**



**Figure 4.6.11. Displacement Transducers Attached to Door of TR6**

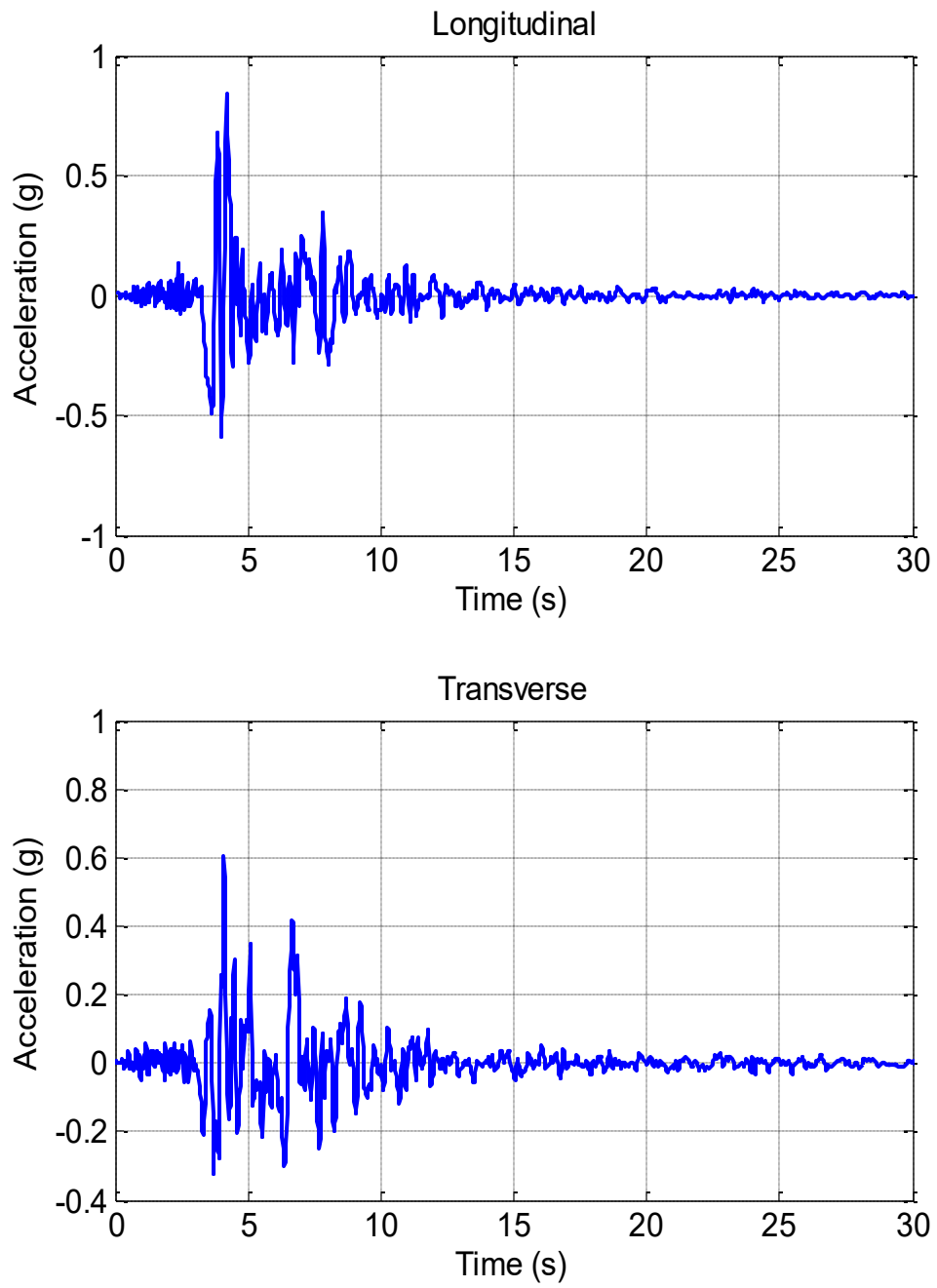


**Figure 4.7.1. Unscaled Sylmar Acceleration Histories**

# CHAPTER 5. EXPERIMENTAL RESULTS

## 5.1. General

This chapter presents the results of the experimental study. Actual material properties as tested in the laboratory are reported together with the response of the bridge with six trucks for the input motions described in Section 4.7.2. This response is compared with that of the bridge without trucks (Levi 2012) and the influence of live load determined. The performance of the bridge is reported in terms of displacement, acceleration, and forces at the support locations.

## 5.2. Material Properties

The materials used in the experiment were tested to obtain the actual properties, such as the compressive strength of the concrete and yield strength of the steel reinforcement. These values were then used to refine the analytical model.

### 5.2.1. Concrete

The target strength for the concrete was 5.5 ksi. To determine the compressive strength of the concrete cylinders, four sets of three concrete cylinders were made following the guidelines of ASTM C31 for compressive tests at 7, 14, 21, and 28 days, respectively. Along with these sets, an extra set of concrete cylinders was made to test compressive strength on the day of the experiment. Before each test, the cylinders were capped with sulfur to ensure a level surface following the guidelines of ASTM C617. Capping was typically done 24 hours before testing to ensure the sulfur had reached full strength. Cylinders were tested in a compressive machine following the guidelines of ASTM C39, as shown in Figure 5.2.1. A summary of test results is tabulated in Table 5.2.1 and plotted in Figure 5.2.2. The 28-day average compressive strength was found to be approximately equal to the expected compressive strength of 5.5 ksi. However, the test-day average compressive strength was approximately 23% higher at 6.7 ksi.

### 5.2.2. Steel Reinforcement

The steel reinforcement was specified as A706 grade steel. Both longitudinal and spiral reinforcement were tested following the requirements of ASTM A37015. The test setup used a strain gauge and an 8 in extensometer to measure the strain. Tensile stress was calculated and plotted against the strain to determine the yield strength, yield strain, and ultimate load, as shown in Figure 5.2.3 and summarized in Table 5.2.2. From the figure, the yield point is about 68 ksi as expected, and the ultimate stress is about 112 ksi

for the #3 bars and 100 ksi for #5 bars. These values are 17 ksi and 5 ksi higher than the expected value of 95 ksi, respectively.

### **5.2.3. Section Analysis**

Although differences were observed in the columns properties from the two experiments (with and without live load), numerical sectional analysis showed that both columns have similar moment-curvature relationship, as seen in Figure 5.2.4. Therefore, the columns from both experiments were deemed to have the same capacity and ductility and the effect of the differences in material properties on their performance was considered minimal.

## **5.3. Shake Tables Performance**

The performance of a shake table system may be measured in two ways; 1) ability to repeat a motion from one experiment the next, and 2) ability to reproduce the target (desired) motions. The performance of the shake table array used for this project, is discussed below using both measures.

Table 5.3.1 compares PGA values for the no-live and live load experiments for earthquake runs from 10 to 350% DE. Excellent repeatability of the table motions was achieved with the average difference in PGA in the longitudinal and transverse directions being 5.64% and 8.64% respectively. Seventy percent of the runs had differences less than 5% but the remainder had discrepancies ranging up to 34%. It is noted that the runs with the greatest error (50, 75 and 100% DE) were those when the shear keys failed or were about to fail. Comparisons of table performance with and without live load may also be seen in Figures 5.3.1 through 5.3.10 where response histories are plotted for displacement, velocity and acceleration. Again excellent repeatability is demonstrated.

In addition, response spectra for the target and achieved motions for the two cases with and without live load, are given for all earthquake runs (10 - 350% DE) in Figures 5.3.11 through 5.3.20 for acceleration, Figures 5.3.21 through 5.3.30 for velocity, and Figures 5.3.31 through 5.3.40 for displacement. Again excellent performance is demonstrated, particularly in the period range of interest, from 0.5 to 1.5 s.

## **5.4. Bridge Experimental Dynamic Properties**

Low-amplitude white noise excitation was applied before each ground motion run and after the last run, to quantify the dynamic properties of the system and changes to these properties with increasing levels of earthquake excitation. The displacement amplitudes of the white noise motions were chosen to be 0.02 in (rms) for the runs prior to 20% DE and 0.035 in (rms) afterwards. The white noise excitation frequency was chosen to range between 0 and 10 Hz. The results of these runs are presented below.

### 5.4.1. System Frequency

Power spectral density (PSD) spectra were generated from the longitudinal and transverse acceleration histories recorded at midspan of the middle girder during each run. Figures 5.4.1 through 5.4.11 show these spectra for the longitudinal and transverse directions for both the live load and no-live load cases. The PSD spectra were generated using a window size of 512 Hz and a Hanning window.

Figures 5.4.12 and 5.4.13 plot the fundamental frequency obtained from the PSD spectra against white noise run number and show a steady decrease in frequency with increasing run number. In other words the frequency of the bridge is decreasing with increasing levels of earthquake excitation (which is applied between each white noise run) and indicates a softening of the structure due to increasing damage in the columns at the higher levels of shaking.

### 5.4.2. System Damping

From the PSD spectra described in the previous section, the system damping ratio can be estimated using the half-power bandwidth method. This method calculates the damping ratio as follows:

$$\zeta_{est} = \frac{f_2 - f_1}{f_r} \quad (5.4.1)$$

where:

$\zeta_{est}$  = estimated damping ratio

$f_r$  = resonant frequency (i.e., frequency with the largest response amplitude)

$f_1, f_2$  = frequencies at which the response amplitude is  $1/\sqrt{2}$  times the resonant amplitude and  $f_1 < f_2$

Figures 5.4.14 and 5.4.15 plot the damping ratio in the longitudinal and transverse directions, respectively, against the white noise run number and show essentially no change in the transverse direction and a slight increase in the longitudinal direction, despite increasing levels of damage in the columns as noted above. These plots also show the damping ratio is of the order of 15-20% which is high compared to the 5% value usually assumed for elastic bridge response. It is clear that the low level nature of the white noise excitation activated a source of damping that was only present at small strain and insensitive to the extent of the column damage. One possibility is in the friction sliders at the abutments which did not slip during the white noise runs but the Teflon pads did deform a few hundreds of an inch, possibly in a plastic manner. More work is required to understand this phenomenon.

## 5.5. Bridge Displacement

One of the most useful parameters to quantify the effect of live load on seismic response is displacement and particularly column drift. Displacement responses at the deck and top-of-bent levels are compared in this section.

Figures 5.5.1 to 5.5.10 show deck displacement histories measured at the center of the middle span for the live load and no-live load cases. It is observed that the peak displacements when live load was on the bridge are consistently less than those when no live load was present. This beneficial effect is generally more pronounced in the moderate amplitude runs (100%DE) than in the higher runs (350% DE).

This same observation may be made when comparing the displacement response at the top of the north and south bents. Figures 5.5.11 through 5.5.20 plot the displacement histories at the top of the north bent, with and without live load, while Figures 5.5.21 through 5.5.30 plot these histories for the south bent. The reduction of displacement is also observed in the post-peak displacement history. It is also observed that the resultant response of the longitudinal and transverse displacements is dictated by the longitudinal response (North-South direction of the bridge) and that the vehicles are more effective in this direction. This may be because the fundamental mode of each truck is a pitching mode with a period of 0.8 s (Figure 3.8.1) and since the trucks are aligned principally in the NS direction on the bridge, this mode could be strongly activated, leading to a reduction in response in this direction. In the transverse direction the rolling mode of the vehicle is likely to dominate but with a period of 0.6 sec (Figure 3.8.3) it will not be as strongly excited. These plots also show that the presence of vehicles elongates the period of the structure, but not significantly. Plots of the orbital displacement at the top of the bent for different runs are given in Figures 5.5.31 to 5.5.40 for the north bent, and Figures 5.5.41 to 5.5.50 for the south bent. It is shown that the orbital area of the bent is reduced when the live load is present, which is in agreement with previous observations. Nonetheless, the orbital shape remains similar. In other words, the presence of live load does not alter the direction of bridge movement during a particular earthquake motion. The displacement of the bents during the higher amplitude runs became more asymmetric due to the inelasticity that occurs in the bents.

The maximum resultant displacement of the top of the north bent during the 100% DE run without live load was found to be 2.64 in, and with live load it was 1.68 in, i.e., approximately 36% less. At the top of the south bent for the same earthquake level, the maximum displacement was found to be 2.83 in without live load and 1.92 in with live load, i.e., approximately 32% less. For the 300% DE run, those figures became 7.40 in and 6.96 in for the north bent corresponding approximately to a 6% reduction, and 8.67 in and 8.02 in for the south bent corresponding approximately to an 8% reduction. Maximum displacements, with and without live load at the top of north and south bents, are plotted against earthquake level in Figures 5.5.51 and 5.5.52, respectively.

Girder uplift was observed at the abutments during the experiments with and without live load. This upward displacement is due to the curvature of the superstructure and becomes larger with increasing lateral load at the higher earthquake levels. Figures 5.5.53 and 5.5.54 show these displacements at the north and south abutments, measured

at the bottom of the outer and inner bays during the 350% DE runs, with and without live load. A positive displacement indicates the bridge deck is moving upward. Uplift begins at the inner girder and is larger at the north abutment than the south. It can be observed from Figures 5.5.5.3 and 5.5.5.4 that the maximum uplift with live load is about the same or less as the uplift without live load.

## **5.6. Bridge Acceleration**

Figure 5.6.1 to 5.6.10 and Figures 5.6.11 to 5.6.20 show acceleration histories recorded at the base (i.e., table acceleration), top of the bent, and deck levels, with and without live load, for the north and south bents respectively. From these figures it is seen that the maximum acceleration is lower at the deck level compared to the top of the bent, and the maximum accelerations with live load are generally lower than those without live load.

Acceleration histories at the deck level of the mid-span of the middle girder are plotted in Figures 5.6.21 through 5.6.30 together with PSD spectra. It is observed that contrary to the displacement, the resultant acceleration history is dominated by the transverse acceleration especially during the higher amplitude runs where the shear keys were not present and the bridge was free to move in the radial direction at the abutments. In addition, from the frequency analysis, similar results were observed for the responses with and without live load.

## **5.7. Bridge Forces and Moments**

Forces and moments at the supports were calculated using the load cells located under each girder at the north and south abutments, and the north and south bents. This section presents the results from the load cell readings as well as processed data that may be used to characterize the performance of the bridge.

### **5.7.1. Force and Moment Histories from Load Cells**

The load cells were numbered from north to south, inner girder to outer girder. For example, the load cell located under the middle girder at the north bent is LC #5, the load cell under the outer girder at the south abutment is LC #12. It is to be noted that the axial readings from LC #4 and LC#11 were corrupted during the 100% DE and 150% DE runs in the no-live load case.

For each run, a four-second buffer was added to the recorded data before the earthquake motion began. This four-second buffer was used to determine the initial loads in the bridge, and from this data, the axial load under dead load was found to be in good agreement with the calculated weight. After comparing the axial load in the entire system, the dead load at each bent was determined from the first run.

Figures 5.7.1 to 5.7.5 show histories of axial force, shear force in the tangential and radial directions, and moment in tangential and radial directions in the three load cells located on the top of south bent during the 100% DE run. The offset between the axial load with and without live load is due to the additional weight of the vehicles.

### 5.7.2. Calculation of Force and Moment at Bottom of the Bent

Some response quantities were measured in the longitudinal (x-, N-S) and transverse (y-, E-W) directions and some in the radial (R) and tangential (T) directions. To transform longitudinal and transverse quantities to radial and tangential directions, as shown in Figure 5.7.6, the following transformation equation was used:

$$\begin{Bmatrix} Q_T \\ Q_R \end{Bmatrix} = \begin{bmatrix} \cos \theta & \sin \theta \\ -\sin \theta & \cos \theta \end{bmatrix} \begin{Bmatrix} Q_X \\ Q_Y \end{Bmatrix} \quad (5.7.1)$$

As mentioned previously, load cells were placed only at the top of the bents. Therefore, to obtain shear forces and moments at the bottom of the bents, additional calculation is required.

The axial force at the bottom of a column is assumed to be equal to the axial force at the top plus the weight of the bent, so that:

$$N_{bot} = N_{top} + W_{bent} \quad (5.7.2)$$

where:

$$N_{bot} = \text{Axial force at the top of the bent (k)}$$

$$N_{top} = \text{Axial force at the bottom of the bent (k)}$$

$$W_{bent} = \text{Weight of the bent (column, cap, and added weight) (k)}$$

The calculation of the shear forces at the bottom of the bents takes into account the bent cap inertia forces, as follows:

$$V_{t,bot} = V_{t,top} - W_{bent} \ddot{u}_{t,bent} \quad (5.7.3)$$

$$V_{r,bot} = V_{r,top} - W_{bent} \ddot{u}_{r,bent} \quad (5.7.4)$$

where:

$$V_{t,bot} = \text{Tangential shear at the bottom of the bent (k)}$$

$$V_{r,bot} = \text{Radial shear at the bottom of the bent (k)}$$

$$V_{t,top} = \text{Tangential shear at the top of the bent (k)}$$

$$V_{r,top} = \text{Radial shear at the top of the bent (k)}$$

$$\ddot{u}_{t,bent} = \text{Tangential acceleration at the top of the bent (g)}$$

$$\ddot{u}_{r,bent} = \text{Radial acceleration at the top of the bent (g)}$$

Similarly, moments at the bottom of the bents were calculated from the moments, shear and inertia forces at the top, neglecting the contribution due to the axial force (i.e. the P-Δ effect), as follows:

$$M_{t,bot} = M_{t,top} + V_{t,top} (L_c + H_{bent}) - W_{bent} \ddot{u}_{t,bent} (L_c + H_{bent}) \quad (5.7.5)$$

$$M_{r,bot} = M_{r,top} + V_{r,top} (0.5L_c) - W_{bent} \ddot{u}_{r,bent} (0.5L_c) \quad (5.7.6)$$

where:

$M_{t,bot}$  = Tangential moment in the bottom of the bent (k.in)

$M_{r,bot}$  = Radial moment at the bottom of the bent (k.in)

$M_{t,top}$  = Tangential moment at the top of the bent (k.in)

$M_{r,top}$  = Radial moment at the top of the bent (k.in)

$L_c$  = Column height (in) = 92 in

$H_{bent}$  = Bent cap height (in) = 24 in

Equation (5.7.5) is based on the assumption that the bent acts in single curvature in the tangential direction, i.e. no moment restraint is provided by the superstructure to the top of the bent due to the pinned connection at this location. However, in the radial direction the bent is assumed to act in double curvature, due to the torsional stiffness of the superstructure and the moment connection provided to the cap beam by the eccentric axial forces in the bearings. This behavior is reflected in Equation (5.7.6).

For the double curvature deformation in the radial direction, the column was assumed to deform in a cubic shape that has an inflection point at the mid-height of the column, i.e., 46 in from the footing. This assumption was verified by calculating the location histories of the inflection points. An example is shown in Figures 5.7.7 for 100% DE case. These calculations were based on the following steps:

- a. A cubic equation for the deformed shape of the column is assumed, i.e.,  $y = ax^3 + bx^2 + cx + d$ , where  $a$ ,  $b$ , and  $c$  are constants and  $x, y$  are variables as shown in Figure 5.7.8.
- b. From the boundary conditions that  $y = 0$  and  $y' = 0$  at  $x = 0$ , the equation reduces to  $y = ax^3 + bx^2$ .
- c. To obtain the constants  $a$  and  $b$ , the boundary conditions at the top of the bent are used, i.e., at  $x = L_c$ ,  $y = \Delta_r$  and  $y' = \varphi$ , where  $\Delta_r$  is the radial displacement of the column and  $\varphi$  is the angle of rotation of the top of the bent (rad) obtained from the difference of vertical displacements at the two ends of the bent over the bent width as illustrated in Figure 5.7.8. This requires solving two simultaneous equations.
- d. After the two constants  $a$  and  $b$  are obtained, the equation is derived twice to find the value of  $x$  at which the curvature is zero (the point of inflection), i.e., solve  $6ax + 2b = 0$  to find  $x$ .
- e. The procedure is repeated for the entire response history.

It is seen in the abovementioned plots that the inflection point varies from time to time but the value falls between 40 and 50 in. Therefore, it was considered acceptable to assume the location of inflection point remains constant at the mid-height of the column.

Force and moment histories at the bottom of the north and south bents are shown in Figures 5.7.9 to 5.7.28. It is seen that for the lower amplitude runs up to 100% DE, live load reduces the demand in the column but the opposite is true for the higher amplitude runs. The maximum resultant moments at the bottom of the bents calculated from each run are plotted in Figures 5.7.29 and 5.7.30 for the north and south bents, respectively. These values are compared to the cracking moment ( $M_{cr}$ ), yield moment ( $M_y$ ), and ultimate moment ( $M_u$ ) obtained from a section analysis. It is seen that the values calculated are still reasonably within the limits given by the section analysis. In addition, Figures 5.7.31 and 5.7.32 the same moments obtained from static equilibrium. Comparing Figures 5.7.29 and 5.7.30 to Figures 5.7.31 and 5.7.32, the maximum resultant moments calculated with the assumptions made earlier have good agreement with those calculated from static equilibrium. However, the latter depends on the axial reading of the load cell which for some cases were deemed unreliable.

It is also important to note that the resultant moment (i.e., vector summation of the tangential and radial moments) at the bottom of the columns is larger than the resultant moment at the top of the columns. This is because the columns behave in single curvature in the tangential direction and double curvature in the radial direction.

### **5.7.3. Force vs. Displacement and Moment vs. Curvature Relationships**

Another measurement of column performance is to examine the shear force versus displacement hysteresis loops. The column shear forces were calculated as in the previous section the resultant shear in the bent plotted against the resultant displacement at each location, as shown in Figures 5.7.33 through 5.7.52 for both bents. These plots show a general trend that live load increases the maximum shear force demand due to the additional weight of the vehicles but reduces the maximum displacement. Figures 5.7.53 and 5.7.54 show a direct comparison of the maximum resultant shear versus maximum resultant displacement for the north and south bents with and without live load for each earthquake run. It is observed that during the low amplitude runs, the beneficial effect of live load is more pronounced and as the earthquake amplitude increases, this beneficial effect becomes less

It is evident in Figures 5.7.37 and 5.7.47 that there is minor hysteretic behavior in the bents at 100% DE, but it is less in the case with live load. This hysteresis is indicative of bar yield which is confirmed in Section 5.8.2. While both bents appear to have the same behavior, the key difference is the maximum shear force values. During the higher amplitude runs, the effect of yielding in the bents becomes evident as hysteretic behavior is clearly seen in the tangential direction of the bent and stiffness degradation occurs. While both bents are showing hysteretic behavior and stiffness loss, the south bent is yielding in flexure earlier than the north bent and attracting lower shear forces than the north. The extent of yield is consequently greater in the south column and gives rise to

more severe cracking in the plastic hinge region of this bent (Section 5.8.1). Maximum shear demands in the north and south columns due to column yielding were 76 k and 62 k, respectively. The shear capacity was calculated to be 221 k (Levi, 2011).

The average curvature in the plastic hinge region was calculated from the displacements measured by the inductive transducers attached to the outside of column in the expected hinge region. First the average strain on opposite sides of the column was calculated as the vertical displacement measured by the transducers divided by the gauge length. Then using Bernoulli's principle of plane sections remaining plane, the average curvature was computed as the difference in strain on the opposite sides of the column, divided by the horizontal distance between the instruments as shown in Figure 5.7.55 and summarized below:

$$\phi_i = \frac{\varepsilon_{i,1} - \varepsilon_{i,2}}{x_{i,1} + D + x_{i,2}} \quad (5.7.7)$$

where:

- $\phi_i$  = Curvature at location  $i$  (1/in)
- $\varepsilon_{i,1}$  = Recorded strain by transducer 1 at location  $i$  (Equation 5.7.8)
- $\varepsilon_{i,2}$  = Recorded strain by transducer 2 at location  $i$  (Equation 5.7.8)
- $x_{i,1}$  = Distance from the column face to the centroid of the transducer 1 at location  $i$  (in)
- $x_{i,2}$  = Distance from the column face to the centroid of the transducer 2 at location  $i$  (in)
- $D$  = Column diameter (in)

Strains  $\varepsilon_{i,1}$  and  $\varepsilon_{i,2}$  are obtained using the following equation:

$$\varepsilon_{i,j} = \frac{\Delta_{i,j}}{l_{i,j}} \quad (5.7.8)$$

where:

- $\varepsilon_{i,j}$  = Recorded strain on transducer  $j$  at location  $i$
- $\Delta_{i,j}$  = Displacement of transducer  $j$  at location  $i$  (in)
- $l_{i,j}$  = Initial length of transducer  $j$  at location  $i$  (in)

Rotation due to bond slip was calculated using two displacement transducers mounted at the BH level. These transducers measured the relative displacement between this mounting point at approximately 1 in above the footing surface, and the footing itself.

The resultant moment-curvature plots at the bottom of the bents are shown in Figures 5.7.56 through 5.7.65 for the north bent and Figures 5.7.66 through 5.7.75 for the south bent. The moment-curvature relation obtained from the section analysis is plotted in the same figure so that the state of inelasticity can be visually compared. It may be

observed that the bottom of the bent experienced extensive inelasticity in the higher amplitudes motion, which is consistent with the expected location of the plastic hinge zone. This inelasticity started to occur during the 100% DE run and progressively increased through the last run. However, no yielding was found to occur at the top of either bent. Maximum and minimum curvatures are given in Figures 5.7.76 and 5.7.77.

## **5.8. Column Damage**

Column damage in the live load and no-live load cases may be compared in terms of the degree of cracking and spalling, as well as the extent of rebar yielding. It was observed that the extent of damage in the columns with live load present was less than with no-live load. Details are given below.

### **5.8.1. Cracking and Spalling**

Minor hairline cracks (0.2 mm) started to occur during the 20% DE, and cracks propagated up to the 100% DE run. After the 100% DE run, and the failure of the abutment shear keys, cracks continued to propagate and but were concentrated at the bottom of the columns in the hinge zones, with a few flexural cracks at the mid-height of the column. Longer and wider cracks (approximately 0.4 mm) occurred during the 150% DE and minor spalling of the cover concrete was observed on both columns. During the 200% DE run, cracks opened up to a width of 1 mm and spalling was more severe in south column. Two spiral bars were visible in the north column and five spiral bars were visible in the south column. During the 250% DE run, spalling became more evident and penetrated deeper into the core concrete, but was still concentrated in the bottom hinge area. Two longitudinal bars were visible in both the north and south columns along with five and six spiral bars visible in north and south columns, respectively. During the 300% DE run, spalling continued to spread and parts of the core concrete became visible. In the north column, three longitudinal bars and six spiral bars were visible and four longitudinal bars and eight spiral bars were visible in the south column. Also, vertical and shear cracks propagated to a greater extent. Last, during the 350% DE run, spalling became more extensive and additional core concrete was exposed. At the end of the experiment, five longitudinal bars and seven spiral bars were visible in the north column and seven longitudinal bars and nine spiral bars were visible with one longitudinal bar about to buckle in the south column.

As noted in Section 5.5.5 the presence of live load reduced the displacements in the columns which in turn reduced the damage in the columns. This is clearly seen in Figures 5.8.1 and 5.8.2 which show that the extent of spalling is less in the case with live load than without, for both the north and south columns. Since concrete spalling implies significant yield in the reinforcement, less spalling implies lower yield strains due to the presence of the live load. This observation is confirmed in Section 5.8.2.

### 5.8.2. Reinforcement Yield Strain

Strain gauges were placed on the longitudinal and spiral reinforcement in the expected plastic hinge zones, as described in Chapter 4. A total of 64 gauges were installed divided between the top and bottom zones of each column. When examining this data, the strain gauges readings were placed in three groups: (1) top and bottom column zones, (2) north and south bent, and (3) longitudinal and spiral reinforcement. Separating the strains into these groups allows for easier understanding of the recorded data. Maximum and minimum strains for each bar along the length of the column for each test are shown in Table 5.8.1 through Table 5.8.20. When examining the min/max table, a value is highlighted when it exceeds the calculated yield strain determined from material testing. If a strain gauge was broken during construction, the value is labeled as “Pre-Test Break.” If a specific location on a rebar does not have a strain gauge attached, the table reads “N/A”. Strain readings in the range of 15 to 20% strain (150,000 – 200,000  $\mu\epsilon$ ) usually means the gauge has been damaged, and any gauge with a reading in this range is listed as “Broken.” Using this guideline, a total of ten strain gauges were lost during construction of the columns and an additional nine gauges were “broken” during experimental testing.

When examining the data, yield of the first longitudinal rebar occurred during the 75% DE. During this motion, two and three longitudinal bars in the north and south columns respectively, exceeded yield with maximum strains approximately twice the theoretical yield strain calculated from the material tests. This yielding of the rebar also occurred during the same run that the shear keys at the abutment reached their ultimate capacity and failed. During a visible inspection after this run, flexural cracking appeared around the circumference of the column. During the next run, yield occurred in all longitudinal reinforcement in both columns and began to progress up the height of the column. Yielding of the reinforcement in compression started to occur during the 100% DE, when one longitudinal bar had compressive strains slightly in excess of the calculated yield strain from material testing. During the 150% DE run, two longitudinal bars in the north bent and three bars in the south bent began to yield in compression accompanied by noticeable spalling. At this point, tensile strains in the column started to increase markedly and spiral and longitudinal reinforcement became visible. Finally, during the 350% DE run, longitudinal bars began to buckle and strains reached 12,000 to 35,000  $\times 10^{-6}$ . However, the extent of rebar yielding in this case with live load, was found to be less than that observed in the no-live load case as reported by Levi (2011).

### 5.8.3. Post-Experiment Torsional Stiffness

After completing the experiment, the torsional stiffness of each bent was measured. Results from applying an eccentric static horizontal load to one end of the bent cap are shown in Figures 5.8.3 and 5.8.4.

Fitting a line to the observed data gives torsional stiffnesses of 13,223 k.in/rad and 10,212 k.in/rad for the north and south bents respectively. Comparing to the theoretical value, these values are about 10% of the usually assumed value of 0.2 JG/L

for a cracked section torsional stiffness. Levi (2011) reports values of 3% of 0.2 JG/L for the case without live load.

It is apparent these columns have suffered a serious degradation in their torsional stiffness during the experiment due, no doubt, to the curvature in the bridge. However, the loss on stiffness was not as severe when live load was present.

## 5.9. Shear Key Performance

As noted in Section 4.4, sacrificial shear keys were installed at the abutments of the bridge model to protect the shake tables from high overturning moments. In the live load experiment, the shear keys failed during the 100% DE run whereas for the no-live load case, the shear keys failed during the 75% DE run. Since the ultimate strength of the key was the same in both experiments (25 k) the radial shear force in the device at 75% DE was less when live load was present than when it was absent. In other words, live load reduced the radial shear forces at the abutments, and it took a larger earthquake (100% DE) to generate sufficient force to fail the key when live load was present.

Response histories of shear force in the keys at the north and south abutments are shown in Figures 5.9.1 through 5.9.5 for earthquakes from 10% through 100% DE respectively. It can be observed that the shear keys did indeed fail at loads close to their ultimate strength (25 k). For the no-live load experiment, the north and south shear keys failed at different times, but for the live load experiment, both keys failed almost simultaneously. At the instant of failure, the sudden release of strain energy caused short duration pulses in the acceleration and displacement histories of the superstructure.

## 5.10. Discussion

Key findings from the experimental work reported in this chapter can be summarized as follows:

1. The input table motions for the live load and no-live load cases are essentially the same in the period range of interest, and thus the results from both experiments (with and without live load) may be directly compared.
2. Live load reduces the demand in the structure, which is seen by the decrease in the displacements, accelerations, and internal forces. This effect also delays the formation of cracks and concrete spalling in the columns and reduces column damage for the same level of earthquake excitation.
3. Yielding in the column for the live load case was found to be less than the no-live load case. This was shown by the strain gage readings as well as from the moment-curvature plots.
4. Superstructure uplift at the abutments was less when live load was present.
5. The reduction in torsional stiffness of the single column bents was less when live load was present.

It is clear that live load had a beneficial effect on the seismic response of the curved bridge model used in this experiment, subject to the selected earthquake motion. Possible reasons for this effect are discussed below.

1. *Non-identical experimental conditions between the two cases giving an inadvertent advantage to the live load case.* Examples are differences in table input motions, material properties, and initial conditions, but as noted below, none of these were found to be significant.

- The average table accelerations in the longitudinal and transverse directions for the live load and no-live load cases are comparable in value and the differences are acceptably small, as shown in Table 5.3.1. The acceleration, velocity, and displacement spectra for both cases are also similar particularly in the period range of interest, as noted in Section 5.3. This means that the input motions for both cases are essentially the same.
- As expected, differences in material properties were observed, but they were determined to have no substantive effect on column performance as shown in the moment-curvature plots in Figure 5.2.4. However the extent of deck cracking escalated from the no-live load case to the live load experiment due to the assembly-disassembly process undertaken between each experiment, making the superstructure more flexible and lengthening the transverse period slightly.
- The assembly-disassembly process just mentioned was observed to also cause different initial conditions over the supports and at splice points due to construction tolerances. For this reason, the two bridge structures used for the no-live load and live load cases might not have been identical but the differences (locked-in, self-equilibrating forces in the superstructure) are not believed to have affected the dynamic response of the bridge.

2. *Longer period and increased damping of the system when live load is present placing the structure in a more favorable part of the acceleration response spectrum.*

Even though the live load is sprung (and not rigidly attached to the bridge) the fundamental period of the system becomes longer when live load is present. This period shift results in lower spectral accelerations, but in this case the shift is slight and this effect is small. However the additional damping in the system due to the live load, further reduces the response (Figure 5.10.1), and together (period shift and damping) these effects may be significant. It is noted however that although these effects may help explain the reduced forces in the live load experiment, they do not explain the reduced displacements, since these increase with period and decrease with damping and the net result is small unless the period shift is large.

3. *Reduced structural response due a tuned-mass-damper effect of the live load.* Tuned mass dampers (TMD) have been used to reduce the demand in structures due to wind load by adding another degree-of-freedom and

associated mode of vibration with a carefully chosen frequency and shape. However, this beneficial effect is achieved only for a narrow range of frequency ratios, but the range may be broadened by introducing damping to the TMD as discussed in Appendix A and shown in Figures A.3 and A.5, for undamped and 5%-damped structures, respectively. The horizontal axis in these figures is the ratio of the frequency of a harmonic exciting force to the frequency of the structure, and the vertical axis is the deformation response factor or magnification factor, which is the ratio of the maximum dynamic response to the static response. In these figures, beneficial frequency ratios are those where the deformation response factor of a structure with a TMD is less than without a TMD. For a more versatile system, multiple tuned mass dampers (MTMD) may be placed on a structure. Since an MTMD may be tuned to multiple operating frequencies as compared to a TMD, which is tuned to a single operating frequency, they are attractive for structures that have greater participation from the higher modes. Recent research has also shown that TMDs and MTMDs with nonlinear stiffness, have greater bandwidth than linear devices. Since a truck suspension is nonlinear, the theory behind these devices, also known as a nonlinear energy sink (NES), may provide the best explanation of the observed behavior. Energy sinks have shown attractive results for controlling the seismic response of buildings and it is very possible that the six trucks, each with heavily damped bilinear rear suspensions, are acting as an NES with equally favorable results.

Of the above possible reasons for beneficial response, the first is judged to have only a minimal impact, and the second offers only a partial explanation. However the third reason, the tuned-mass-damper effect, appears to be significant, particularly in this case where there are six trucks on the bridge, each of them acting as a tuned mass damper. As briefly described above and discussed in detail in Appendix A, multiple tuned mass dampers with nonlinear properties offer the most likely explanation for the beneficial response observed in these experiments. Further work is required to validate this explanation.

## **5.11. Summary**

Experimental results have been presented in this chapter to quantify the effect of live load on the seismic response of a large-scale model bridge. It is shown that the presence of live load reduced the demand in the structure, as evidenced by a decrease in displacements, accelerations, and internal forces. It also delayed the formation of cracks and concrete spalling in the columns and reduced column damage for the same level of earthquake excitation. Girder uplift at the abutments and degradation of column torsional stiffness was less with live load on the bridge. Possible explanations for this beneficial behavior are noted.

However, these observations may not be true for other bridges, different ground motions and other vehicle types. An analytical parameter study is required quantify the factors governing live load effects and their limitations.

**Table 5.2.1. Concrete Compression Test Summary**

Day	Compressive Strength, $f'_c$ (ksi)
7	3.991
14	4.685
21	4.823
28	5.434
Test Day	6.676

**Table 5.2.2. Rebar Tension Test Summary**

Property	#5 Rebar	#3 Rebar
Yield Stress, $f_y$ (ksi)	63.90	62.34
Yield Strain, $\epsilon_y$ ( $\mu\epsilon$ )	2,470	4,105
Ultimate Stress, $f_u$ (ksi)	111.68	99.67
Modulus of Elasticity, E (ksi)	25,863	15,185

**Table 5.3.1. Comparison of Average Table Accelerations for No-Live Load and Live Load Experiments**

%Design Earthquake	Average Table Longitudinal Acceleration			Average Table Transverse Acceleration		
	With LL (g)	Without LL (g)	Difference (%)	With LL (g)	Without LL (g)	Difference (%)
10	0.054	0.055	-1.85	0.035	0.036	-2.86
20	0.109	0.111	-1.84	0.079	0.080	-1.27
50	0.265	0.310	-16.98	0.181	0.202	-11.60
75	0.427	0.456	-6.79	0.268	0.341	-27.24
100	0.742	0.613	17.38	0.506	0.331	34.59
150	0.853	0.878	-2.93	0.473	0.469	0.85
200	1.104	1.086	1.63	0.575	0.572	0.52
250	1.385	1.332	3.83	0.715	0.690	3.50
300	1.614	1.577	2.29	0.816	0.828	-1.47
350	1.861	1.877	-0.86	0.961	0.985	-2.50
Average difference			5.64			8.64

**Table 5.4.1. Estimation of Period and Damping Ratio**A. Longitudinal Direction

<b>White Noise</b>	<b>With LL</b>		<b>Without LL</b>	
	<b>Period (s)</b>	<b>Damping (%)</b>	<b>Period (s)</b>	<b>Damping (%)</b>
1	0.36	18.10	0.33	14.43
2	0.33	10.00	0.33	11.21
3	0.40	11.23	0.44	18.26
4	0.36	17.95	0.47	13.85
5	0.36	9.33	0.50	25.65
6	0.40	12.34	0.50	16.02
7	0.36	3.72	0.36	15.17
8	0.44	14.53	0.57	19.56
9	0.44	22.37	0.44	17.07
10	0.36	11.43	0.40	16.52
11	0.44	18.18	0.50	24.49

B. Transverse Direction

<b>White Noise</b>	<b>With LL</b>		<b>Without LL</b>	
	<b>Period (s)</b>	<b>Damping (%)</b>	<b>Period (s)</b>	<b>Damping (%)</b>
1	0.33	19.80	0.40	19.74
2	0.44	11.02	0.44	40.33
3	0.40	22.82	0.50	14.93
4	0.40	27.62	0.44	22.63
5	0.44	16.39	0.57	13.10
6	0.36	12.28	0.50	20.47
7	0.80	15.44	0.57	20.15
8	0.80	18.24	0.57	20.02
9	0.40	9.85	0.50	10.17
10	0.57	50.93	0.57	25.17
11	0.80	43.50	0.57	20.43

**Table 5.8.1. North Bent Longitudinal and Spiral Reinforcement Strains (10% DE)**

A. Longitudinal Reinforcement

Bar	BS, Bot	BH, Bot	MH, Bot	TH, Bot	TH, Top	MH, Top	BH, Top	BS, Top
#1_Max	281.4	366.6	485.0	170.2	N/A	359.6	419.0	N/A
#1_Min	137.4	176.8	249.1	-65.5	N/A	274.6	327.3	N/A
#2_Max	163.6	327.1	353.4	405.8	457.9	516.5	483.8	294.2
#2_Min	98.2	222.4	242.2	281.4	379.4	431.5	411.9	222.3
#3_Max	222.5	320.6	288.3	320.6	N/A	287.8	255.1	N/A
#3_Min	45.8	52.3	91.7	104.7	N/A	202.8	170.1	N/A
#4_Max	177.7	229.0	255.2	242.1	286.4	320.3	347.1	235.5
#4_Min	92.2	111.3	163.6	130.9	214.8	254.9	275.1	170.1
#5_Max	N/A	392.6	458.4	N/A	N/A	385.8	516.6	N/A
#5_Min	N/A	261.8	307.8	N/A	N/A	307.3	444.7	N/A
#6_Max	N/A	294.3	405.6	N/A	N/A	Broken	PT Break	N/A
#6_Min	N/A	137.3	222.4	N/A	N/A	Broken	PT Break	N/A
#7_Max	N/A	216.1	229.0	N/A	N/A	281.3	353.3	N/A
#7_Min	N/A	32.7	98.2	N/A	N/A	189.7	255.1	N/A
#8_Max	N/A	366.4	333.9	N/A	N/A	372.6	346.5	N/A
#8_Min	N/A	143.9	196.4	N/A	N/A	294.2	281.1	N/A

B. Spiral Reinforcement

Bar	BH,Bot	MH,Bot	TH,Bot	TH,Top	BH,Top
#1_Max	91.6	92.1	98.2	163.6	163.5
#1_Min	13.1	32.9	26.2	104.7	91.6
#2_Max	PT Break	117.9	196.4	137.3	137.3
#2_Min	PT Break	45.8	117.8	91.6	71.9
#3_Max	137.4	189.7	229.1	143.8	157.0
#3_Min	65.4	111.2	150.6	71.9	85.1
#4_Max	117.8	111.2	117.9	163.7	150.3
#4_Min	39.3	52.3	39.3	85.1	91.5

Note: PT Break = Pre-Test Break

**Table 5.8.2. South Bent Longitudinal and Spiral Reinforcement Strains (10% DE)**

A. Longitudinal Reinforcement

Bar	BS, Bot	BH, Bot	MH, Bot	TH, Bot	TH, Top	MH, Top	BH, Top	BS, Top
#1_Max	13.8	524.9	372.6	393.2	N/A	449.0	470.0	N/A
#1_Min	-110.4	269.3	193.2	220.8	N/A	359.2	366.3	N/A
#2_Max	338.2	510.8	462.2	545.4	442.3	504.2	379.8	200.3
#2_Min	255.4	400.3	365.6	455.6	393.9	449.0	324.5	158.9
#3_Max	282.8	386.6	262.3	317.5	N/A	269.3	200.3	N/A
#3_Min	89.7	6.9	-20.7	117.4	N/A	179.6	110.5	N/A
#4_Max	132.1	172.5	83.1	110.4	82.9	165.7	Broken	200.2
#4_Min	7.0	-82.8	-20.8	-69.0	6.9	110.5	Broken	158.8
#5_Max	N/A	738.8	490.5	N/A	N/A	470.0	738.8	N/A
#5_Min	N/A	504.0	310.9	N/A	N/A	387.1	635.3	N/A
#6_Max	N/A	611.5	338.2	N/A	N/A	373.0	297.2	N/A
#6_Min	N/A	291.9	151.8	N/A	N/A	297.1	221.1	N/A
#7_Max	N/A	241.7	144.9	N/A	N/A	207.1	276.3	N/A
#7_Min	N/A	-110.5	-96.6	N/A	N/A	124.3	179.6	N/A
#8_Max	N/A	324.6	213.9	N/A	N/A	290.2	518.3	N/A
#8_Min	N/A	69.1	96.6	N/A	N/A	207.3	400.8	N/A

B. Spiral Reinforcement

Bar	BH,Bot	MH,Bot	TH,Bot	TH,Top	BH,Top
#1_Max	96.7	110.4	82.8	117.4	165.8
#1_Min	48.3	62.1	34.5	76.0	124.4
#2_Max	193.3	96.7	97.7	110.5	320.0
#2_Min	145.0	48.3	48.8	69.1	83.5
#3_Max	117.3	151.9	158.6	152.0	124.3
#3_Min	75.9	89.8	110.4	103.6	82.9
#4_Max	103.5	124.3	110.8	158.8	PT Break
#4_Min	62.1	76.0	62.3	110.5	PT Break

Note: PT Break = Pre-Test Break

**Table 5.8.3. North Bent Longitudinal and Spiral Reinforcement Strains (20% DE)**

A. Longitudinal Reinforcement

Bar	BS, Bot	BH, Bot	MH, Bot	TH, Bot	TH, Top	MH, Top	BH, Top	BS, Top
#1_Max	366.5	484.4	688.2	667.8	N/A	392.3	464.8	N/A
#1_Min	65.5	78.6	157.3	157.1	N/A	248.5	294.6	N/A
#2_Max	163.6	372.9	399.2	458.2	470.9	516.5	477.3	274.6
#2_Min	91.6	124.3	183.3	216.0	346.7	411.9	385.7	209.2
#3_Max	268.3	373.0	334.2	379.5	N/A	287.8	255.1	N/A
#3_Min	-137.4	-327.2	-65.5	-202.8	N/A	130.8	111.2	N/A
#4_Max	197.5	274.9	294.5	287.9	299.5	339.9	340.6	229.0
#4_Min	-13.2	0.0	91.6	65.4	182.3	222.2	248.9	163.6
#5_Max	N/A	510.4	576.2	N/A	N/A	411.9	536.2	N/A
#5_Min	N/A	183.2	235.7	N/A	N/A	281.2	418.5	N/A
#6_Max	N/A	333.6	458.0	N/A	N/A	Broken	PT Break	N/A
#6_Min	N/A	-26.2	65.4	N/A	N/A	Broken	PT Break	N/A
#7_Max	N/A	262.0	287.9	N/A	N/A	287.8	359.8	N/A
#7_Min	N/A	-268.5	-13.1	N/A	N/A	117.8	170.1	N/A
#8_Max	N/A	431.8	406.0	N/A	N/A	392.3	372.6	N/A
#8_Min	N/A	19.6	124.4	N/A	N/A	261.5	248.4	N/A

B. Spiral Reinforcement

Bar	BH,Bot	MH,Bot	TH,Bot	TH,Top	BH,Top
#1_Max	85.1	92.1	85.1	157.0	157.0
#1_Min	13.1	19.7	19.6	91.6	85.0
#2_Max	PT Break	111.3	183.3	130.8	137.3
#2_Min	PT Break	39.3	117.8	78.5	65.4
#3_Max	124.3	176.7	216.0	130.7	150.5
#3_Min	58.9	104.7	130.9	52.3	85.1
#4_Max	85.1	104.7	111.3	150.6	137.3
#4_Min	26.2	32.7	32.7	85.1	85.0

Note: PT Break = Pre-Test Break

**Table 5.8.4. South Bent Longitudinal and Spiral Reinforcement Strains (20% DE)**

A. Longitudinal Reinforcement

Bar	BS, Bot	BH, Bot	MH, Bot	TH, Bot	TH, Top	MH, Top	BH, Top	BS, Top
#1_Max	96.6	690.6	496.7	531.2	N/A	497.3	518.4	N/A
#1_Min	-172.5	34.5	138.0	151.8	N/A	324.6	338.7	N/A
#2_Max	345.1	524.6	482.9	559.2	449.2	518.0	379.8	200.3
#2_Min	200.2	255.4	282.8	379.7	366.3	428.2	310.7	152.0
#3_Max	337.9	455.6	324.5	379.7	N/A	297.0	221.0	N/A
#3_Min	-69.0	-559.2	-220.9	-34.5	N/A	145.0	41.4	N/A
#4_Max	201.6	282.9	166.3	207.1	138.1	186.4	Broken	207.1
#4_Min	-83.4	-317.4	-90.1	-172.5	-20.7	96.7	Broken	151.9
#5_Max	N/A	876.9	607.9	N/A	N/A	504.6	780.3	N/A
#5_Min	N/A	352.1	248.7	N/A	N/A	359.4	607.7	N/A
#6_Max	N/A	722.7	407.2	N/A	N/A	393.8	304.1	N/A
#6_Min	N/A	-236.3	13.8	N/A	N/A	248.7	179.7	N/A
#7_Max	N/A	331.5	213.9	N/A	N/A	227.8	317.7	N/A
#7_Min	N/A	-490.3	-248.4	N/A	N/A	82.9	124.3	N/A
#8_Max	N/A	462.7	331.2	N/A	N/A	324.7	601.2	N/A
#8_Min	N/A	-172.7	55.2	N/A	N/A	165.8	345.5	N/A

B. Spiral Reinforcement

Bar	BH,Bot	MH,Bot	TH,Bot	TH,Top	BH,Top
#1_Max	96.7	110.4	75.9	117.4	165.8
#1_Min	48.3	41.4	27.6	69.1	96.7
#2_Max	186.4	96.7	90.7	110.5	396.6
#2_Min	138.1	41.4	48.8	62.2	215.7
#3_Max	117.3	145.0	158.6	152.0	131.2
#3_Min	62.1	75.9	110.4	103.6	82.9
#4_Max	103.5	124.3	103.9	151.9	PT Break
#4_Min	55.2	69.1	62.3	103.6	PT Break

Note: PT Break = Pre-Test Break

**Table 5.8.5. North Bent Longitudinal and Spiral Reinforcement Strains (50% DE)**

A. Longitudinal Reinforcement

Bar	BS, Bot	BH, Bot	MH, Bot	TH, Bot	TH, Top	MH, Top	BH, Top	BS, Top
#1_Max	569.4	746.3	1206.0	1099.9	N/A	464.2	563.0	N/A
#1_Min	-183.3	-543.3	-989.7	-667.8	N/A	170.0	150.6	N/A
#2_Max	196.4	497.2	543.2	641.4	529.8	555.7	503.4	281.2
#2_Min	13.1	-490.7	-510.5	-549.8	248.6	340.0	320.4	176.5
#3_Max	490.8	641.3	629.0	680.5	N/A	386.0	327.0	N/A
#3_Min	-654.4	-1347.9	-1736.4	-1302.0	N/A	39.3	32.7	N/A
#4_Max	342.3	438.5	543.1	497.3	377.6	411.8	379.9	242.1
#4_Min	-276.5	-713.3	-752.5	-575.8	104.2	163.4	209.6	150.5
#5_Max	N/A	700.2	969.1	N/A	N/A	464.2	601.6	N/A
#5_Min	N/A	-464.6	-1145.9	N/A	N/A	196.2	287.7	N/A
#6_Max	N/A	477.4	772.0	N/A	N/A	Broken	PT Break	N/A
#6_Min	N/A	-771.8	-1334.6	N/A	N/A	Broken	PT Break	N/A
#7_Max	N/A	576.3	713.3	N/A	N/A	418.7	477.6	N/A
#7_Min	N/A	-1008.6	-1433.2	N/A	N/A	32.7	45.8	N/A
#8_Max	N/A	759.0	798.8	N/A	N/A	496.9	464.2	N/A
#8_Min	N/A	-667.4	-779.2	N/A	N/A	170.0	137.3	N/A

B. Spiral Reinforcement

Bar	BH,Bot	MH,Bot	TH,Bot	TH,Top	BH,Top
#1_Max	72.0	85.5	78.5	150.5	150.4
#1_Min	-26.2	-13.2	-13.1	78.5	85.0
#2_Max	PT Break	144.1	242.2	124.3	124.2
#2_Min	PT Break	26.2	98.2	71.9	58.9
#3_Max	124.3	150.5	216.0	124.2	144.0
#3_Min	39.3	72.0	98.2	52.3	72.0
#4_Max	104.7	111.2	104.8	144.0	137.3
#4_Min	0.0	32.7	6.5	72.0	78.4

Note: PT Break = Pre-Test Break

**Table 5.8.6. South Bent Longitudinal and Spiral Reinforcement Strains (50% DE)**

A. Longitudinal Reinforcement

Bar	BS, Bot	BH, Bot	MH, Bot	TH, Bot	TH, Top	MH, Top	BH, Top	BS, Top
#1_Max	393.4	1167.1	993.5	1048.6	N/A	663.1	711.9	N/A
#1_Min	-448.6	-1035.9	-800.3	-344.9	N/A	214.1	179.7	N/A
#2_Max	565.9	607.4	710.5	690.3	511.4	573.3	414.3	221.0
#2_Min	-34.5	-890.4	-310.4	62.1	262.6	345.3	262.4	124.3
#3_Max	613.8	835.3	586.8	683.4	N/A	366.0	317.7	N/A
#3_Min	-724.1	-2008.9	-1574.1	-1373.7	N/A	-20.7	-165.8	N/A
#4_Max	528.3	683.2	554.2	566.0	317.7	269.3	Broken	248.6
#4_Min	-361.5	-1083.4	-990.6	-683.3	-179.6	34.5	Broken	131.2
#5_Max	N/A	1263.5	967.1	N/A	N/A	587.6	932.2	N/A
#5_Min	N/A	-600.7	-379.9	N/A	N/A	276.5	469.5	N/A
#6_Max	N/A	1195.2	814.3	N/A	N/A	476.7	373.2	N/A
#6_Min	N/A	-1723.3	-1366.4	N/A	N/A	131.3	6.9	N/A
#7_Max	N/A	621.6	469.3	N/A	N/A	310.7	428.2	N/A
#7_Min	N/A	-1560.8	-1318.1	N/A	N/A	0.0	-34.5	N/A
#8_Max	N/A	849.5	690.0	N/A	N/A	476.7	856.8	N/A
#8_Min	N/A	-1181.0	-1221.4	N/A	N/A	69.1	152.0	N/A

B. Spiral Reinforcement

Bar	BH,Bot	MH,Bot	TH,Bot	TH,Top	BH,Top
#1_Max	103.6	110.4	82.8	110.5	179.6
#1_Min	13.8	-13.8	-34.5	55.3	76.0
#2_Max	214.0	117.4	118.6	110.5	410.5
#2_Min	145.0	27.6	34.9	55.2	-410.5
#3_Max	117.3	117.4	158.6	145.1	117.4
#3_Min	34.5	13.8	75.9	96.7	76.0
#4_Max	110.4	131.2	103.9	165.7	PT Break
#4_Min	34.5	41.4	41.5	103.6	PT Break

Note: PT Break = Pre-Test Break

**Table 5.8.7. North Bent Longitudinal and Spiral Reinforcement Strains (75% DE)**

A. Longitudinal Reinforcement

Bar	BS, Bot	BH, Bot	MH, Bot	TH, Bot	TH, Top	MH, Top	BH, Top	BS, Top
#1_Max	713.4	896.8	1455.1	1374.9	N/A	549.2	648.1	N/A
#1_Min	-720.0	-1688.9	-2458.0	-2010.0	N/A	104.6	19.6	N/A
#2_Max	229.1	641.2	726.5	818.1	601.8	594.9	562.2	320.4
#2_Min	-78.6	-1367.4	-1106.1	-1250.1	222.4	326.9	333.4	209.2
#3_Max	746.0	981.5	1061.5	1131.9	N/A	529.9	418.6	N/A
#3_Min	-1295.7	-2218.2	<b>-2542.4</b>	-2113.3	N/A	26.2	-32.7	N/A
#4_Max	467.3	582.4	739.4	680.5	442.7	470.6	438.8	281.3
#4_Min	-539.7	-1335.0	-1400.3	-1079.6	71.6	163.4	235.8	176.6
#5_Max	N/A	870.4	1211.4	N/A	N/A	549.2	653.9	N/A
#5_Min	N/A	-1099.4	-2036.5	N/A	N/A	176.5	215.8	N/A
#6_Max	N/A	647.5	1033.7	N/A	N/A	Broken	PT Break	N/A
#6_Min	N/A	-1811.7	<b>-2754.3</b>	N/A	N/A	Broken	PT Break	N/A
#7_Max	N/A	779.4	1066.7	N/A	N/A	510.3	601.9	N/A
#7_Min	N/A	-1532.5	-2094.1	N/A	N/A	26.2	-6.5	N/A
#8_Max	N/A	1131.9	1237.5	N/A	N/A	621.1	568.8	N/A
#8_Min	N/A	-1989.0	-1885.8	N/A	N/A	124.2	85.0	N/A

B. Spiral Reinforcement

Bar	BH,Bot	MH,Bot	TH,Bot	TH,Top	BH,Top
#1_Max	111.2	98.6	91.6	196.3	183.1
#1_Min	-32.7	-26.3	-19.6	98.1	91.6
#2_Max	PT Break	183.3	268.4	163.5	183.1
#2_Min	PT Break	72.0	111.3	104.6	91.5
#3_Max	157.1	183.2	222.6	163.4	176.7
#3_Min	26.2	32.7	85.1	58.8	91.6
#4_Max	130.9	150.5	150.6	183.3	189.6
#4_Min	0.0	39.3	0.0	98.2	98.0

Note: PT Break = Pre-Test Break, Value in bold =Yielded

**Table 5.8.8. South Bent Longitudinal and Spiral Reinforcement Strains (75% DE)**

A. Longitudinal Reinforcement

Bar	BS, Bot	BH, Bot	MH, Bot	TH, Bot	TH, Top	MH, Top	BH, Top	BS, Top
#1_Max	690.2	1616.0	1524.7	1510.8	N/A	891.0	926.2	N/A
#1_Min	-1104.3	-2258.3	-2283.6	-1835.0	N/A	89.8	-20.7	N/A
#2_Max	759.2	655.7	972.7	932.0	580.5	621.6	441.9	234.8
#2_Min	-400.3	-1677.3	-1207.2	-545.4	207.3	324.6	241.7	138.1
#3_Max	937.9	1007.9	918.2	1166.6	N/A	476.5	455.9	N/A
#3_Min	-1655.2	<b>-4542.4</b>	<b>-3099.8</b>	<b>-2864.8</b>	N/A	-518.0	-373.0	N/A
#4_Max	716.0	904.0	817.5	759.2	393.7	317.6	Broken	290.0
#4_Min	-862.0	-1904.6	-1828.9	-1339.0	-345.3	6.9	Broken	138.1
#5_Max	N/A	1408.5	1153.6	N/A	N/A	718.9	1111.7	N/A
#5_Min	N/A	-1650.1	-1671.7	N/A	N/A	214.3	276.2	N/A
#6_Max	N/A	1236.9	1159.4	N/A	N/A	559.6	456.1	N/A
#6_Min	N/A	<b>-3863.5</b>	-2456.8	N/A	N/A	-228.0	-110.6	N/A
#7_Max	N/A	794.2	683.2	N/A	N/A	386.6	524.9	N/A
#7_Min	N/A	<b>-2790.1</b>	<b>-2498.3</b>	N/A	N/A	-283.1	-200.3	N/A
#8_Max	N/A	1118.9	1083.4	N/A	N/A	656.3	1119.4	N/A
#8_Min	N/A	-2217.0	-2359.9	N/A	N/A	-48.4	-55.3	N/A

B. Spiral Reinforcement

Bar	BH,Bot	MH,Bot	TH,Bot	TH,Top	BH,Top
#1_Max	138.1	89.7	82.8	124.3	214.2
#1_Min	-13.8	-75.9	-89.7	69.1	48.4
#2_Max	234.8	131.2	139.6	138.1	431.3
#2_Min	158.8	0.0	20.9	76.0	<b>-6810.9</b>
#3_Max	131.1	124.3	158.6	152.0	138.1
#3_Min	27.6	0.0	-6.9	96.7	89.8
#4_Max	138.0	124.3	103.9	165.7	PT Break
#4_Min	41.4	13.8	-13.8	103.6	PT Break

Note: PT Break = Pre-Test Break, Value in bold =Yielded

**Table 5.8.9. North Bent Longitudinal and Spiral Reinforcement Strains (100% DE)**

A. Longitudinal Reinforcement

Bar	BS, Bot	BH, Bot	MH, Bot	TH, Bot	TH, Top	MH, Top	BH, Top	BS, Top
#1_Max	1210.9	1237.2	1940.2	464.8	N/A	653.9	746.3	N/A
#1_Min	-1930.8	<b>-9047.0</b>	<b>-14295.6</b>	<b>-210672.6</b>	N/A	-261.5	-268.4	N/A
#2_Max	648.0	399.1	1138.8	1295.9	765.3	640.7	608.0	340.0
#2_Min	-333.8	<b>-5508.9</b>	<b>-2696.4</b>	<b>-2840.6</b>	-91.6	-111.1	274.6	163.5
#3_Max	1282.6	948.8	1028.8	1105.7	N/A	673.8	523.3	N/A
#3_Min	-2453.9	<b>-10161.9</b>	<b>-8315.2</b>	<b>-6431.6</b>	N/A	-229.0	-222.4	N/A
#4_Max	1013.7	497.4	484.2	1138.5	546.8	529.5	491.2	287.9
#4_Min	-2159.0	<b>-6825.6</b>	<b>-7204.3</b>	<b>-2748.1</b>	-319.0	-124.2	52.4	124.3
#5_Max	N/A	647.9	838.2	N/A	N/A	529.6	673.5	N/A
#5_Min	N/A	<b>-3481.4</b>	<b>-6705.3</b>	N/A	N/A	-39.2	-45.8	N/A
#6_Max	N/A	457.8	1413.1	N/A	N/A	Broken	PT Break	N/A
#6_Min	N/A	<b>-6834.7</b>	<b>-11730.3</b>	N/A	N/A	Broken	PT Break	N/A
#7_Max	N/A	851.4	1158.3	N/A	N/A	536.4	634.6	N/A
#7_Min	N/A	<b>-2475.6</b>	<b>-3317.9</b>	N/A	N/A	-150.5	-157.0	N/A
#8_Max	N/A	1890.8	2029.8	N/A	N/A	771.4	660.3	N/A
#8_Min	N/A	<b>-13458.3</b>	<b>-9500.9</b>	N/A	N/A	-483.8	-241.9	N/A

B. Spiral Reinforcement

Bar	BH,Bot	MH,Bot	TH,Bot	TH,Top	BH,Top
#1_Max	78.5	72.3	78.5	183.2	170.1
#1_Min	-39.3	-124.9	-104.7	45.8	91.6
#2_Max	PT Break	163.7	189.9	157.0	170.0
#2_Min	PT Break	26.2	-32.7	85.0	71.9
#3_Max	150.5	124.3	163.7	150.3	176.7
#3_Min	19.6	-13.1	19.6	45.8	85.1
#4_Max	170.2	130.9	91.7	183.3	163.4
#4_Min	-72.0	-19.6	-124.4	85.1	85.0

Note: PT Break = Pre-Test Break, Value in bold=Yielded

**Table 5.8.10. South Bent Longitudinal and Spiral Reinforcement Strains (100% DE)**

A. Longitudinal Reinforcement

Bar	BS, Bot	BH, Bot	MH, Bot	TH, Bot	TH, Top	MH, Top	BH, Top	BS, Top
#1_Max	1076.7	2334.3	<b>2911.5</b>	2193.7	N/A	1056.8	1112.8	N/A
#1_Min	-2056.7	<b>-13881.2</b>	<b>-11894.2</b>	<b>-8830.1</b>	N/A	-697.6	-490.7	N/A
#2_Max	855.8	448.7	1145.1	1256.4	608.1	628.5	455.7	234.8
#2_Min	-1621.9	<b>-6667.8</b>	<b>-3056.0</b>	-2105.5	-6.9	152.0	200.2	117.4
#3_Max	2124.2	1201.2	1891.7	2416.1	N/A	732.1	683.8	N/A
#3_Min	-2220.7	<b>-12916.3</b>	<b>-8988.9</b>	<b>-6999.7</b>	N/A	-1070.5	-787.4	N/A
#4_Max	834.2	800.5	817.5	759.2	442.0	324.5	Broken	310.7
#4_Min	-2301.0	<b>-10082.1</b>	<b>-6858.3</b>	<b>-2643.4</b>	-752.8	-365.9	Broken	82.9
#5_Max	N/A	1436.1	1208.9	N/A	N/A	850.2	1291.3	N/A
#5_Min	N/A	<b>-14616.5</b>	<b>-9781.7</b>	N/A	N/A	-103.7	-193.3	N/A
#6_Max	N/A	694.9	1380.2	N/A	N/A	711.5	573.6	N/A
#6_Min	N/A	<b>-15857.2</b>	<b>-6556.1</b>	N/A	N/A	-704.6	-317.9	N/A
#7_Max	N/A	856.4	766.0	N/A	N/A	441.9	628.5	N/A
#7_Min	N/A	<b>-11996.1</b>	<b>-11476.8</b>	N/A	N/A	-704.3	-642.3	N/A
#8_Max	N/A	1229.4	1221.4	N/A	N/A	732.3	1257.6	N/A
#8_Min	N/A	<b>-10297.9</b>	<b>-10454.0</b>	N/A	N/A	-697.8	-525.2	N/A

B. Spiral Reinforcement

Bar	BH,Bot	MH,Bot	TH,Bot	TH,Top	BH,Top
#1_Max	103.6	48.3	48.3	110.5	214.2
#1_Min	-145.0	-193.2	-158.8	41.4	-6.9
#2_Max	241.7	138.1	111.6	158.8	438.3
#2_Min	145.0	-221.0	-160.5	76.0	<b>-4821.2</b>
#3_Max	124.2	110.5	137.9	152.0	131.2
#3_Min	-27.6	-75.9	-137.9	69.1	69.1
#4_Max	138.0	96.7	69.2	165.7	PT Break
#4_Min	27.6	-221.0	-235.4	89.8	PT Break

Note: PT Break = Pre-Test Break, Value in bold =Yielded

**Table 5.8.11. North Bent Longitudinal and Spiral Reinforcement Strains (150% DE)**

A. Longitudinal Reinforcement

Bar	BS, Bot	BH, Bot	MH, Bot	TH, Bot	TH, Top	MH, Top	BH, Top	BS, Top
#1_Max	1577.4	307.7	2182.7	<b>23294.6</b>	N/A	784.6	844.5	N/A
#1_Min	<b>-2552.6</b>	<b>-15082.7</b>	<b>-18438.1</b>	<b>-210672.6</b>	N/A	-385.8	-386.3	N/A
#2_Max	1446.6	-732.8	1138.8	1158.5	811.1	673.4	575.3	307.3
#2_Min	-693.9	<b>-13889.9</b>	<b>-11178.3</b>	<b>-12036.5</b>	-248.6	58.8	300.7	163.5
#3_Max	2061.3	-1315.2	1002.5	1131.9	N/A	686.9	510.2	N/A
#3_Min	<b>-2957.8</b>	<b>-20834.2</b>	<b>-17135.0</b>	<b>-11705.1</b>	N/A	-686.9	-385.9	N/A
#4_Max	2126.1	-1380.8	1086.2	1086.1	579.4	503.3	445.4	268.2
#4_Min	<b>-3218.7</b>	<b>-17119.7</b>	<b>-15436.0</b>	<b>-8878.9</b>	-481.7	-248.4	65.5	117.8
#5_Max	N/A	-104.7	-432.2	N/A	N/A	601.5	784.7	N/A
#5_Min	N/A	<b>-7872.5</b>	<b>-15080.5</b>	N/A	N/A	-170.0	-176.6	N/A
#6_Max	N/A	-673.7	1773.0	N/A	N/A	Broken	PT Break	N/A
#6_Min	N/A	<b>-17580.6</b>	<b>-24834.6</b>	N/A	N/A	Broken	PT Break	N/A
#7_Max	N/A	235.8	287.9	N/A	N/A	543.0	634.6	N/A
#7_Min	N/A	<b>-11795.2</b>	<b>-15444.3</b>	N/A	N/A	-837.4	-464.5	N/A
#8_Max	N/A	<b>3755.5</b>	<b>3968.0</b>	N/A	N/A	830.3	686.4	N/A
#8_Min	N/A	<b>-22520.0</b>	<b>-16539.8</b>	N/A	N/A	-660.3	-294.2	N/A

B. Spiral Reinforcement

Bar	BH,Bot	MH,Bot	TH,Bot	TH,Top	BH,Top
#1_Max	45.8	6.6	13.1	163.6	170.1
#1_Min	-183.2	-315.6	-307.6	-10559.3	65.4
#2_Max	PT Break	131.0	144.0	137.3	150.4
#2_Min	PT Break	-209.5	-183.3	71.9	58.9
#3_Max	124.3	98.1	130.9	137.3	157.0
#3_Min	-65.4	-575.8	-72.0	26.1	65.4
#4_Max	202.9	91.6	-6.5	157.1	163.4
#4_Min	-222.5	-235.6	-537.0	52.4	65.4

Note: PT Break = Pre-Test Break, Value in bold =Yielded

**Table 5.8.12. South Bent Longitudinal and Spiral Reinforcement Strains (150% DE)**

A. Longitudinal Reinforcement

Bar	BS, Bot	BH, Bot	MH, Bot	TH, Bot	TH, Top	MH, Top	BH, Top	BS, Top
#1_Max	1594.3	2348.1	<b>5202.0</b>	<b>3966.7</b>	N/A	1146.6	1216.5	N/A
#1_Min	<b>-4092.8</b>	<b>-12541.4</b>	<b>-16868.6</b>	<b>-15535.5</b>	N/A	-1112.0	-698.1	N/A
#2_Max	1663.3	-1118.2	876.1	1111.4	573.6	649.3	476.4	234.8
#2_Min	<b>-2574.4</b>	<b>-17277.0</b>	<b>-11058.1</b>	<b>-8145.9</b>	-138.2	-13.8	124.3	96.7
#3_Max	<b>4186.2</b>	1960.6	<b>3051.5</b>	<b>2733.6</b>	N/A	801.1	732.1	N/A
#3_Min	<b>-5627.6</b>	<b>-27289.2</b>	<b>-17805.1</b>	<b>-17050.5</b>	N/A	-1512.5	-1118.9	N/A
#4_Max	1418.2	<b>-4361.3</b>	-2272.2	-96.6	455.8	345.2	Broken	317.6
#4_Min	<b>-7320.2</b>	<b>-23600.8</b>	<b>-20041.4</b>	<b>-10615.1</b>	-801.1	-448.8	Broken	76.0
#5_Max	N/A	-2126.5	41.4	N/A	N/A	871.0	1367.2	N/A
#5_Min	N/A	<b>-24876.4</b>	<b>-18713.7</b>	N/A	N/A	-352.5	-290.0	N/A
#6_Max	N/A	1362.0	<b>2594.9</b>	N/A	N/A	773.7	622.0	N/A
#6_Min	N/A	<b>-25960.7</b>	<b>-14168.2</b>	N/A	N/A	-1098.4	-559.8	N/A
#7_Max	N/A	-2361.9	-338.2	N/A	N/A	490.2	649.2	N/A
#7_Min	N/A	<b>-4302.6</b>	<b>-19282.1</b>	N/A	N/A	-1097.8	-960.0	N/A
#8_Max	N/A	-462.7	779.7	N/A	N/A	842.8	1375.1	N/A
#8_Min	N/A	<b>-20133.0</b>	<b>-18161.7</b>	N/A	N/A	-1036.3	-739.4	N/A

B. Spiral Reinforcement

Bar	BH,Bot	MH,Bot	TH,Bot	TH,Top	BH,Top
#1_Max	787.4	-13.8	20.7	96.7	214.2
#1_Min	-400.6	-558.9	-393.5	13.8	-55.3
#2_Max	207.1	41.4	7.0	145.0	438.3
#2_Min	-186.4	-808.0	-614.1	41.4	<b>-3708.1</b>
#3_Max	89.7	69.0	110.4	138.1	103.6
#3_Min	-186.3	-303.8	-296.6	48.4	6.9
#4_Max	131.1	-27.6	-20.8	138.1	PT Break
#4_Min	0.0	-435.0	-436.2	69.1	PT Break

Note: PT Break = Pre-Test Break, Value in bold =Yielded

**Table 5.8.13. North Bent Longitudinal and Spiral Reinforcement Strains (200% DE)**

A. Longitudinal Reinforcement

Bar	BS, Bot	BH, Bot	MH, Bot	TH, Bot	TH, Top	MH, Top	BH, Top	BS, Top
#1_Max	1891.6	137.5	2962.7	Broken	N/A	863.1	896.9	N/A
#1_Min	<b>-5196.9</b>	<b>-16359.2</b>	<b>-20116.1</b>	Broken	N/A	-385.8	-405.9	N/A
#2_Max	661.1	-1066.4	1760.5	556.3	811.1	706.1	693.0	359.6
#2_Min	-576.0	<b>-14936.8</b>	<b>-16610.4</b>	<b>-19412.9</b>	-235.5	-71.9	39.2	98.1
#3_Max	2395.0	-1452.6	766.7	1413.3	N/A	713.0	523.3	N/A
#3_Min	<b>-9848.4</b>	<b>-31643.9</b>	<b>-25030.9</b>	<b>-18686.3</b>	N/A	-811.2	-477.5	N/A
#4_Max	<b>2837.0</b>	-1492.1	1629.3	1406.8	546.8	451.0	497.7	300.9
#4_Min	<b>-9669.4</b>	<b>-25718.7</b>	<b>-23582.6</b>	<b>-13675.0</b>	-442.7	-287.6	-91.7	98.1
#5_Max	N/A	163.6	-176.8	N/A	N/A	778.1	935.1	N/A
#5_Min	N/A	<b>-10581.8</b>	<b>-18439.7</b>	N/A	N/A	-202.7	-287.7	N/A
#6_Max	N/A	-1523.9	1576.7	N/A	N/A	Broken	PT Break	N/A
#6_Min	N/A	<b>-26429.7</b>	<b>-31658.2</b>	N/A	N/A	Broken	PT Break	N/A
#7_Max	N/A	-2194.0	-1269.6	N/A	N/A	654.2	700.0	N/A
#7_Min	N/A	<b>-20224.0</b>	<b>-23853.6</b>	N/A	N/A	-1105.6	-660.7	N/A
#8_Max	N/A	<b>6366.1</b>	<b>4989.4</b>	N/A	N/A	804.1	660.3	N/A
#8_Min	N/A	<b>-29265.5</b>	<b>-21797.7</b>	N/A	N/A	-627.6	-300.7	N/A

B. Spiral Reinforcement

Bar	BH,Bot	MH,Bot	TH,Bot	TH,Top	BH,Top
#1_Max	-26.2	-78.9	-98.2	163.6	157.0
#1_Min	-458.0	-637.8	-732.9	-1975.8	71.9
#2_Max	PT Break	26.2	72.0	163.5	150.4
#2_Min	PT Break	-353.6	-438.6	91.6	85.0
#3_Max	58.9	-32.7	58.9	137.3	150.5
#3_Min	-222.5	-798.2	-189.9	26.1	78.5
#4_Max	91.6	-45.8	-137.5	157.1	143.8
#4_Min	-412.4	-549.6	-792.4	78.6	78.4

Note: PT Break = Pre-Test Break, Value in bold =Yielded

**Table 5.8.14. South Bent Longitudinal and Spiral Reinforcement Strains (200% DE)**

A. Longitudinal Reinforcement

Bar	BS, Bot	BH, Bot	MH, Bot	TH, Bot	TH, Top	MH, Top	BH, Top	BS, Top
#1_Max	2112.0	<b>7610.5</b>	<b>8430.8</b>	<b>3166.4</b>	N/A	1236.3	1251.0	N/A
#1_Min	<b>-7633.4</b>	<b>-6139.5</b>	<b>-10645.5</b>	<b>-21075.0</b>	N/A	-1188.0	-725.7	N/A
#2_Max	2208.6	<b>-3195.9</b>	1172.7	828.4	587.4	642.3	469.5	234.8
#2_Min	<b>-5631.9</b>	<b>-24234.7</b>	<b>-16659.5</b>	<b>-13896.4</b>	-235.0	-214.1	6.9	62.2
#3_Max	<b>4986.3</b>	2147.0	<b>2630.4</b>	1967.4	N/A	821.8	752.9	N/A
#3_Min	<b>-10565.6</b>	<b>-40460.9</b>	<b>-27808.8</b>	<b>-23698.2</b>	N/A	-1664.4	-1236.3	N/A
#4_Max	1174.8	<b>-5513.7</b>	<b>-3290.6</b>	-980.1	372.9	303.8	Broken	310.7
#4_Min	<b>-11220.1</b>	<b>-30004.7</b>	<b>-23699.2</b>	<b>-13541.6</b>	-739.0	-497.1	Broken	89.8
#5_Max	N/A	<b>-2913.6</b>	-594.1	N/A	N/A	919.4	1367.2	N/A
#5_Min	N/A	<b>-27065.1</b>	<b>-21877.6</b>	N/A	N/A	-490.8	-531.7	N/A
#6_Max	N/A	<b>2585.0</b>	<b>3850.9</b>	N/A	N/A	808.3	628.9	N/A
#6_Min	N/A	<b>-38642.3</b>	<b>-21814.7</b>	N/A	N/A	-1340.2	-711.8	N/A
#7_Max	N/A	-2203.1	641.8	N/A	N/A	538.5	759.7	N/A
#7_Min	N/A	-3853.7	<b>-3643.9</b>	N/A	N/A	-1222.1	-1056.7	N/A
#8_Max	N/A	131.2	2035.6	N/A	N/A	918.8	1527.1	N/A
#8_Min	N/A	<b>-27336.7</b>	<b>-20942.5</b>	N/A	N/A	-1195.2	-843.0	N/A

B. Spiral Reinforcement

Bar	BH,Bot	MH,Bot	TH,Bot	TH,Top	BH,Top
#1_Max	2148.0	-165.6	-75.9	96.7	214.2
#1_Min	290.1	-2166.7	-814.6	6.9	-69.1
#2_Max	<b>4764.3</b>	-186.5	-125.6	117.4	389.6
#2_Min	<b>-187734.1</b>	-1077.3	-711.8	20.7	<b>-36538.3</b>
#3_Max	27.6	13.8	20.7	145.1	76.0
#3_Min	-324.4	-510.9	-544.9	48.4	-13.8
#4_Max	151.8	-179.5	-131.6	138.1	PT Break
#4_Min	-48.3	-704.4	-823.9	76.0	PT Break

Note: PT Break = Pre-Test Break, Value in bold =Yielded

**Table 5.8.15. North Bent Longitudinal and Spiral Reinforcement Strains (250% DE)**

A. Longitudinal Reinforcement

Bar	BS, Bot	BH, Bot	MH, Bot	TH, Bot	TH, Top	MH, Top	BH, Top	BS, Top
#1_Max	2094.5	39.3	<b>5283.0</b>	Broken	N/A	902.3	936.2	N/A
#1_Min	<b>-6401.2</b>	<b>-17766.6</b>	<b>-20732.2</b>	Broken	N/A	-470.8	-504.1	N/A
#2_Max	1341.9	-13.1	2362.6	-1106.1	850.3	804.2	843.4	411.9
#2_Min	-274.9	<b>-10579.4</b>	<b>-21178.6</b>	<b>-25663.6</b>	-399.0	-594.9	-313.8	-39.2
#3_Max	<b>2892.3</b>	-2021.9	314.5	922.5	N/A	726.1	542.9	N/A
#3_Min	<b>-14893.6</b>	<b>-41701.2</b>	<b>-33064.4</b>	<b>-25778.7</b>	N/A	-955.1	-614.8	N/A
#4_Max	<b>2883.0</b>	-314.1	2283.7	968.4	540.3	549.1	596.0	314.0
#4_Min	<b>-17568.2</b>	<b>-33355.8</b>	<b>-33718.3</b>	<b>-19184.3</b>	-618.4	-640.6	-465.0	26.2
#5_Max	N/A	1230.3	929.8	N/A	N/A	941.6	1105.1	N/A
#5_Min	N/A	<b>-14861.6</b>	<b>-24483.7</b>	N/A	N/A	-294.2	-503.5	N/A
#6_Max	N/A	-470.9	45.8	N/A	N/A	Broken	PT Break	N/A
#6_Min	N/A	<b>-28849.6</b>	<b>-13536.0</b>	N/A	N/A	Broken	PT Break	N/A
#7_Max	N/A	<b>-2770.3</b>	-2316.6	N/A	N/A	686.9	732.7	N/A
#7_Min	N/A	<b>-27513.3</b>	<b>-30064.0</b>	N/A	N/A	-1576.6	-1053.3	N/A
#8_Max	N/A	<b>7138.1</b>	<b>8643.1</b>	N/A	N/A	699.5	594.9	N/A
#8_Min	N/A	<b>-36135.4</b>	<b>-27952.7</b>	N/A	N/A	-725.7	-346.5	N/A

B. Spiral Reinforcement

Bar	BH,Bot	MH,Bot	TH,Bot	TH,Top	BH,Top
#1_Max	-111.2	-111.8	-170.1	1105.7	150.4
#1_Min	-1144.9	-1262.5	-1066.6	<b>-13411.8</b>	78.5
#2_Max	PT Break	-65.5	130.9	157.0	143.9
#2_Min	PT Break	-602.4	-608.9	65.4	52.3
#3_Max	-32.7	-183.2	-13.1	124.2	150.5
#3_Min	-327.2	-916.0	-451.7	26.1	72.0
#4_Max	-19.6	-196.3	-216.1	144.0	143.8
#4_Min	-628.4	-961.9	-864.5	58.9	71.9

Note: PT Break = Pre-Test Break, Value in bold =Yielded

**Table 5.8.16. South Bent Longitudinal and Spiral Reinforcement Strains (250% DE)**

A. Longitudinal Reinforcement

Bar	BS, Bot	BH, Bot	MH, Bot	TH, Bot	TH, Top	MH, Top	BH, Top	BS, Top
#1_Max	1946.3	<b>9316.3</b>	1855.9	<b>3897.7</b>	N/A	1250.2	1264.9	N/A
#1_Min	<b>-9352.0</b>	<b>-2783.2</b>	<b>-5050.2</b>	<b>-21923.6</b>	N/A	-1222.5	-767.2	N/A
#2_Max	2291.4	<b>-3402.9</b>	1076.1	414.2	594.3	676.9	483.4	234.8
#2_Min	<b>-11070.5</b>	<b>-29811.9</b>	<b>-23654.4</b>	<b>-17838.2</b>	-311.0	-331.5	-62.1	55.3
#3_Max	<b>5103.5</b>	1504.9	<b>2526.8</b>	1725.8	N/A	814.9	739.0	N/A
#3_Min	<b>-14600.1</b>	<b>-55558.6</b>	<b>-36279.9</b>	<b>-14220.3</b>	N/A	-1761.1	-1333.0	N/A
#4_Max	931.5	<b>-5693.2</b>	<b>-4925.5</b>	-1097.4	372.9	310.7	Broken	303.8
#4_Min	<b>-14459.6</b>	<b>-35601.3</b>	<b>-28409.9</b>	<b>-16164.3</b>	-649.2	-435.0	Broken	82.9
#5_Max	N/A	<b>-3044.8</b>	-677.0	N/A	N/A	953.9	1394.8	N/A
#5_Min	N/A	<b>-26057.0</b>	<b>-21373.3</b>	N/A	N/A	-573.7	-662.9	N/A
#6_Max	N/A	<b>3106.1</b>	<b>2877.8</b>	N/A	N/A	759.9	608.1	N/A
#6_Min	N/A	<b>-51247.4</b>	<b>-29392.2</b>	N/A	N/A	-1471.4	-787.8	N/A
#7_Max	N/A	-814.9	1131.8	N/A	N/A	649.0	870.2	N/A
#7_Min	N/A	<b>-3315.0</b>	<b>-3567.9</b>	N/A	N/A	-1346.4	-1187.9	N/A
#8_Max	N/A	1360.6	-558.9	N/A	N/A	953.4	1561.7	N/A
#8_Min	N/A	<b>-32475.3</b>	<b>-7604.2</b>	N/A	N/A	-1077.7	-711.7	N/A

B. Spiral Reinforcement

Bar	BH,Bot	MH,Bot	TH,Bot	TH,Top	BH,Top
#1_Max	1871.8	-572.7	-172.6	89.8	200.4
#1_Min	835.7	<b>-2711.8</b>	-1063.1	0.0	-82.9
#2_Max	483.3	-303.9	-209.3	69.1	Broken
#2_Min	<b>-88249.6</b>	-1077.3	-900.2	6.9	Broken
#3_Max	-34.5	-6.9	-117.3	138.1	48.3
#3_Min	-234.6	-586.9	-710.4	48.4	-34.5
#4_Max	69.0	-193.4	-207.7	131.2	PT Break
#4_Min	-186.3	-711.3	-1211.6	69.1	PT Break

Note: PT Break = Pre-Test Break, Value in bold =Yielded

**Table 5.8.17. North Bent Longitudinal and Spiral Reinforcement Strains (300% DE)**

A. Longitudinal Reinforcement

Bar	BS, Bot	BH, Bot	MH, Bot	TH, Bot	TH, Top	MH, Top	BH, Top	BS, Top
#1_Max	1799.9	-386.2	<b>12368.5</b>	Broken	N/A	921.9	949.3	N/A
#1_Min	<b>-6650.0</b>	<b>-17583.3</b>	<b>-19880.1</b>	Broken	N/A	-575.4	-628.5	N/A
#2_Max	2304.1	<b>6320.2</b>	<b>2892.8</b>	<b>-2834.1</b>	1040.0	895.7	1033.0	477.3
#2_Min	-379.7	<b>-3513.4</b>	<b>-26983.7</b>	<b>-30533.2</b>	-556.0	-1333.7	-627.6	-274.6
#3_Max	<b>3108.3</b>	<b>-2676.3</b>	-235.9	-490.7	N/A	739.2	536.3	N/A
#3_Min	<b>-20279.1</b>	<b>-42813.5</b>	<b>-41707.2</b>	<b>-31503.7</b>	N/A	-1177.5	-863.4	N/A
#4_Max	1935.2	2225.0	<b>3239.0</b>	301.0	631.5	666.7	713.9	320.6
#4_Min	<b>-25322.1</b>	<b>-40508.7</b>	<b>-41518.1</b>	<b>-23548.5</b>	-963.5	-1072.0	-936.6	-215.9
#5_Max	N/A	<b>3808.6</b>	1257.3	N/A	N/A	1124.6	1288.2	N/A
#5_Min	N/A	<b>-17911.1</b>	<b>-30403.2</b>	N/A	N/A	-405.4	-719.3	N/A
#6_Max	N/A	0.0	-1256.1	N/A	N/A	Broken	PT Break	N/A
#6_Min	N/A	<b>-21308.6</b>	<b>-6660.1</b>	N/A	N/A	Broken	PT Break	N/A
#7_Max	N/A	<b>-5488.3</b>	<b>-6190.8</b>	N/A	N/A	647.6	726.2	N/A
#7_Min	N/A	<b>-34331.0</b>	<b>-34592.6</b>	N/A	N/A	-2119.6	-1635.5	N/A
#8_Max	N/A	<b>5221.1</b>	<b>14654.0</b>	N/A	N/A	634.1	594.9	N/A
#8_Min	N/A	<b>-41664.0</b>	<b>-30323.0</b>	N/A	N/A	-843.3	-418.4	N/A

B. Spiral Reinforcement

Bar	BH,Bot	MH,Bot	TH,Bot	TH,Top	BH,Top
#1_Max	-307.5	-236.7	-248.7	1890.7	137.4
#1_Min	-2342.1	-2150.2	-1223.7	<b>-16643.7</b>	58.9
#2_Max	PT Break	-137.5	183.3	137.3	130.8
#2_Min	PT Break	-1106.6	-1080.2	32.7	13.1
#3_Max	-130.9	-268.3	13.1	117.7	124.3
#3_Min	-425.4	-1092.7	-628.5	0.0	45.8
#4_Max	-242.2	-327.2	-268.5	117.8	130.7
#4_Min	-1577.4	-1622.7	-1060.9	32.7	39.2

Note: PT Break = Pre-Test Break, Value in bold =Yielded

**Table 5.8.18. South Bent Longitudinal and Spiral Reinforcement Strains (300% DE)**

A. Longitudinal Reinforcement

Bar	BS, Bot	BH, Bot	MH, Bot	TH, Bot	TH, Top	MH, Top	BH, Top	BS, Top
#1_Max	1801.4	<b>8998.6</b>	441.5	<b>4946.3</b>	N/A	1250.2	1264.9	N/A
#1_Min	<b>-9931.7</b>	-2161.6	<b>-4394.8</b>	<b>-20205.8</b>	N/A	-1146.6	-725.7	N/A
#2_Max	1483.9	<b>-4438.3</b>	<b>79455.7</b>	-759.4	587.4	683.8	476.4	676.9
#2_Min	<b>-16895.6</b>	<b>-28673.0</b>	<b>-29069.6</b>	<b>-19964.4</b>	-373.2	-400.6	-179.5	338.5
#3_Max	<b>5006.9</b>	1960.6	2450.9	1042.4	N/A	787.3	732.1	N/A
#3_Min	<b>-19931.2</b>	<b>-72858.6</b>	<b>-43963.9</b>	<b>-11051.8</b>	N/A	-1809.4	-1395.2	N/A
#4_Max	896.8	<b>-4803.0</b>	<b>-5410.4</b>	-987.0	435.1	352.1	Broken	338.3
#4_Min	<b>-17747.8</b>	<b>-41418.6</b>	<b>-31617.4</b>	<b>-17696.5</b>	-856.4	-538.6	Broken	-13.8
#5_Max	N/A	<b>-3113.9</b>	-193.4	N/A	N/A	1009.2	1539.8	N/A
#5_Min	N/A	<b>-26126.1</b>	<b>-20717.1</b>	N/A	N/A	-573.7	-725.0	N/A
#6_Max	N/A	-569.8	-103.5	N/A	N/A	683.9	545.9	N/A
#6_Min	N/A	<b>-65075.5</b>	<b>-26141.7</b>	N/A	N/A	-1526.7	-850.0	N/A
#7_Max	N/A	<b>5683.8</b>	1559.7	N/A	N/A	704.3	980.7	N/A
#7_Min	N/A	<b>-2589.8</b>	<b>-3243.6</b>	N/A	N/A	-1470.6	-1298.4	N/A
#8_Max	N/A	<b>3536.2</b>	-1152.4	N/A	N/A	953.4	1589.3	N/A
#8_Min	N/A	<b>-34353.9</b>	<b>-5823.9</b>	N/A	N/A	-918.8	-608.1	N/A

B. Spiral Reinforcement

Bar	BH,Bot	MH,Bot	TH,Bot	TH,Top	BH,Top
#1_Max	2493.4	-993.6	-262.3	82.9	179.6
#1_Min	739.0	<b>-4002.1</b>	-1297.8	-6.9	-96.7
#2_Max	<b>5157.9</b>	-386.7	-244.2	62.2	Broken
#2_Min	<b>-32210.7</b>	-1243.0	-1116.5	-34.5	Broken
#3_Max	-41.4	-34.5	-124.1	131.2	34.5
#3_Min	-324.4	-745.7	-675.9	48.4	-48.3
#4_Max	-55.2	-221.0	-380.8	124.3	PT Break
#4_Min	-345.0	-738.9	-1537.1	48.3	PT Break

Note: PT Break = Pre-Test Break, Value in bold =Yielded

**Table 5.8.19. North Bent Longitudinal and Spiral Reinforcement Strains (350% DE)**

A. Longitudinal Reinforcement

Bar	BS, Bot	BH, Bot	MH, Bot	TH, Bot	TH, Top	MH, Top	BH, Top	BS, Top
#1_Max	425.4	Broken	<b>25576.1</b>	Broken	N/A	941.6	962.4	N/A
#1_Min	<b>-5236.2</b>	Broken	<b>-21040.3</b>	Broken	N/A	-634.2	-739.8	N/A
#2_Max	<b>2500.5</b>	<b>9722.3</b>	<b>3017.1</b>	<b>-4103.8</b>	1445.5	1157.2	1287.9	555.8
#2_Min	-602.2	-1936.6	<b>-33247.0</b>	<b>-29983.4</b>	-699.9	-8636.5	-1183.3	-647.3
#3_Max	<b>2866.2</b>	<b>-6936.0</b>	-1788.9	-1164.6	N/A	745.8	529.8	N/A
#3_Min	<b>-25468.3</b>	<b>-13289.7</b>	<b>-48358.1</b>	<b>-36672.5</b>	N/A	-1360.7	-1013.8	N/A
#4_Max	612.2	<b>5215.7</b>	<b>4423.4</b>	-831.0	696.6	764.8	858.0	372.9
#4_Min	<b>-33431.5</b>	<b>-45632.8</b>	<b>-46275.2</b>	<b>-26322.8</b>	-2044.1	-1810.7	-1460.5	-438.3
#5_Max	N/A	<b>4757.5</b>	-1486.4	N/A	N/A	1203.1	1379.8	N/A
#5_Min	N/A	<b>-19514.4</b>	<b>-35962.6</b>	N/A	N/A	-601.5	-1033.2	N/A
#6_Max	N/A	1026.8	-2433.7	N/A	N/A	Broken	PT Break	N/A
#6_Min	N/A	<b>-14859.8</b>	<b>-5116.1</b>	N/A	N/A	Broken	PT Break	N/A
#7_Max	N/A	<b>-8494.3</b>	<b>-7898.8</b>	N/A	N/A	647.6	752.3	N/A
#7_Min	N/A	<b>-43310.0</b>	<b>-35201.2</b>	N/A	N/A	-2335.5	-1923.3	N/A
#8_Max	N/A	<b>3284.4</b>	<b>40838.8</b>	N/A	N/A	673.4	640.7	N/A
#8_Min	N/A	<b>-46152.3</b>	<b>-27311.0</b>	N/A	N/A	-1006.8	-666.8	N/A

B. Spiral Reinforcement

Bar	BH,Bot	MH,Bot	TH,Bot	TH,Top	BH,Top
#1_Max	-157.0	-670.7	-333.7	157.0	150.4
#1_Min	-1949.6	<b>-2696.0</b>	-1616.3	<b>-5135.7</b>	52.3
#2_Max	PT Break	-229.2	170.2	124.3	104.6
#2_Min	PT Break	-1689.4	-1263.5	-26.2	-6.5
#3_Max	-242.1	-379.5	45.8	104.6	117.8
#3_Min	-562.8	-1164.6	-635.0	-6.5	39.3
#4_Max	-674.2	-523.5	-301.3	104.8	117.7
#4_Min	<b>-3920.7</b>	-2335.9	-1257.4	0.0	19.6

Note: PT Break = Pre-Test Break, Value in bold =Yielded

**Table 5.8.20. South Bent Longitudinal and Spiral Reinforcement Strains (350% DE)**

A. Longitudinal Reinforcement

Bar	BS, Bot	BH, Bot	MH, Bot	TH, Bot	TH, Top	MH, Top	BH, Top	BS, Top
#1_Max	1656.4	<b>8853.6</b>	-531.2	<b>5884.5</b>	N/A	1208.7	1230.3	N/A
#1_Min	<b>-9669.5</b>	-1560.8	-3780.8	<b>-17315.3</b>	N/A	-1222.5	-794.9	N/A
#2_Max	303.7	<b>-3278.7</b>	Broken	-1988.2	628.9	773.6	552.4	711.4
#2_Min	<b>-24515.1</b>	<b>-28866.3</b>	Broken	<b>-21200.1</b>	-380.1	-400.6	-207.2	103.6
#3_Max	<b>5172.5</b>	<b>2692.3</b>	1332.4	690.3	N/A	808.0	752.9	N/A
#3_Min	<b>-27193.3</b>	<b>-92885.4</b>	<b>-43439.2</b>	<b>-9643.6</b>	N/A	-1837.0	-1450.5	N/A
#4_Max	20.9	<b>-4892.7</b>	<b>-7481.8</b>	-1221.6	511.1	421.2	Broken	386.7
#4_Min	<b>-20730.1</b>	<b>-44544.7</b>	<b>-35891.7</b>	<b>-17323.8</b>	-1111.9	-780.2	Broken	-193.3
#5_Max	N/A	-1311.8	538.8	N/A	N/A	1140.5	1747.0	N/A
#5_Min	N/A	<b>-28231.9</b>	<b>-23252.3</b>	N/A	N/A	-608.3	-697.4	N/A
#6_Max	N/A	<b>-8178.7</b>	2208.4	N/A	N/A	635.6	539.0	N/A
#6_Min	N/A	<b>-87075.4</b>	<b>-10289.7</b>	N/A	N/A	-1478.4	-801.6	N/A
#7_Max	N/A	<b>10773.7</b>	1683.9	N/A	N/A	697.3	980.7	N/A
#7_Min	N/A	-994.5	-2394.7	N/A	N/A	-1574.2	-1629.9	N/A
#8_Max	N/A	<b>5104.1</b>	-1159.3	N/A	N/A	911.9	1513.3	N/A
#8_Min	N/A	<b>-33815.2</b>	<b>-5071.7</b>	N/A	N/A	-967.2	-656.5	N/A

B. Spiral Reinforcement

Bar	BH,Bot	MH,Bot	TH,Bot	TH,Top	BH,Top
#1_Max	815.0	-1711.2	-331.4	76.0	179.6
#1_Min	-393.7	<b>-4864.6</b>	-1636.1	-6.9	-89.8
#2_Max	Broken	-469.6	-258.2	55.2	Broken
#2_Min	Broken	-1415.7	-1660.8	-48.3	Broken
#3_Max	27.6	13.8	-131.0	131.2	27.6
#3_Min	-407.2	-759.5	-1076.0	41.4	-62.2
#4_Max	-117.3	-227.9	-540.0	110.5	PT Break
#4_Min	-476.2	-1519.2	-1897.1	34.5	PT Break

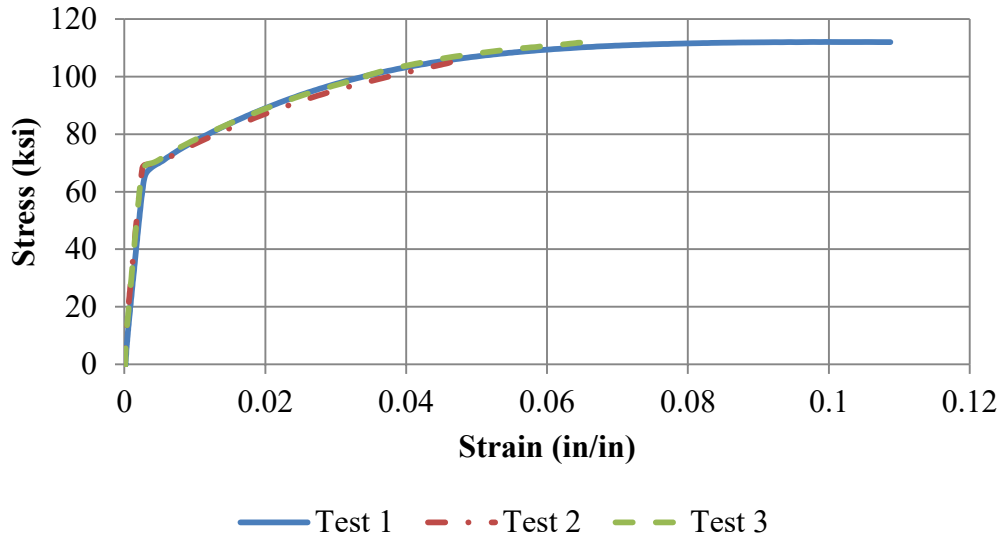
Note: PT Break = Pre-Test Break, Value in bold =Yielded



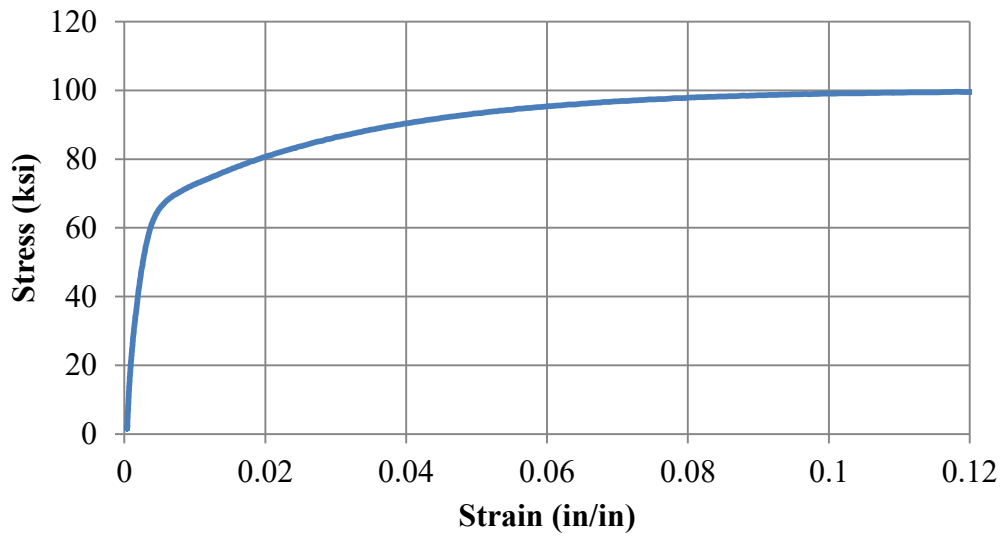
**Figure 5.2.1. Typical Concrete Compression Test**



**Figure 5.2.2. Typical Steel Tension Test**



(a)



(b)

**Figure 5.2.3. Stress vs. Strain Results from (a) #5 and (b) #3 Rebar Tests**

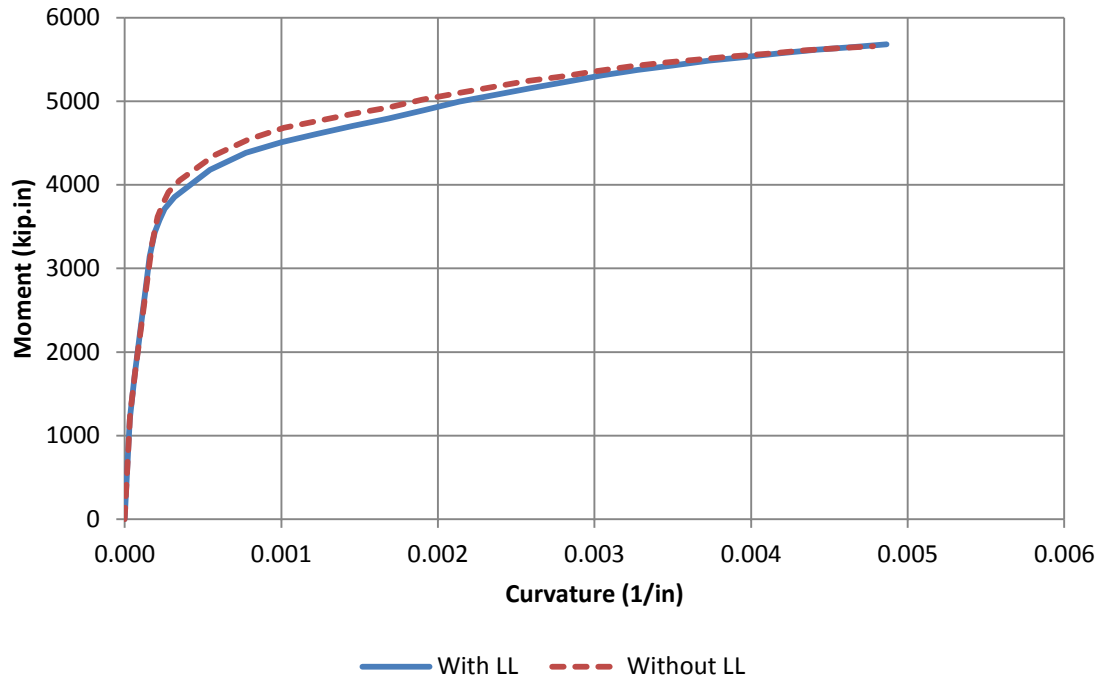


**Figure 5.2.4. Analytical Moment vs. Curvature Comparison for Columns in No-Live Load and Live Load Experiments under Dead Load**

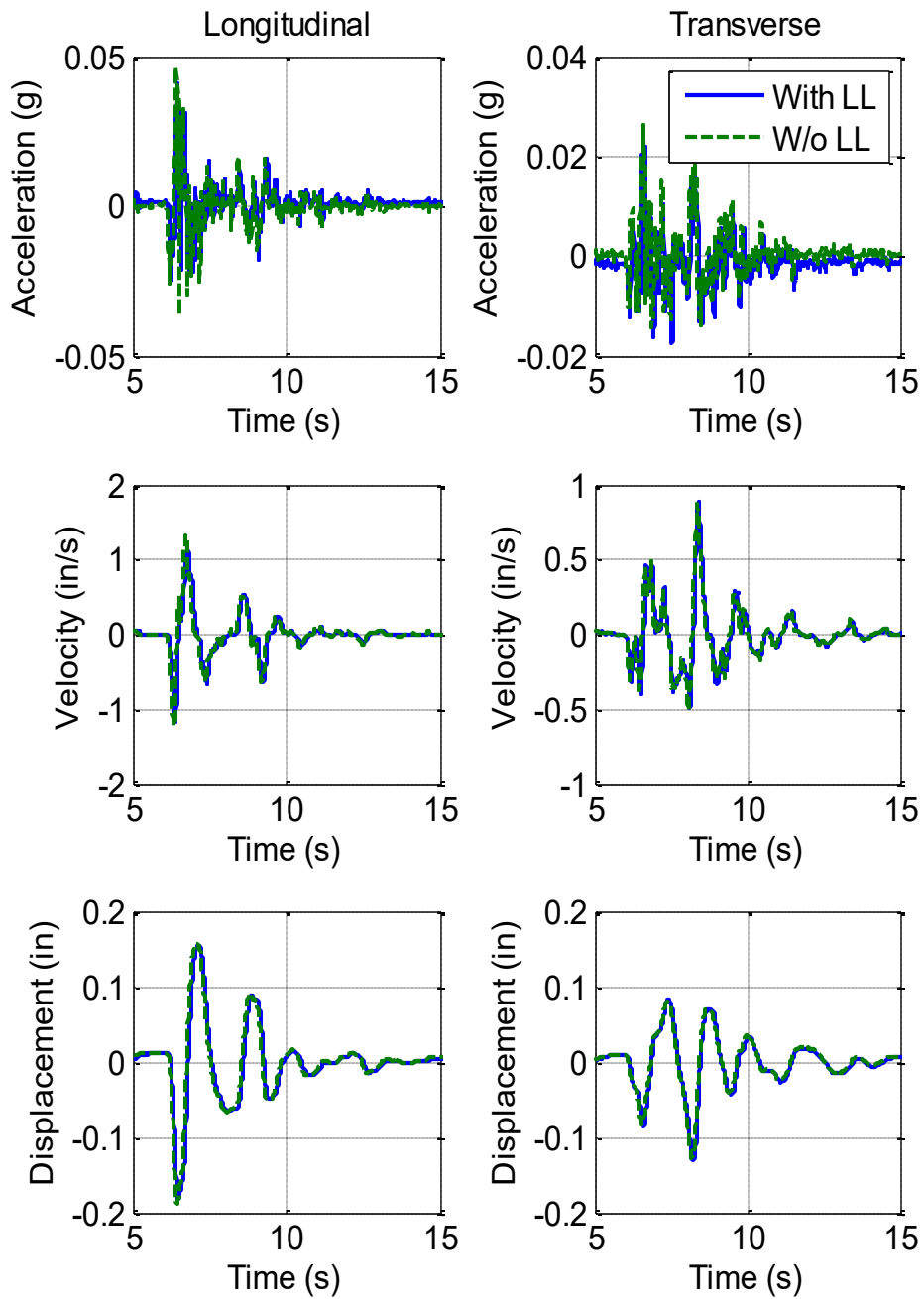


**Figure 5.3.1. Histories of Average Table Motion (10% DE)**

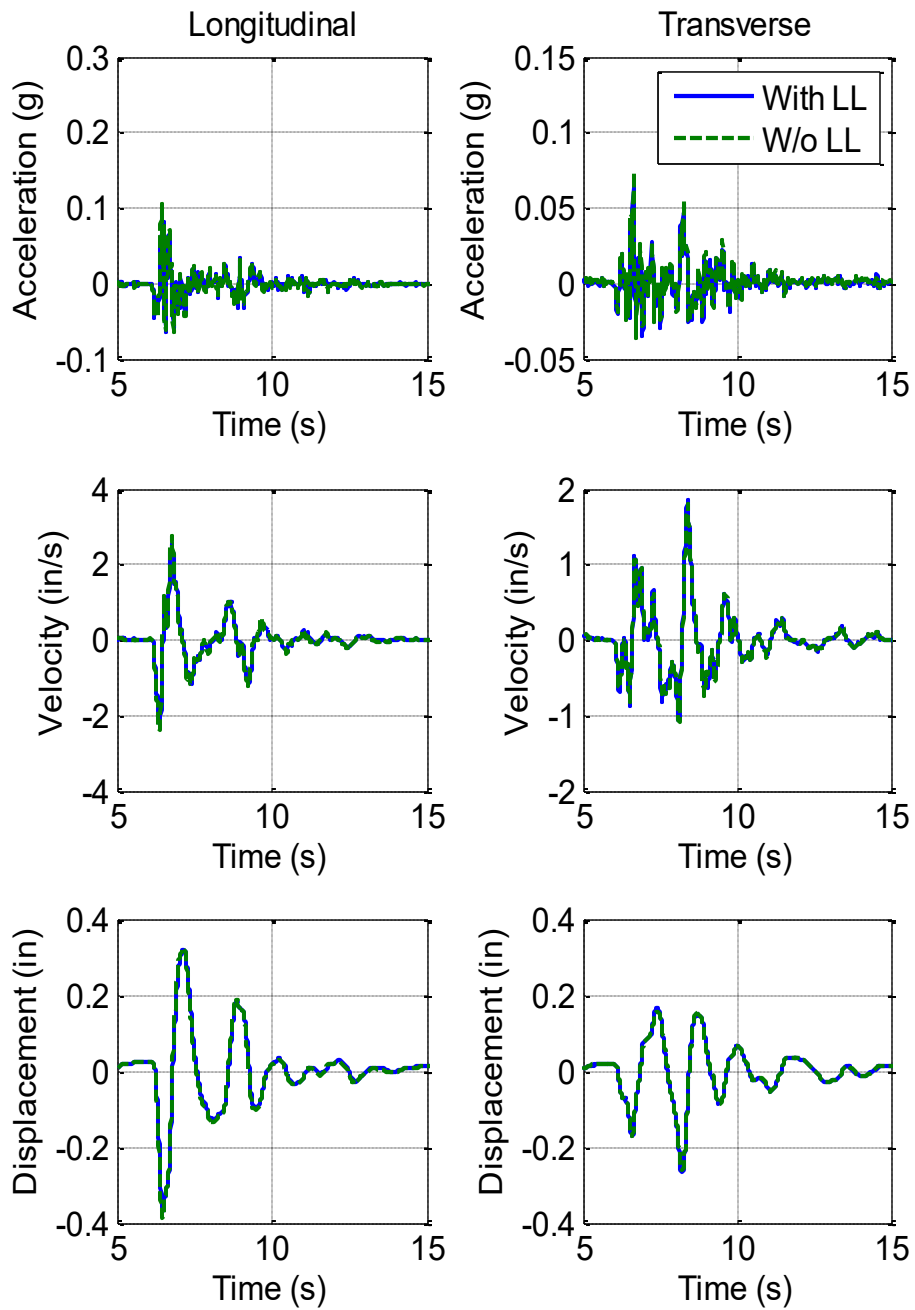


**Figure 5.3.2. Histories Average of Table Motion (20% DE)**

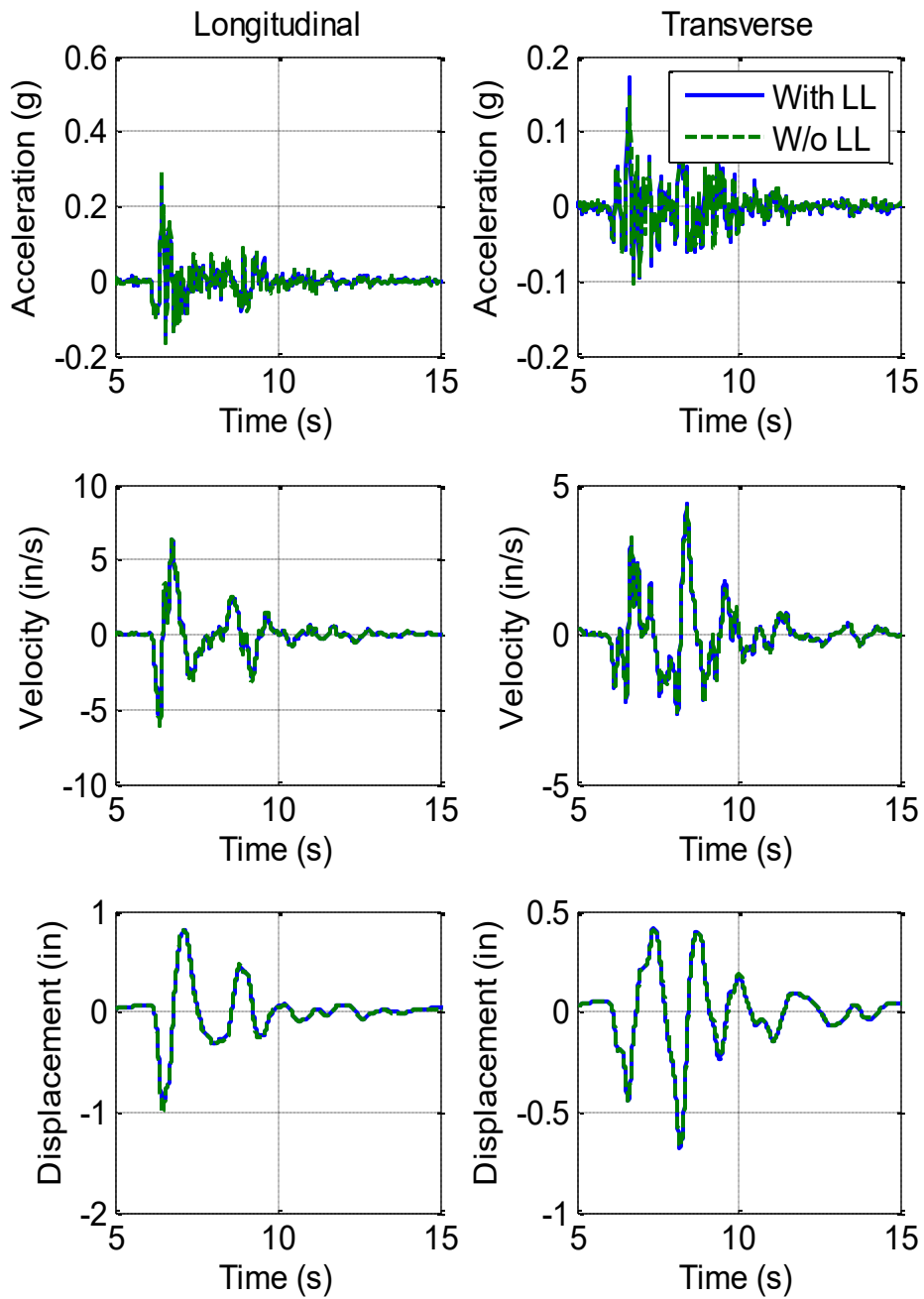


**Figure 5.3.3. Histories of Average Table Motion (50% DE)**

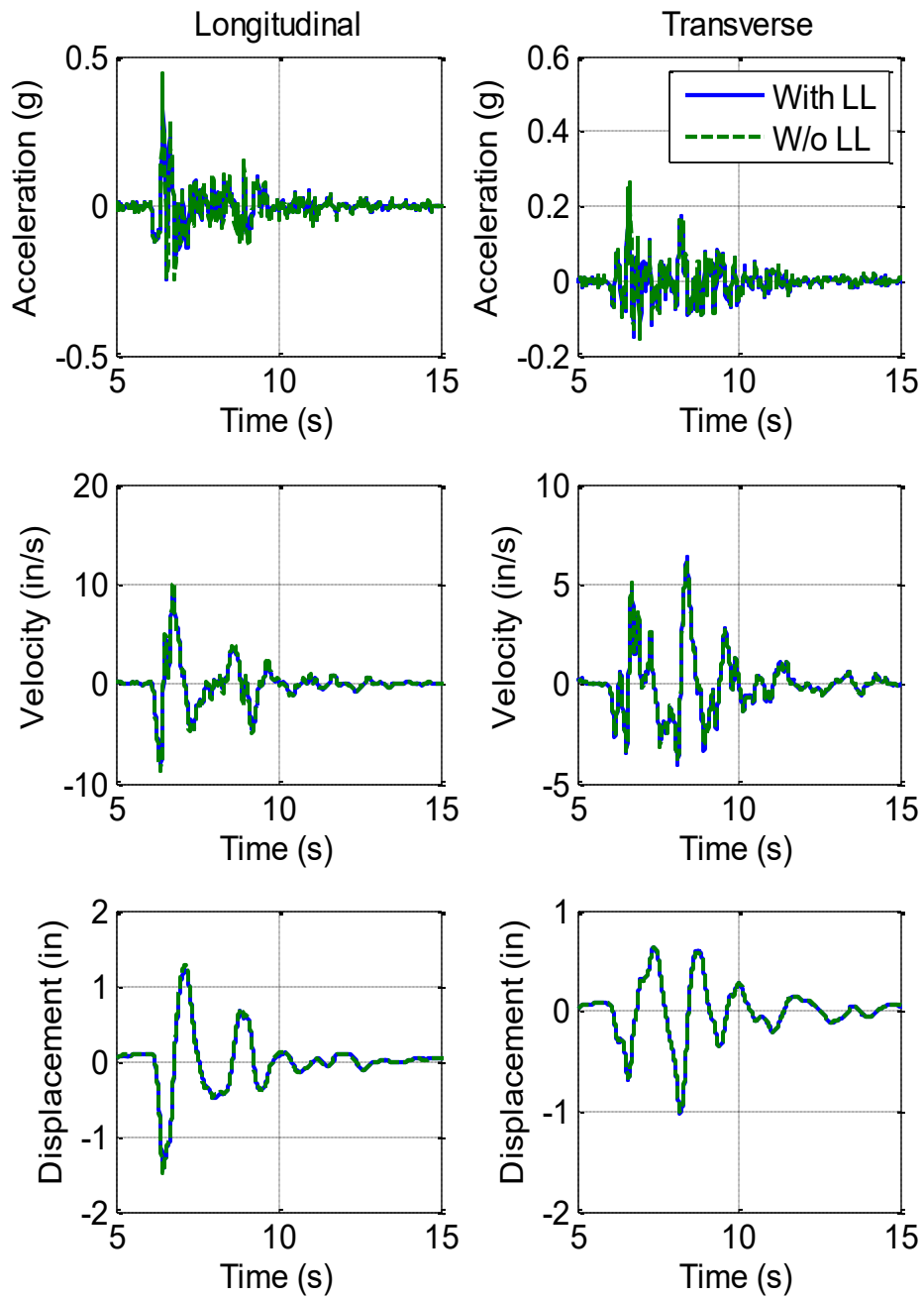


**Figure 5.3.4. Histories of Average Table Motion (75% DE)**

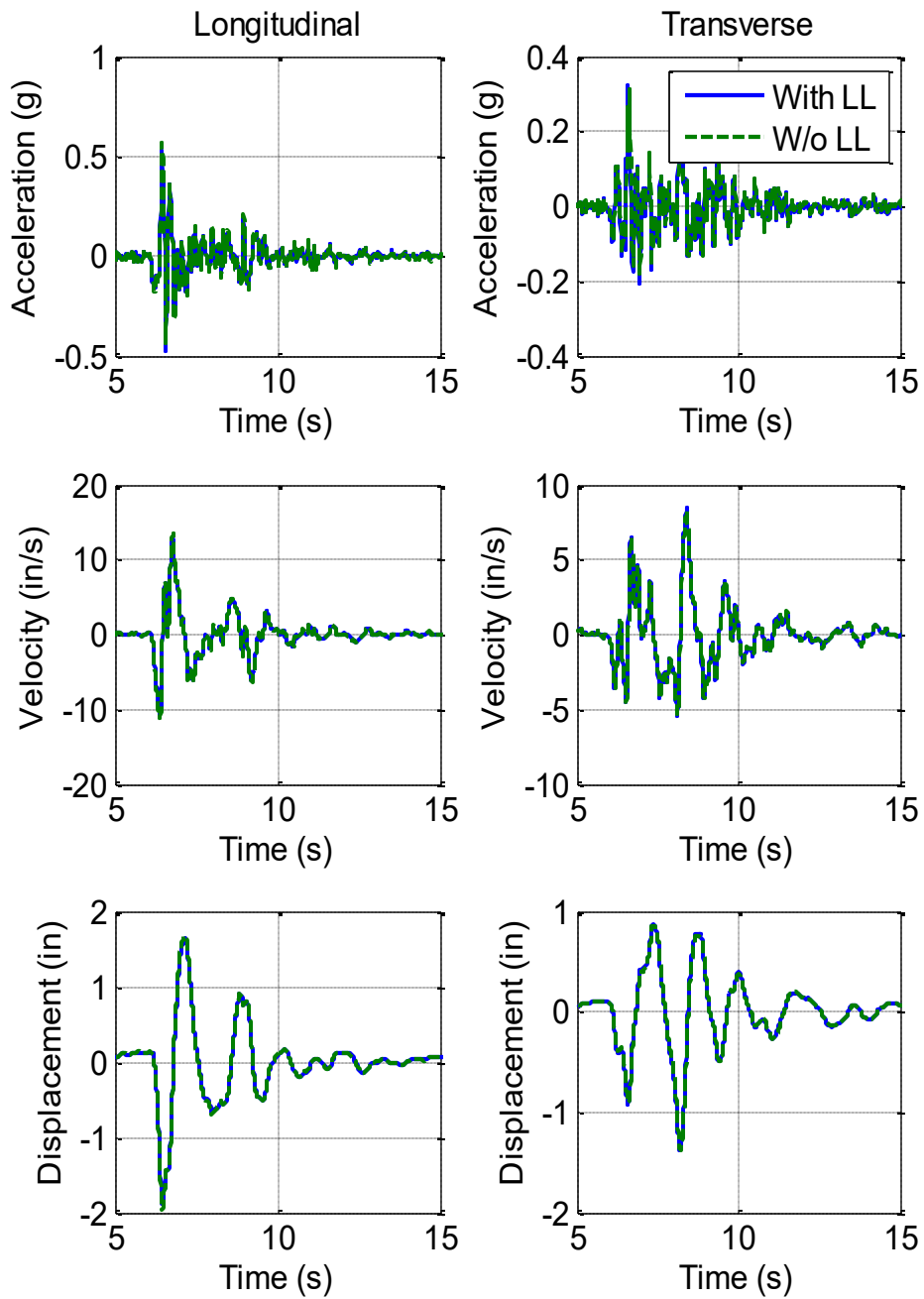


**Figure 5.3.5. Histories of Average Table Motion (100% DE)**

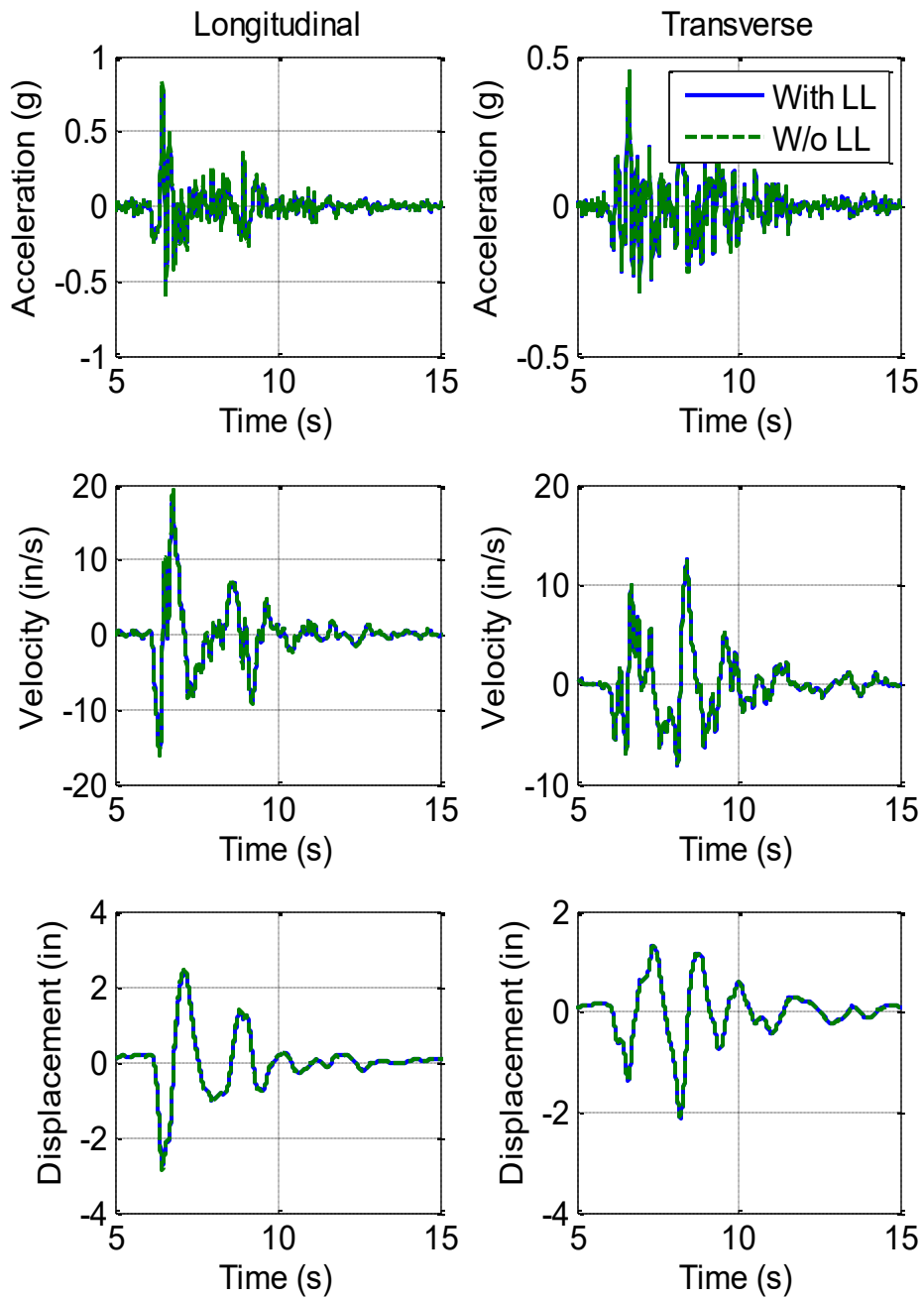


**Figure 5.3.6. Histories of Average Table Motion (150% DE)**

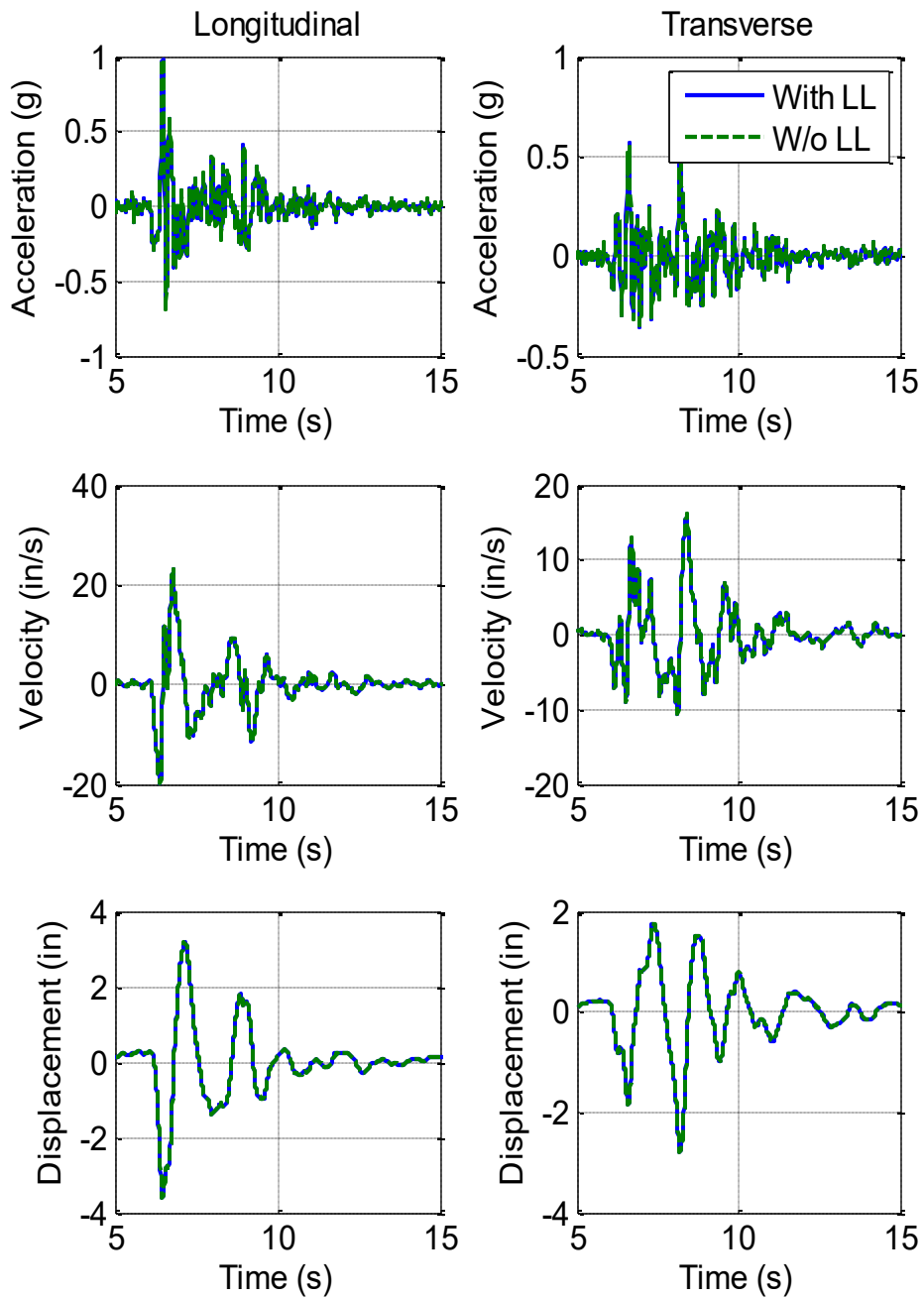


**Figure 5.3.7. Histories of Average Table Motion (200% DE)**

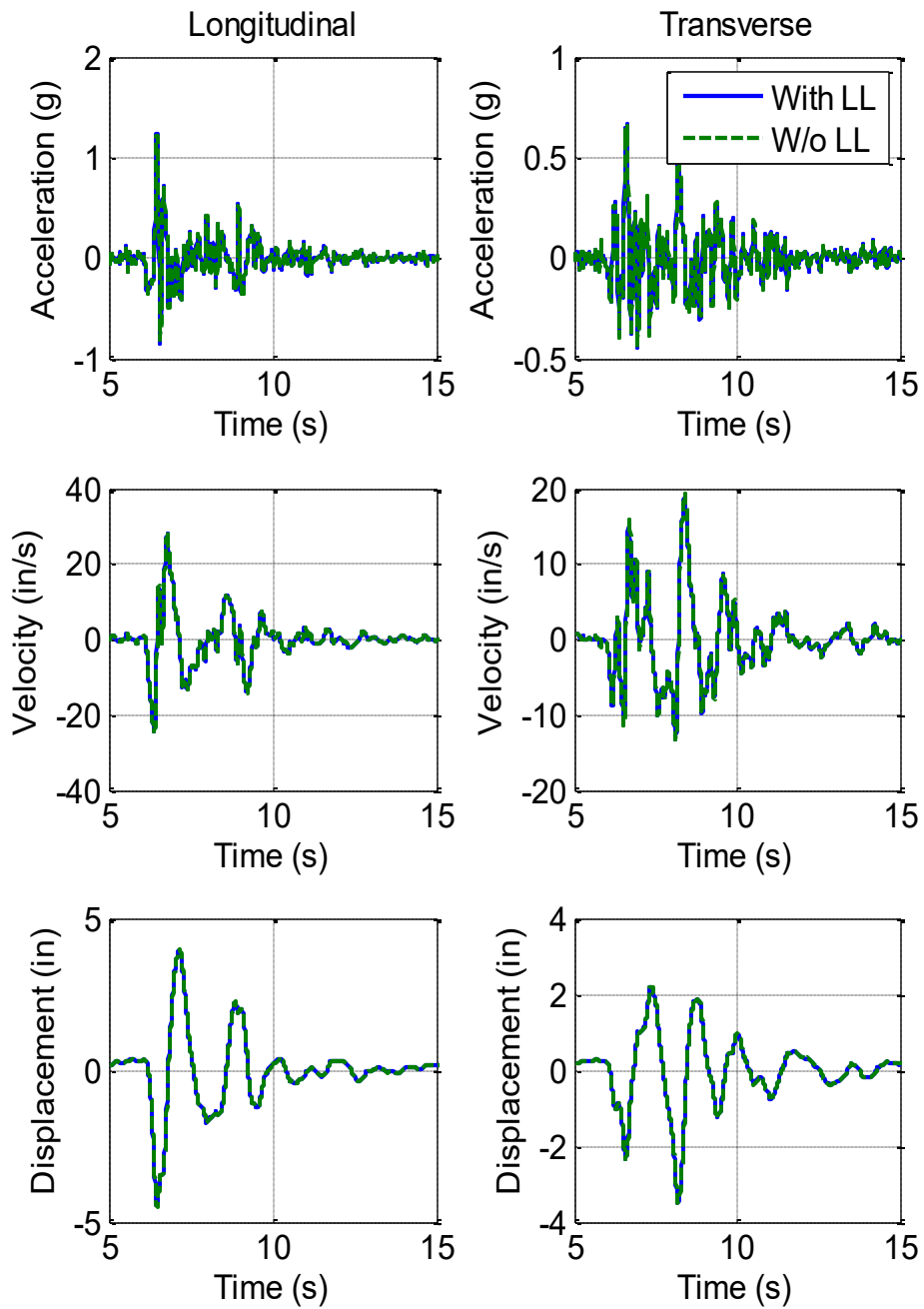


**Figure 5.3.8. Histories of Average Table Motion (250% DE)**

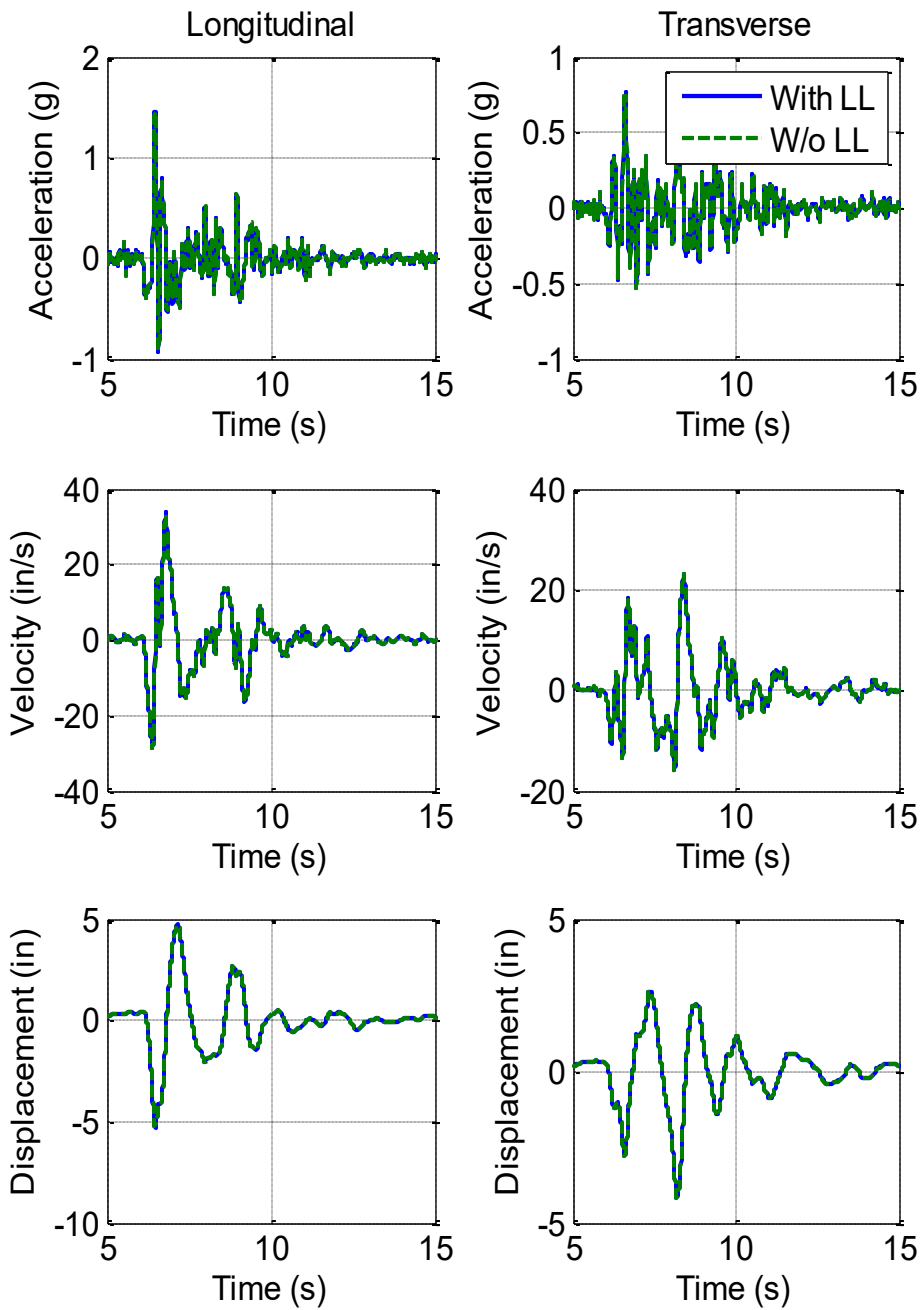


**Figure 5.3.9. Histories of Average Table Motion (300% DE)**

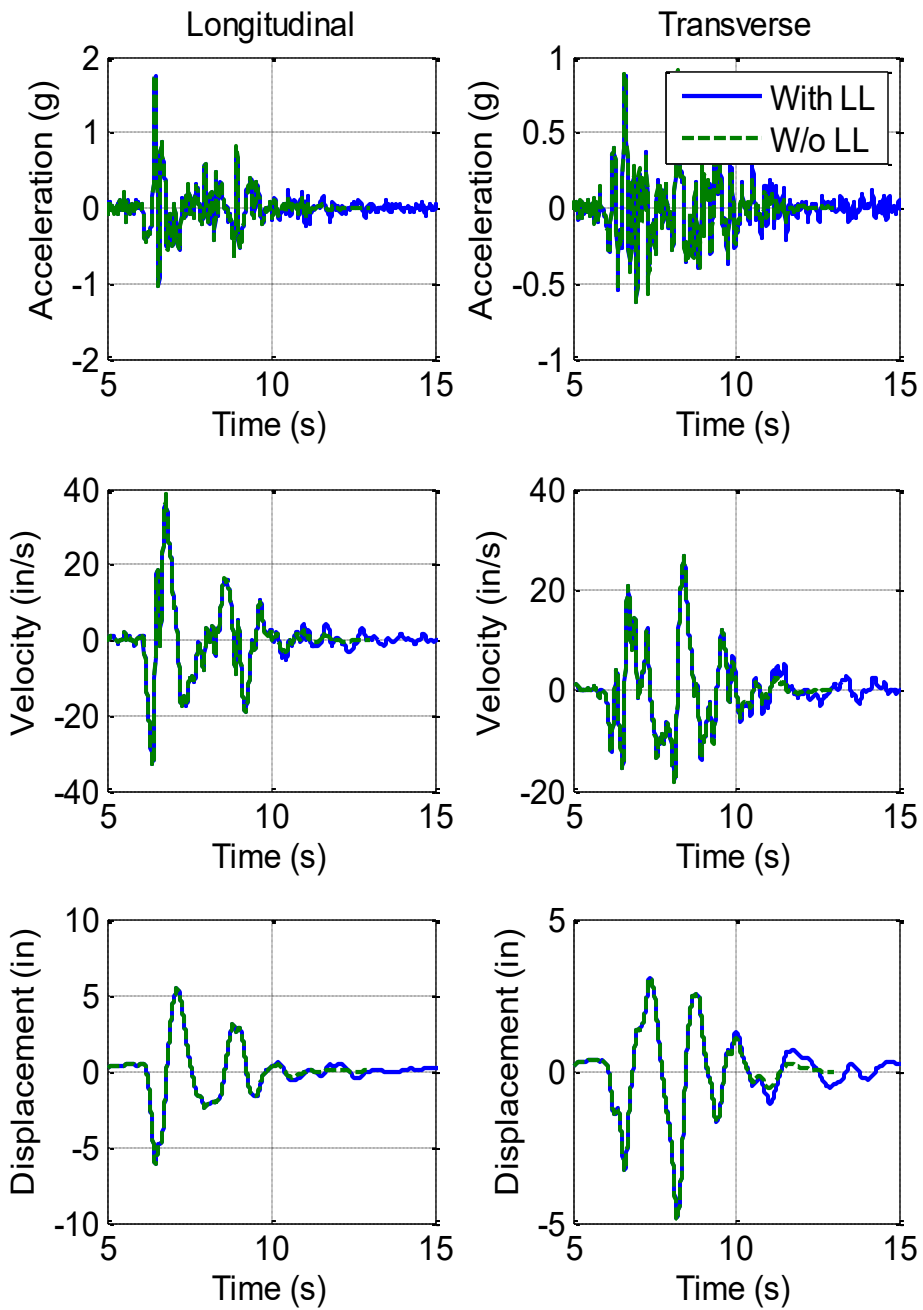


**Figure 5.3.10. Histories of Average Table Motion (350% DE)**

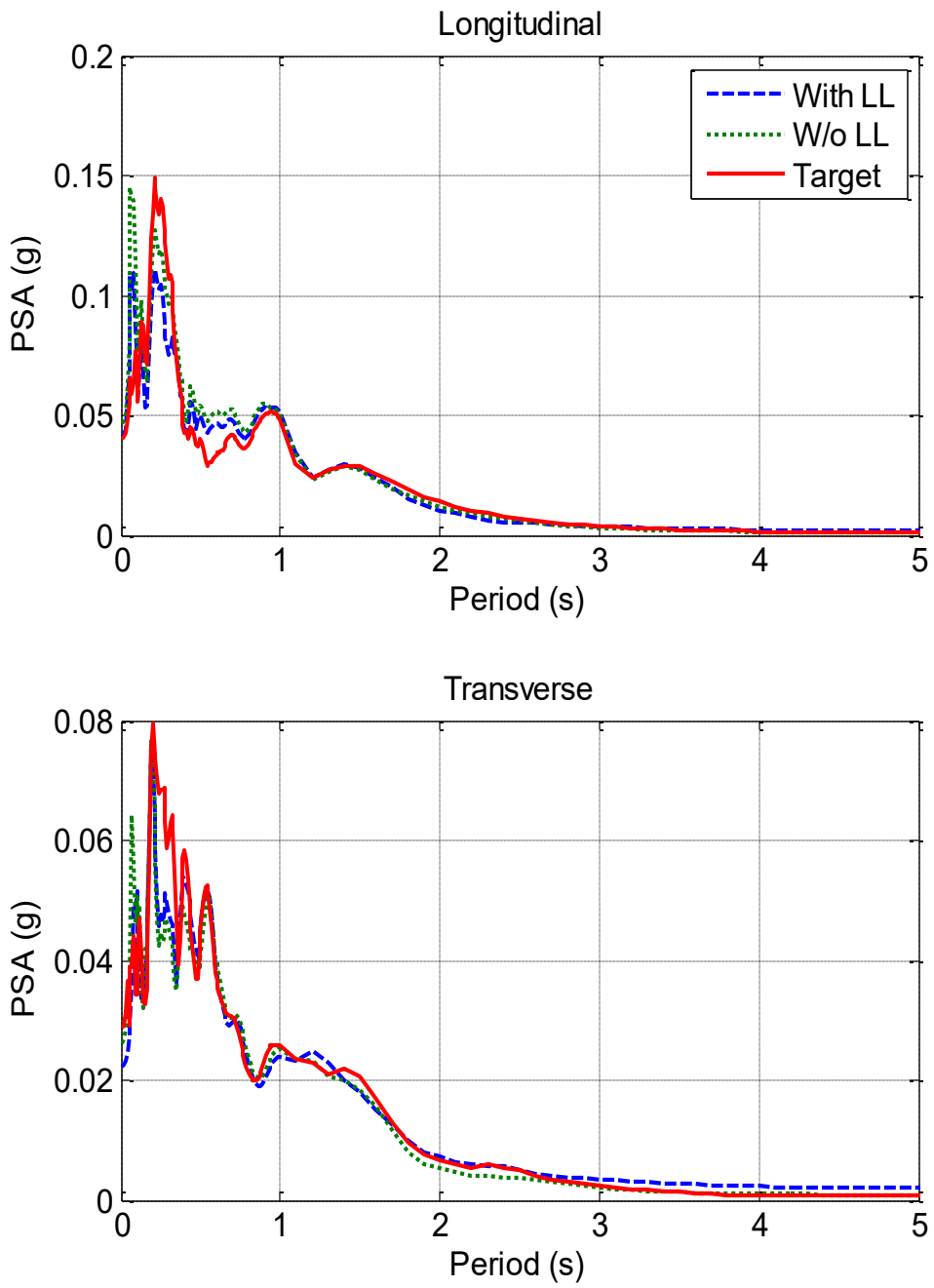


**Figure 5.3.11. Acceleration Response Spectra for Average Table Motion (10% DE)**

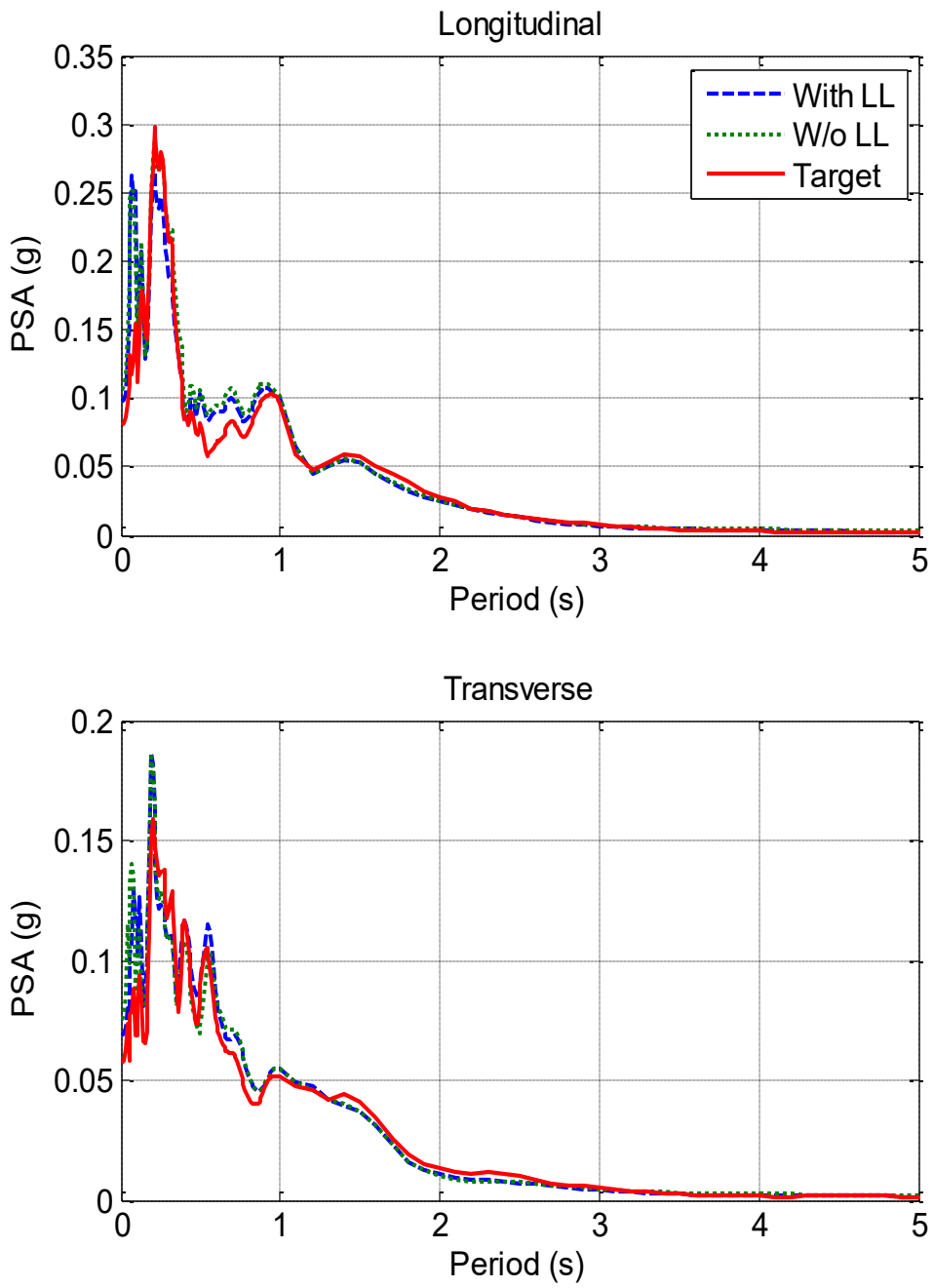


**Figure 5.3.12. Acceleration Response Spectra for Average Table Motion (20% DE)**

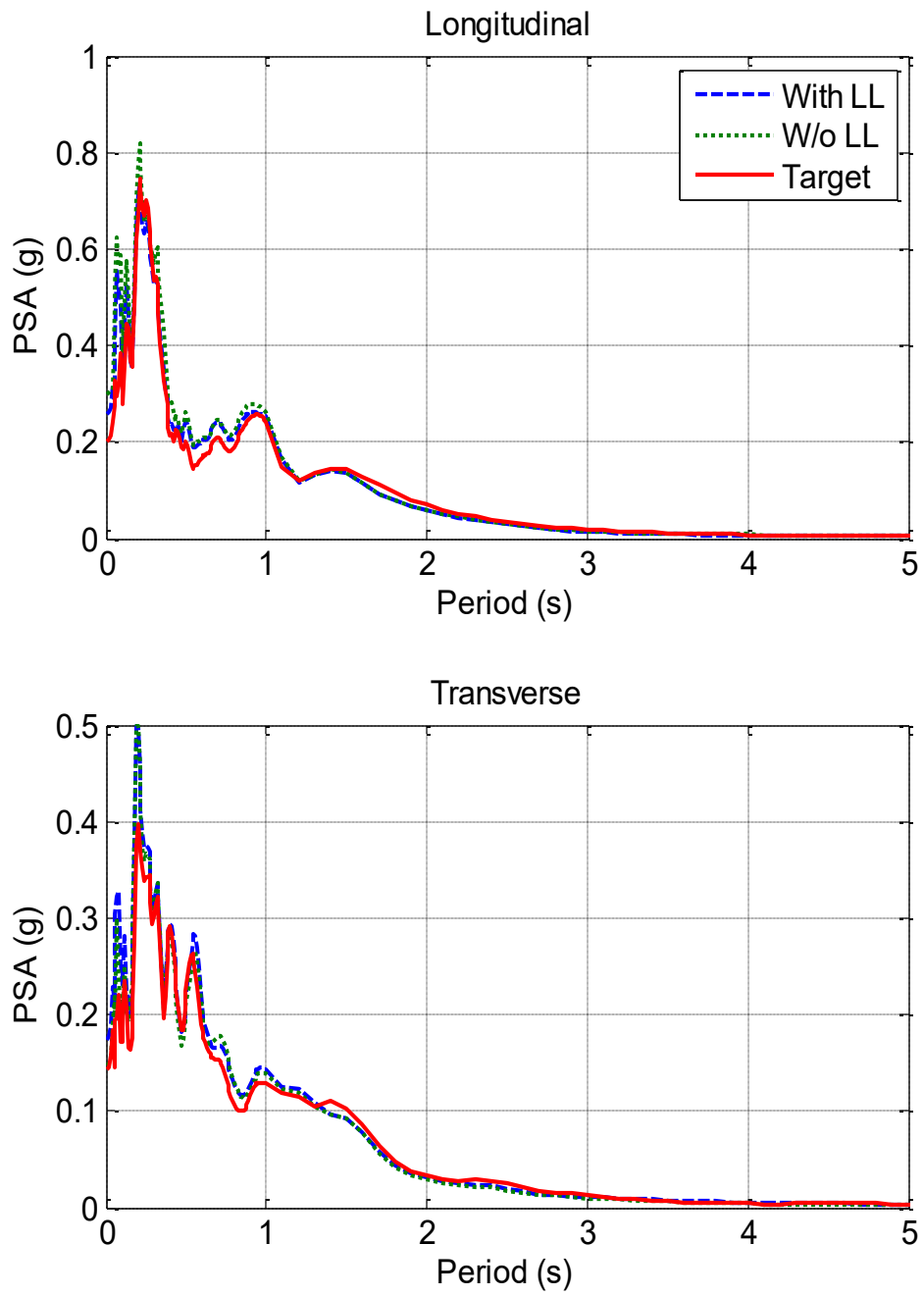


**Figure 5.3.13. Acceleration Response Spectra for Average Table Motion (50% DE)**

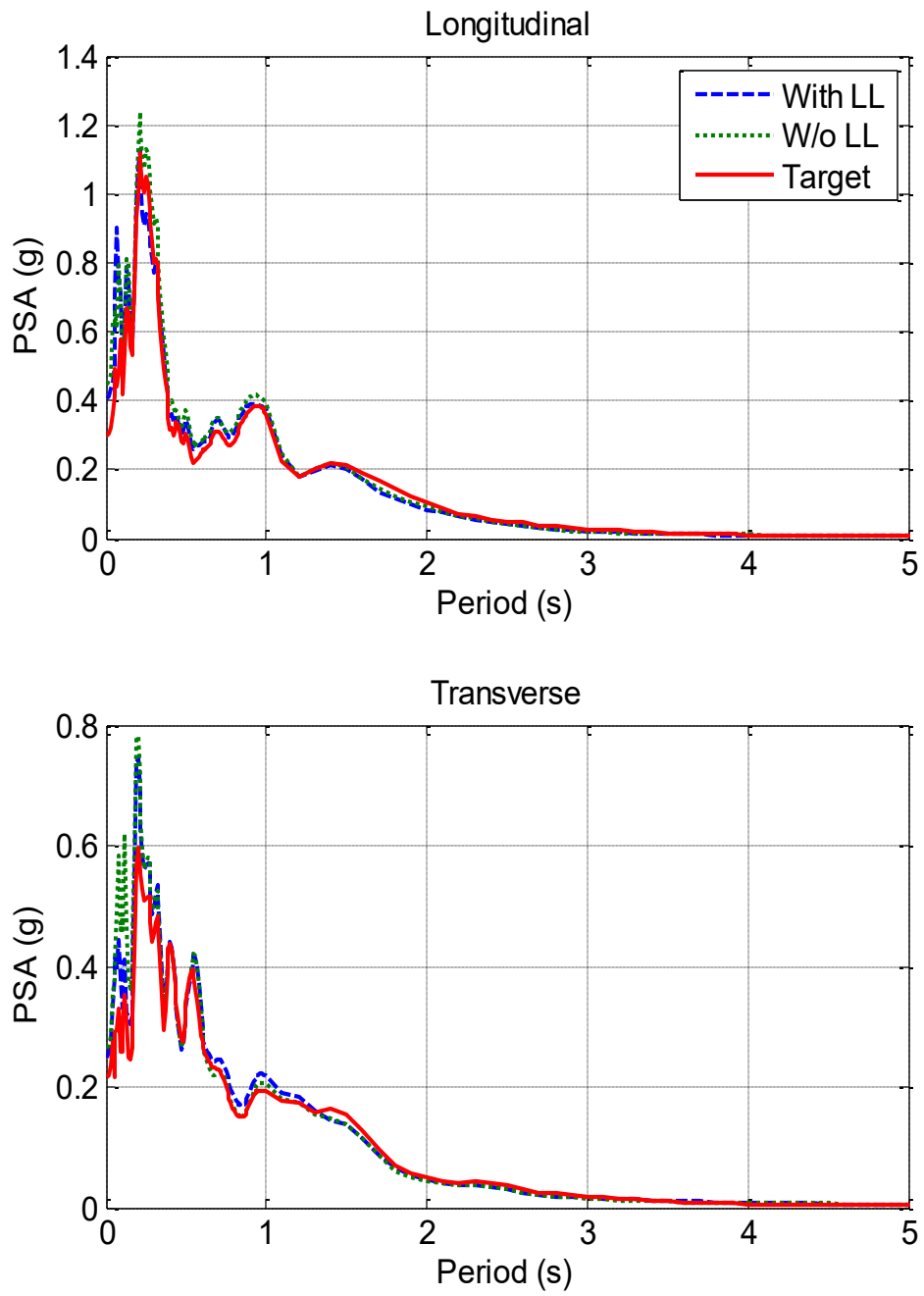


**Figure 5.3.14. Acceleration Response Spectra for Average Table Motion (75% DE)**

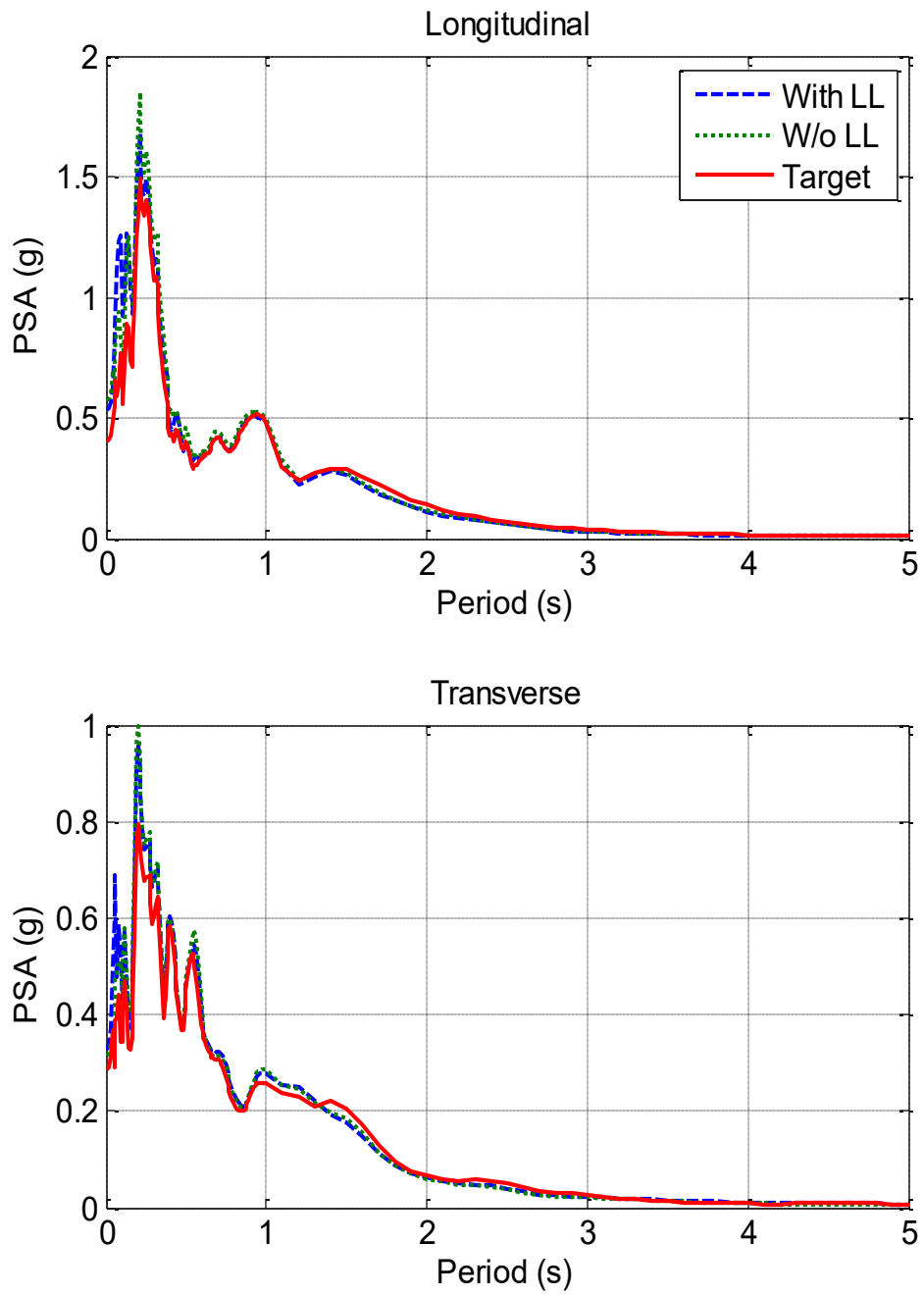


**Figure 5.3.15. Acceleration Response Spectra for Average Table Motion (100% DE)**

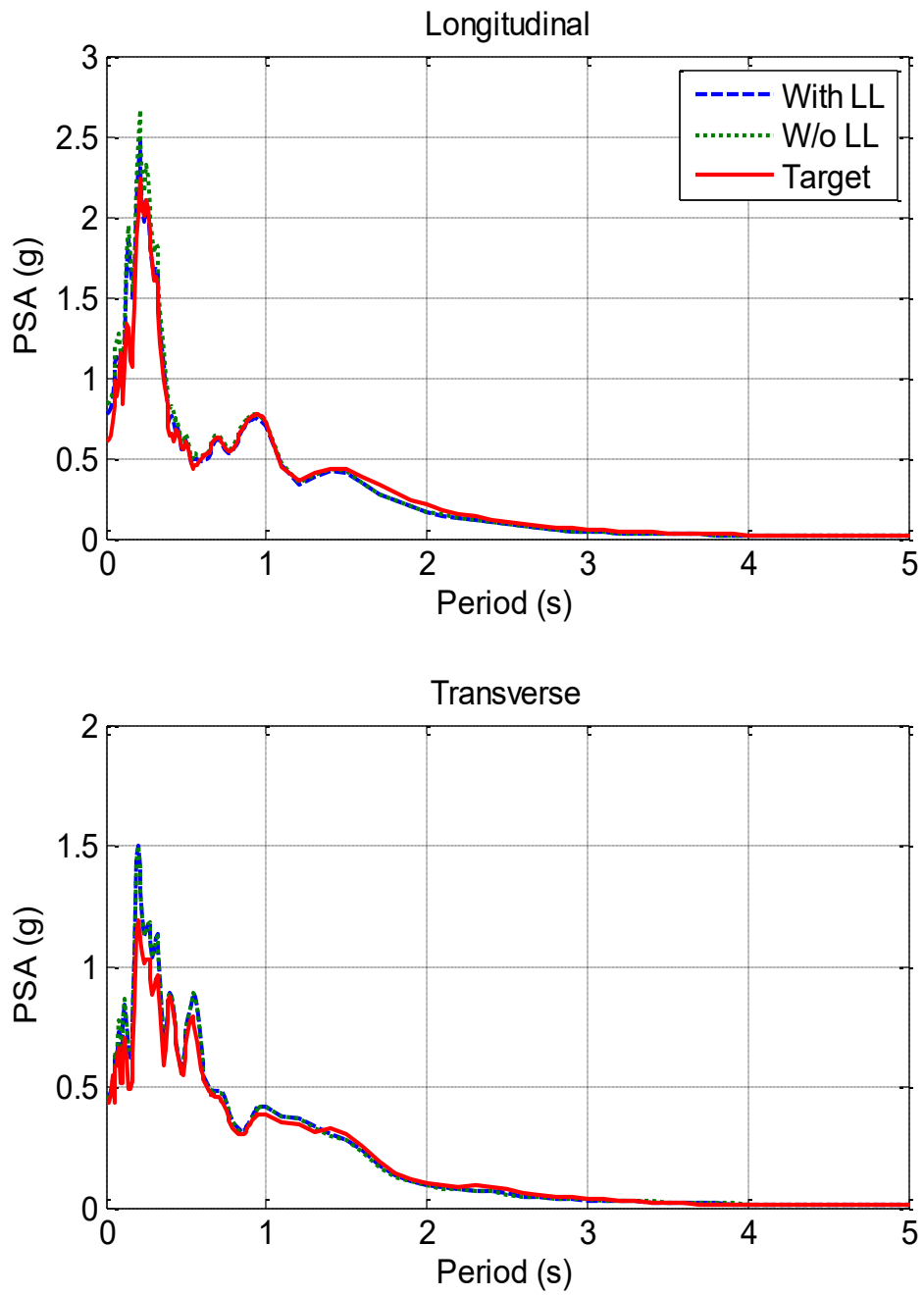


**Figure 5.3.16. Acceleration Response Spectra for Average Table Motion (150% DE)**

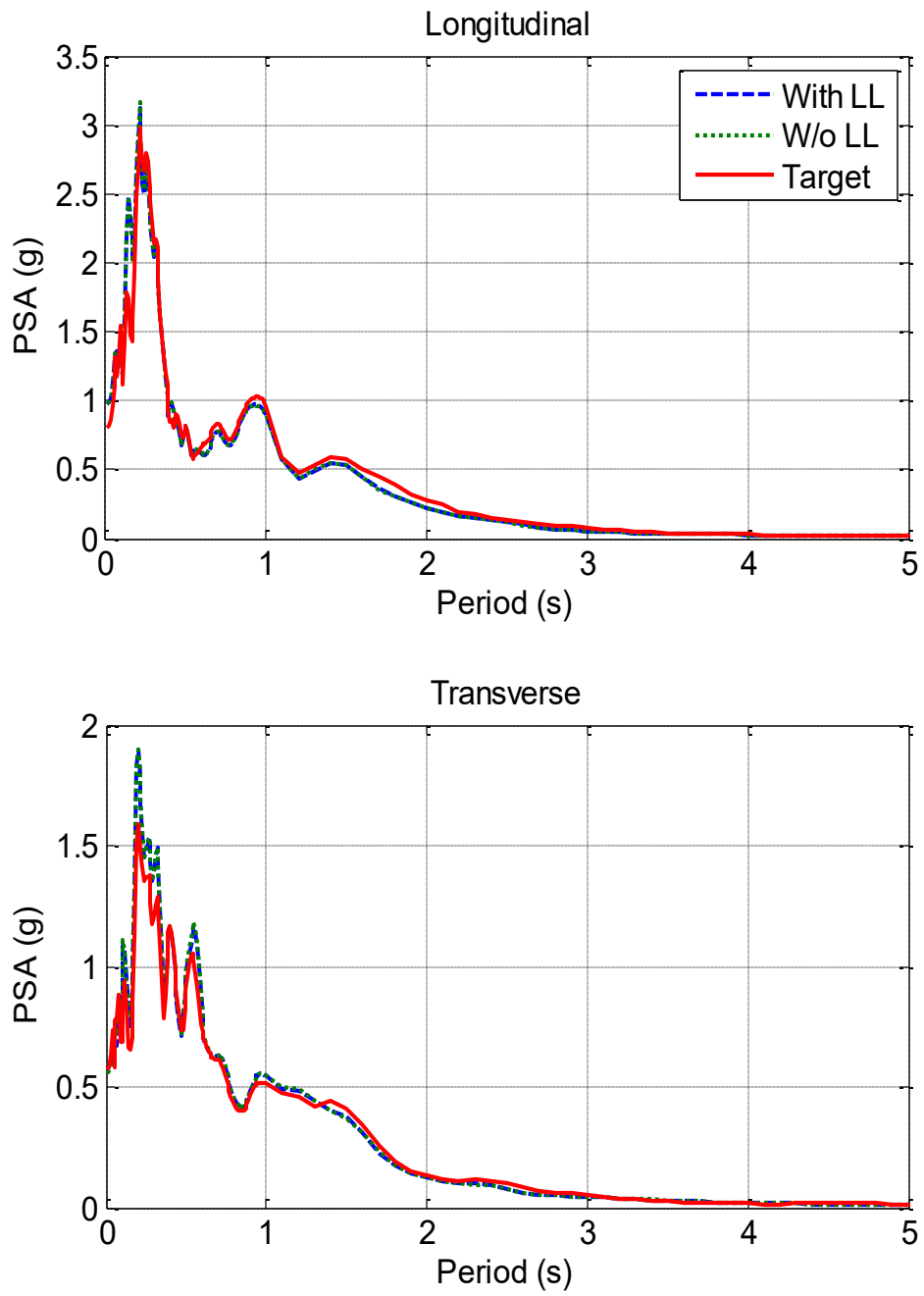


**Figure 5.3.17. Acceleration Response Spectra for Average Table Motion (200% DE)**

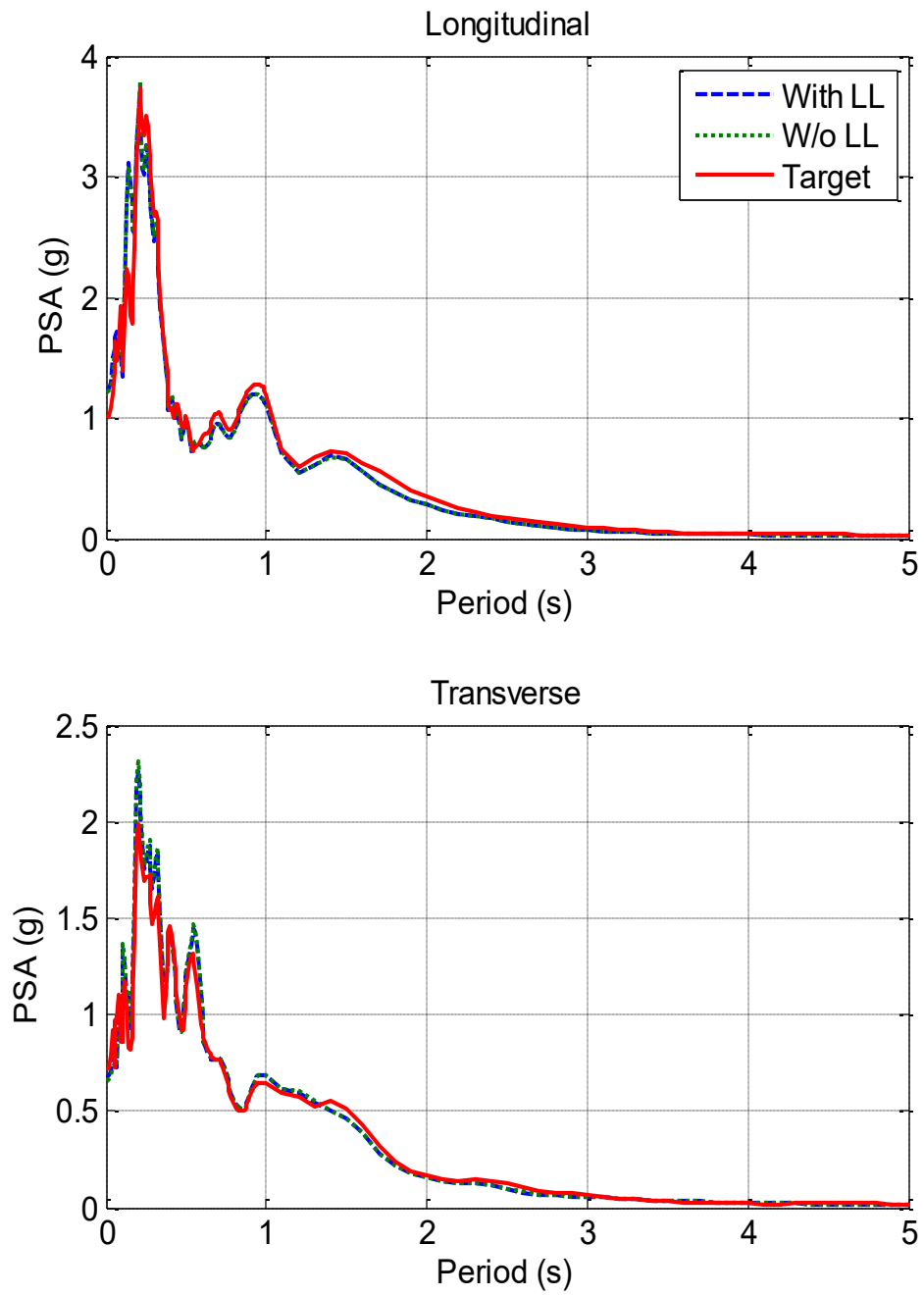


**Figure 5.3.18. Acceleration Response Spectra for Average Table Motion (250% DE)**

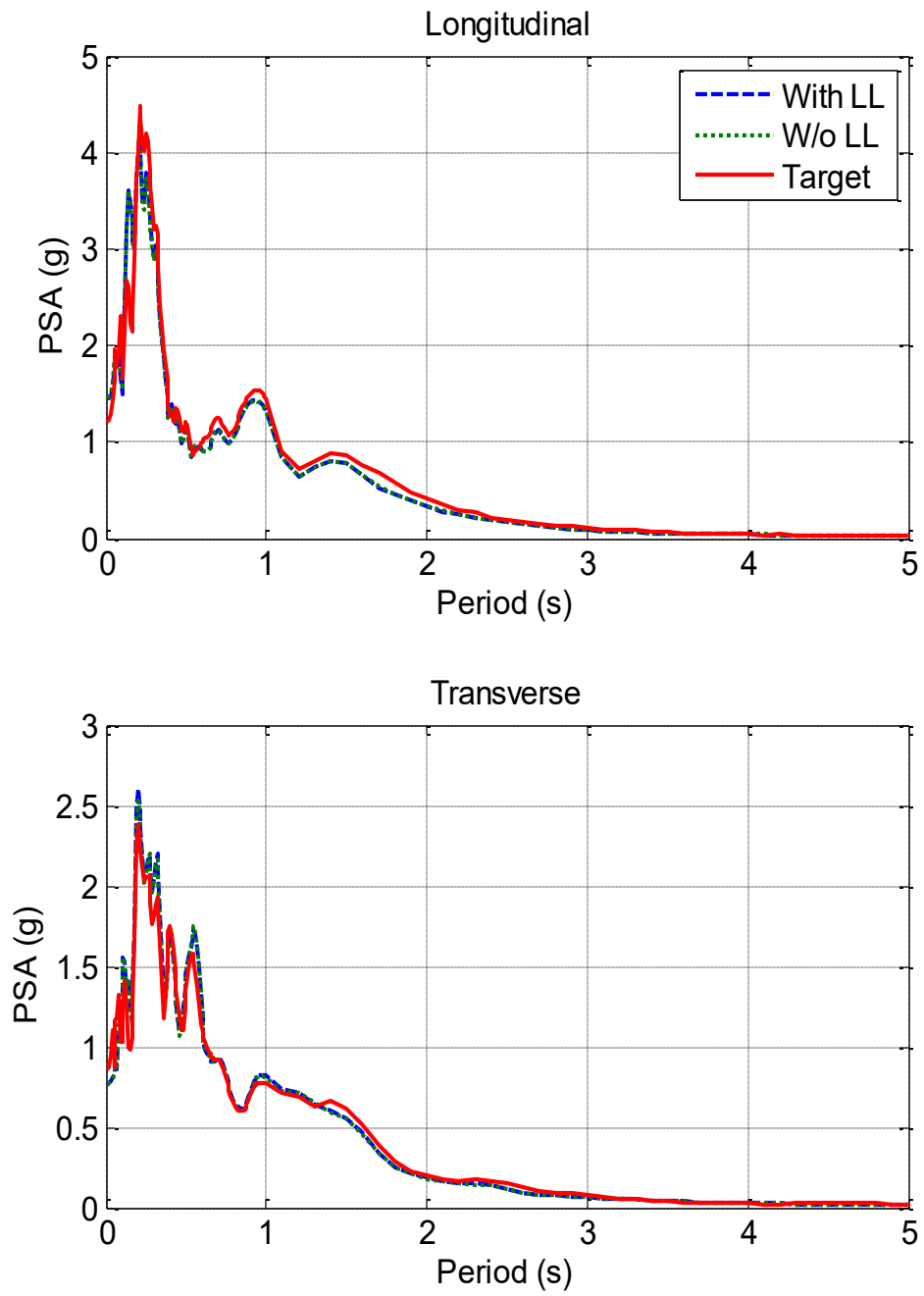


**Figure 5.3.19. Acceleration Response Spectra for Average Table Motion (300% DE)**

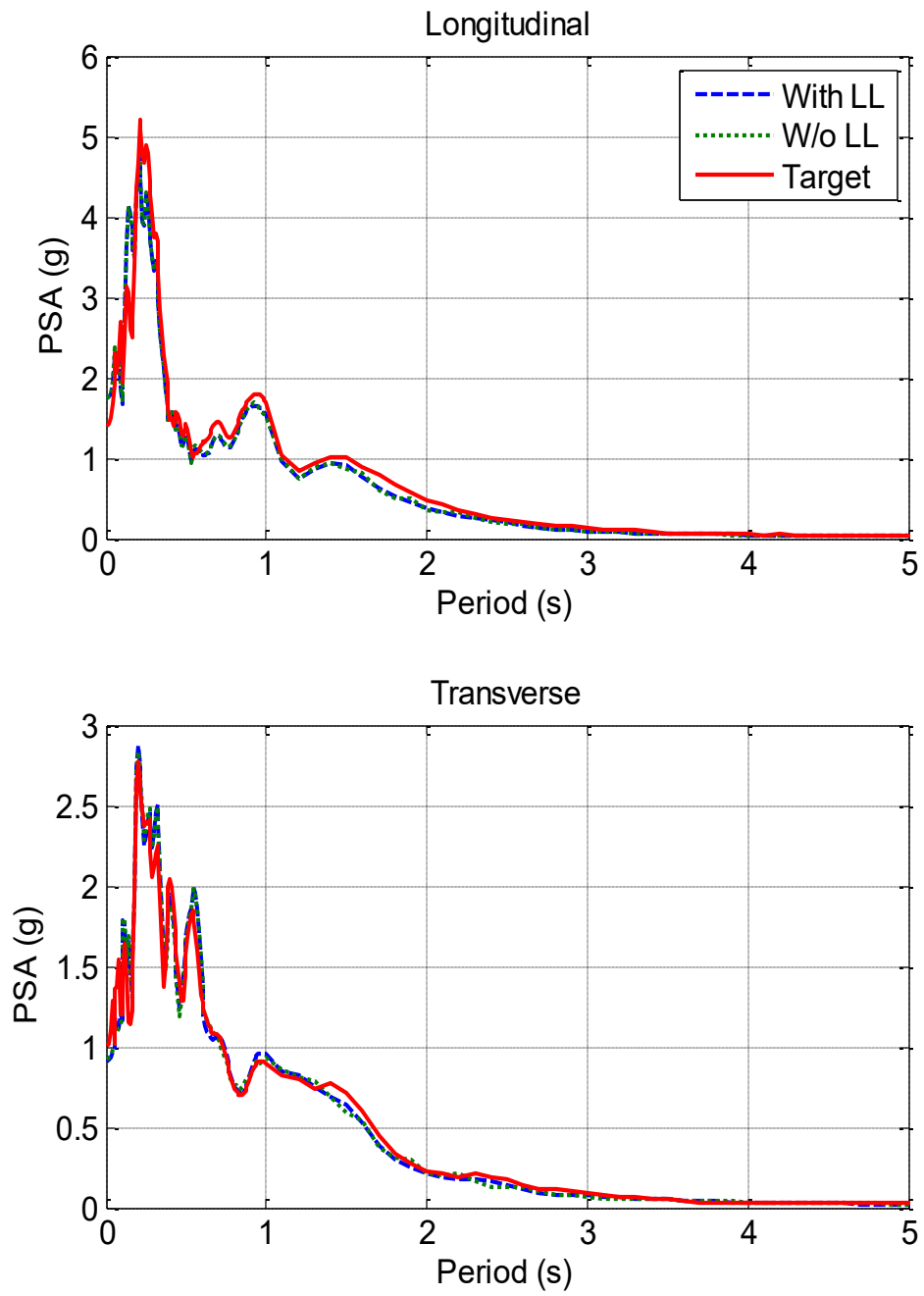


**Figure 5.3.20. Acceleration Response Spectra for Average Table Motion (350% DE)**

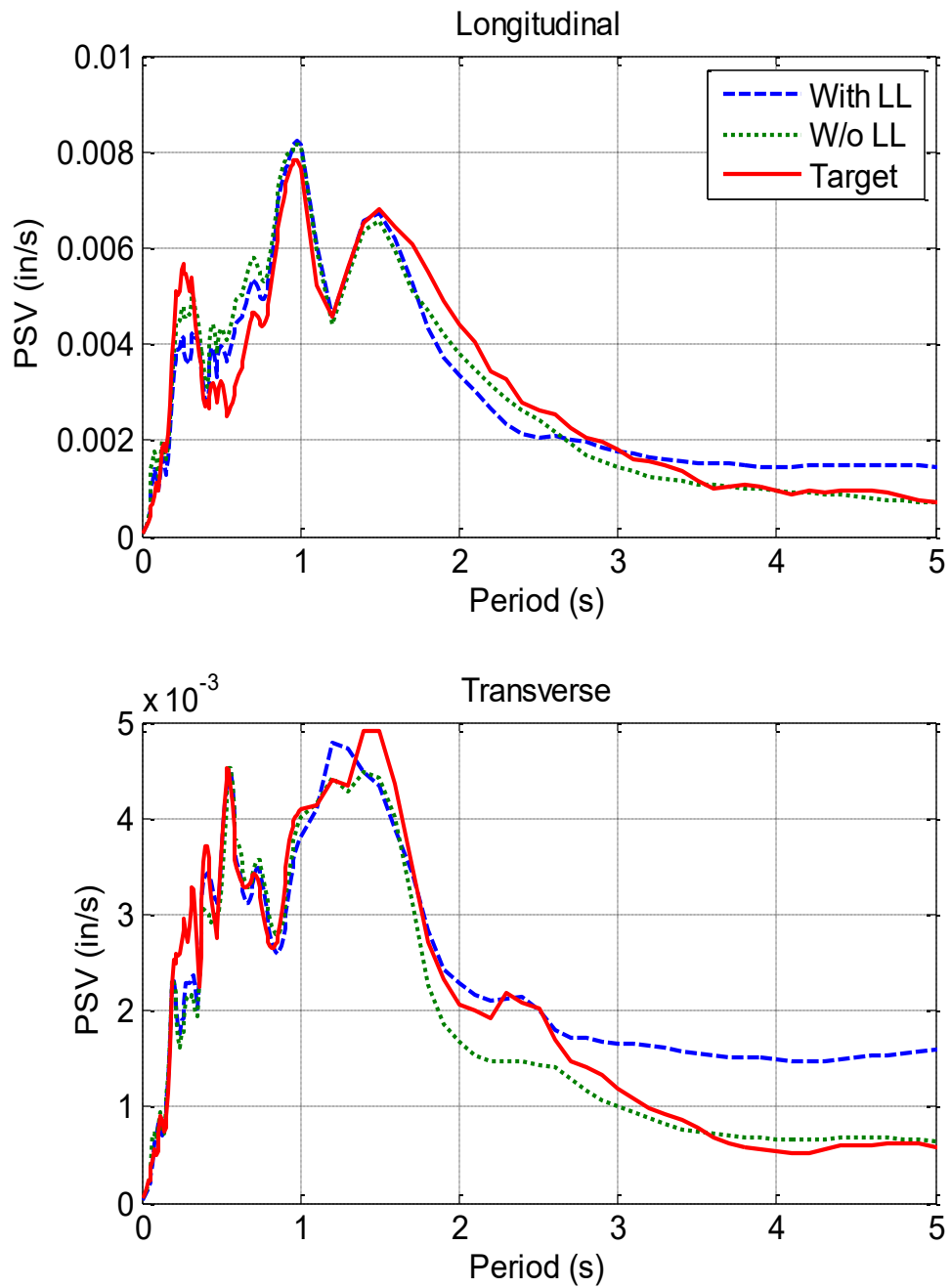


**Figure 5.3.21. Velocity Response Spectra for Average Table Motion (10% DE)**

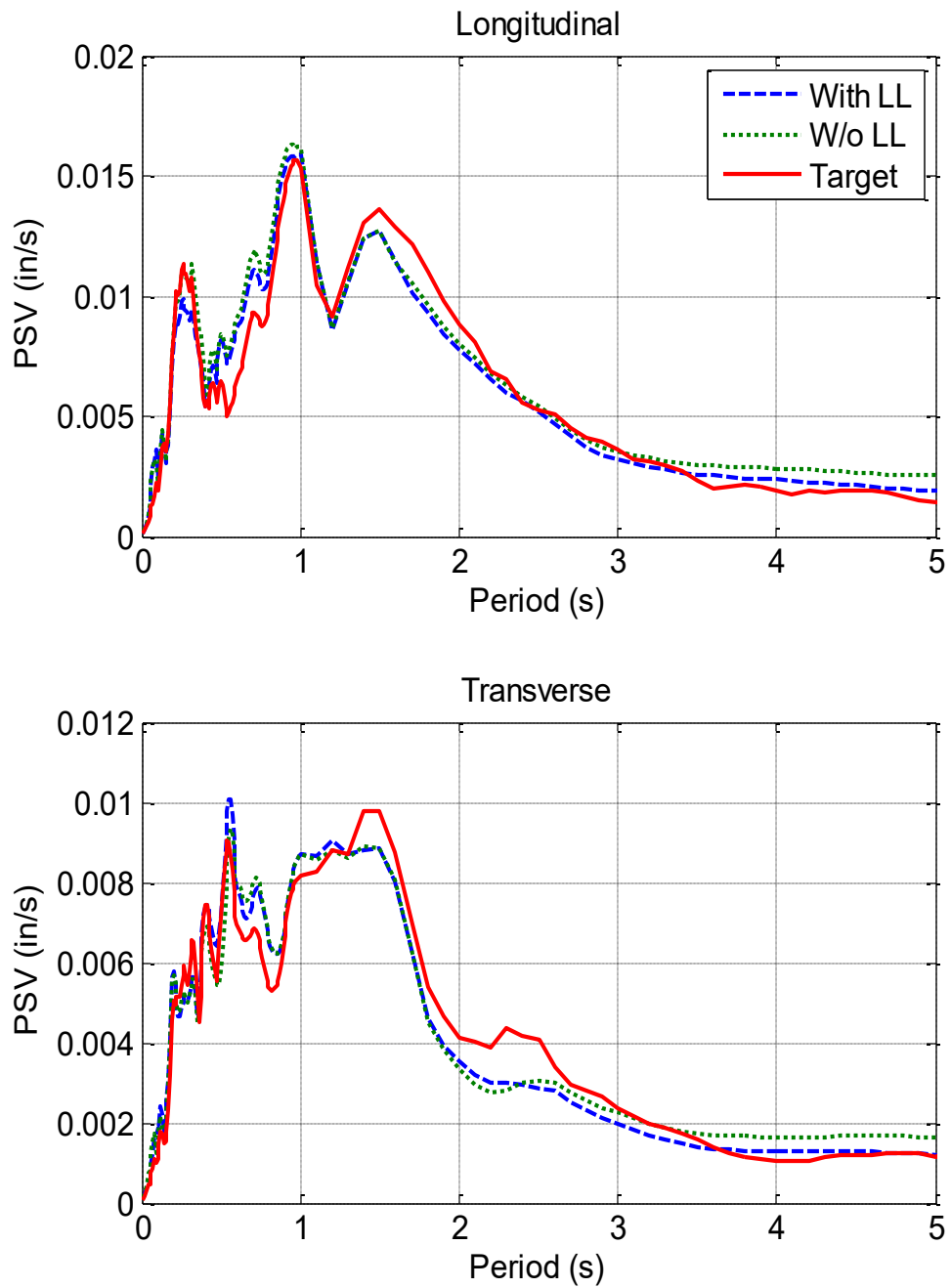


**Figure 5.3.22. Velocity Response Spectra for Average Table Motion (20% DE)**

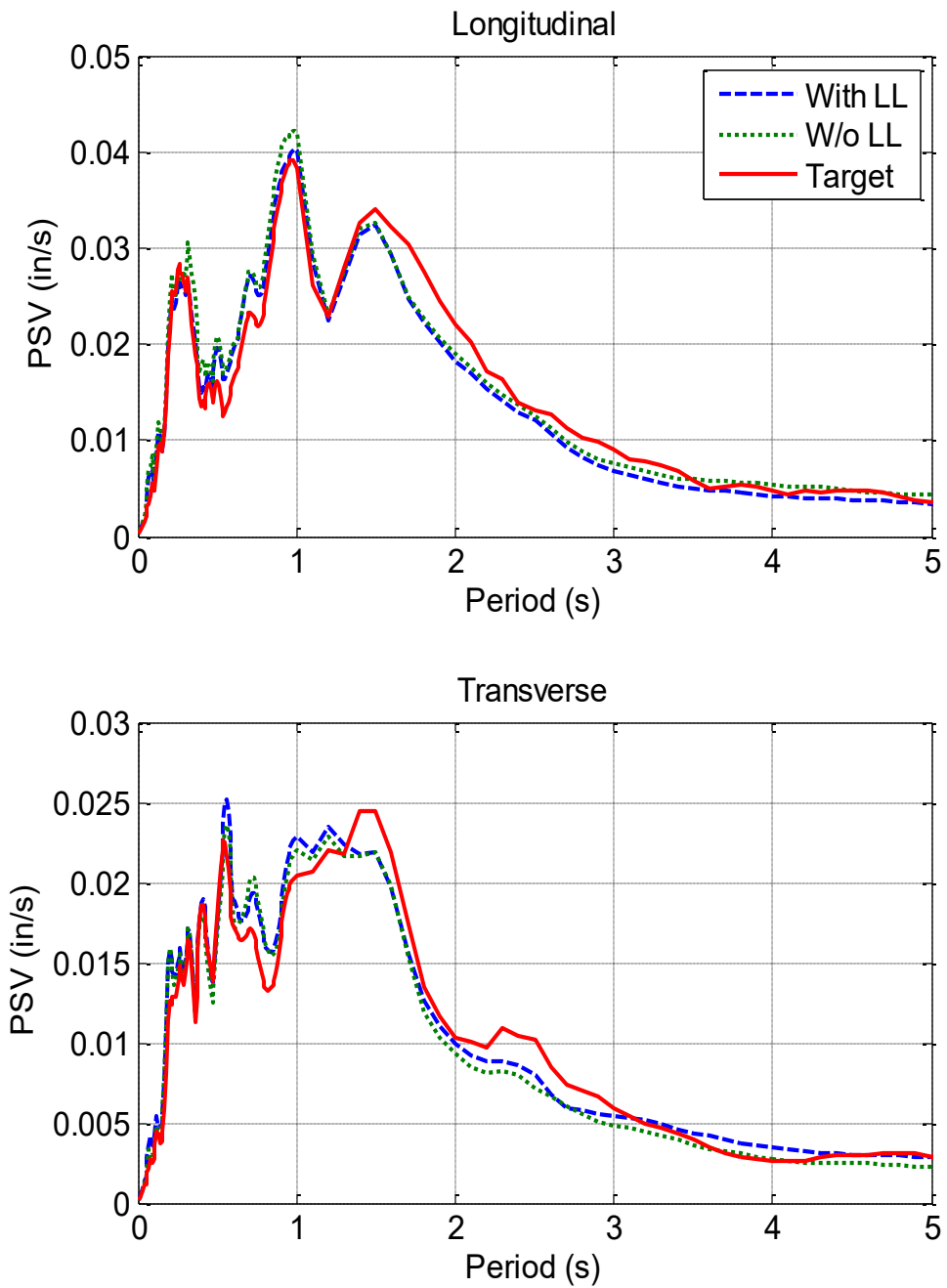


**Figure 5.3.23. Velocity Response Spectra for Average Table Motion (50% DE)**

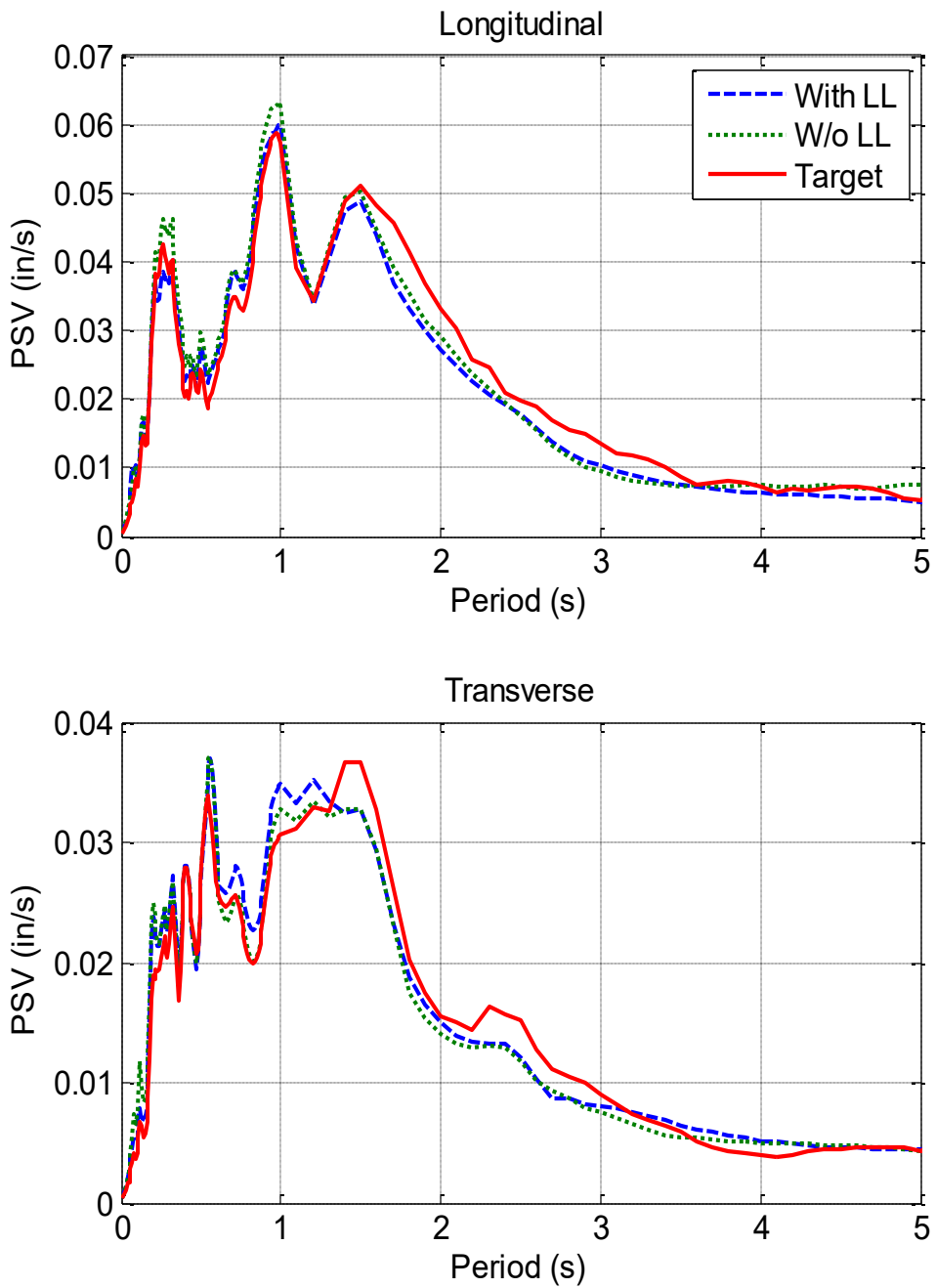


**Figure 5.3.24. Velocity Response Spectra for Average Table Motion (75% DE)**

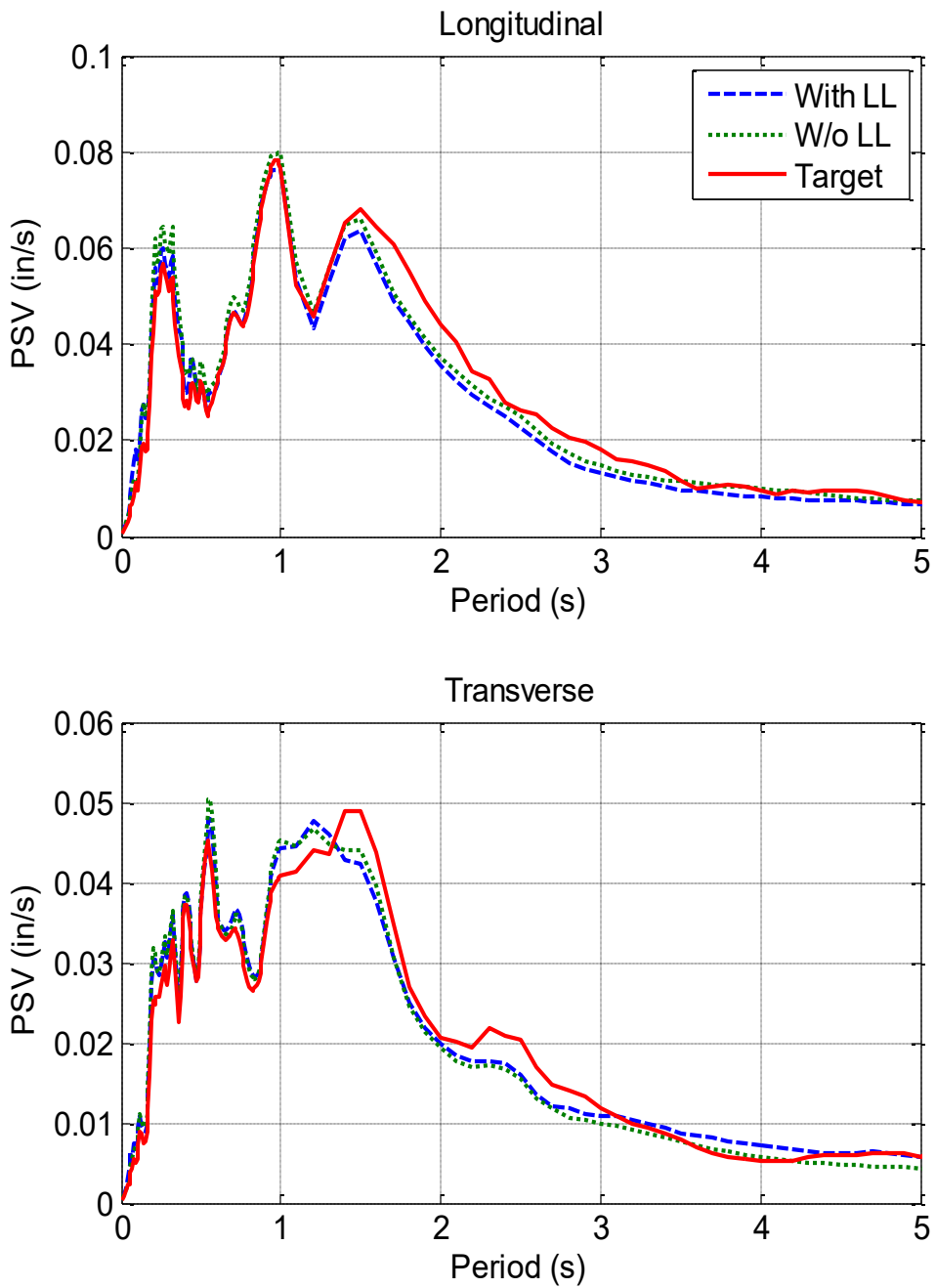


**Figure 5.3.25. Velocity Response Spectra for Average Table Motion (100% DE)**

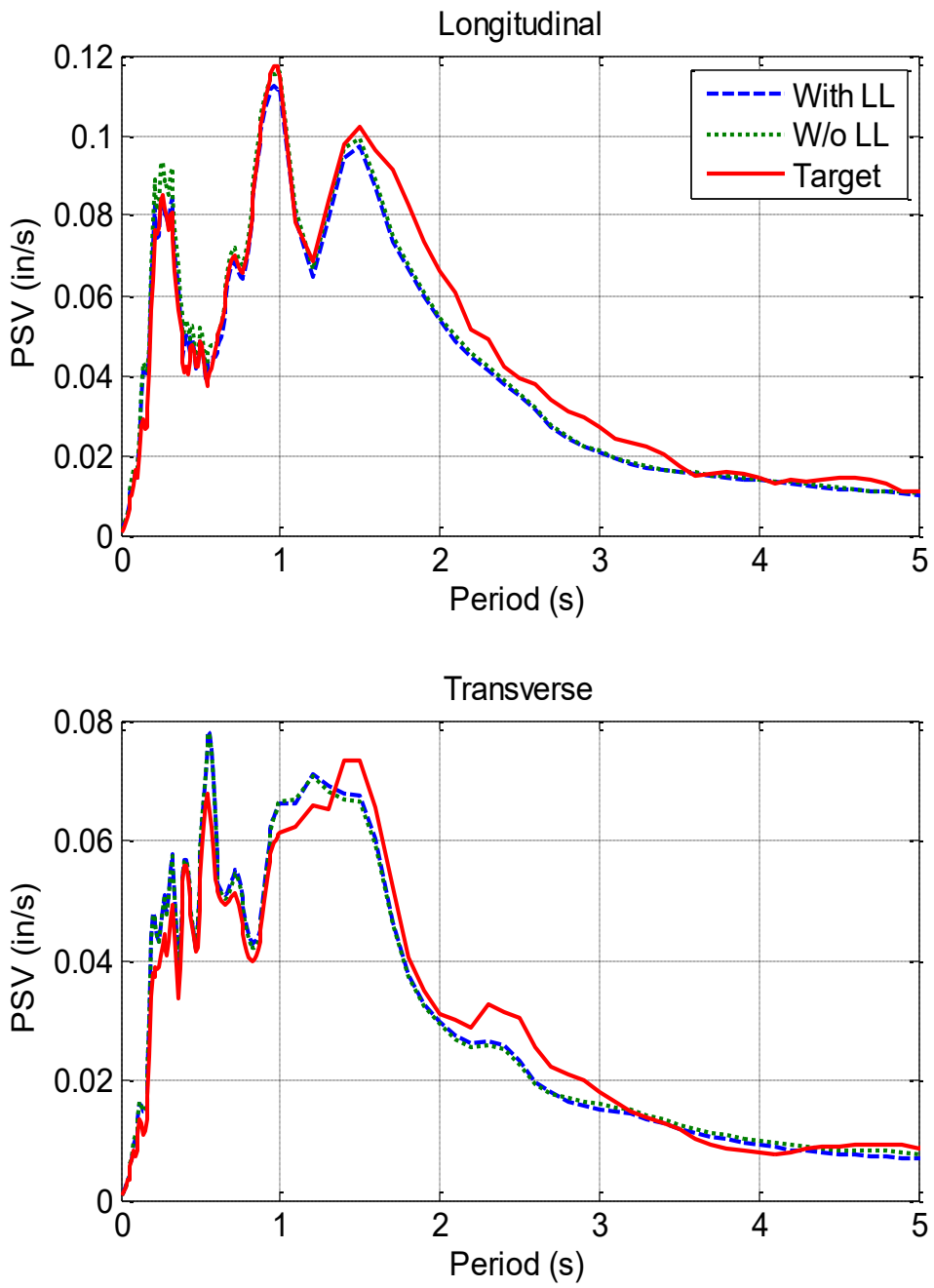


**Figure 5.3.26. Velocity Response Spectra for Average Table Motion (150% DE)**

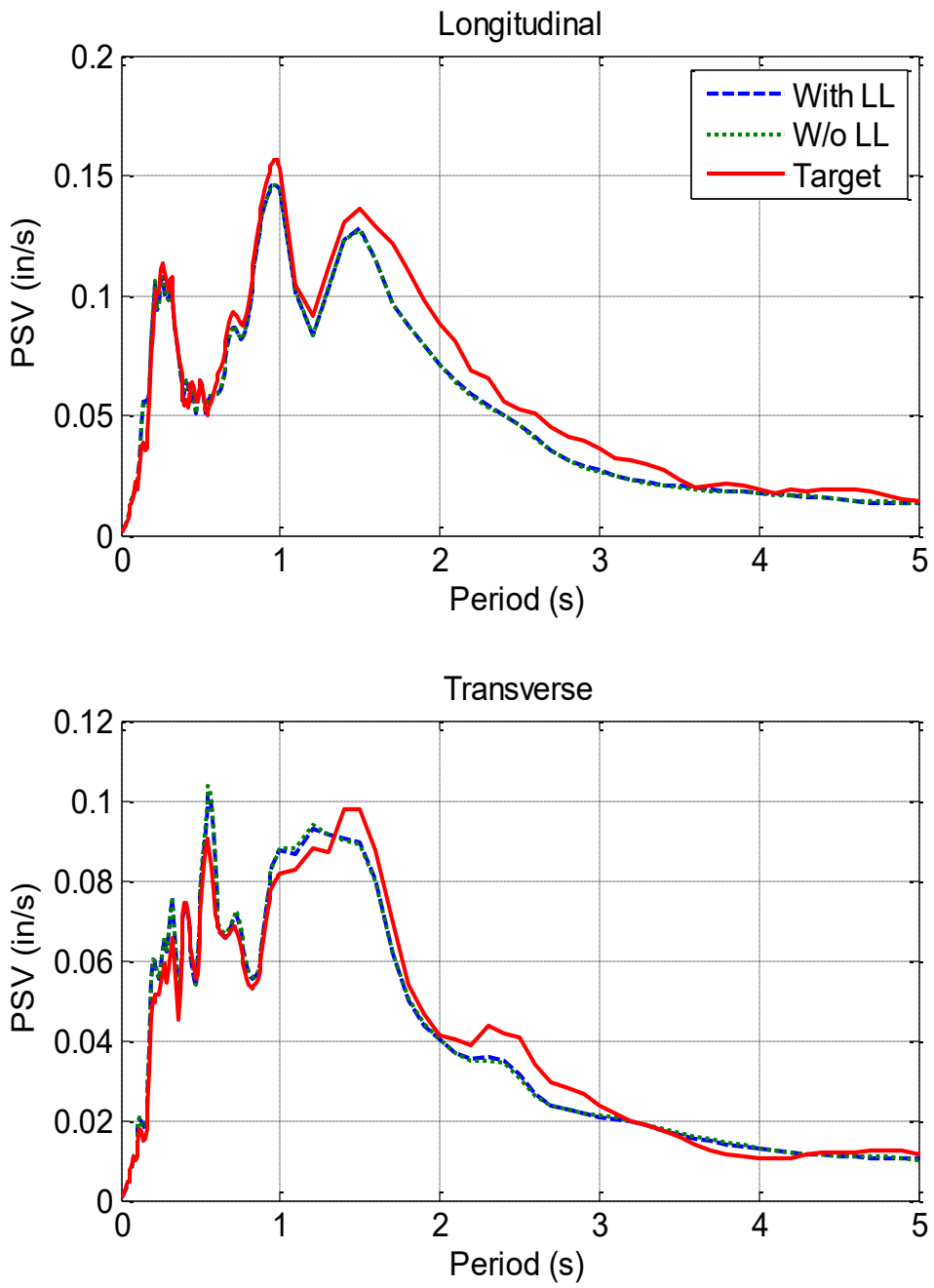


**Figure 5.3.27. Velocity Response Spectra for Average Table Motion (200% DE)**

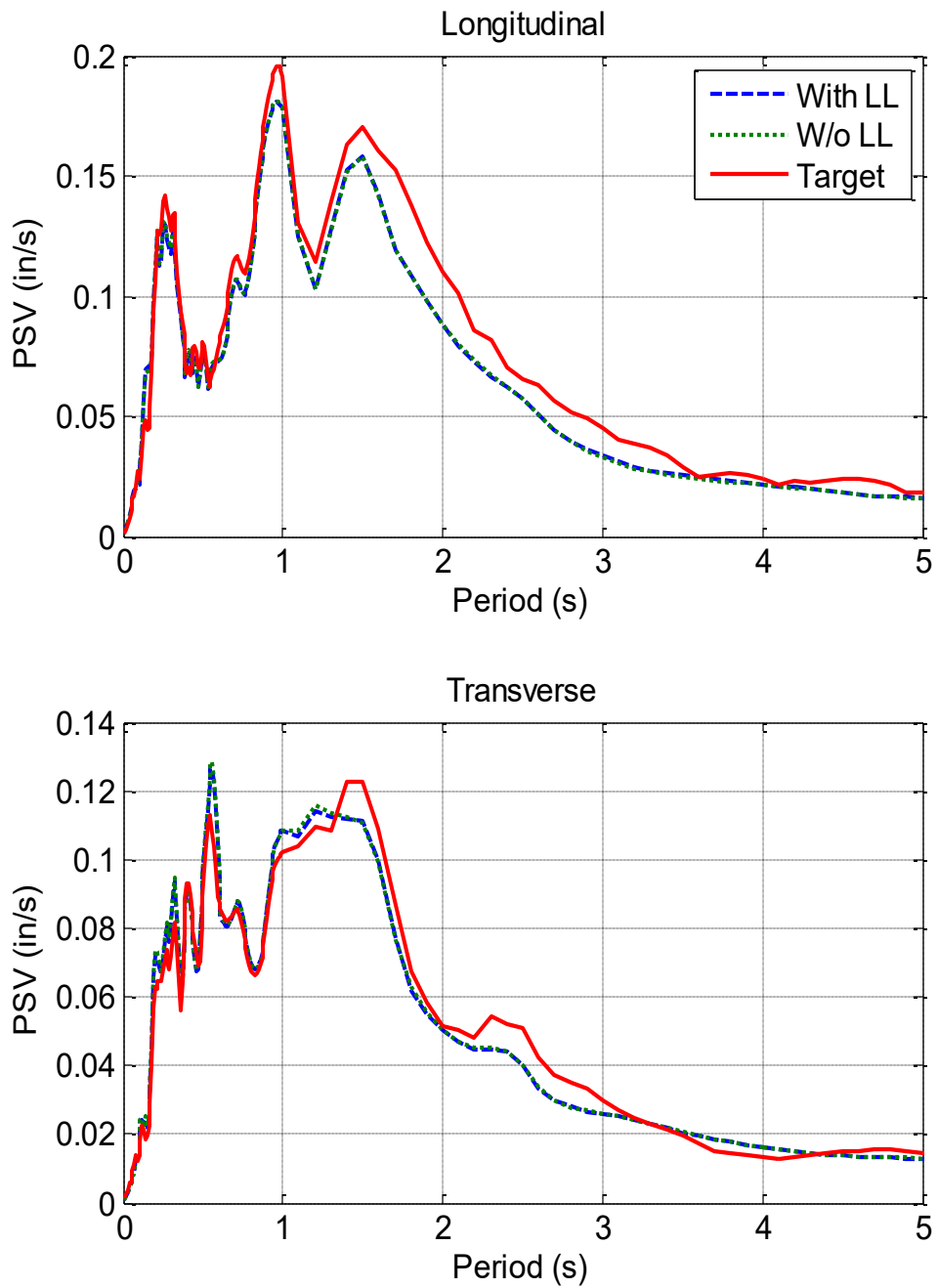


Figure 5.3.28. Velocity Response Spectra for Average Table Motion (250% DE)

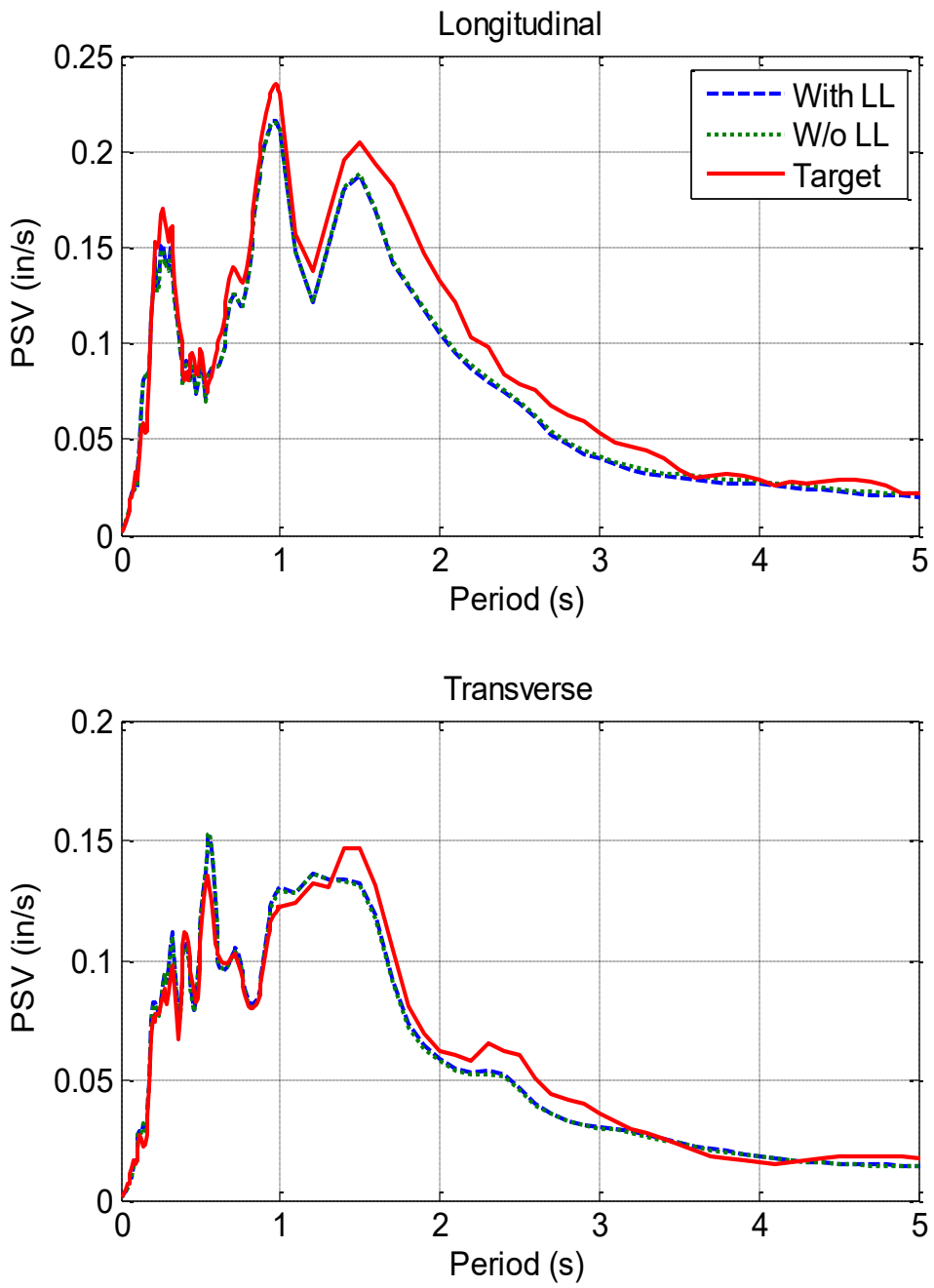
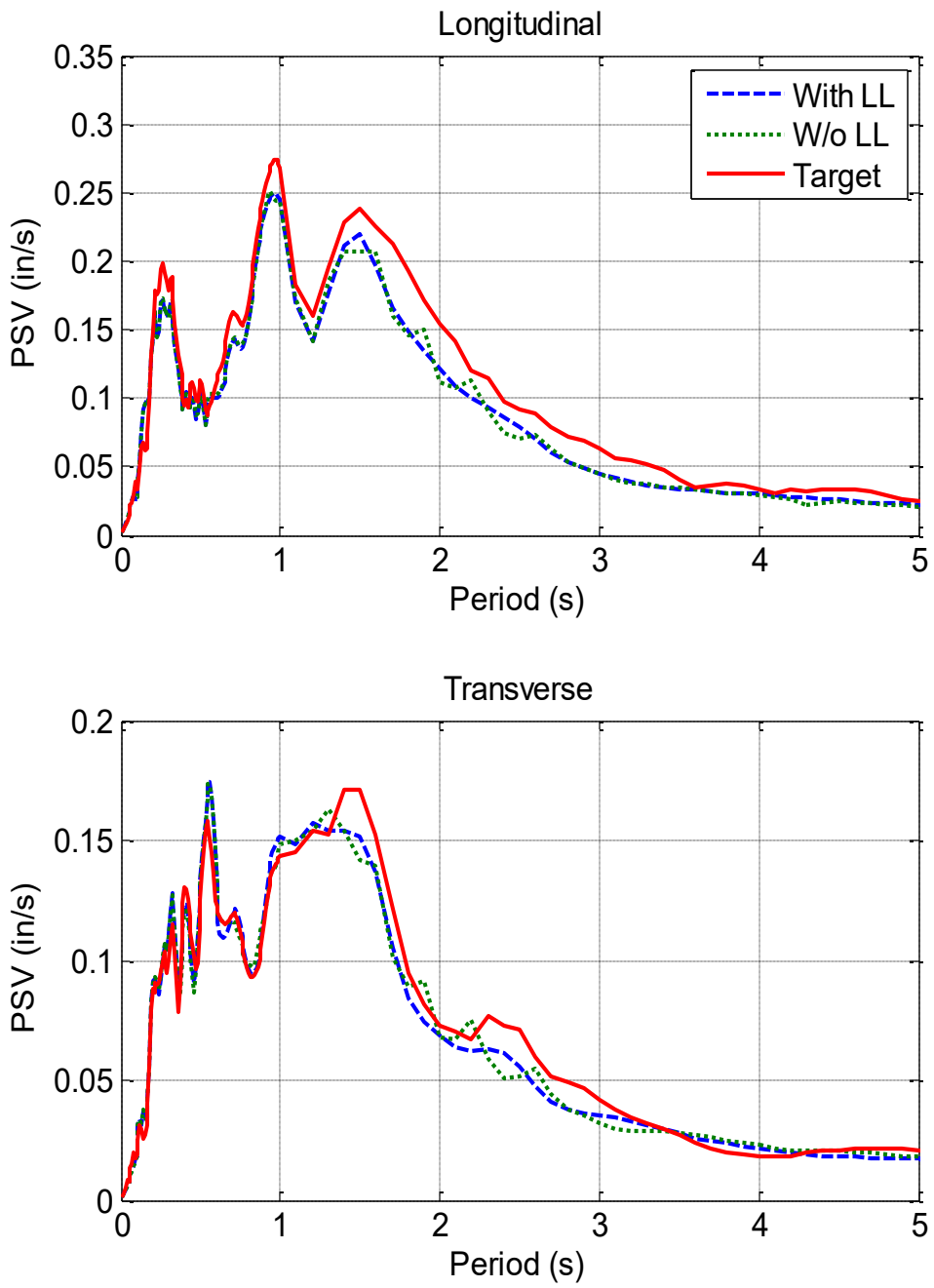
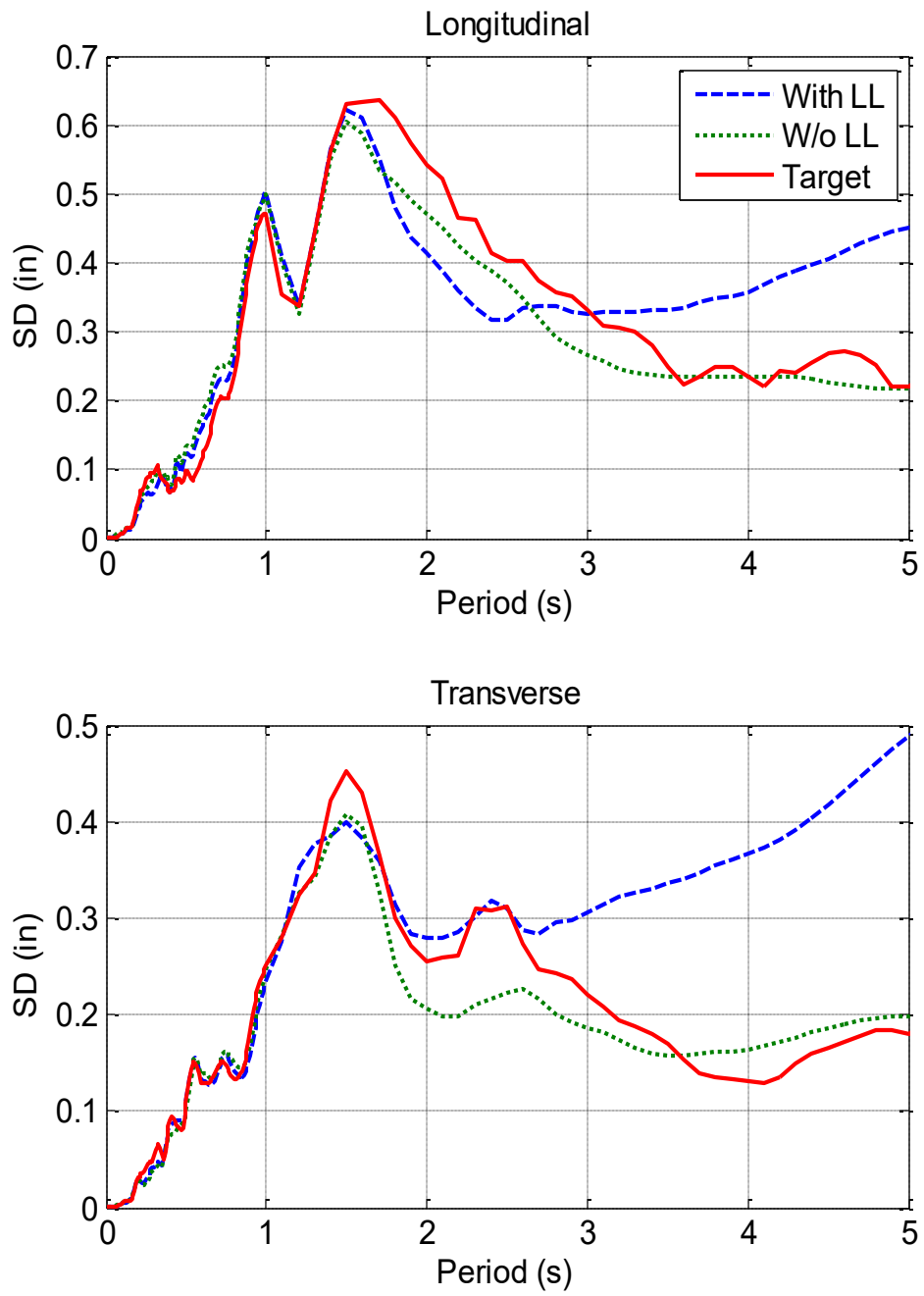


Figure 5.3.29. Velocity Response Spectra for Average Table Motion (300% DE)



**Figure 5.3.30. Velocity Response Spectra for Average Table Motion (350% DE)**



**Figure 5.3.31. Displacement Response Spectra for Average Table Motion (10% DE)**

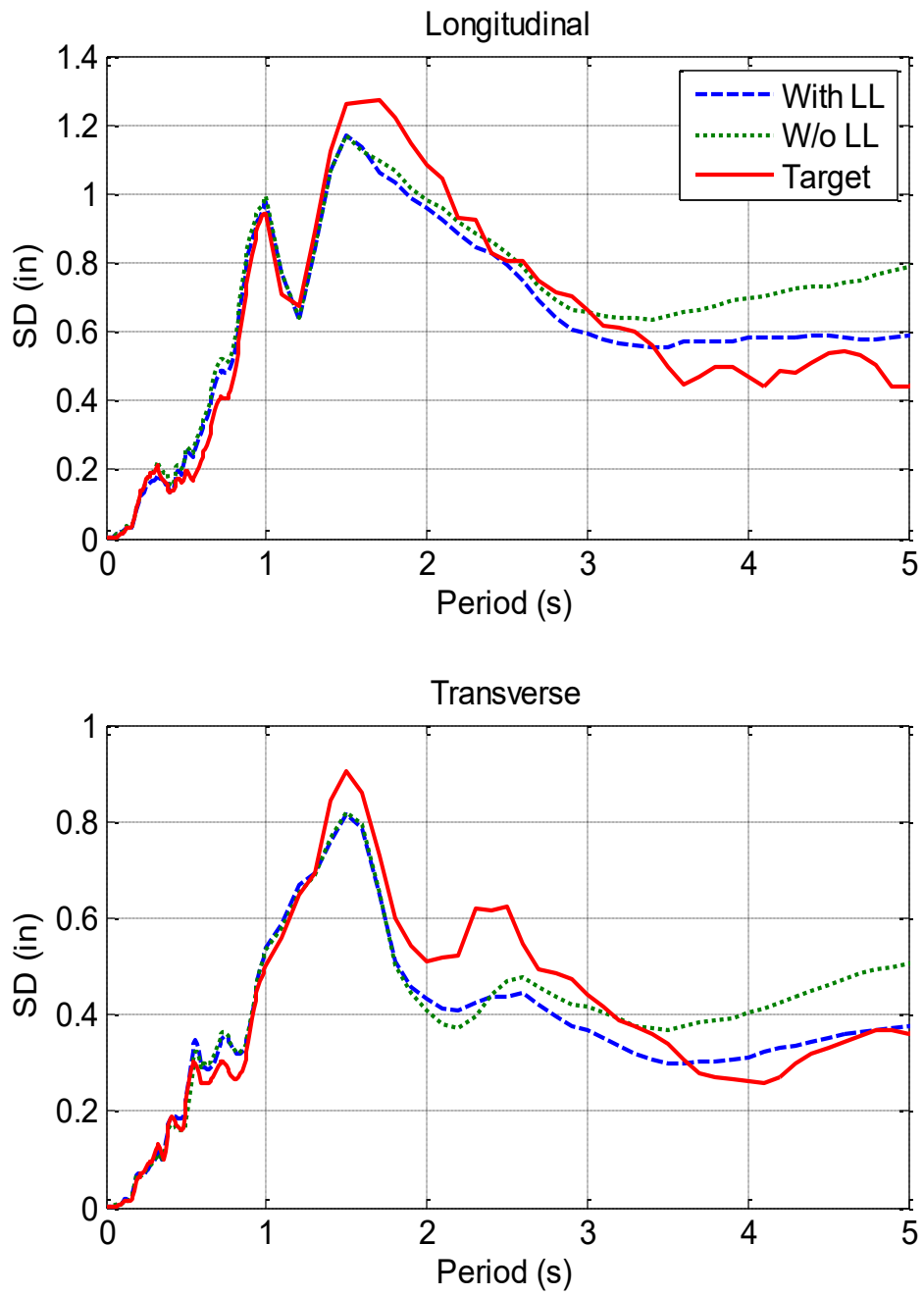


**Figure 5.3.32. Displacement Response Spectra for Average Table Motion (20% DE)**

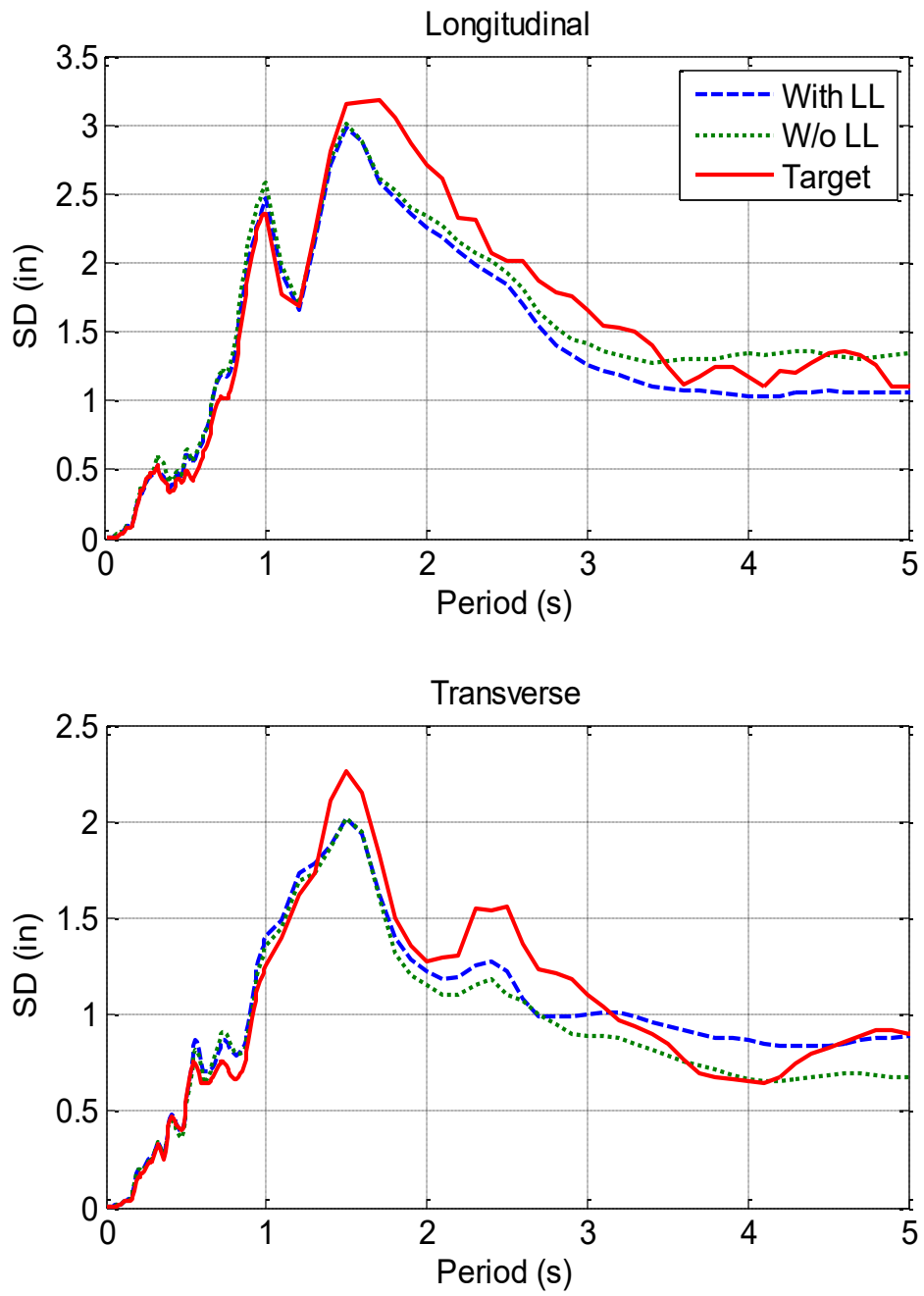


**Figure 5.3.33. Displacement Response Spectra for Average Table Motion (50% DE)**

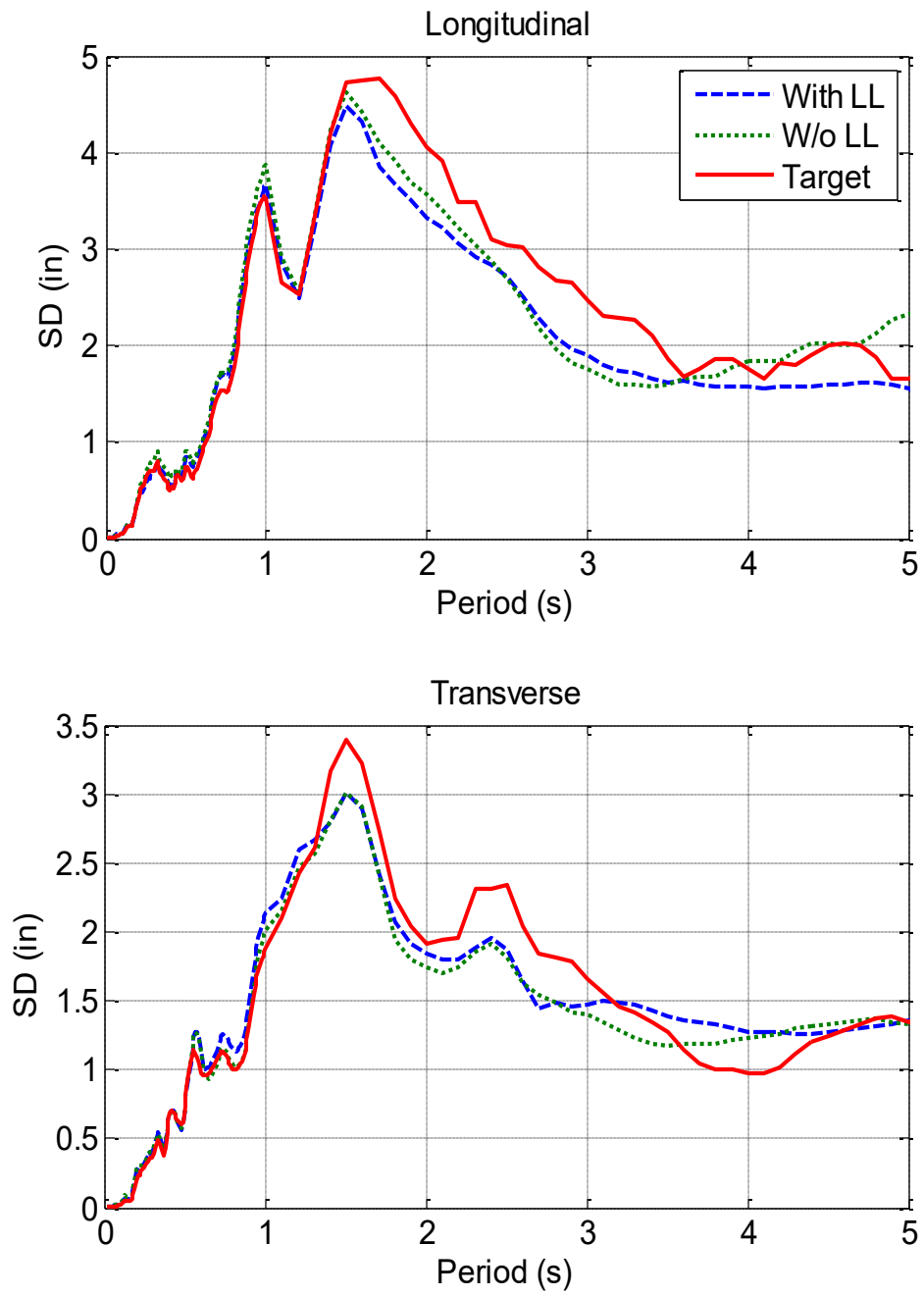


**Figure 5.3.34. Displacement Response Spectra for Average Table Motion (75% DE)**

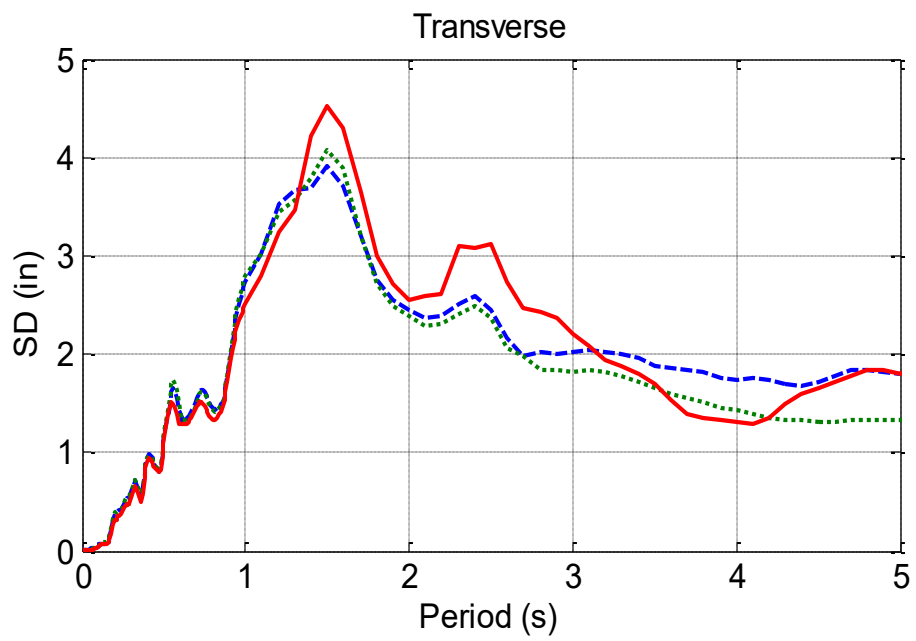
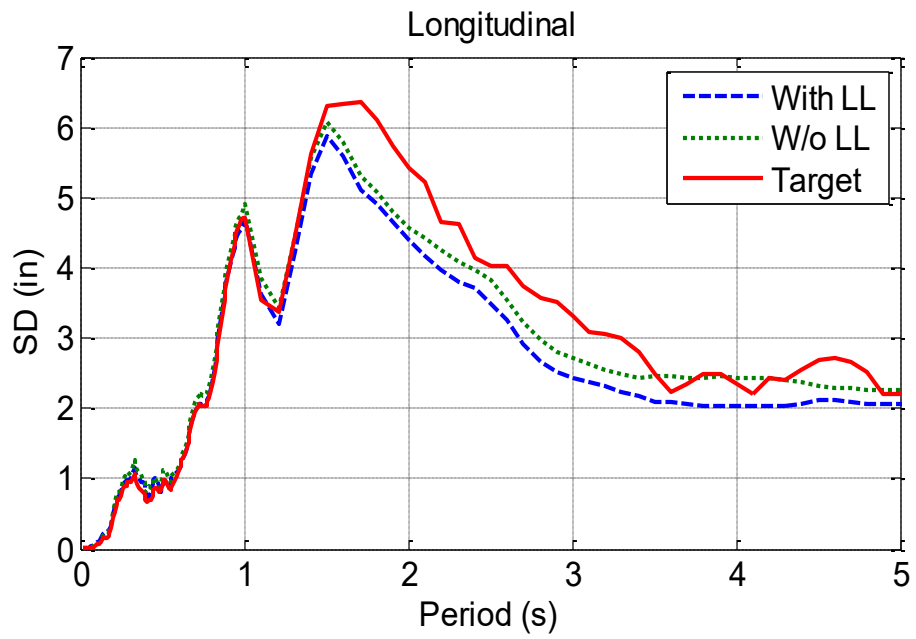


**Figure 5.3.35. Displacement Response Spectra for Average Table Motion (100% DE)**

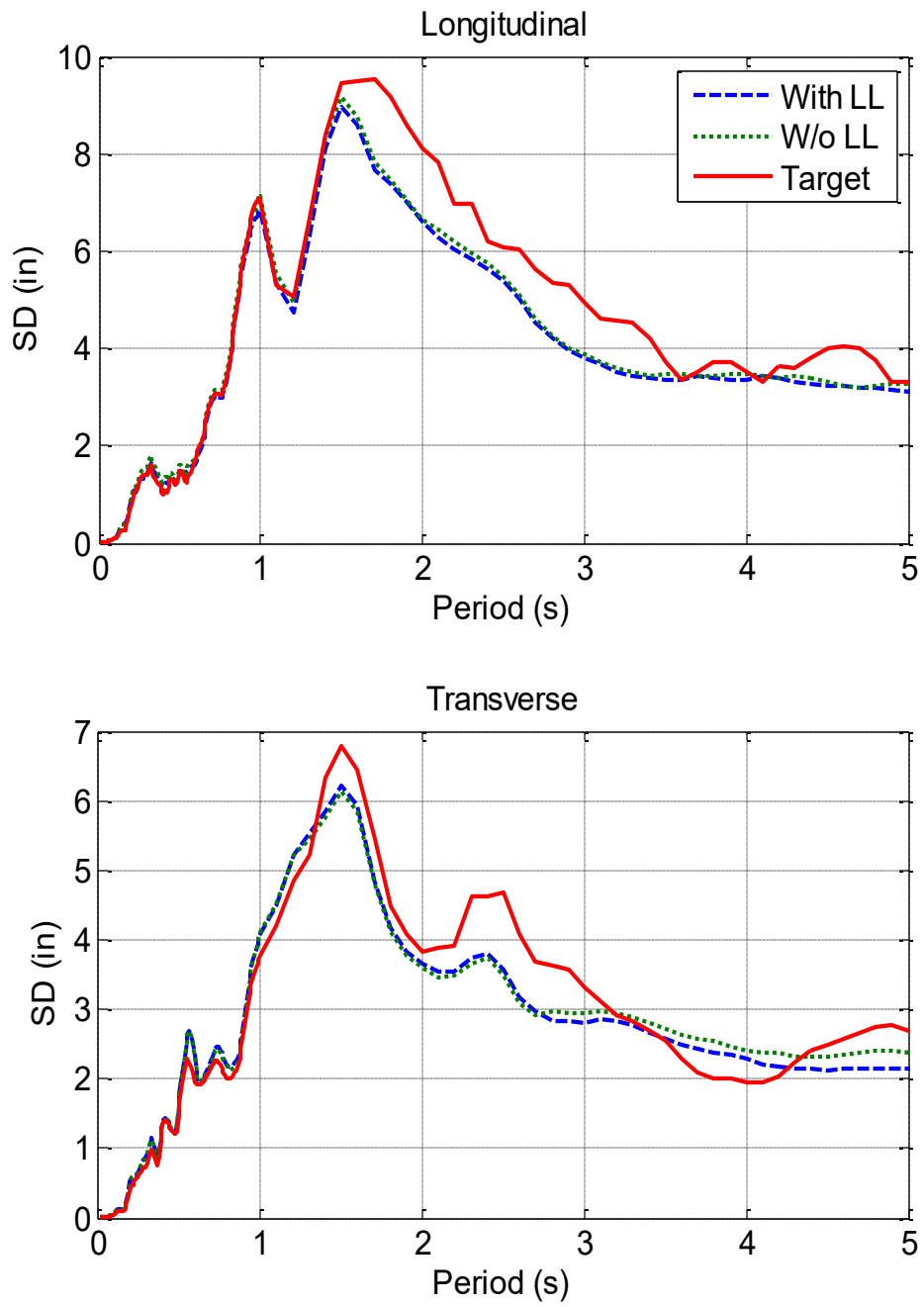


**Figure 5.3.36. Displacement Response Spectra for Average Table Motion (150% DE)**

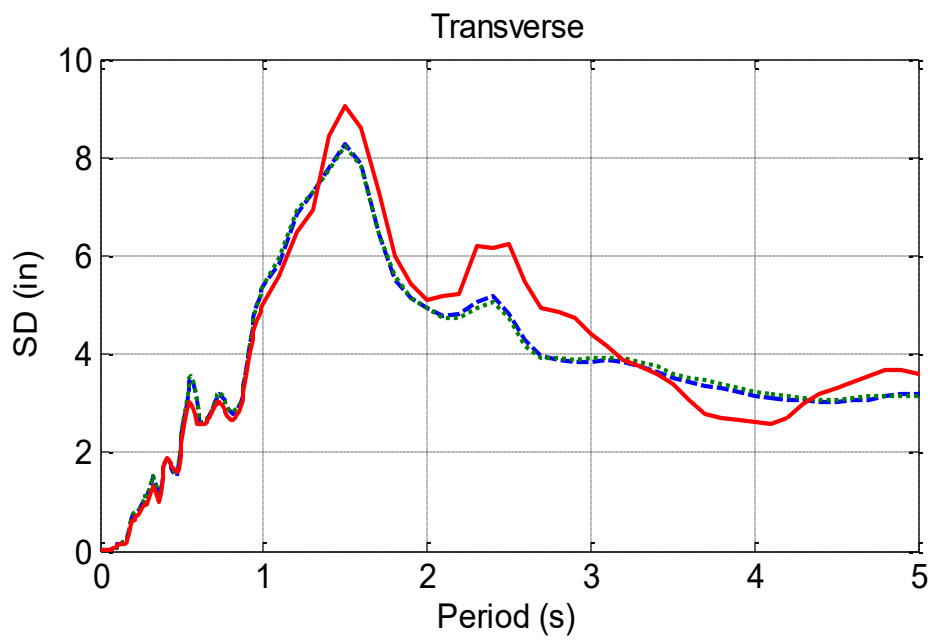
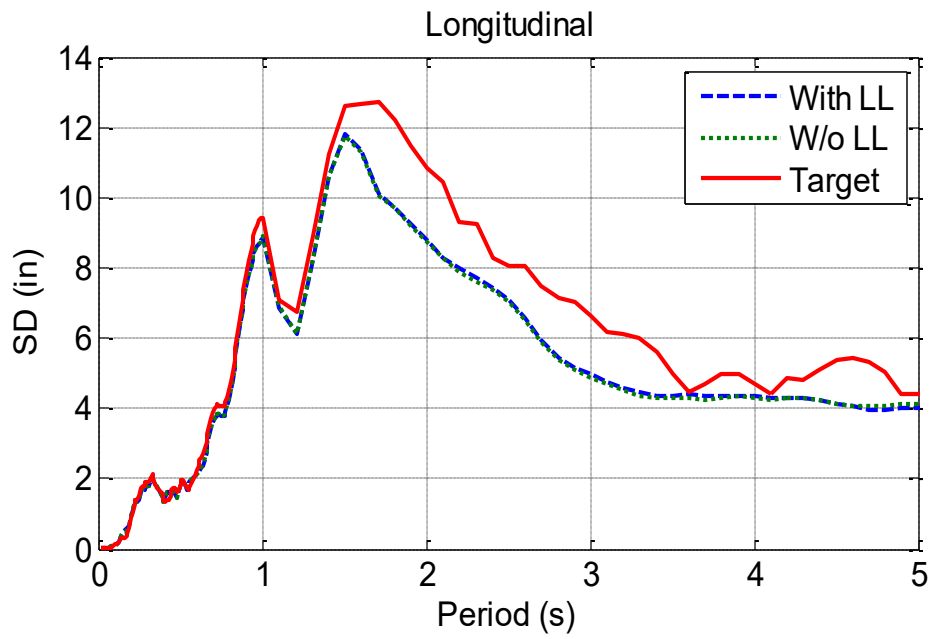


**Figure 5.3.37. Displacement Response Spectra for Average Table Motion (200% DE)**

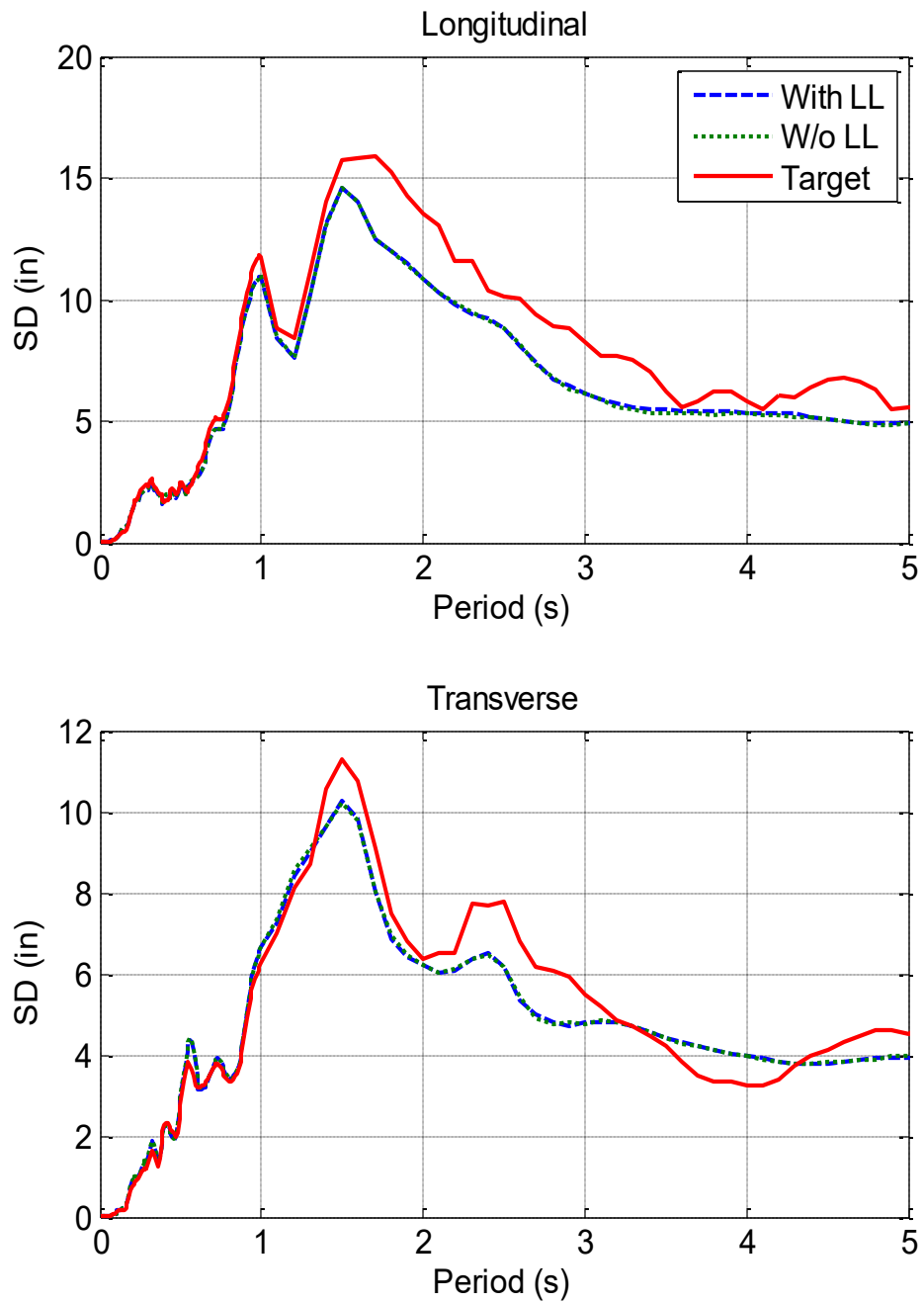


**Figure 5.3.38. Displacement Response Spectra for Average Table Motion (250% DE)**

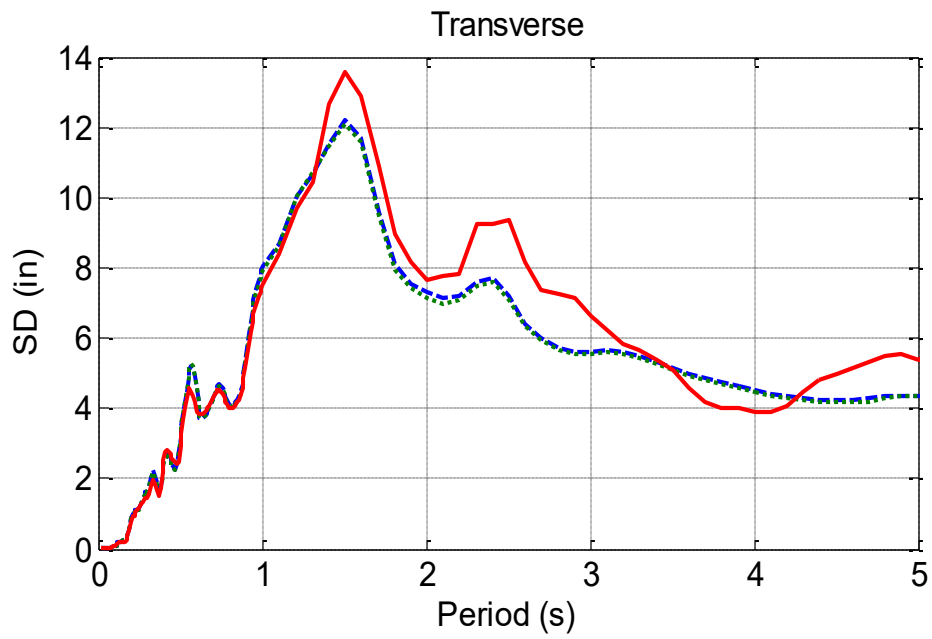
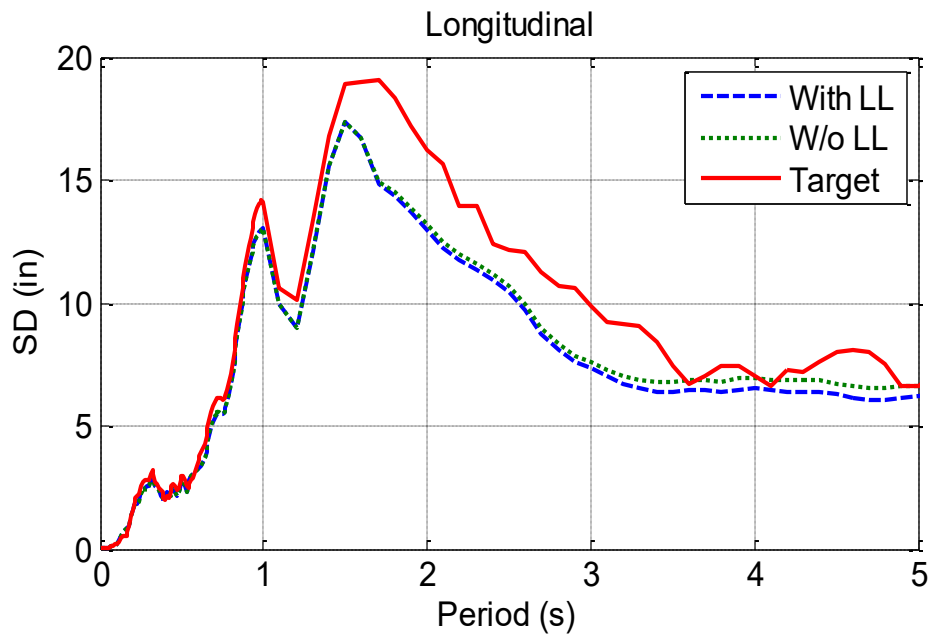


**Figure 5.3.39. Displacement Response Spectra for Average Table Motion (300% DE)**

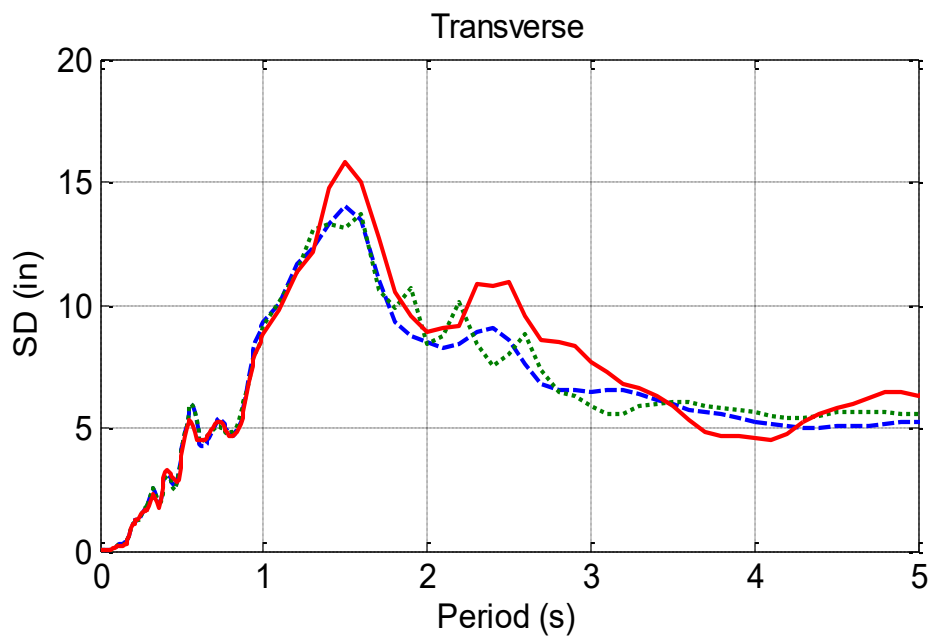
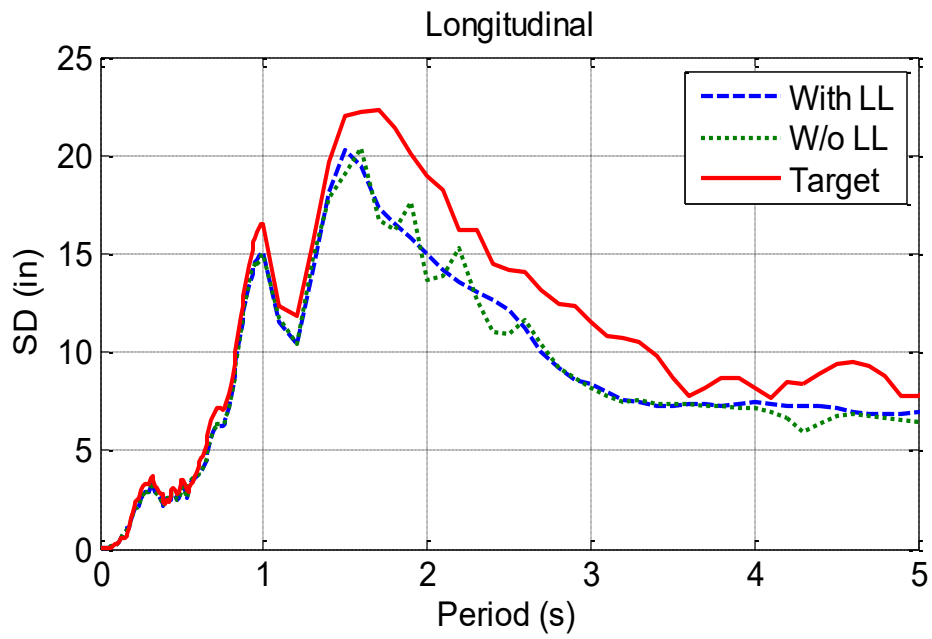


**Figure 5.3.40. Displacement Response Spectra for Average Table Motion (350% DE)**

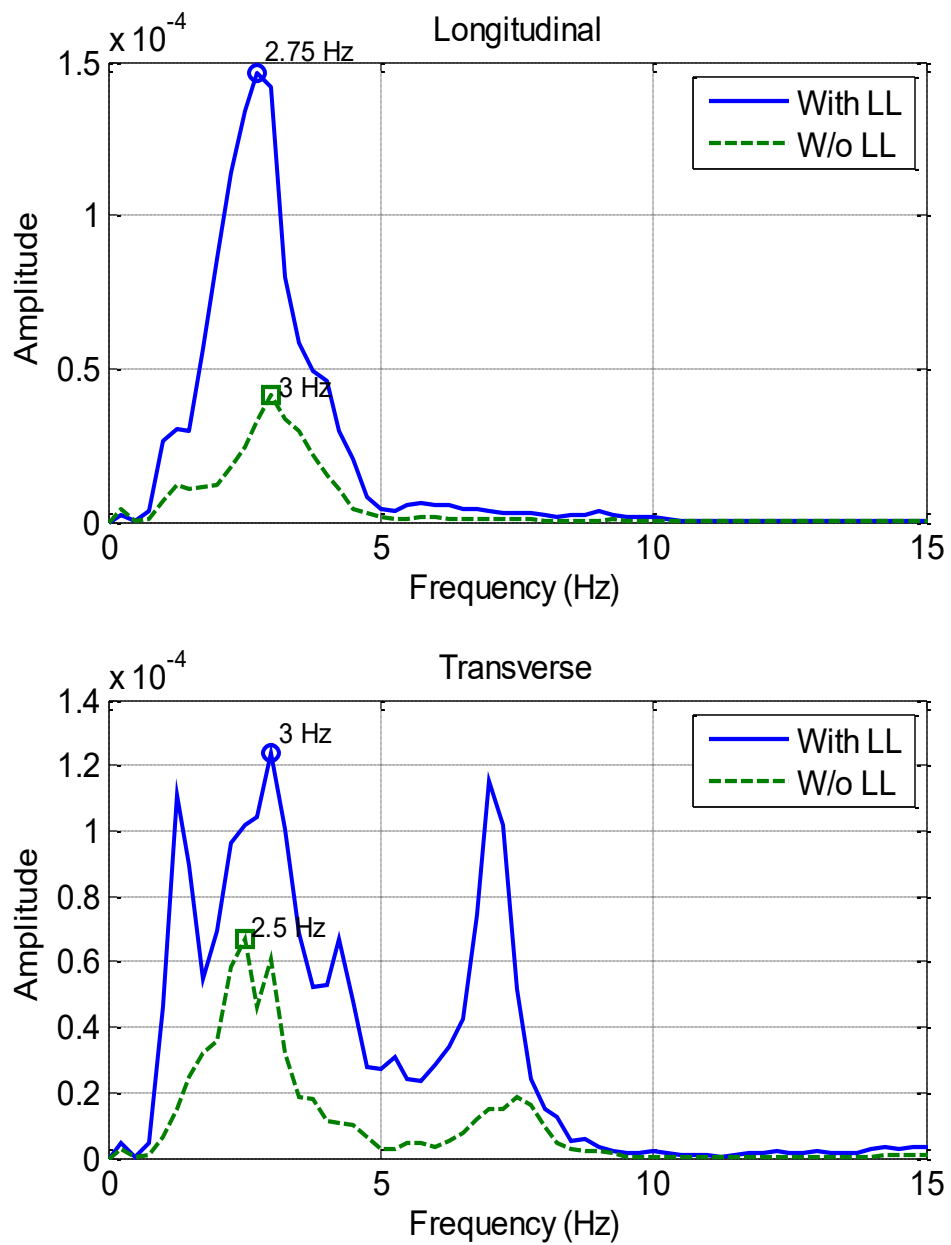


**Figure 5.4.1. Power Spectral Density of Deck Acceleration in Longitudinal Direction (White Noise #1)**

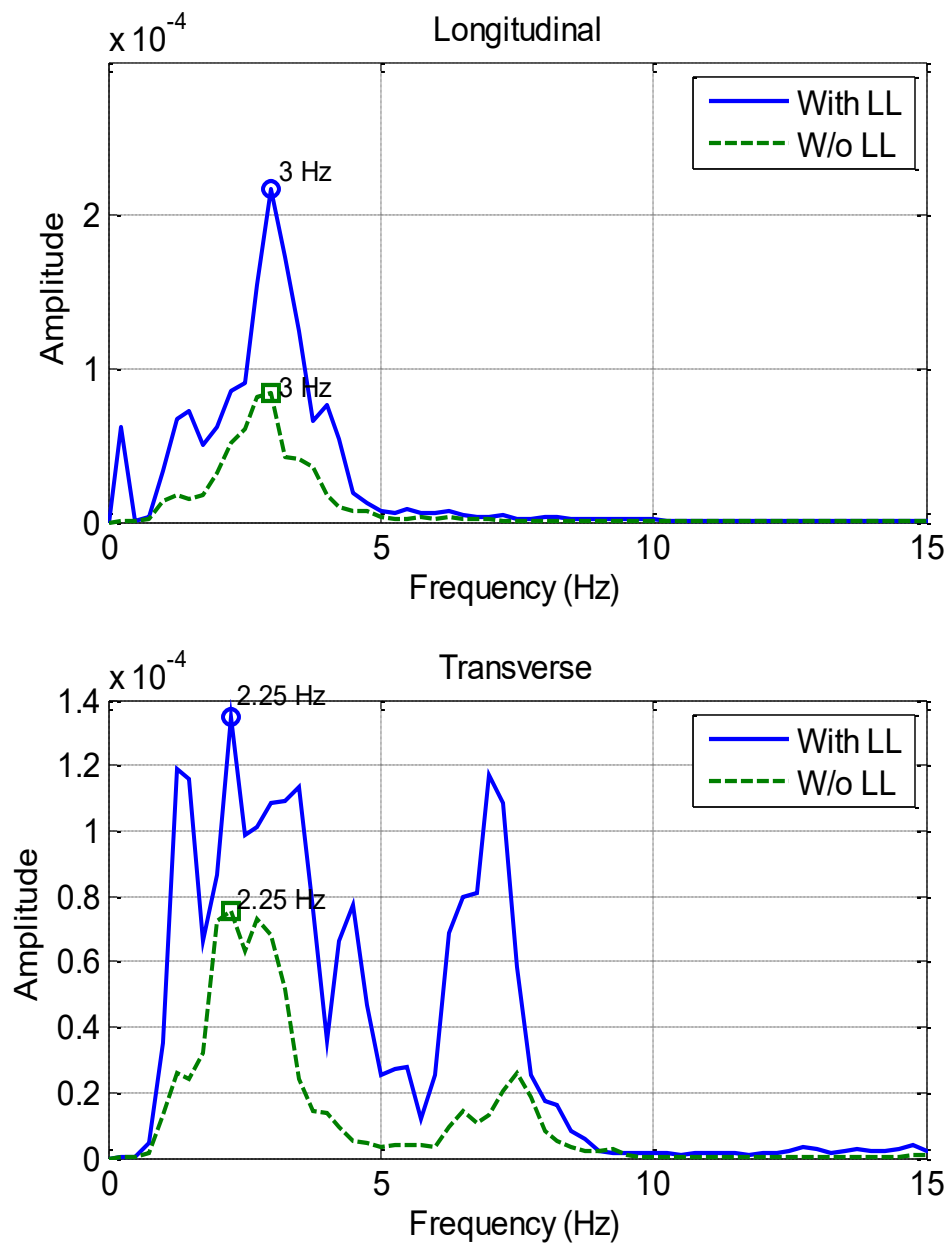


**Figure 5.4.2. Power Spectral Density of Deck Acceleration in Longitudinal Direction (White Noise #2)**

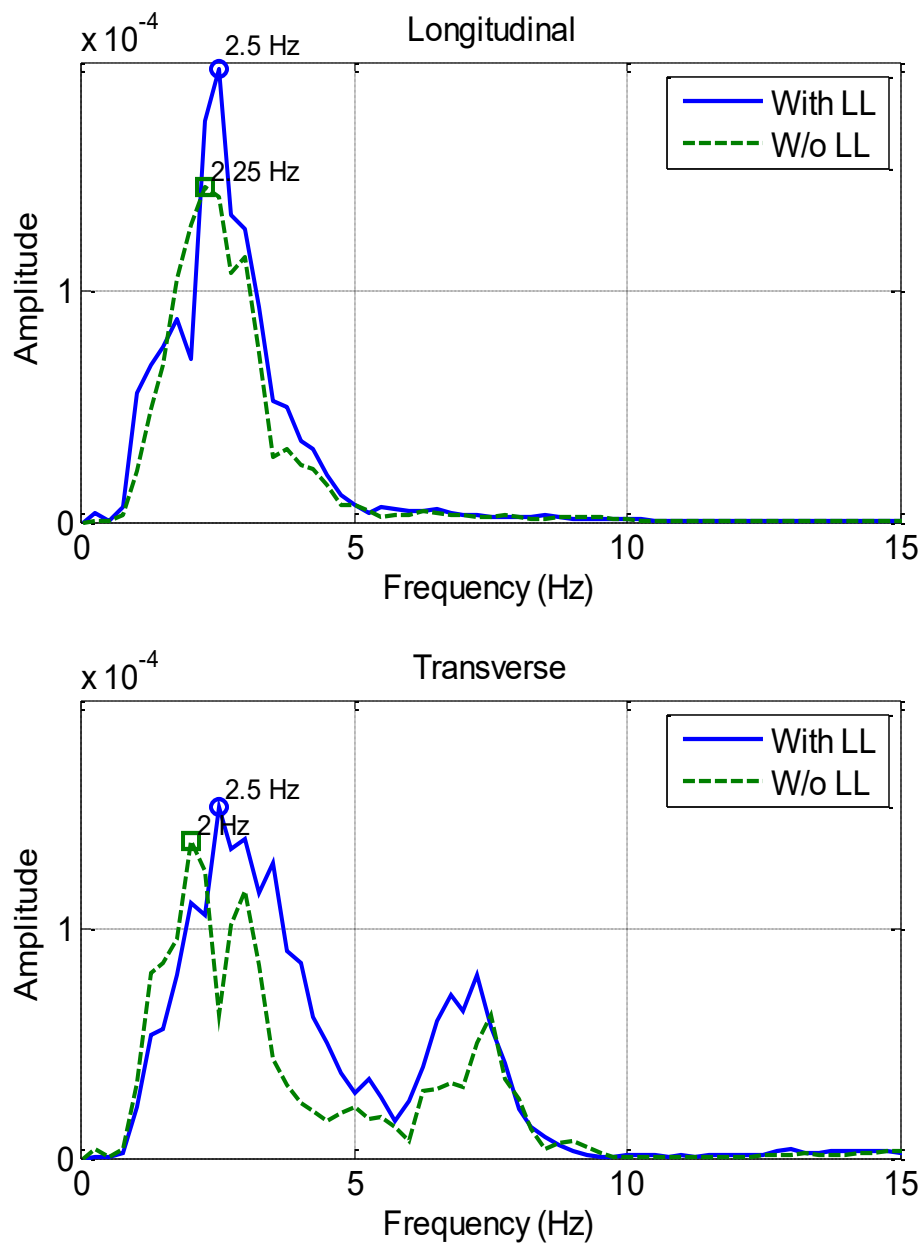


**Figure 5.4.3. Power Spectral Density of Deck Acceleration in Longitudinal Direction (White Noise #3)**

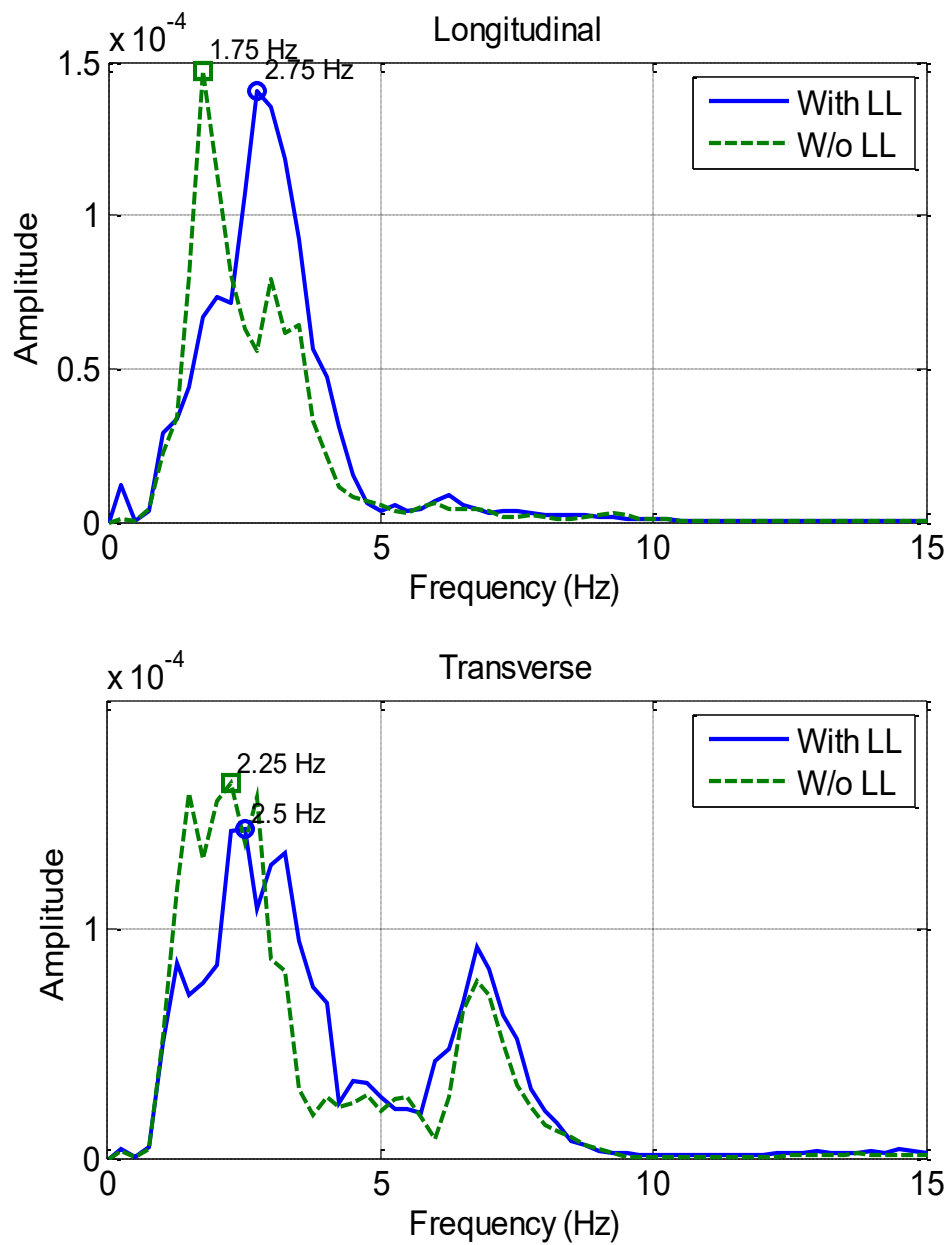


**Figure 5.4.4. Power Spectral Density of Deck Acceleration in Longitudinal Direction (White Noise #4)**

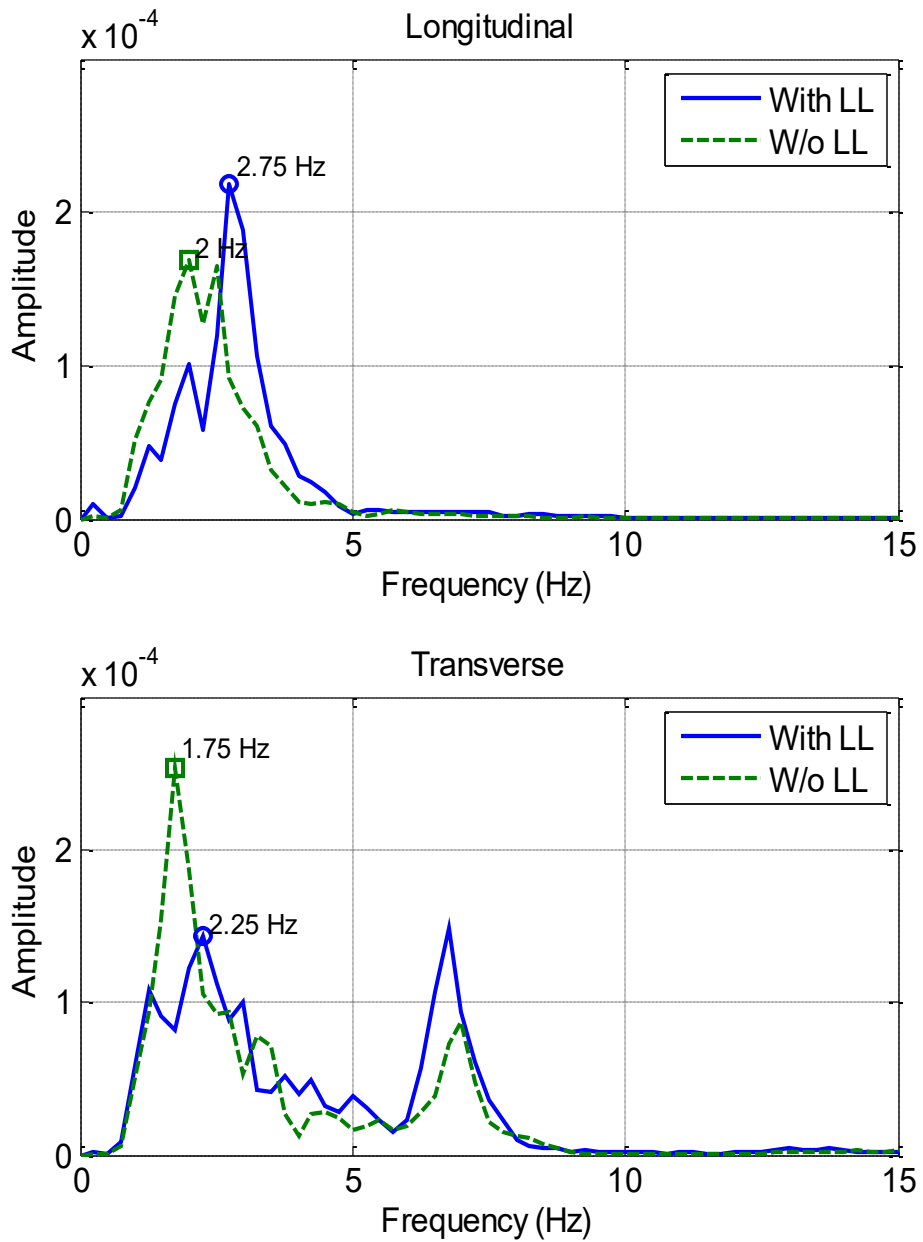


**Figure 5.4.5. Power Spectral Density of Deck Acceleration in Longitudinal Direction (White Noise #5)**

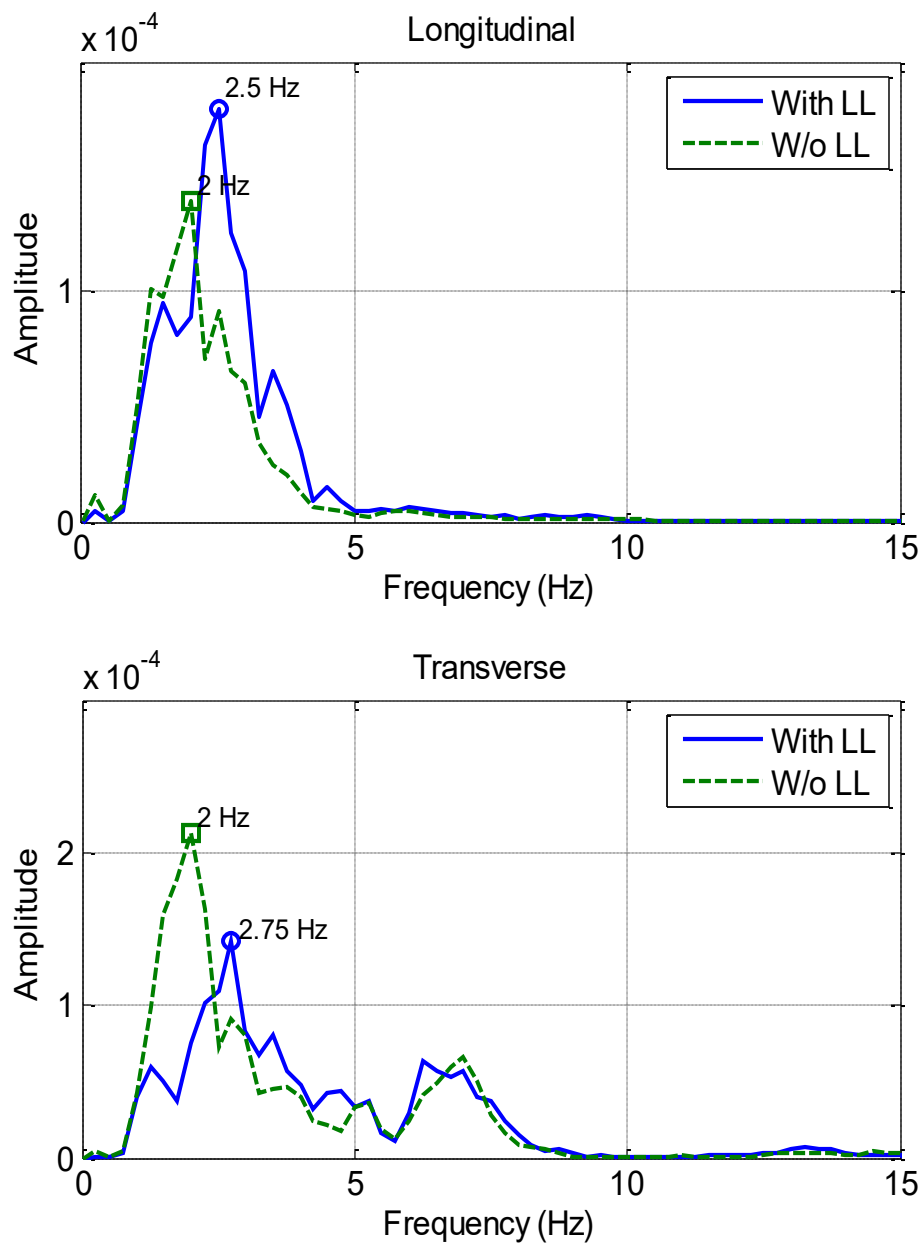


**Figure 5.4.6. Power Spectral Density of Deck Acceleration in Longitudinal Direction (White Noise #6)**

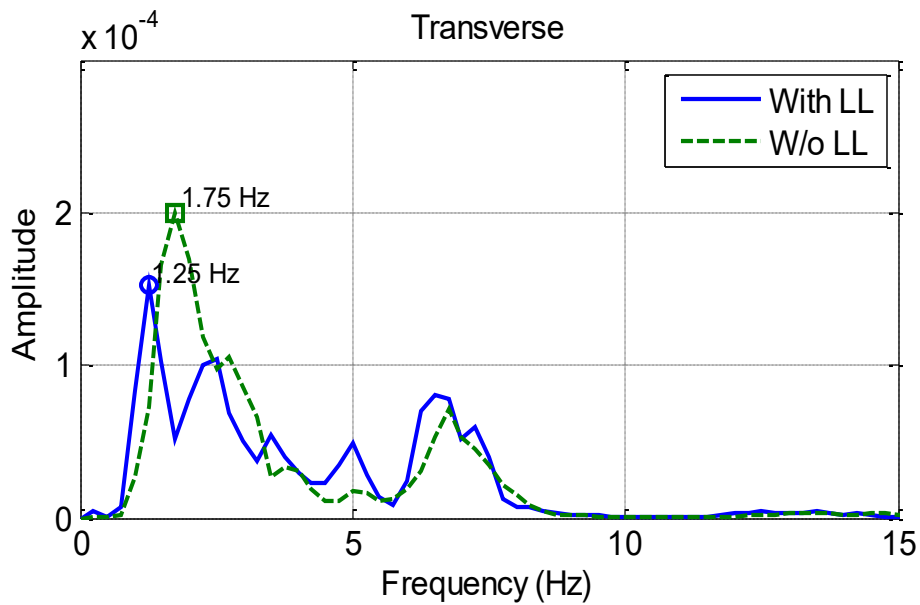
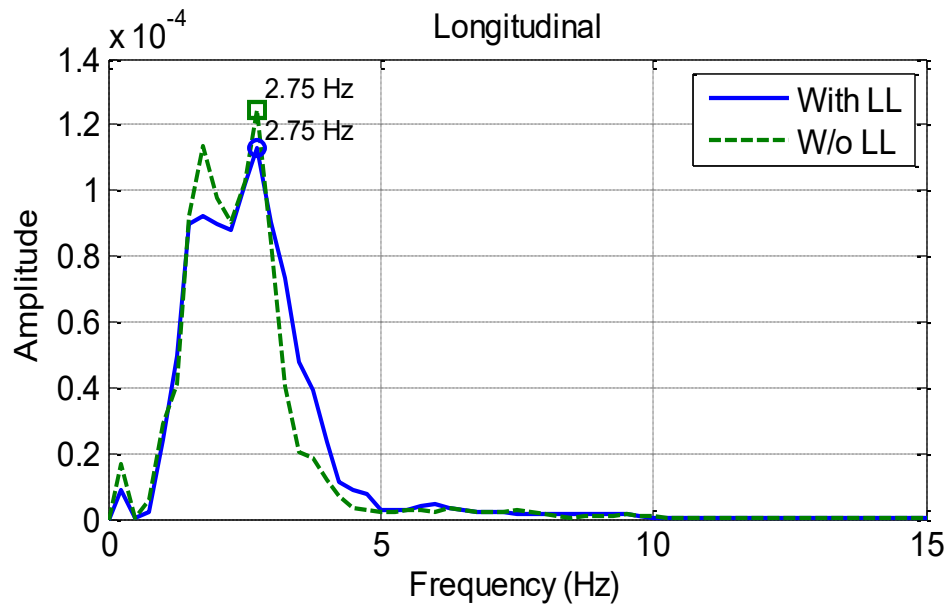


**Figure 5.4.7. Power Spectral Density of Deck Acceleration in Longitudinal Direction (White Noise #7)**

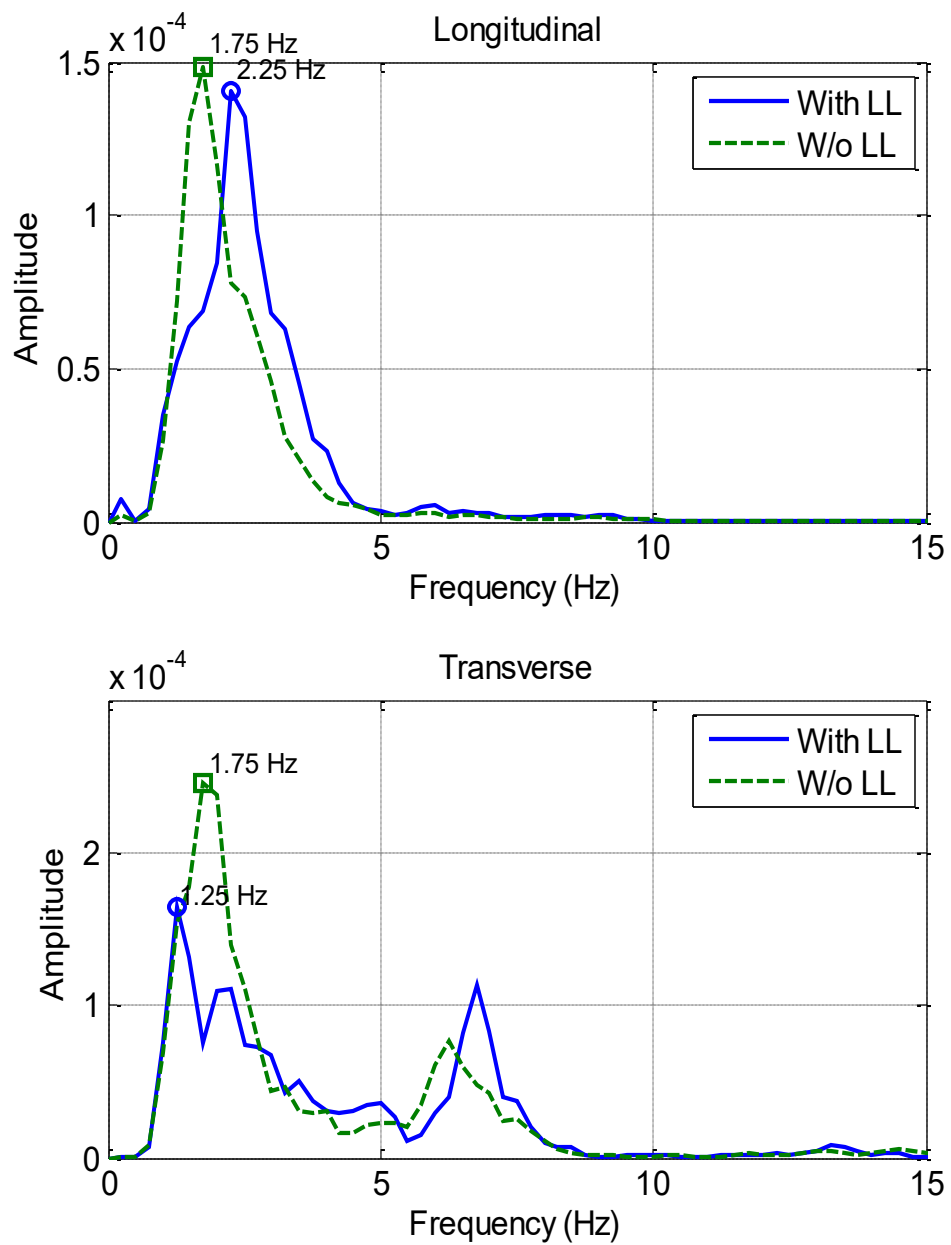


**Figure 5.4.8. Power Spectral Density of Deck Acceleration in Longitudinal Direction (White Noise #8)**

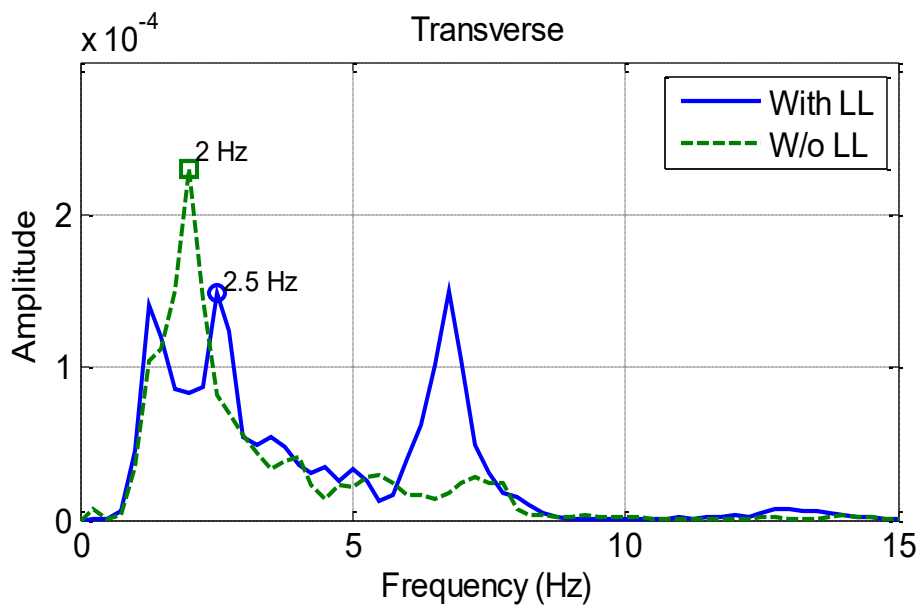
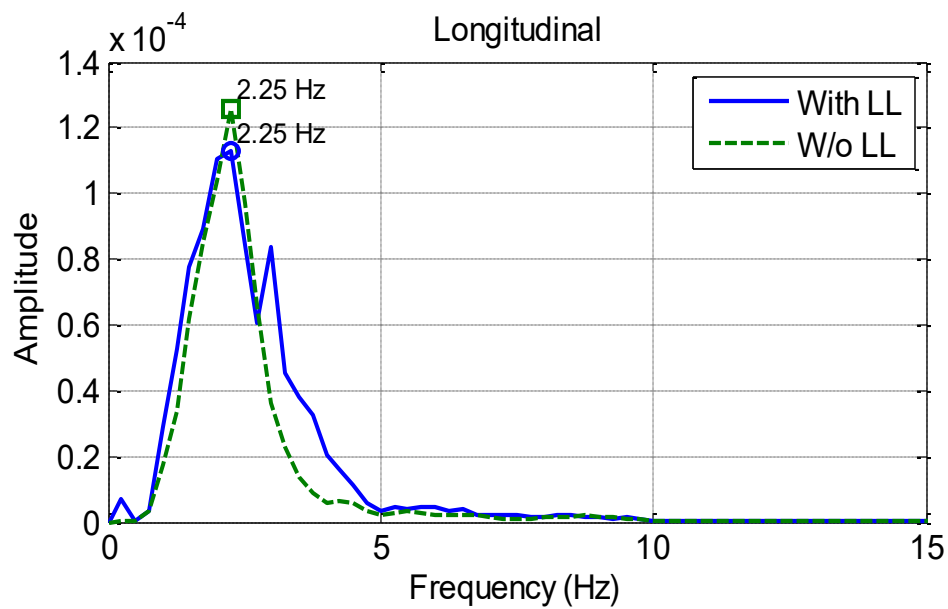


**Figure 5.4.9. Power Spectral Density of Deck Acceleration in Longitudinal Direction (White Noise #9)**

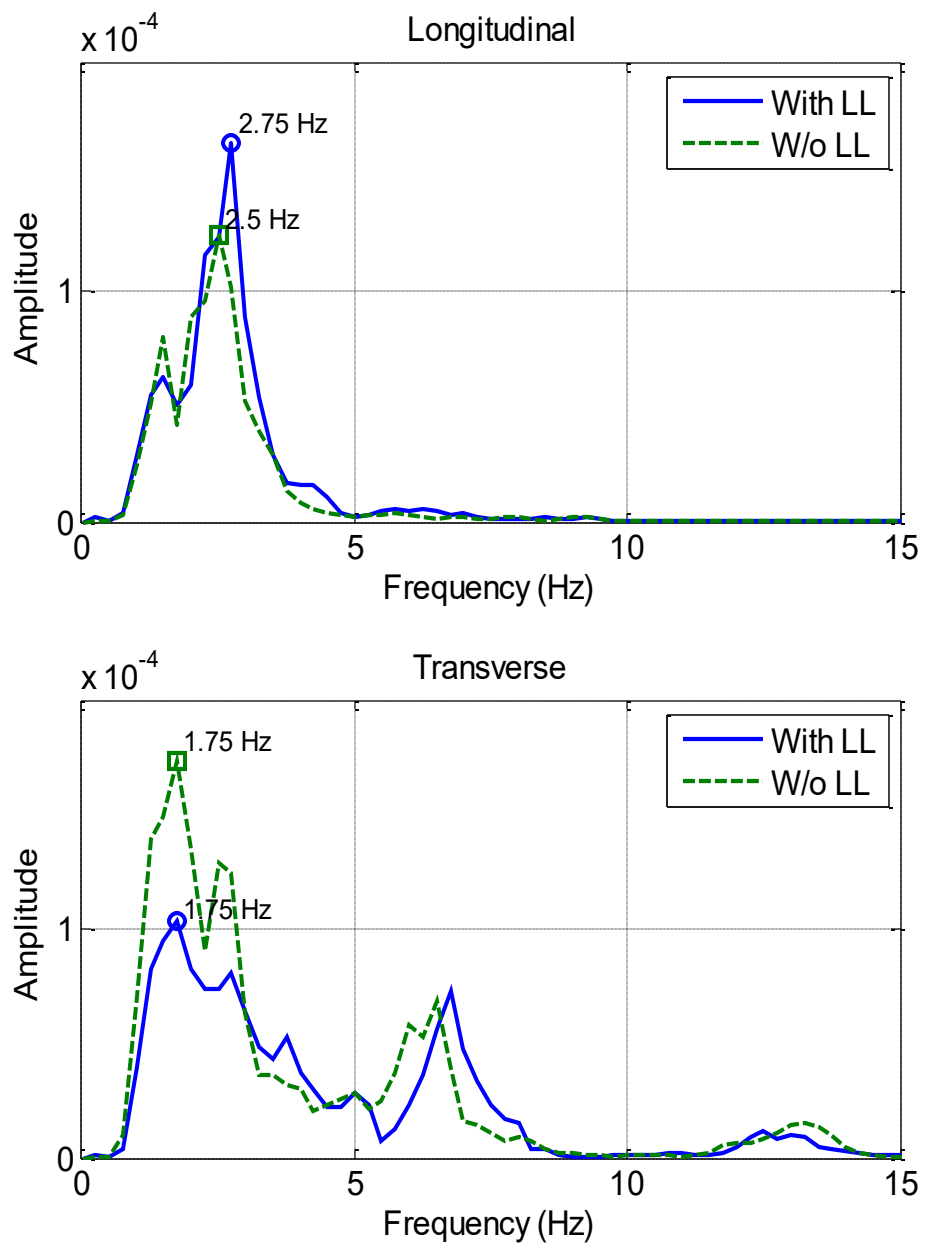


**Figure 5.4.10. Power Spectral Density of Deck Acceleration in Longitudinal Direction (White Noise #10)**

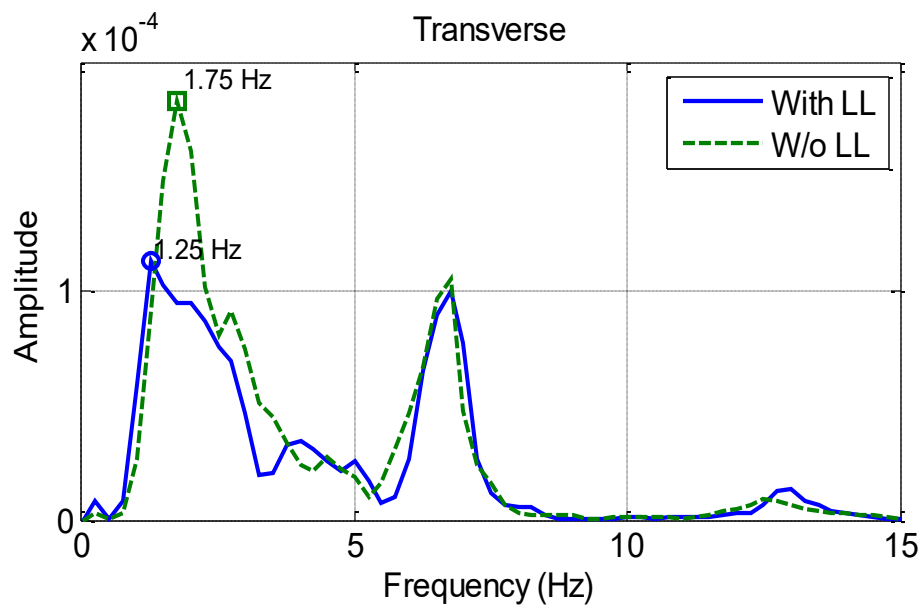
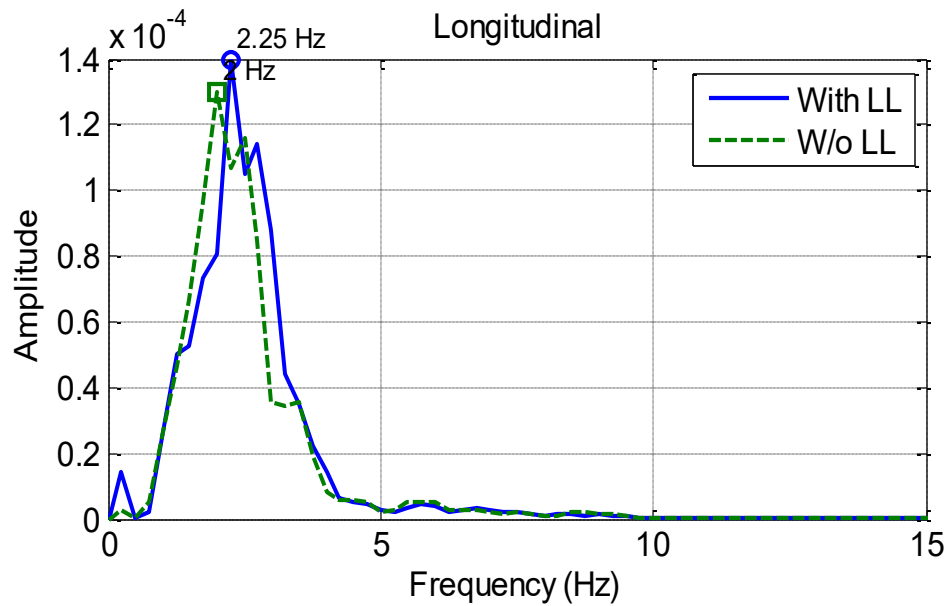


**Figure 5.4.11. Power Spectral Density of Deck Acceleration in Longitudinal Direction (White Noise #11)**

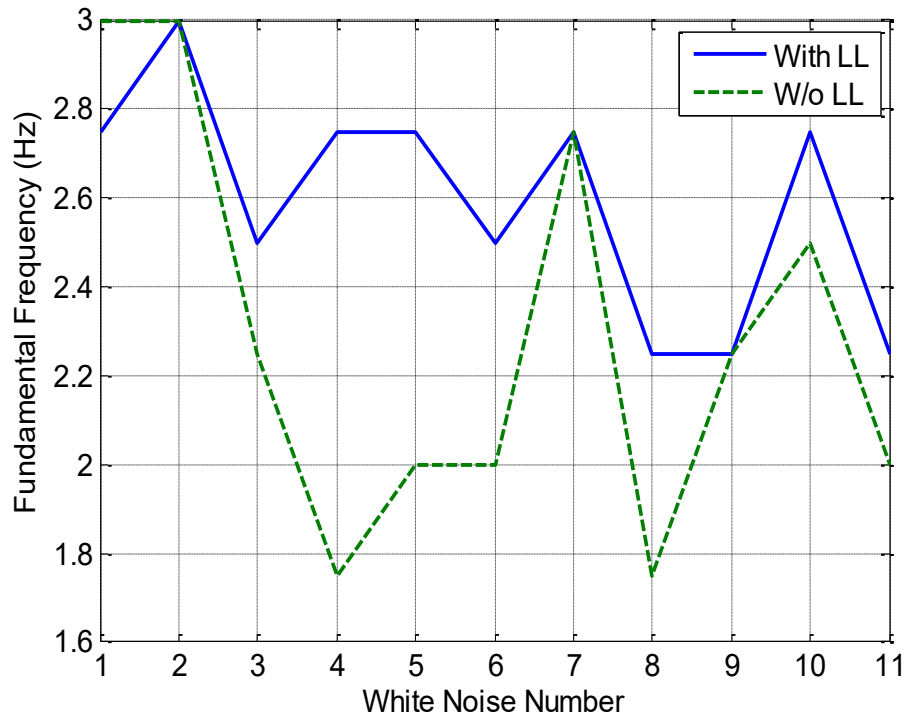


**Figure 5.4.12. Fundamental Frequency in Longitudinal Direction**

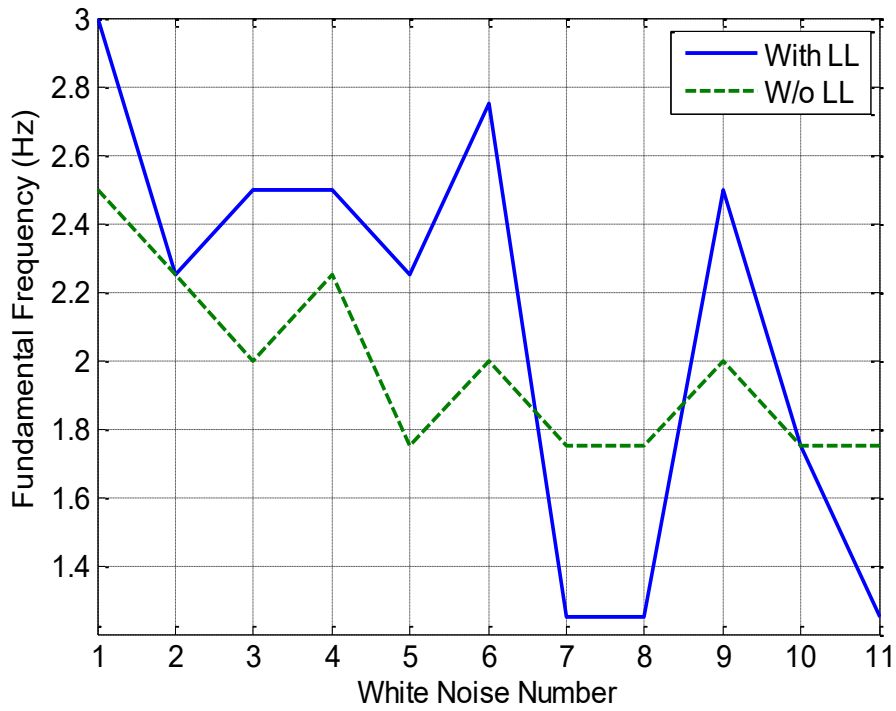


**Figure 5.4.13. Fundamental Frequency in Transverse Direction**

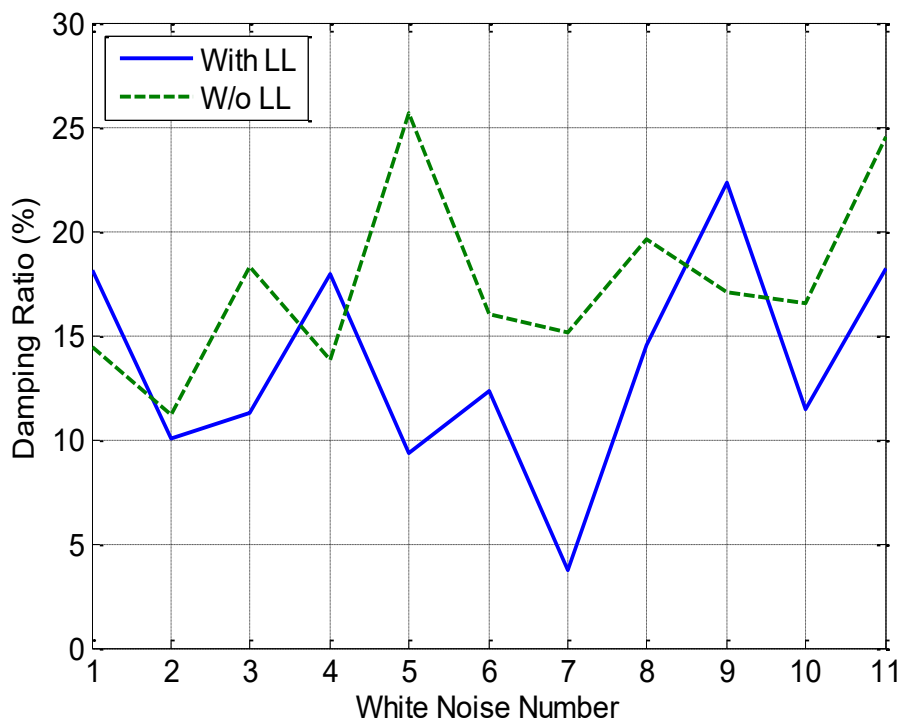


**Figure 5.4.14. Damping Ratio in Longitudinal Direction**

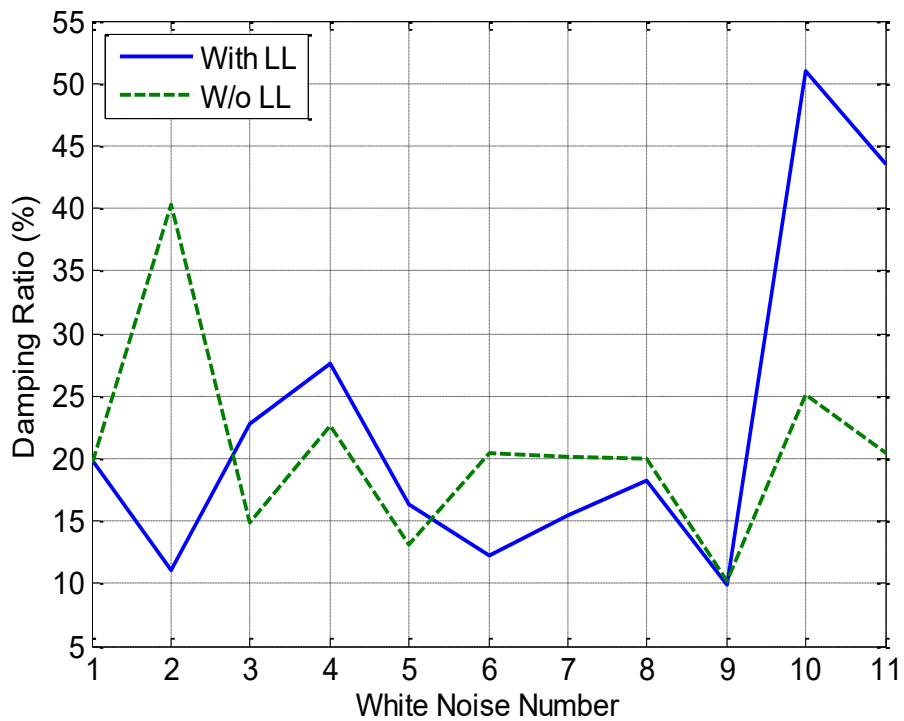


**Figure 5.4.15. Damping Ratio in Transverse Direction**

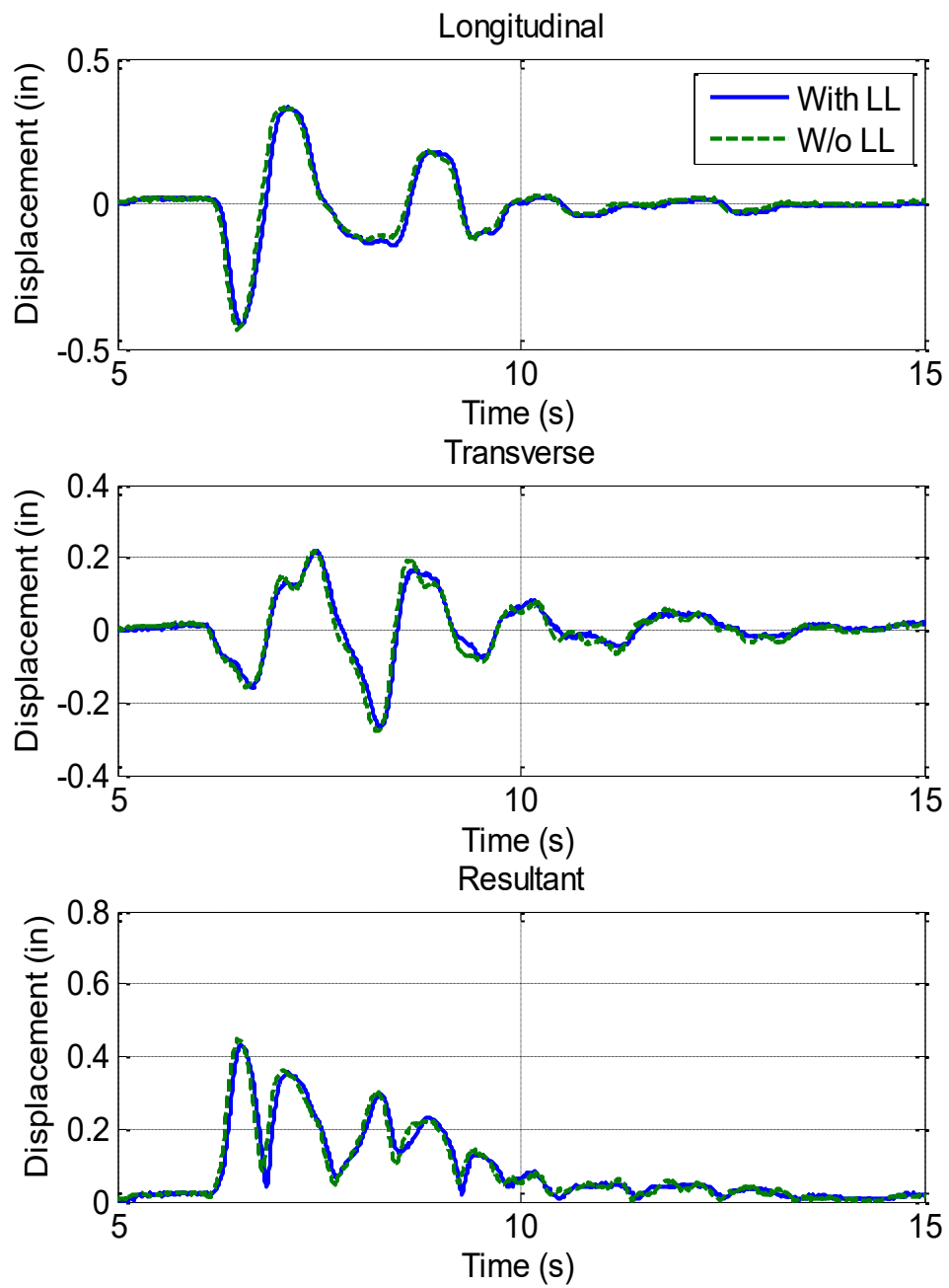


**Figure 5.5.1. Relative Displacement at Middle Span on Middle Girder (10% DE)**

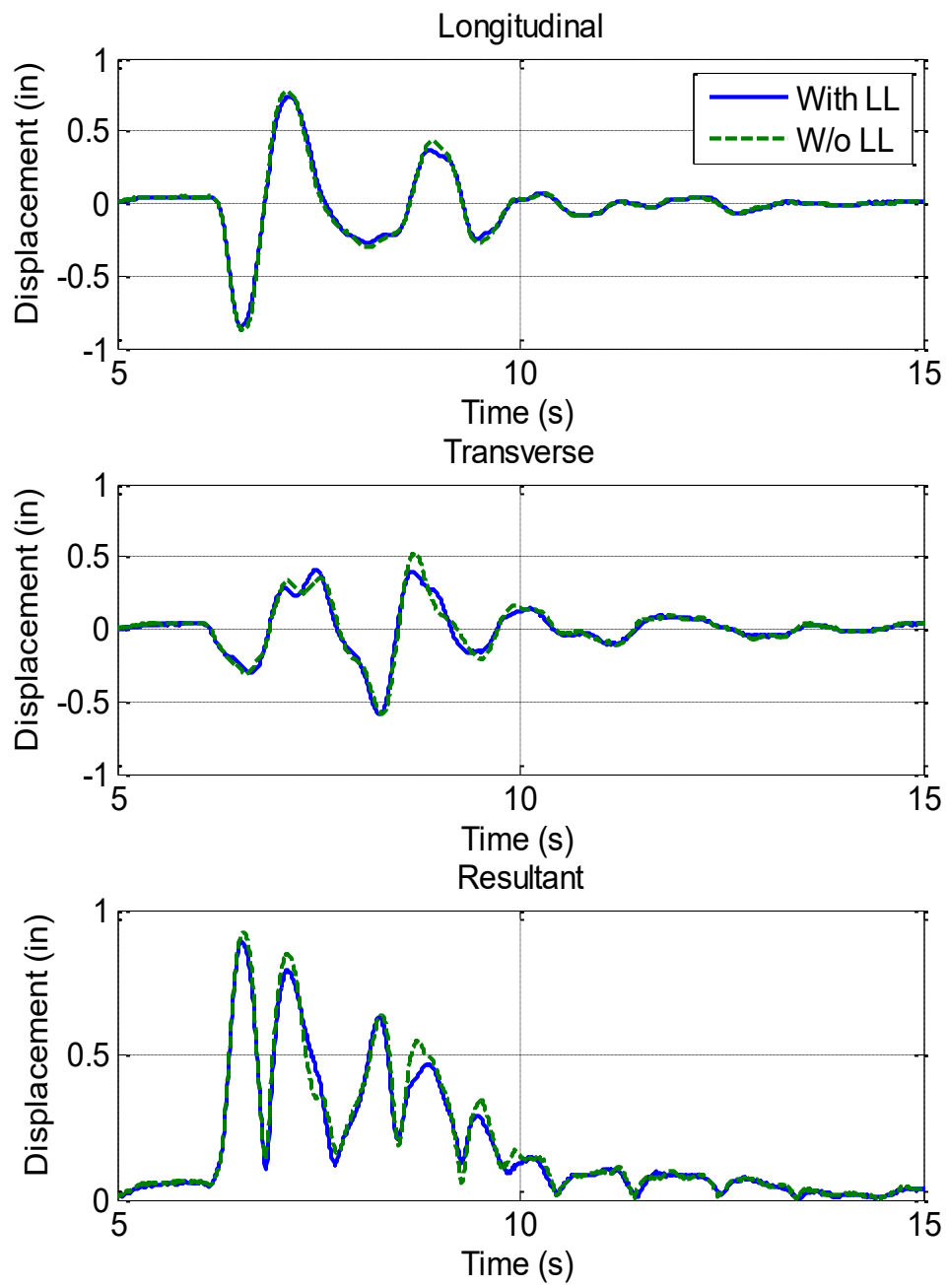


**Figure 5.5.2. Relative Displacement at Middle Span on Middle Girder (20% DE)**

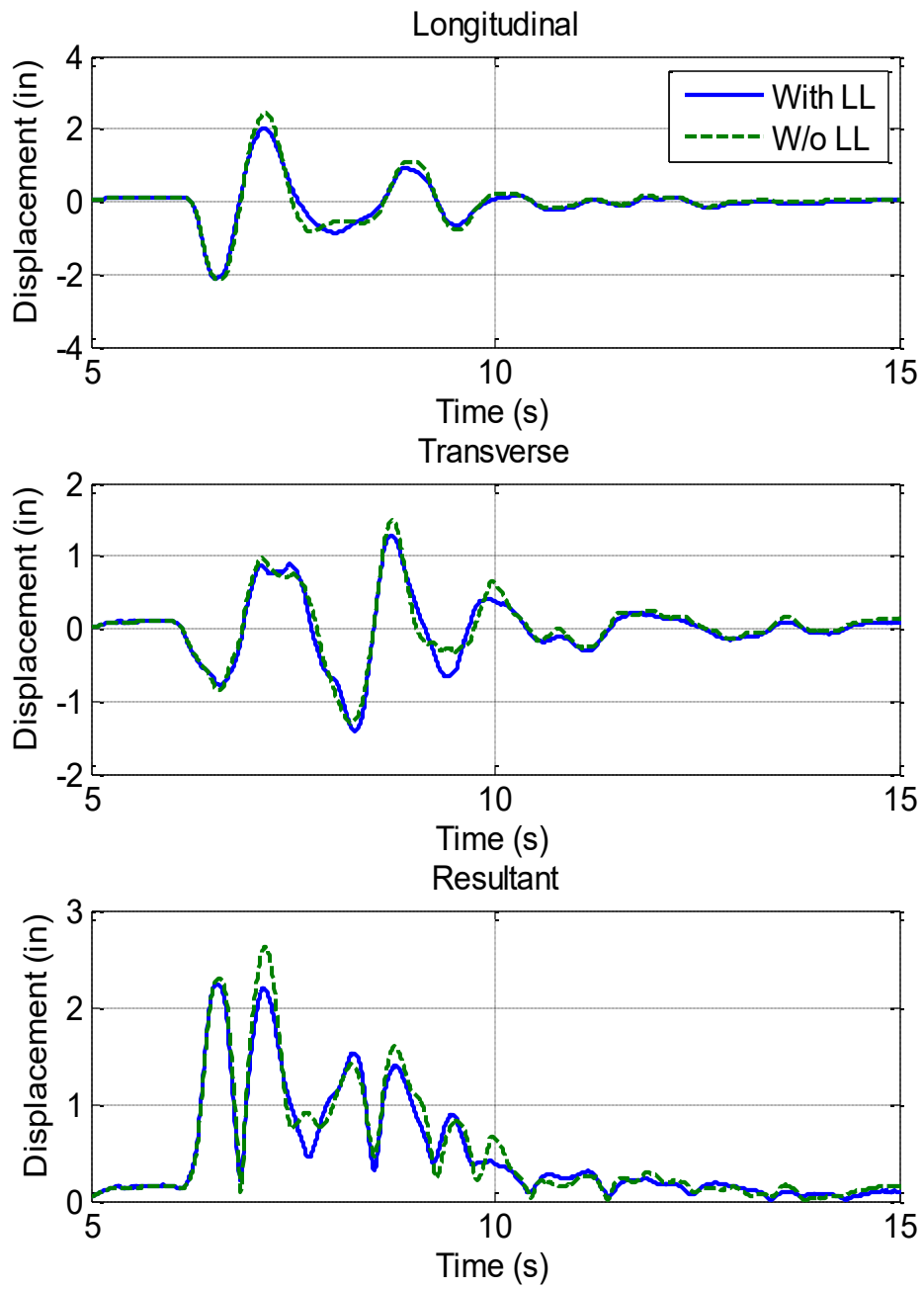


**Figure 5.5.3. Relative Displacement at Middle Span on Middle Girder (50% DE)**

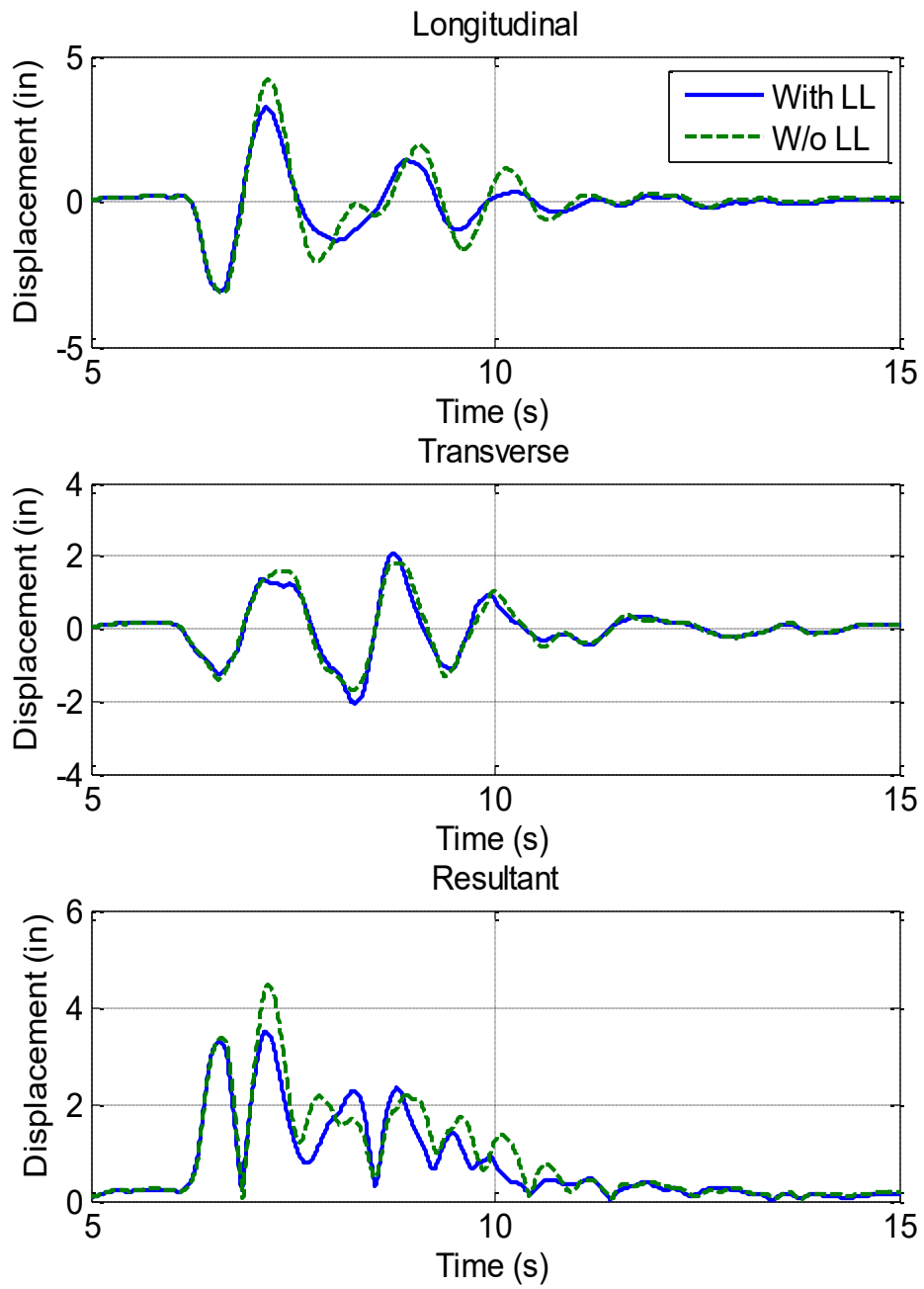


**Figure 5.5.4. Relative Displacement at Middle Span on Middle Girder (75% DE)**

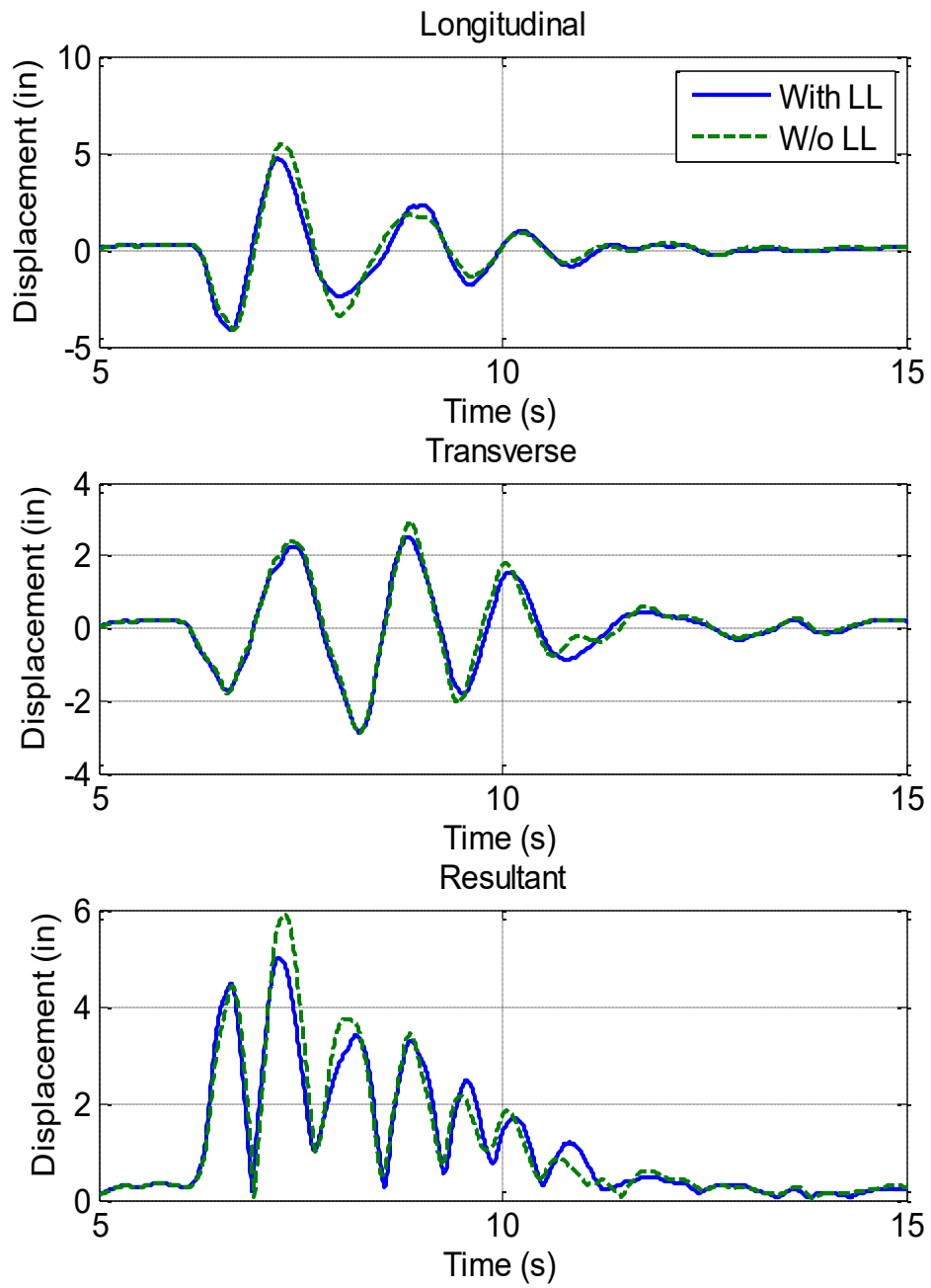


**Figure 5.5.5. Relative Displacement at Middle Span on Middle Girder (100% DE)**

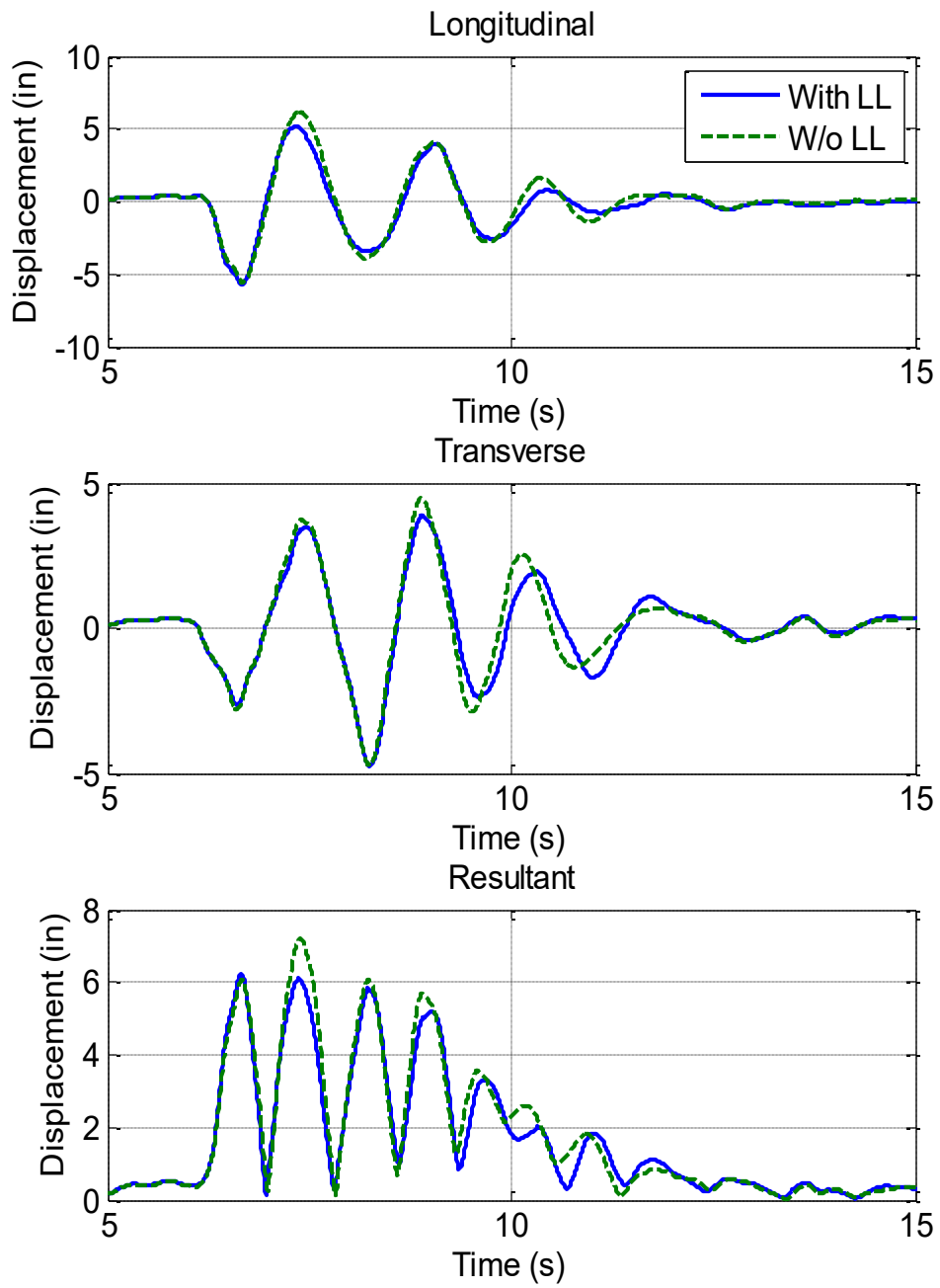


**Figure 5.5.6. Relative Displacement at Middle Span on Middle Girder (150% DE)**

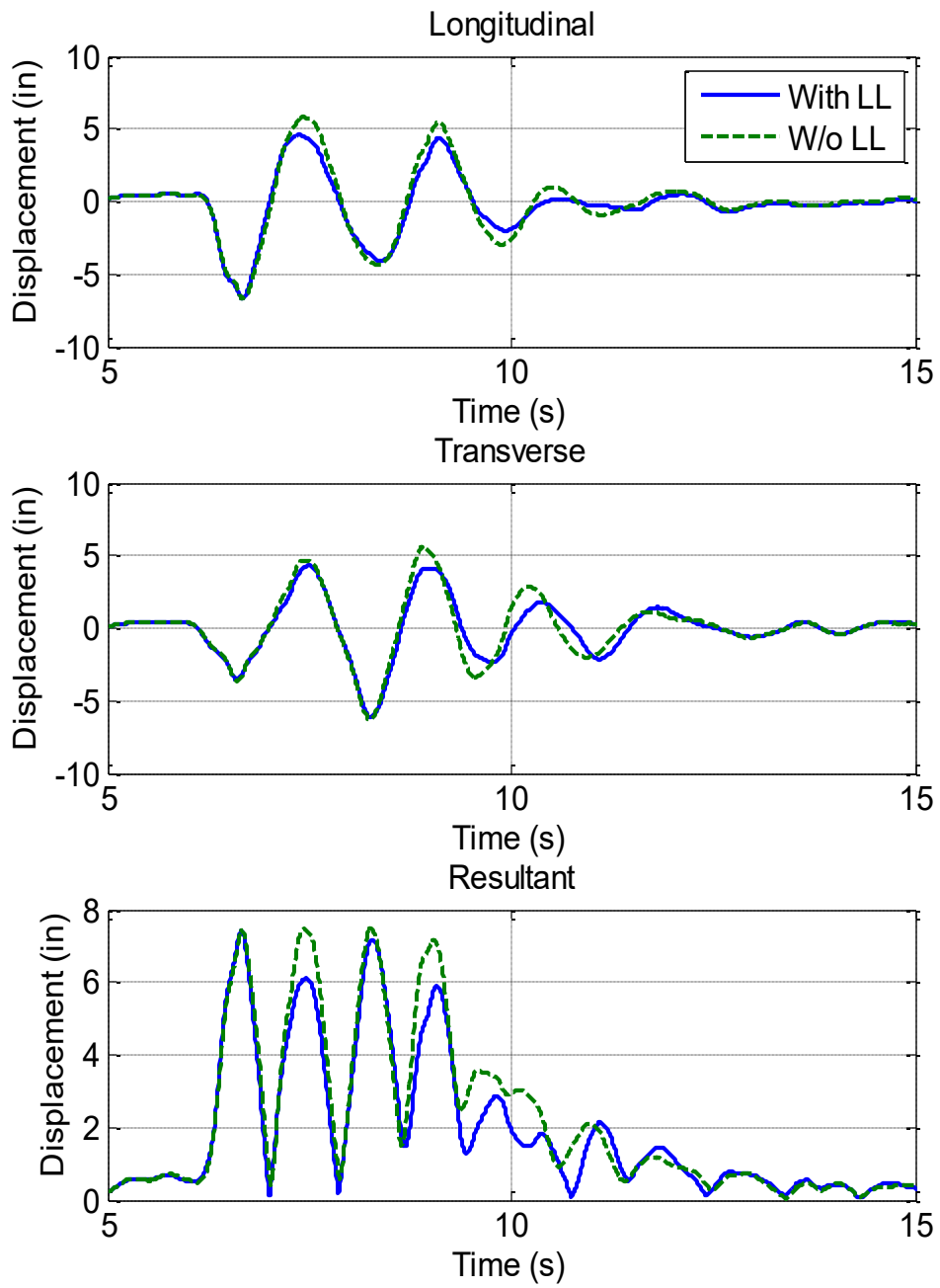


**Figure 5.5.7. Relative Displacement at Middle Span on Middle Girder (200% DE)**

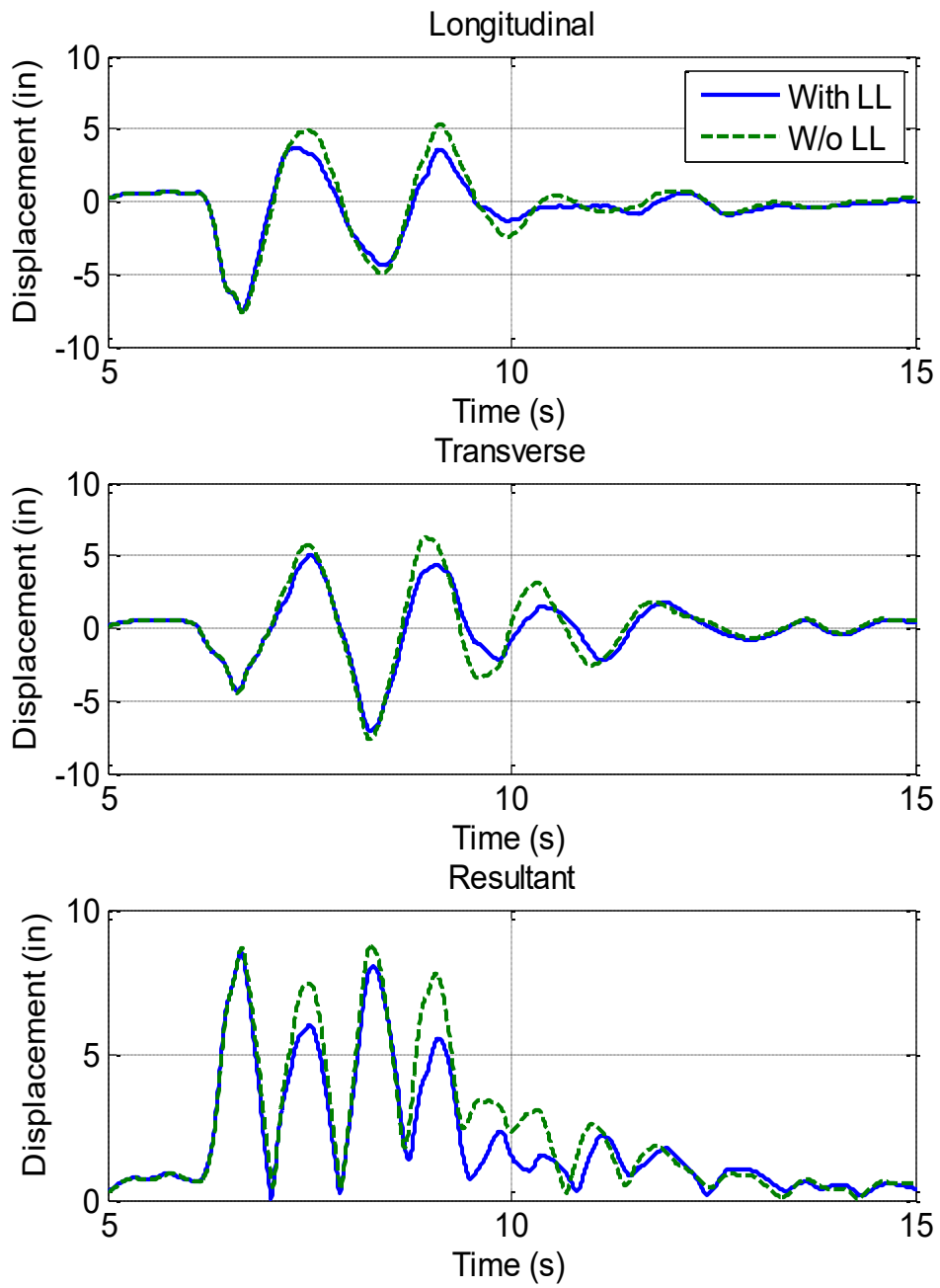


**Figure 5.5.8. Relative Displacement at Middle Span on Middle Girder (250% DE)**

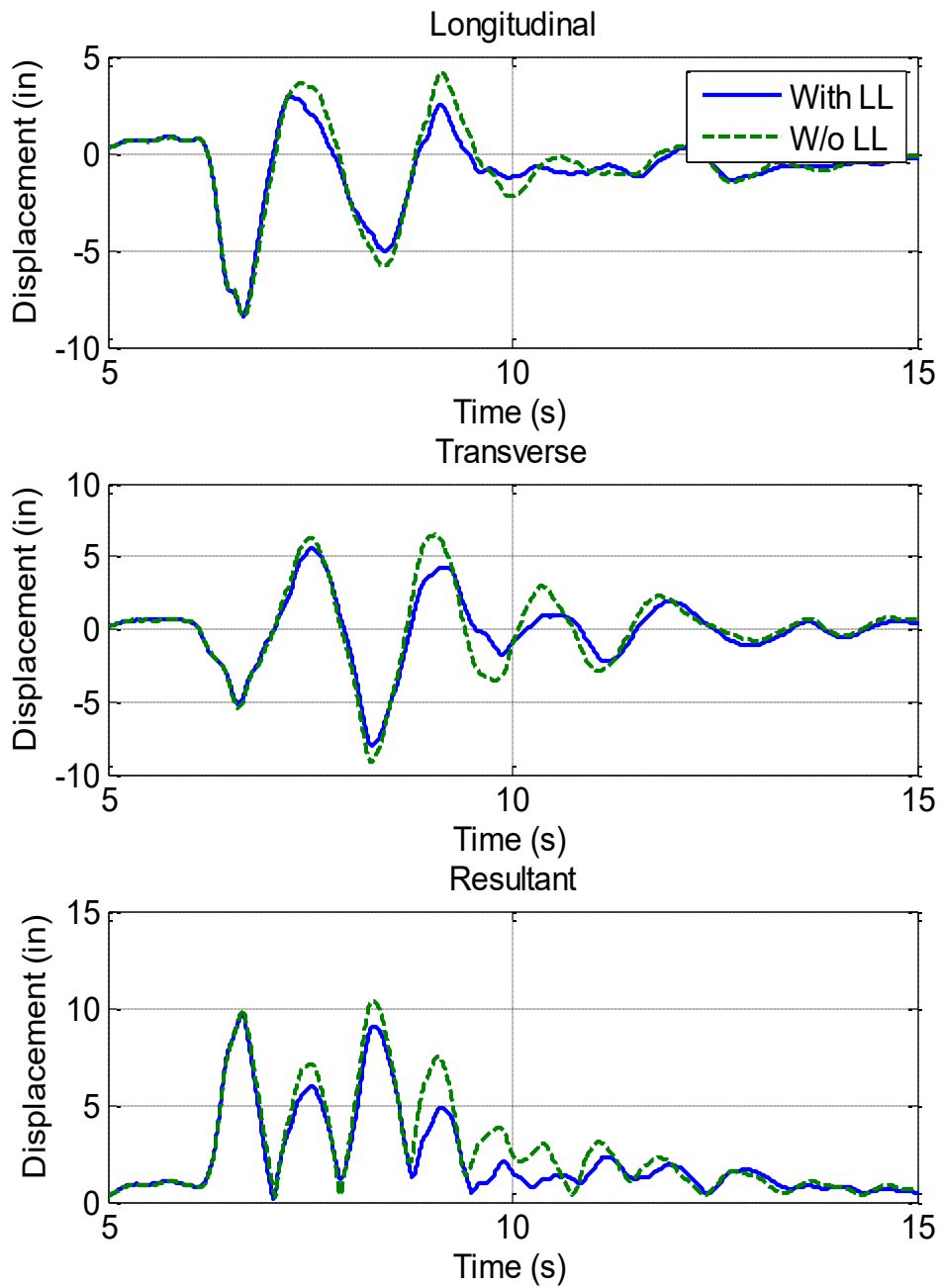


**Figure 5.5.9. Relative Displacement at Middle Span on Middle Girder (300% DE)**

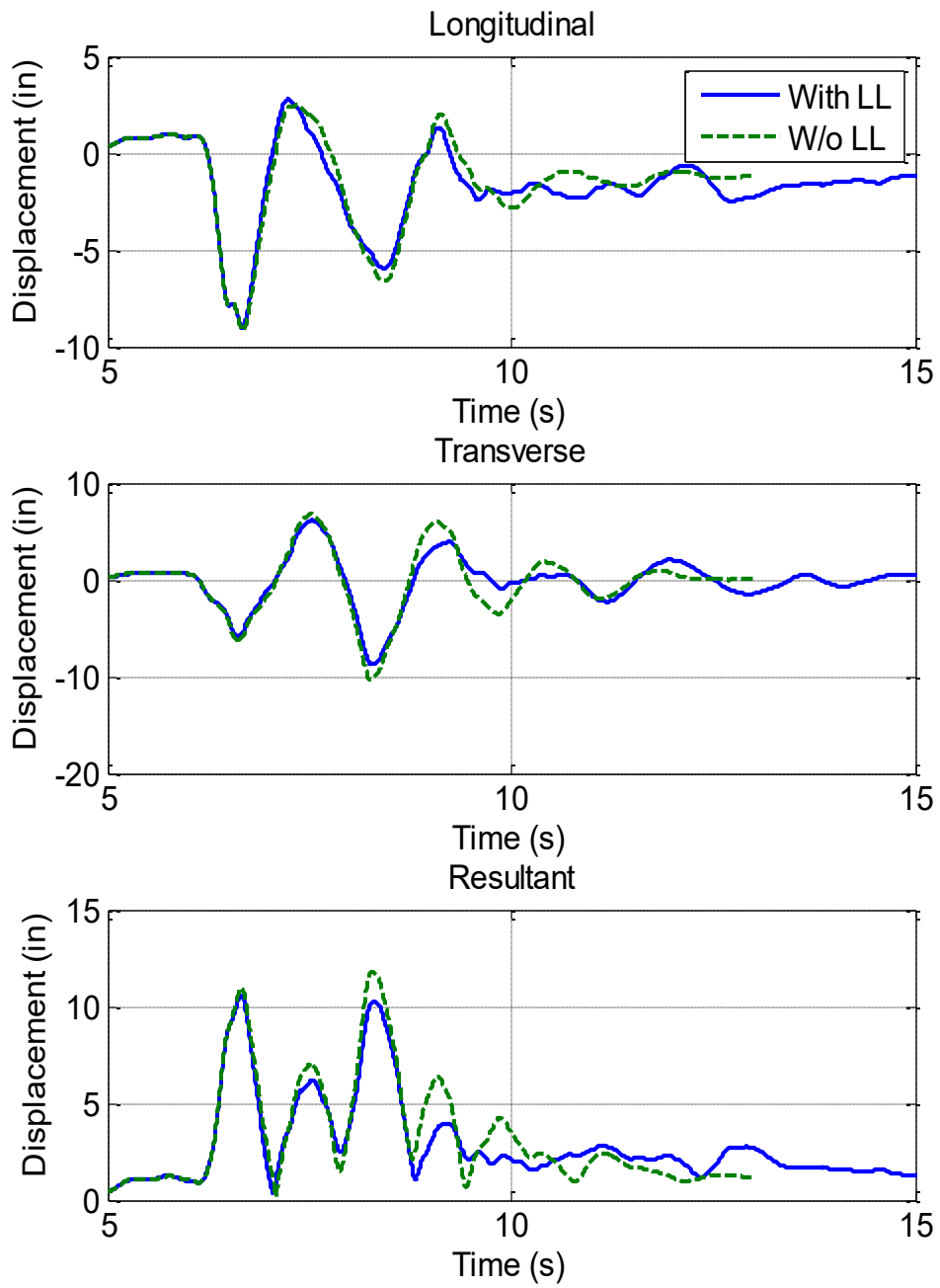


**Figure 5.5.10. Relative Displacement at Middle Span on Middle Girder (350% DE)**

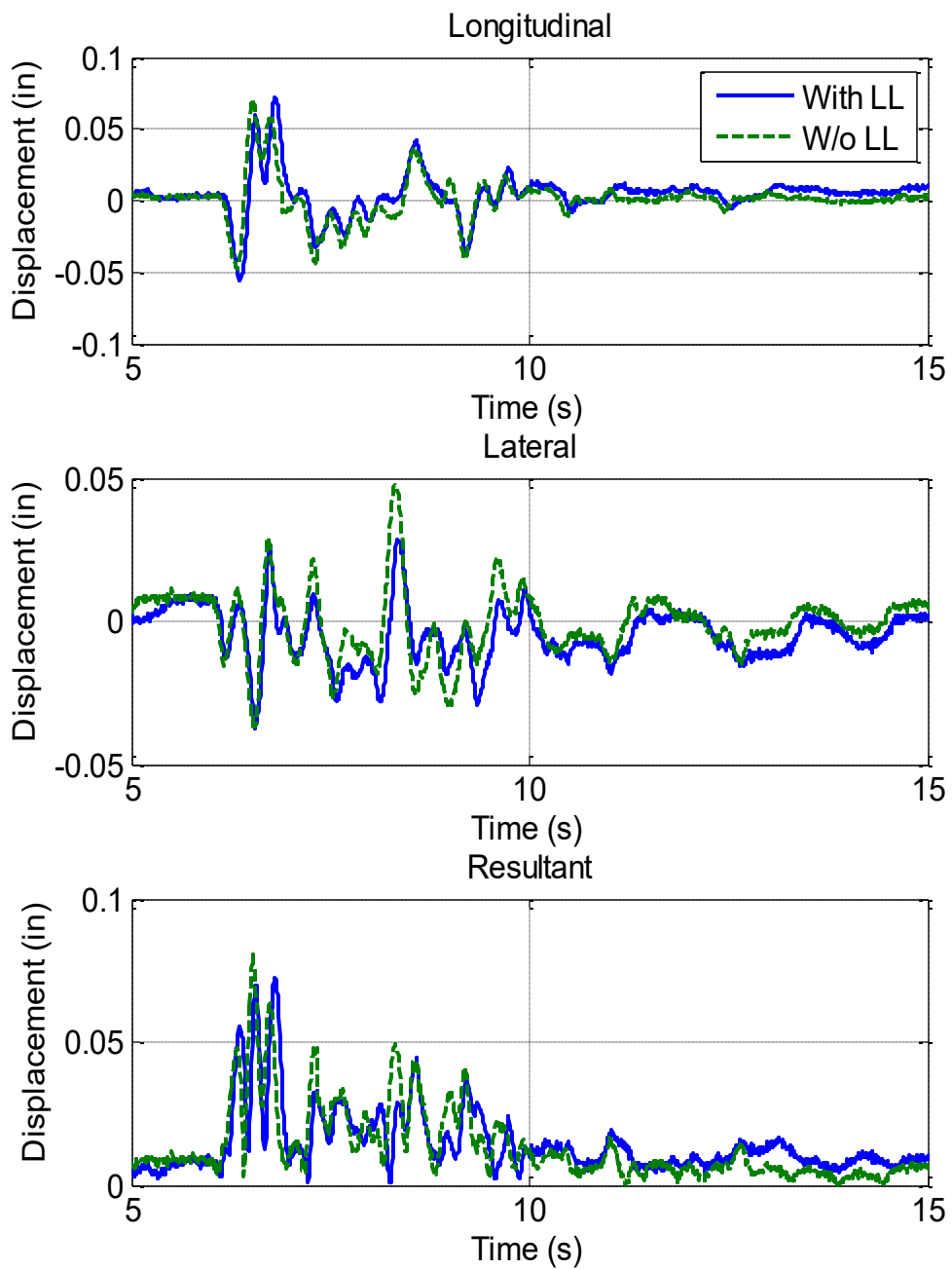


**Figure 5.5.11. Relative Displacement at the Top of North Bent (10% DE)**

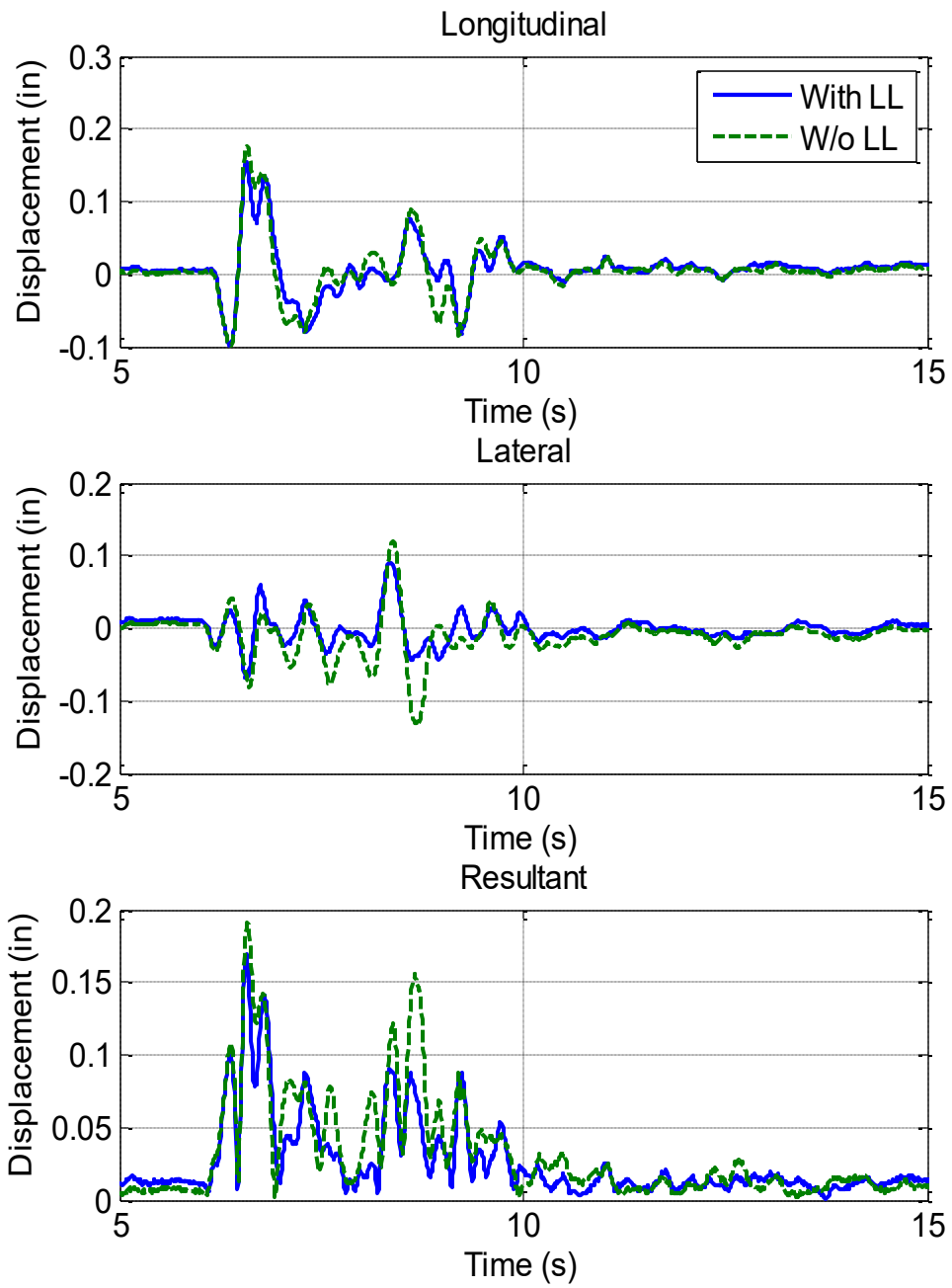


**Figure 5.5.12. Relative Displacement at the Top of North Bent (20% DE)**

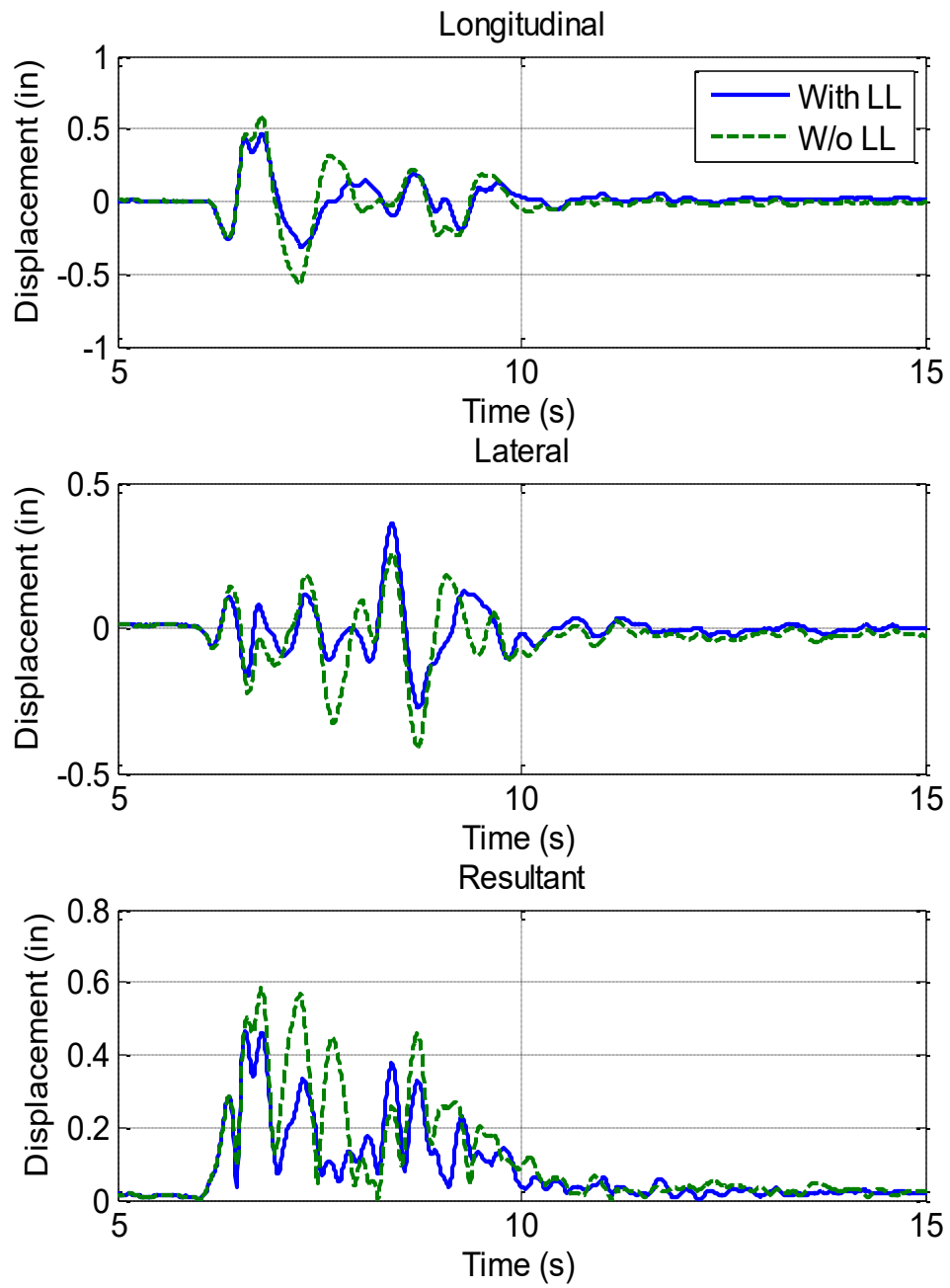


**Figure 5.5.13. Relative Displacement at the Top of North Bent (50% DE)**

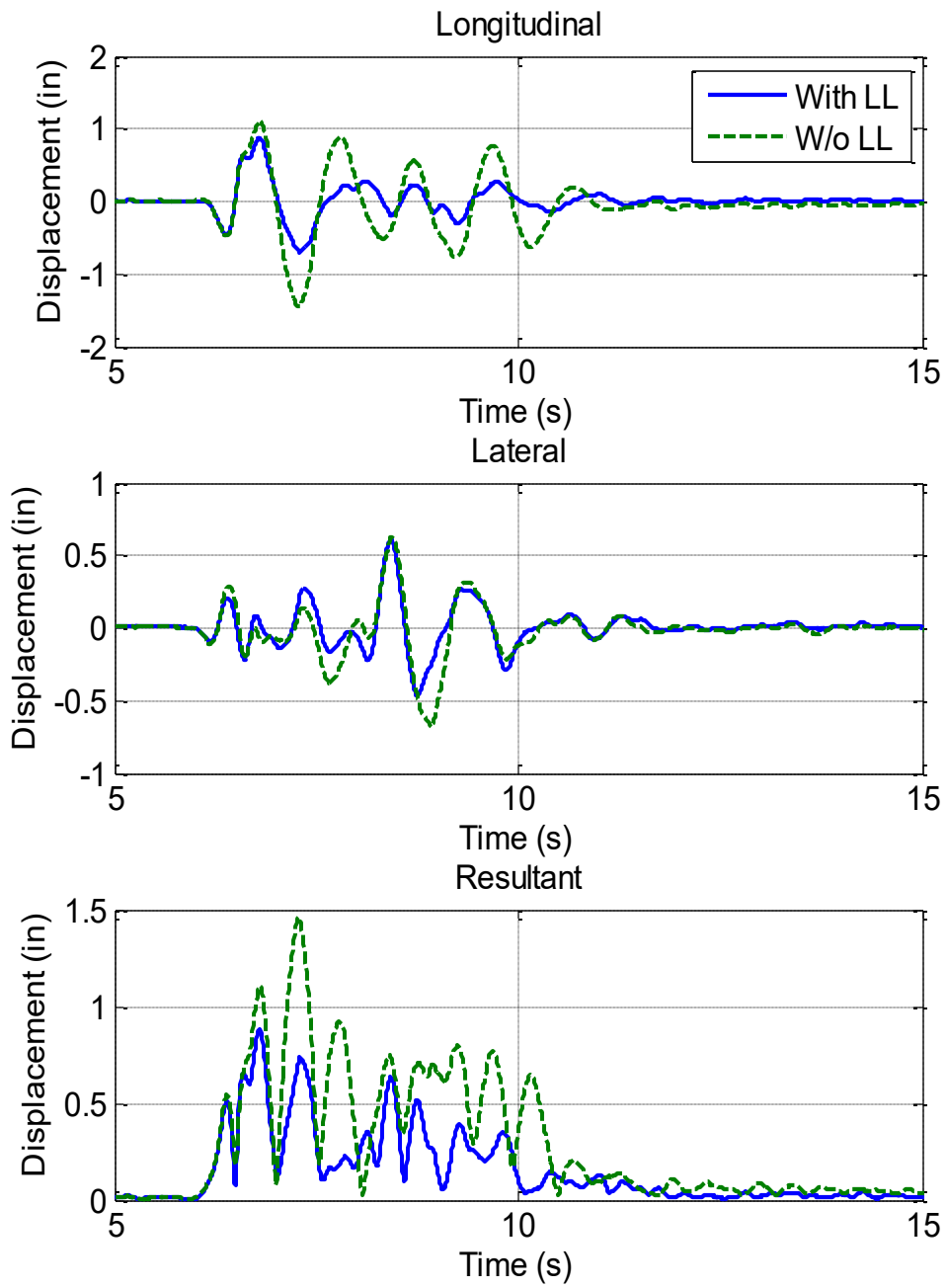


**Figure 5.5.14. Relative Displacement at the Top of North Bent (75% DE)**

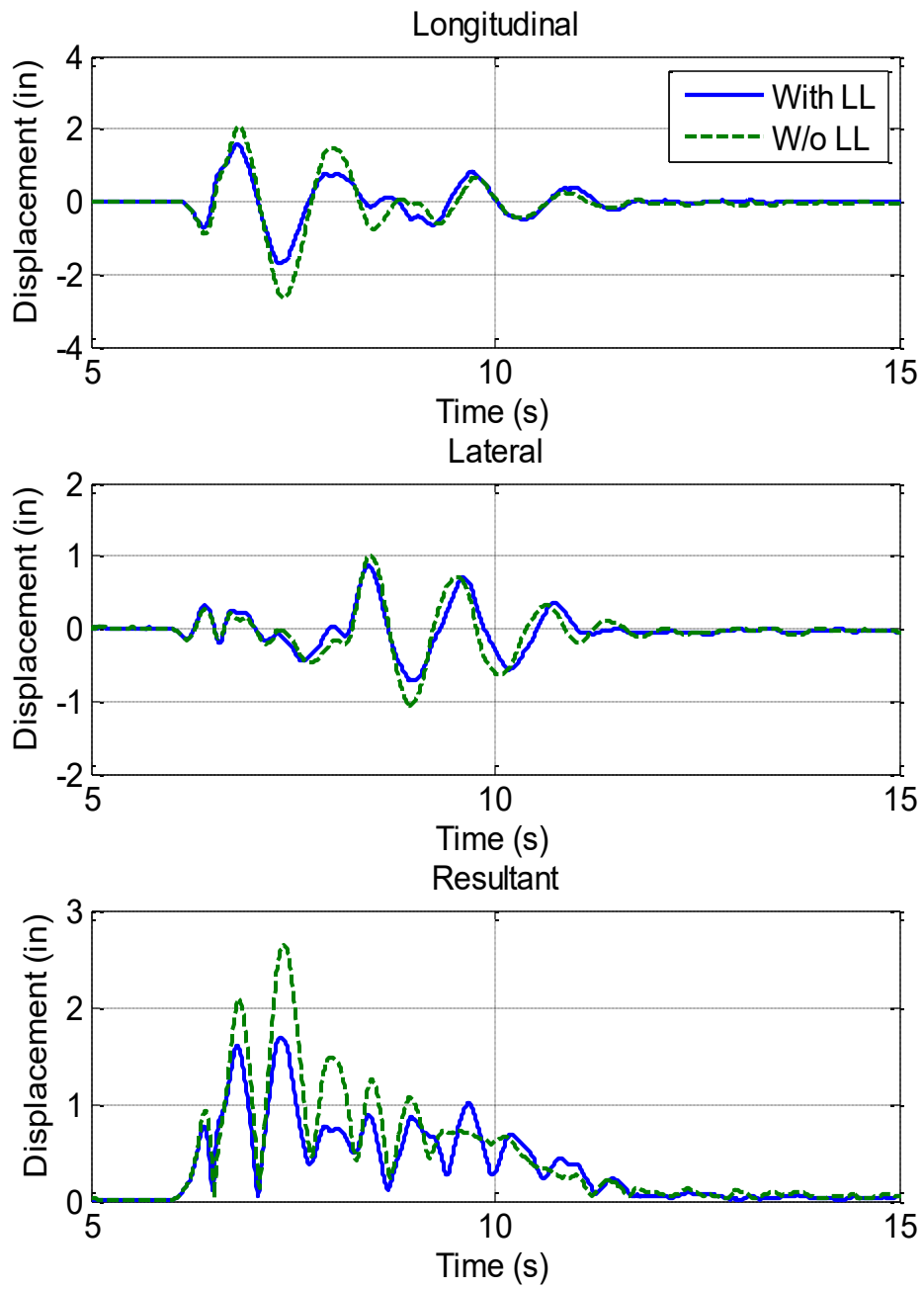


**Figure 5.5.15. Relative Displacement at the Top of North Bent (100% DE)**

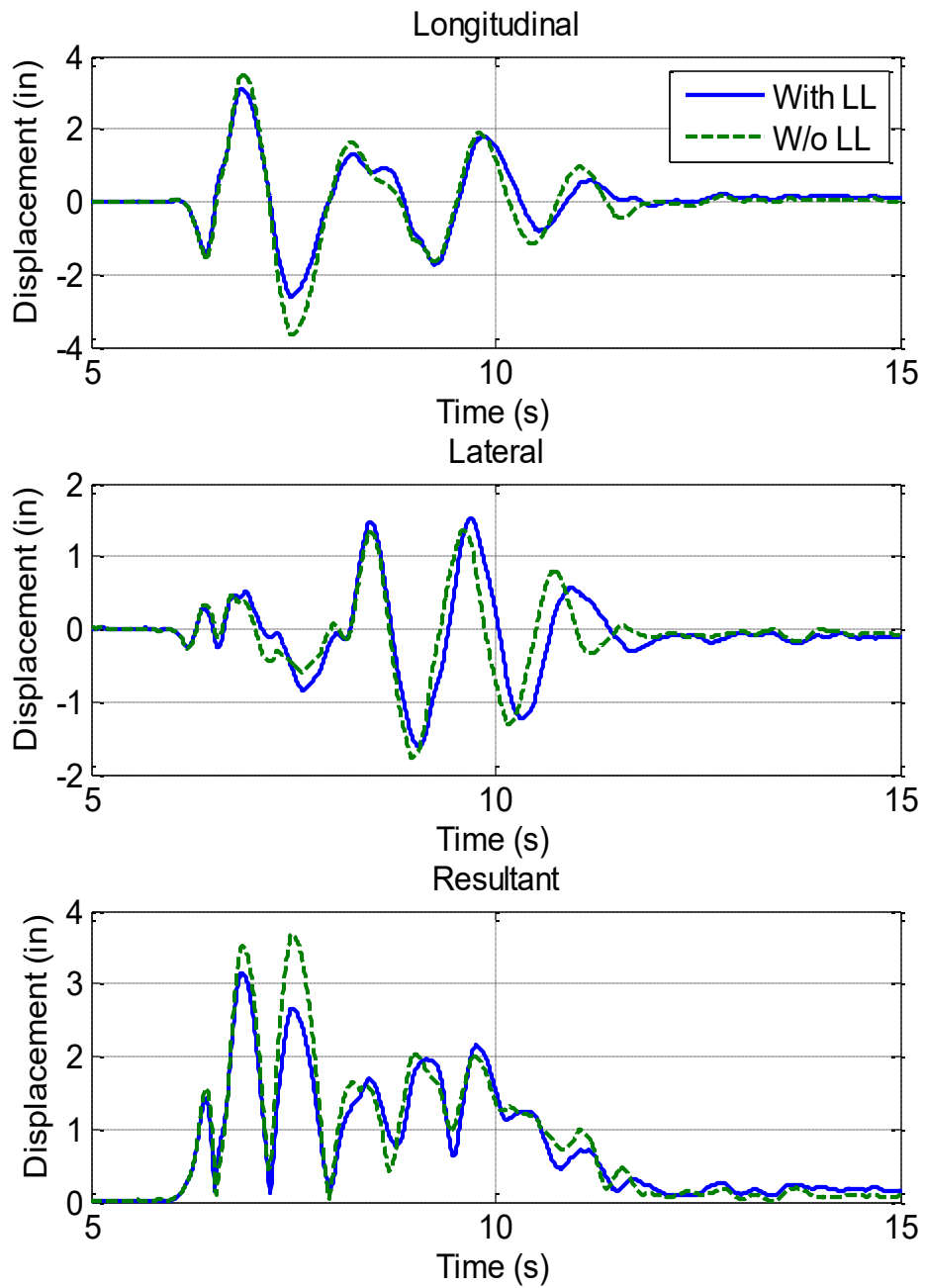


**Figure 5.5.16. Relative Displacement at the Top of North Bent (150% DE)**

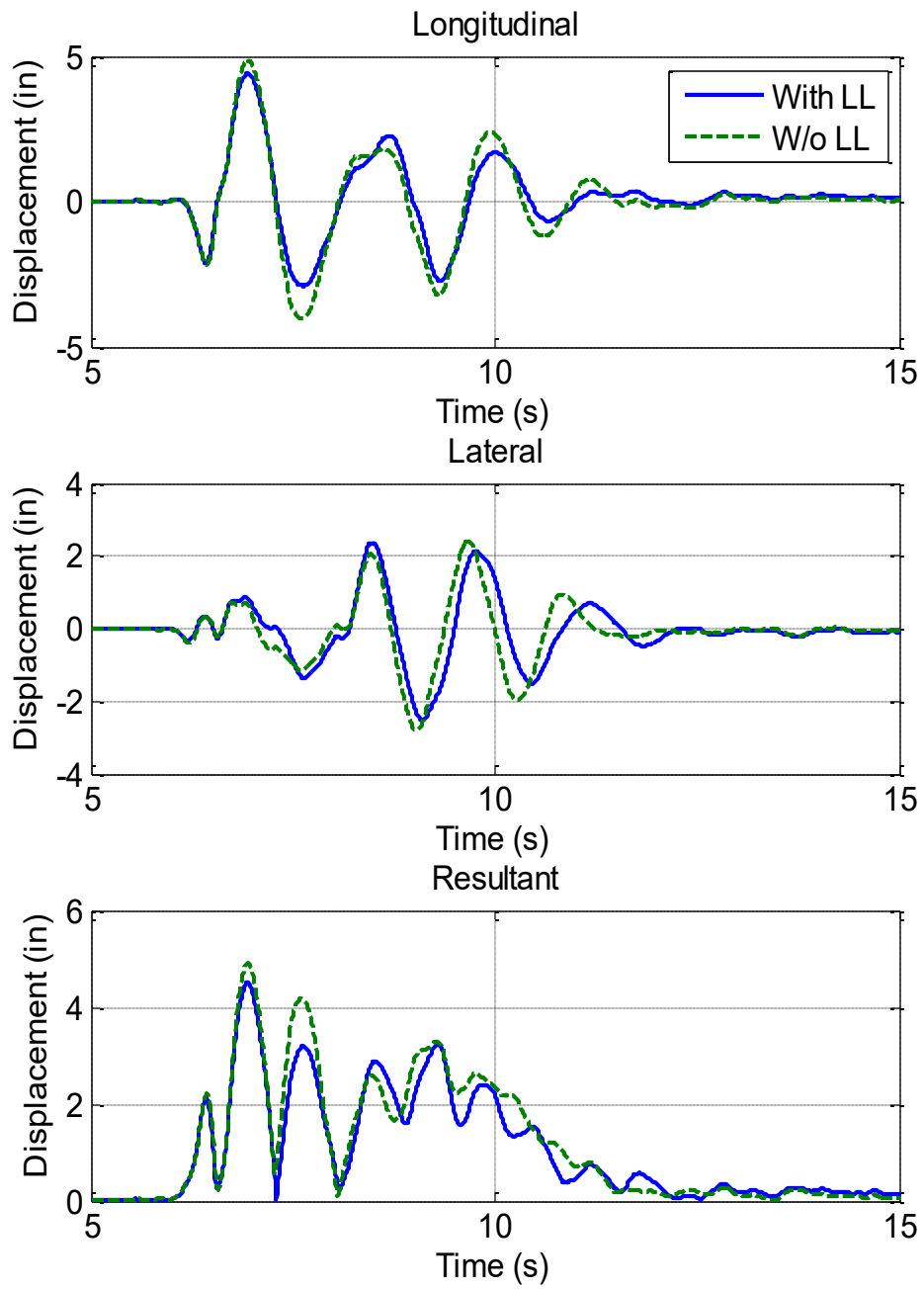


**Figure 5.5.17. Relative Displacement at the Top of North Bent (200% DE)**

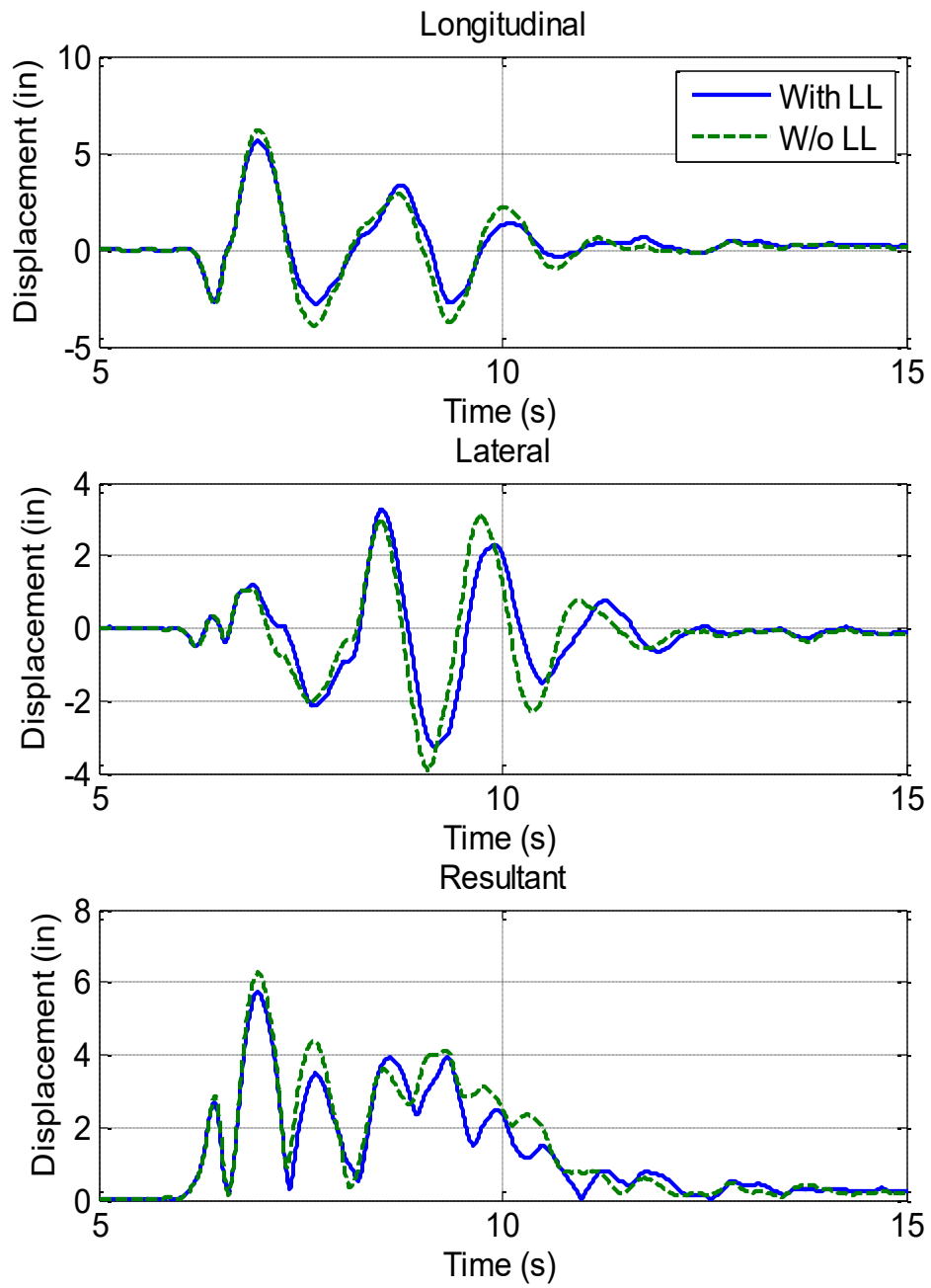


**Figure 5.5.18. Relative Displacement at the Top of North Bent (250% DE)**

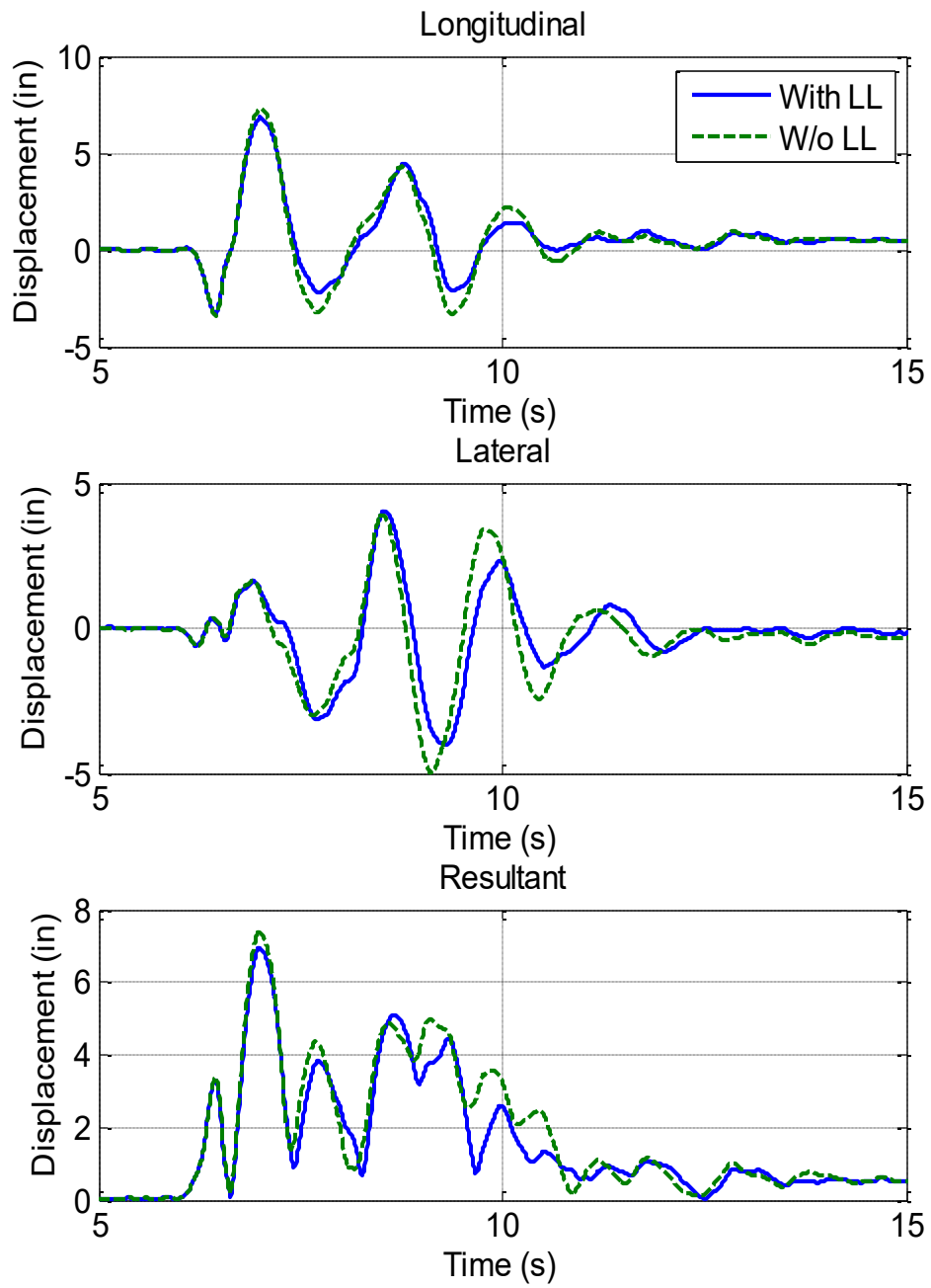


**Figure 5.5.19. Relative Displacement at the Top of North Bent (300% DE)**

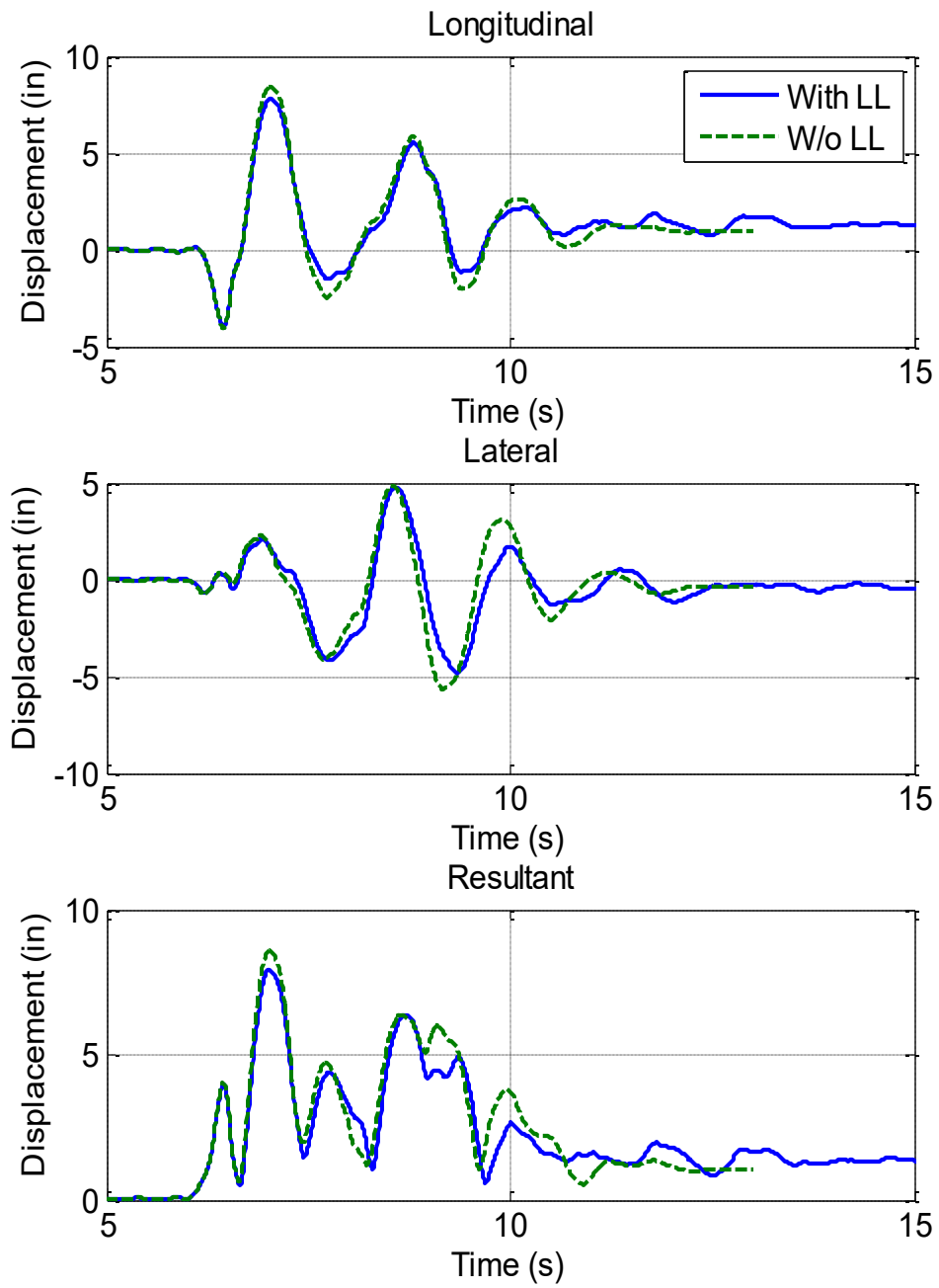


**Figure 5.5.20. Relative Displacement at the Top of North Bent (350% DE)**

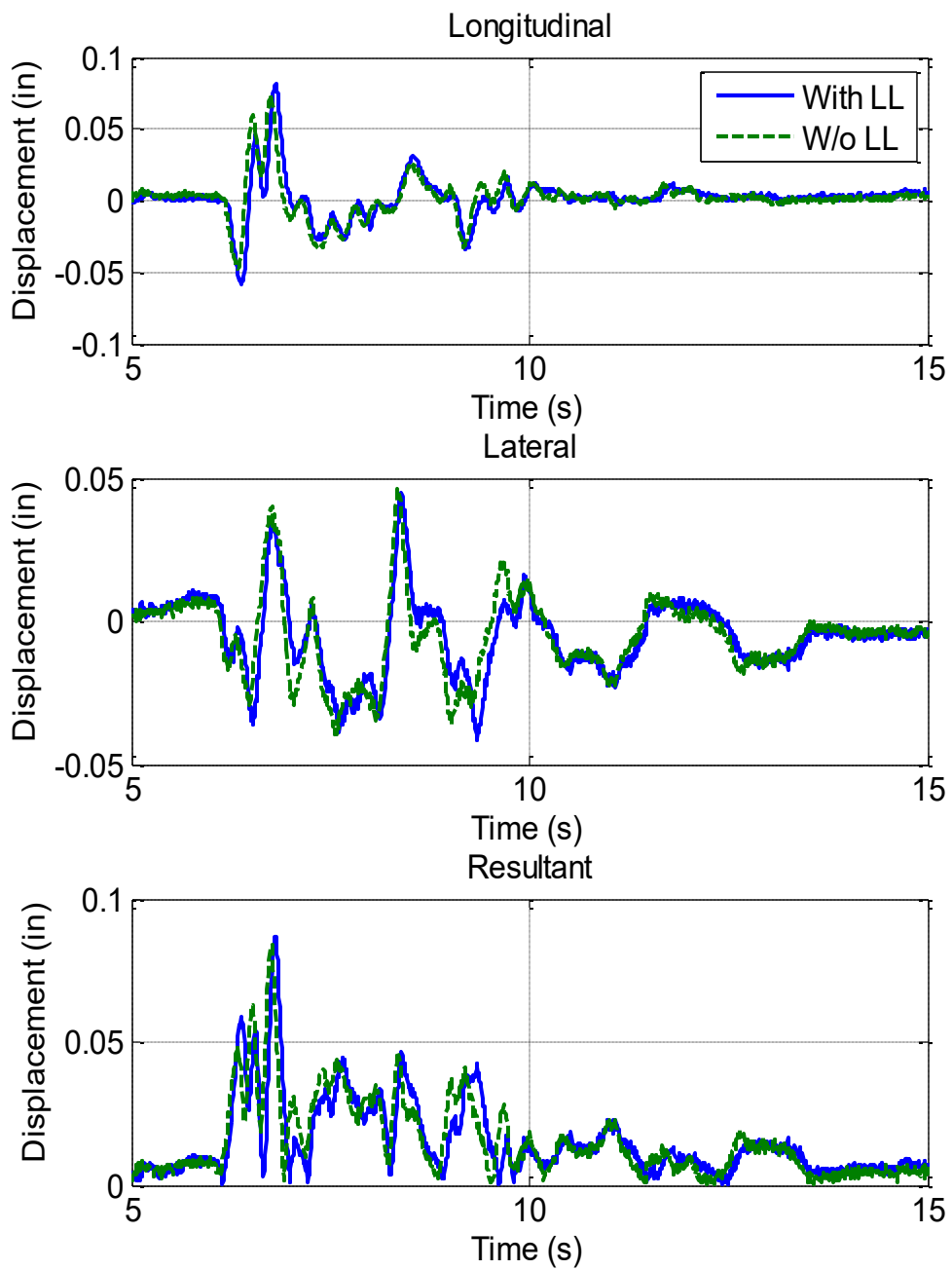


**Figure 5.5.21. Relative Displacement at the Top of South Bent (10% DE)**

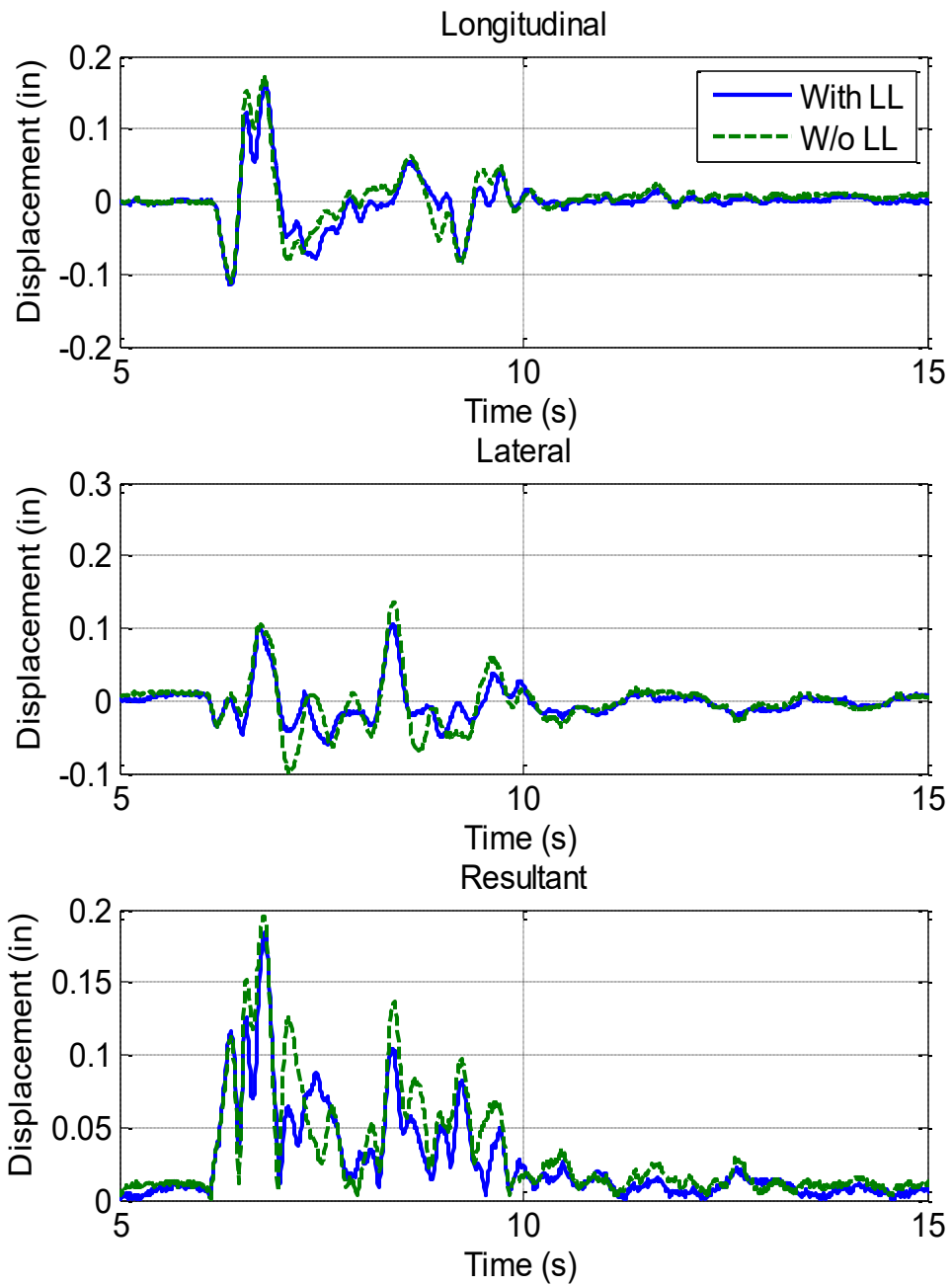


**Figure 5.5.22. Relative Displacement at the Top of South Bent (20% DE)**

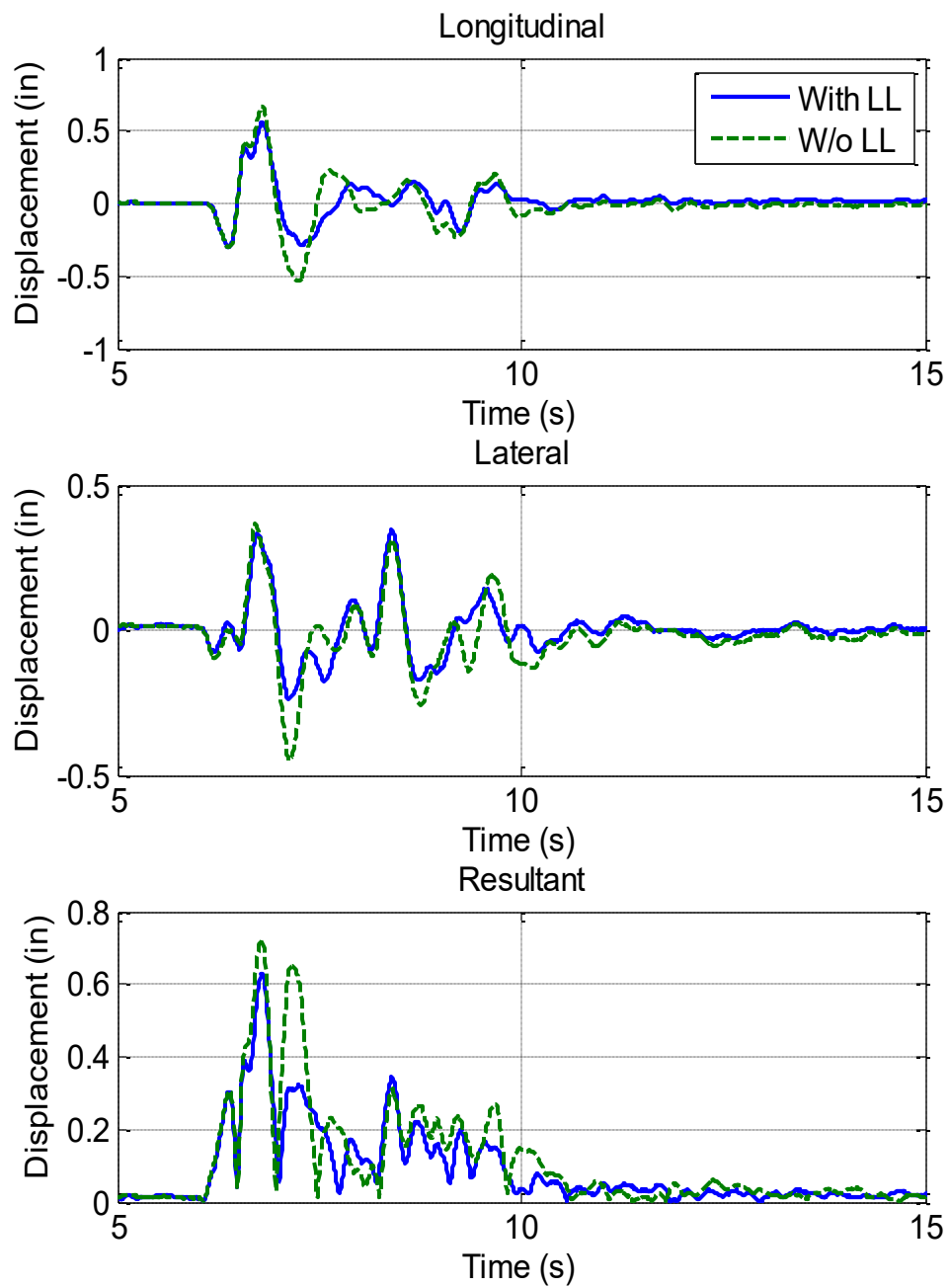


**Figure 5.5.23. Relative Displacement at the Top of South Bent (50% DE)**

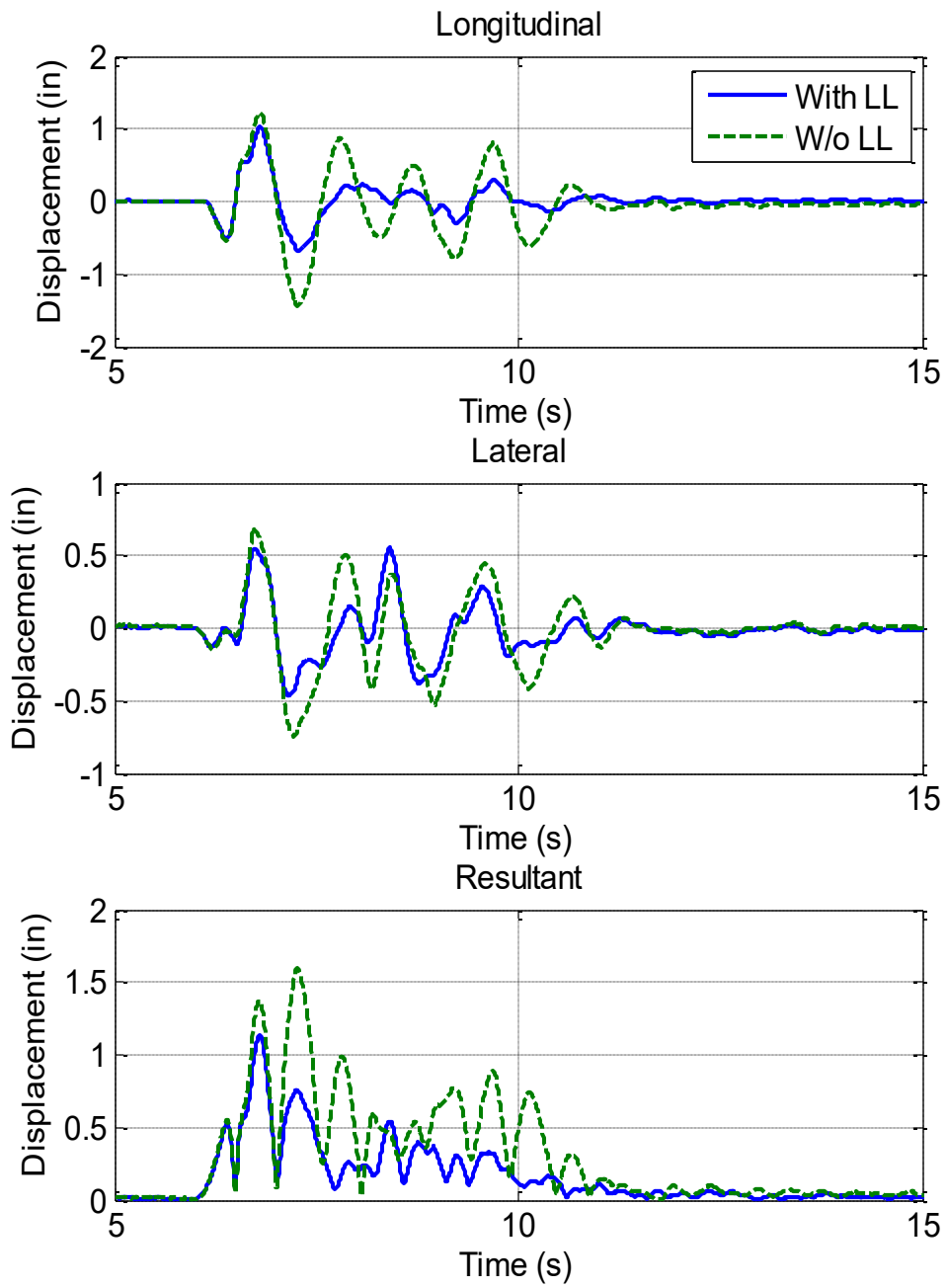


**Figure 5.5.24. Relative Displacement at the Top of South Bent (75% DE)**

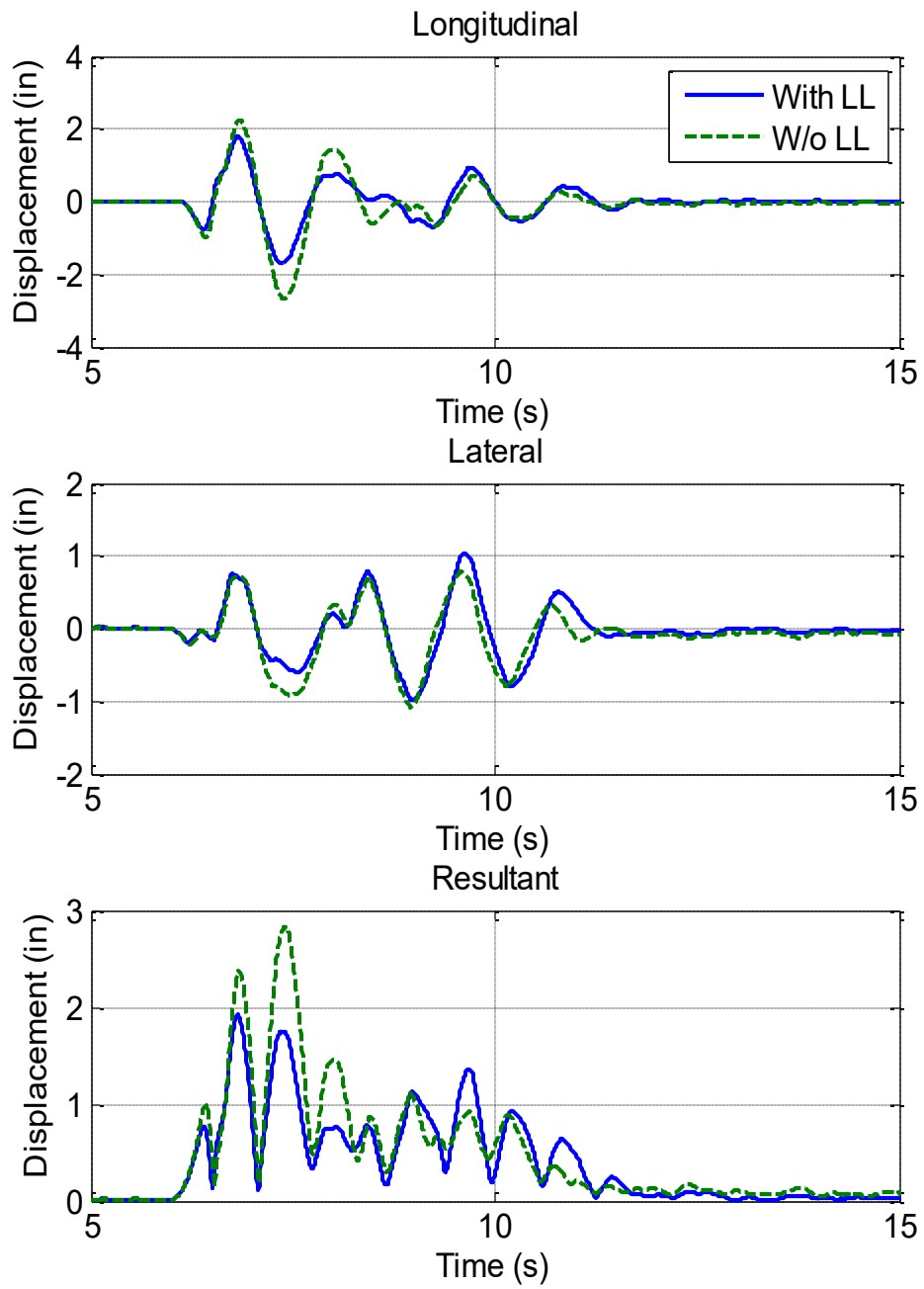


**Figure 5.5.25. Relative Displacement at the Top of South Bent (100% DE)**

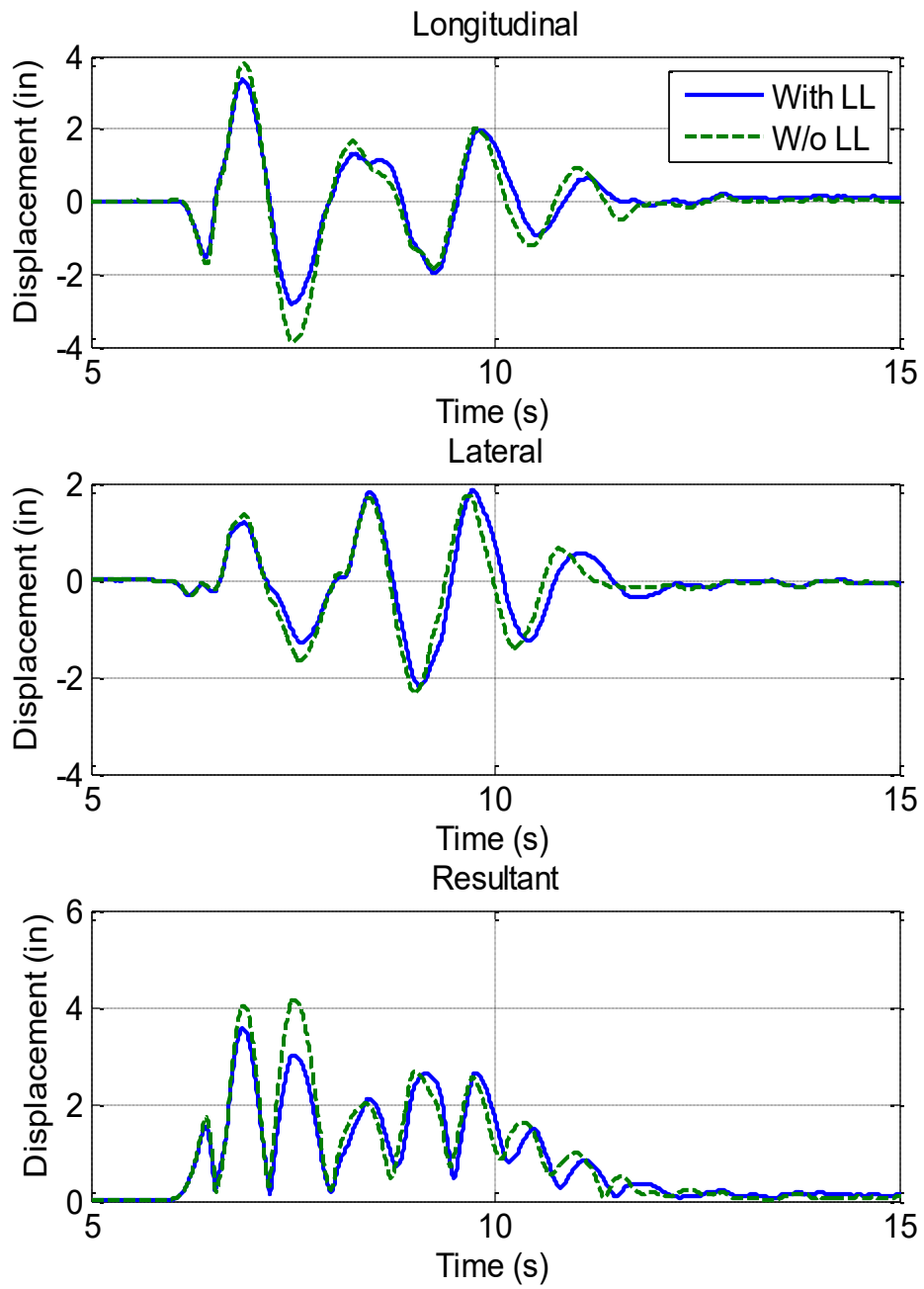


**Figure 5.5.26. Relative Displacement at the Top of South Bent (150% DE)**

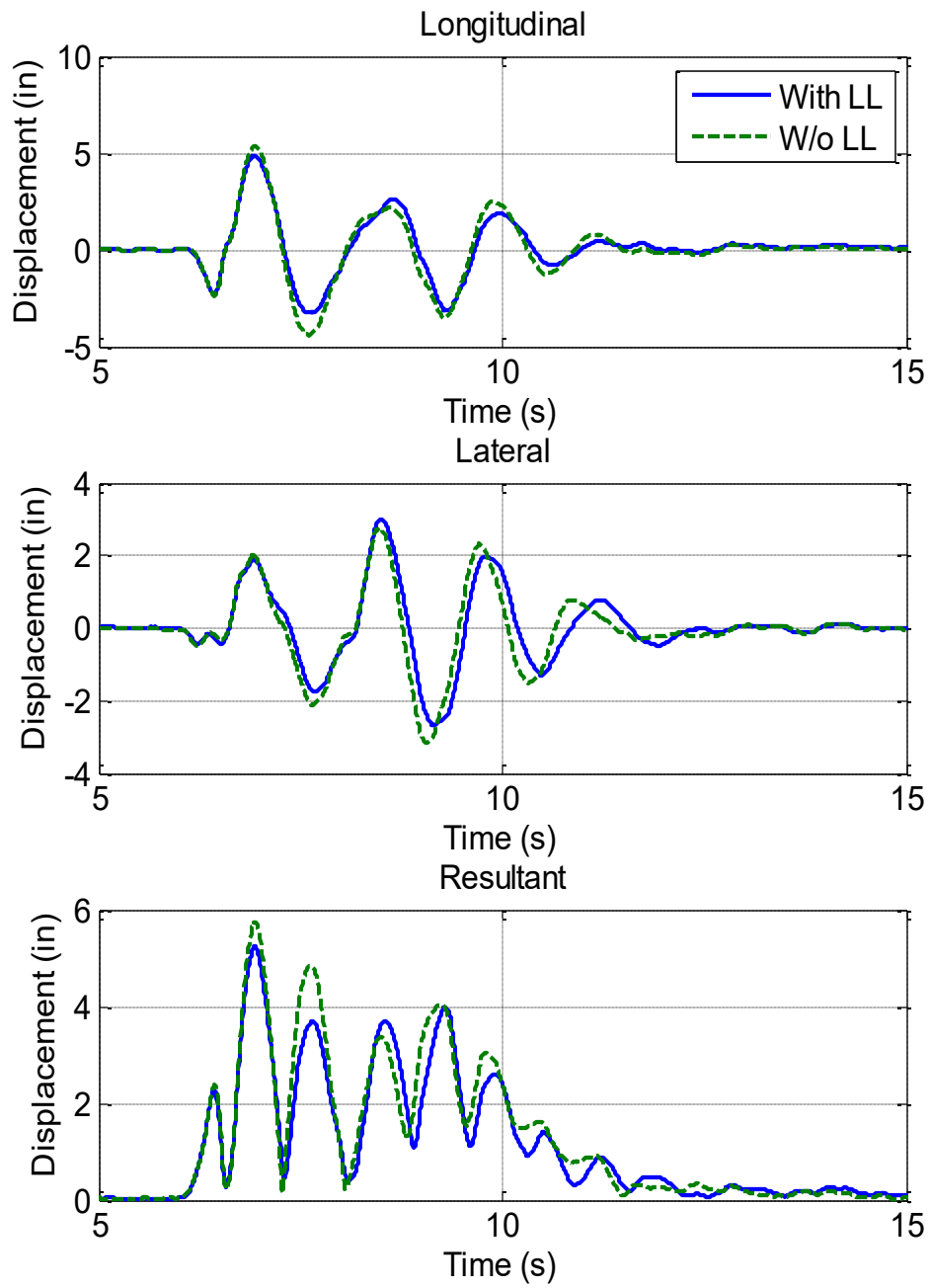


**Figure 5.5.27. Relative Displacement at the Top of South Bent (200% DE)**

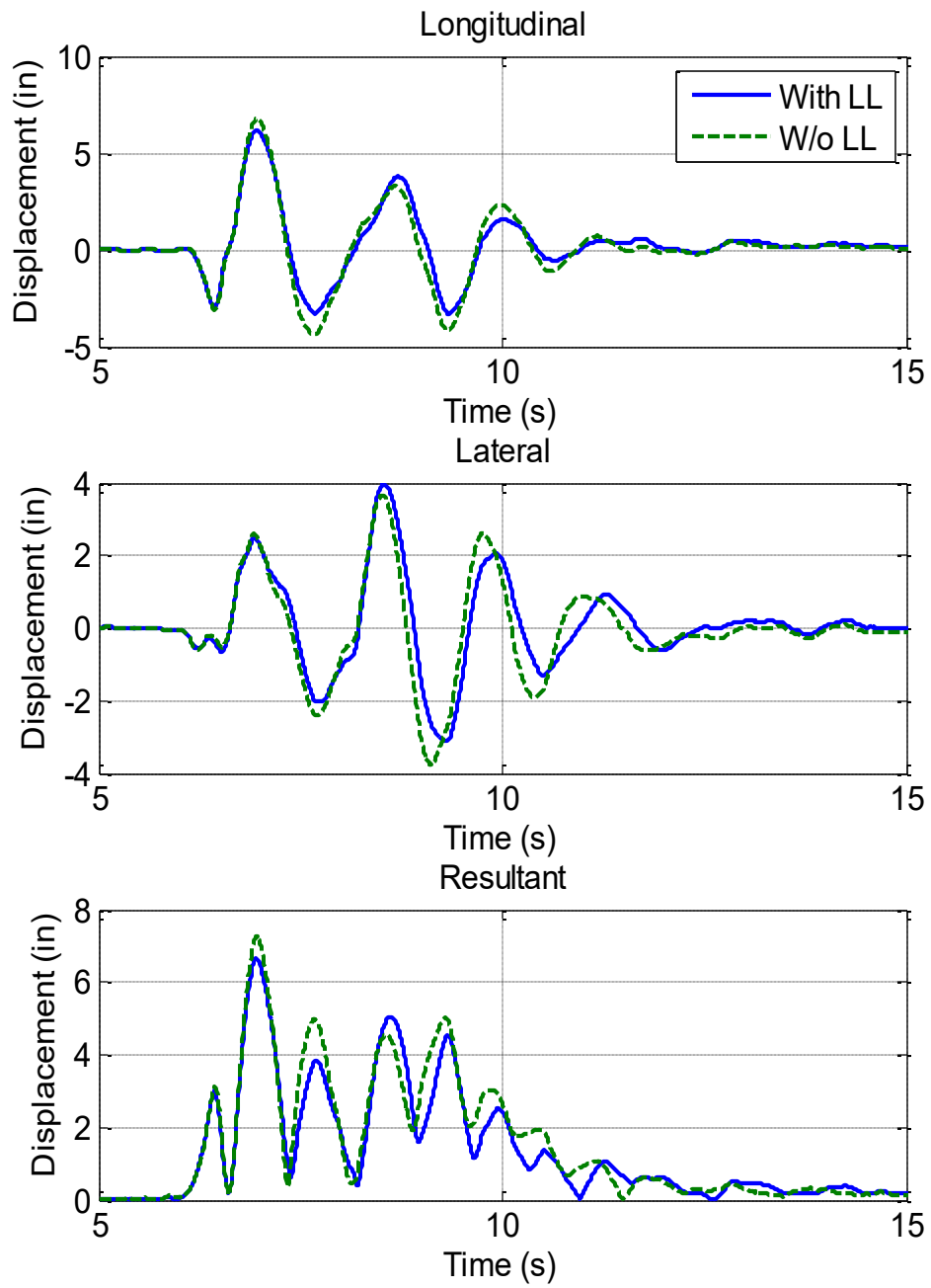


**Figure 5.5.28. Relative Displacement at the Top of South Bent (250% DE)**

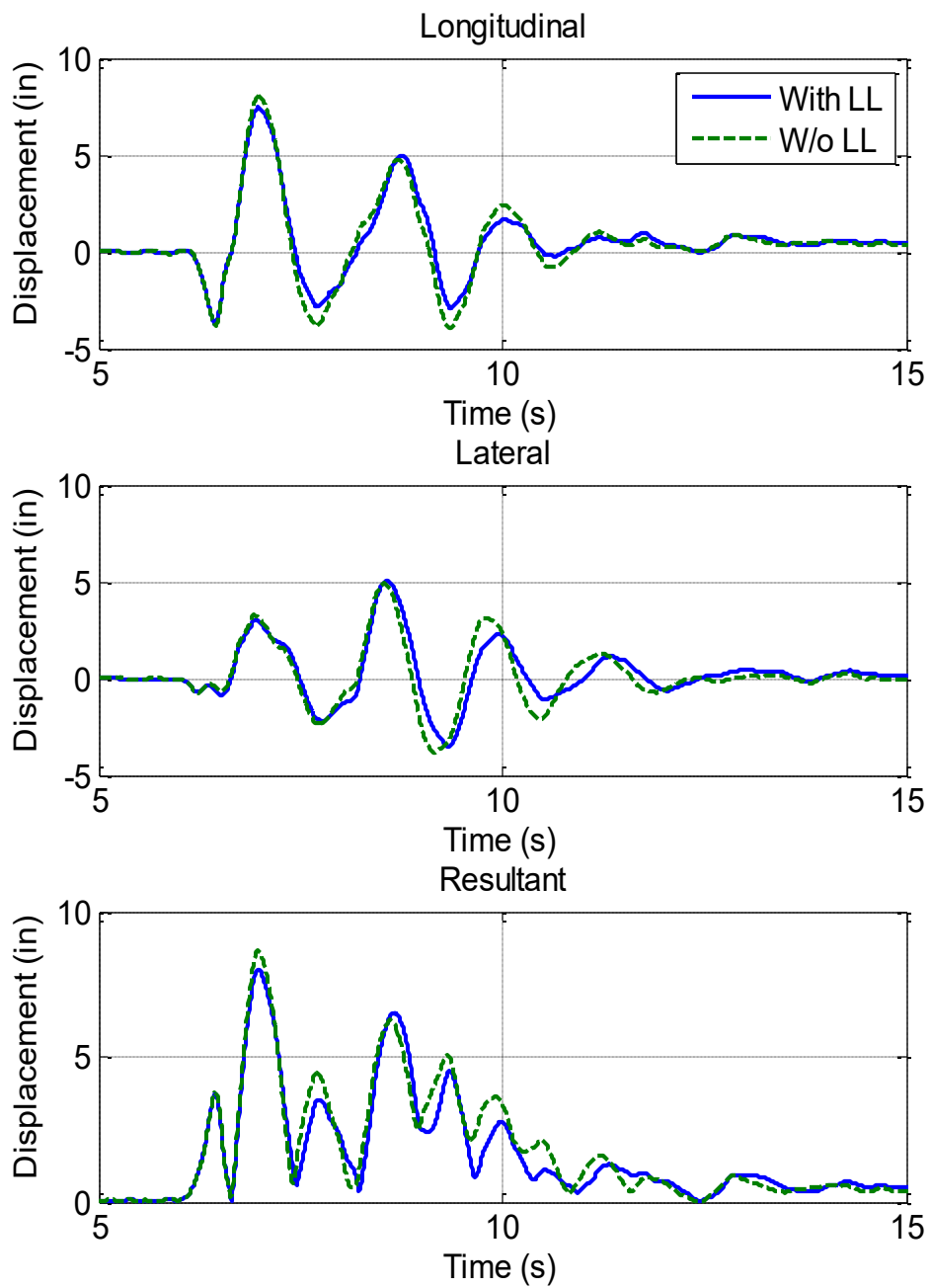


**Figure 5.5.29. Relative Displacement at the Top of South Bent (300% DE)**

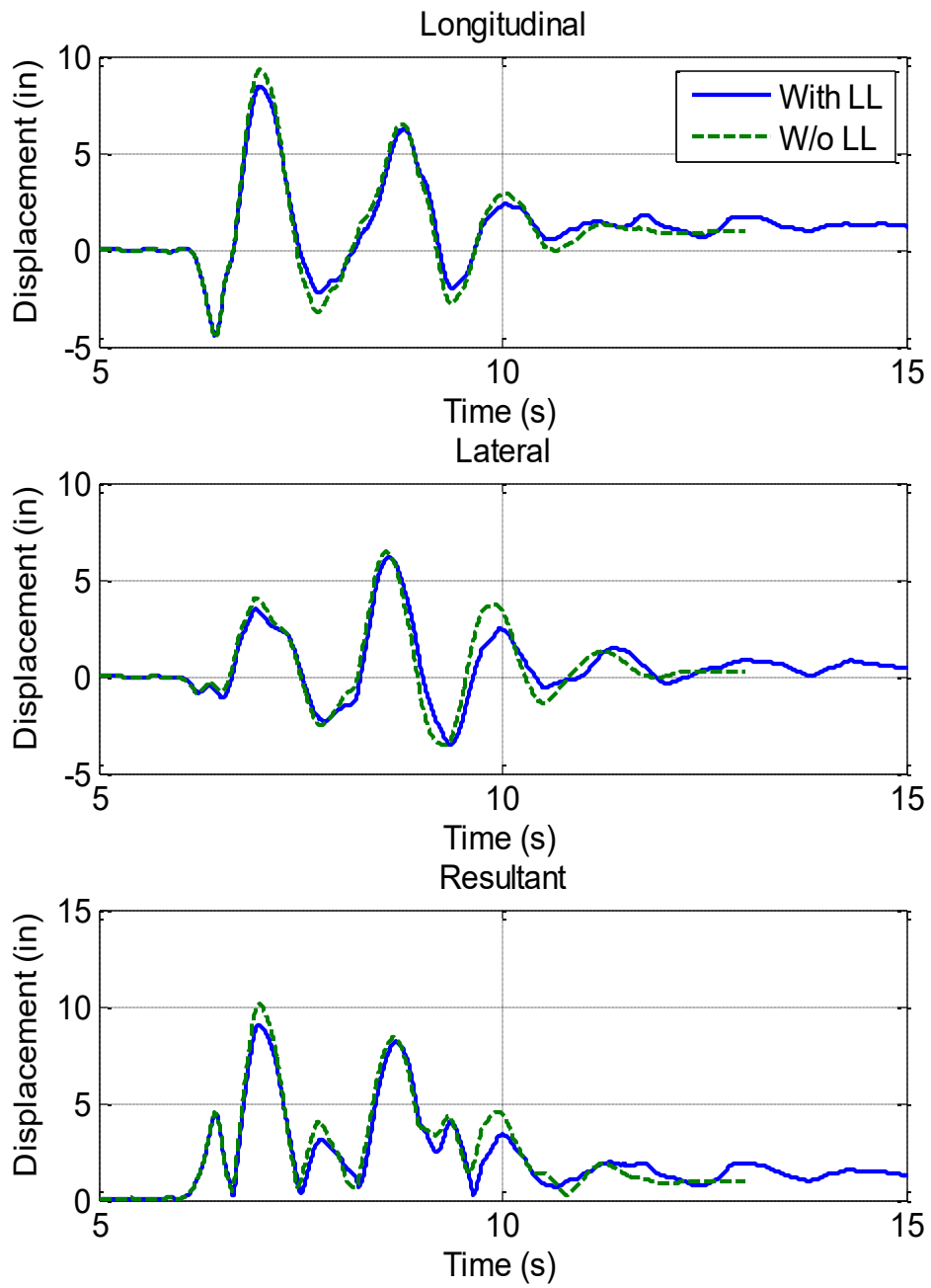


**Figure 5.5.30. Relative Displacement at the Top of South Bent (350% DE)**

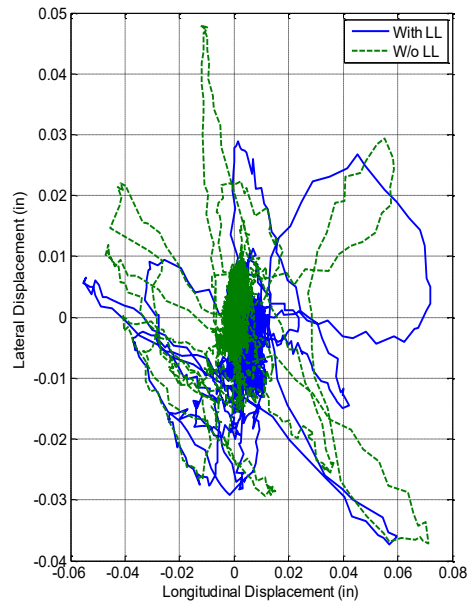


**Figure 5.5.31. Orbital Displacement at the Top of North Bent (10% DE)**

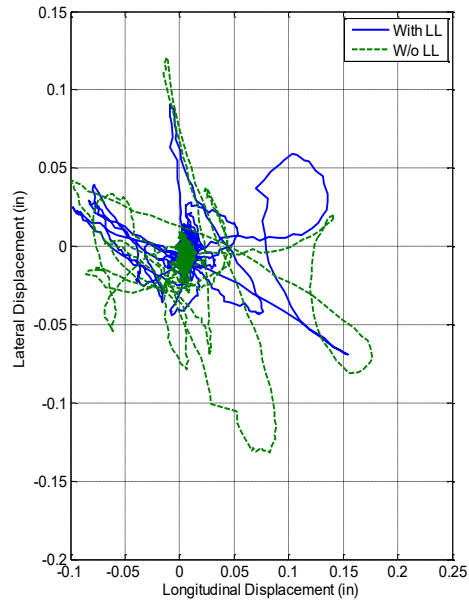


**Figure 5.5.32. Orbital Displacement at the Top of North Bent (20% DE)**

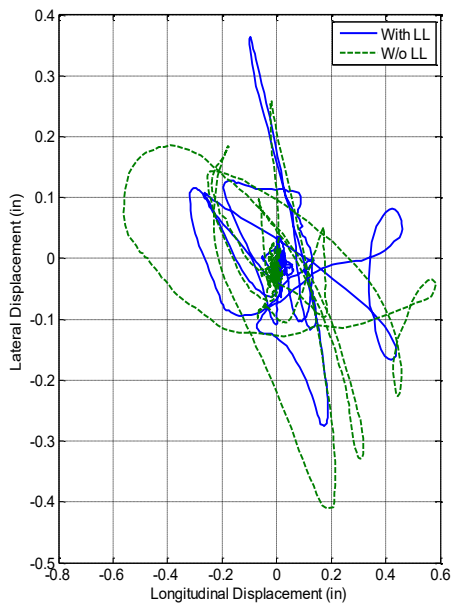


**Figure 5.5.33. Orbital Displacement at the Top of North Bent (50% DE)**

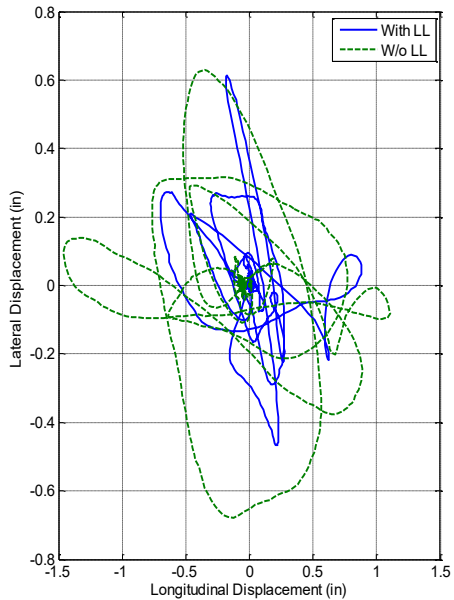


**Figure 5.5.34. Orbital Displacement at the Top of North Bent (75% DE)**

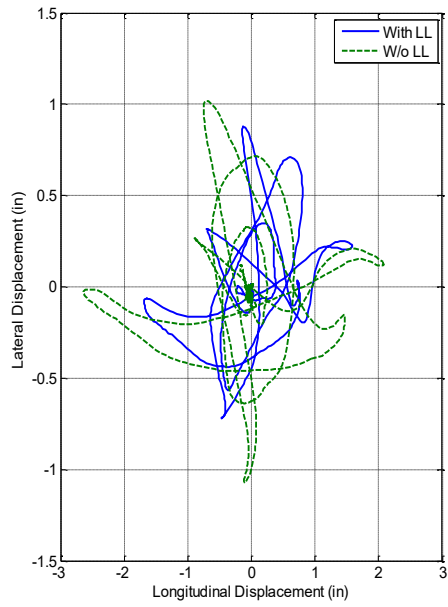


**Figure 5.5.35. Orbital Displacement at the Top of North Bent (100% DE)**

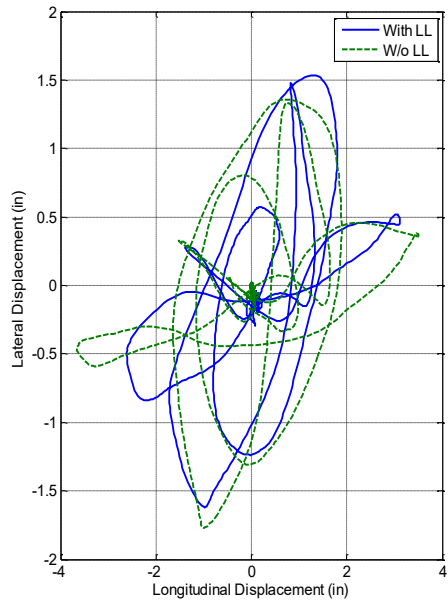


**Figure 5.5.36. Orbital Displacement at the Top of North Bent (150% DE)**

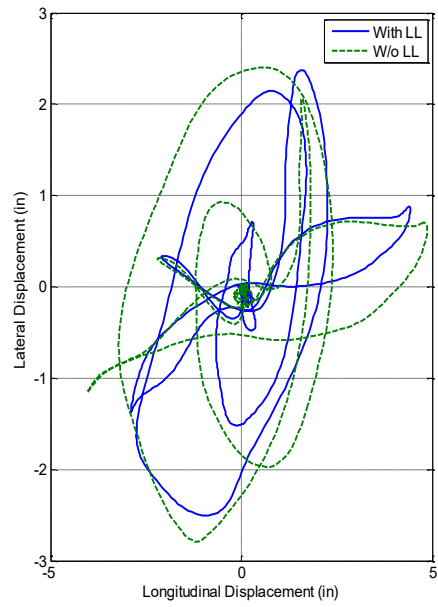


**Figure 5.5.37. Orbital Displacement at the Top of North Bent (200% DE)**

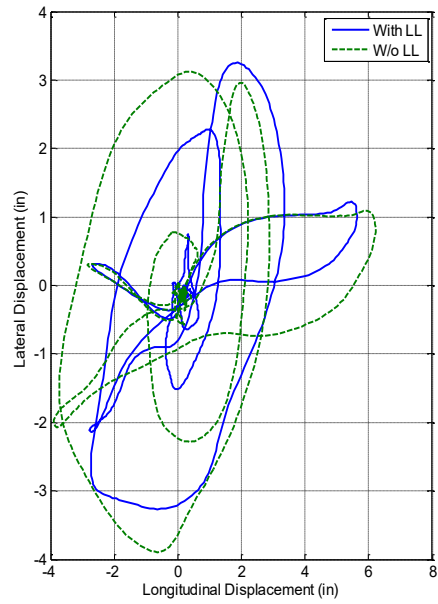


**Figure 5.5.38. Orbital Displacement at the Top of North Bent (250% DE)**

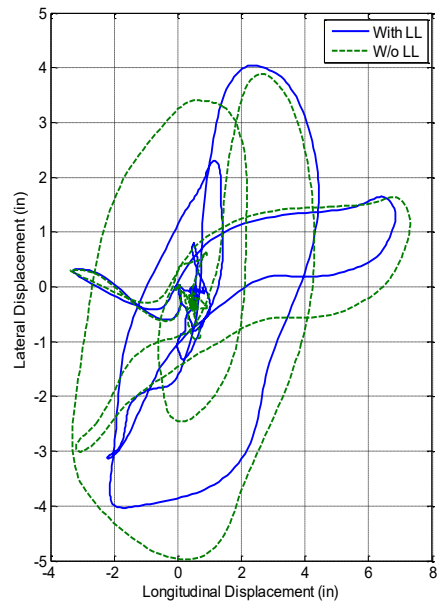


**Figure 5.5.39. Orbital Displacement at the Top of North Bent (300% DE)**

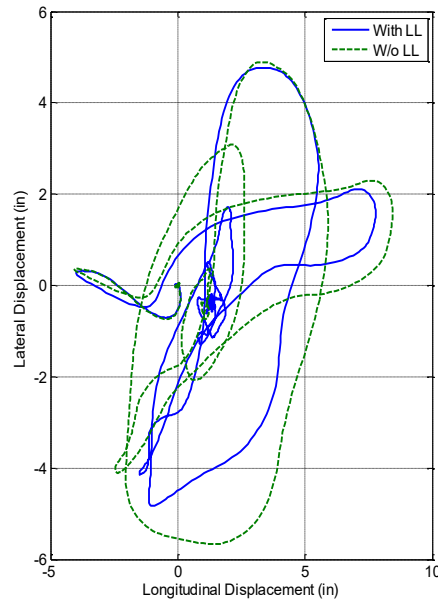


**Figure 5.5.40. Orbital Displacement at the Top of North Bent (350% DE)**

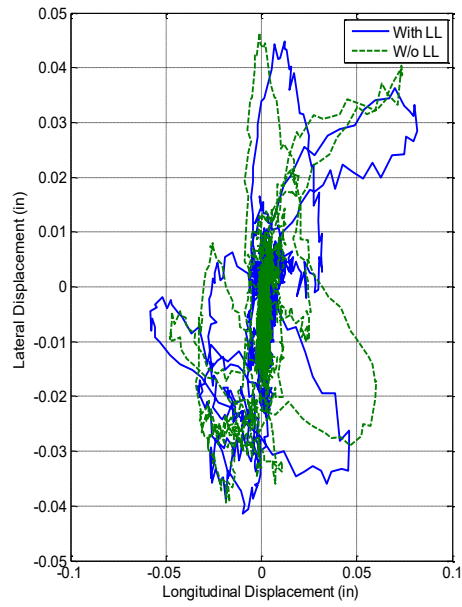


**Figure 5.5.41. Orbital Displacement at the Top of South Bent (10% DE)**

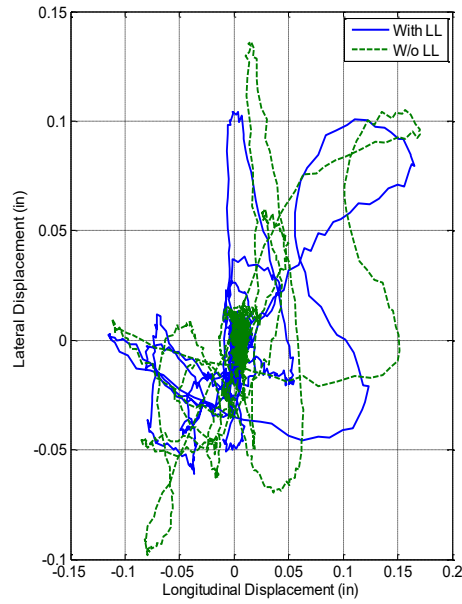


**Figure 5.5.42. Orbital Displacement at the Top of South Bent (20% DE)**

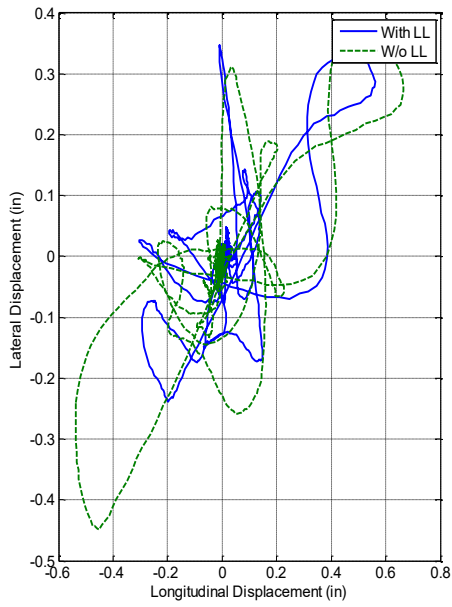


**Figure 5.5.43. Orbital Displacement at the Top of South Bent (50% DE)**

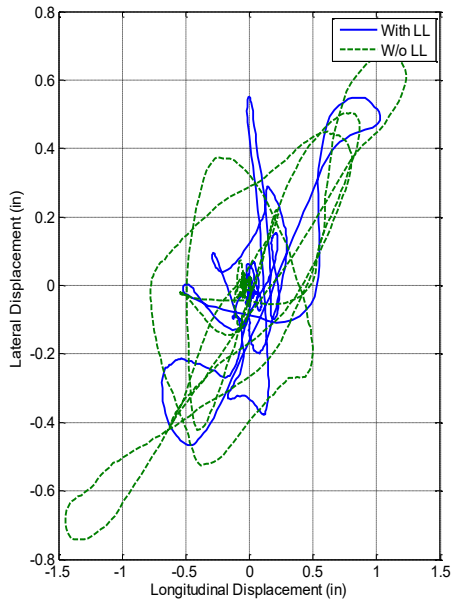


**Figure 5.5.44. Orbital Displacement at the Top of South Bent (75% DE)**

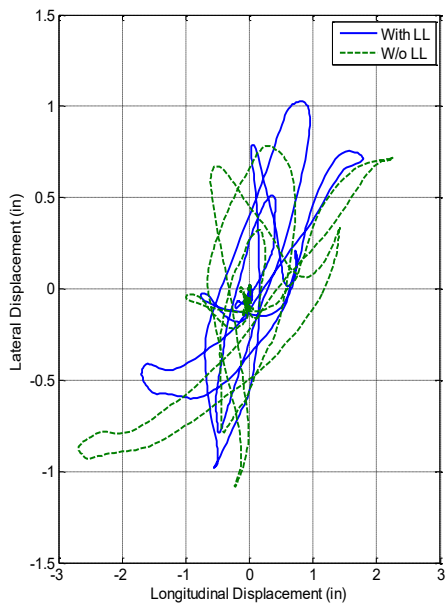


**Figure 5.5.45. Orbital Displacement at the Top of South Bent (100% DE)**

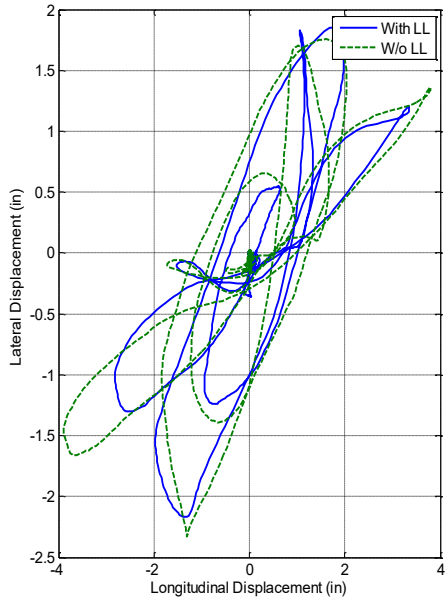


**Figure 5.5.46. Orbital Displacement at the Top of South Bent (150% DE)**

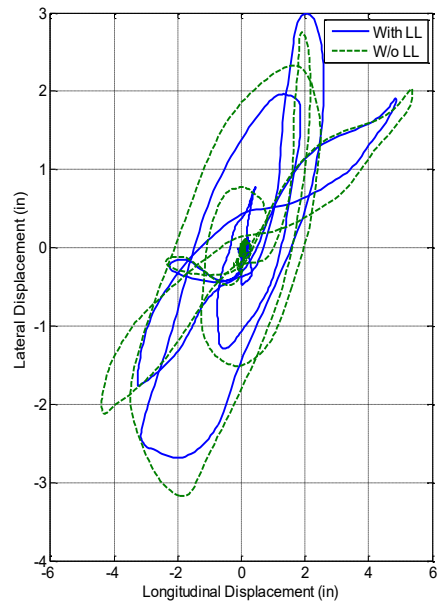


**Figure 5.5.47. Orbital Displacement at the Top of South Bent (200% DE)**

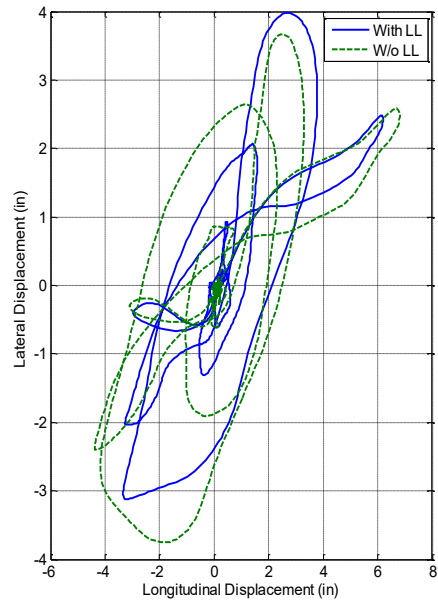


**Figure 5.5.48. Orbital Displacement at the Top of South Bent (250% DE)**

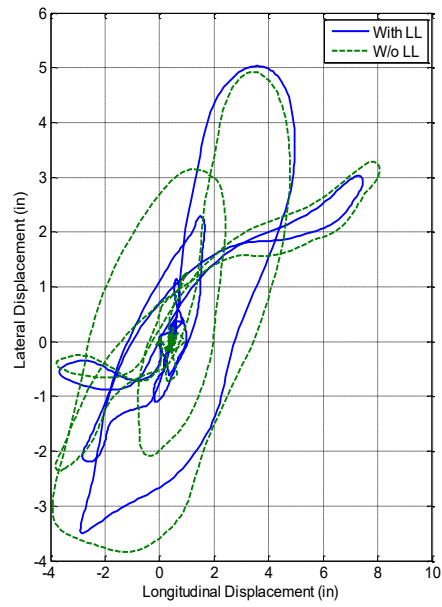


**Figure 5.5.49. Orbital Displacement at the Top of South Bent (300% DE)**

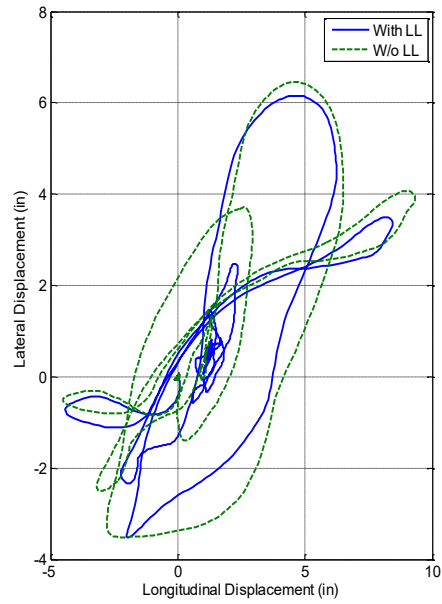


**Figure 5.5.50. Orbital Displacement at the Top of South Bent (350% DE)**

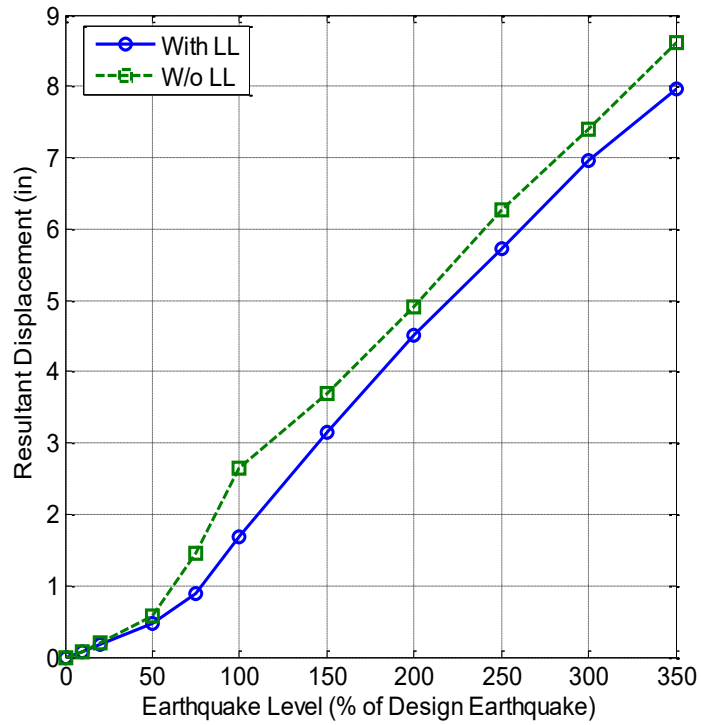


**Figure 5.5.51. Maximum Displacement at Top of North Bent**

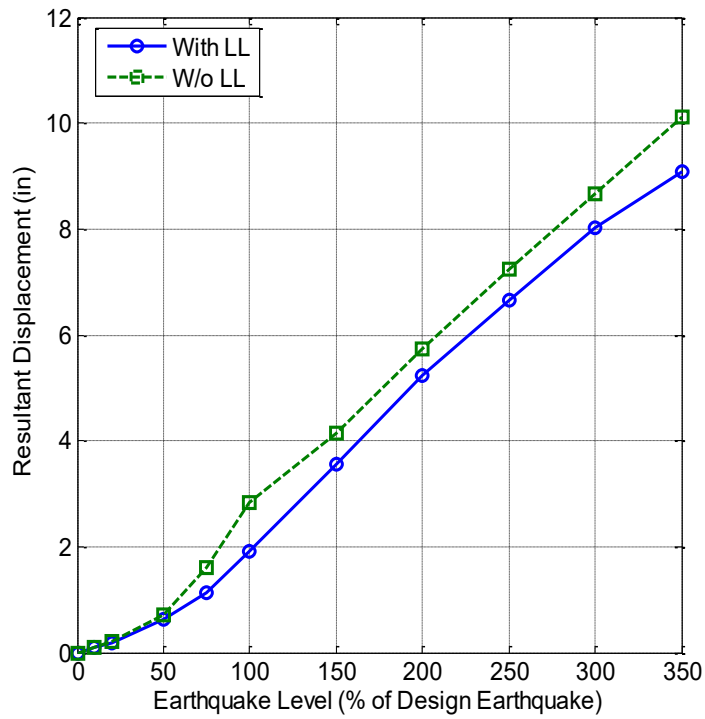
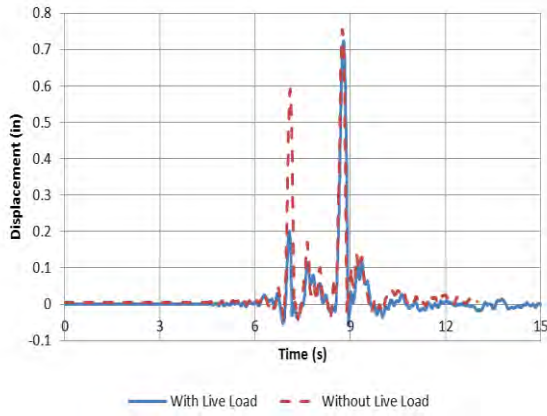
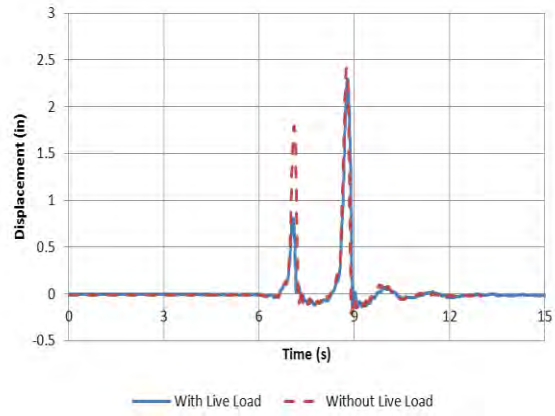


**Figure 5.5.52. Maximum Displacement at Top of South Bent**

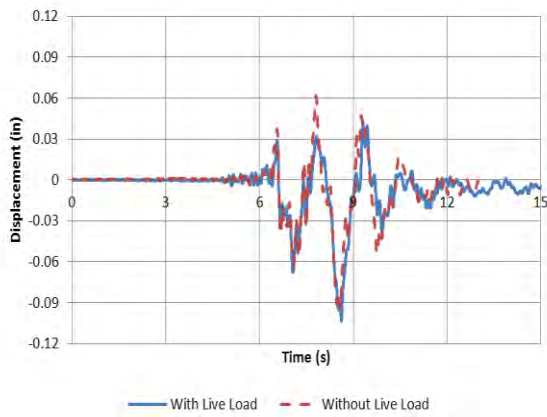


(a)

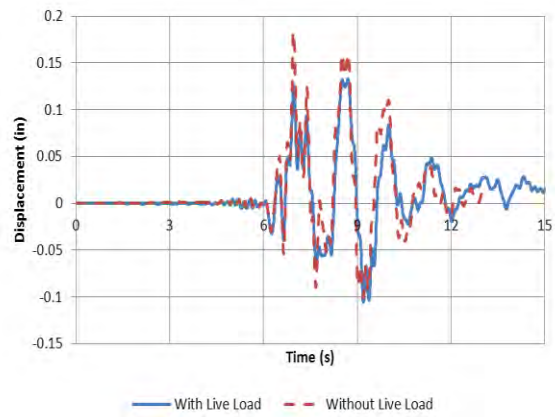


(b)

**Figure 5.5.53. Displacement Histories of Superstructure at North Abutment (a) Outer and (b) Inner Bay Response (350% DE)**



(a)



(b)

**Figure 5.5.54. Displacement Histories of Superstructure at South Abutment (a) Outer and (b) Inner Bay (350% DE)**

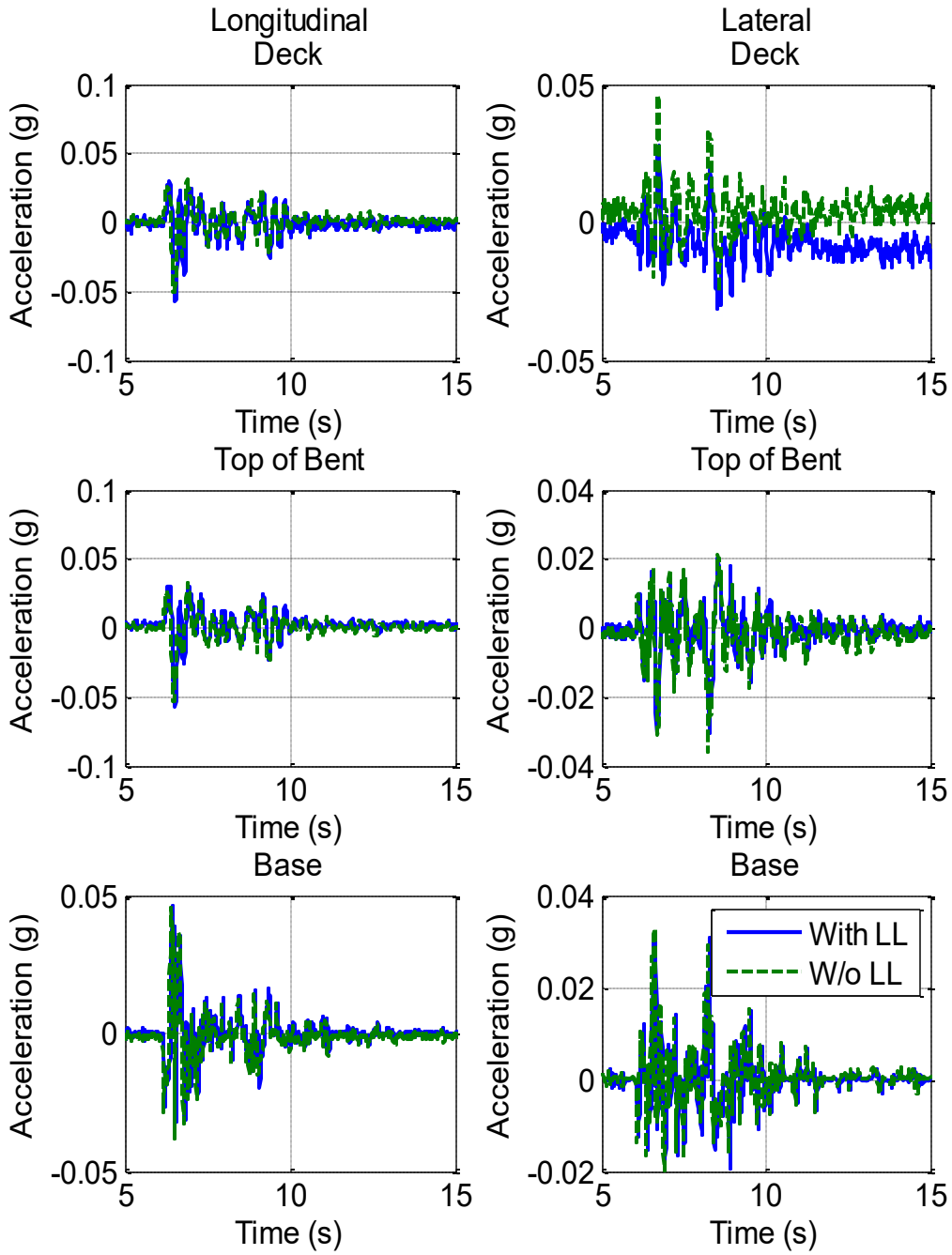


**Figure 5.6.1. Acceleration Histories at Deck, Top of Bent, and Base Levels of North Bent (10% DE)**

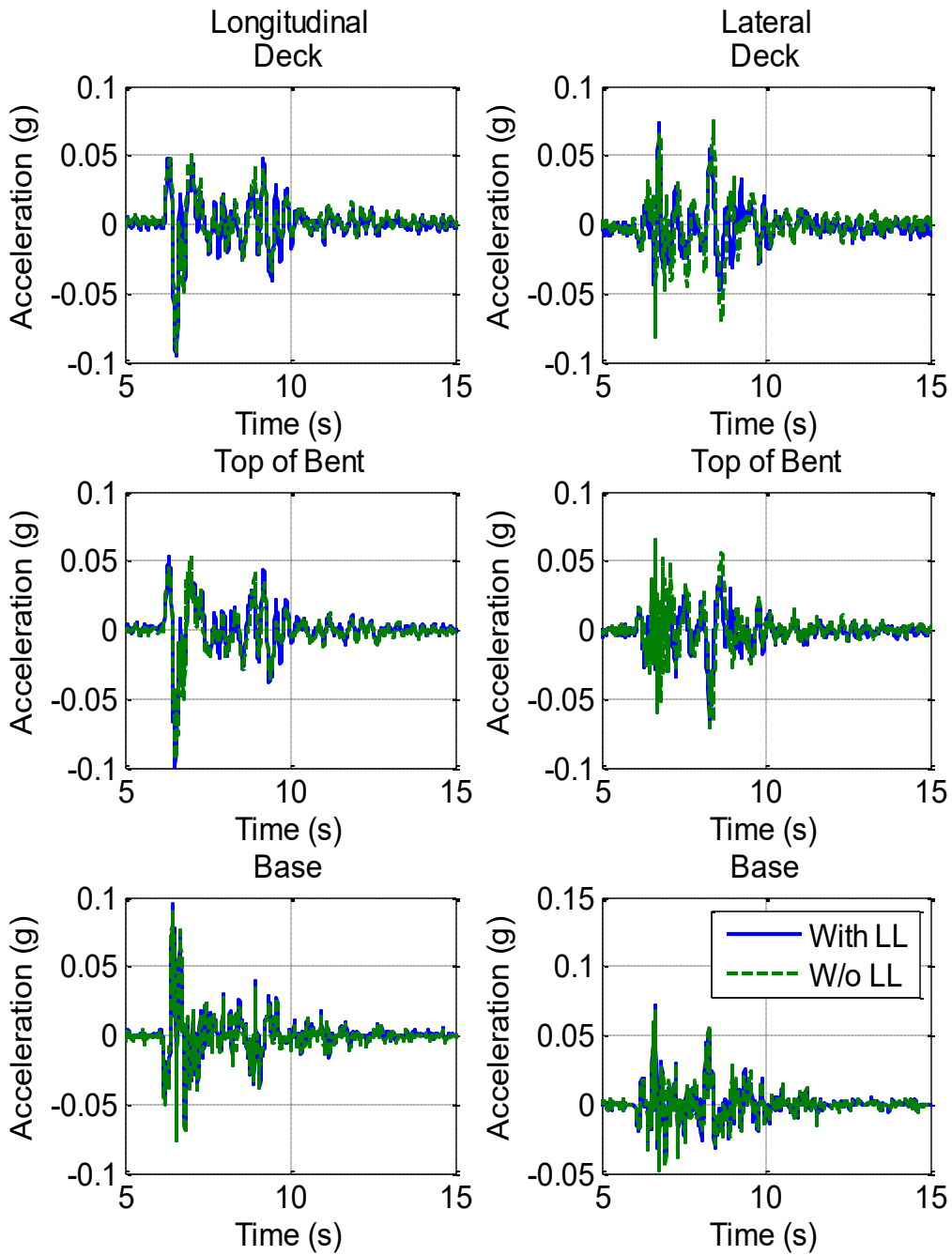


**Figure 5.6.2. Acceleration Histories at Deck, Top of Bent, and Base Levels of North Bent (20% DE)**

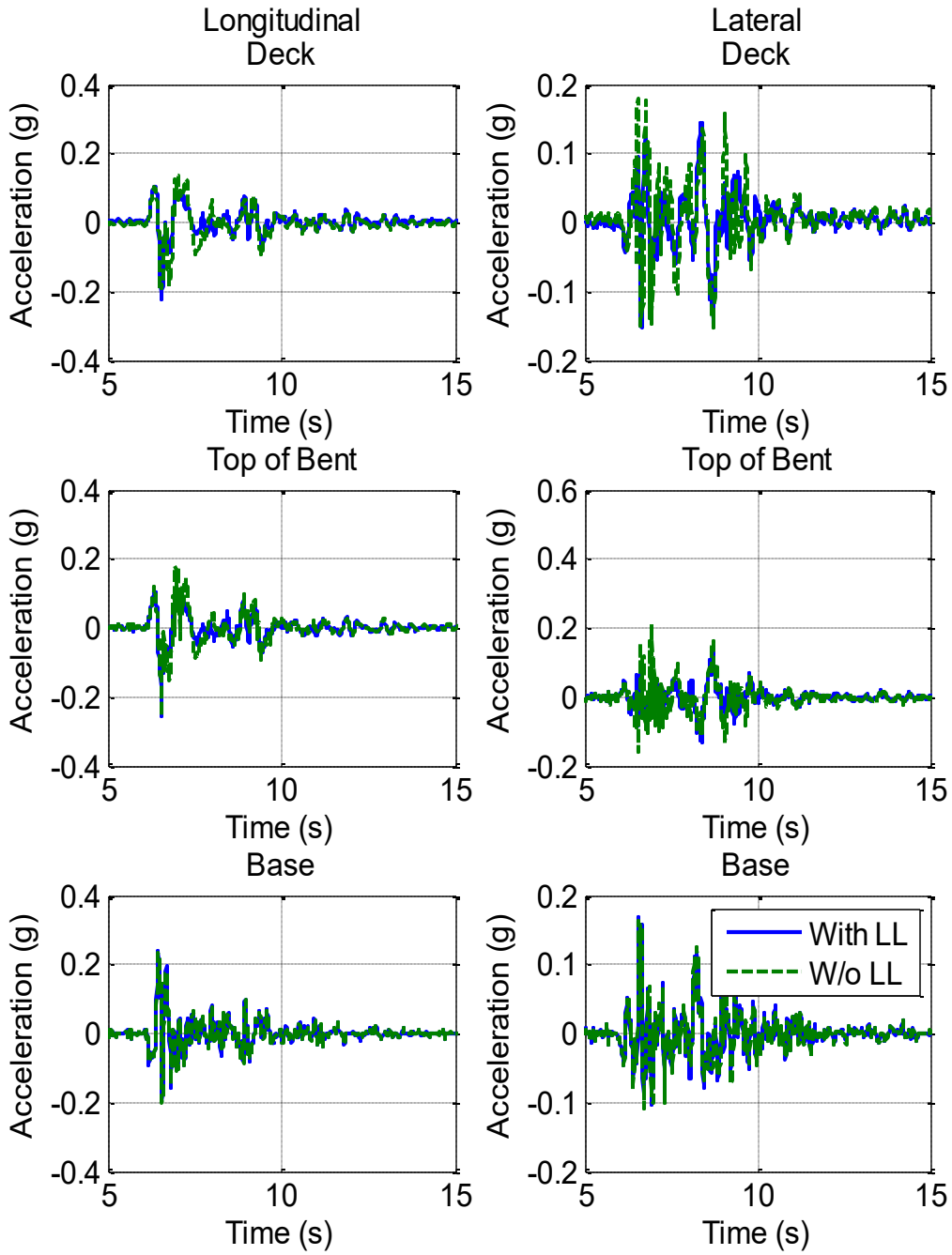


**Figure 5.6.3. Acceleration Histories at Deck, Top of Bent, and Base Levels of North Bent (50% DE)**

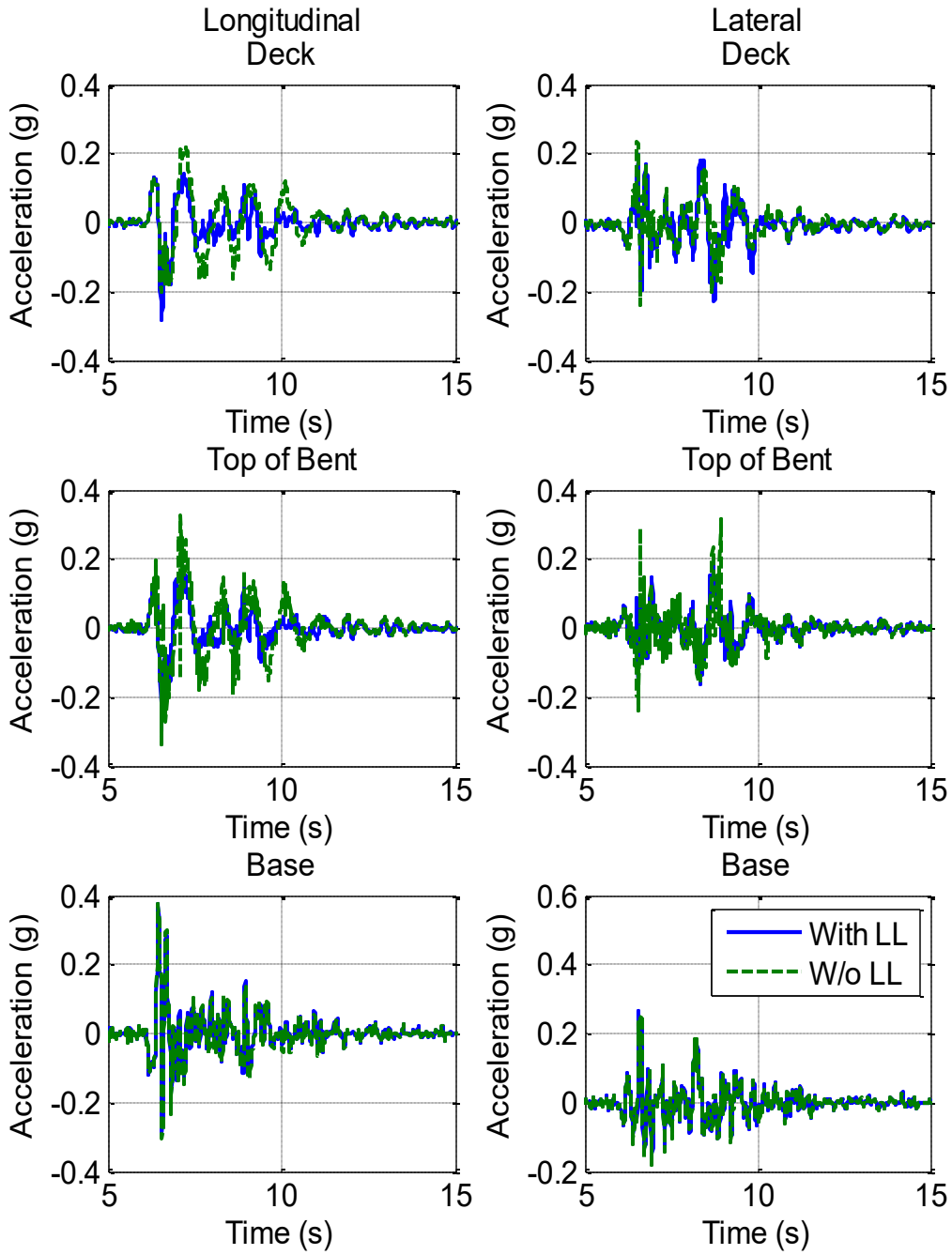


**Figure 5.6.4. Acceleration Histories at Deck, Top of Bent, and Base Levels of North Bent (75% DE)**

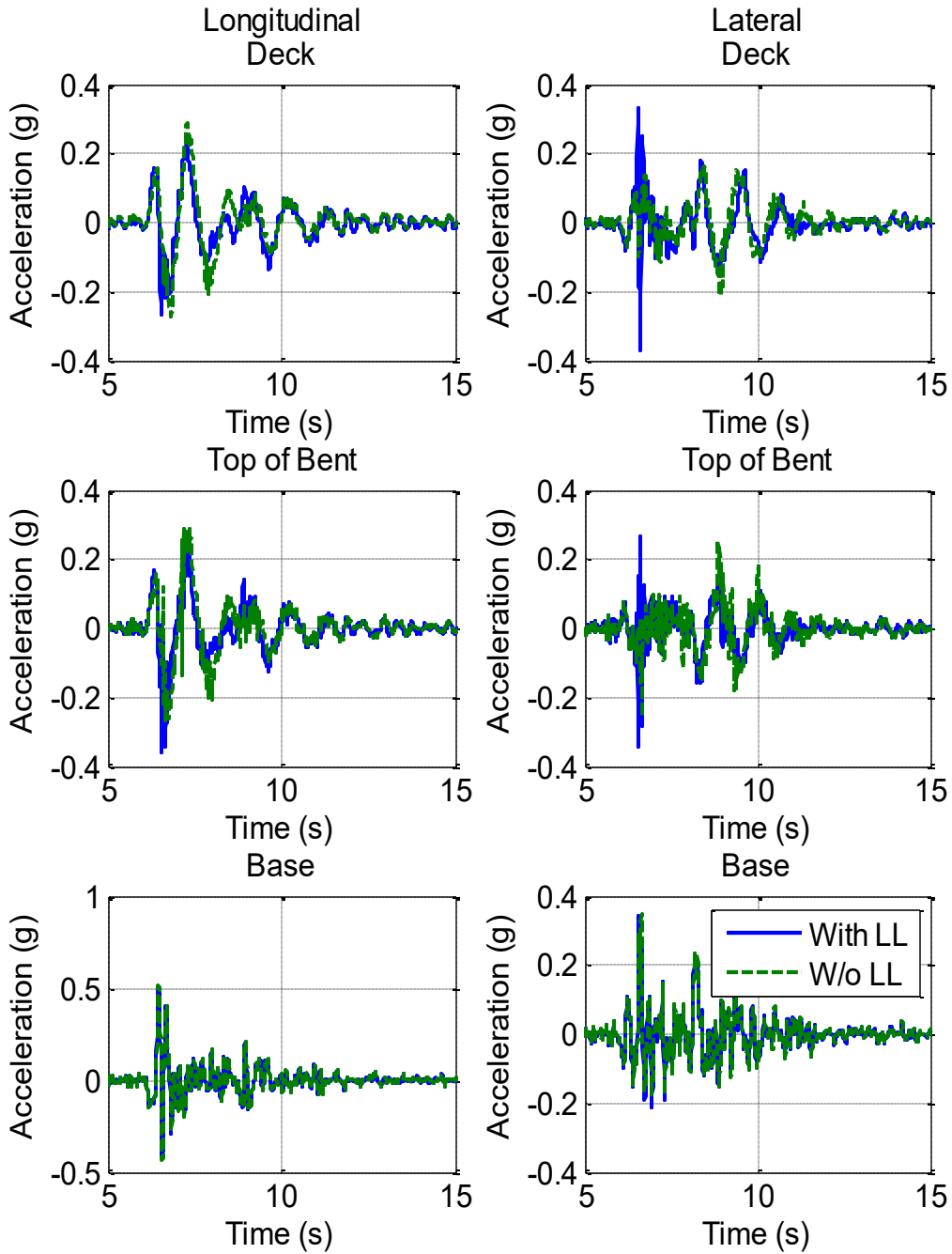


**Figure 5.6.5. Acceleration Histories at Deck, Top of Bent, and Base Levels of North Bent (100% DE)**

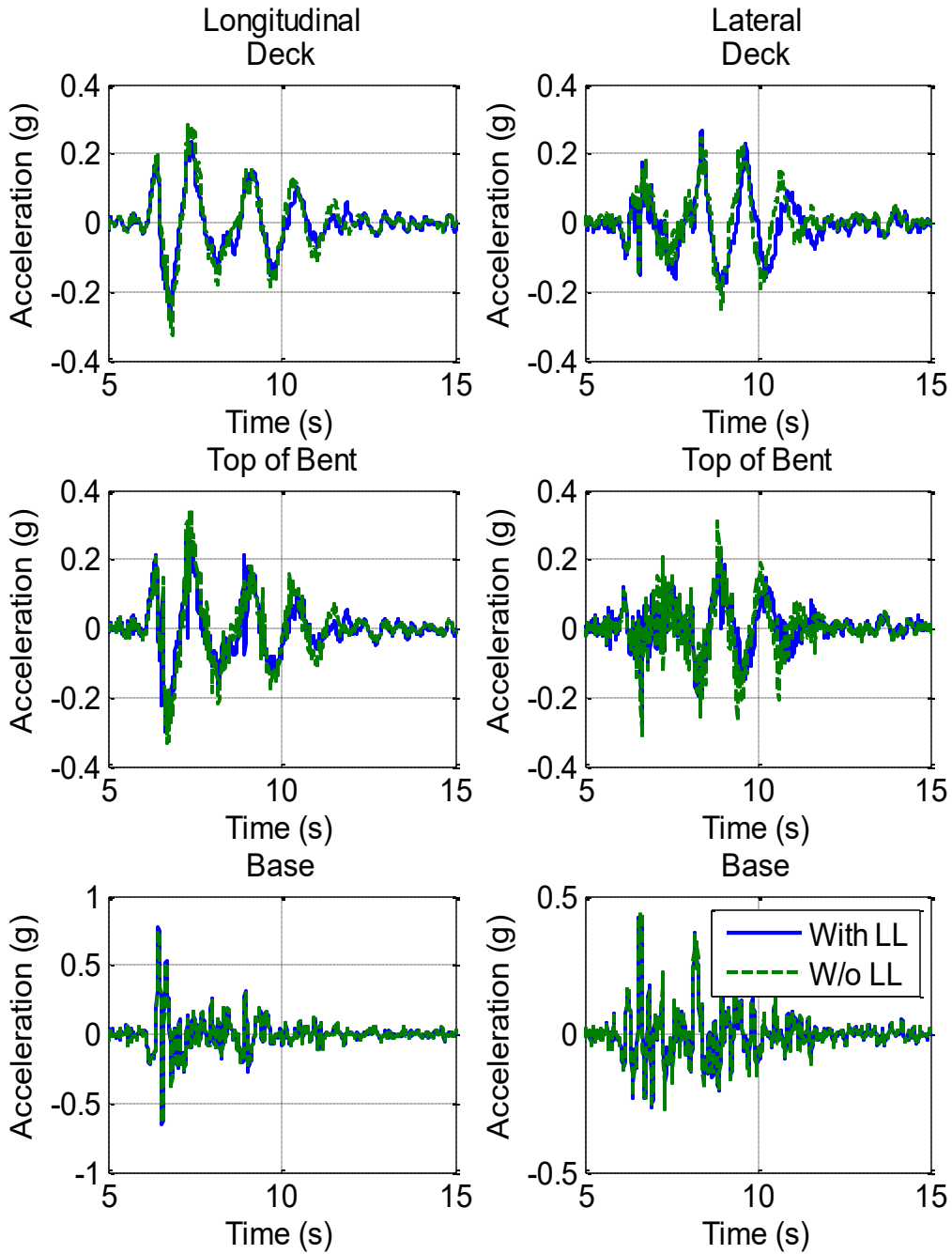


**Figure 5.6.6. Acceleration Histories at Deck, Top of Bent, and Base Levels of North Bent (150% DE)**

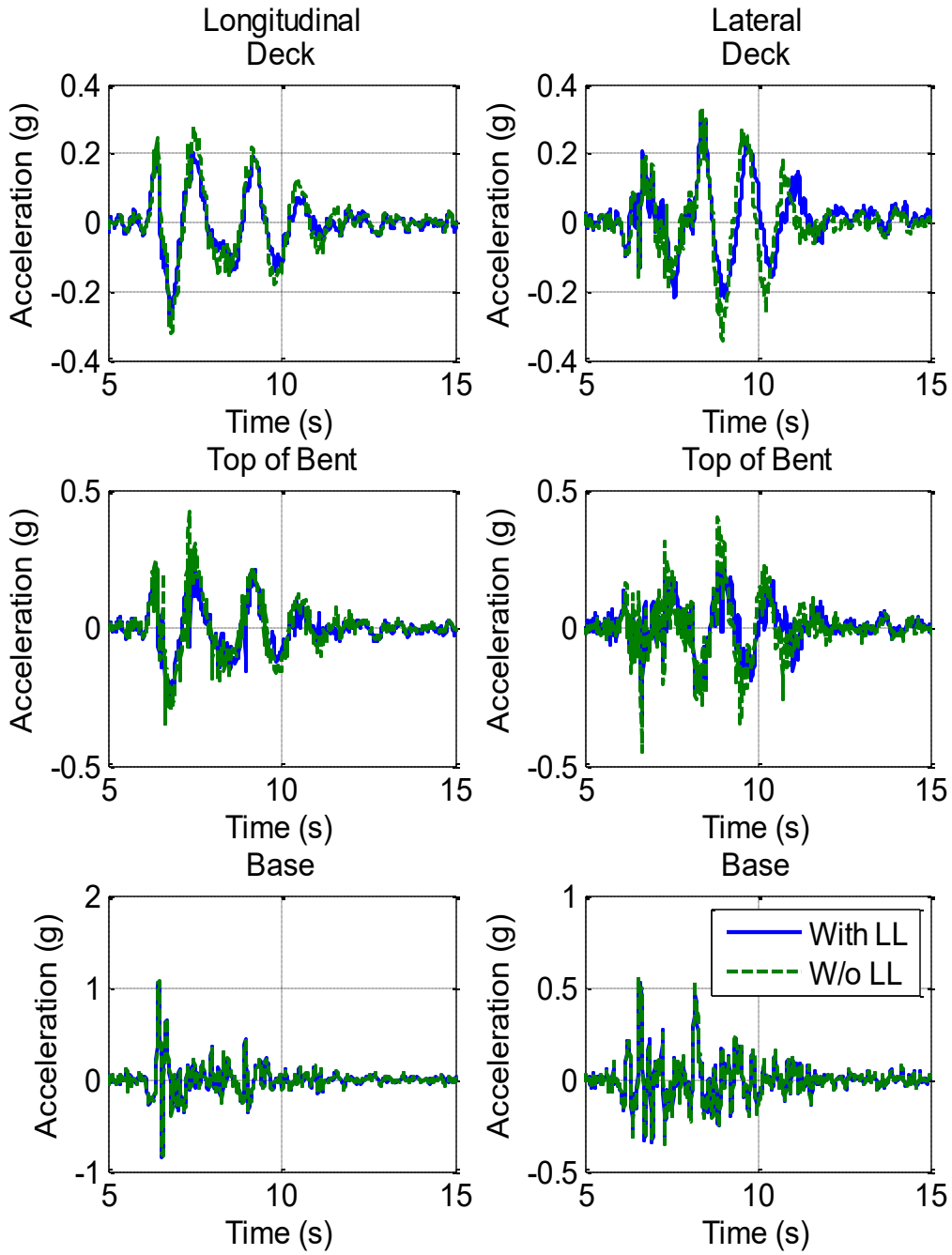


**Figure 5.6.7. Acceleration Histories at Deck, Top of Bent, and Base Levels of North Bent (200% DE)**

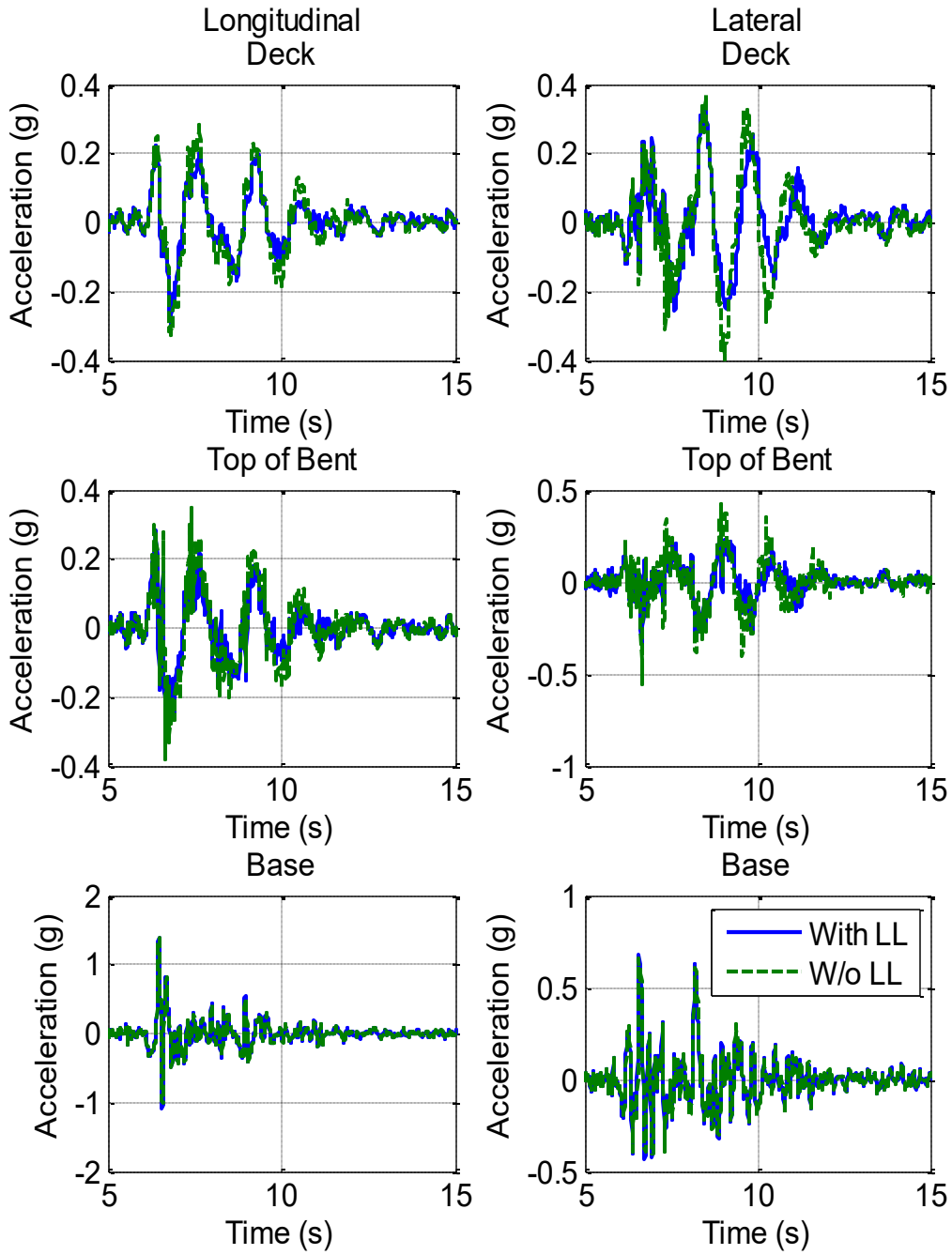


**Figure 5.6.8. Acceleration Histories at Deck, Top of Bent, and Base Levels of North Bent (250% DE)**

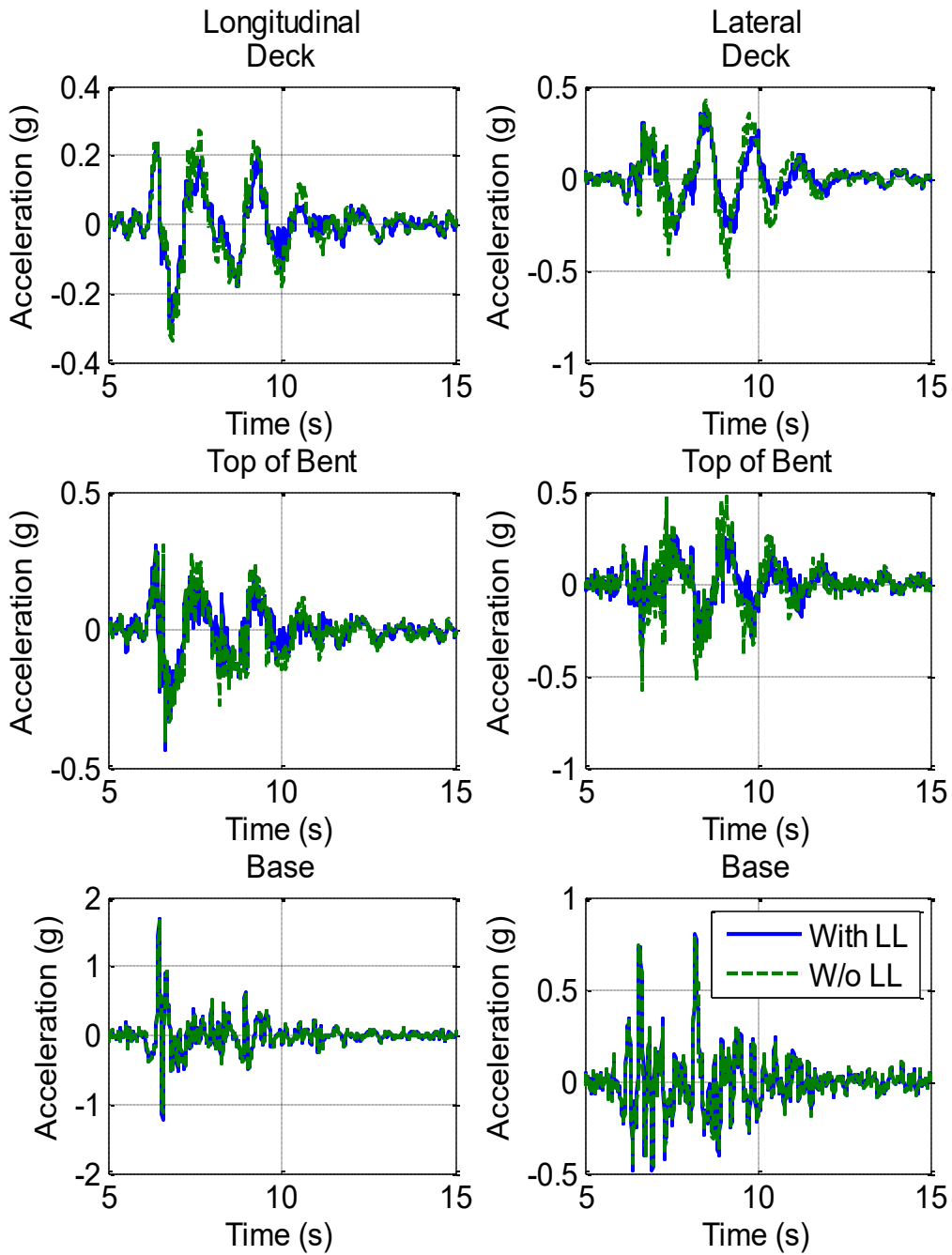


**Figure 5.6.9. Acceleration Histories at Deck, Top of Bent, and Base Levels of North Bent (300% DE)**

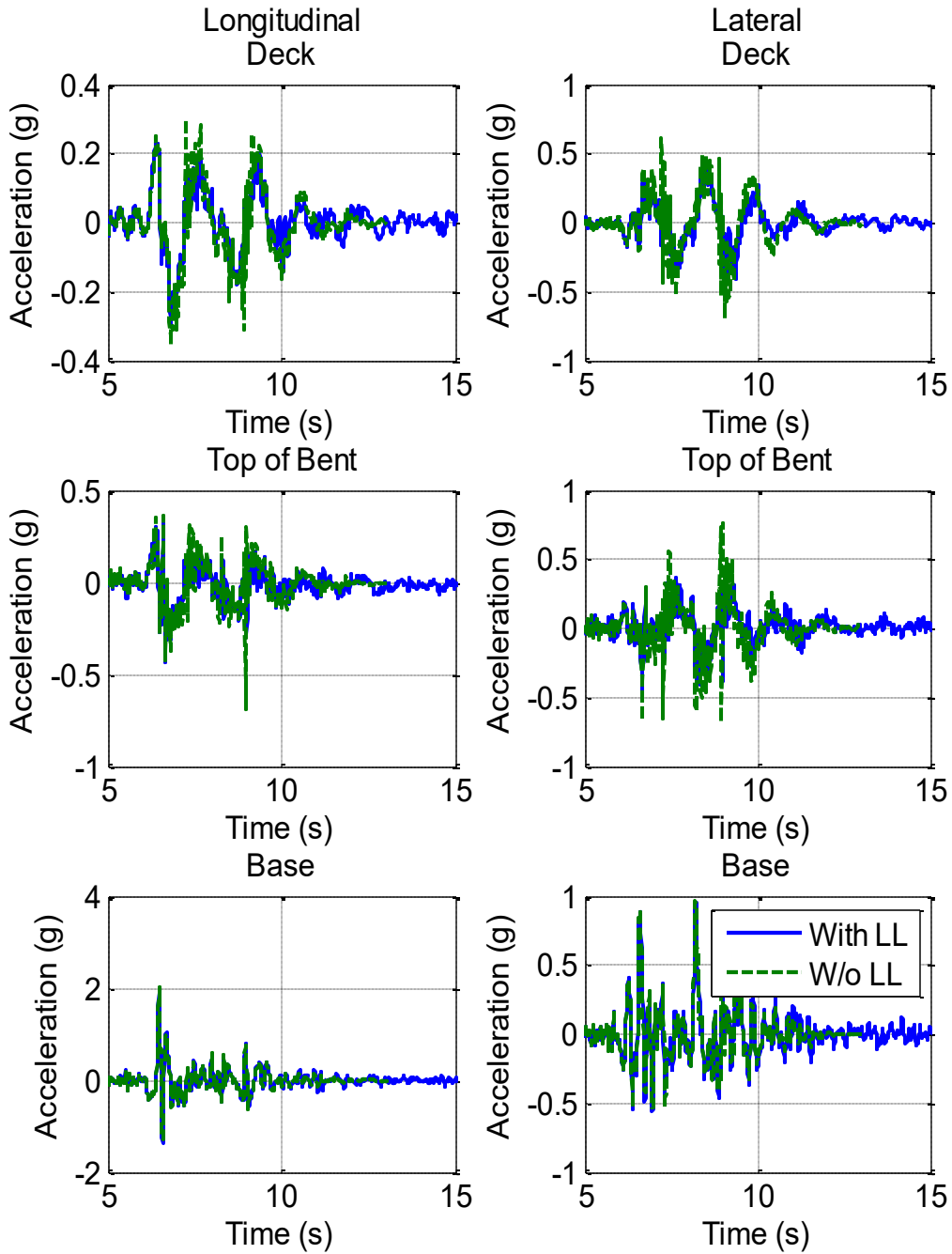


**Figure 5.6.10. Acceleration Histories at Deck, Top of Bent, and Base Levels of North Bent (350% DE)**

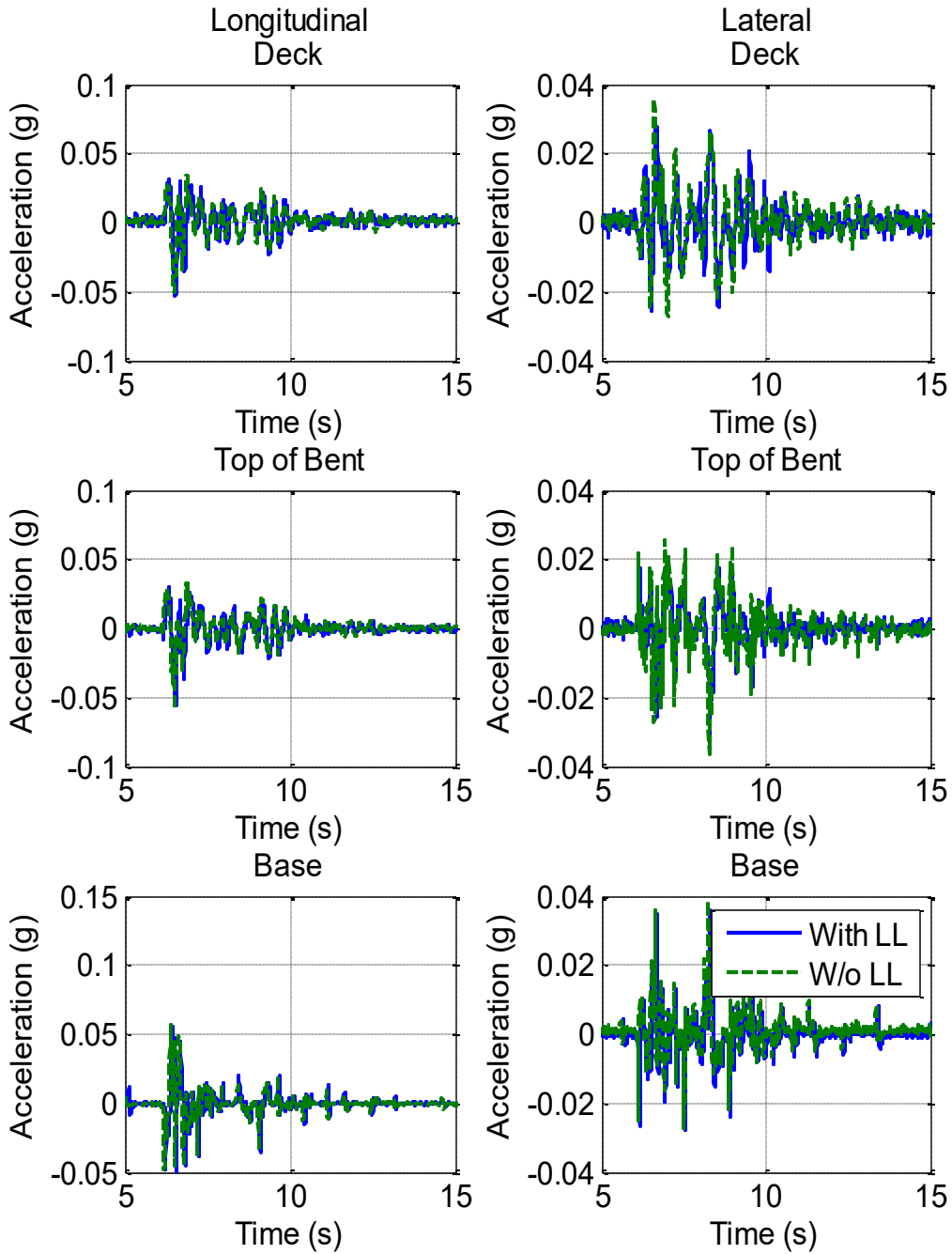


**Figure 5.6.11. Acceleration Histories at Deck, Top of Bent, and Base Levels of South Bent (10% DE)**

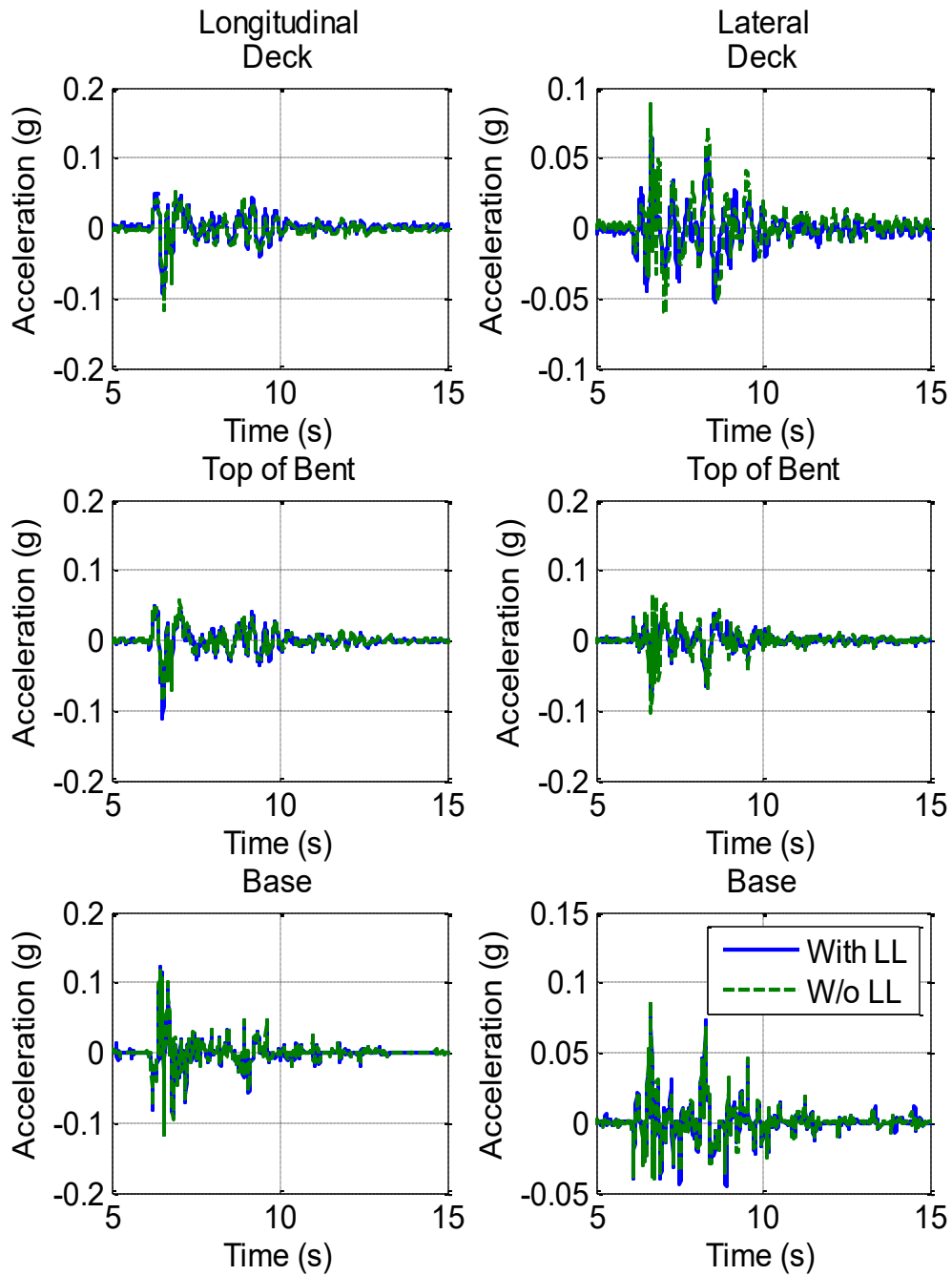


**Figure 5.6.12. Acceleration Histories at Deck, Top of Bent, and Base Levels of South Bent (20% DE)**

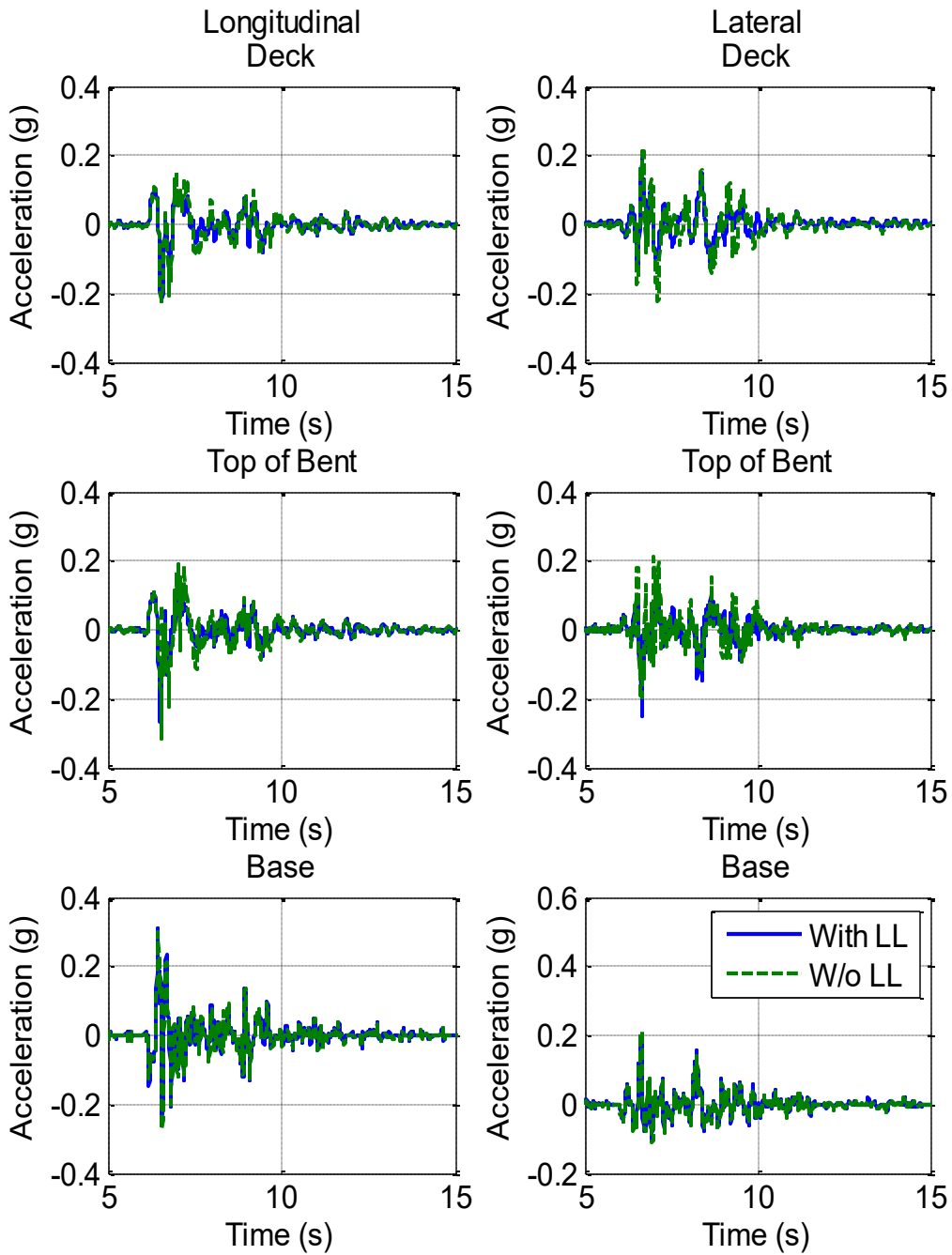


**Figure 5.6.13. Acceleration Histories at Deck, Top of Bent, and Base Levels of South Bent (50% DE)**

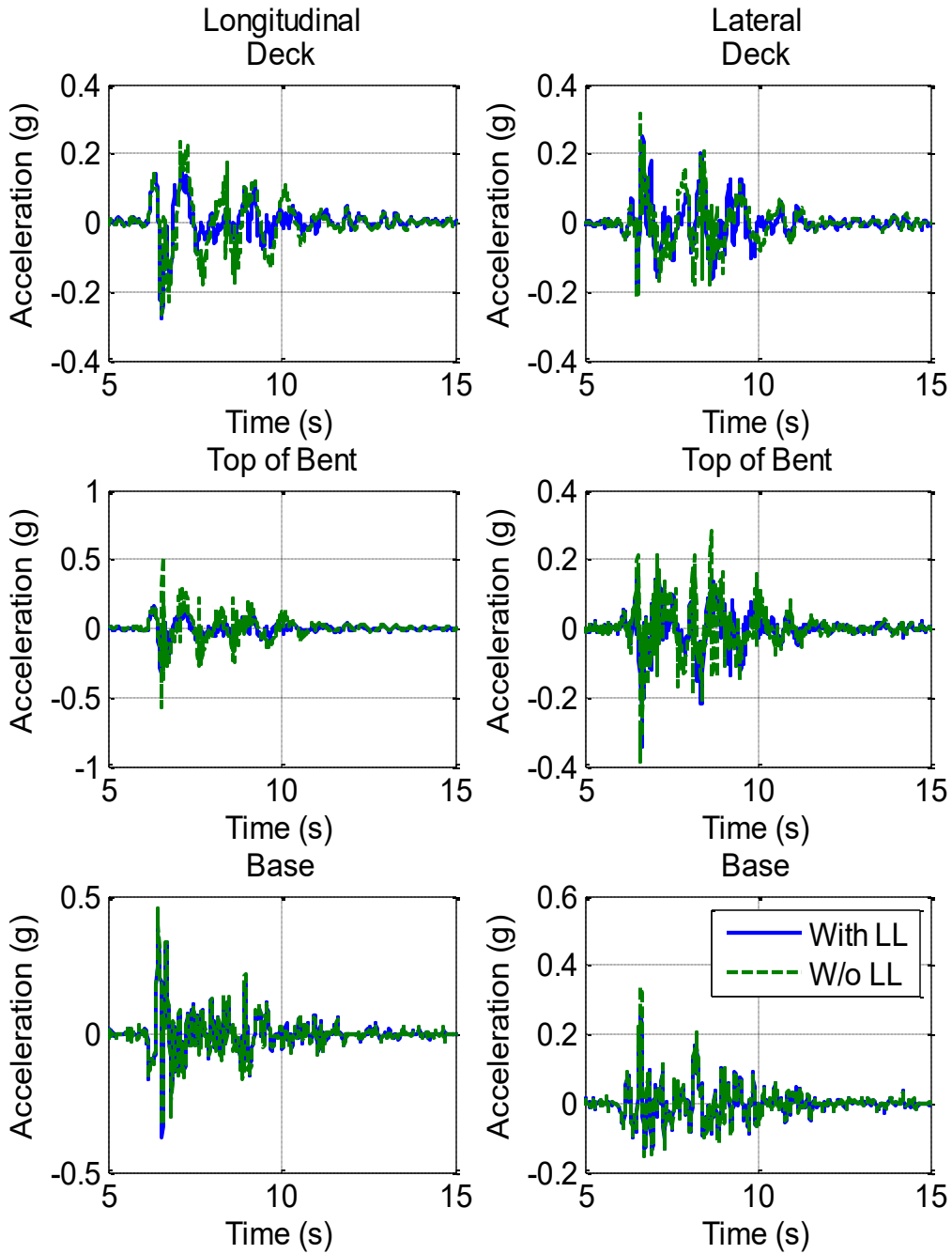


**Figure 5.6.14. Acceleration Histories at Deck, Top of Bent, and Base Levels of South Bent (75% DE)**

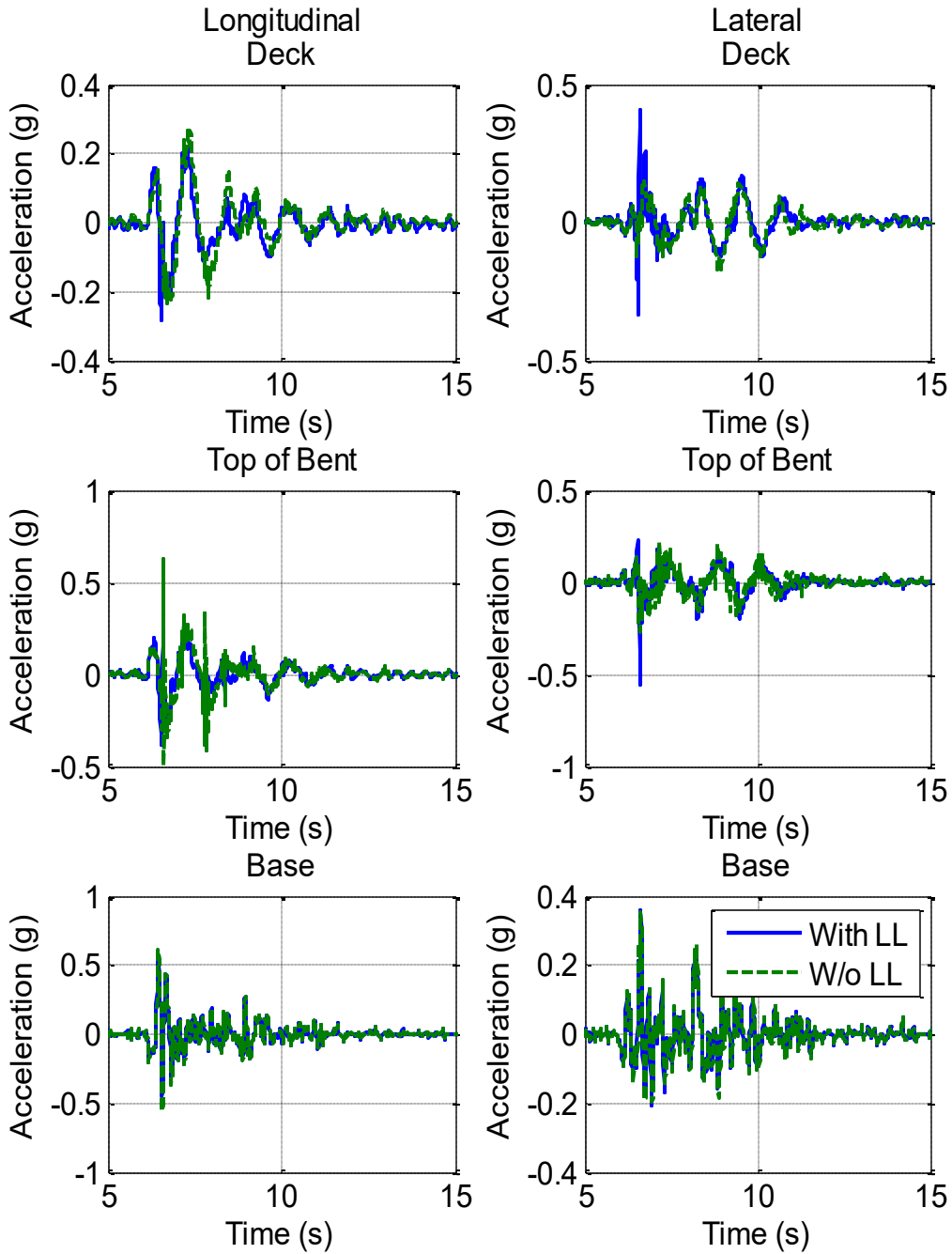


**Figure 5.6.15. Acceleration Histories at Deck, Top of Bent, and Base Levels of South Bent (100% DE)**

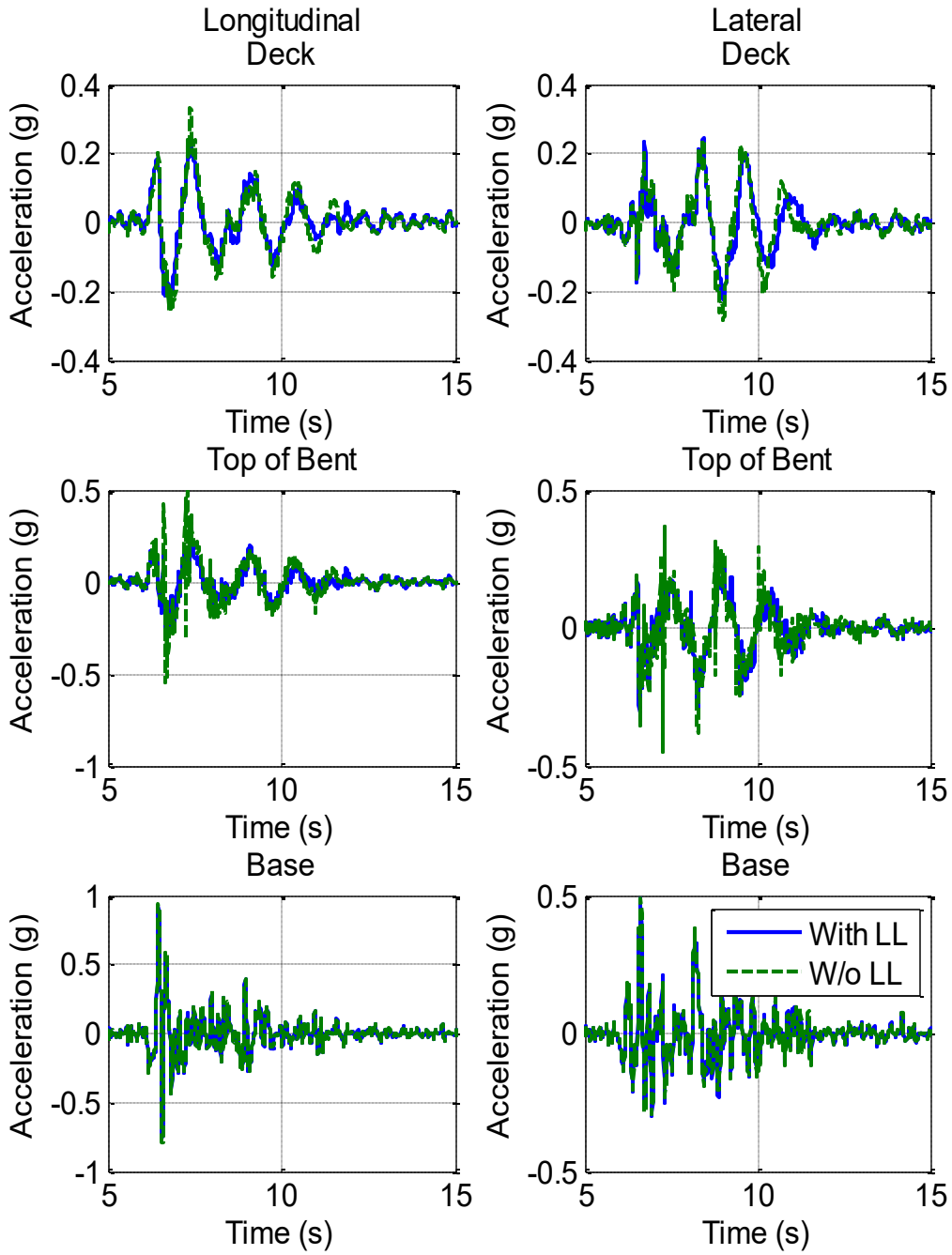


**Figure 5.6.16. Acceleration Histories at Deck, Top of Bent, and Base Levels of South Bent (150% DE)**

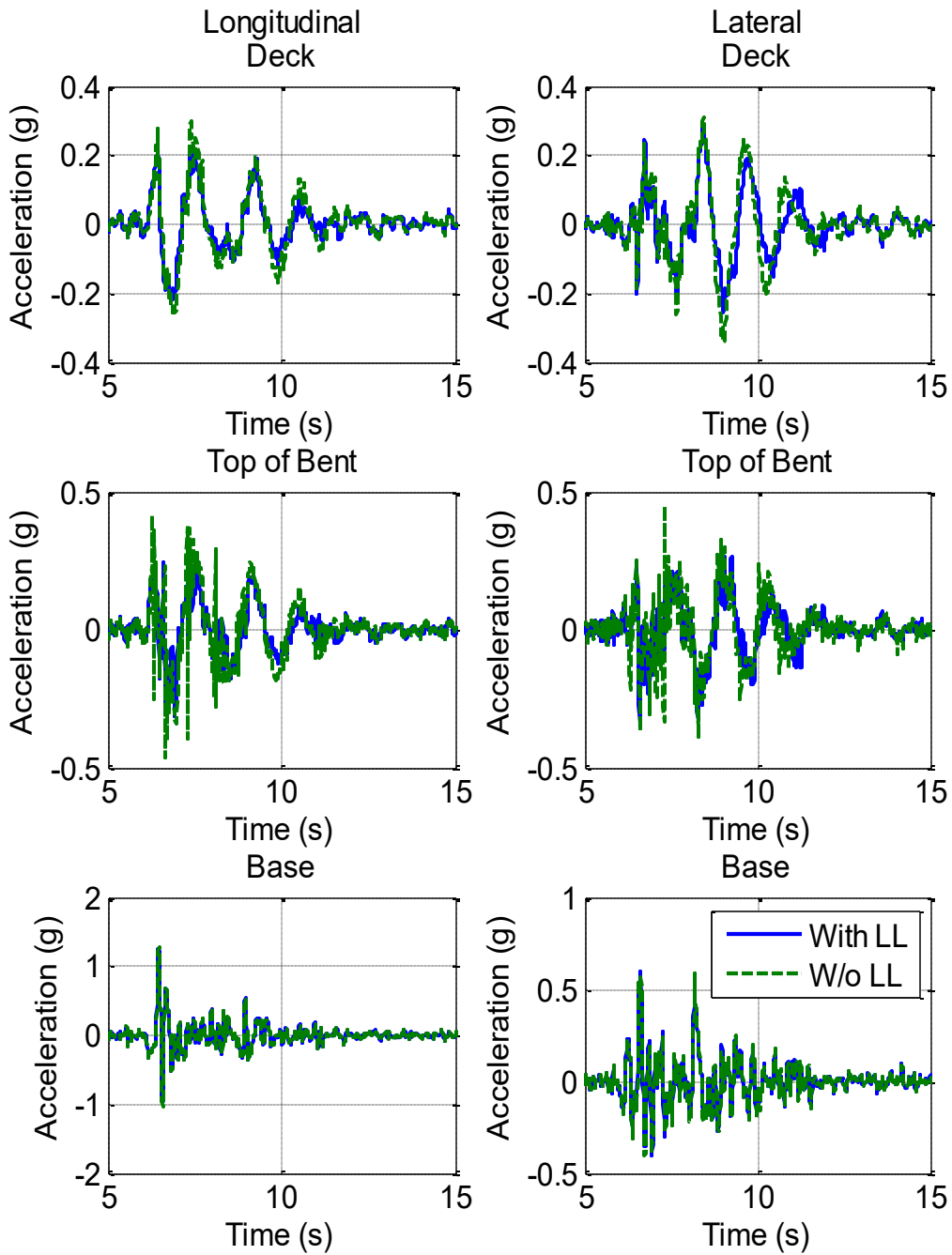


**Figure 5.6.17. Acceleration Histories at Deck, Top of Bent, and Base Levels of South Bent (200% DE)**

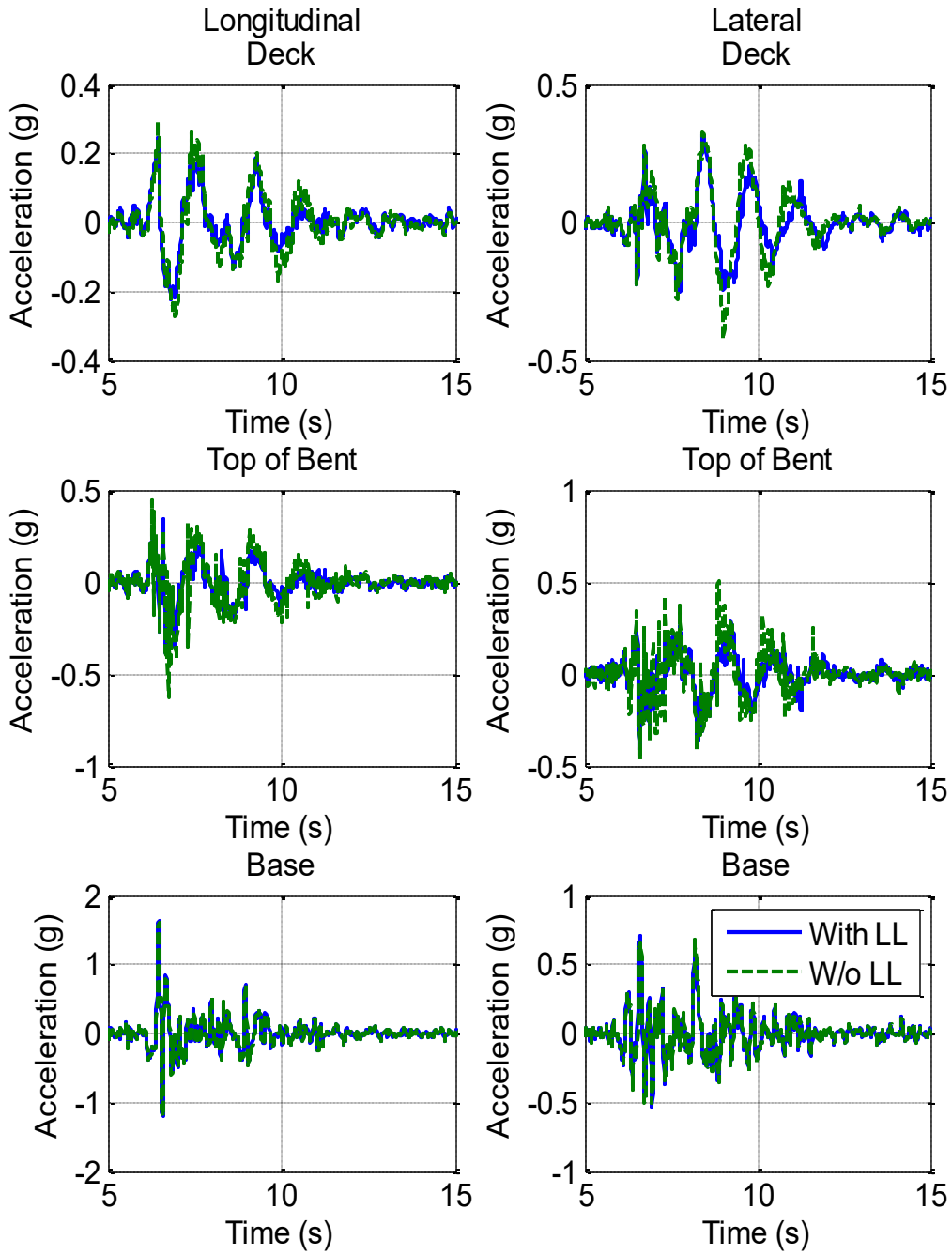


**Figure 5.6.18. Acceleration Histories at Deck, Top of Bent, and Base Levels of South Bent (250% DE)**

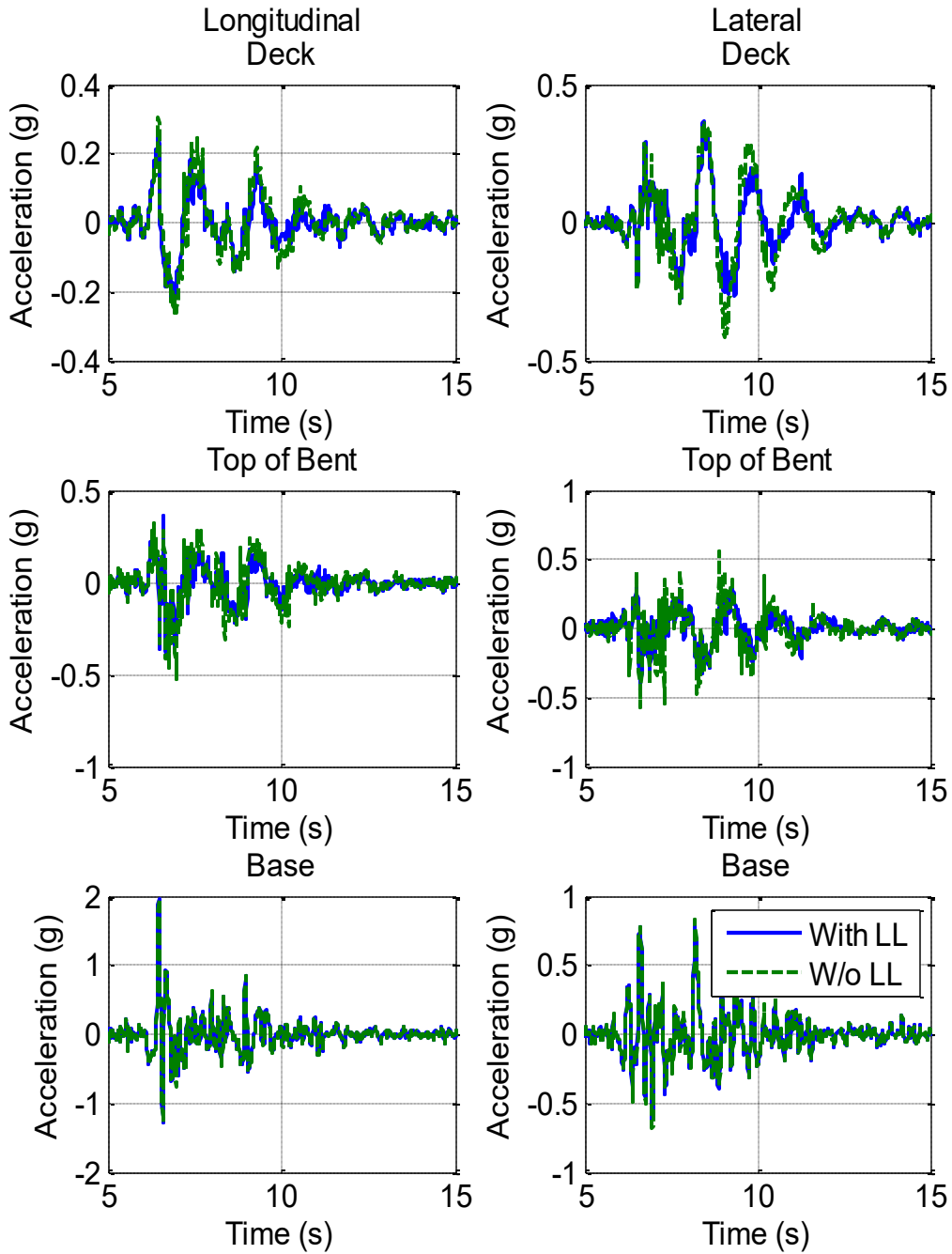


**Figure 5.6.19. Acceleration Histories at Deck, Top of Bent, and Base Levels of South Bent (300% DE)**

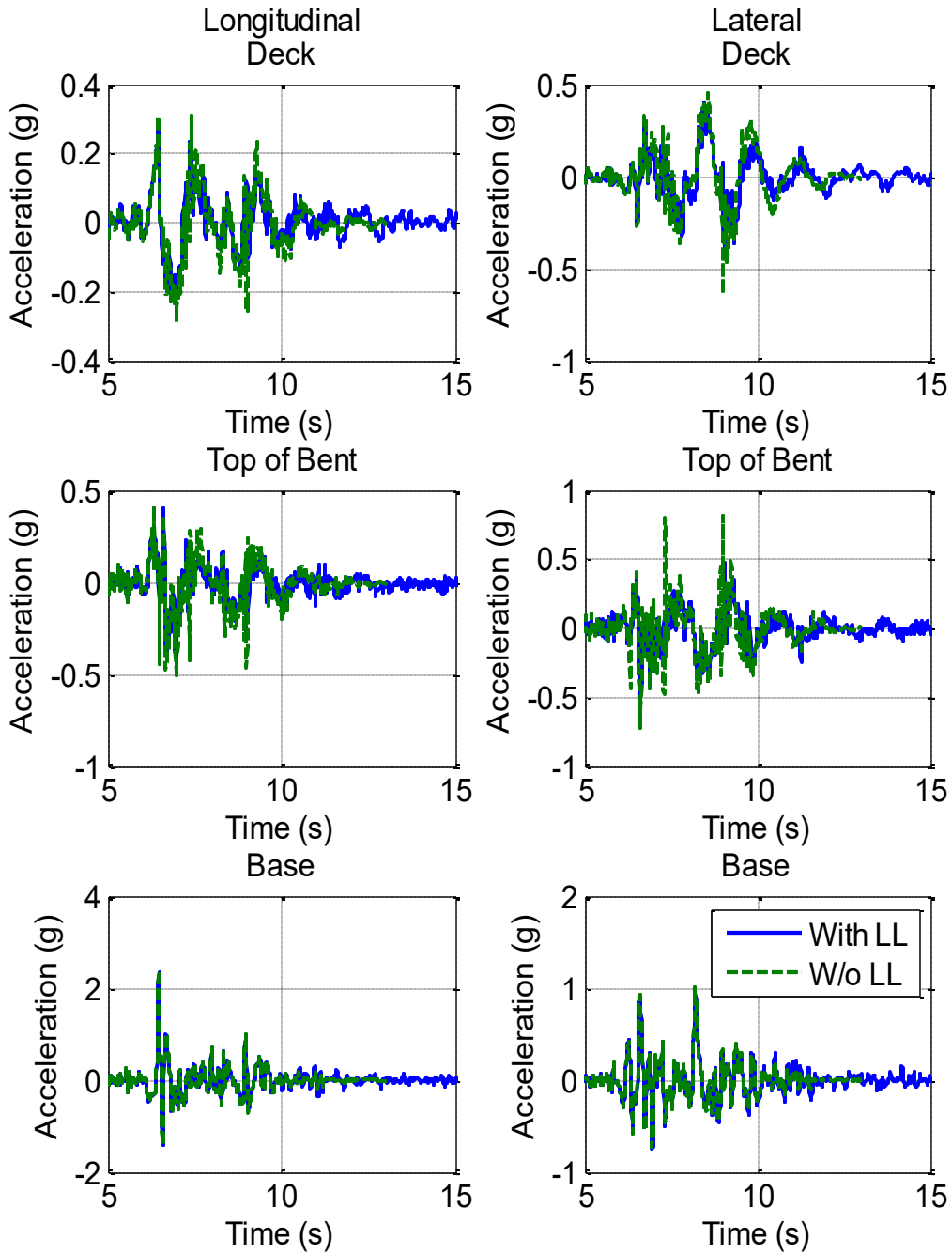


**Figure 5.6.20. Acceleration Histories at Deck, Top of Bent, and Base Levels of South Bent (350% DE)**

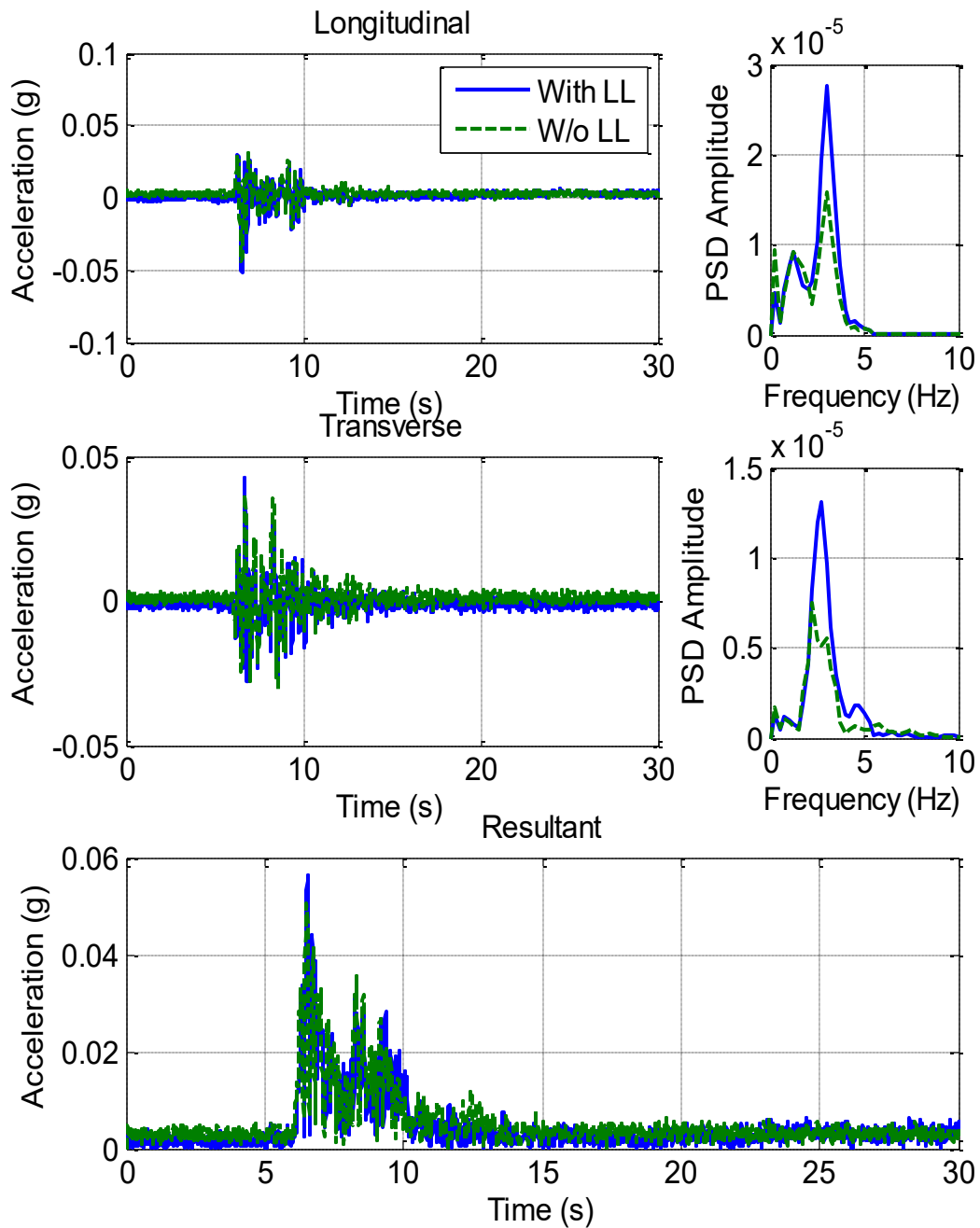


**Figure 5.6.21. Acceleration Histories and PSD Spectra at Mid-Span of Middle Girder (10% DE)**

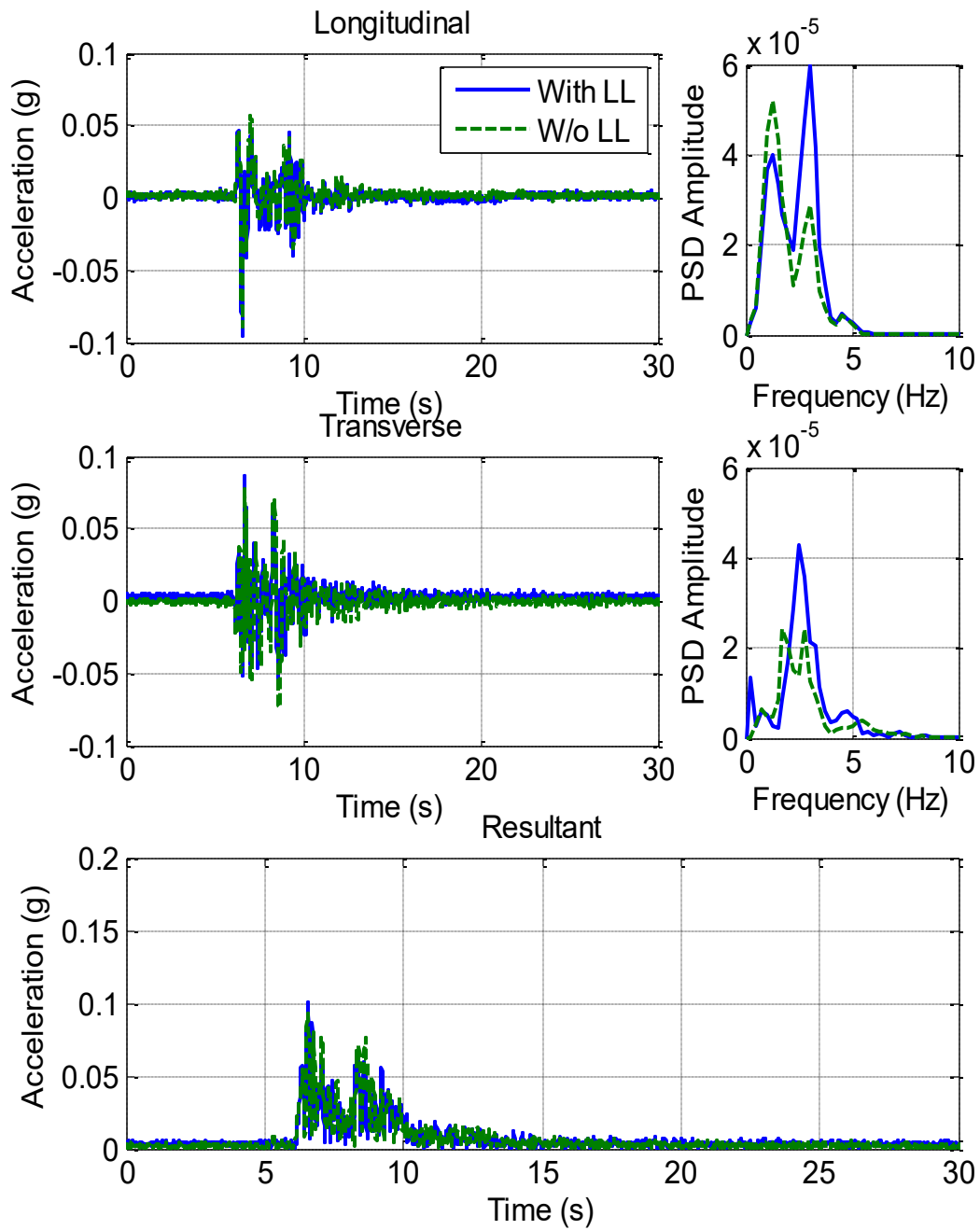


**Figure 5.6.22. Acceleration Histories and PSD Spectra at Mid-Span of Middle Girder (20% DE)**

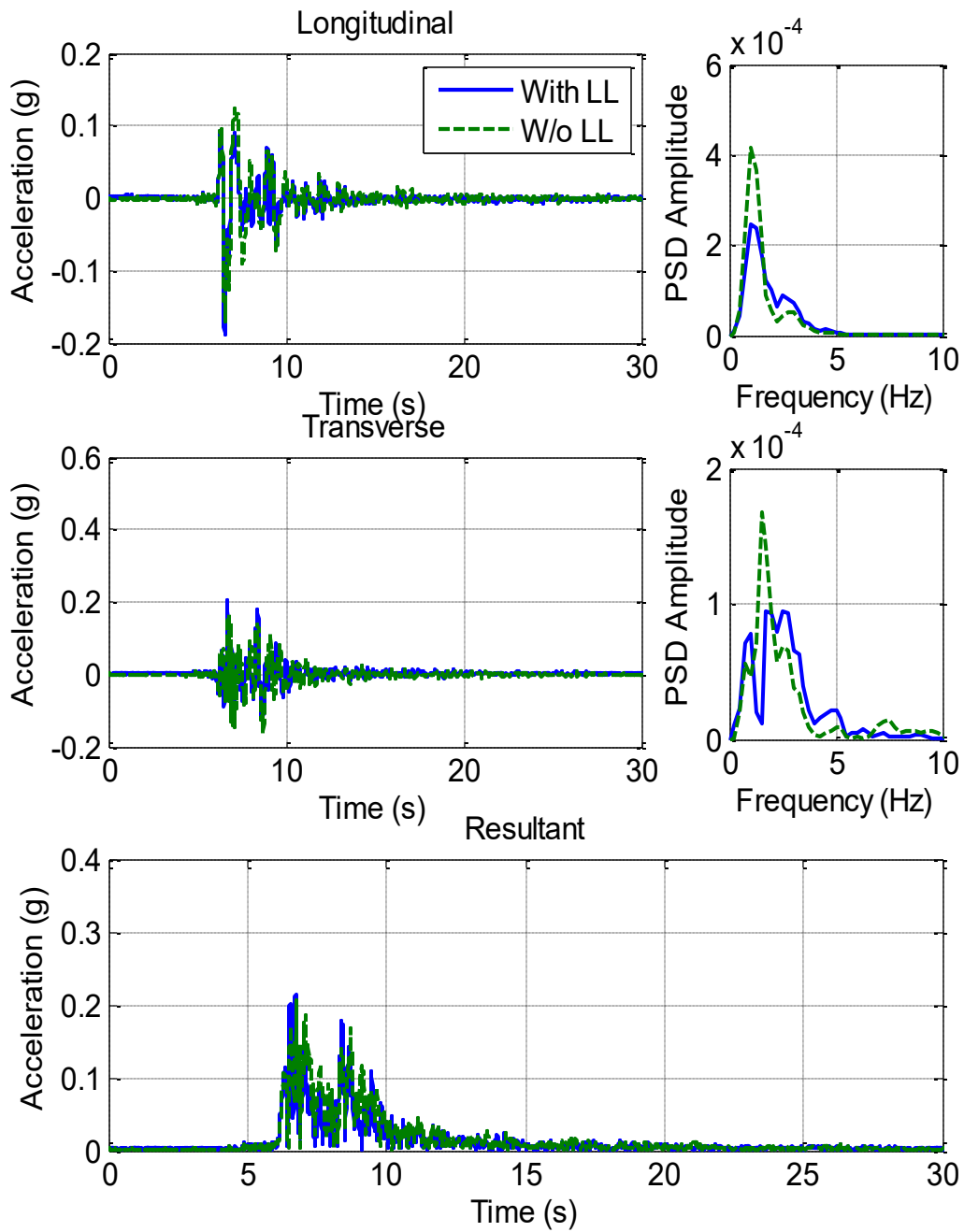


**Figure 5.6.23. Acceleration Histories and PSD Spectra at Mid-Span of Middle Girder (50% DE)**

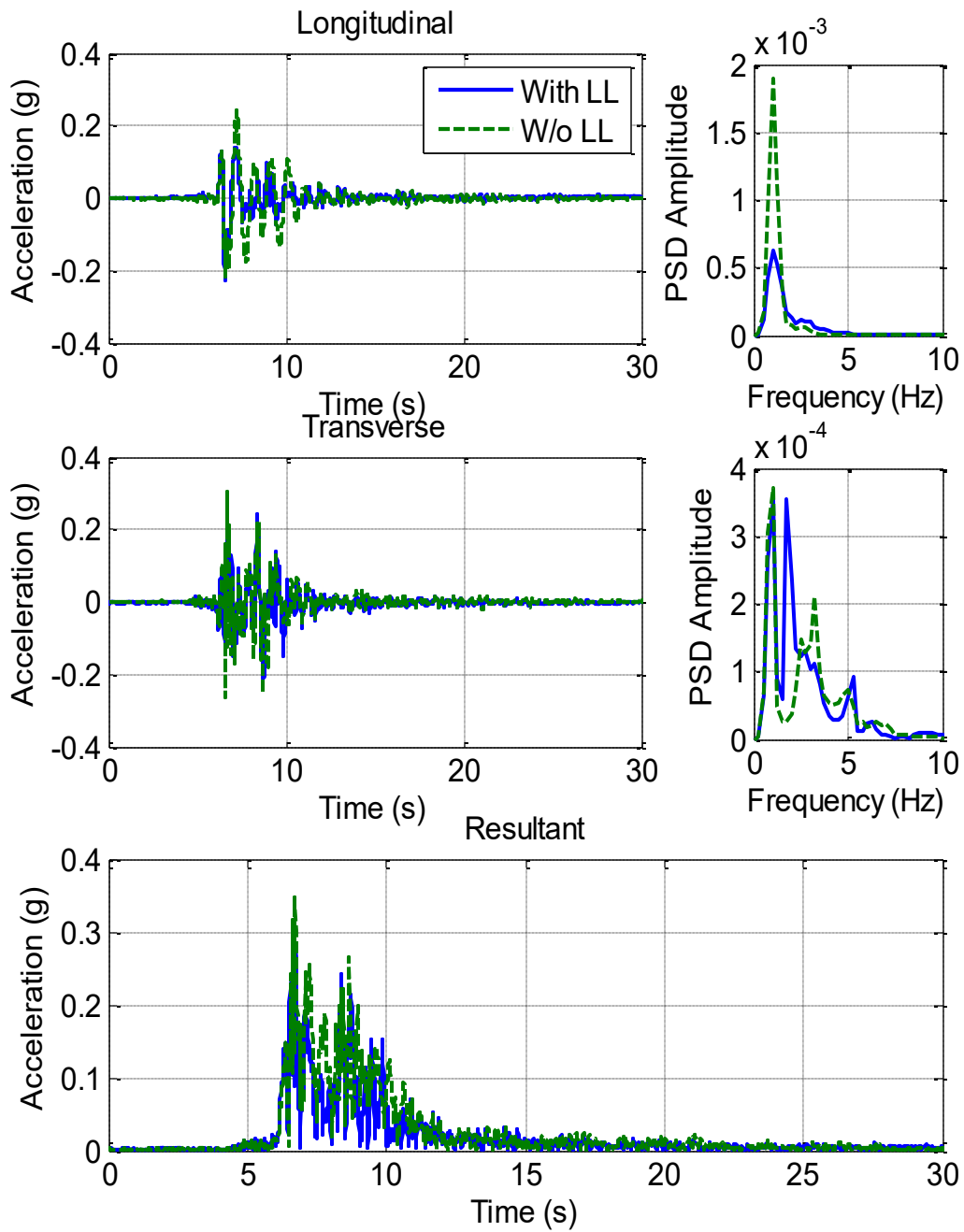


**Figure 5.6.24. Acceleration Histories and PSD Spectra at Mid-Span of Middle Girder (75% DE)**

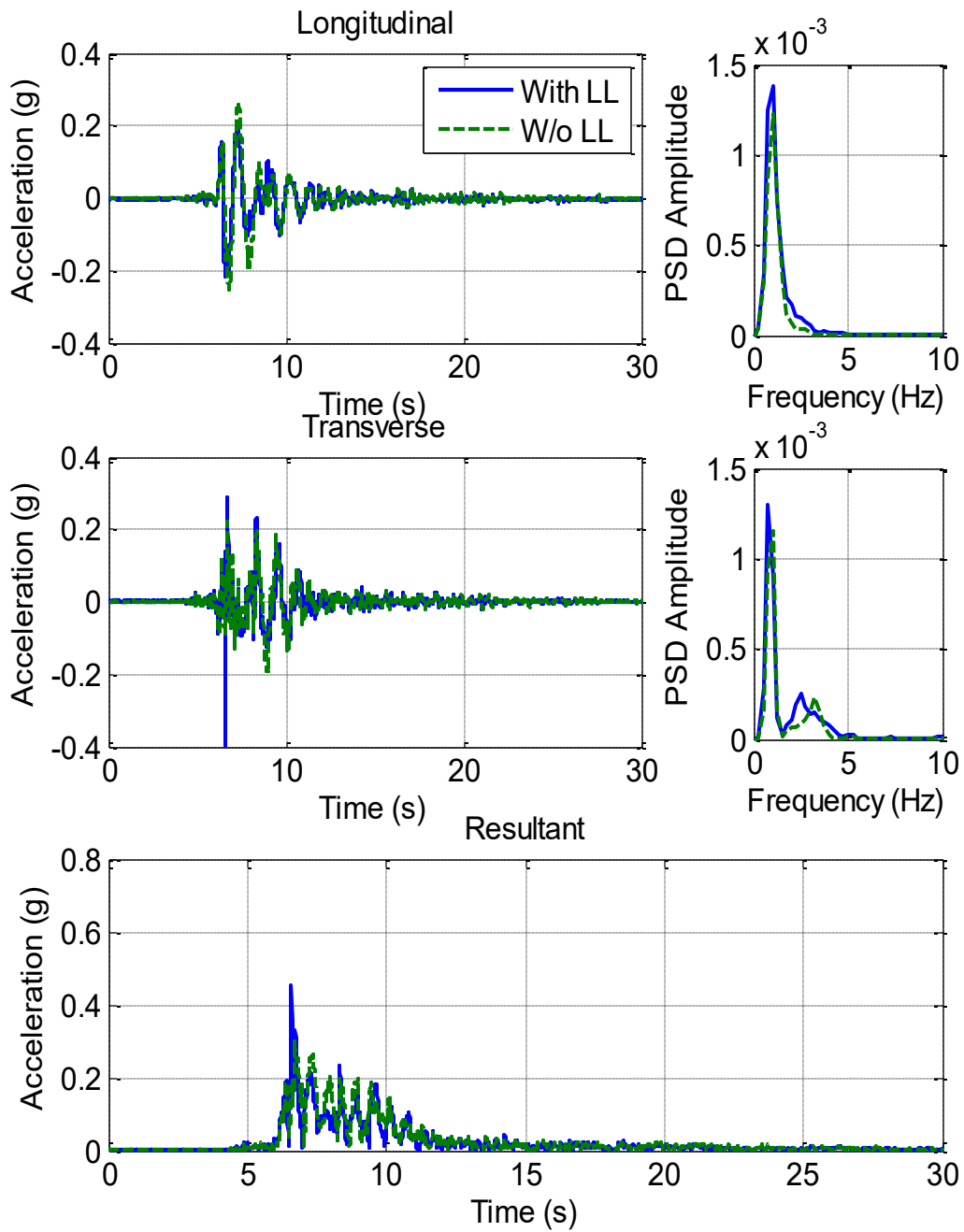


**Figure 5.6.25. Acceleration Histories and PSD Spectra at Mid-Span of Middle Girder (100% DE)**

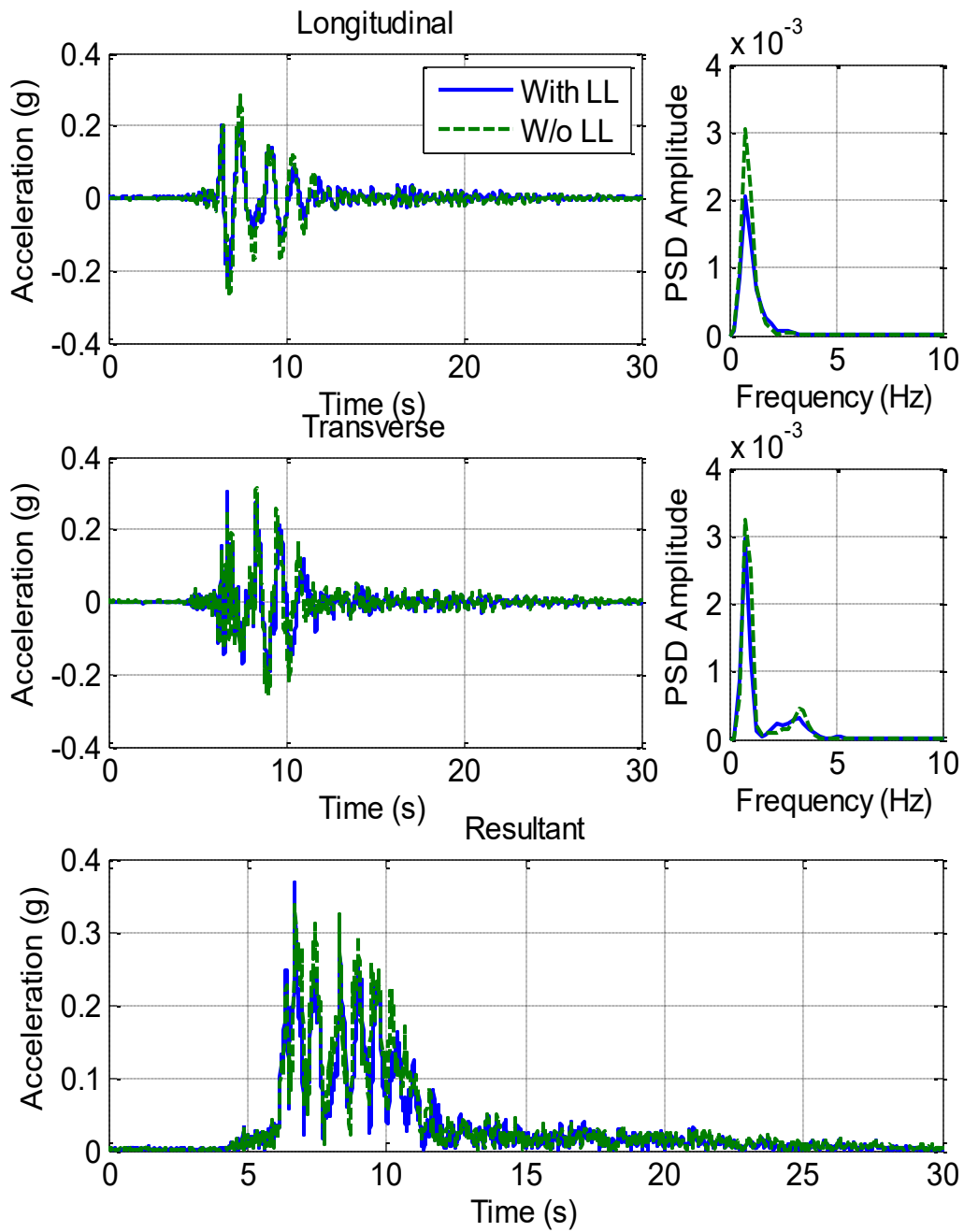


**Figure 5.6.26. Acceleration Histories and PSD Spectra at Mid-Span of Middle Girder (150% DE)**

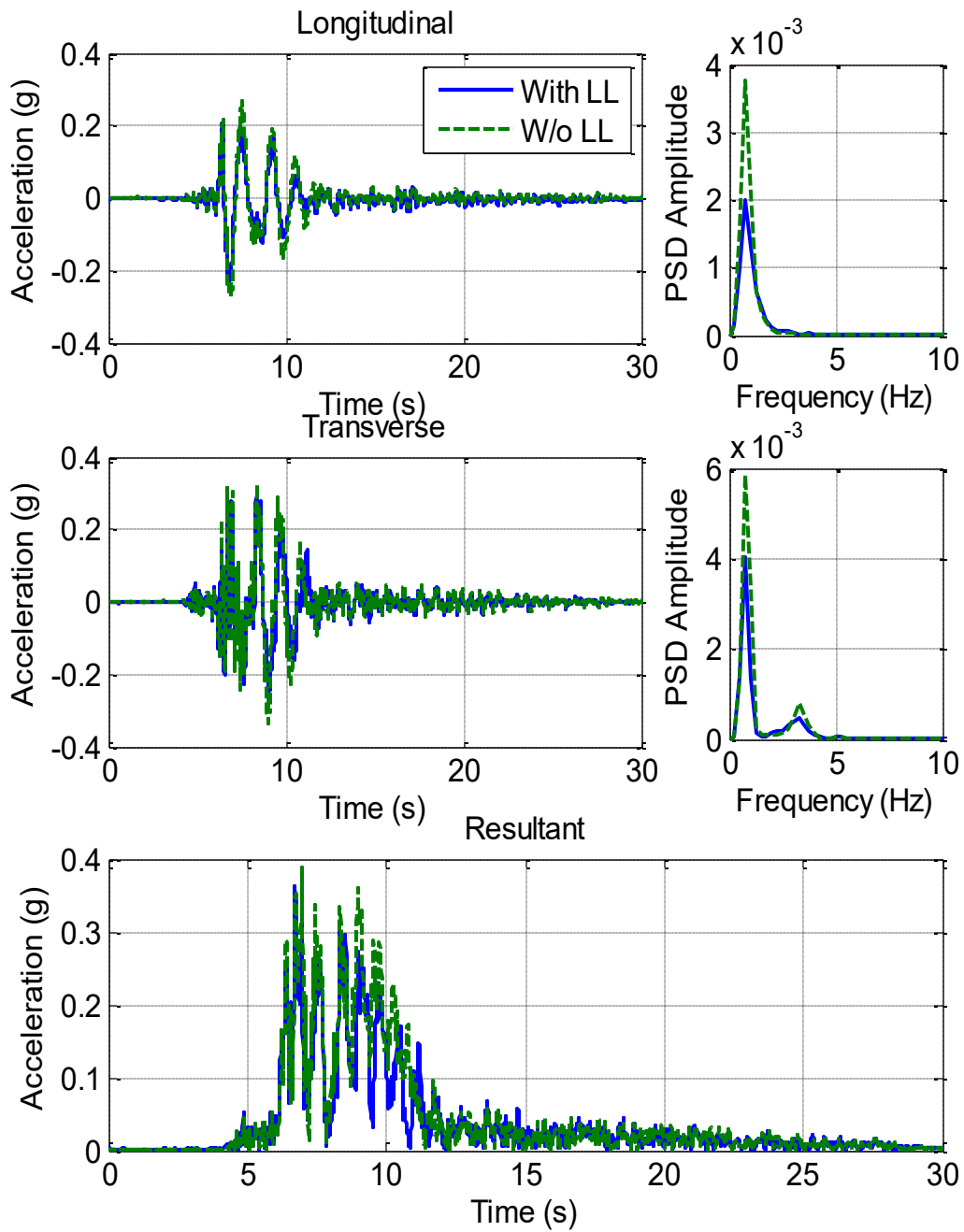


**Figure 5.6.27. Acceleration Histories and PSD Spectra at Mid-Span of Middle Girder (200% DE)**

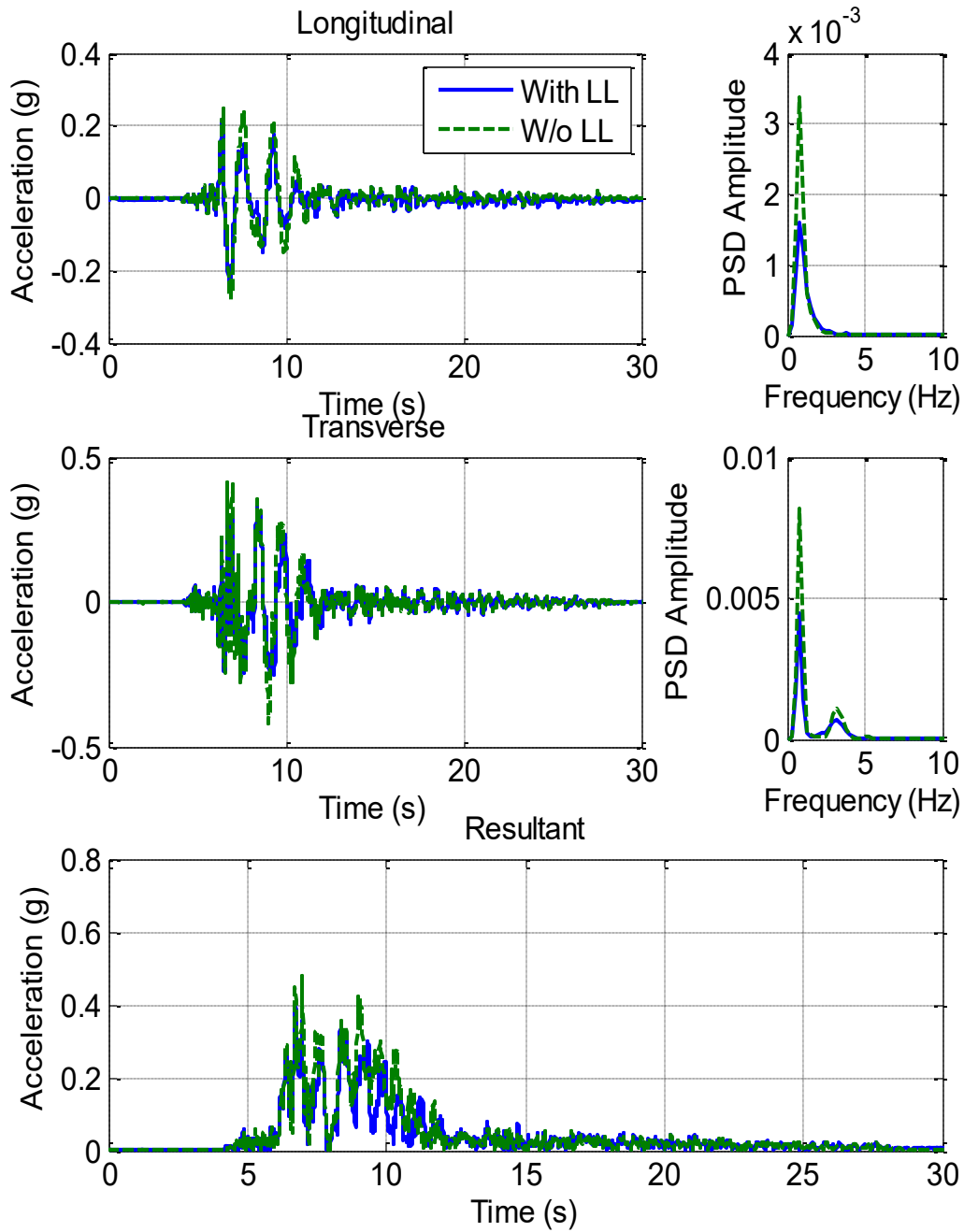


**Figure 5.6.28. Acceleration Histories and PSD Spectra at Mid-Span of Middle Girder (250% DE)**

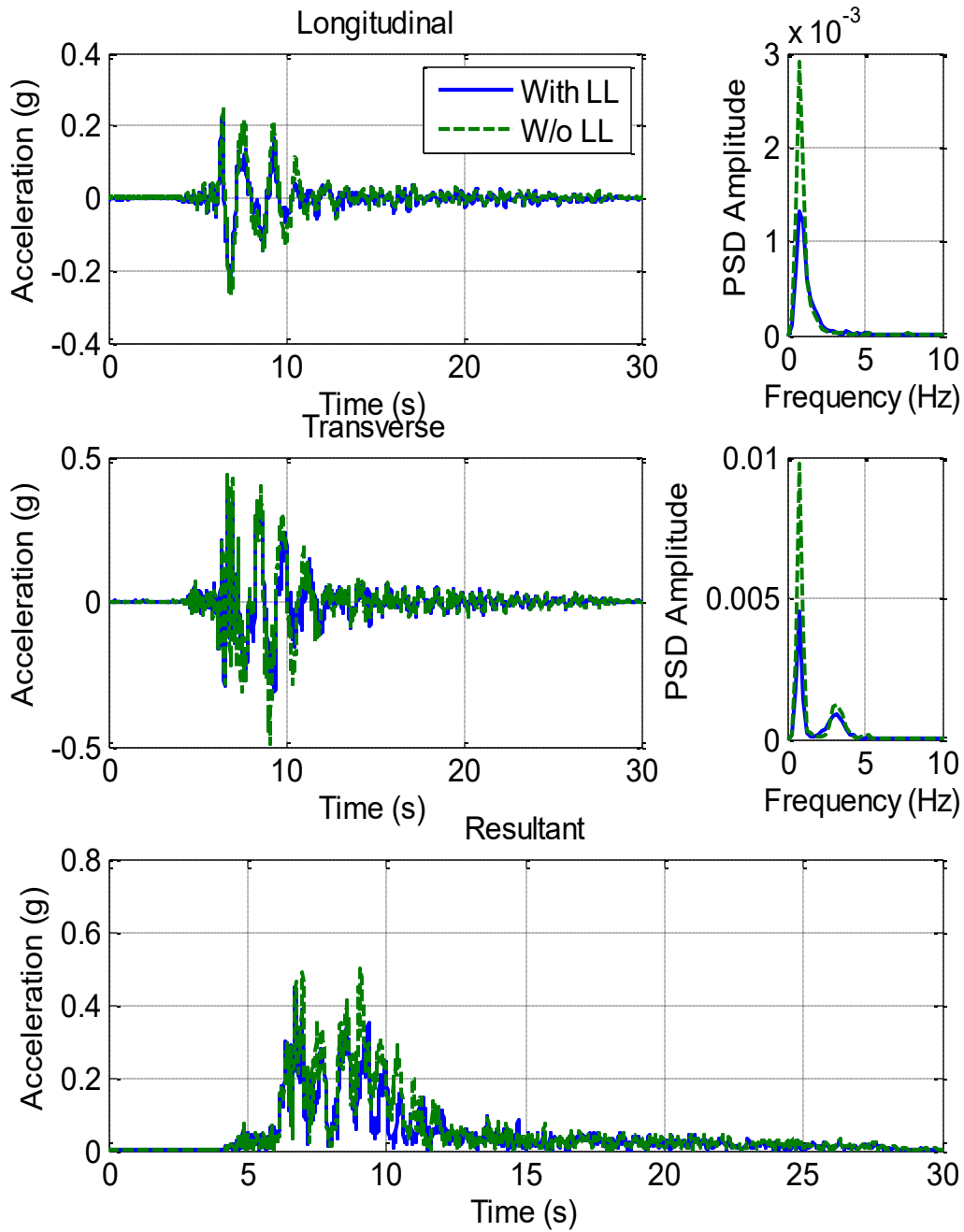


**Figure 5.6.29. Acceleration Histories and PSD Spectra at Mid-Span of Middle Girder (300% DE)**

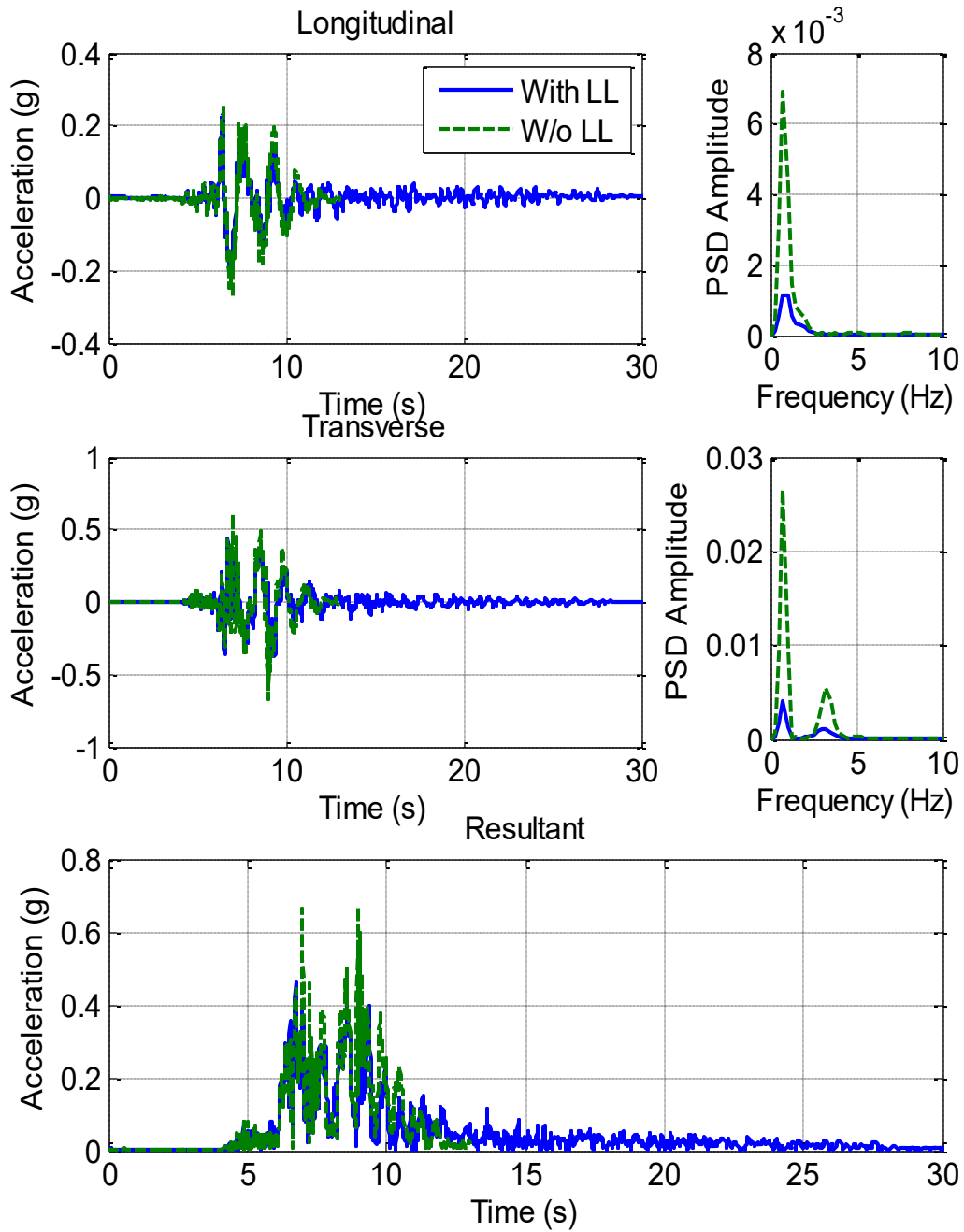


**Figure 5.6.30. Acceleration Histories and PSD Spectra at Mid-Span of Middle Girder (350% DE)**

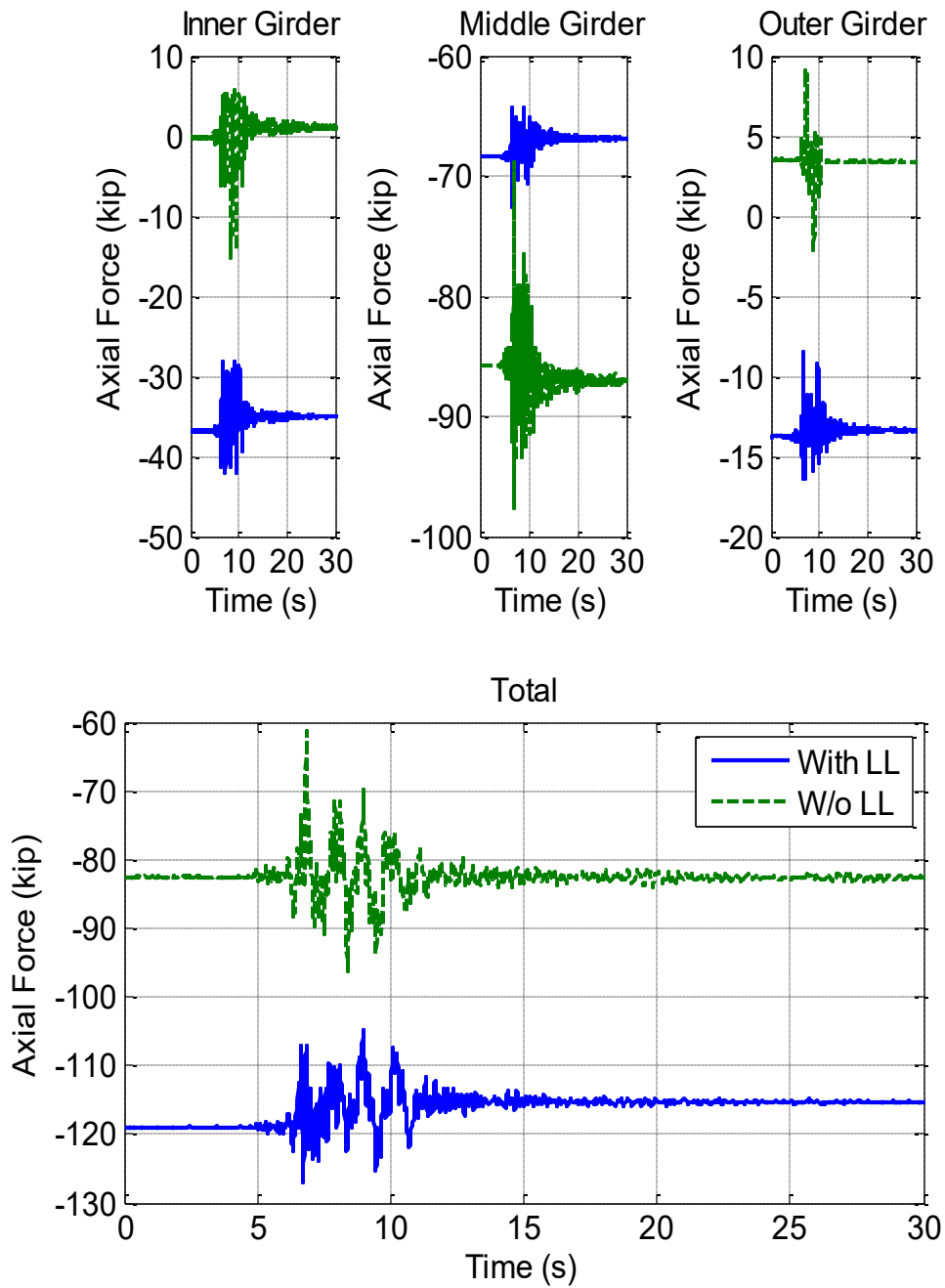
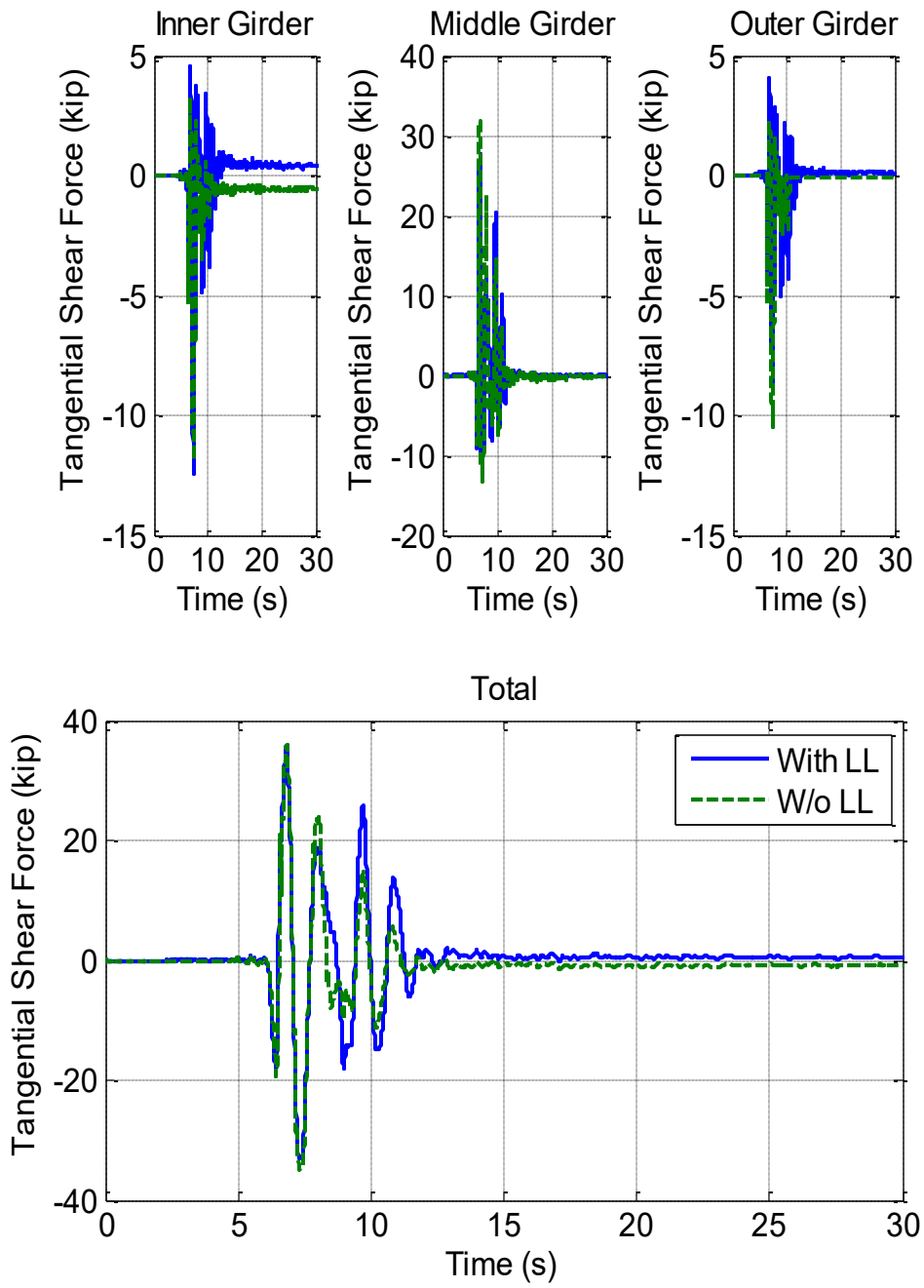
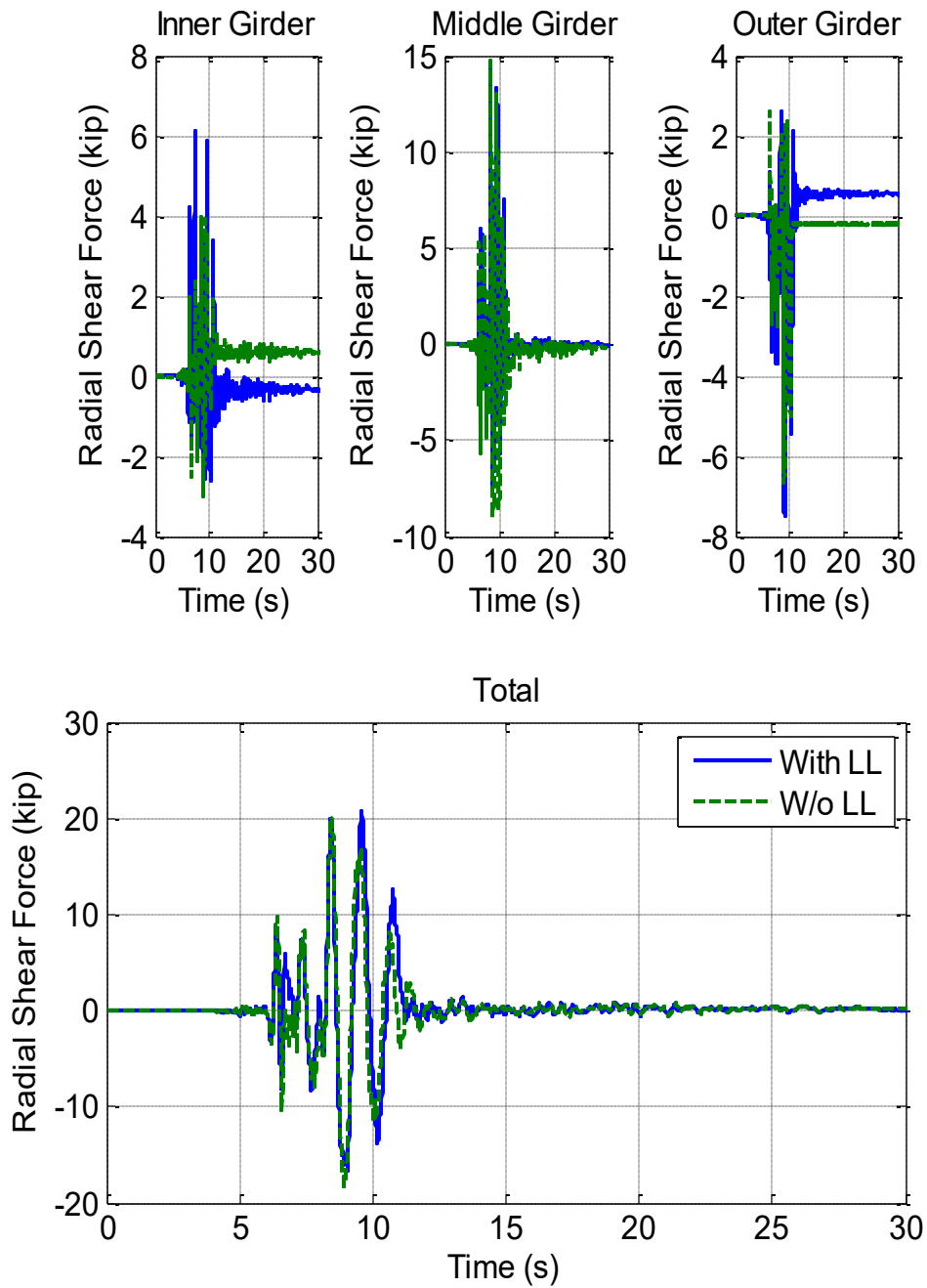


Figure 5.7.1. South Bent Load Cell Axial Force Histories (100% DE)



**Figure 5.7.2. South Bent Load Cell Tangential Shear Force Histories (100% DE)**



**Figure 5.7.3. South Bent Load Cell Radial Shear Force Histories (100% DE)**

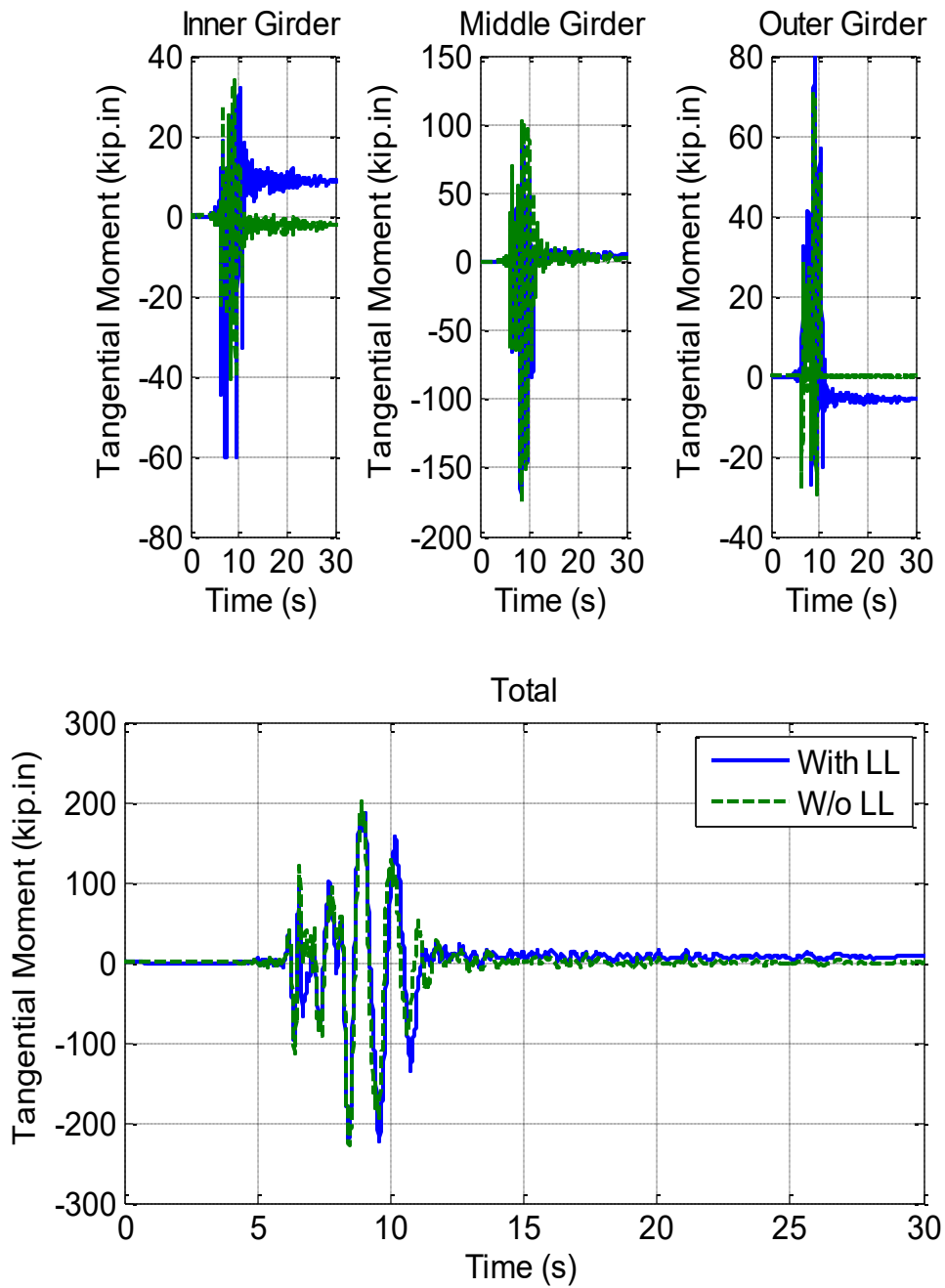


**Figure 5.7.4. South Bent Load Cell Tangential Moment Histories (100% DE)**

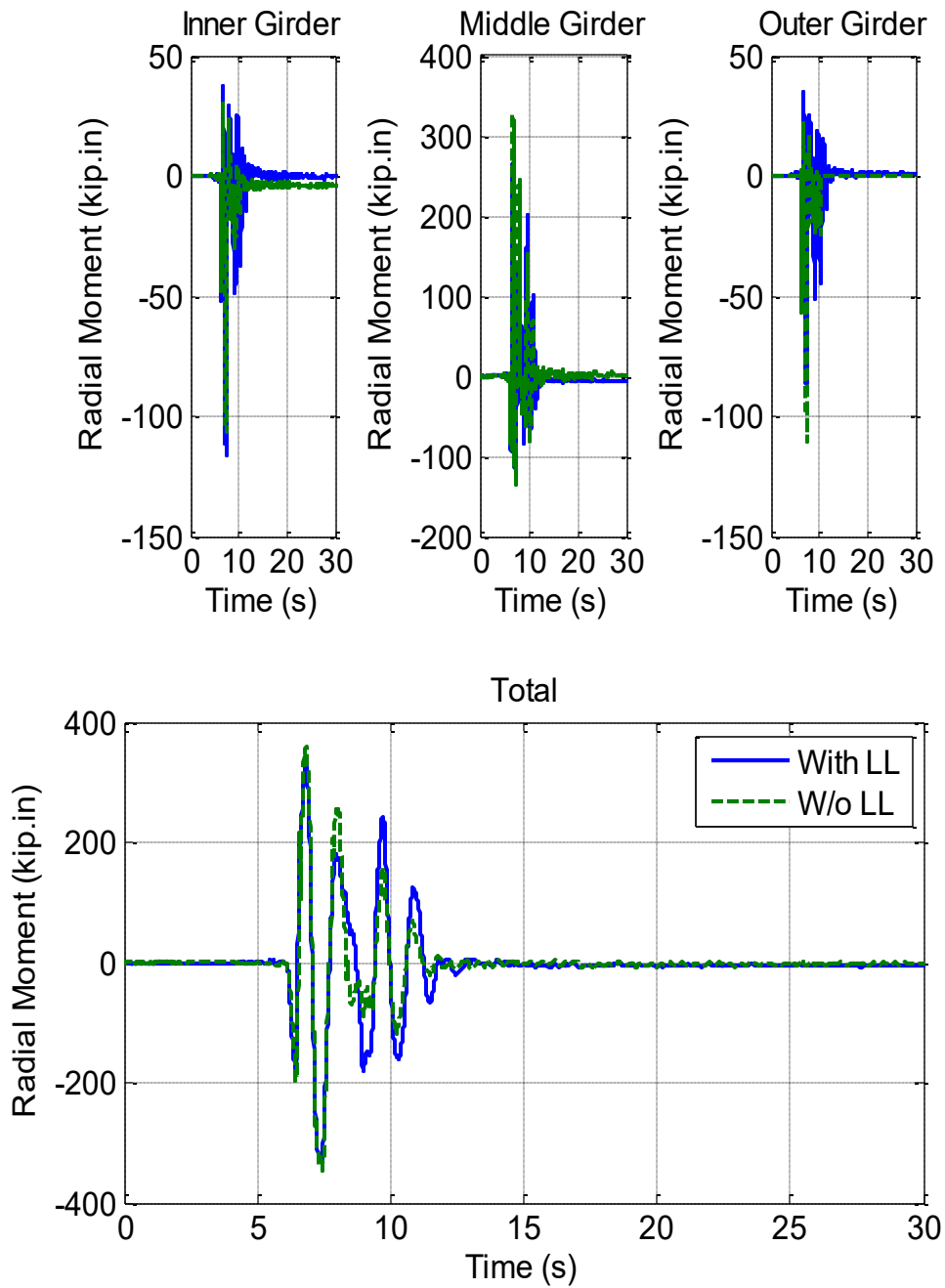


**Figure 5.7.5. South Bent Load Cell Radial Moment Histories (100% DE)**

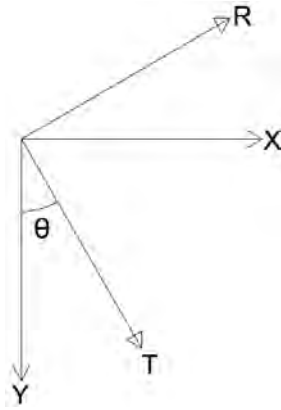


**Figure 5.7.6. Coordinate System Transformation**

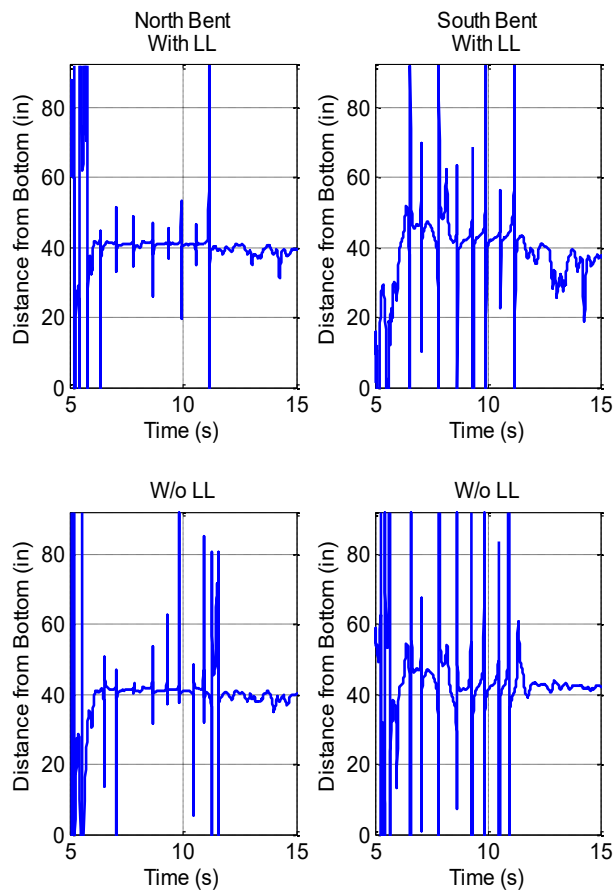


**Figure 5.7.7. Inflection Point Histories in North and South Bents (100% DE)**

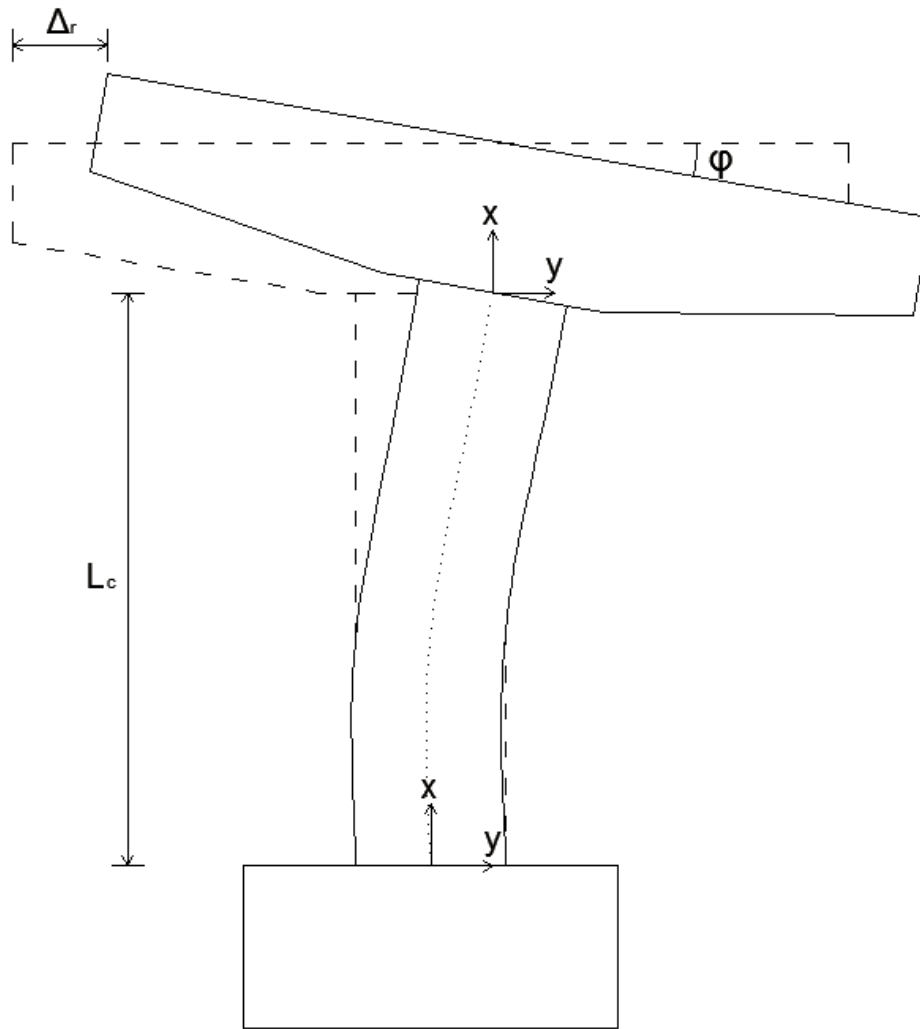


**Figure 5.7.8. Inflection Point Geometry**

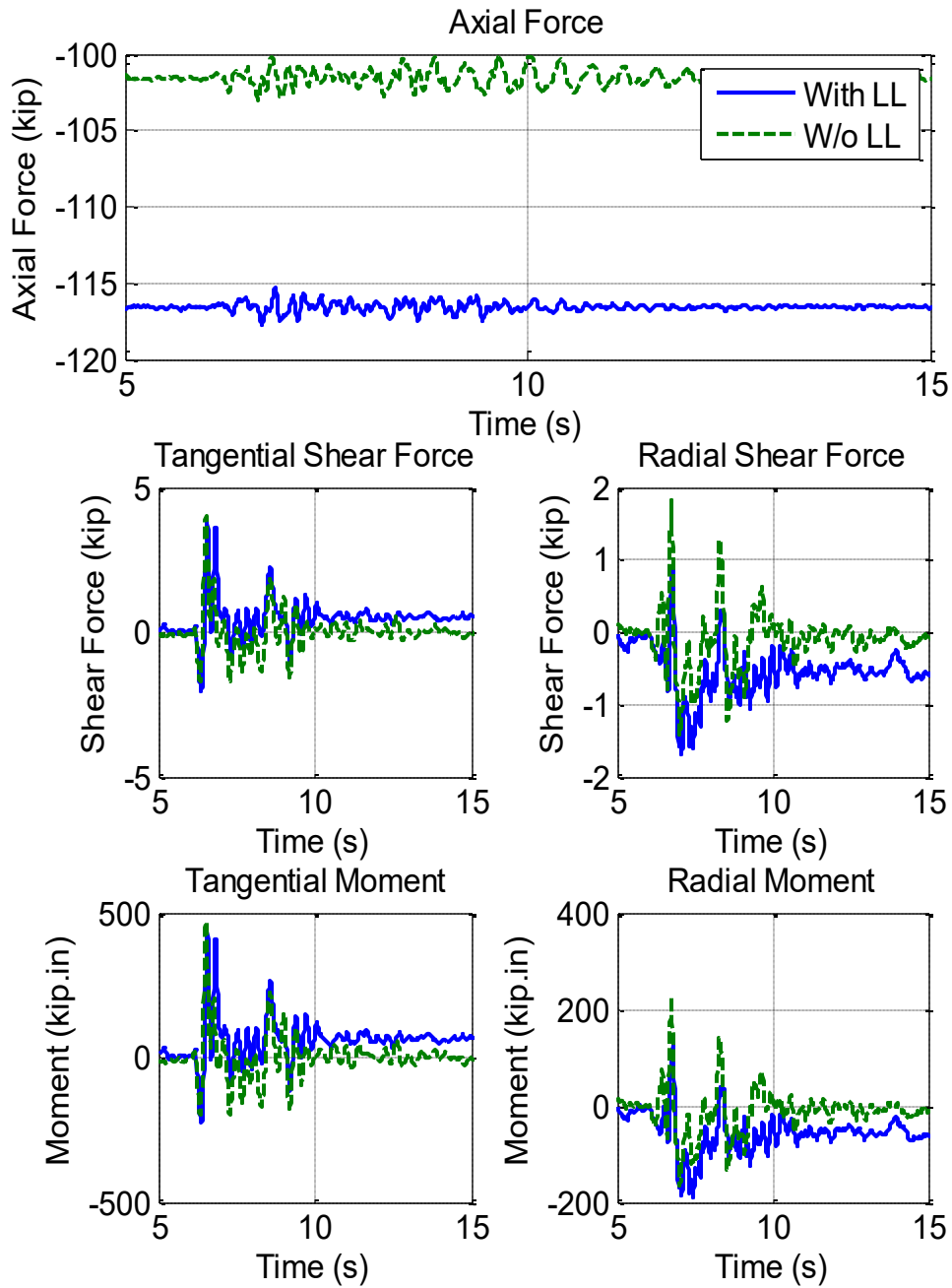


**Figure 5.7.9. Forces and Moments at the Bottom of North Bent (10% DE)**

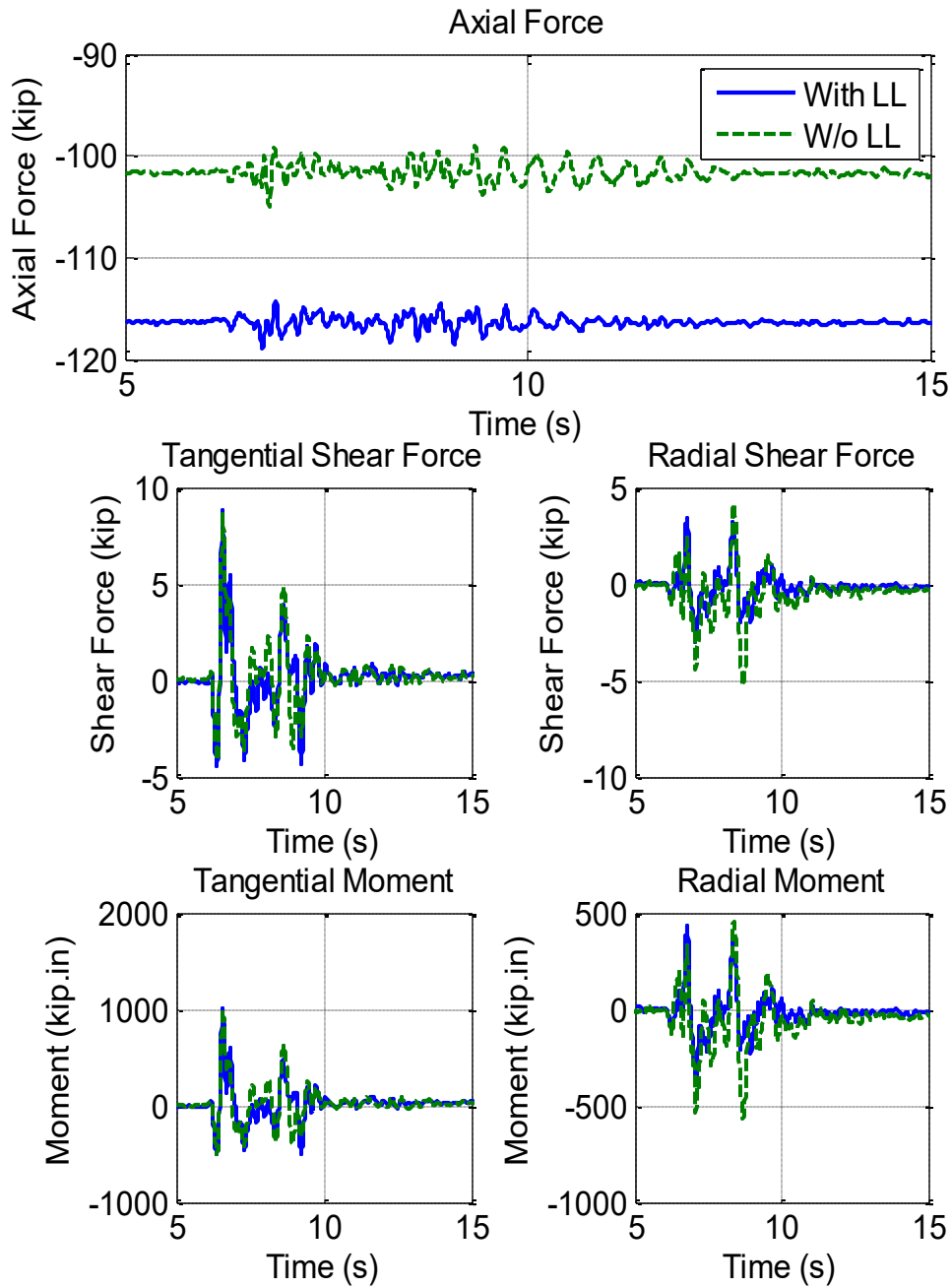


**Figure 5.7.10. Forces and Moments at the Bottom of North Bent (20% DE)**

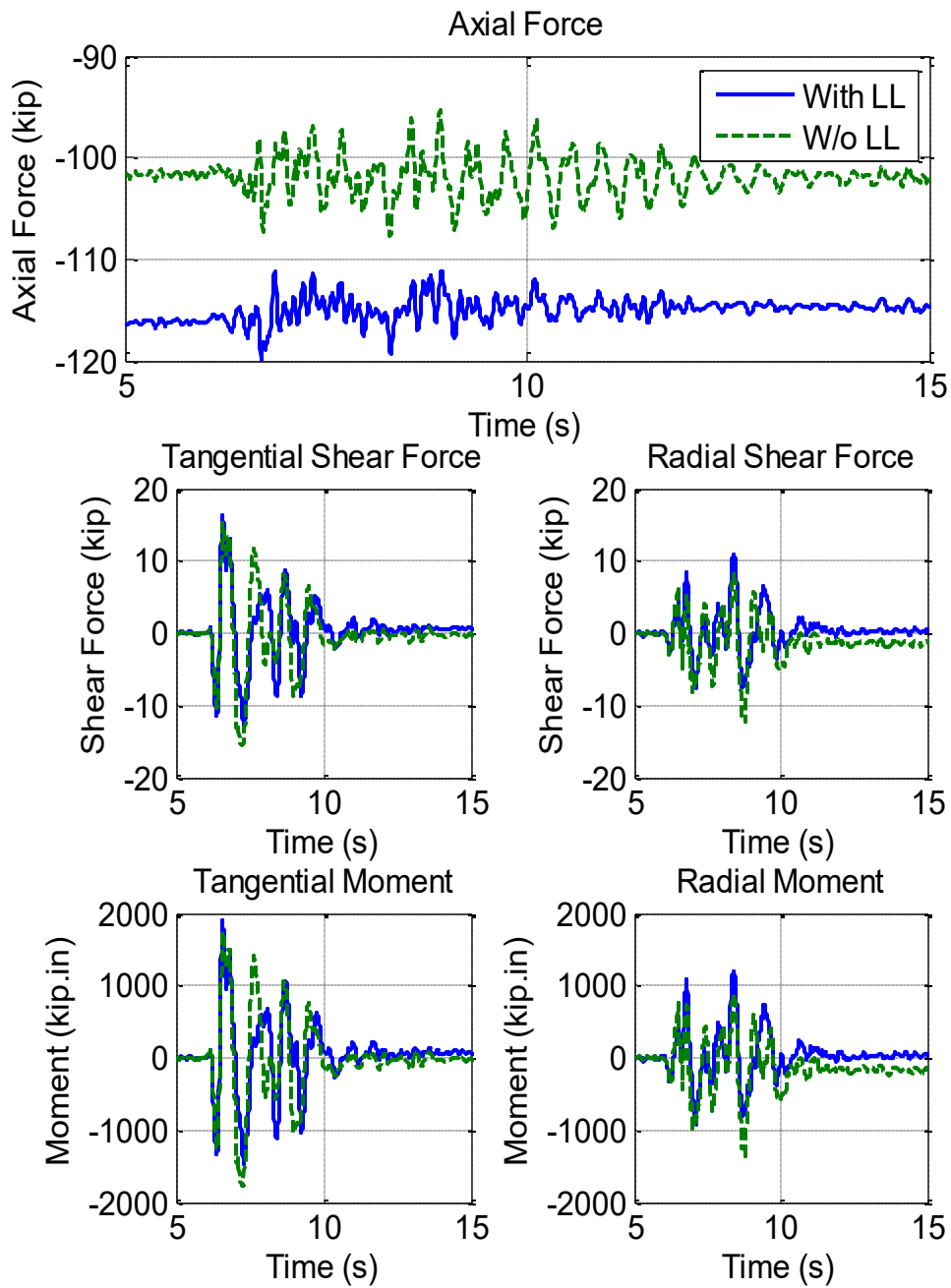


**Figure 5.7.11. Forces and Moments at the Bottom of North Bent (50% DE)**

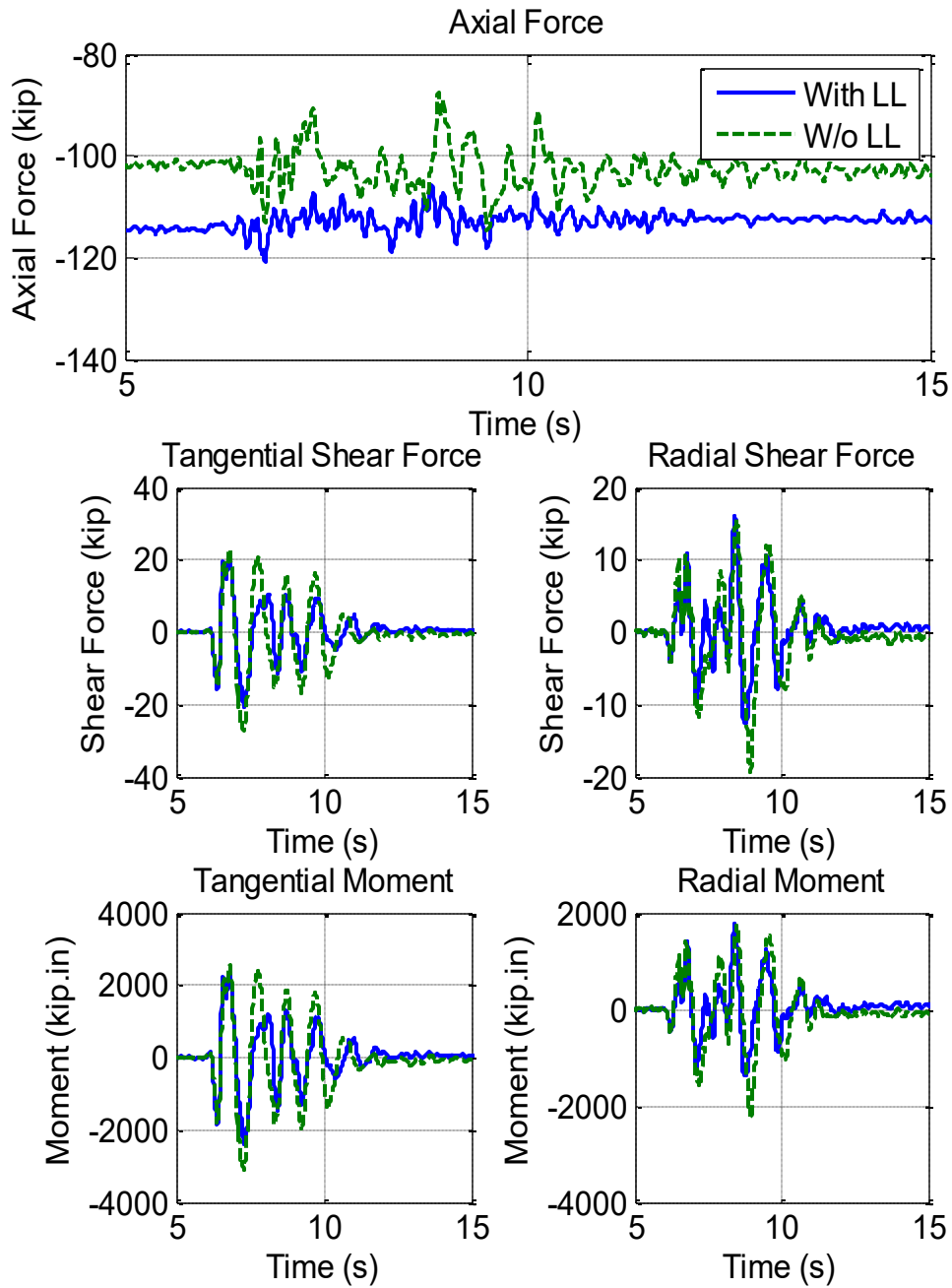


**Figure 5.7.12. Forces and Moments at the Bottom of North Bent (75% DE)**

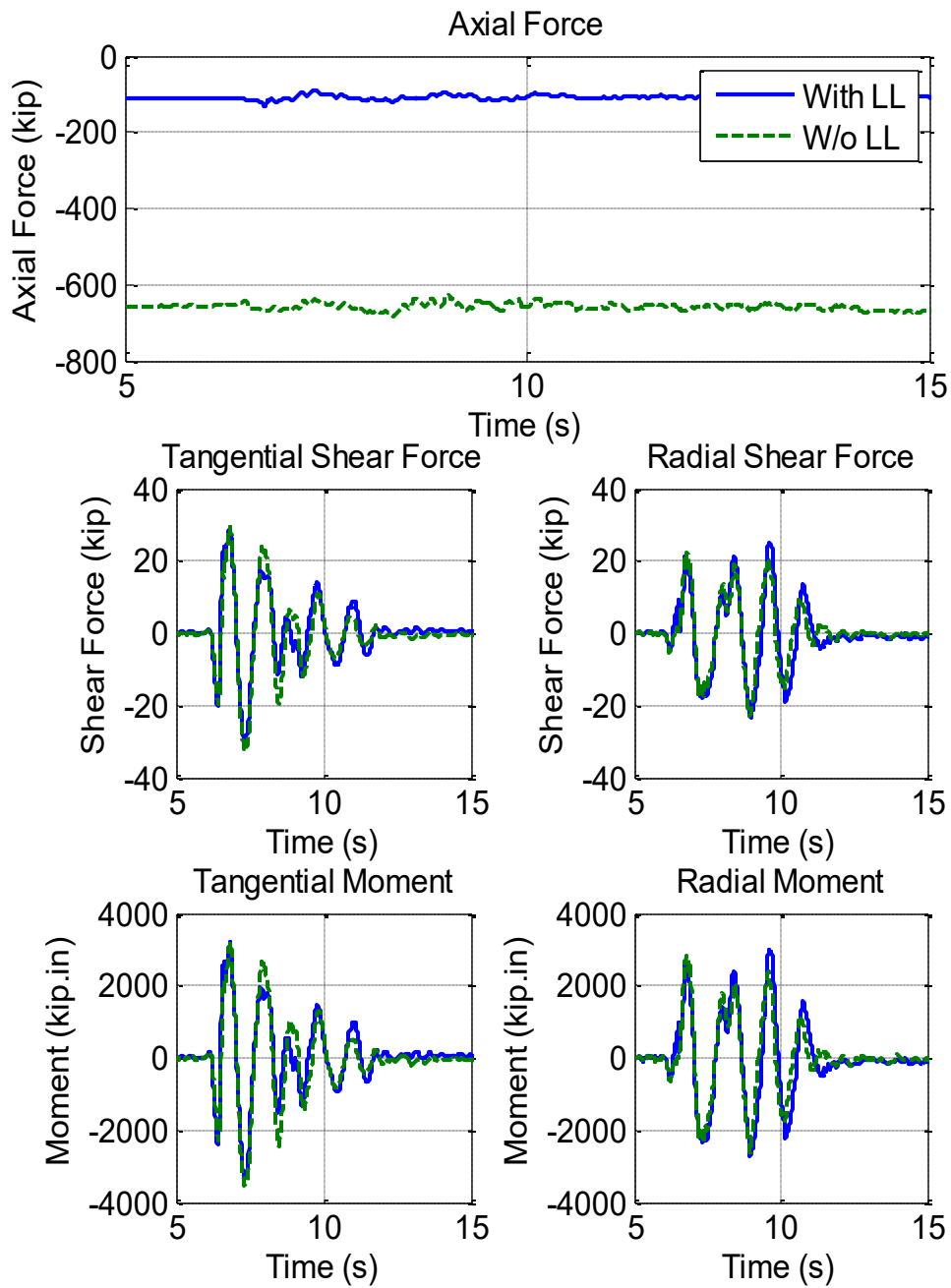


**Figure 5.7.13. Forces and Moments at the Bottom of North Bent (100% DE)**

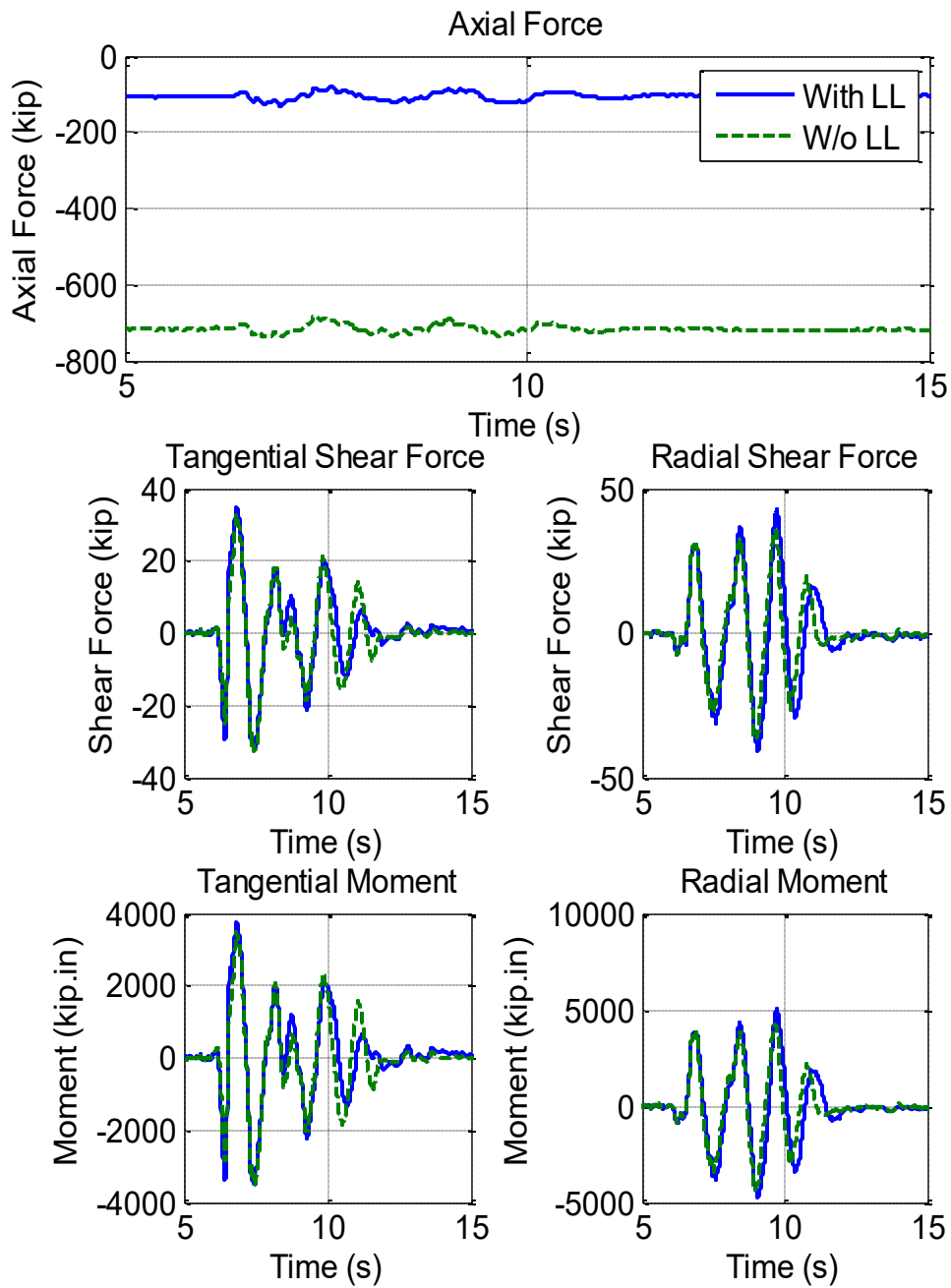


**Figure 5.7.14. Forces and Moments at the Bottom of North Bent (150% DE)**

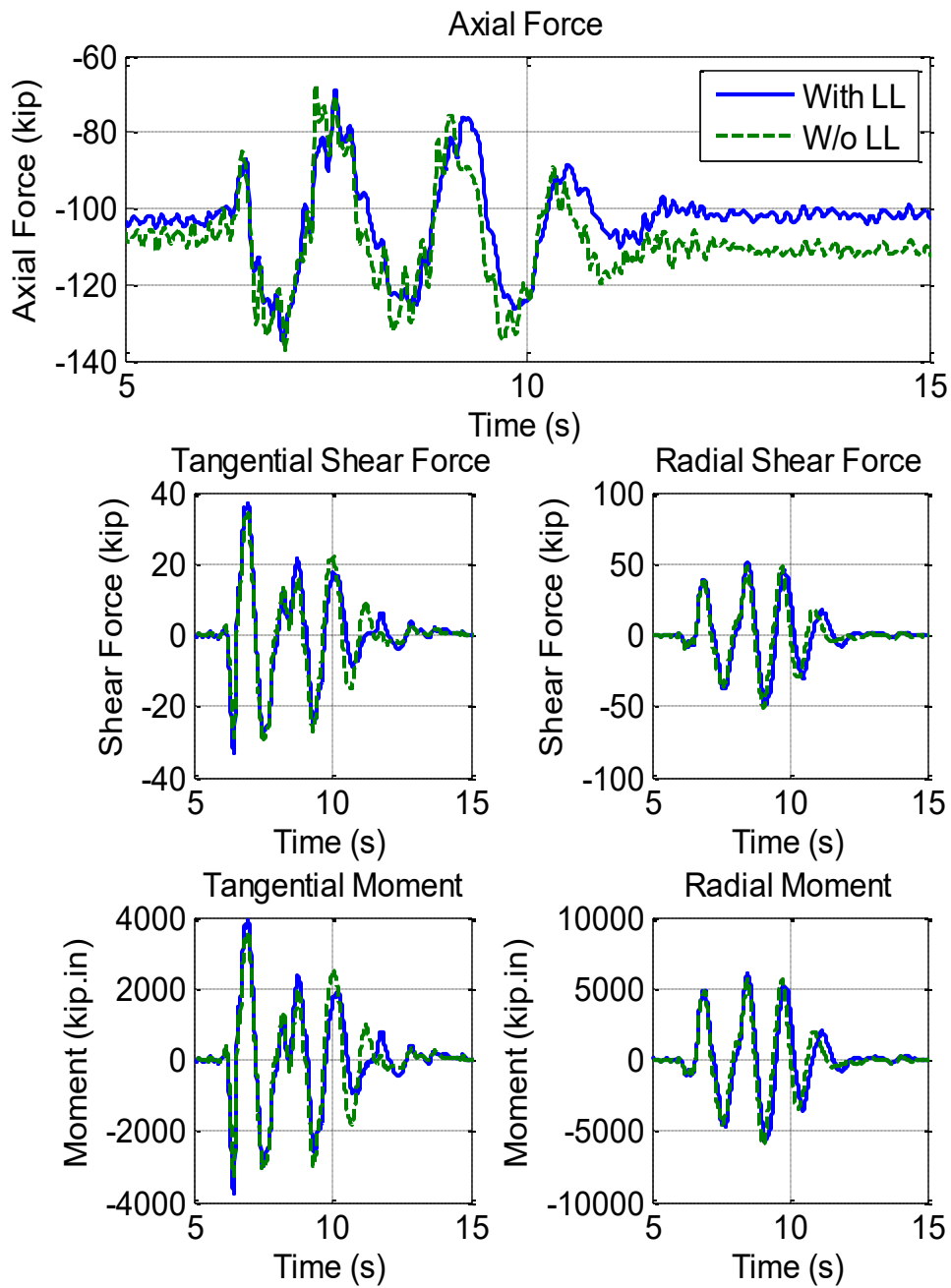


**Figure 5.7.15. Forces and Moments at the Bottom of North Bent (200% DE)**

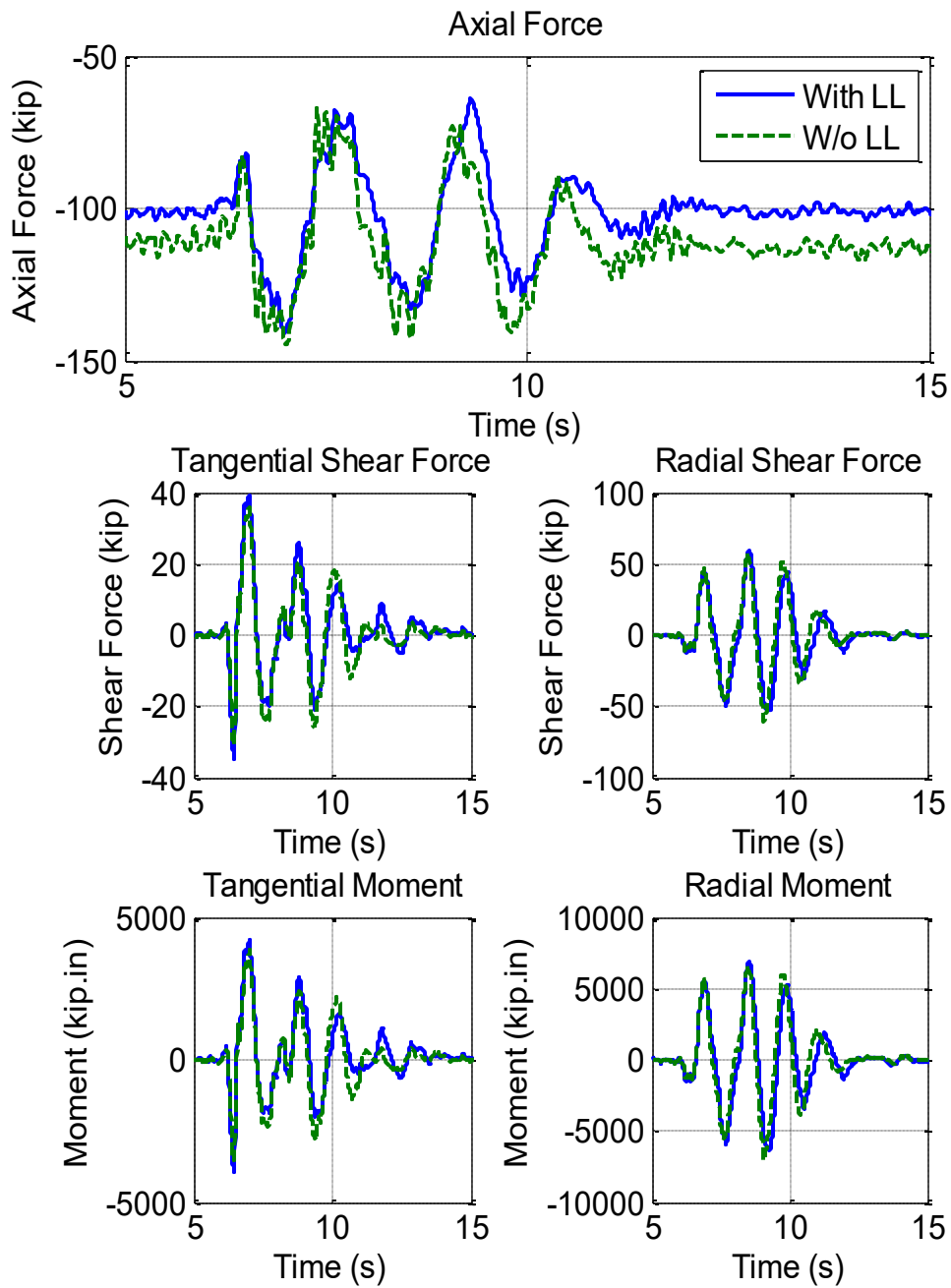


**Figure 5.7.16. Forces and Moments at the Bottom of North Bent (250% DE)**

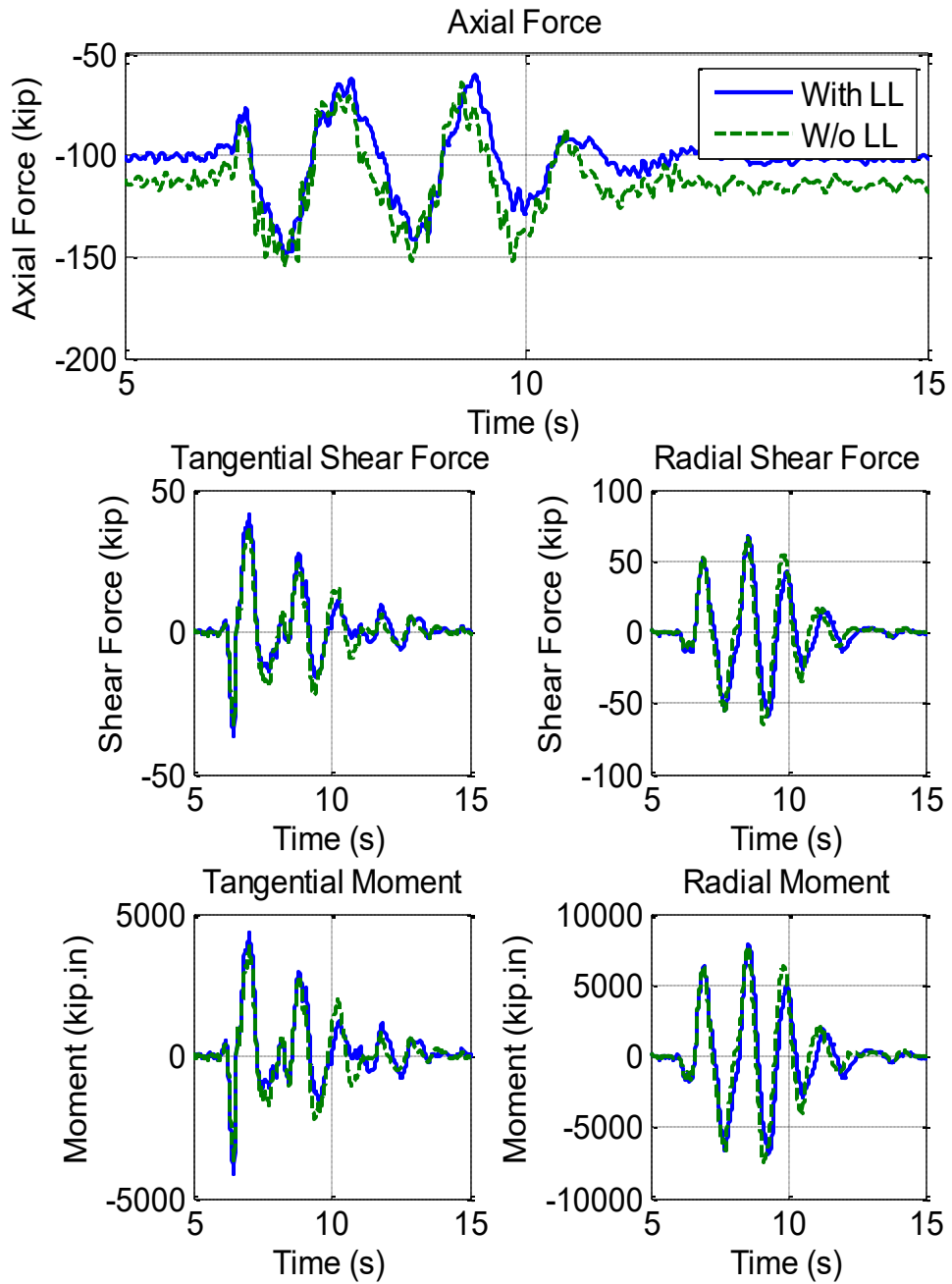


**Figure 5.7.17. Forces and Moments at the Bottom of North Bent (300% DE)**

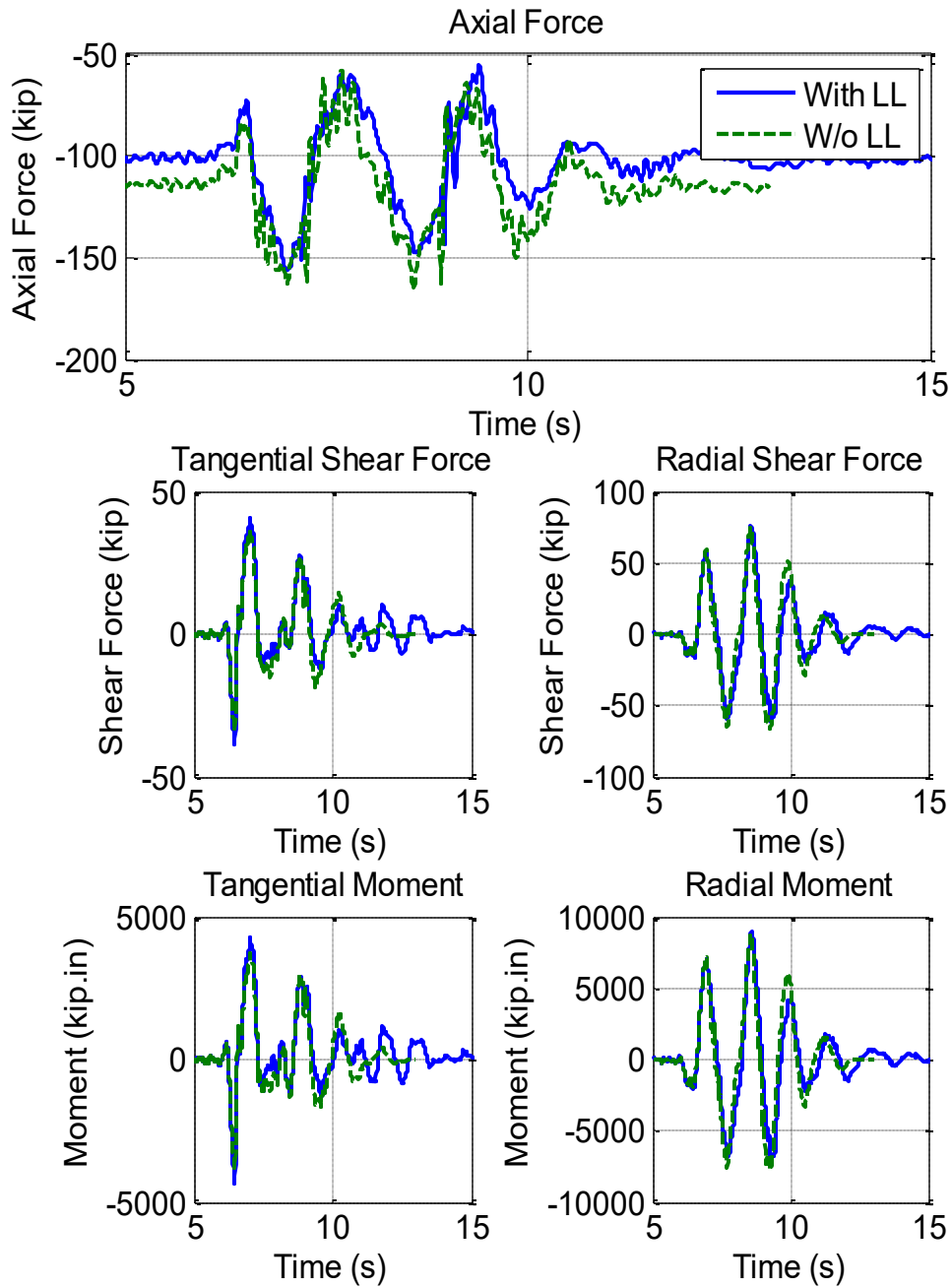


**Figure 5.7.18. Forces and Moments at the Bottom of North Bent (350% DE)**

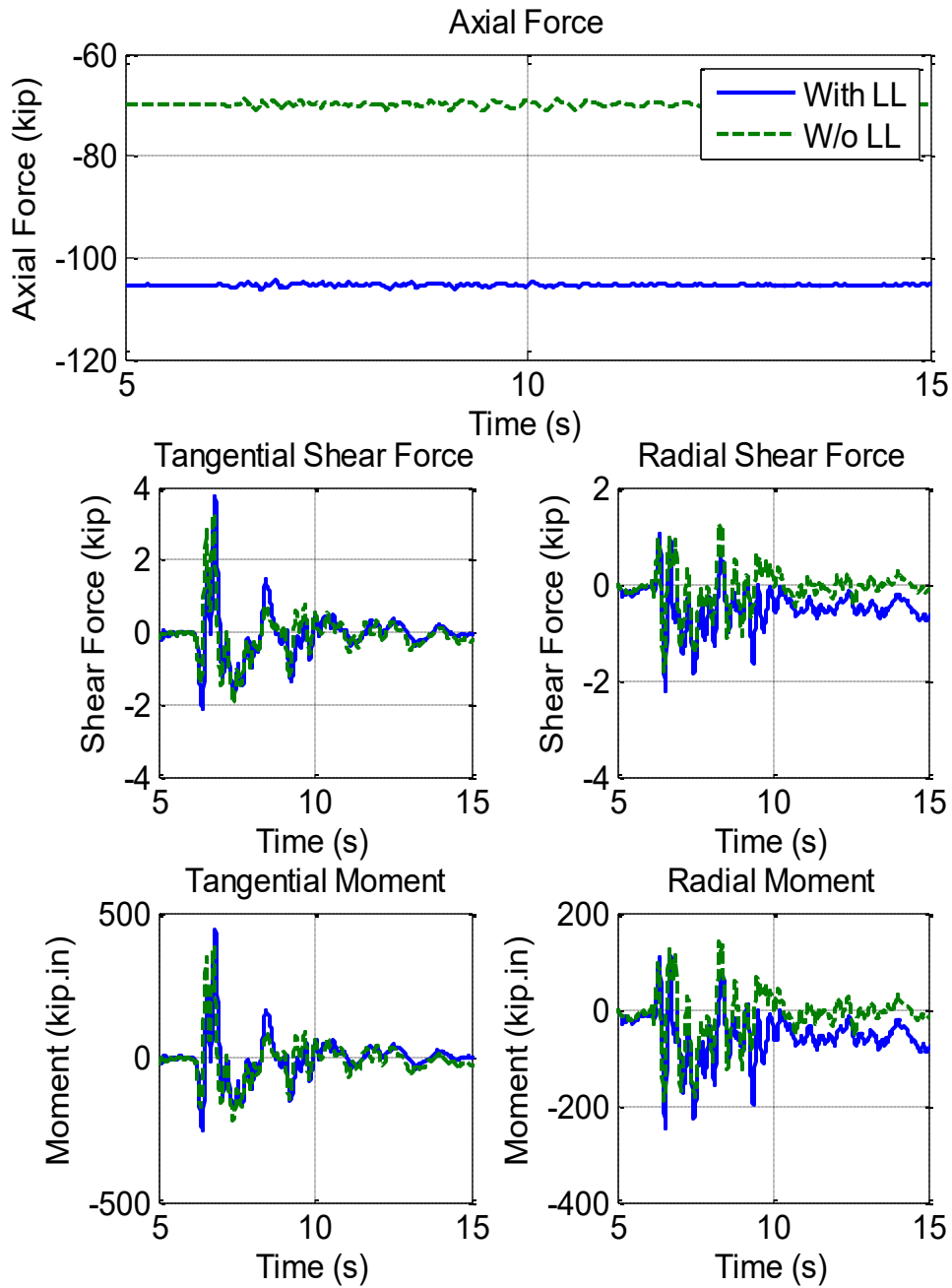


**Figure 5.7.19. Forces and Moments at the Bottom of South Bent (10% DE)**

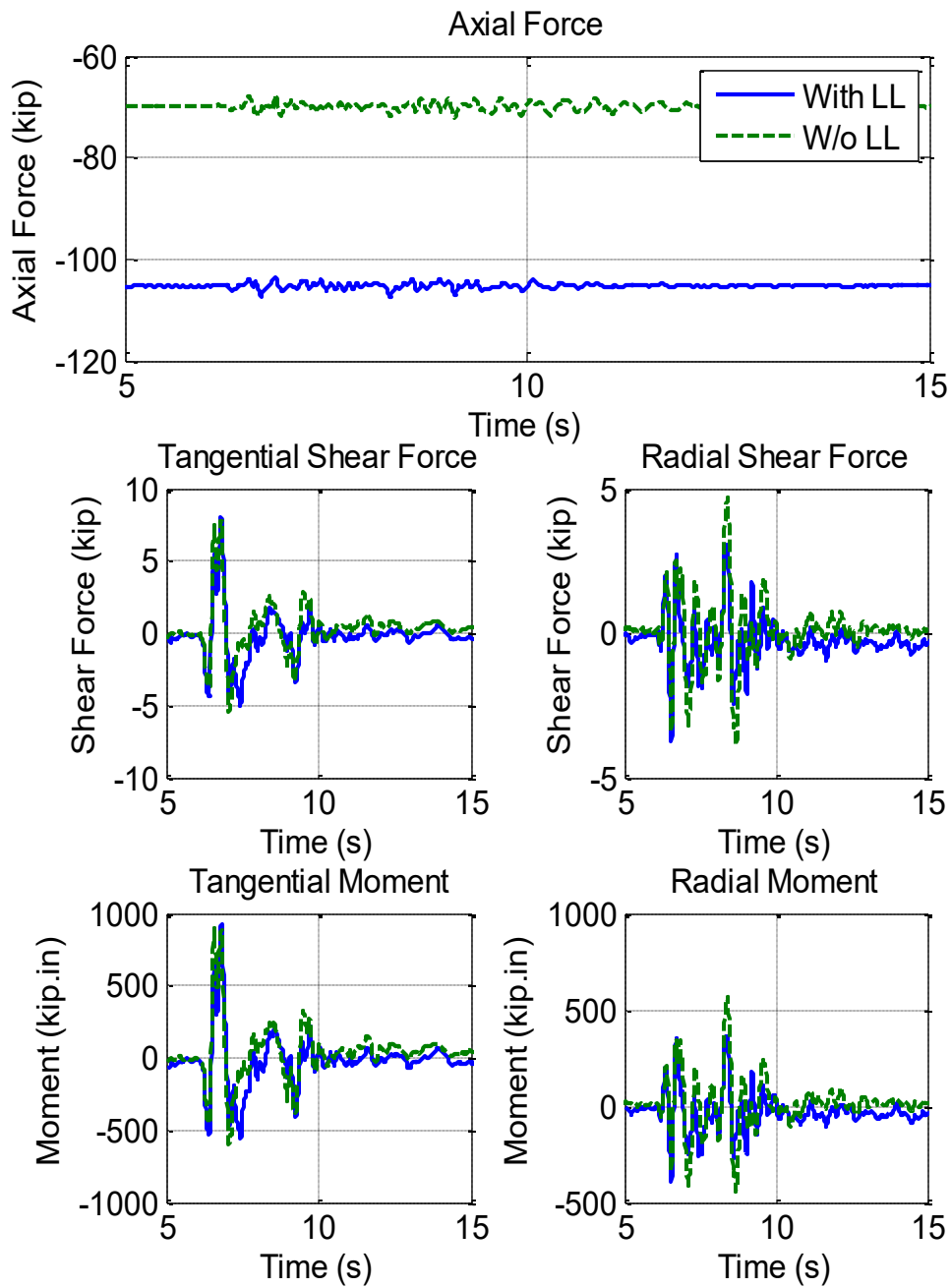


**Figure 5.7.20. Forces and Moments at the Bottom of South Bent (20% DE)**

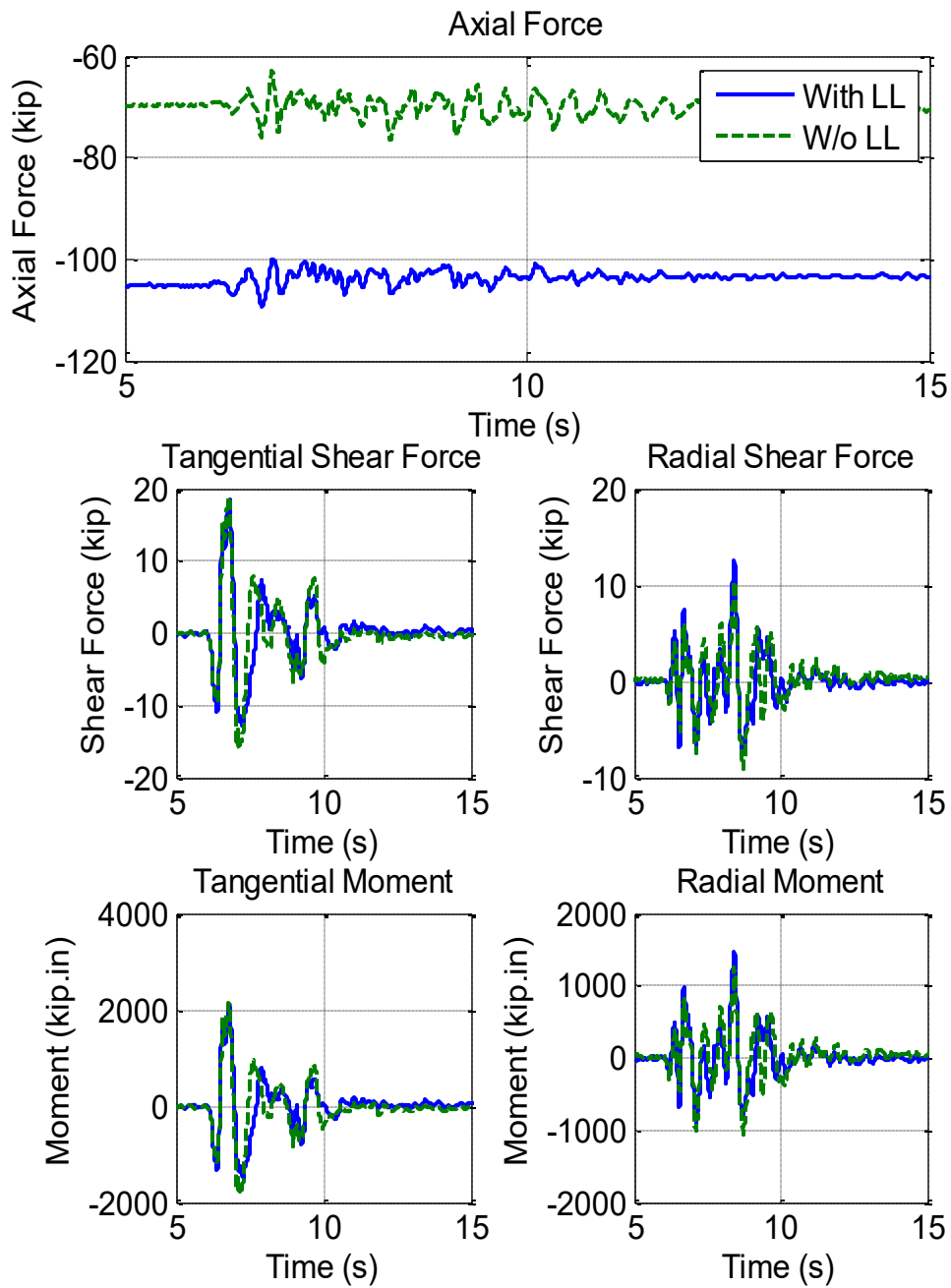


**Figure 5.7.21. Forces and Moments at the Bottom of South Bent (50% DE)**

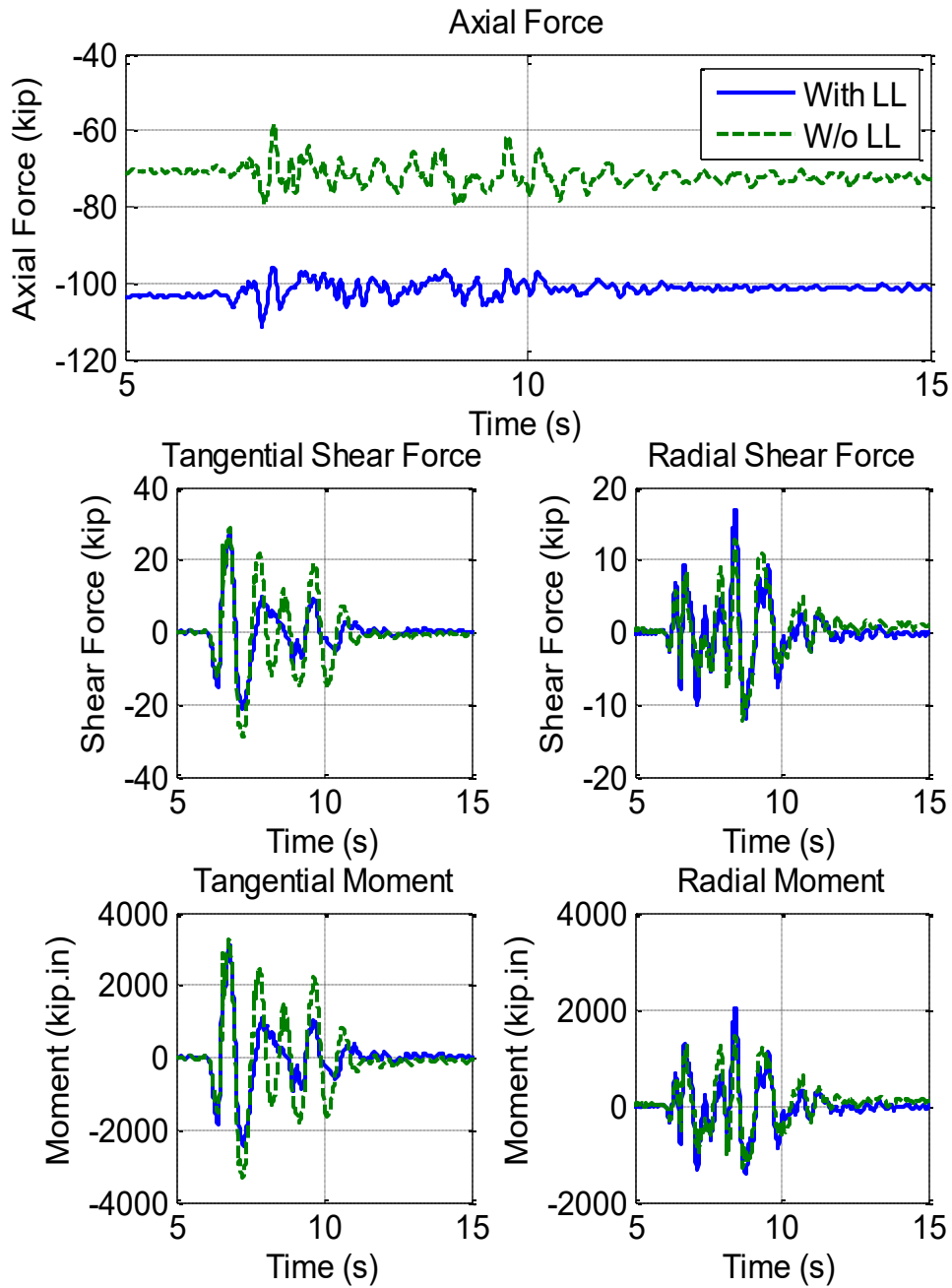


**Figure 5.7.22. Forces and Moments at the Bottom of South Bent (75% DE)**

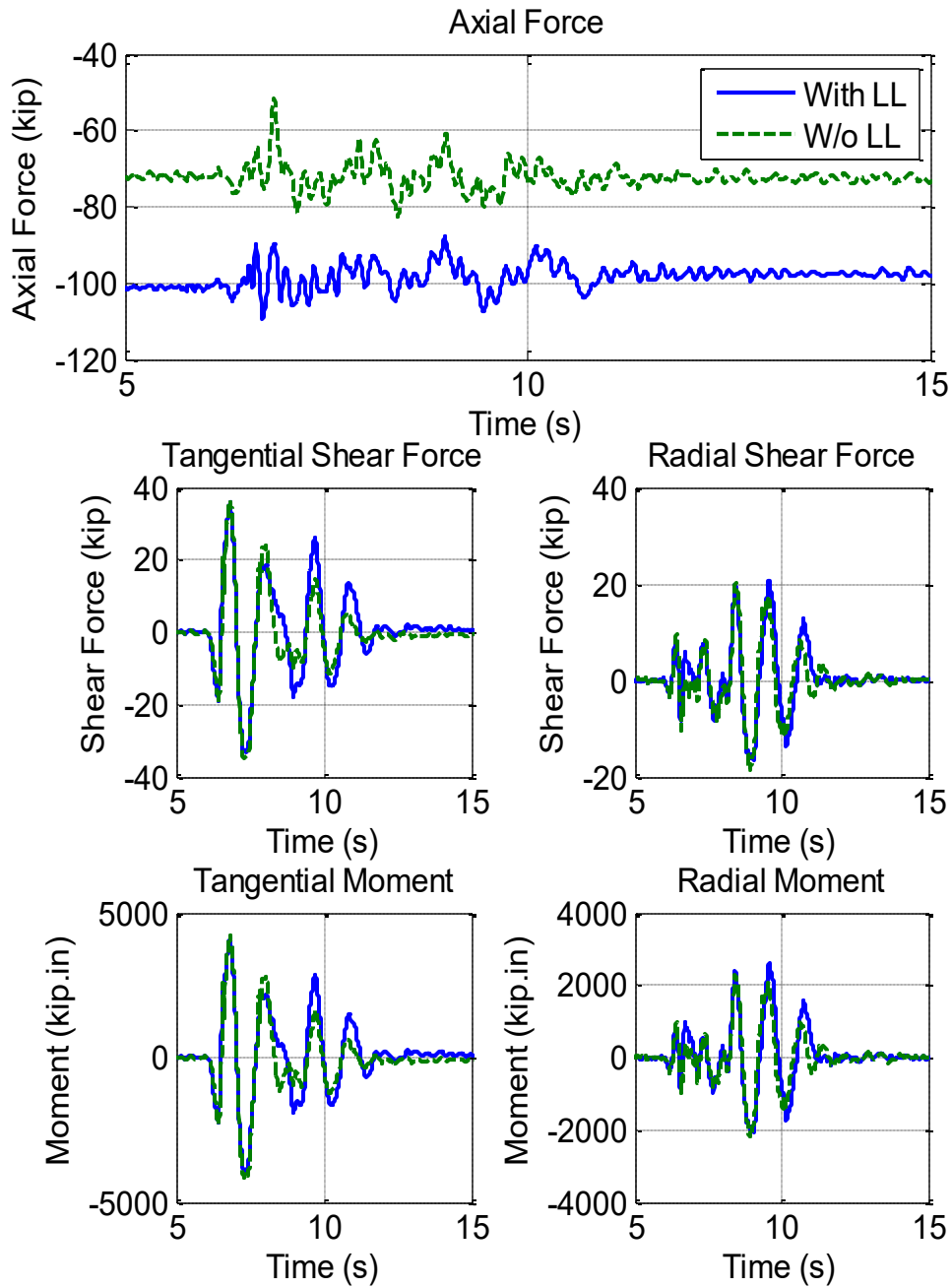


**Figure 5.7.23. Forces and Moments at the Bottom of South Bent (100% DE)**

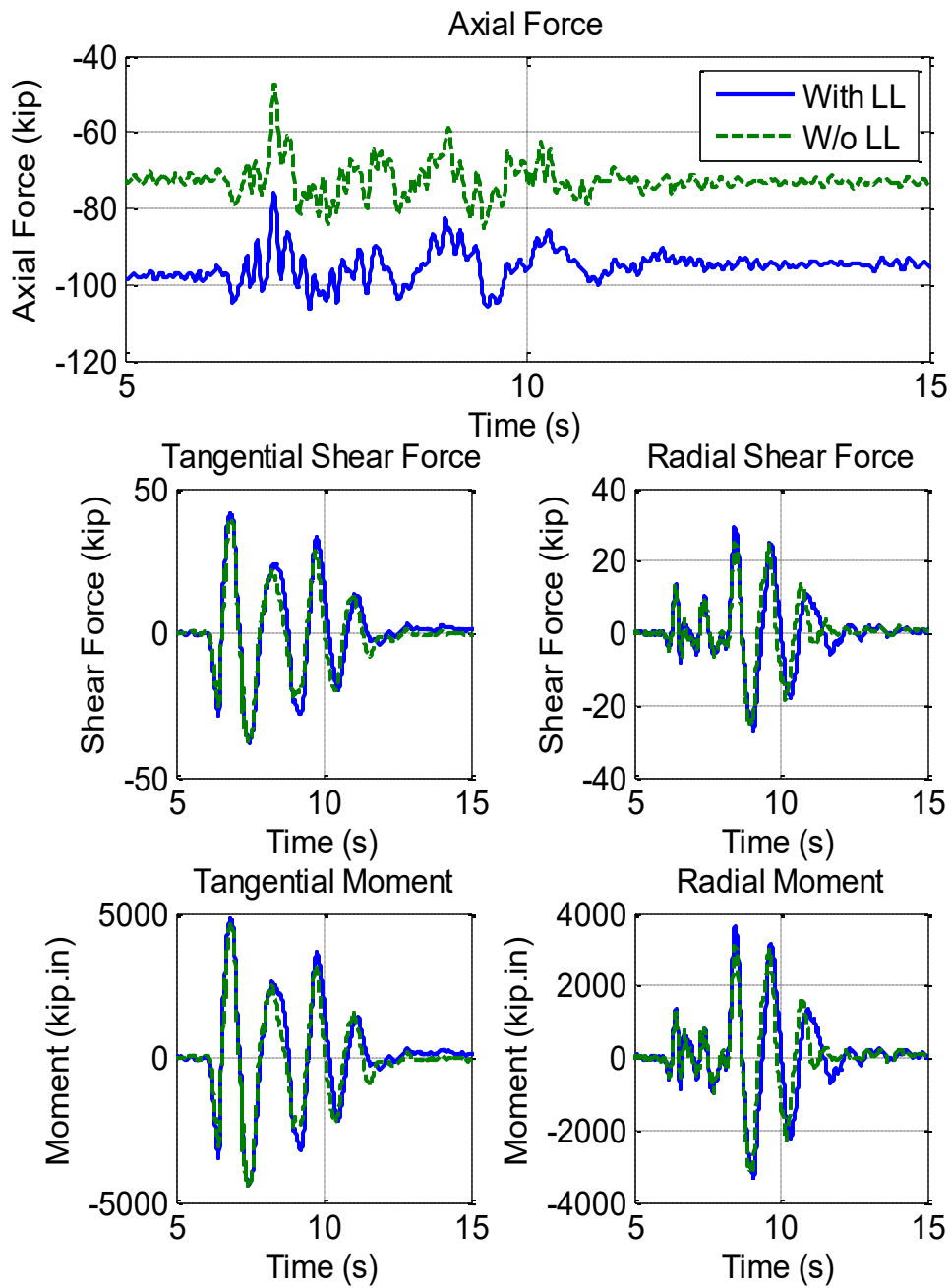


**Figure 5.7.24. Forces and Moments at the Bottom of South Bent (150% DE)**

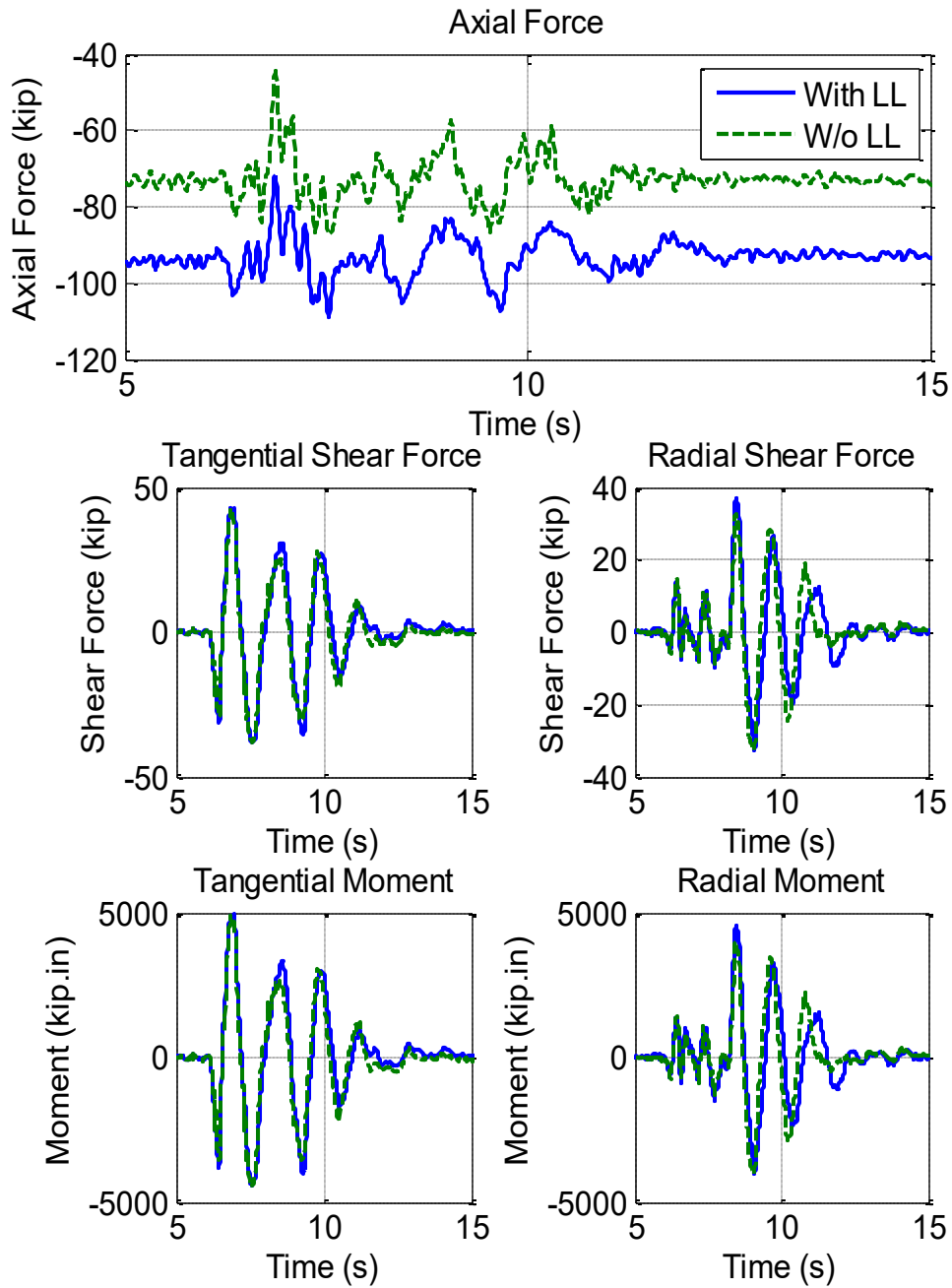
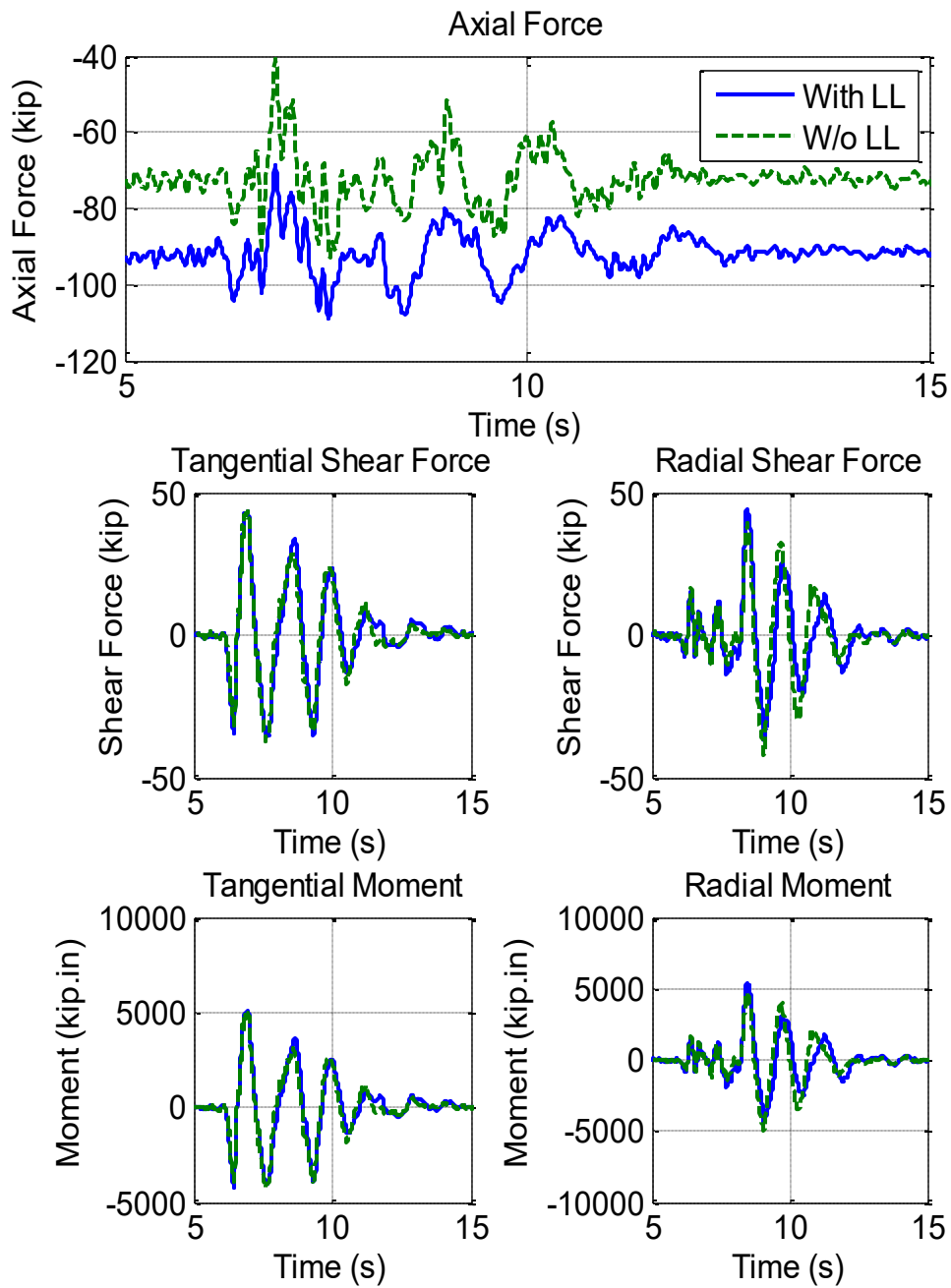
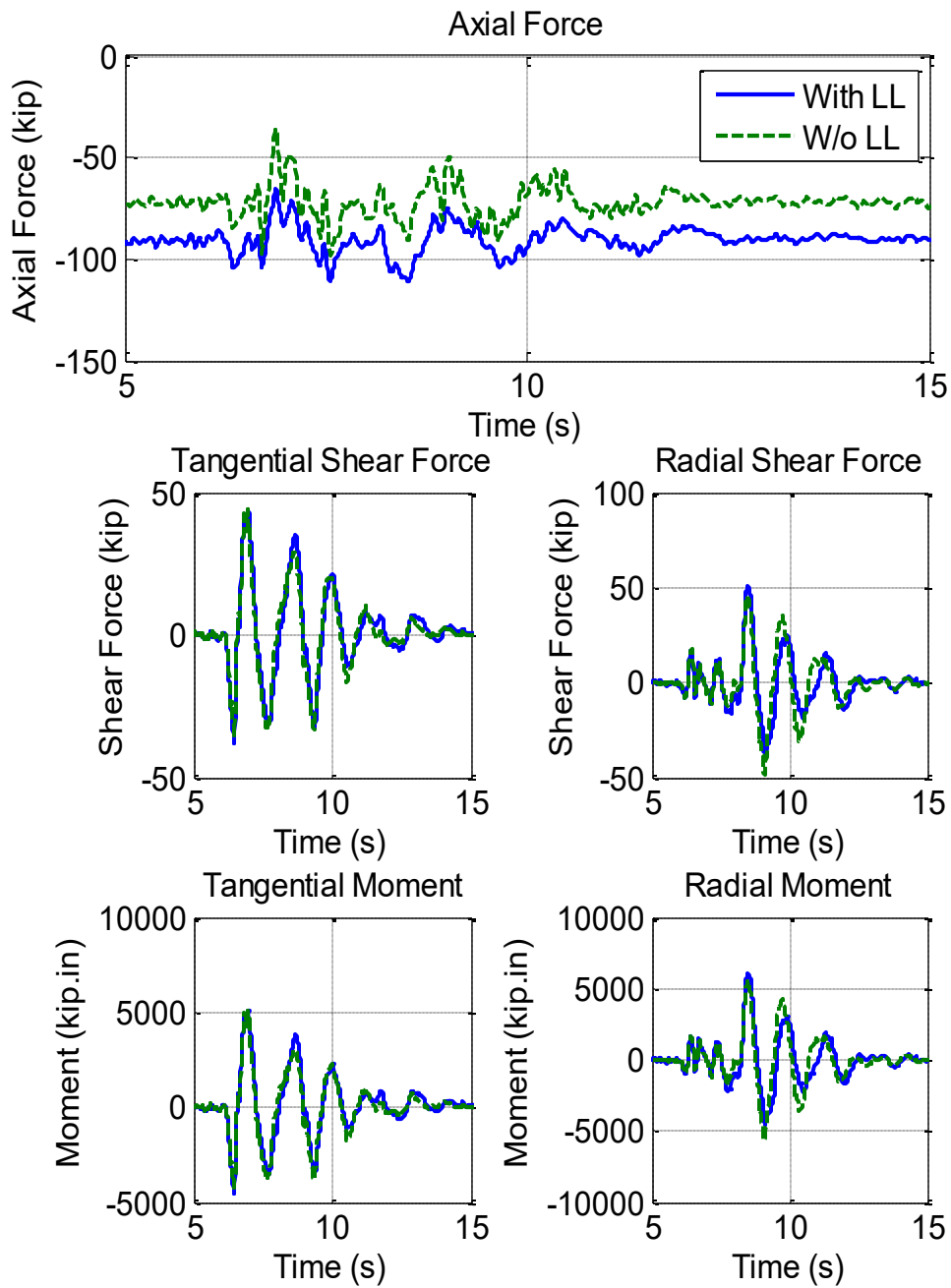


Figure 5.7.25. Forces and Moments at the Bottom of South Bent (200% DE)



**Figure 5.7.26. Forces and Moments at the Bottom of South Bent (250% DE)**



**Figure 5.7.27. Forces and Moments at the Bottom of South Bent (300% DE)**

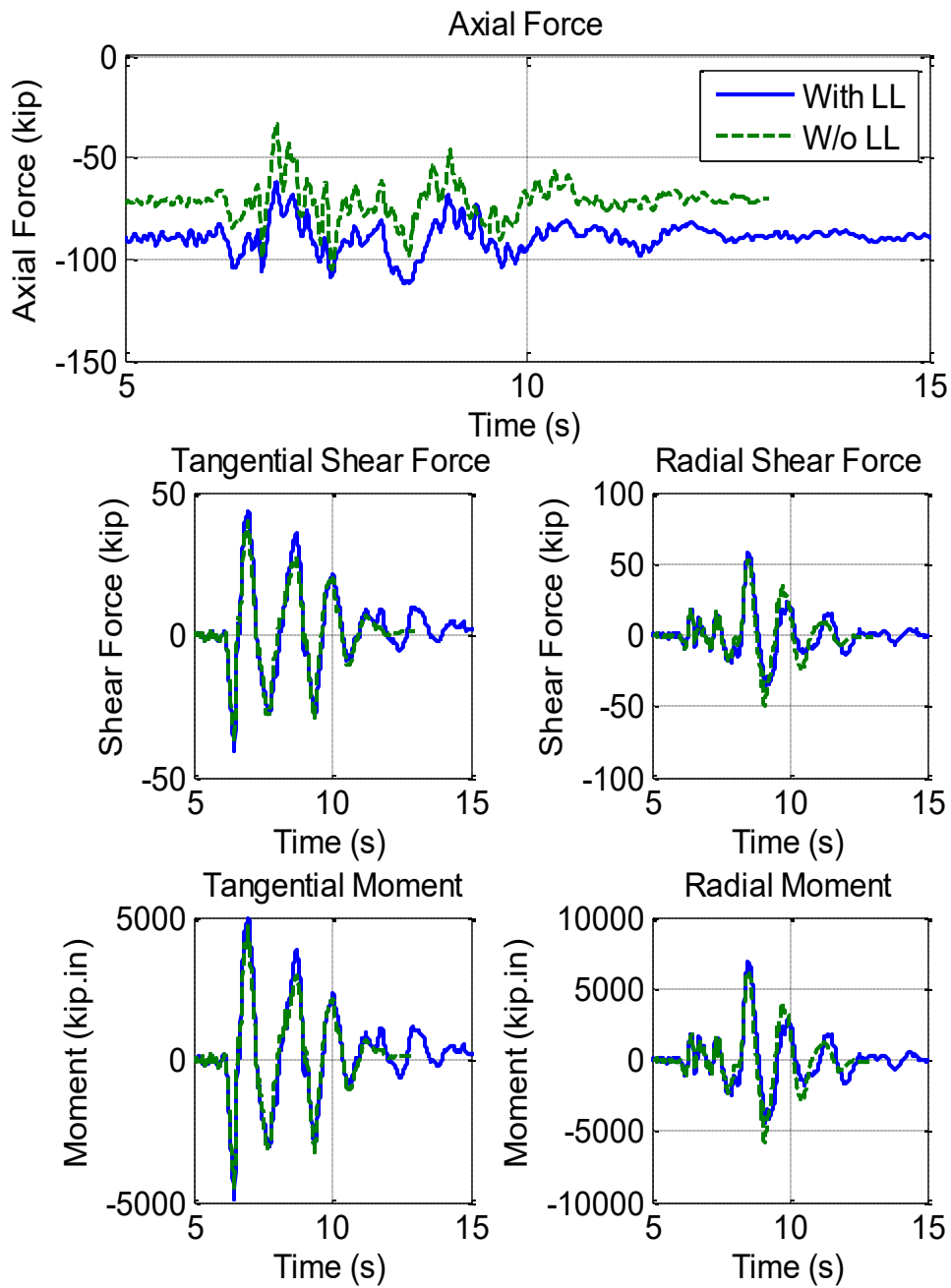


**Figure 5.7.28. Forces and Moments at the Bottom of South Bent (350% DE)**

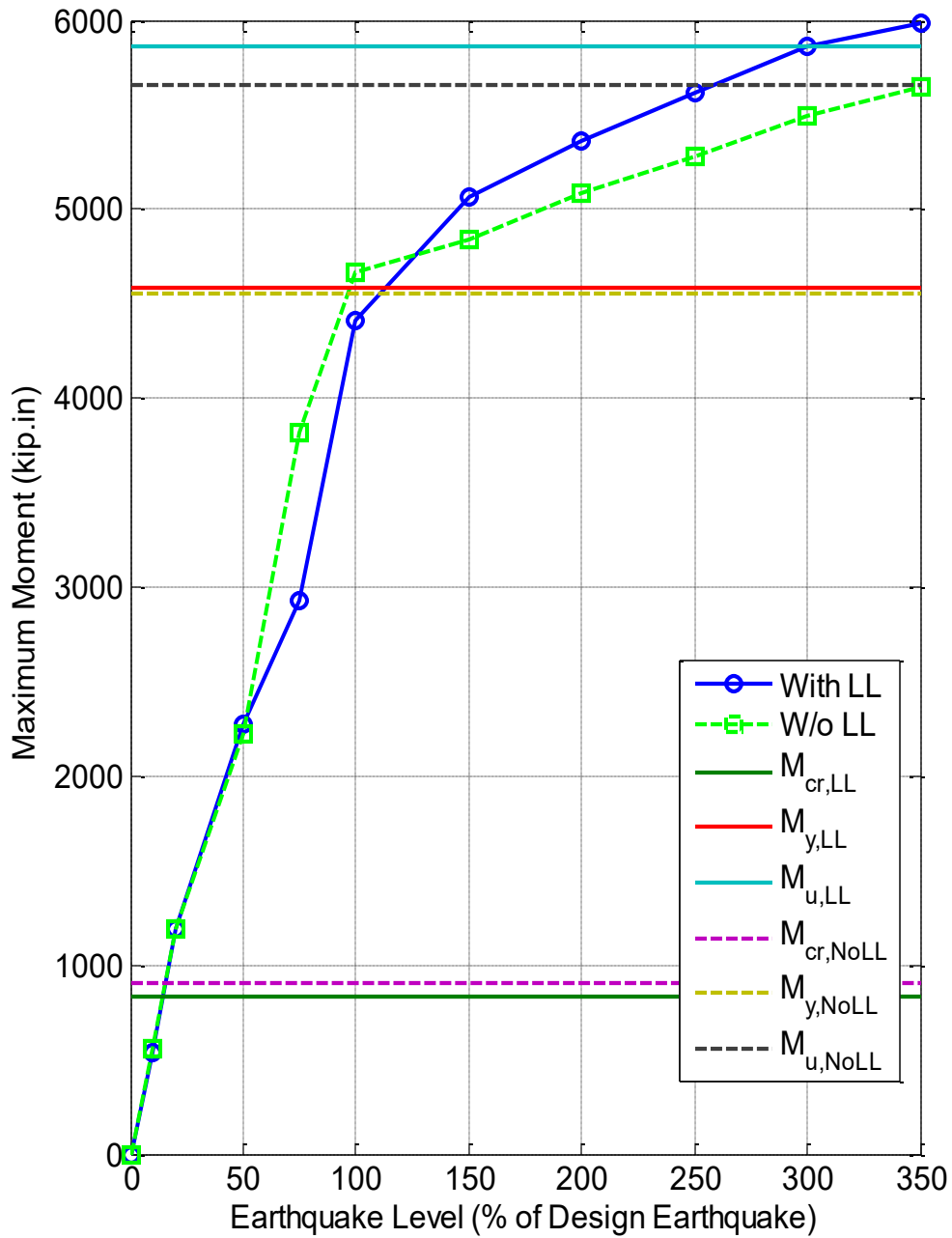


**Figure 5.7.29. Comparison of Maximum Moment at the Bottom of North Bent with and without Live Load**

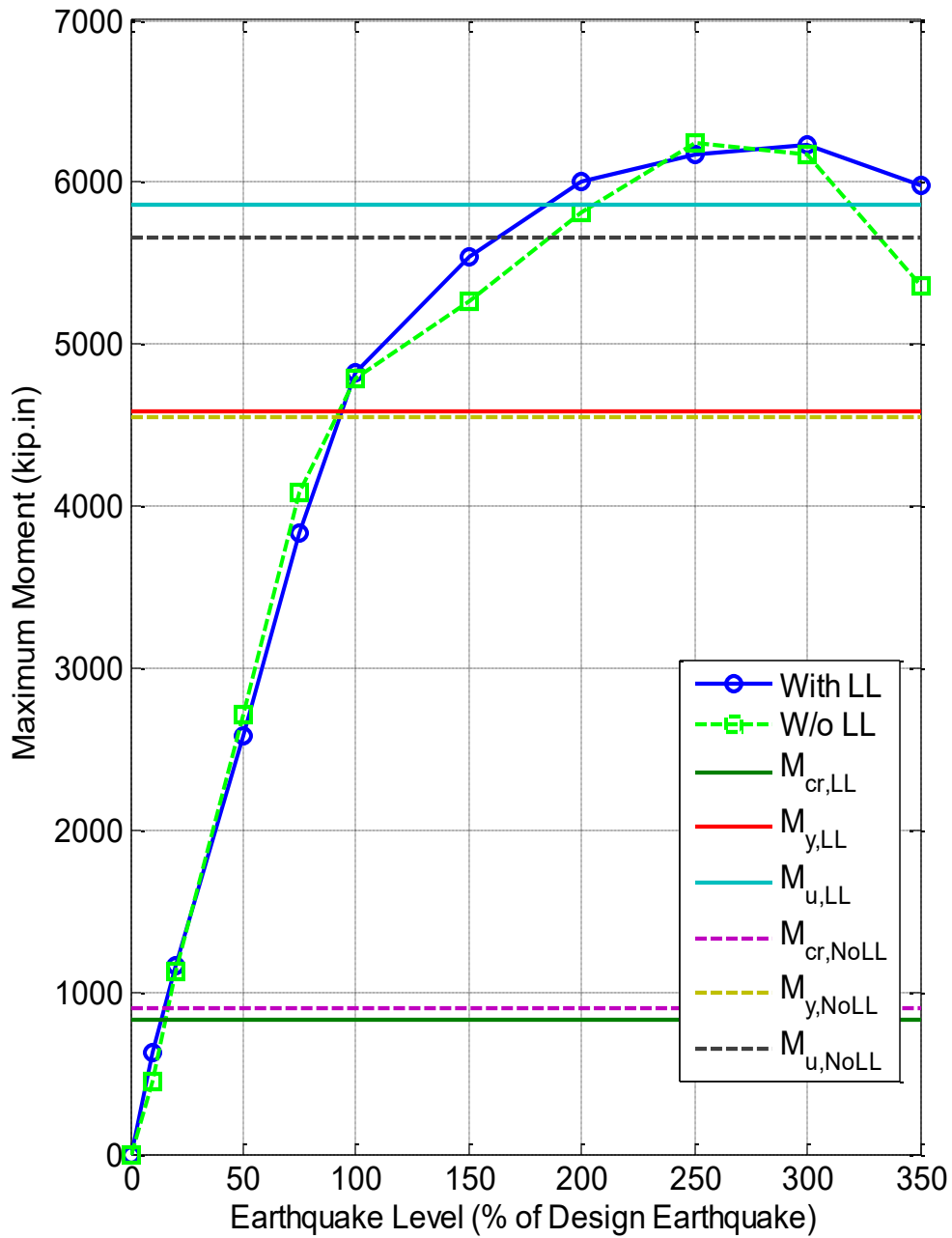


**Figure 5.7.30. Comparison of Maximum Moment at the Bottom of South Bent with and without Live Load**

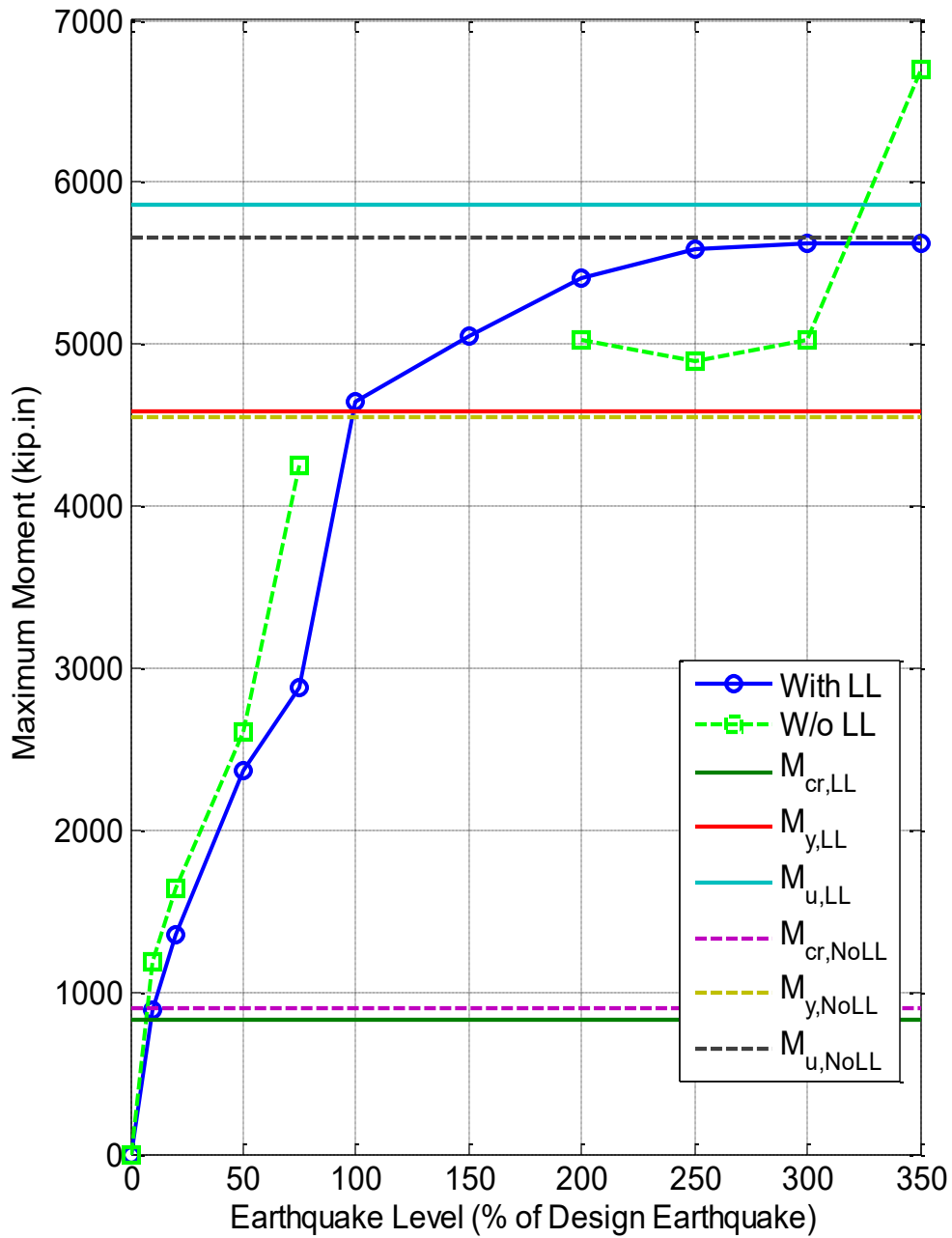


**Figure 5.7.31. Comparison of Maximum Moment Obtained from Statics at the Bottom of North Bent**

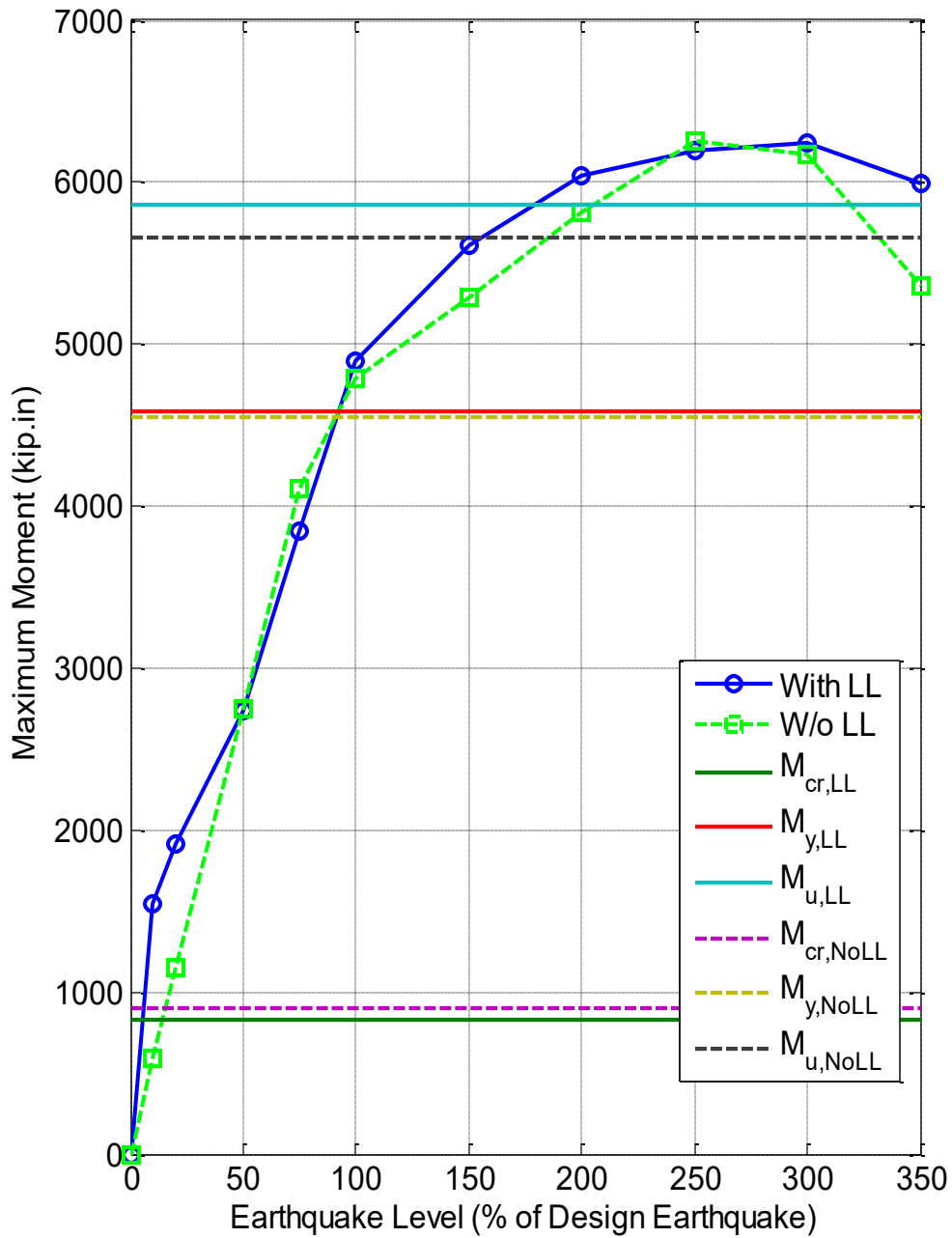


**Figure 5.7.32. Comparison of Maximum Moment Obtained from Statics in the Bottom of South Bent**

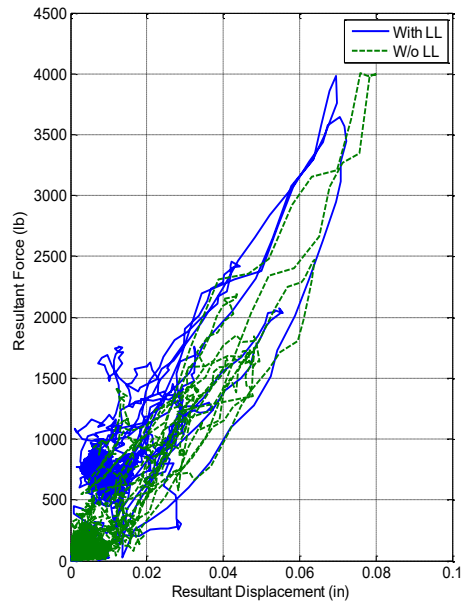


**Figure 5.7.33. Resultant Force vs. Displacement in Bottom of North Bent (10% DE)**

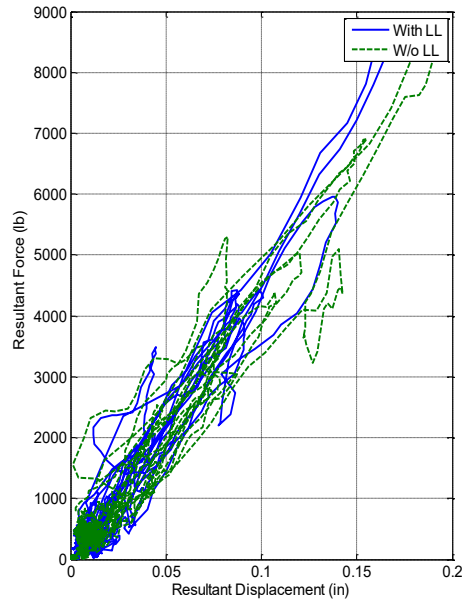


**Figure 5.7.34. Resultant Force vs. Displacement in Bottom of North Bent (20% DE)**

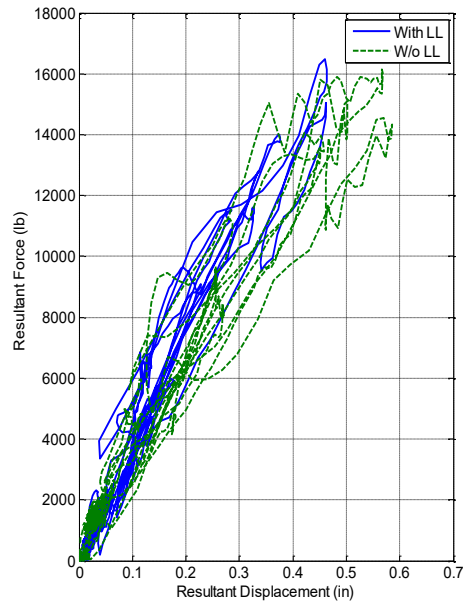


**Figure 5.7.35. Resultant Force vs. Displacement in Bottom of North Bent (50% DE)**

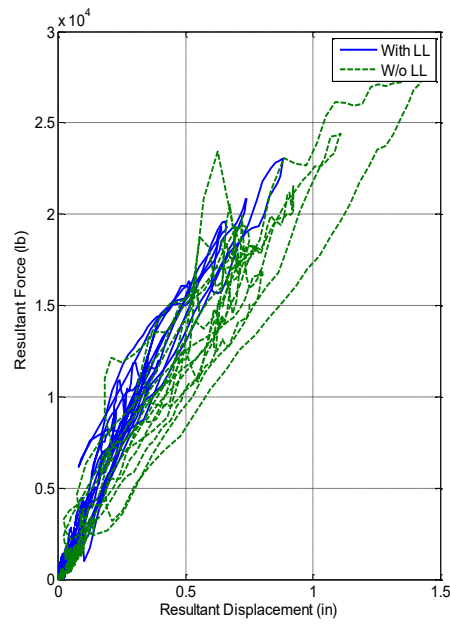


**Figure 5.7.36. Resultant Force vs. Displacement in Bottom of North Bent (75% DE)**

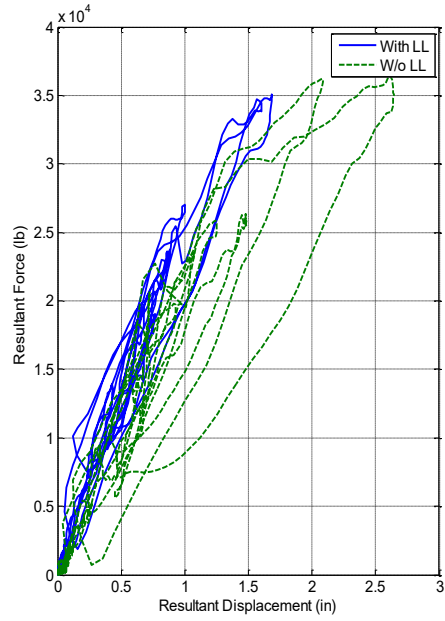


**Figure 5.7.37. Resultant Force vs. Displacement in Bottom of North Bent (100% DE)**

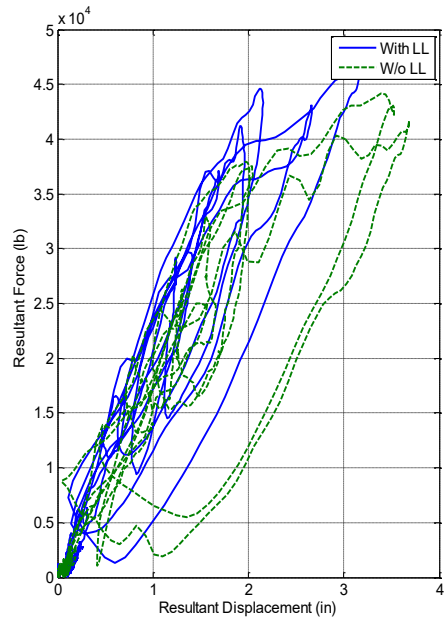


**Figure 5.7.38. Resultant Force vs. Displacement in Bottom of North Bent (150% DE)**

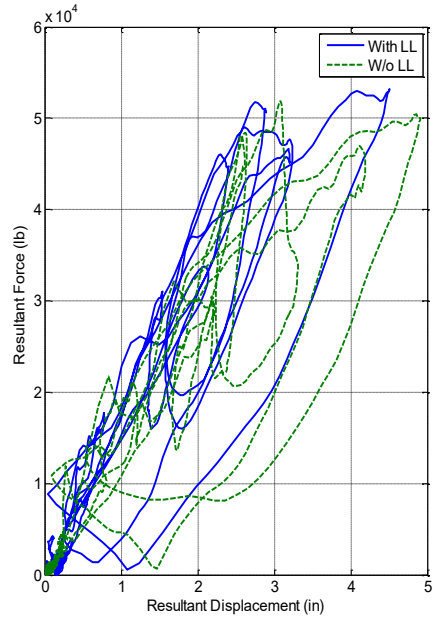


**Figure 5.7.39. Resultant Force vs. Displacement in Bottom of North Bent (200% DE)**

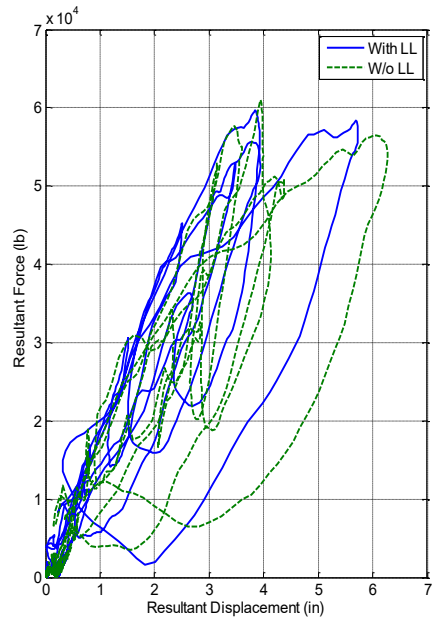


**Figure 5.7.40. Resultant Force vs. Displacement in Bottom of North Bent (250% DE)**

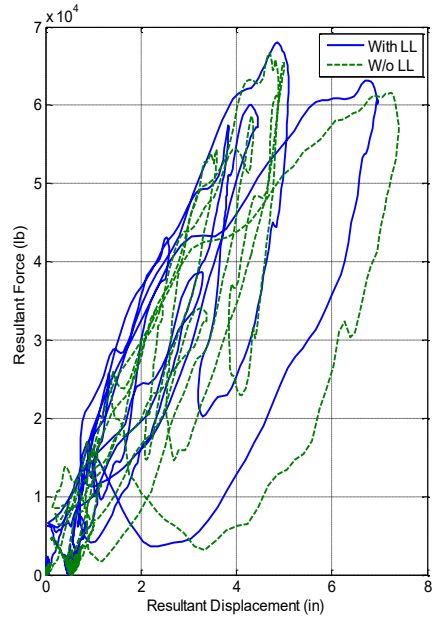


**Figure 5.7.41. Resultant Force vs. Displacement in Bottom of North Bent (300% DE)**

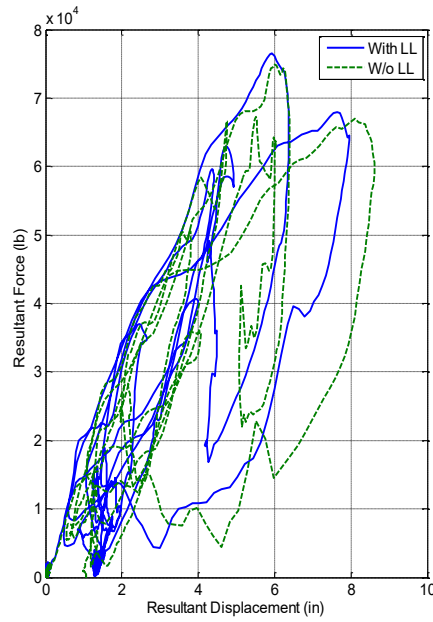


**Figure 5.7.42. Resultant Force vs. Displacement in Bottom of North Bent (350% DE)**

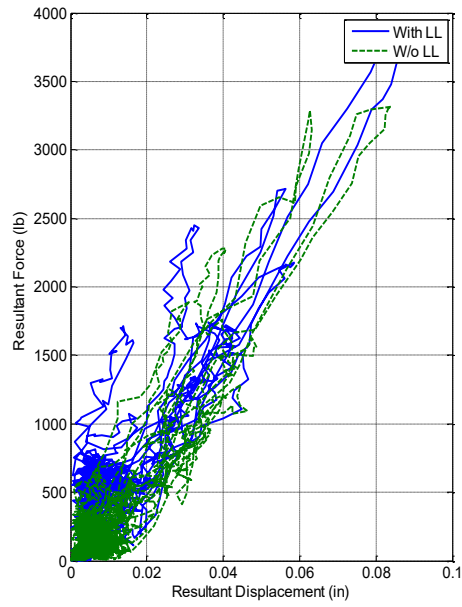


**Figure 5.7.43. Resultant Force vs. Displacement in Bottom of South Bent (10% DE)**

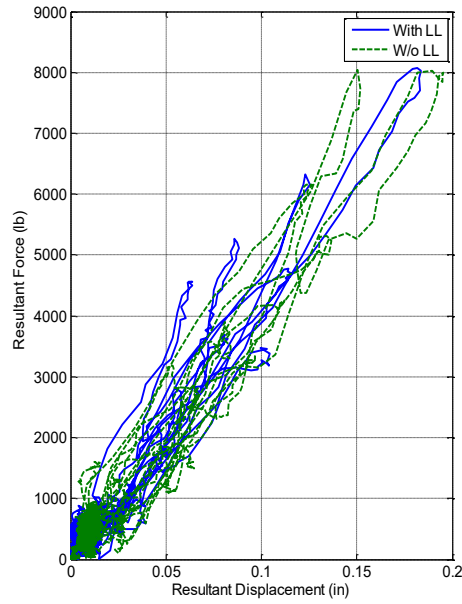


**Figure 5.7.44. Resultant Force vs. Displacement in Bottom of South Bent (20% DE)**

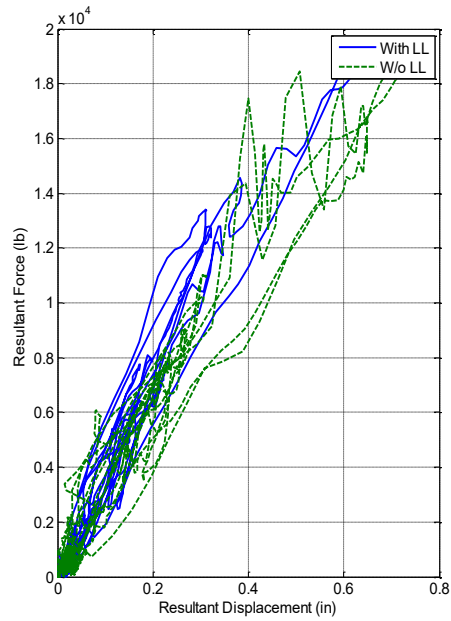


**Figure 5.7.45. Resultant Force vs. Displacement in Bottom of South Bent (50% DE)**

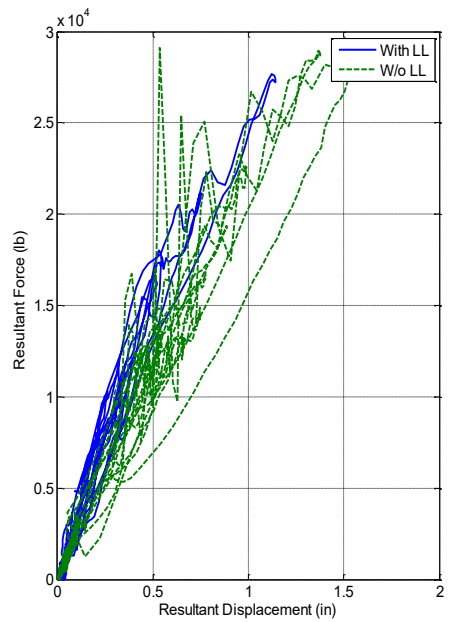


**Figure 5.7.46. Resultant Force vs. Displacement in Bottom of South Bent (75% DE)**

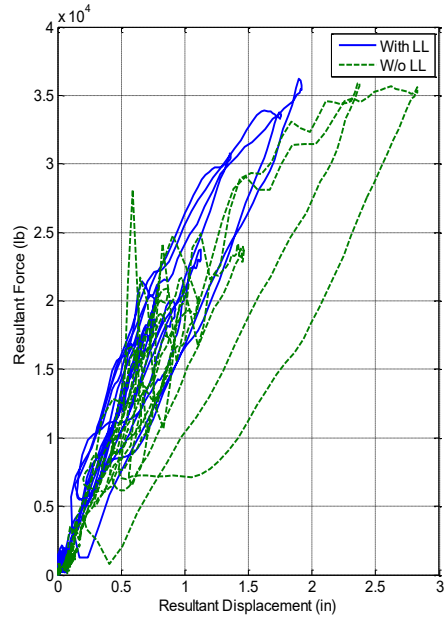


**Figure 5.7.47. Resultant Force vs. Displacement in Bottom of South Bent (100% DE)**

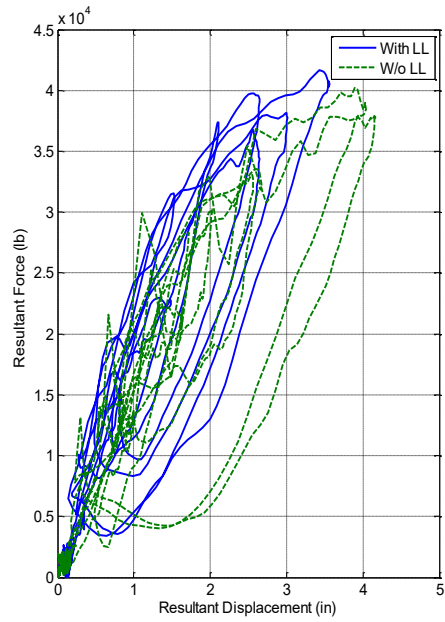


**Figure 5.7.48. Resultant Force vs. Displacement in Bottom of South Bent (150% DE)**

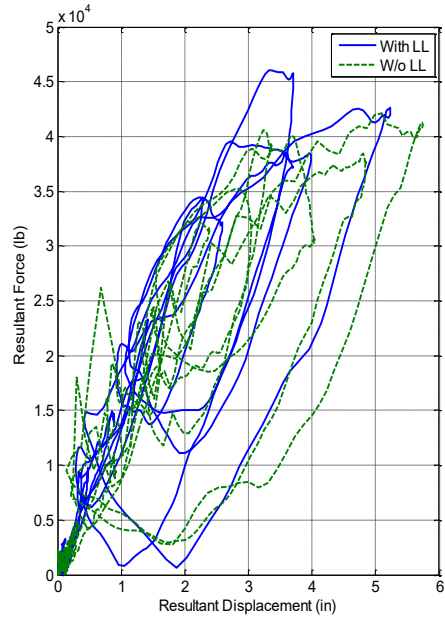


**Figure 5.7.49. Resultant Force vs. Displacement in Bottom of South Bent (200% DE)**

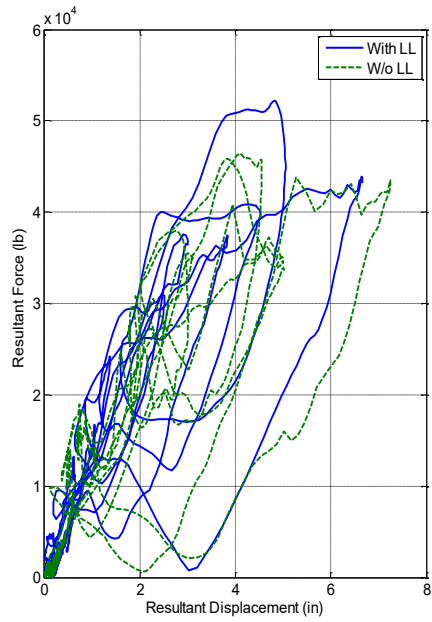


**Figure 5.7.50. Resultant Force vs. Displacement in Bottom of South Bent (250% DE)**

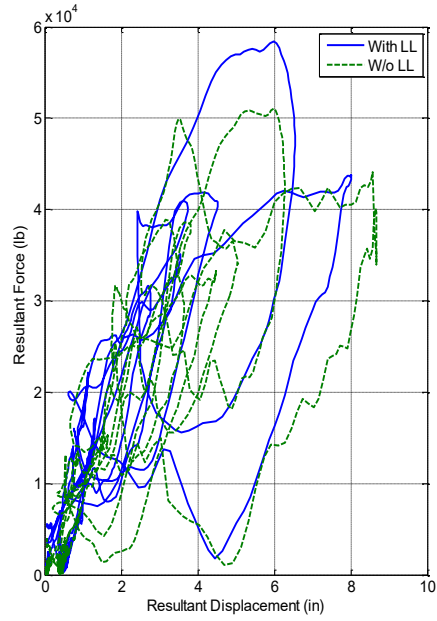


**Figure 5.7.51. Resultant Force vs. Displacement in Bottom of South Bent (300% DE)**

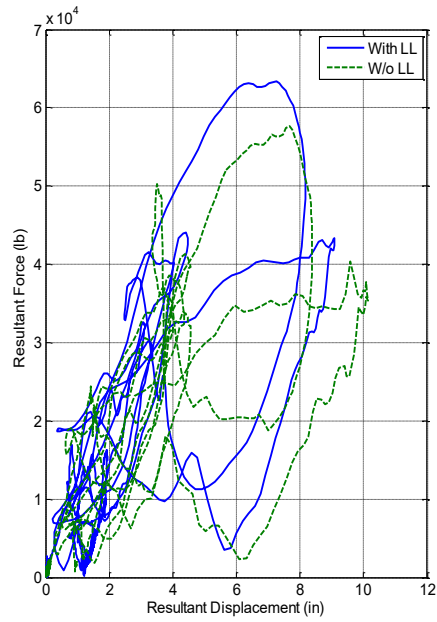


**Figure 5.7.52. Resultant Force vs. Displacement in Bottom of South Bent (350% DE)**

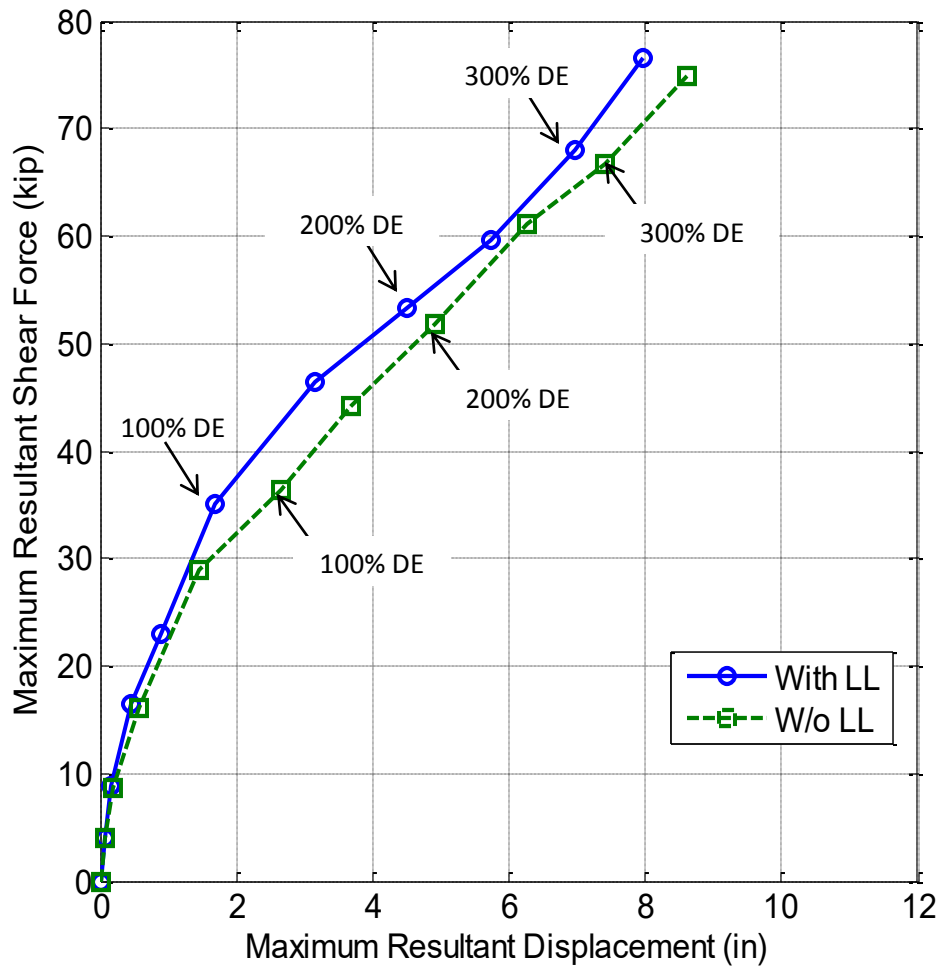


**Figure 5.7.53. North Bent Maximum Resultant Shear Force vs. Displacement with and without Live Load**

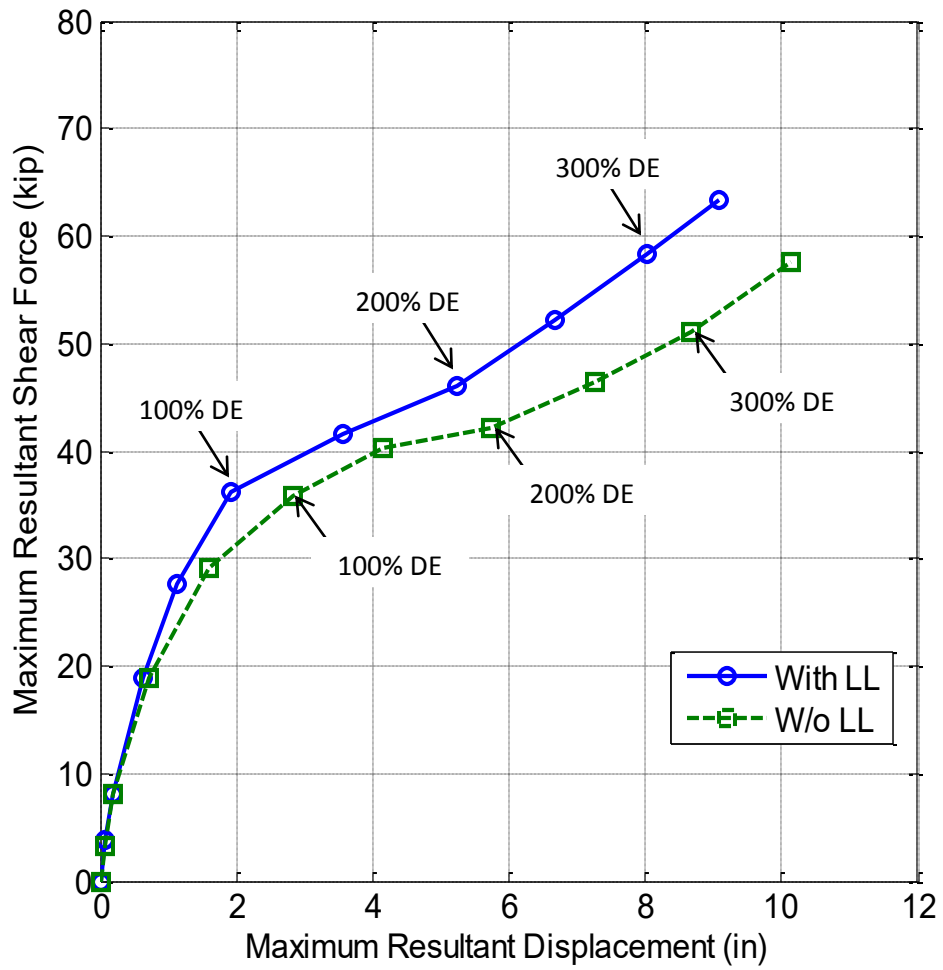


**Figure 5.7.54. South Bent Resultant Shear Force vs. Displacement with and without Live Load**

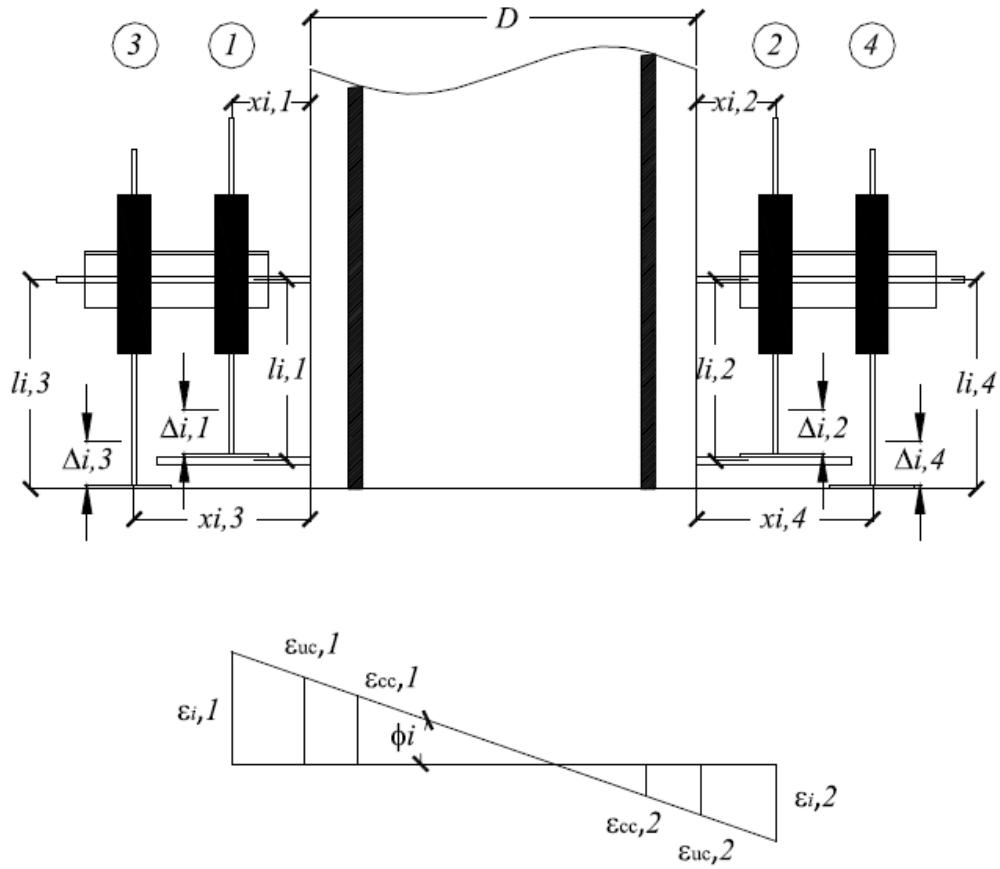
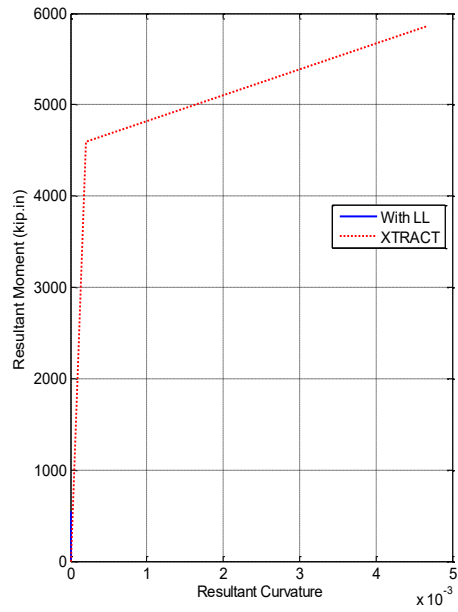
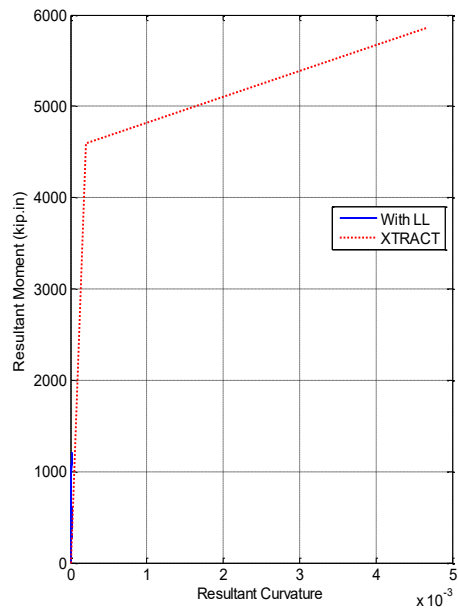


Figure 5.7.55. Illustration of Column Curvature Calculation



**Figure 5.7.56. Resultant Moment vs. Curvature at Bottom of North Bent (10% DE)**



**Figure 5.7.57. Resultant Moment vs. Curvature at Bottom of North Bent (20% DE)**

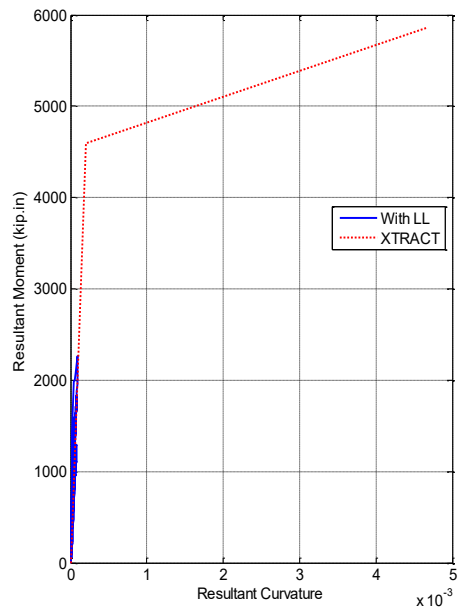


**Figure 5.7.58. Resultant Moment vs. Curvature at Bottom of North Bent (50% DE)**

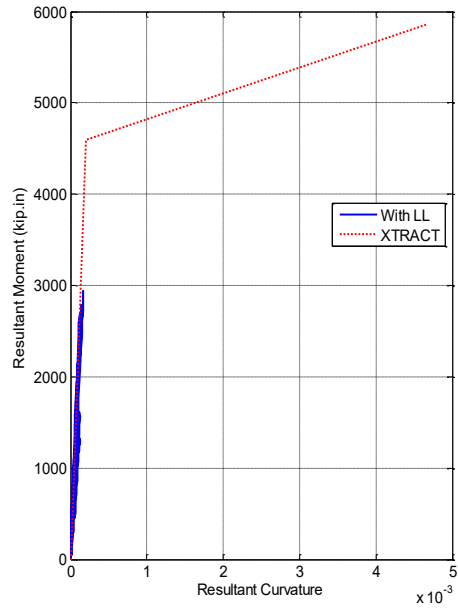


**Figure 5.7.59. Resultant Moment vs. Curvature at Bottom of North Bent (75% DE)**

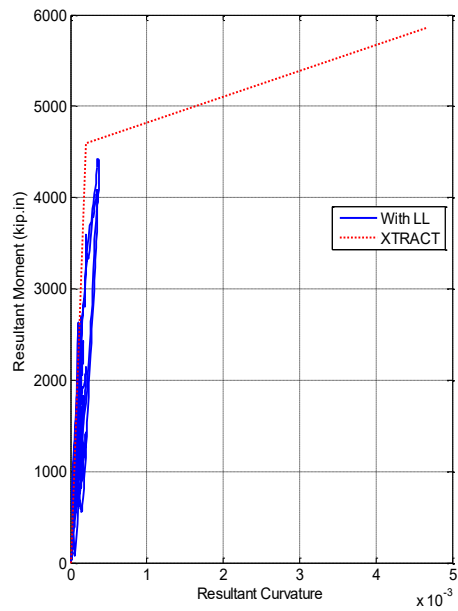


**Figure 5.7.60. Resultant Moment vs. Curvature a Bottom of North Bent (100% DE)**

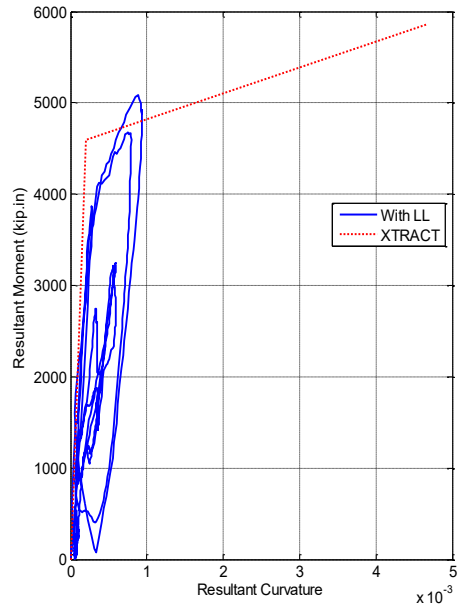


**Figure 5.7.61. Resultant Moment vs. Curvature at Bottom of North Bent (150% DE)**

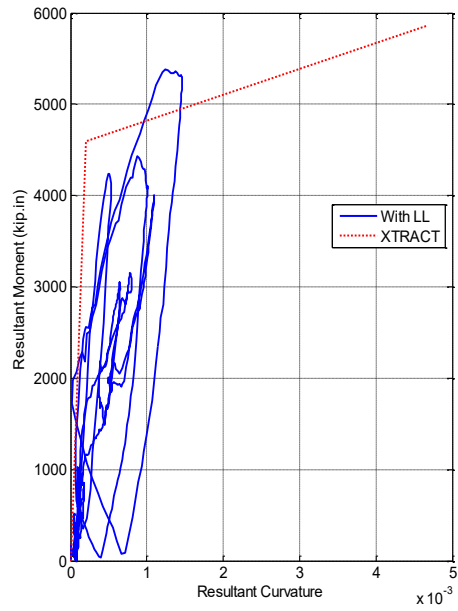


**Figure 5.7.62. Resultant Moment vs. Curvature at Bottom of North Bent (200% DE)**

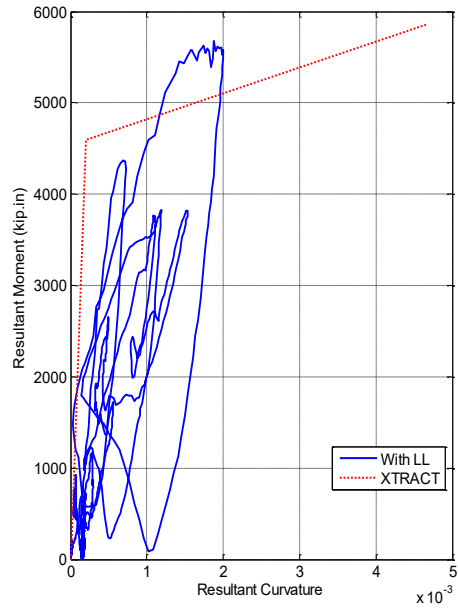


**Figure 5.7.63. Resultant Moment vs. Curvature at Bottom of North Bent (250% DE)**

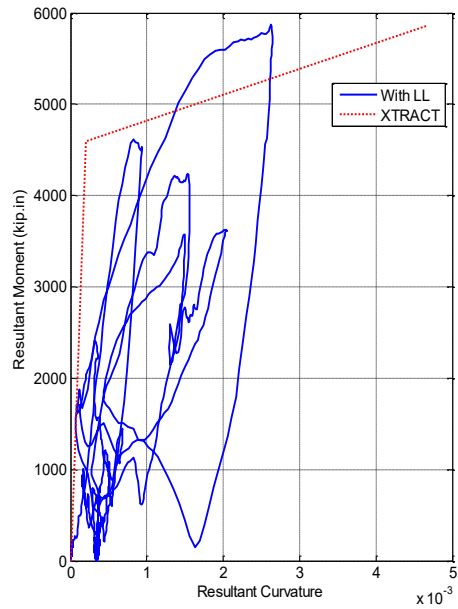


**Figure 5.7.64. Resultant Moment vs. Curvature at Bottom of North Bent (300% DE)**

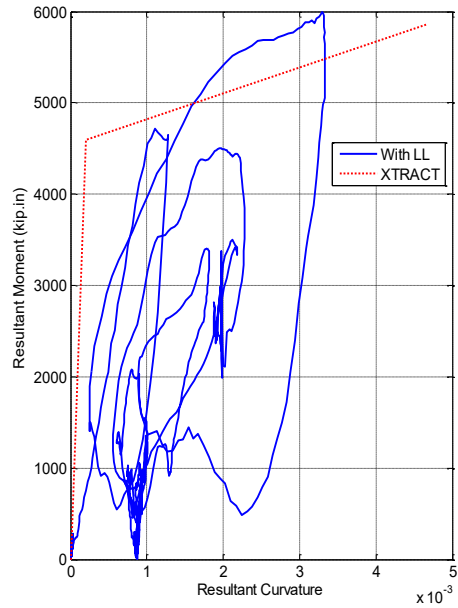


**Figure 5.7.65. Resultant Moment vs. Curvature at Bottom of North Bent (350% DE)**

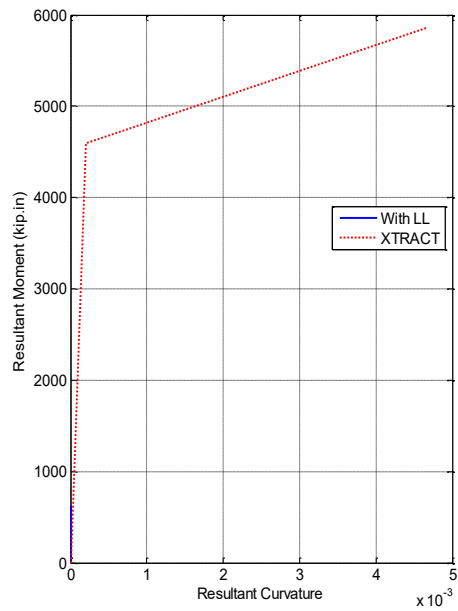


**Figure 5.7.66. Resultant Moment vs. Curvature at Bottom of South Bent (10% DE)**

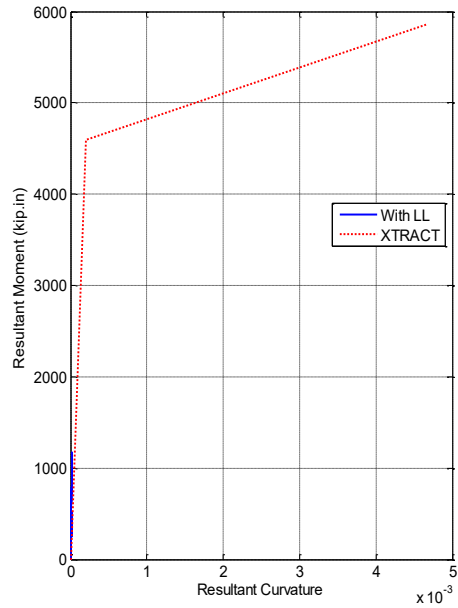


**Figure 5.7.67. Resultant Moment vs. Curvature at Bottom of South Bent (20% DE)**

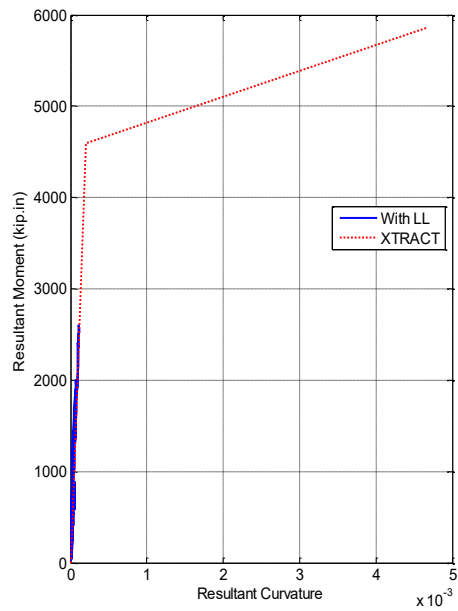


**Figure 5.7.68. Resultant Moment vs. Curvature at Bottom of South Bent (50% DE)**

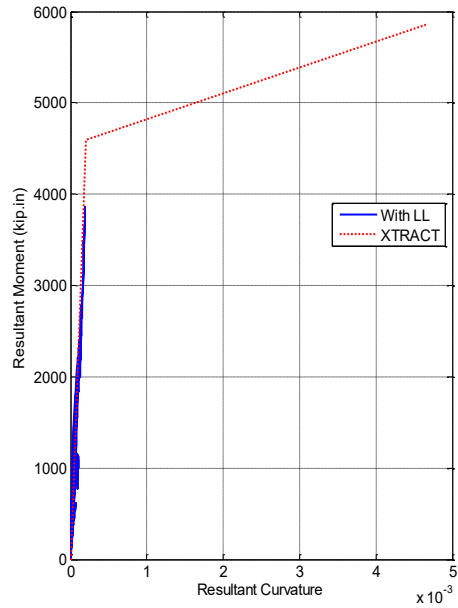


**Figure 5.7.69. Resultant Moment vs. Curvature at Bottom of South Bent (75% DE)**

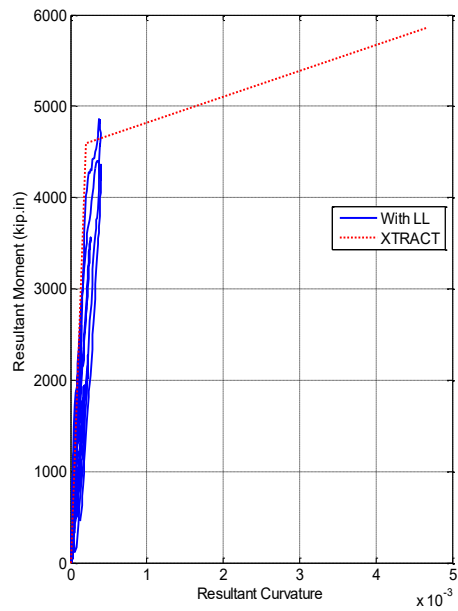


**Figure 5.7.70. Resultant Moment vs. Curvature at Bottom of South Bent (100% DE)**

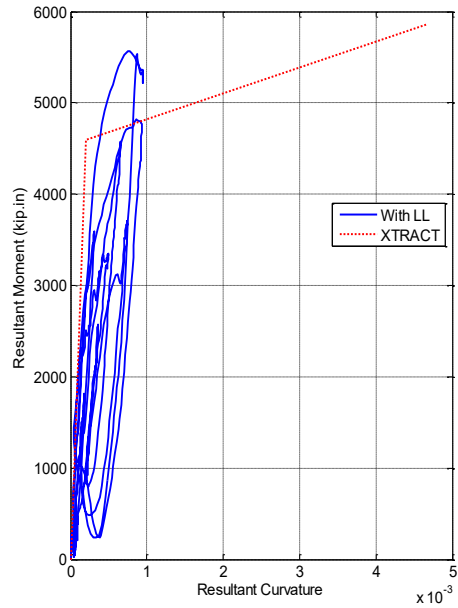


**Figure 5.7.71. Resultant Moment vs. Curvature at Bottom of South Bent (150% DE)**

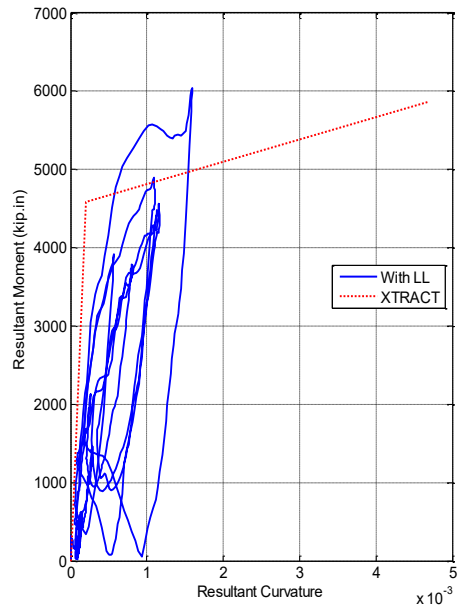


**Figure 5.7.72. Resultant Moment vs. Curvature at Bottom of South Bent (200% DE)**

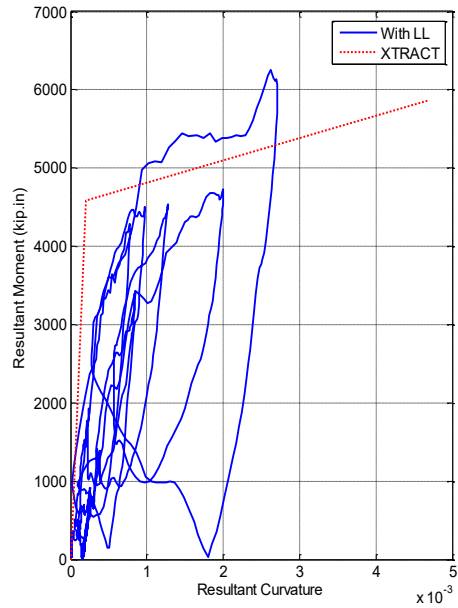


**Figure 5.7.73. Resultant Moment vs. Curvature at Bottom of South Bent (250% DE)**

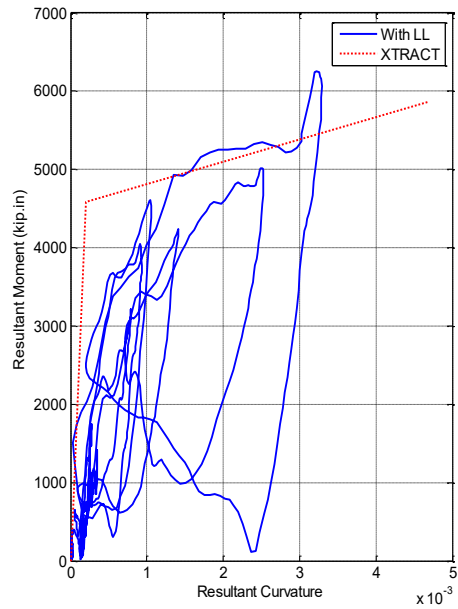


**Figure 5.7.74. Resultant Moment vs. Curvature at Bottom of South Bent (300% DE)**

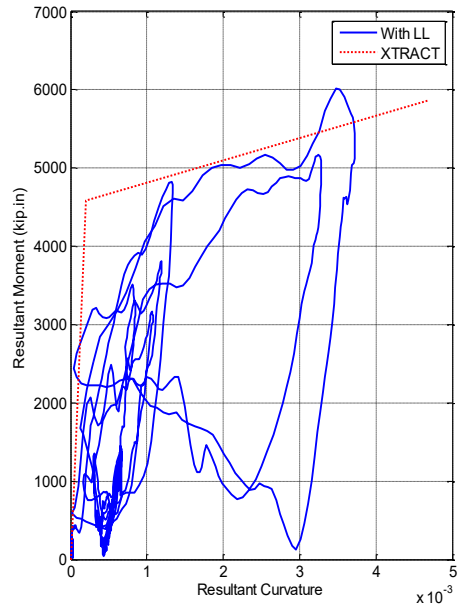


**Figure 5.7.75. Resultant Moment vs. Curvature at Bottom of South Bent (350% DE)**

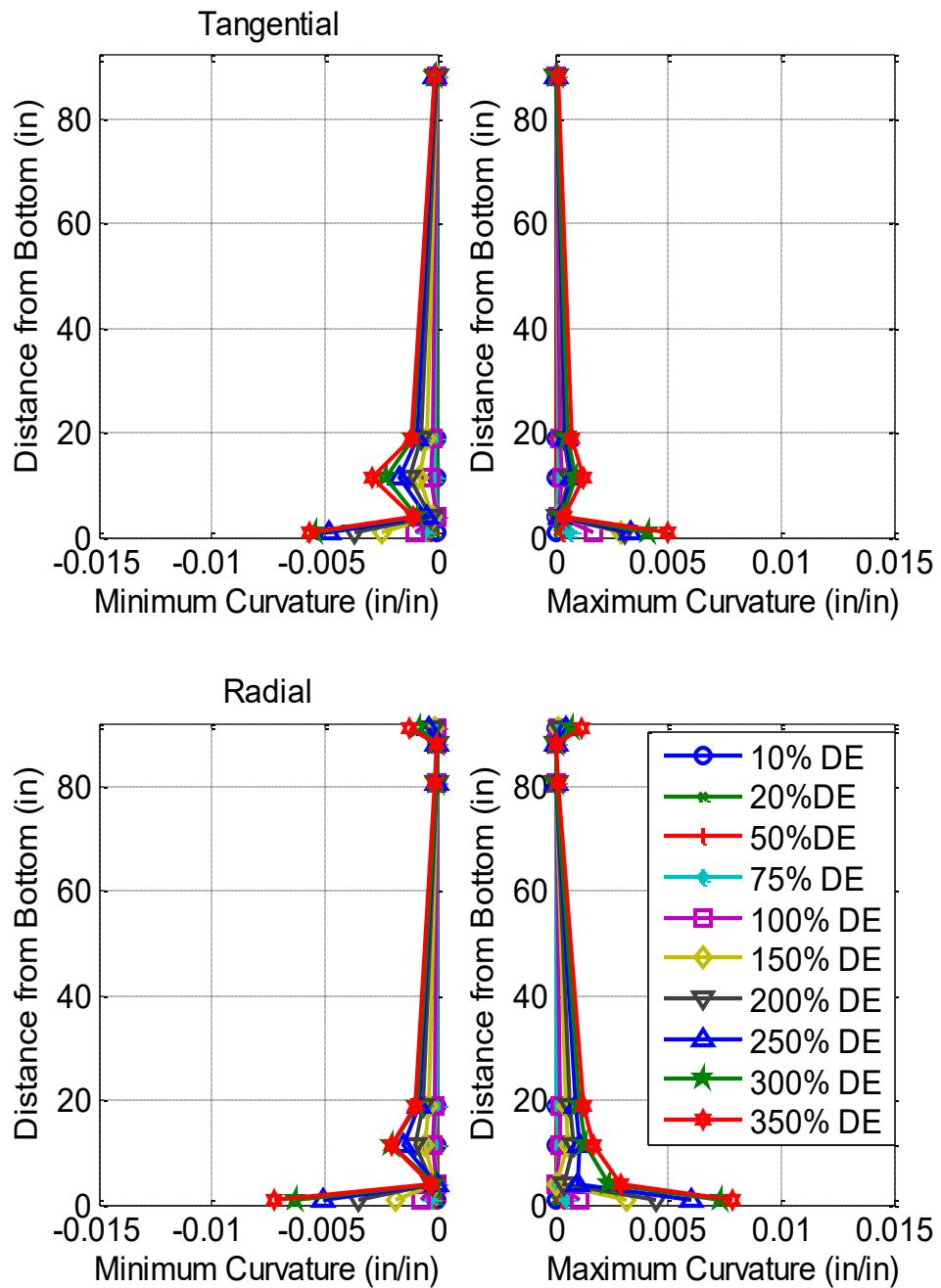


**Figure 5.7.76. Maximum and Minimum Curvatures in North Bent**

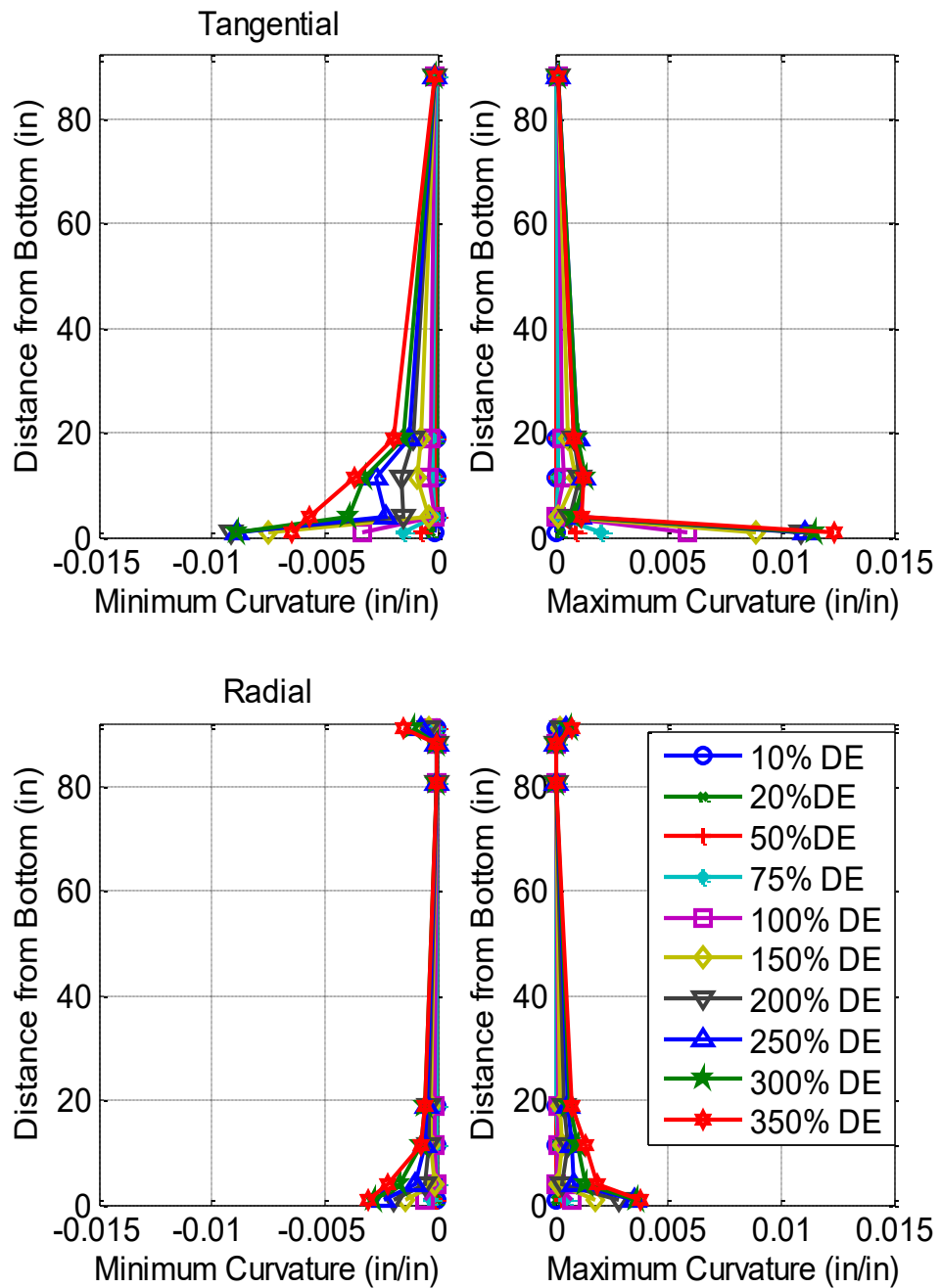


**Figure 5.7.77. Maximum and Minimum Curvatures in South Bent**

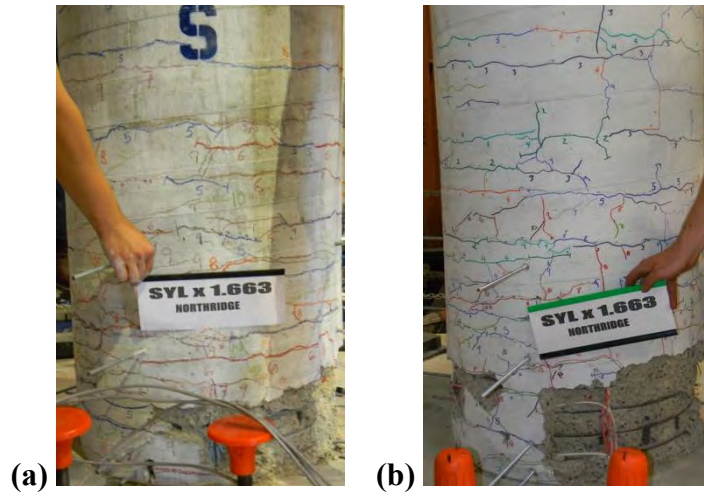


**Figure 5.8.1. Damage on South Face of North Column  
(a) With and (b) Without Live Load After 350% DE Run**

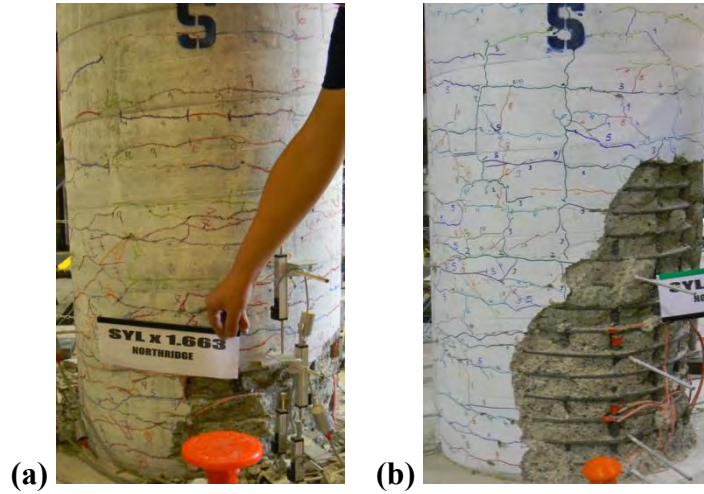


**Figure 5.8.2. Damage on South Face of South Column  
(a) With and (b) Without Live Load After 350% DE Run**

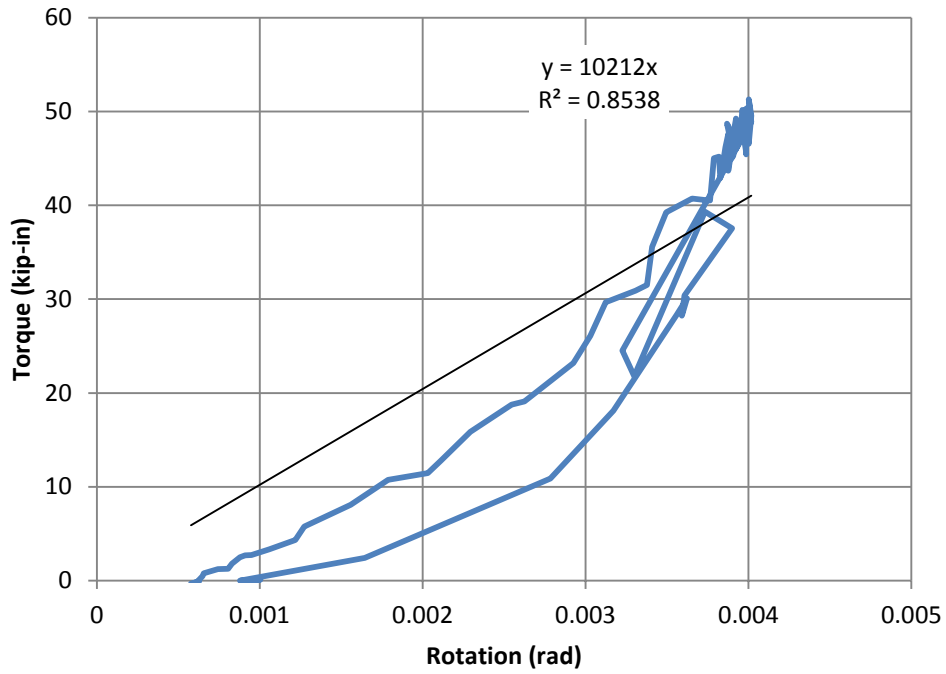


**Figure 5.8.3. North Column Post-Experiment Torque vs. Rotation**

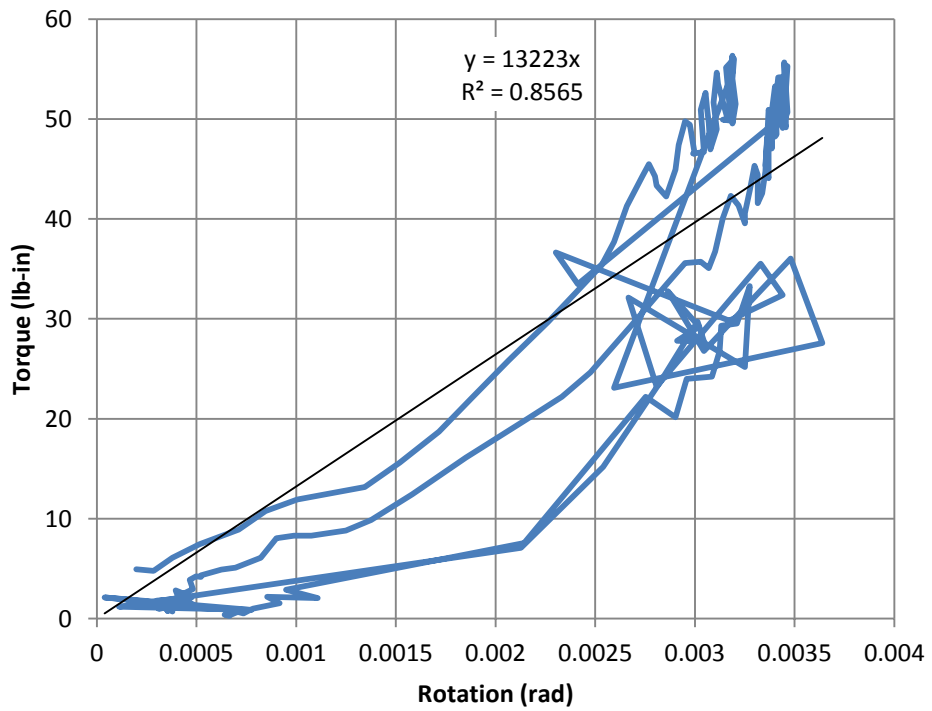
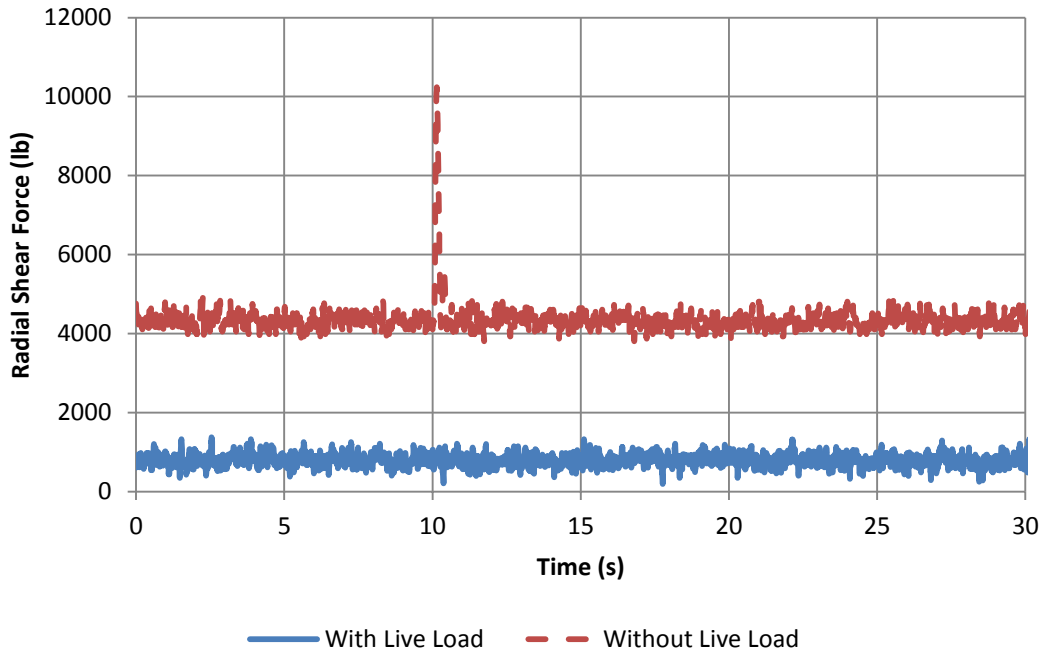
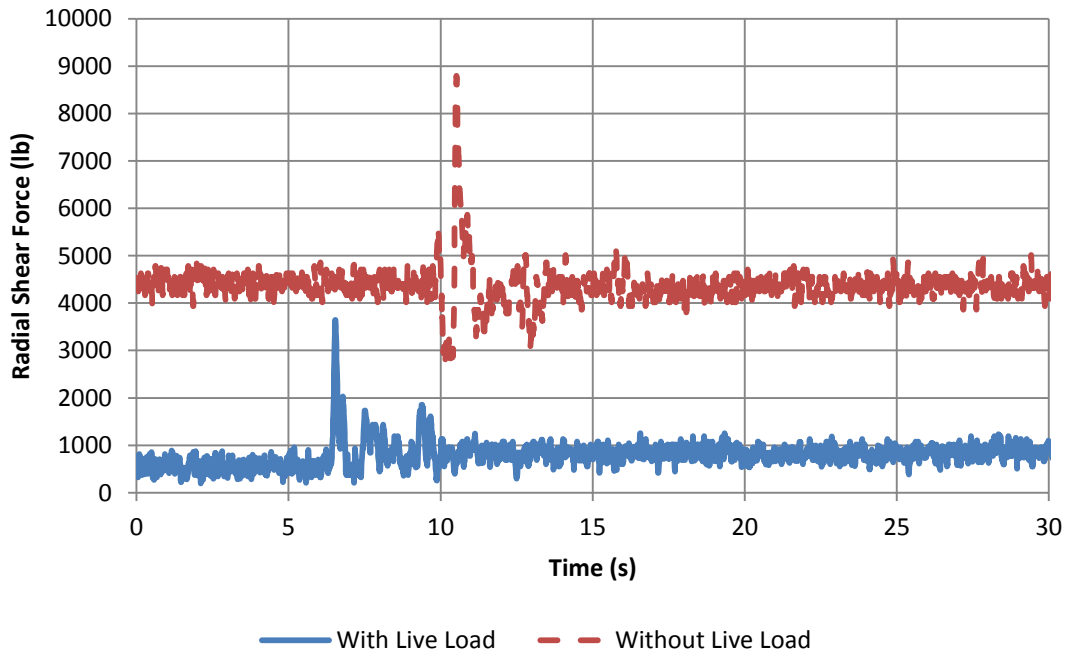


**Figure 5.8.4. South Column Post-Experiment Torque vs. Rotation**

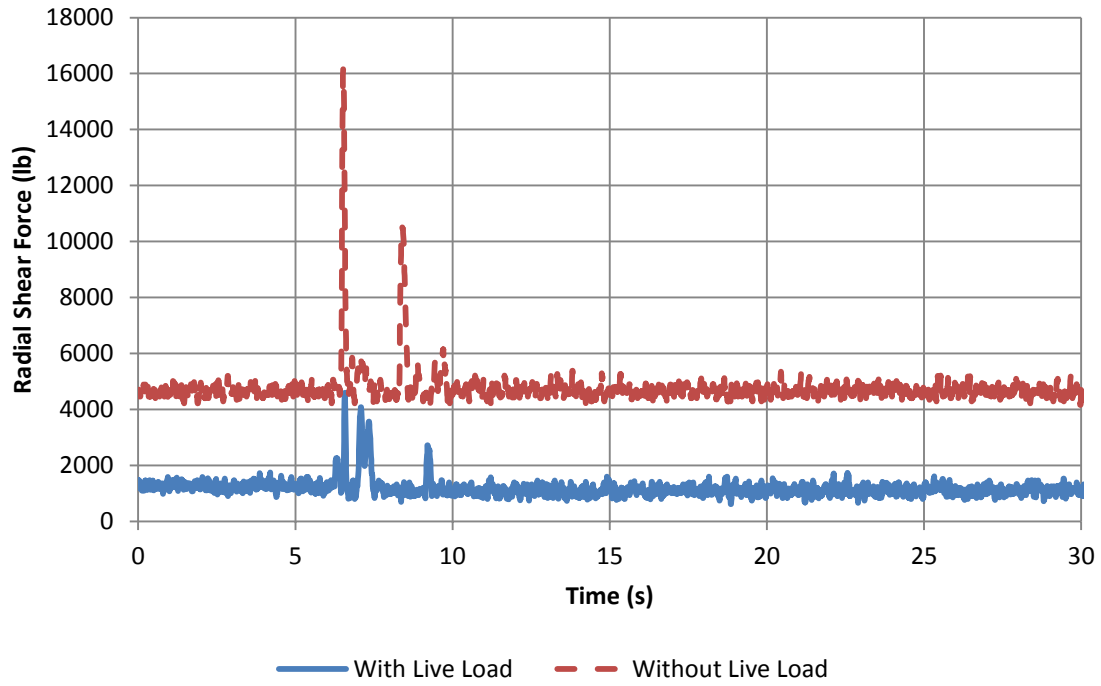


(a)

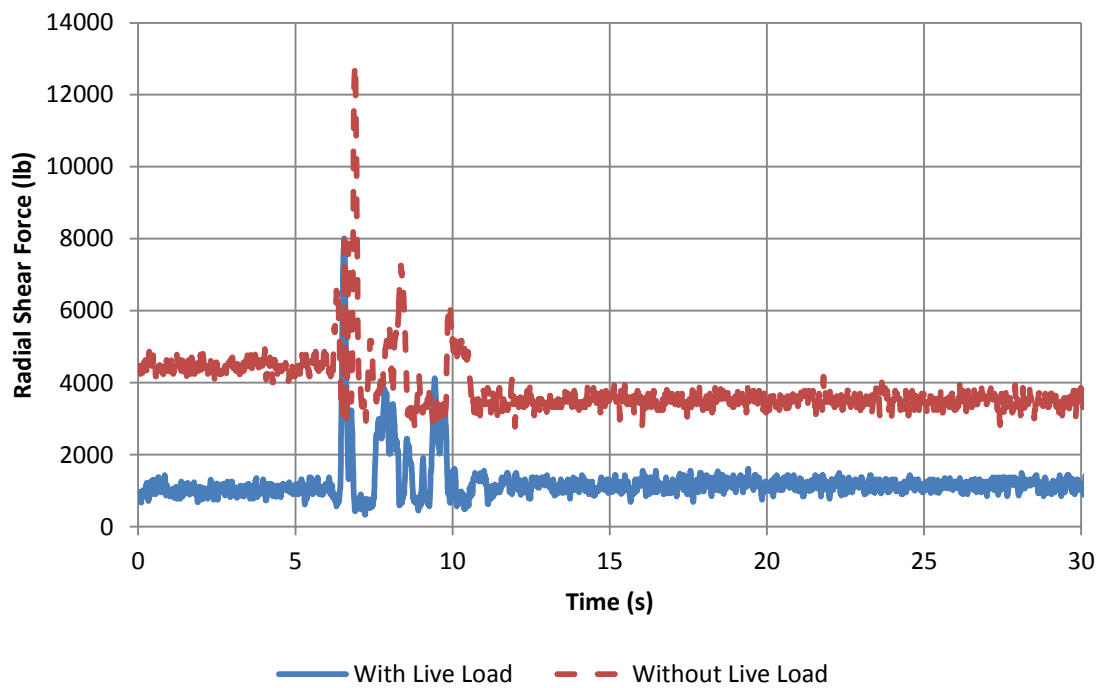


(b)

**Figure 5.9.1. Radial Shear Force in the Shear Key at (a) North and (b) South Abutment during 10% DE Run**

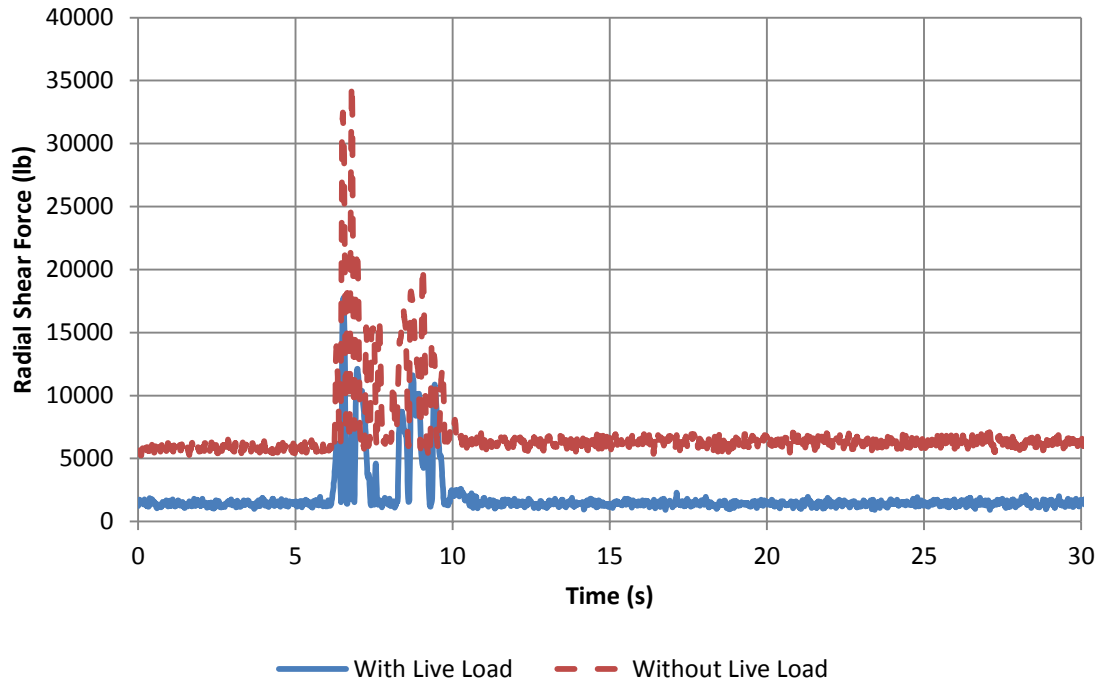


(a)

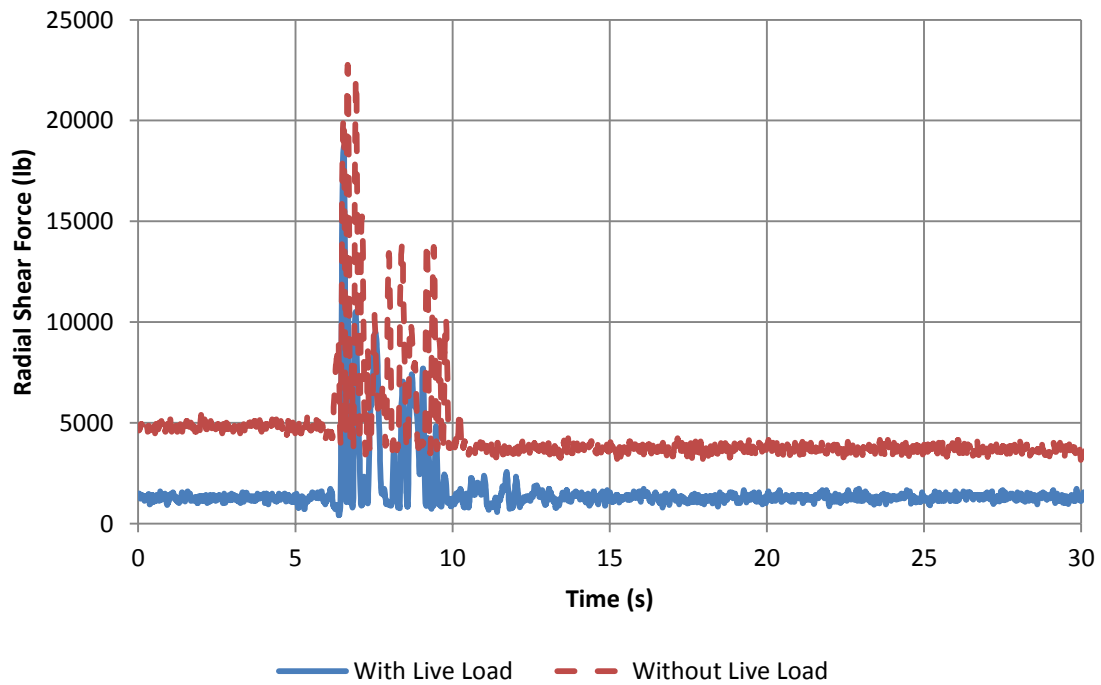


(b)

**Figure 5.9.2. Radial Shear Force in the Shear Key at (a) North and (b) South Abutment during 20% DE Run**

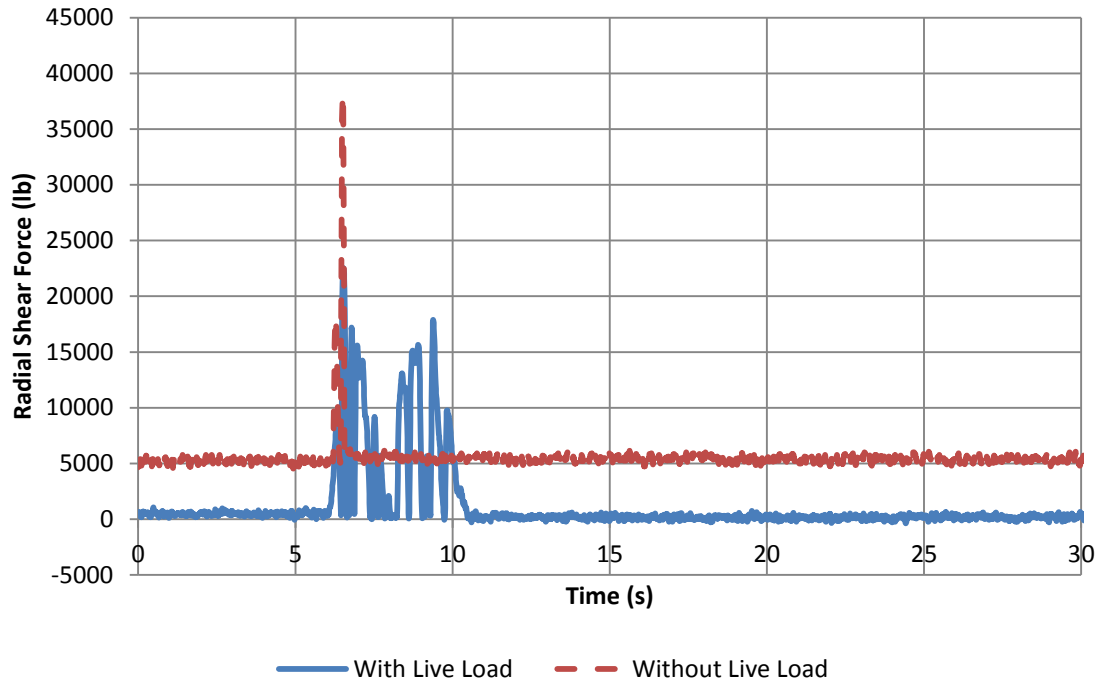


(a)

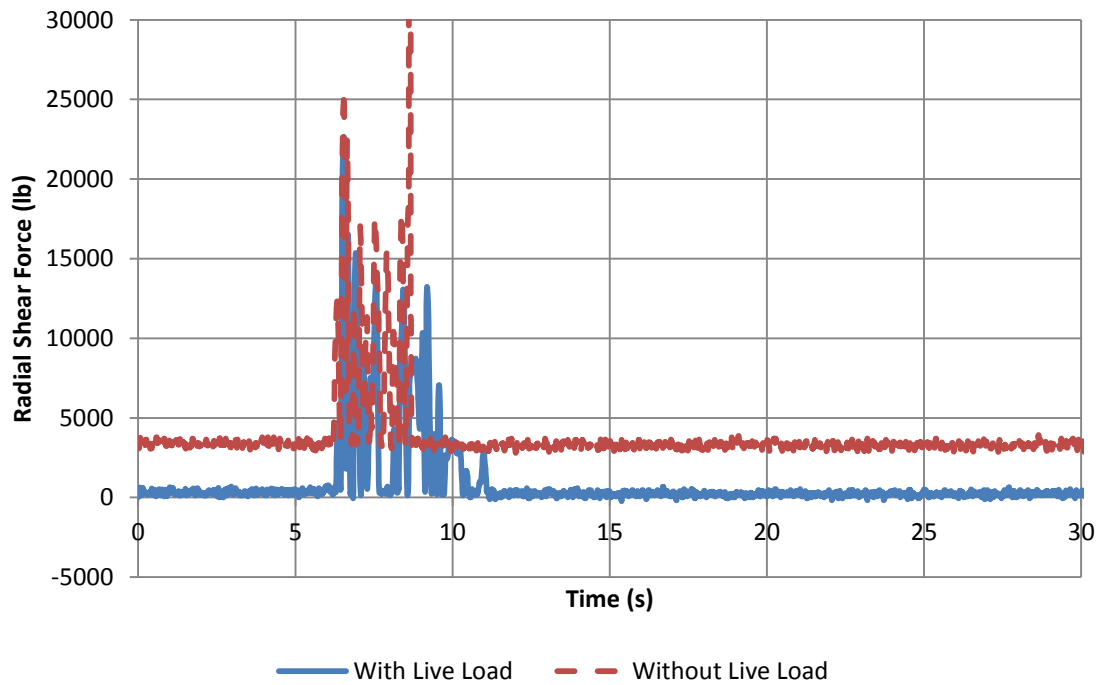


(b)

**Figure 5.9.3. Radial Shear Force in the Shear Key at (a) North and (b) South Abutment during 50% DE Run**

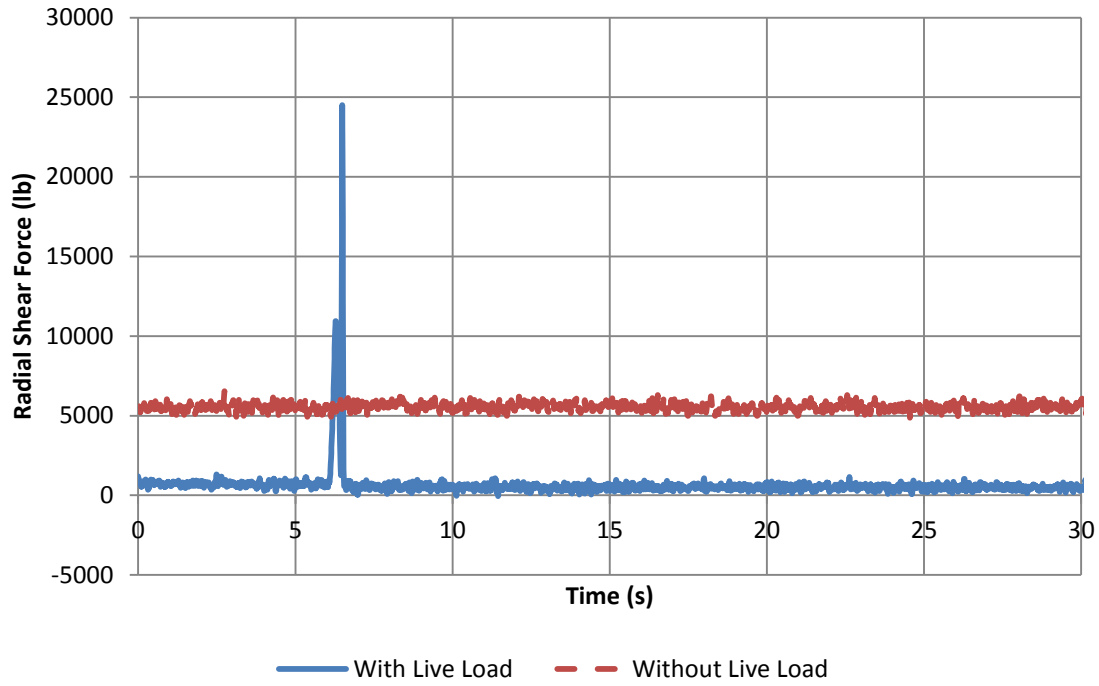


(a)

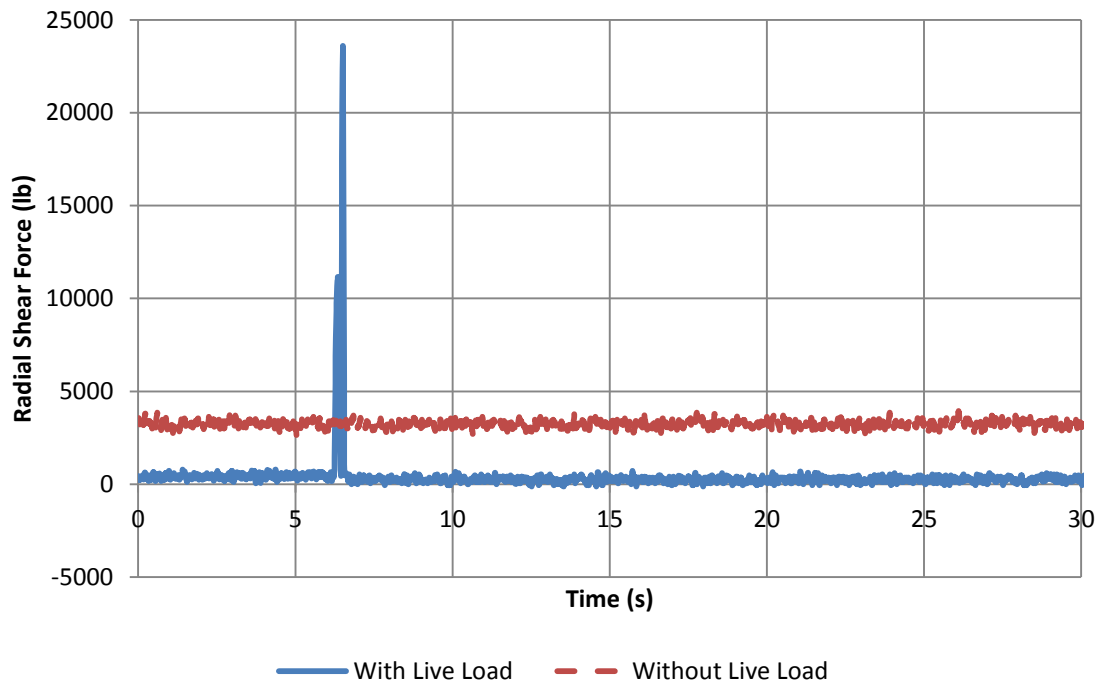


(b)

**Figure 5.9.4. Radial Shear Force in the Shear Key at (a) North and (b) South Abutment during 75% DE Run**



(a)



(b)

**Figure 5.9.5. Radial Shear Force in the Shear Key at (a) North and (b) South Abutment during 100% DE Run**

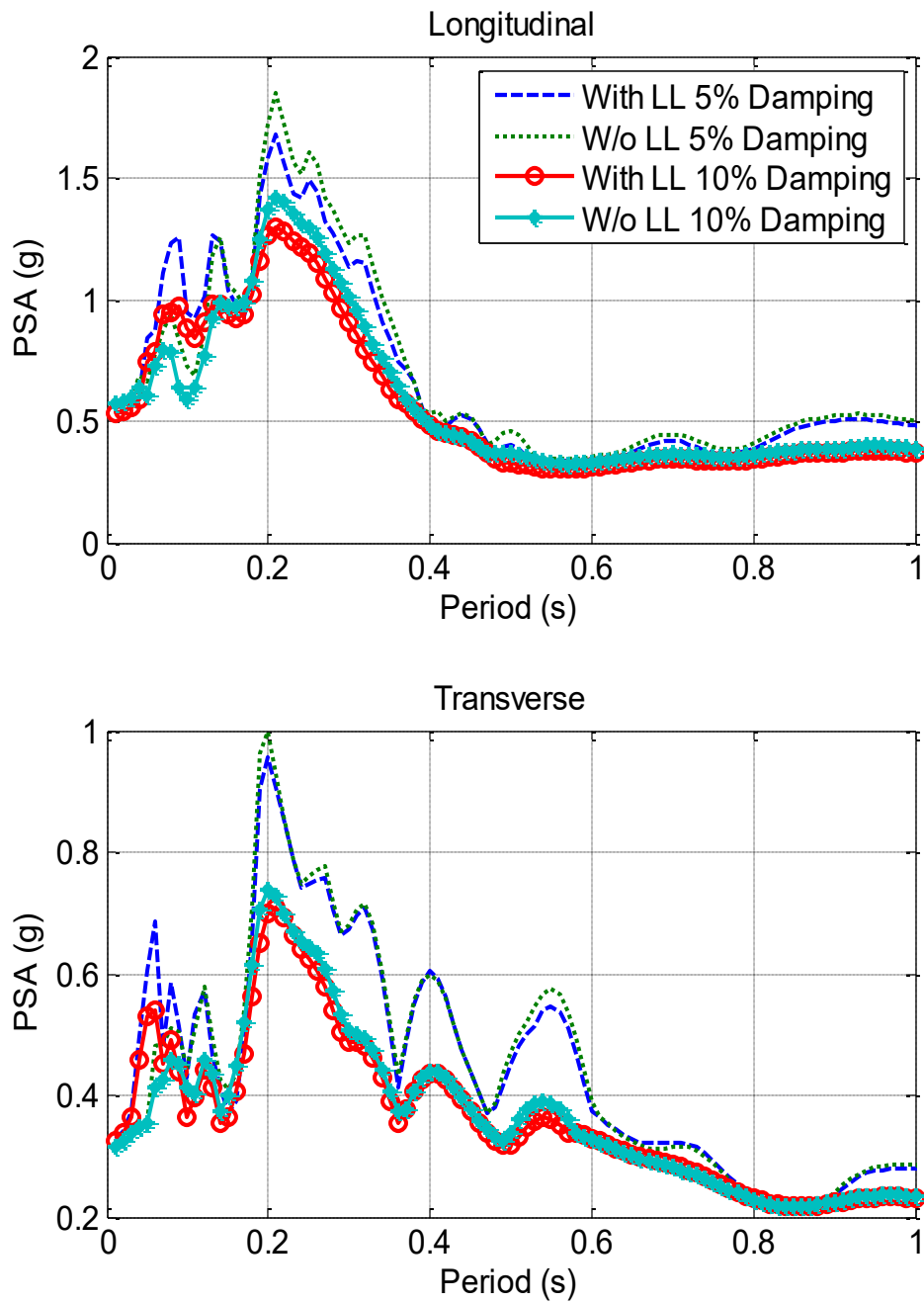


**Figure 5.10.1. Comparison of Table Acceleration Spectra for Various Damping Ratios for the No-Live Load and Live Load Experiments for 100% DE**

# CHAPTER 6. ANALYSIS RESULTS AND VALIDATION OF NUMERICAL MODEL

## 6.1. General

In this chapter an analytical model of the bridge and vehicle is developed and used to obtain numerical results for comparison with those from the experimental study (Chapter 5). In general, good agreement is obtained between the analytical and the experimental results.

## 6.2. Bridge Model and Input Motion

This section describes the analytical model of the bridge developed for the SAP2000 computer software package (CSI, 2011). Modeling assumptions and techniques are discussed. In addition, the acceleration histories used in the analysis are presented.

### 6.2.1. Model Development

Several analytical models were developed by others for use elsewhere in the FHWA Curved Bridge Project including a stick model, a beam-plate model, and a full 3D finite element model (Levi, 2011). The finite element model was chosen for this live load project in view of its superior accuracy and its development is described below. In fact two models were developed: one for each of the two boundary conditions at the abutments according to the status of the shear key located between the inner bay of the cross frame and the abutment seat:

1. Intact shear key and girders restrained in the radial direction but free to move (slide) tangentially, i.e. tangentially free radially restrained case (TFRR).
2. Failed shear key and girders free to move in any direction, i.e. free case (Free).

In addition to these boundary conditions, the girders were free to uplift as necessary. The PTFE and stainless steel bearings at the abutments were modeled with friction elements using coefficients of friction of 0.05 and 0.1 for slow and fast rates of loading respectively. Pinned bearings were assigned to each girder at the bents to allow rotation about any axis but restrain translation and uplift.

The girders and deck slab were modeled using shell elements in order to capture the flexibility of the superstructure. This model used a relatively fine mesh so that the shear studs between the girders and slab could be modeled as discrete link elements. In addition, the mesh layout for the shell elements in the deck slab was adjusted to create a more uniform discretization of the deck to better represent the actual locations of the added mass. The cross-frames, bent caps, and columns were modeled using beam elements.

The abutment towers used in the experiment were also included in the analytical model in order to determine the overturning moments and the axial and shear forces on the tables.

The modulus of elasticity,  $E$ , for the deck slab, bent caps, and columns was calculated from the measured compressive strength of concrete cylinder samples at the time of the experiment. The deck concrete strength was 6.4 ksi and thus the gross  $E$  is 4,842 ksi, calculated according to the AASHTO Specifications. Cracking in the deck slab was modeled using an effective  $E$  equal to 10% of the gross  $E$ . This estimate of the effective  $E$  is based on the measured deflection of the superstructure after the added weights were placed on deck. The column and bent cap concrete compressive strength was 6.37 ksi and thus the gross  $E$  is 4,839 ksi. In the plastic hinge regions, column inelasticity was modeled using fiber hinge elements. The confined and unconfined concrete properties used in the fiber hinge were determined using Mander's model. Reinforcement properties were based on the Park model modified to fit the stress-strain relationship obtained from testing a rebar sample. The actual yield strength was 71 ksi and the modulus of elasticity was 29,000 ksi. The measured modulus of elasticity was between 28,000 and 29,000 ksi. 29,000 ksi was used in the analysis.

Modeling the bents included elements for the column, bent cap, bearings, and load cells, located at their correct elevations. First, link elements representing the pinned bearing were used to connect the lower flange of the girder to the top of the load cell. The overall length of the link included the 1 in attachment plate placed on the bottom of the girder to attach to the bearing. Next, the load cell was modeled as a frame element between the top of the bent cap and the bottom of the pin bearing. This element included the height of the leveling plate and grout. The bent cap was developed using multiple sections to correctly model the beam's taper. This element was then inserted along the top center cardinal point unlike other elements which are typically inserted about the centroid. SAP2000 defines cardinal points in nine locations along the cross-section of a frame element, left, center, right, bottom, middle, and top. By selecting the appropriate cardinal point for the insertion point, the model was updated accordingly. Once this was completed, a rigid element was inserted into the model that was 24 inches in height to connect the top of the bent cap to the top of the column. This element was developed using the diameter of the column and modifying the properties of the section to create a rigid element with no mass or weight. This element was necessary due to the location of the insertion point for the bent cap. The column was modeled using three frame elements, two elements that were 14.855 inches long and one that was 62.29 inches long. The two smaller elements were placed at each end of the column in the locations of the expected plastic hinges; their length was chosen match plastic hinge length for this column. These elements were assigned a PMM fiber hinge to model the nonlinear effects of the columns. A total of 41 fibers were used to capture the progression of core damage in each column, as shown in Figure 6.2.1. The bottom of each column was assigned a fixed base condition which is a reasonable assumption in view of the stiffness and weight of the footing that was bolted to the table platen.

The column was assigned property modifiers. These modifiers were based on recommendations by Aviram *et al.* (2008) and included:

$$I_{eff} = \frac{M_y}{E \phi_y} \quad (6.2.1)$$

$$J_{eff} = 0.2J_g \quad (6.2.2)$$

$$A_{v,eff} = 0.8A_{v,g} \quad (6.2.3)$$

where:

- $I_{eff}$  = Effective moment of inertia
- $M_y$  = Moment at first yield in the reinforcing steel
- $E$  = Elastic modulus
- $\phi_y$  = Curvature at first yield in the reinforcing steel
- $J_{eff}$  = Effective torsional resistance
- $J_g$  = Gross torsional resistance
- $A_{v,eff}$  = Effective shear area
- $A_{v,g}$  = Gross shear area

The above recommendations anticipate cracking in the columns due to gravity and wind loads (and in the case of the experiment in Chapter 4, moving the columns from the fabrication yard to the shake tables). Aviram et. al. (2008) also recommend placing the plastic hinges at the midpoint of each hinge with the assumption of constant plastic curvature throughout the hinge zone. Using the above equations, the value of the effective moment of inertia was calculated to be approximately 30% of the gross moment of inertia. In addition, as noted above, the modulus of elasticity for the deck slab was reduced to 10% of the gross value to account for cracking of the slab during handling and minor damage from previous experiments.

With the model complete, the additional mass necessary to satisfy the similitude scaling laws was added to the model. Since the exact location of the additional mass would not be known until the mass was placed on the deck, a preliminary estimate of the mass location was used. However, due to the way the deck was modeled, with shell elements following radial and tangential directions, the deck elements could not match the actual dimensions of the lead and steel baskets exactly. Thus, the locations of the corners of the steel and lead baskets were determined to select the outer boundaries of the additional mass. The shell elements were then selected in accordance with these areas and grouped together in the tangential direction of the bridge. The area for each section was then determined and the correct load and mass assigned to the area elements. To assign the additional mass to the bent cap, first, a line load was assigned to the frame in the locations where the additional mass would be located. This represented the actual additional mass on the bent cap. However, since SAP2000 does not have a mechanism to model mass on a frame at specific locations, the mass for this weight was assigned along the entire length of the bent cap instead of at the true location. The final 3D model in SAP2000 is shown in Figure 6.2.2.

### **6.2.2. Input Motion for Nonlinear Response History Analysis**

The acceleration histories used as the input motion for the analytical study were taken to be the average achieved table accelerations of all four shake tables in the longitudinal and transverse directions, as mentioned in the previous chapter. After averaging all four table accelerations in each direction, filtering and base correction were applied to the acceleration history. Figure 6.2.3 shows an example of the table input accelerations in the longitudinal and transverse directions for the 100% DE excitation.

## **6.3. Vehicle Model**

Based on work described in Chapter 3, a 3D numerical model to represent the vehicle was also developed.

### **6.3.1. Model Development**

As described in Chapter 3 the vehicle model used in this study was based on the model by Kim *et al.* (2005) as shown in Figure 2.7.6. This model was improved to more accurately represent the behavior of the vehicles used in the experiment. The final model was a 16 degree-of-freedom mass-spring-damper system as shown in Figure 6.3.1.

### **6.3.2. Vehicle Properties**

As described in Chapter 3, a single truck experiment was carried out prior to the live load experiments in Chapter 4, to determine the properties required to develop an analytical model for the vehicle. Summaries of the vehicle properties for the empty and fully-laden conditions are given in Table 3.8.1. Properties for the fully-laden vehicle were used in the analysis that follows.

## **6.4. Refinements to Analytical Model**

A set of refinements to the analytical model could be implemented to better represent the actual model tested in the laboratory. These refinements include bond slip, strain rate effects, and P- $\Delta$  effects, but all were considered second order effects and none were implemented in the analysis that follows.

Advanced friction elements could also be included at the abutment locations in the numerical model. From the forces recorded in the load cells underneath each girder, the pressure in each slider was found to be low with a maximum value in the range of 700-800 psi. Therefore the coefficient of friction of the slider is probably in the range of 10% to 20%. The modal damping ratios used for the development of the Rayleigh damping matrix could also be refined to better represent the damping in the structure

from sources other than friction at the abutments and hysteretic damping in the plastic hinges.

## **6.5. Structural Response and Comparison with Experimental Results**

In this section, the results of the analytical study are presented. These results include displacements, accelerations, forces, and moments in the structure. Overall performance of the bridge is compared. For the numerical model the shear keys were considered effective up to and including the 75% DE at which time they failed. These keys were removed from the model for the 100% DE and higher runs. All results in this section are for the case with live load.

### **6.5.1. Displacement**

The theoretical displacements at the top of the bents obtained from the analysis are compared to the experiment results. The EI modifier for analysis with live load was chosen to be 60% to represent the damage state corresponding to the experiment. Figures 6.5.1 through 6.5.3 show the analytical and experimental results for the north and south column resultant displacement histories for 100%, 200%, and 300% DE, respectively. It is shown that the analytical results are comparable in magnitude with the experimental results. However, it is also observed that the after-peak response from the numerical model could perhaps be improved by refining the numerical model.

For the higher amplitude runs, the numerical model still shows good agreements with the experiment, although the difference between them increases. Figures 6.5.2 and 6.5.3 show the displacement histories from the 200% DE and 300% DE runs, respectively. In the higher runs, the EI modifier in the plastic hinge area was reduced to simulate the damage accumulation from the previous runs as observed in the experiment. However, a more rigorous protocol-type analysis, i.e., running the analysis from the lower amplitudes up to the higher amplitudes, may give more accurate results.

### **6.5.2. Acceleration**

The acceleration histories in the longitudinal and transverse directions at the middle of the bridge during the 100% DE are shown in Figures 6.5.4. It can be observed that the acceleration response from the analysis agrees well with the experiment result for this earthquake run. The magnitude of the acceleration is within the same range except for the moment when the shear keys failed. The values obtained from the experiment show a jump in the acceleration which is due to the impulse and energy released as the shear keys ruptured. The analysis results do not show this jump since the shear keys were not in place during this run. This is because a satisfactory element to model a failing shear key in real time could not be developed using the element library in SAP2000. For the higher amplitude runs such as 200% DE and 300% DE as shown in Figures 6.5.5 and

6.5.6, the agreement between experiment and the analysis decreases. The analysis results in these runs overestimated the acceleration response of the structure.

### **6.5.3. Forces and Moments**

Good agreement was also obtained for the forces and moments at the bottom of the bents. Figures 6.5.7 through 6.5.9 show the axial force, resultant shear force, and resultant moment histories at the bottom of north and south bents during 100% DE run. These results follow the same trend as the displacement. The magnitudes of the responses are within the same range as in the experiment results. Similarly for the higher amplitude runs, as shown in Figures 6.5.10 through 6.5.15 for 200% DE and 300% DE runs, the analysis results overestimated the demand especially in the post-peak regions.

## **6.6. Analysis of Bridge Model With and Without Live Load**

The numerical model was used to perform analyses on the bridge model with and without live load. For 100% DE, the EI modifier was chosen to be 60% and 30% for analyses with and without live load respectively, which attempts to represent the state of damage in the columns in the two cases. Figure 6.6.1 compares the resultant displacements from the analyses with and without live load. As with the experimental work in Chapter 5, it is shown that the presence of live load has a beneficial effect and reduces the displacement demand on the columns. For higher amplitude earthquakes, such as 200% DE, the beneficial effect is reduced as shown in Figure 6.6.2. It follows the numerical model gives similar results to those observed in the experiments and, as with previous analytical results, further refinements are expected to give better estimation of the maxima and post-peak regions.

## **6.7. Discussion**

The analysis results show very good agreement for the peak responses but this agreement decreases in the after-peak response. However, the overall predictions of the numerical model show promising results and it may be concluded that the observations from the experiment can be captured by the numerical model. The model can be fine-tuned by including the refinements mentioned earlier for future studies.

## **6.8. Summary**

A numerical model of a bridge with live load has been developed and validated against the experimental results in Chapter 5. Response history analyses have been carried out using the SAP2000 software package and results compared against experiment data. It has been shown that the analysis results agree well with the

experimental results. The results from analyses with and without live load show the same trend as observed in the experiment. However, some refinements are indicated and deserve consideration in future developments of the bridge-vehicle model.

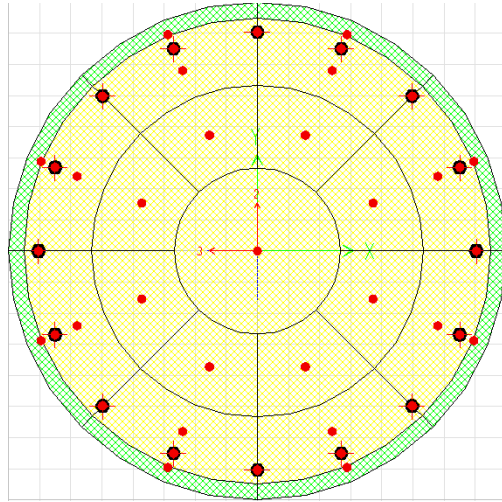


**Figure 6.2.1. Fiber Layout of Column Section**

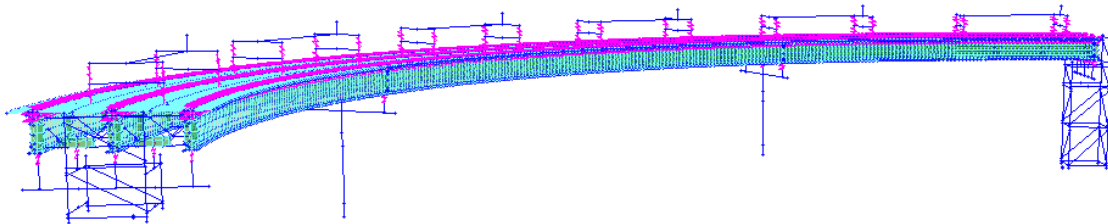
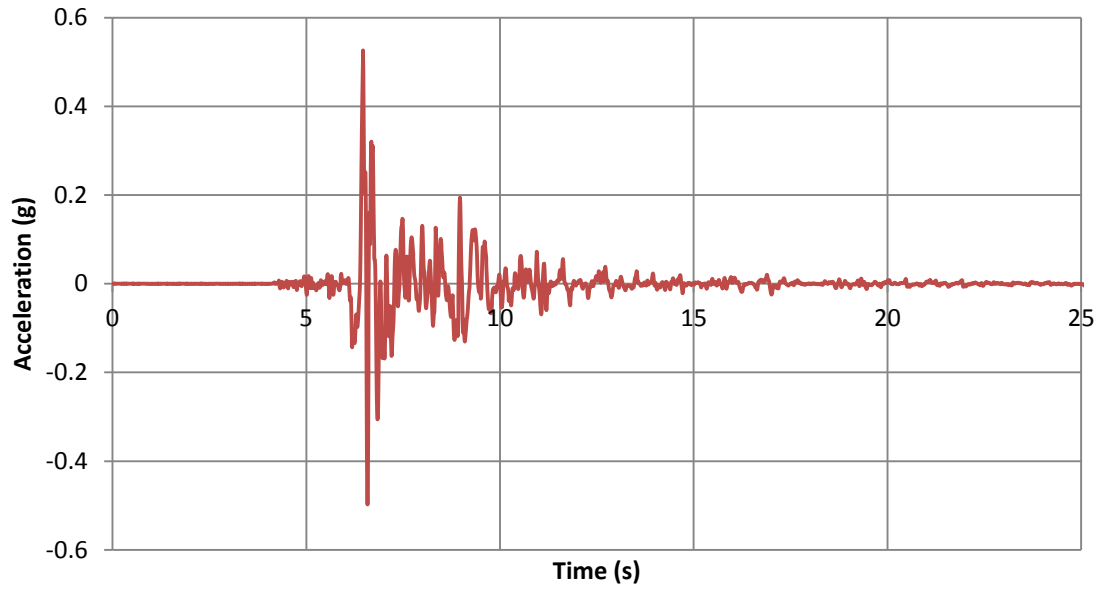
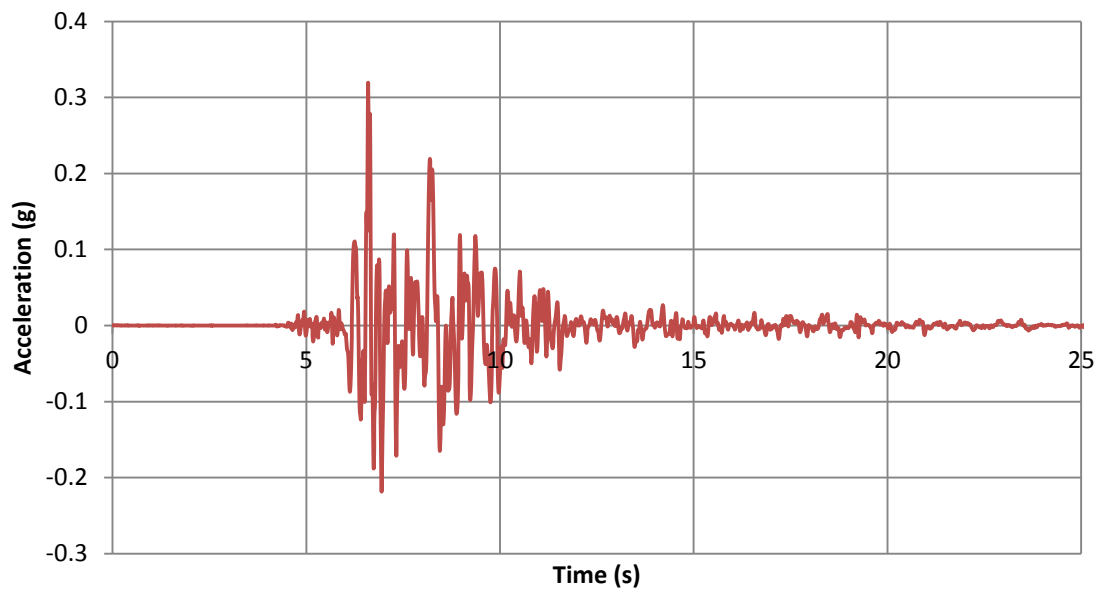


**Figure 6.2.2. 3D Finite Element Model of Bridge and Trucks**



(a)



(b)

**Figure 6.2.3. Input Acceleration History in (a) Longitudinal and (b) Transverse Direction for 100% DE Run**

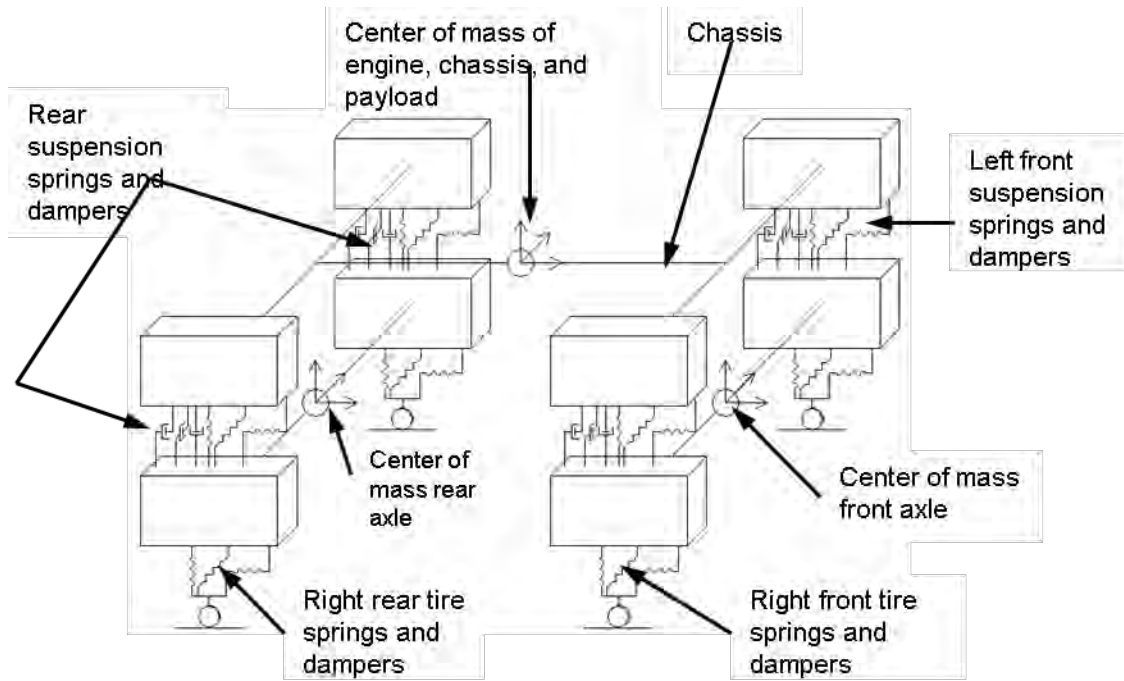
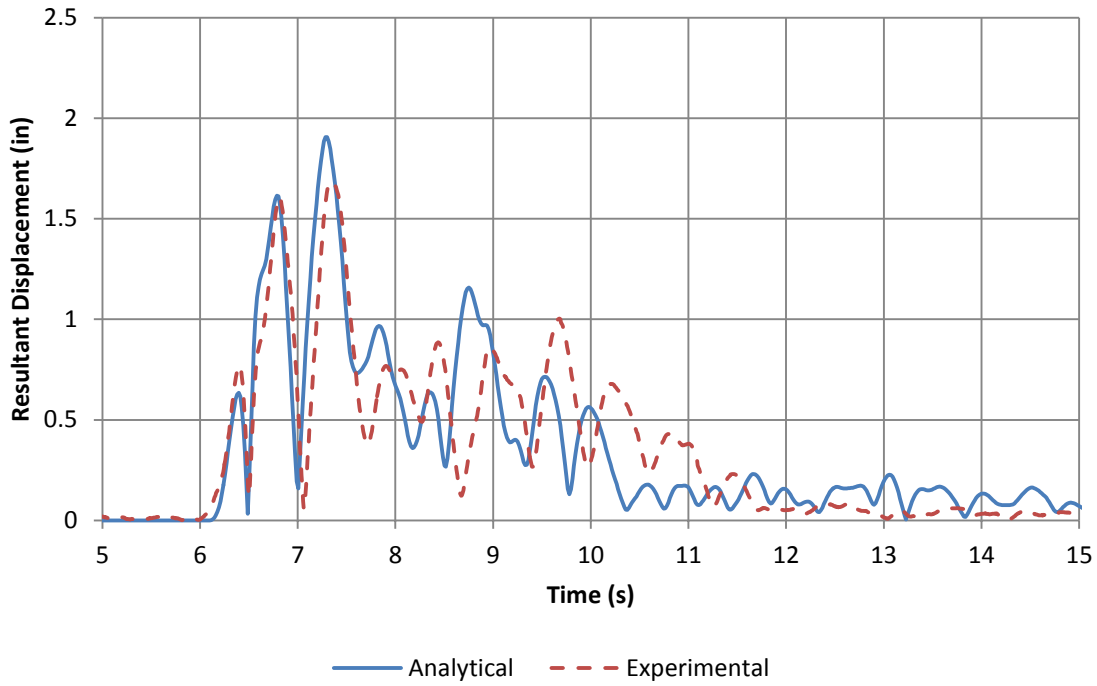
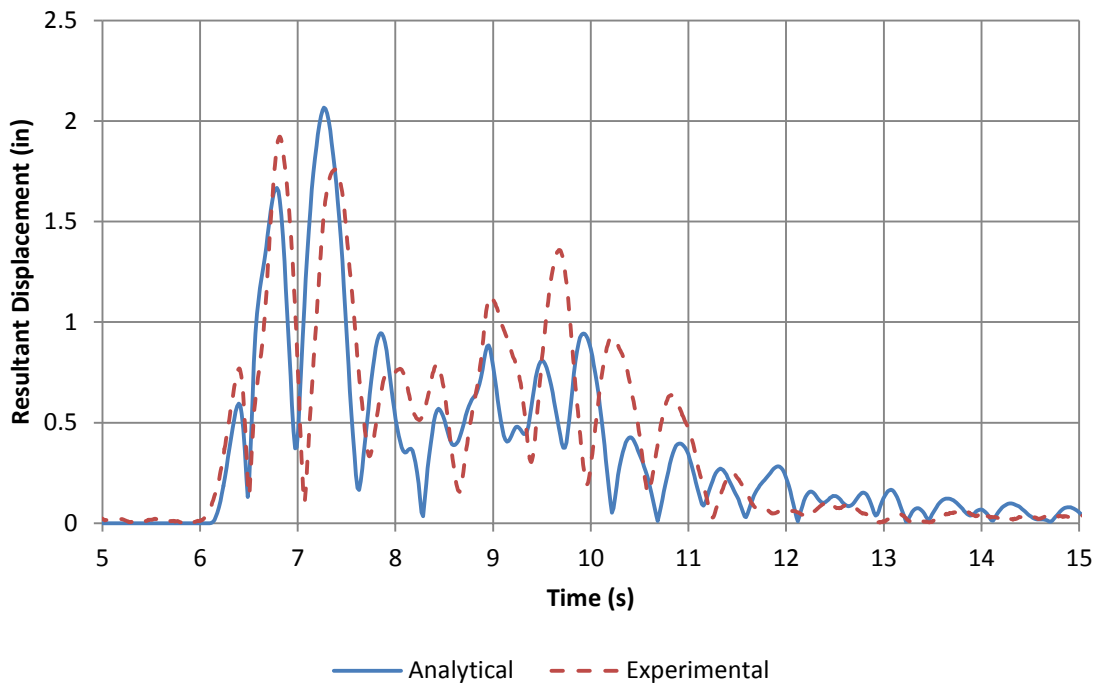


**Figure 6.3.1. 16 Degree-of-Freedom Vehicle Model**

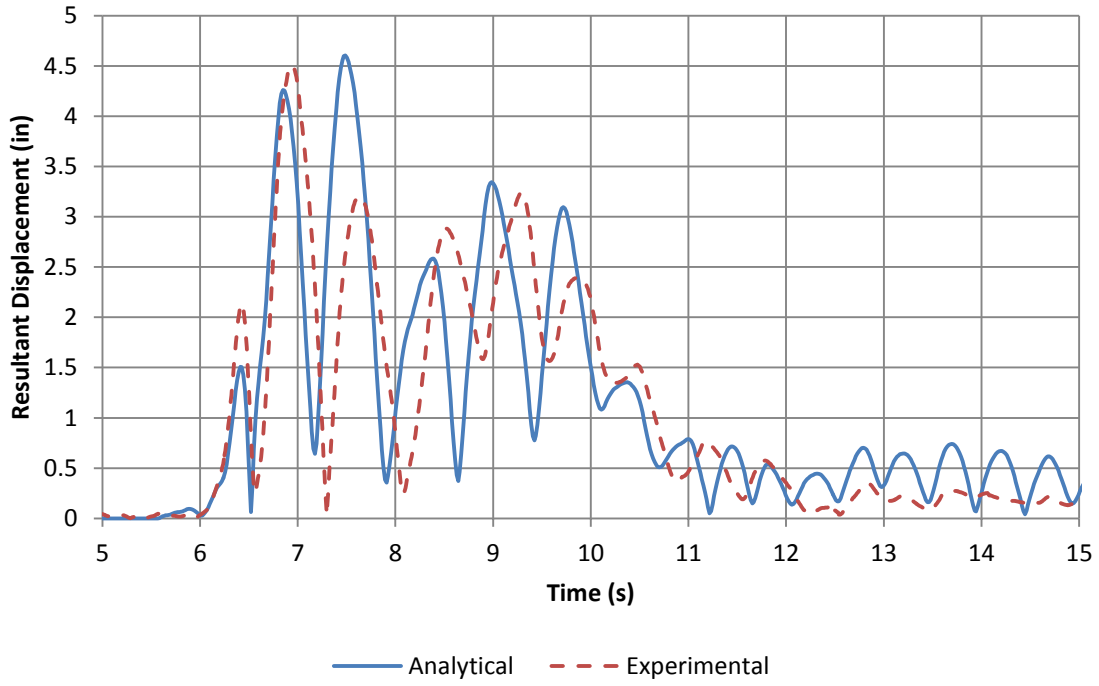


(a)

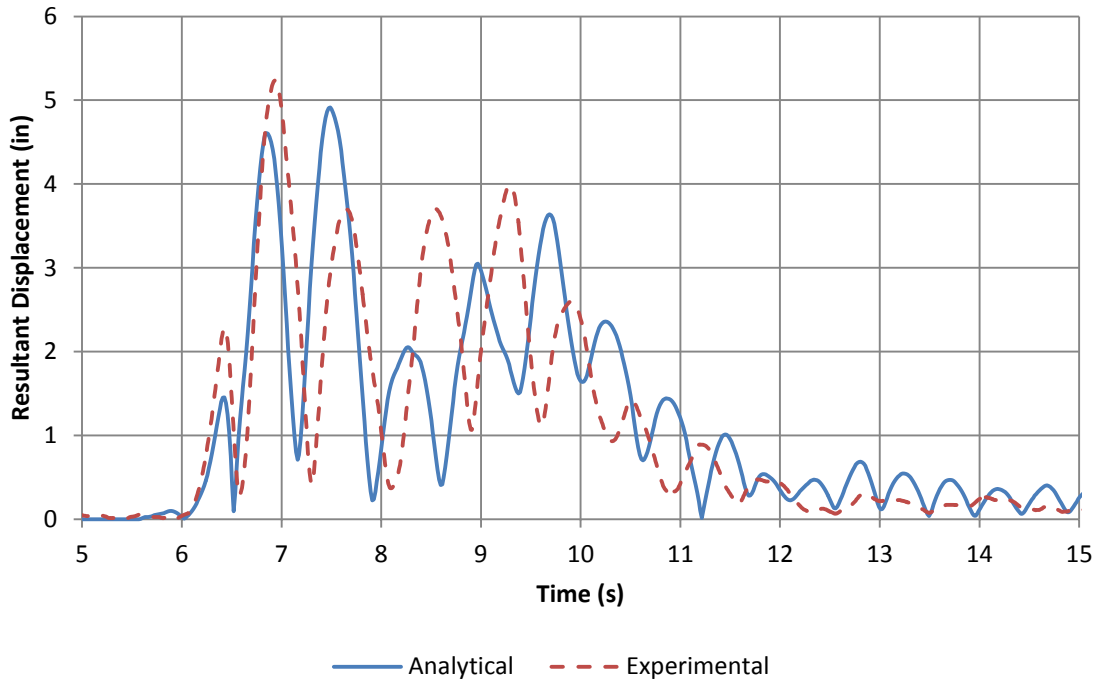


(b)

**Figure 6.5.1. Displacement Histories at the Top of (a) North and (b) South Bent during 100% DE Run**

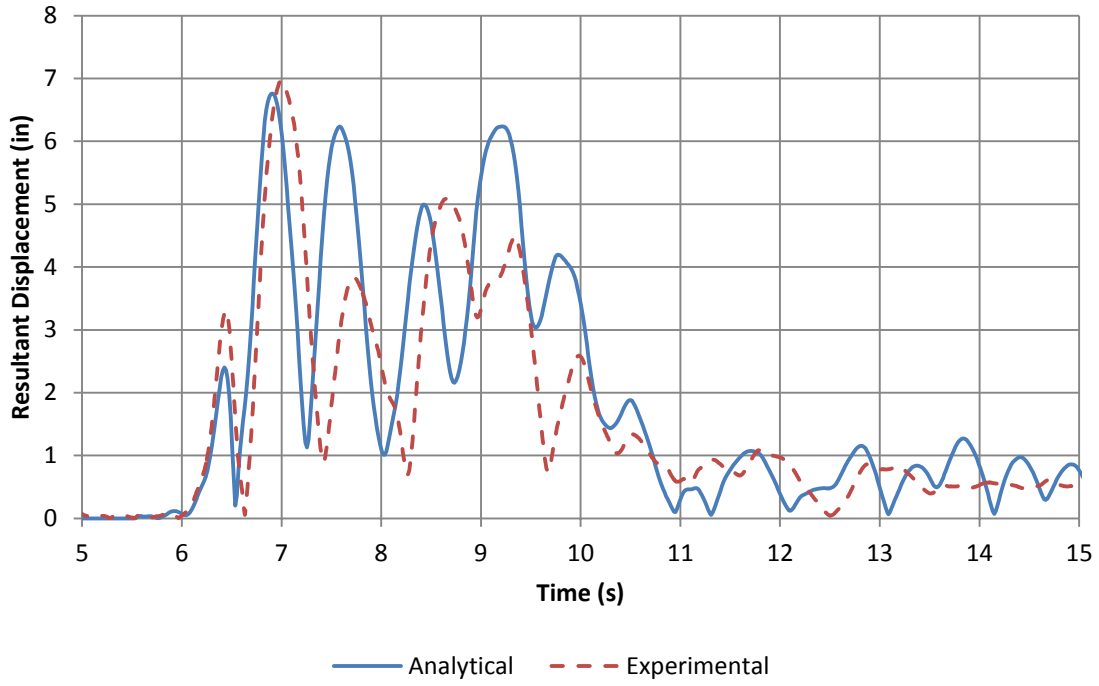


(a)

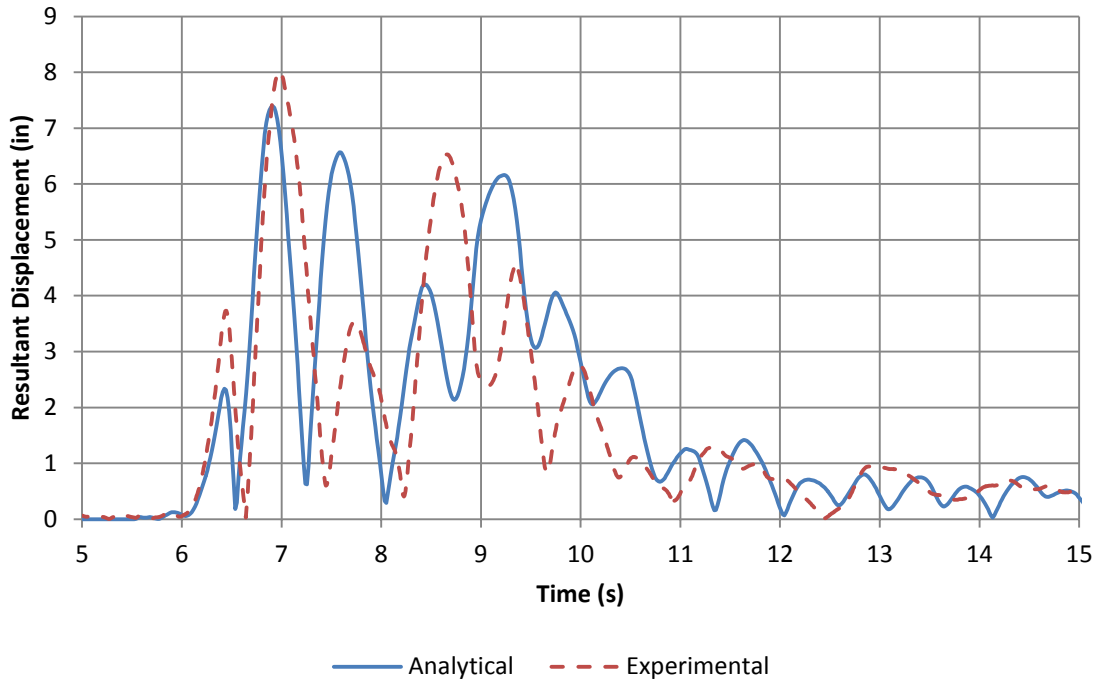


(b)

**Figure 6.5.2. Displacement Histories at the Top of (a) North and (b) South Bents during 200% DE Run**

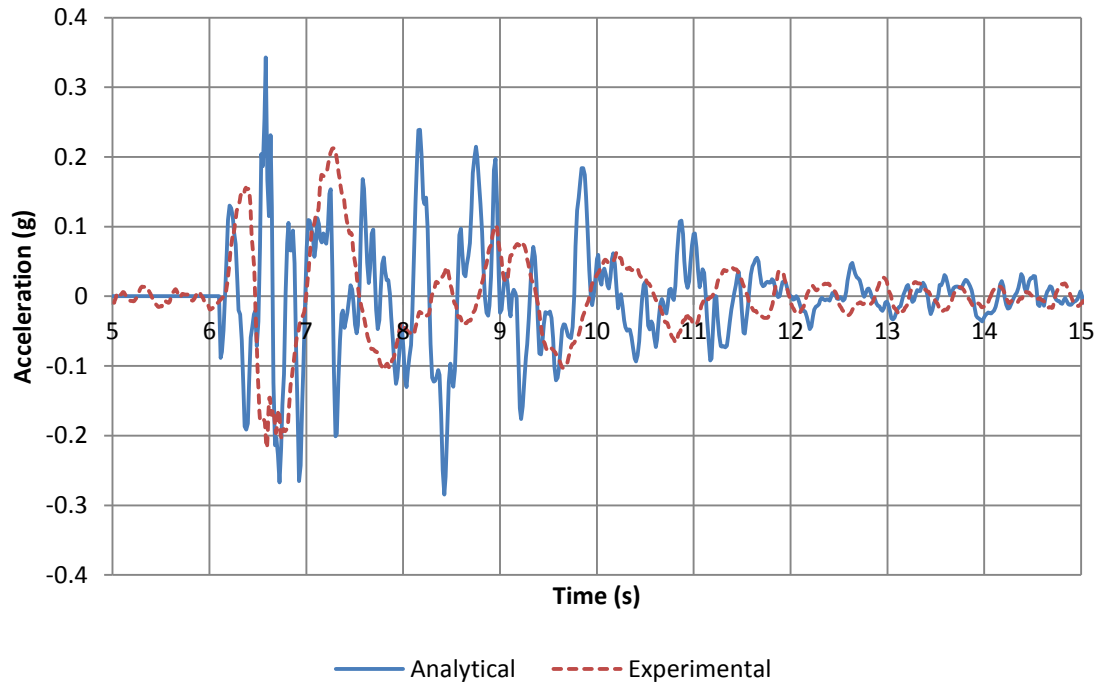


(a)

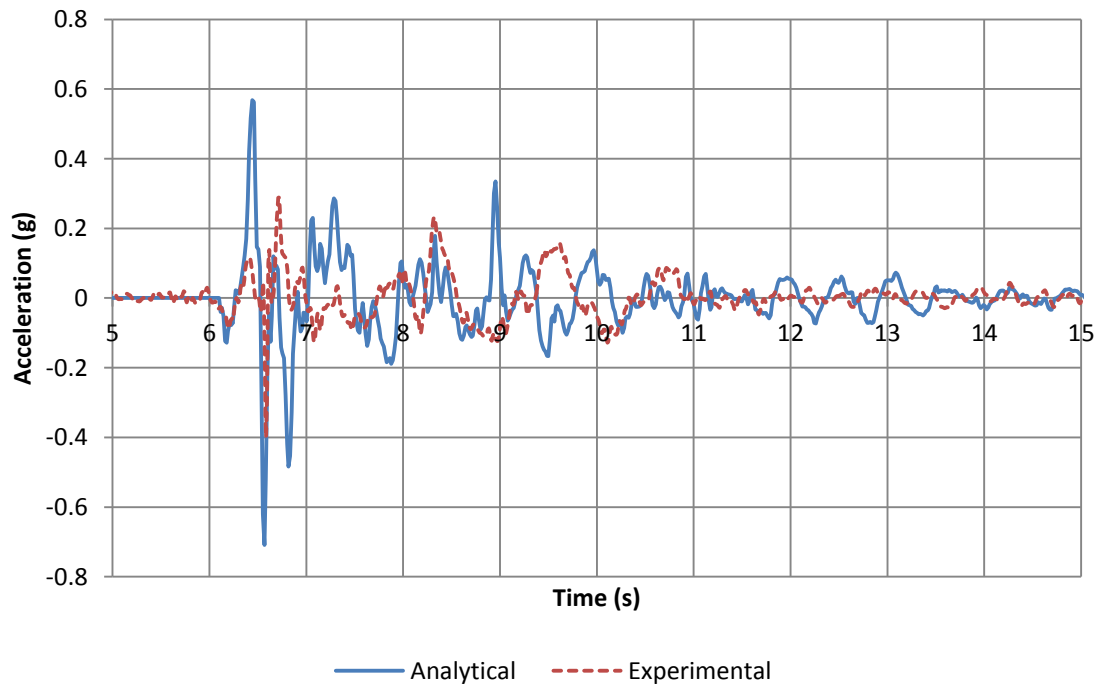


(b)

**Figure 6.5.3. Displacement Histories at the Top of (a) North and (b) South Bents during 300% DE Run**

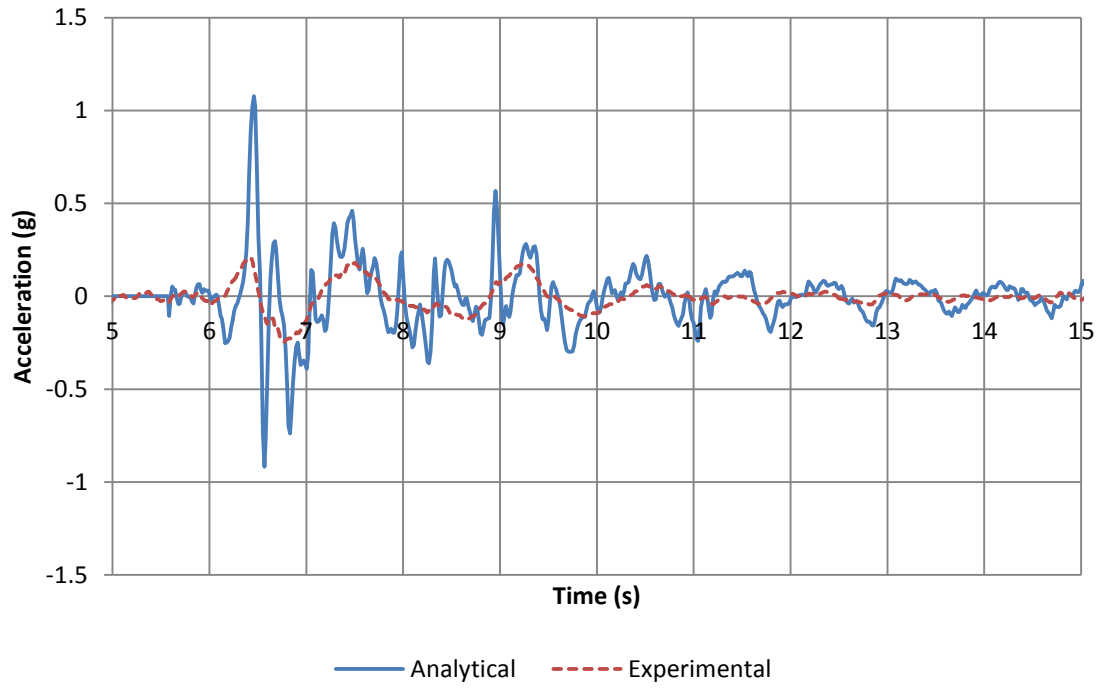


(a)

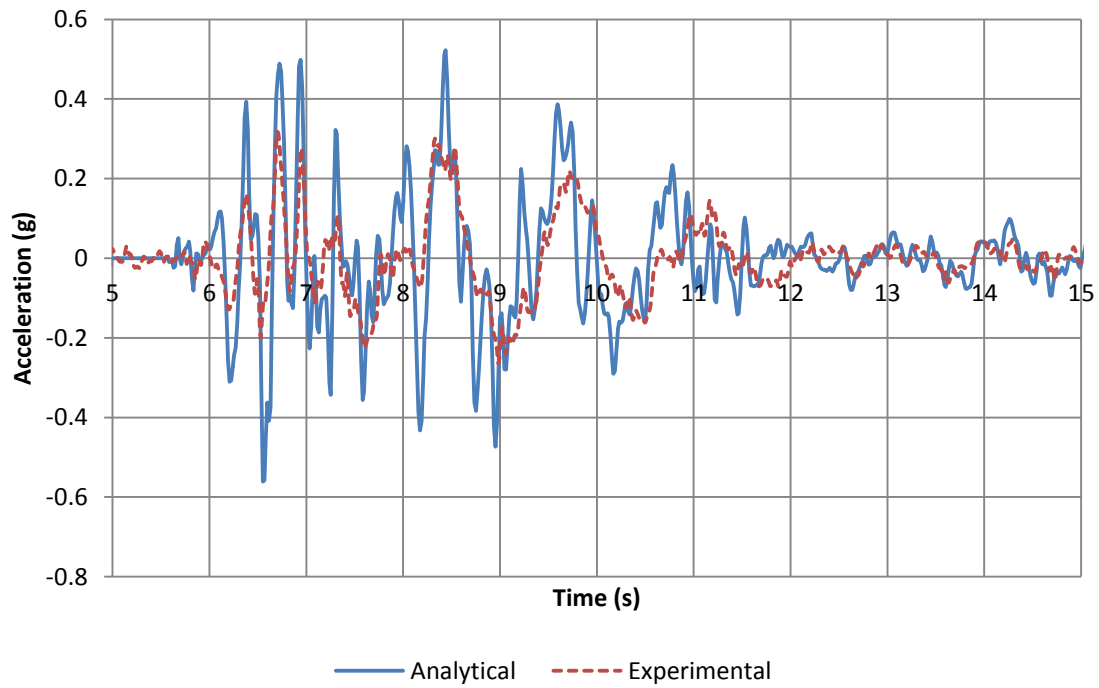


(b)

**Figure 6.5.4. (a) Longitudinal and (b) Transverse Acceleration Histories on the Deck at Mid-Span above Middle Girder during 100% DE Run**

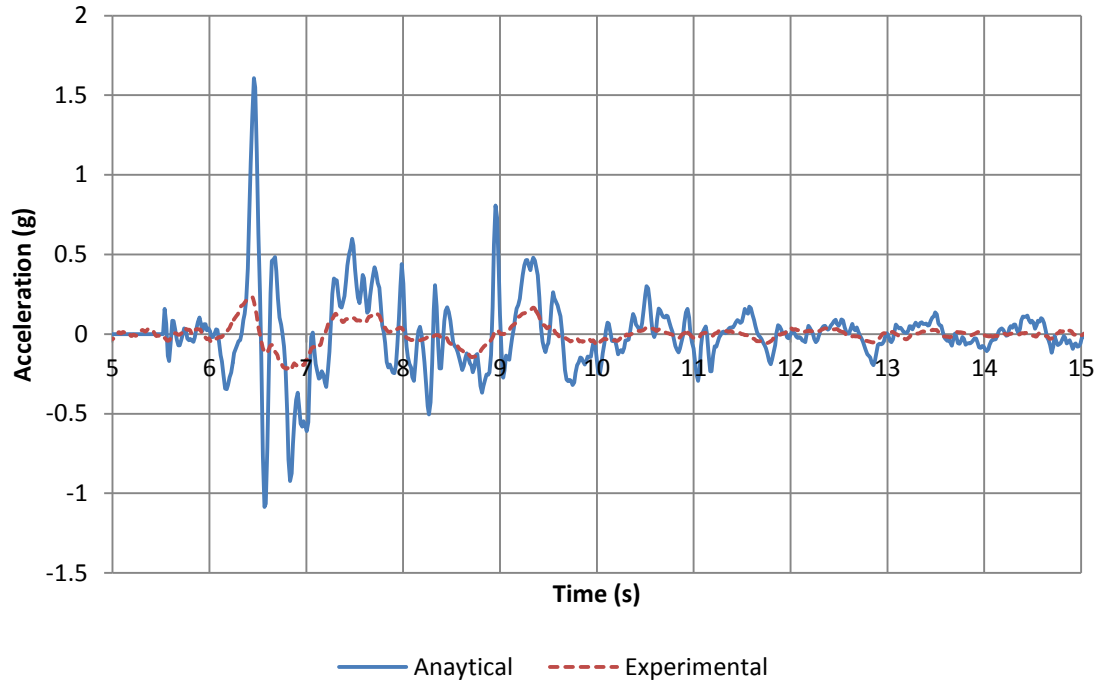


(a)

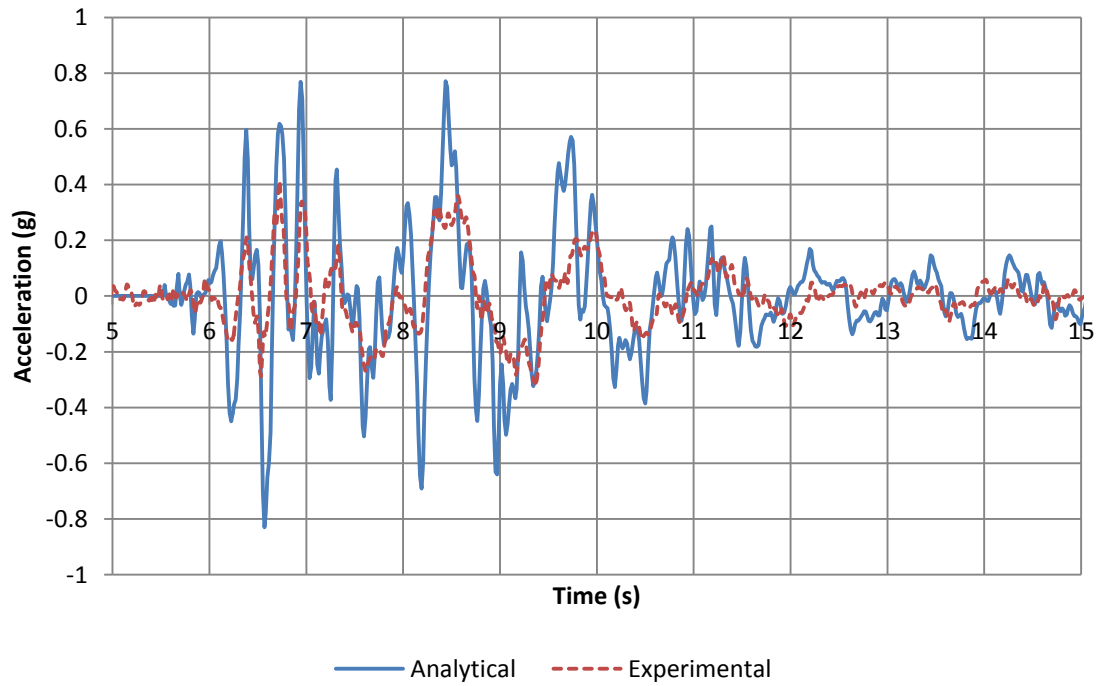


(b)

**Figure 6.5.5. (a) Longitudinal and (b) Transverse Acceleration Histories on the Deck at Mid-Span above Middle Girder during 200% DE Run**

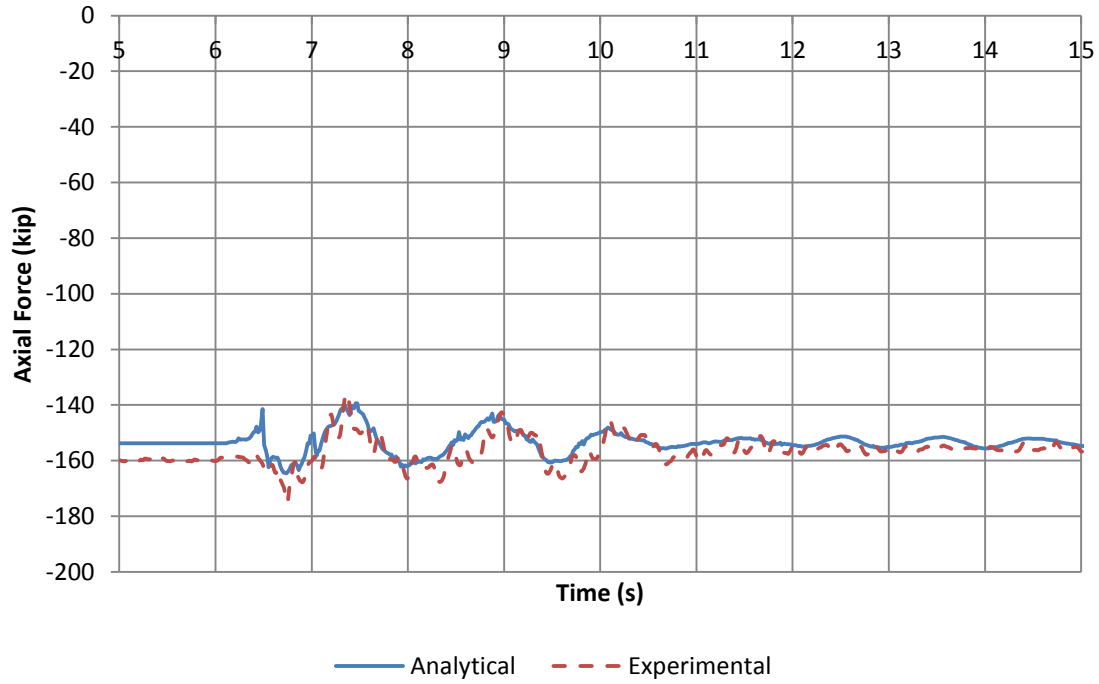


(a)

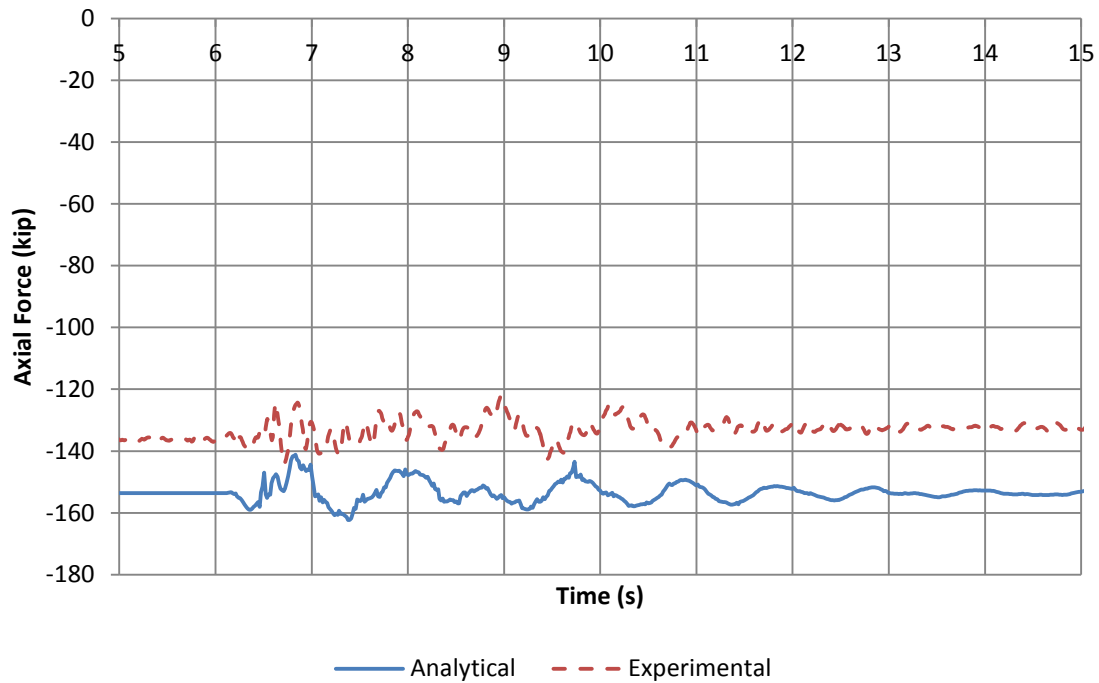


(b)

**Figure 6.5.6. (a) Longitudinal and (b) Transverse Acceleration Histories on the Deck at Mid-Span above Middle Girder during 300% DE Run**

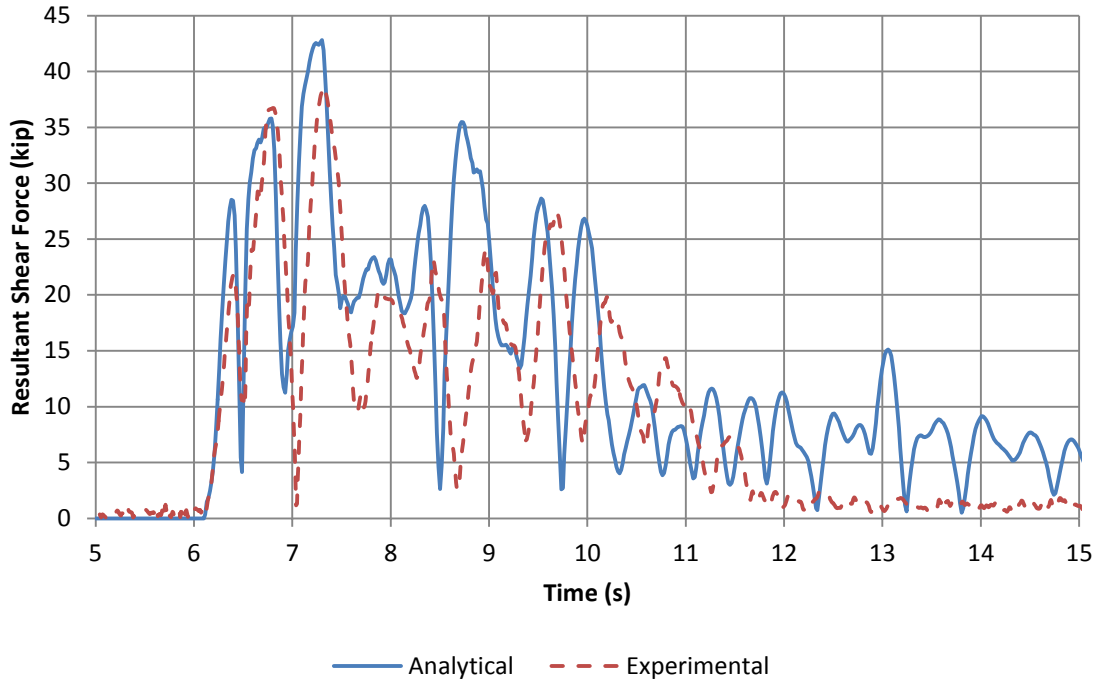


(a)

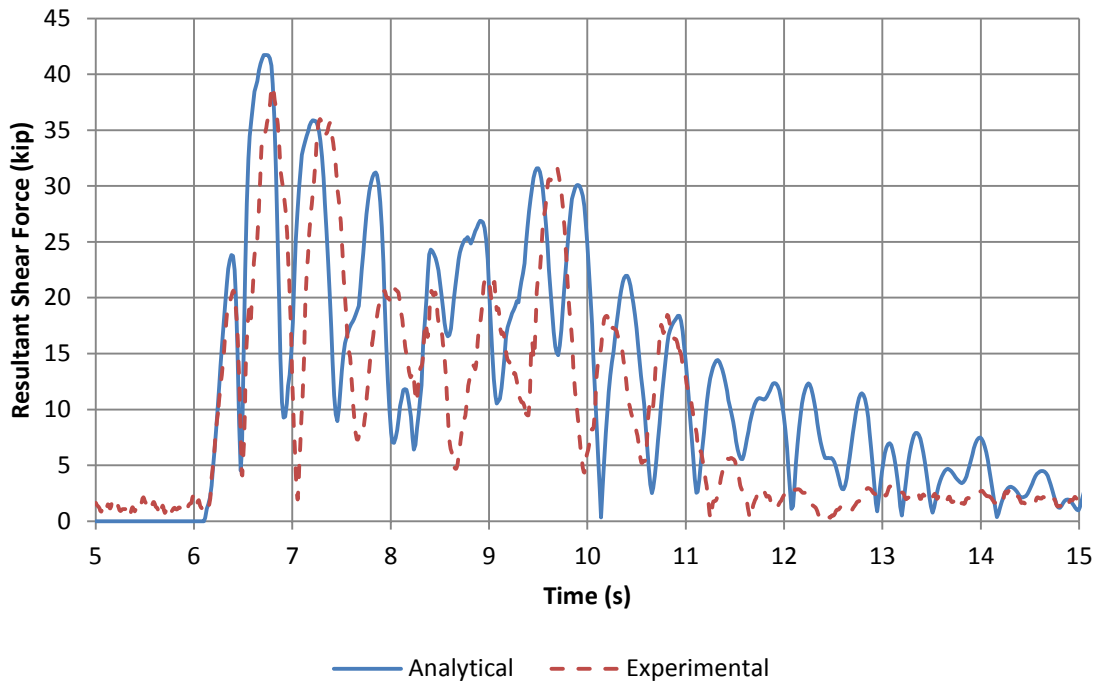


(b)

**Figure 6.5.7. Axial Force Histories at Bottom of (a) North and (b) South Bents during 100%DE Run**

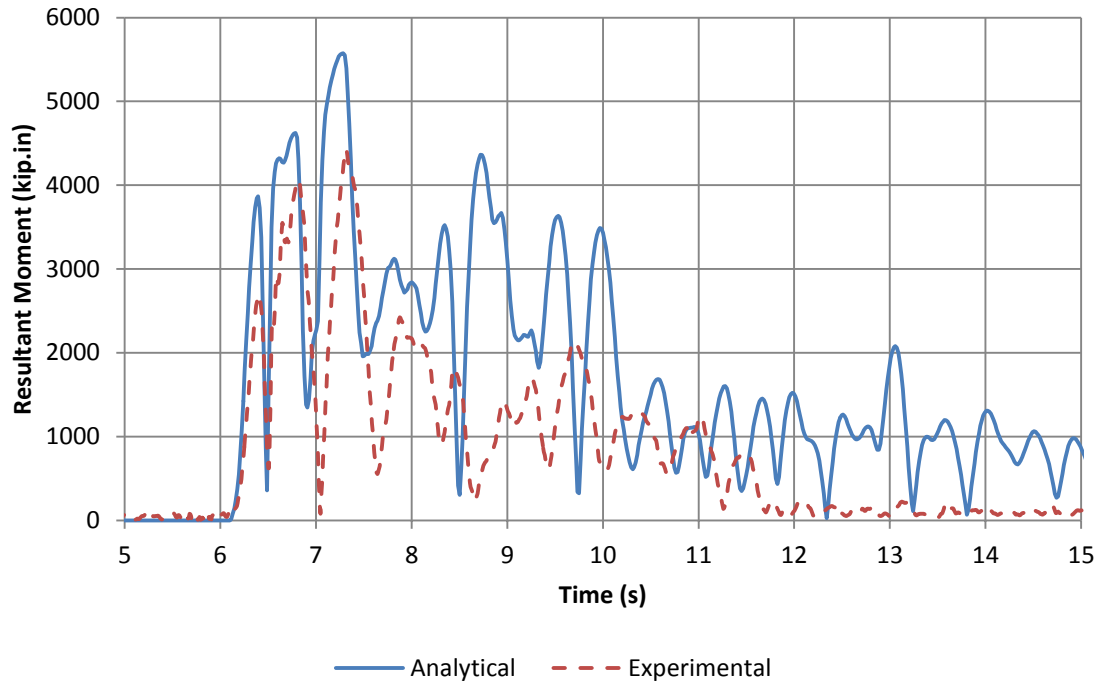


(a)

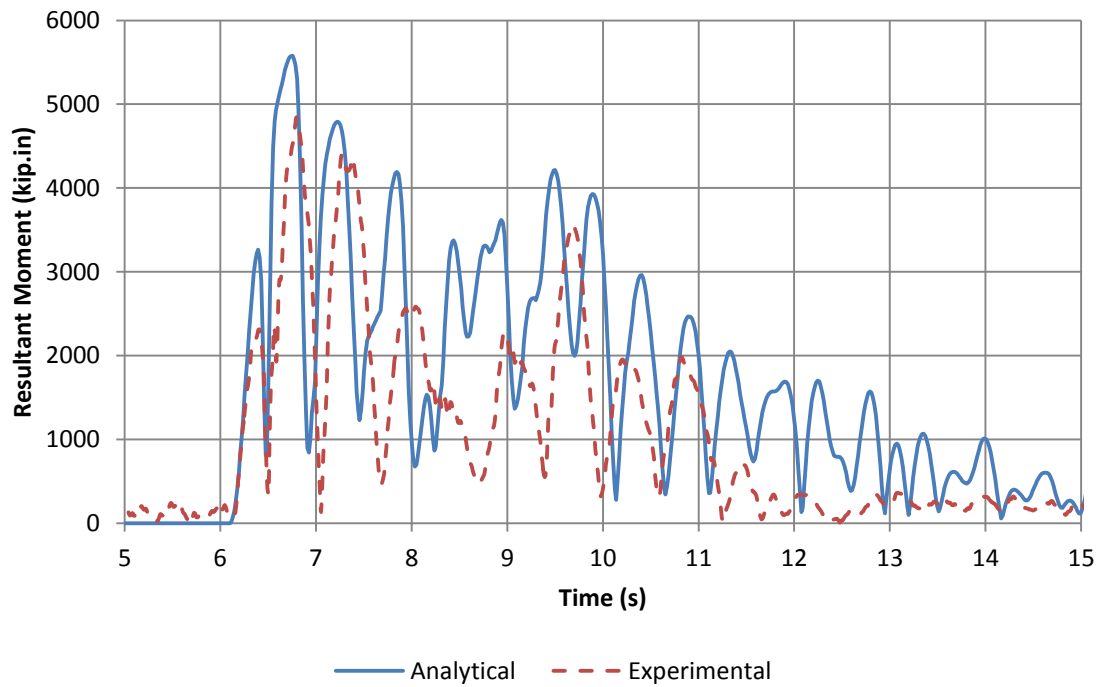


(b)

**Figure 6.5.8. Resultant Shear Force Histories at Bottom of (a) North and (b) South Bents during 100%DE Run**

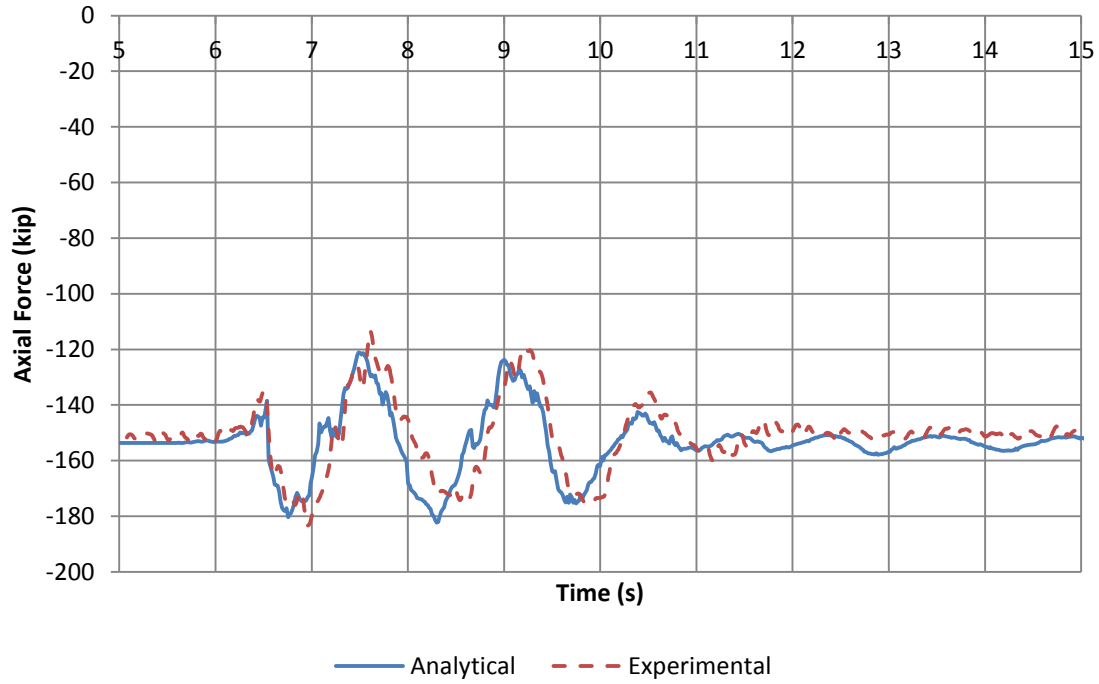


(a)

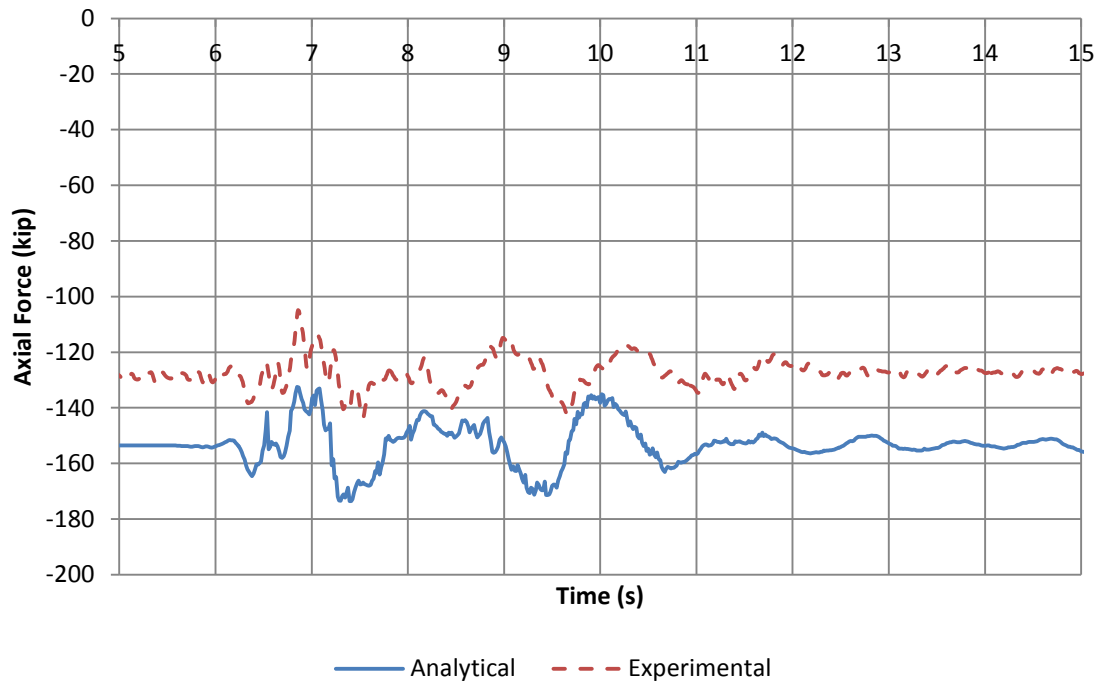


(b)

**Figure 6.5.9. Resultant Moment Histories at Bottom of (a) North and (b) South Bents during 100% DE Run**

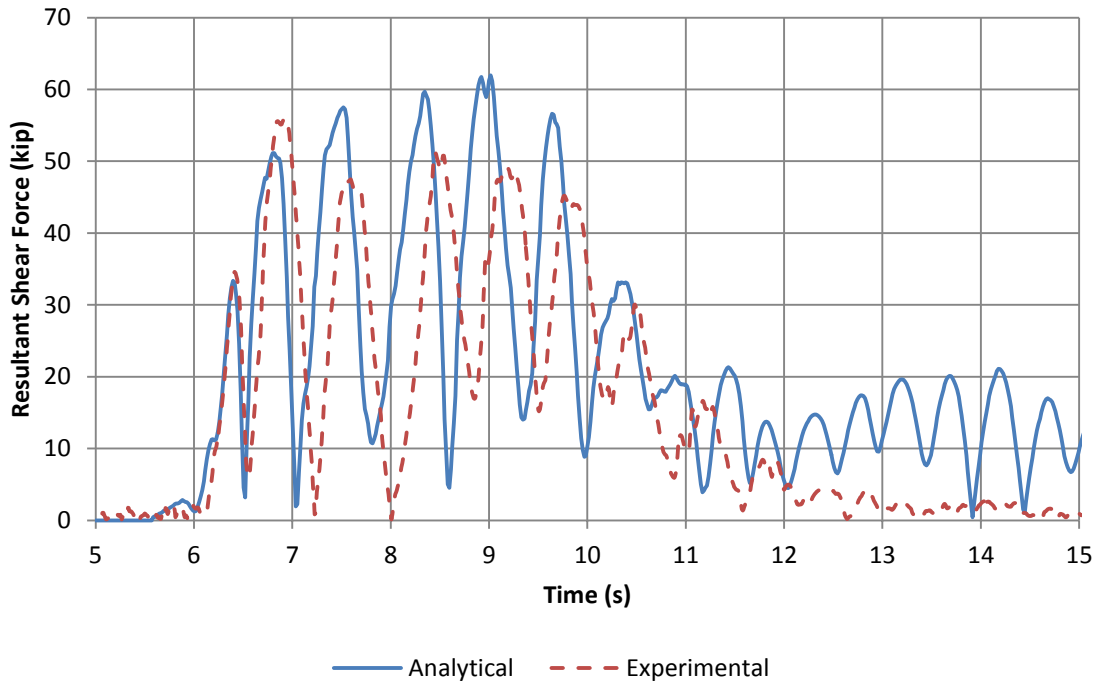


(a)

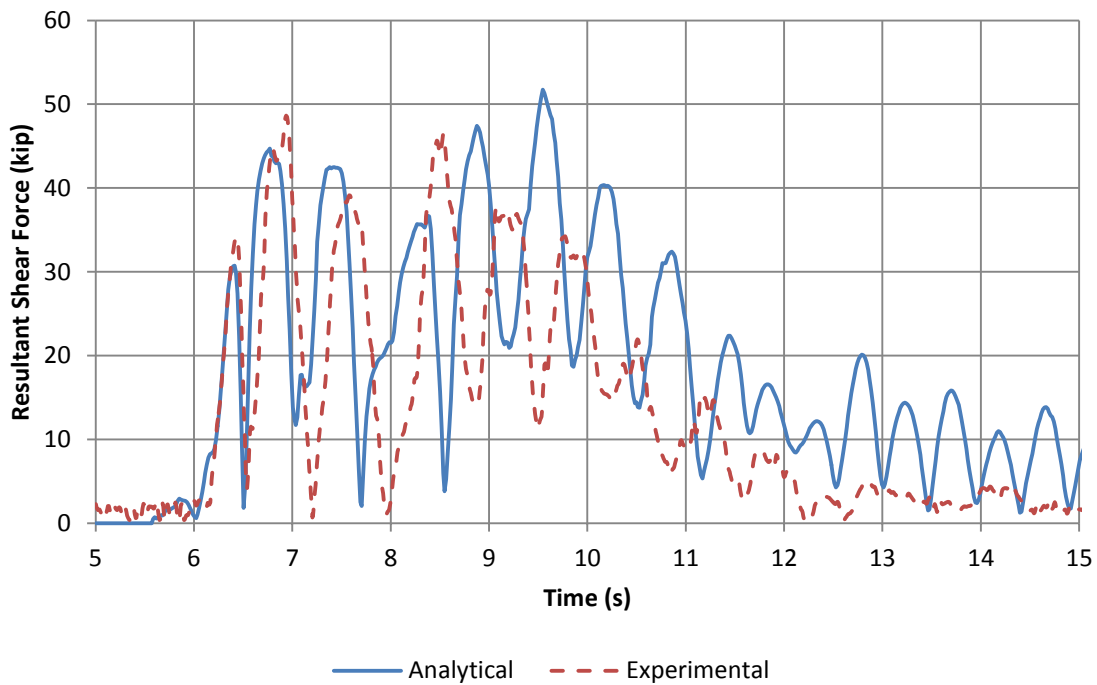


(b)

**Figure 6.5.10. Axial Force Histories at Bottom of (a) North and (b) South Bents during 200% DE Run**

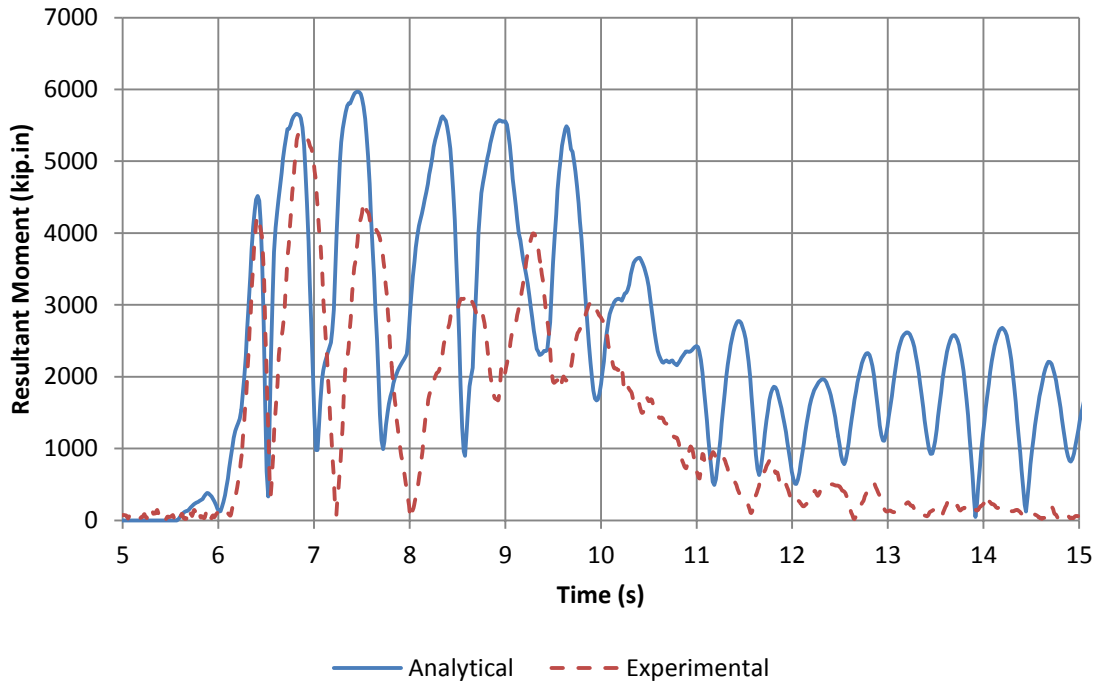


(a)

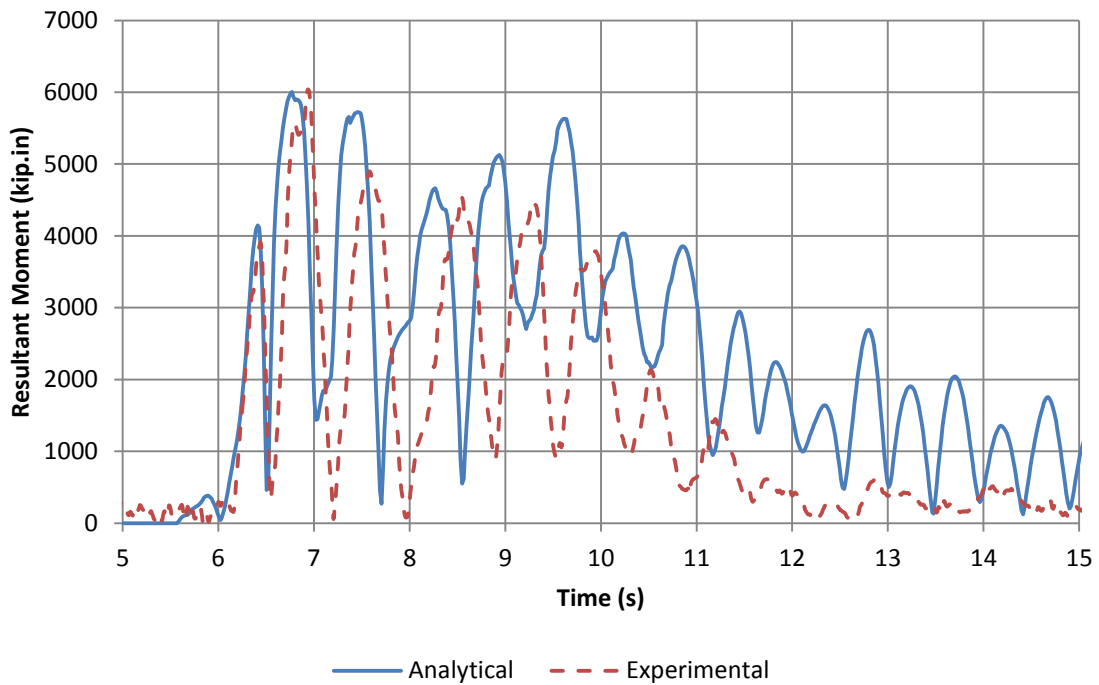


(b)

**Figure 6.5.11. Resultant Shear Force Histories at Bottom of (a) North and (b) South Bents during 200% DE Run**

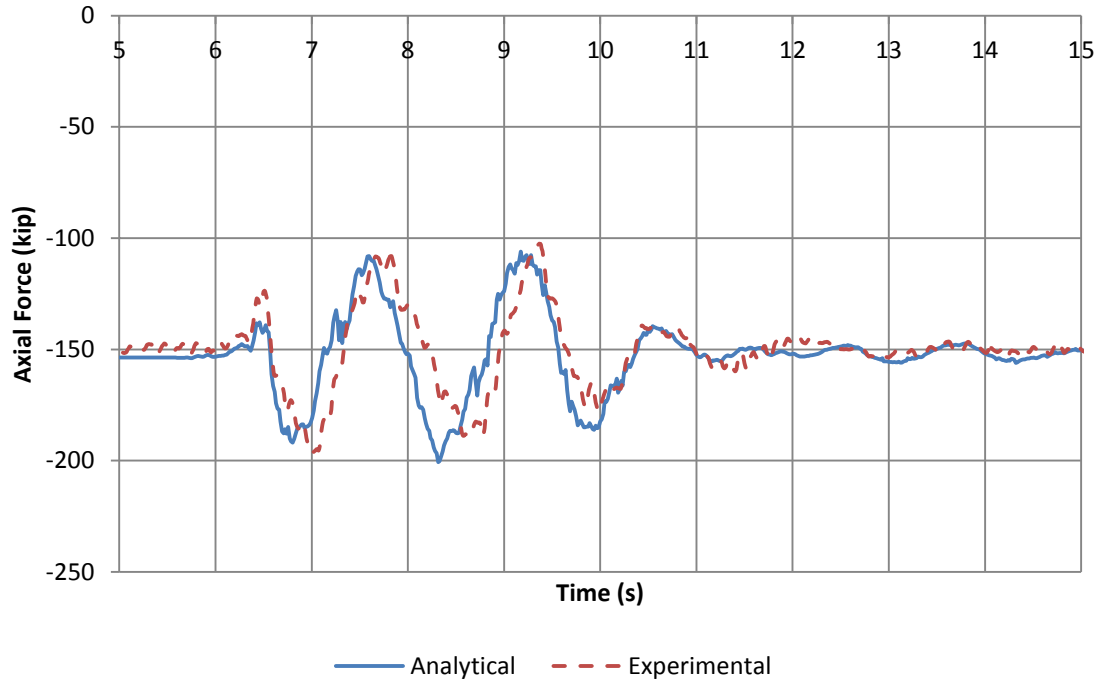


(a)

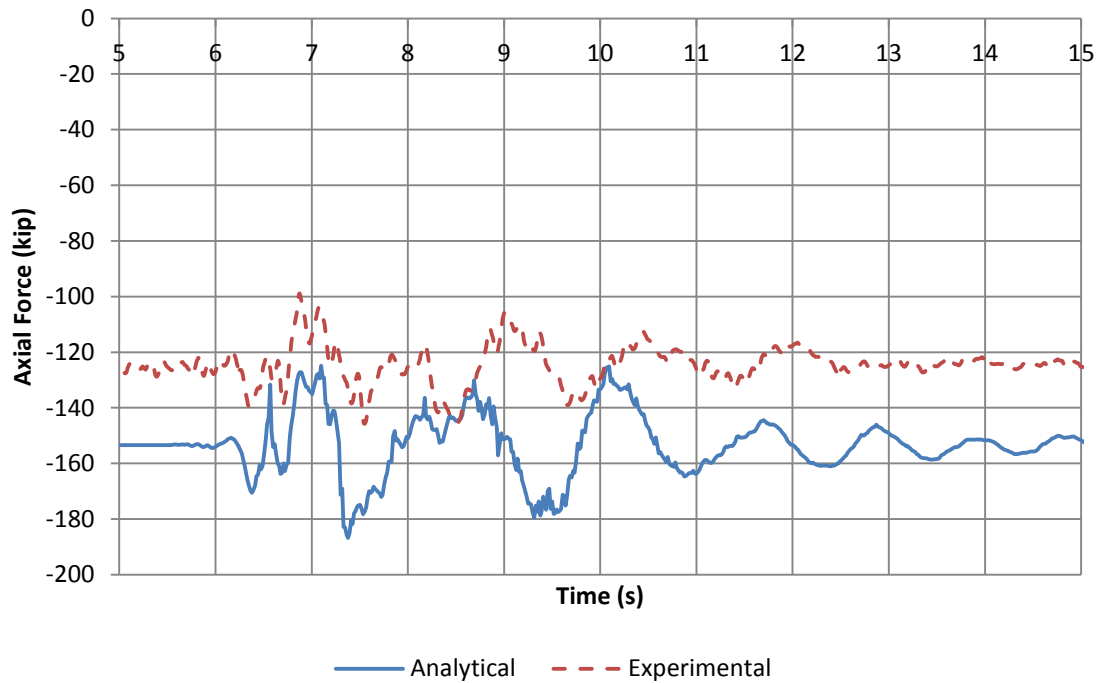


(b)

**Figure 6.5.12. Resultant Moment Histories at Bottom of (a) North and (b) South Bents during 200% DE Run**

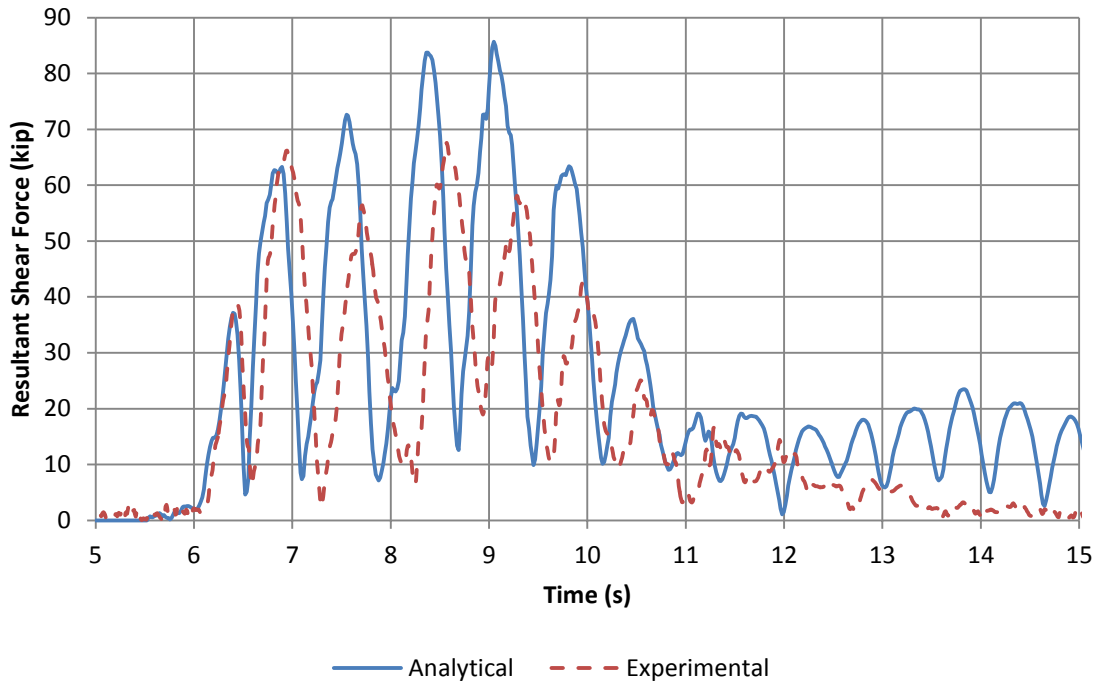


(a)

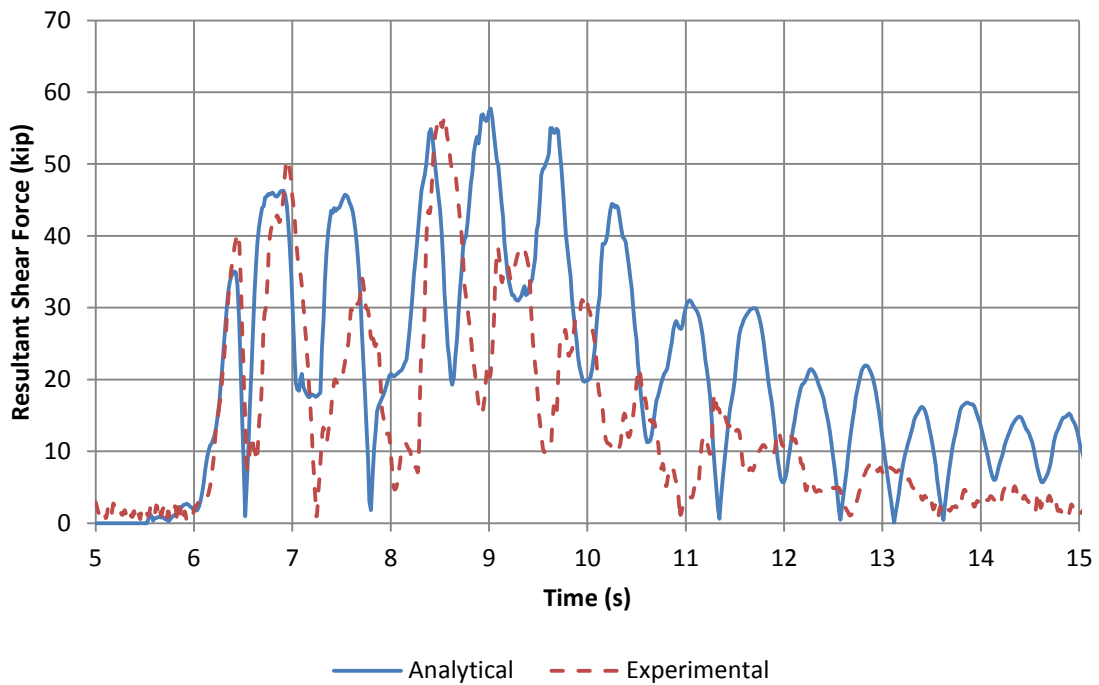


(b)

**Figure 6.5.13. Axial Force Histories at Bottom of (a) North and (b) South Bents during 300% DE Run**

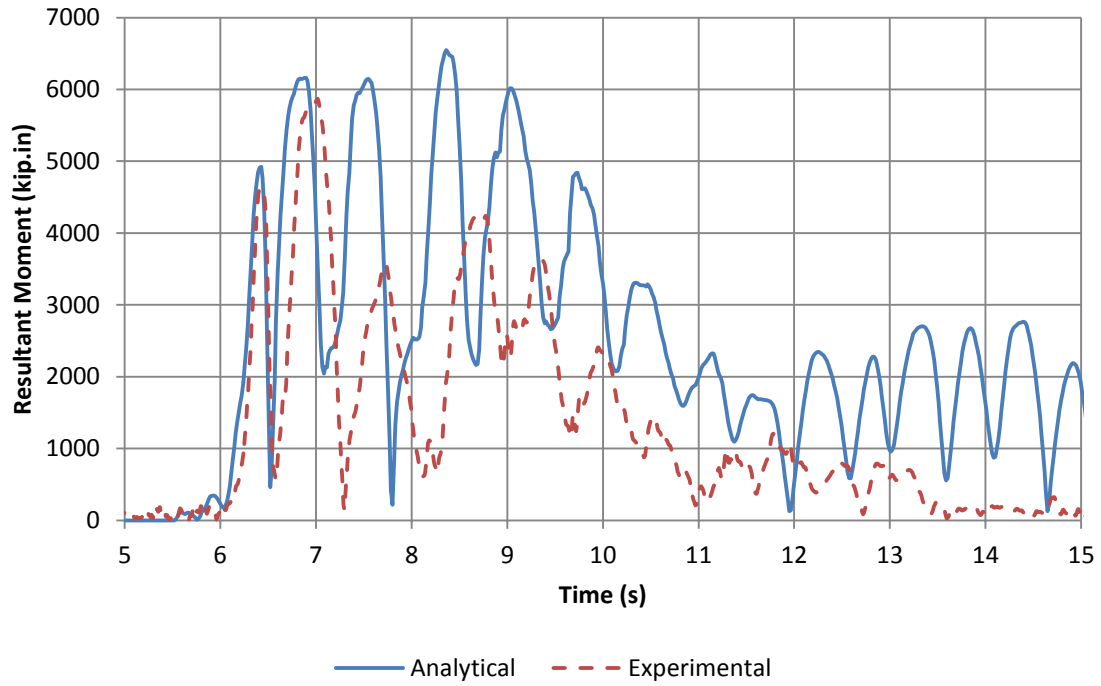


(a)

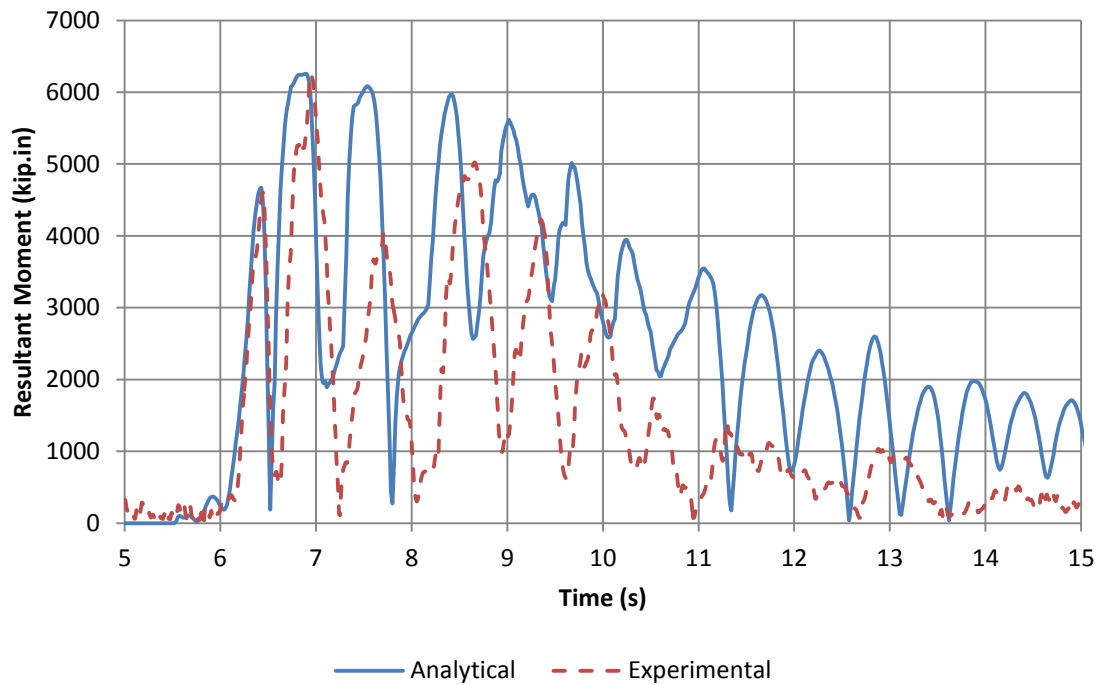


(b)

**Figure 6.5.14. Resultant Shear Force Histories at Bottom of (a) North and (b) South Bents during 300% DE Run**

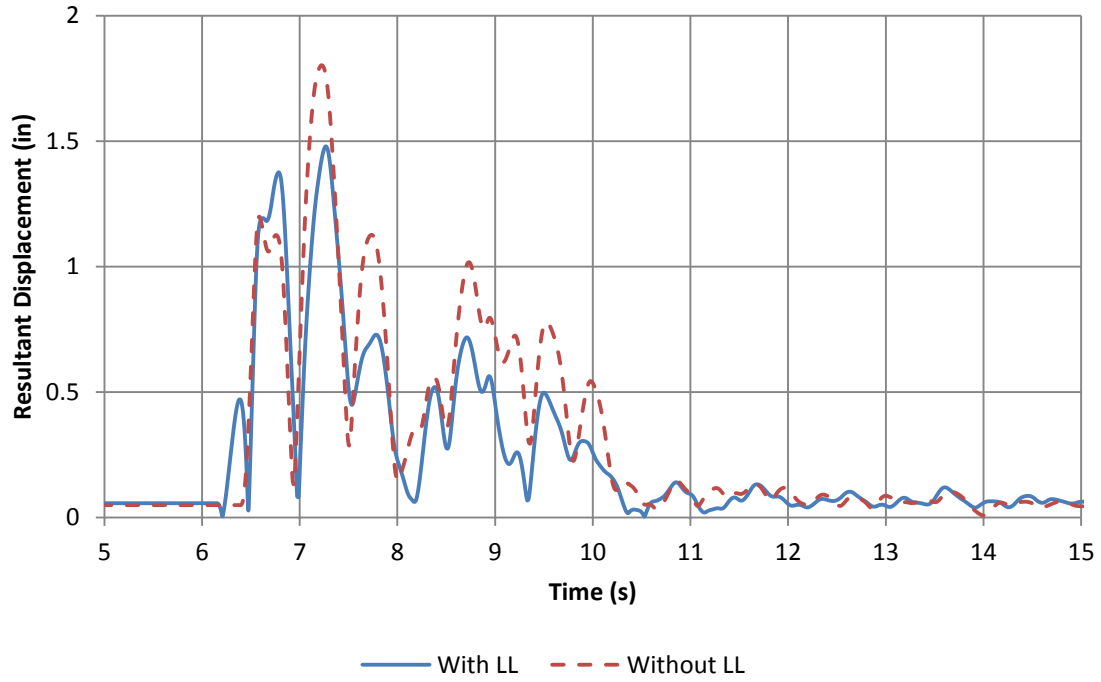


(a)

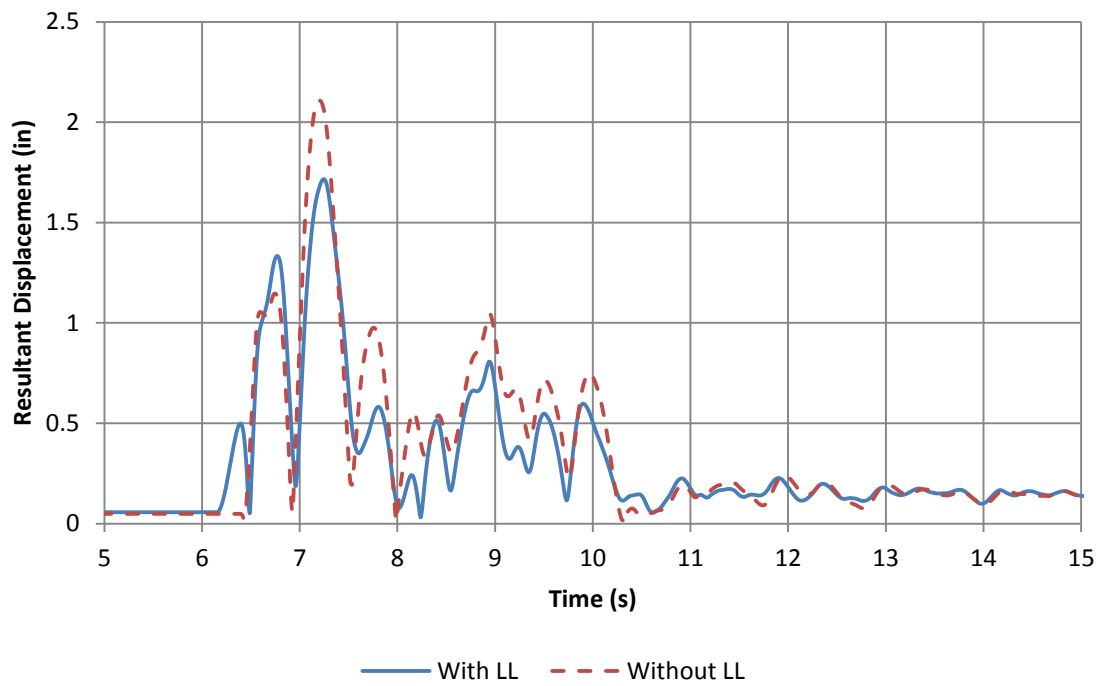


(b)

**Figure 6.5.15. Resultant Moment Histories at Bottom of (a) North and (b) South Bents during 300% DE Run**

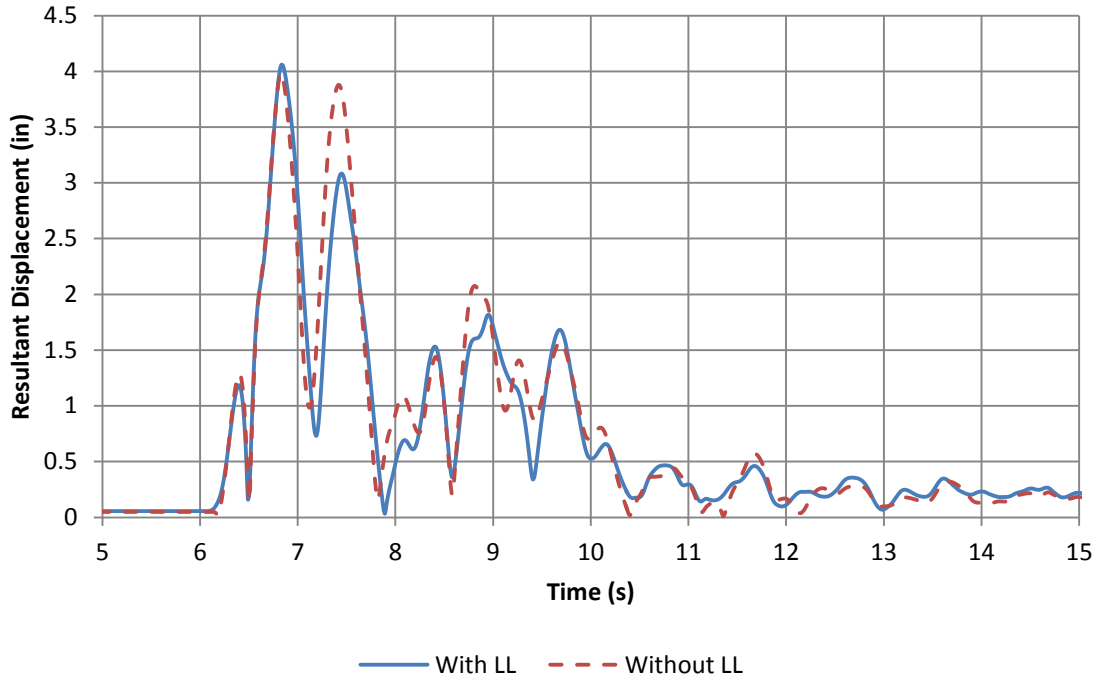


(a)

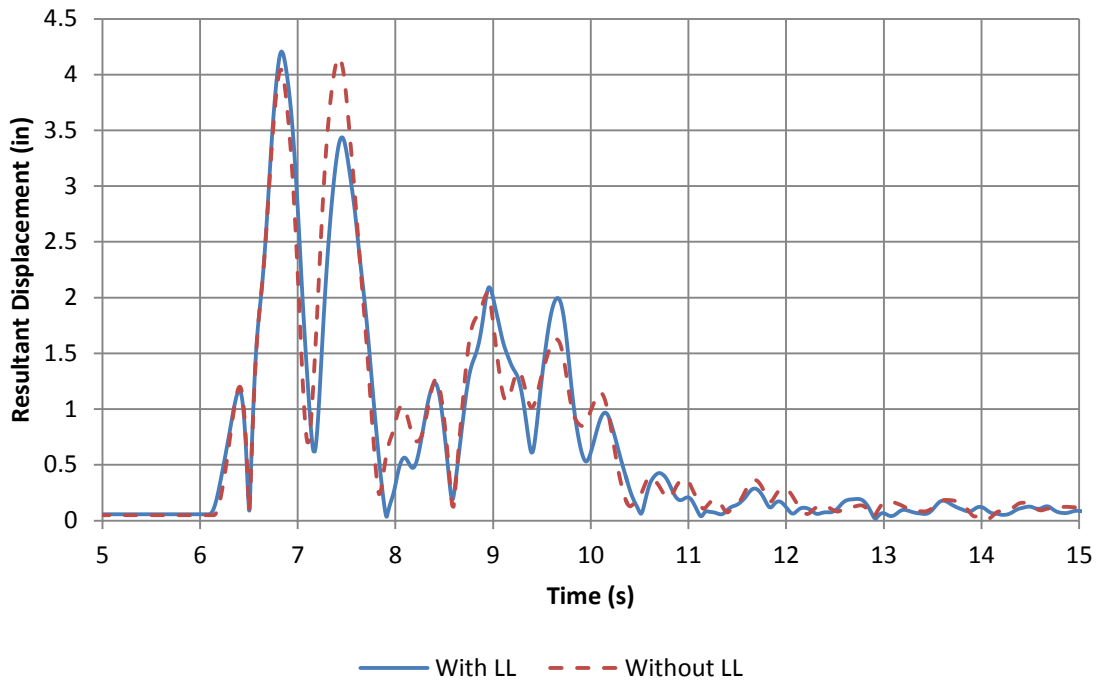


(b)

**Figure 6.6.1. Resultant Displacement Histories from Analyses With and Without Live Load at Top of (a) North and (b) South Bent during 100% DE Run**



(a)



(b)

**Figure 6.6.2. Resultant Displacement Histories from Analyses With and Without Live Load at Top of (a) North and (b) South Bent during 200% DE Run**

## CHAPTER 7. PRELIMINARY PARAMETER STUDY

### 7.1. General

Strictly speaking the results of the experiment described in Chapter 5 apply only to the selected bridge, vehicles, and ground motion described in Chapter 4. However, applications to other bridges, vehicles and ground motions are possible through the use of a calibrated analytical model such as that described in Chapter 6. In this way it is possible to determine if the effects of live load noted in Chapter 5 are unique to the selected bridge or will be found in other bridges. In fact parameter studies may be undertaken with such a model to determine the range of bridge and vehicle types for which these effects are beneficial and gain insight into the factors controlling bridge response to live load. One such parameter study is described in this chapter.

### 7.2. Parameters of Interest

In this preliminary study, the number of parameters of interest was limited to five as follows:

- Live load-to-bridge mass ratio
- Live load period
- Live load damping ratio
- Earthquake ground motion
- Number and location of vehicles

#### 7.2.1. Live Load-to-Bridge Mass Ratio and Live Load Dynamic Properties

The first parameter studied was the mass ratio, i.e., ratio of the mass of the live load to mass of the structure ( $M_v/M_s$ ). A simplified numerical model was used for this study described in Section 7.3. The properties of the live load were adjusted to have mass equal to 1%, 2%, 3%, 4%, 5%, 10%, 15%, 20%, 30%, 40%, and 50% of the structure mass. Then, several cases of live load period were investigated such as periods of 0.25 s, 0.5 s, 0.75 s, and 1.0 s. These variables were chosen to give upper and lower bounds on the response. Displacement ductility demand in the substructure (top of the column) was chosen as the measure of structural response by which to judge the influence of each parameter. For this purpose displacement ductility demand ratios were calculated in which the demand with live load was normalized to the demand without live load. The prototype bridge without live load has a period of 0.75 s.

### **7.2.1. Earthquake Ground Motion**

In this study, three different records were used to represent both near-field and far-field motions. These records were the Sylmar, El Centro, and Takatori motions and each was scaled to have the same spectral acceleration at 1.0 s ( $S_1$ ) as for the bridge in Chapter 4. The scale factors were found to be 0.475, 0.800, and 0.364 for the Sylmar, El Centro, and Takatori records, respectively.

### **7.2.3. Number of Vehicles**

The bridge described in Chapter 4 and trucks described in Chapter 3 were selected for a brief study of the effect of the number and location of the vehicles on the bridge deck. The number of trucks was varied from one to six arranged in 11 different patterns.

## **7.3. Numerical Models**

Both simplified and finite element numerical models were used for this parameter study. The simplified model was developed to reduce the heavy computational effort associated with finite element models and the hundreds of response history analyses required in parameter studies.

### **7.3.1. Stick Model**

A stick model of the prototype bridge in Chapter 4 was developed in SAP2000 but without the curvature. The superstructure was modeled as a single beam element and the columns were modeled as frame elements. Nonlinearity in the columns was included using fiber-element plastic hinges. Each vehicle was modeled as a single degree-of-freedom mass-spring-damper system with the properties adjusted to give the desired range of parameters. The bridge was assumed to have one lane carrying seven vehicles evenly distributed along the length of the bridge. Vehicle properties were varied to have the same range as for the 2DOF Model. The system was subjected to the same two earthquake levels but for the 100% Sylmar record the bridge abutment was modeled as a pin connection, whereas for the 300% record the abutment was modeled as a roller connection to represent the unrestrained condition without the radial shear keys.

### **7.3.2. Finite Element Model**

The finite element model used in this study was the same as that described in Chapter 6. This model was only used to study the effect of the number and location of the vehicles on the bridge.

## 7.4. Parameter Study Results

The results of the preliminary parameter study are presented below. In general, live load was found to alter the dynamic behavior of the structure.

### 7.4.1. Effect of Live Load-to-Structure Mass Ratio, Vehicle Period, and Damping

Figures 7.4.1a and 7.4.1b show plots of column displacement ductility demand ratios against mass ratio for 100% and 300% Sylmar respectively, using the 2DOF model with 0% damping in the live load. As noted previously, the ductility demand ratio is defined as the ductility demand with live load ( $\mu_{d,LL}$ ), divided by the ductility demand without live load ( $\mu_{d,noLL}$ ) for the same set of parameters. A ratio of unity means that the ductility demands or displacements with and without live load are the same. The four curves in each plot show results for different vehicle periods, taken to be 0.25 s, 0.50 s, 0.75 s, and 1.00 s. Similarly, Figures 7.4.2 and 7.4.3 show the same plots but for live load damping ratios of 5% and 25%, respectively. For the case where the system was subjected to 100% Sylmar record in the longitudinal direction with no damping in the live load (0% critical damping ratio) the ductility demand ratios range between 0.75 and 1.25. There are some cases where the live load gives a beneficial effect (e.g., when the period of the live load is longer), but otherwise an adverse effect is observed throughout all cases of mass ratio, vehicle period and earthquake level.

However, when damping is introduced into the live load, the response of the system changed drastically. The presence of live load now gives a beneficial effect for all mass ratios, vehicle periods and earthquake levels (Figures 7.4.5 and 7.4.6). However, this effect of live load damping diminishes at larger damping ratios. This observation has also been made in the application of tuned mass dampers where it has been shown that high levels of damping in the TMD do not always reduce the demand in a structure.

### 7.4.2. Effect of Earthquake Ground Motion

When the earthquake input motion was changed, the observed trend of the ductility demand ratio plot also slightly changed for the stick model. In other words, the earthquake input motion was shown to have a slight impact on the system's response. Two other records were used in the study: El Centro and Takatori records, which were scaled to have the same spectral acceleration at 1.0 s,  $S_1$ , value as the design response spectrum for the prototype bridge.

Ductility demand ratios for the above cases of mass ratio, vehicle period and earthquake level using the El Centro record, are shown in Figures 7.4.7 through 7.4.9 for 0%, 5%, and 25% critical damping in the live load, respectively. The plots for 300% El Centro record show erratic behavior due to the convergence issues in the numerical analysis. The same plots for the Takatori record are shown in Figures 7.4.10 through 7.4.12.

Similar to the previous observations for the Sylmar record, undamped live load gives a beneficial effect in some cases and adverse effects in others depending on the mass ratio and the vehicle period. In general, live load tends to reduce the demand when the system is subjected to 100% design earthquake but increases the demand at larger levels of excitation (300%). These results also corroborate the previous observation that increasing the damping in the live load has a beneficial effect for all cases of mass ratio and vehicle period particularly at the 100% earthquake level of excitation.

### **7.4.3. Effect of Number of Vehicles**

Six truck locations, 1 through 6, were identified along the length of the straight bridge and the effect of various combinations of trucks at these locations was studied. As shown in Table 7.4.1, these combinations included two configurations with only one truck on the bridge, two configurations with two trucks, two configurations with three trucks, two configurations with four trucks, two configurations with five trucks and one configuration with all six trucks.

The two configurations of one vehicle on the bridge comprised only Truck 3 and only Truck 4. Figures 7.4.13a and 7.4.13b show the resultant displacement histories at the top of north and south bents during 100% DE for these two cases, respectively. It is observed that when only one vehicle is present, the displacement of the north column is slightly reduced while the displacement of the south column is slightly increased compared to the case when all six trucks are present.

The two configurations of two vehicles on the bridge comprised Trucks 4 and 6, and Trucks 3 and 4. The resultant displacement histories for these two cases are presented in Figure 7.4.14. Trucks 3 and 4 are located closest to the center of the bridge. In this location the resultant displacement demand is increased compared to when all six trucks are present. However, the opposite observation is true when Trucks 4 and 6 are present, at which time the resultant displacement demand is decreased.

The two configurations of three vehicles on the bridge comprised Trucks 1, 3, and 5, and Trucks 2, 4 and 6. The resultant displacement histories for these two cases are presented in Figure 7.4.15 where it is seen that the latter case gives the greatest maximum resultant displacement demand of all cases. These were found to be 2.02 in and 2.26 in for the north and south bents, respectively.

While the greatest maximum resultant displacement was found in the case where three vehicles are present, the least maximum resultant displacement was found in the case where four vehicles are present. As shown in Figure 7.4.16, the least maximum bent displacements were obtained when Trucks 1, 2, 5, and 6 are present. These displacements are 1.75 in for the north bent and 1.93 in for the south bent. Note that Trucks 1 and 2 are located on the north end of the bridge while Trucks 5 and 6 are located on the south end of the bridge. In addition, when four vehicles were grouped on one side of the bridge such as the case when Trucks 3, 4, 5, and 6 are present, the displacements of the columns are very close to the case when all six trucks are present.

The resultant displacement histories from cases when five vehicles are present are shown in Figure 7.4.17. Similarly, two cases were investigated. One is when Trucks 1, 2, 3, 4, and 5 are present and the other is when Trucks 1, 2, 3, 5, and 6 are present. From these two cases, the displacements of the columns were found to be very similar to the case when all six trucks are present.

Table 7.4.1 summarizes the maximum resultant displacements at the top of north and south bents obtained for the different configurations. The mass ratio is the ratio of the mass of the vehicle(s) to the total mass of the structure and it is seen to range from 3.1% to 18.8%. The displacement ratio is the ratio of maximum displacement of a particular case to the maximum displacement when all trucks are present.

It is shown in this table that the maximum displacement varies over a range from about +7% to -8%, when the number of vehicles is changed. In addition, in cases of the same mass ratio, the seismic response of the structure can differ depending on the placement of the vehicles.

## **7.5. Discussion**

The preliminary parameter study described in this chapter has shown that live load can give beneficial or adverse effects on the seismic response of bridges. Simple and numerically efficient models were used to show the influence of several factors on response including mass ratio, vehicle period and damping, and earthquake ground motion. In general undamped vehicles give beneficial effects at mass ratios less than 10% and adverse effects at higher ratios for all vehicle periods and earthquake levels. However, a modest amount of vehicle damping (5% of critical) gave favorable results for all mass ratios and vehicle periods particularly at the design level earthquake. Beneficial effects were also observed at 300% of the design earthquake but they were not as marked as at the lower level.

These results are consistent with the experimental results reported in Chapter 5 where beneficial effects are reported for a bridge vehicle system with a mass ratio of 19%, truck period of 0.8 s and truck damping of 10-15%, subject two levels of the Sylmar ground motion. Furthermore the benefit was more evident at 100% of the ground motion than at 300%. This consistency gives confidence in the results of the parameter study.

The results from the study on the effect of the number and placement of vehicles on the bridge where the mass ratio varies from 3 to 19 %, are also consistent with the above observations.

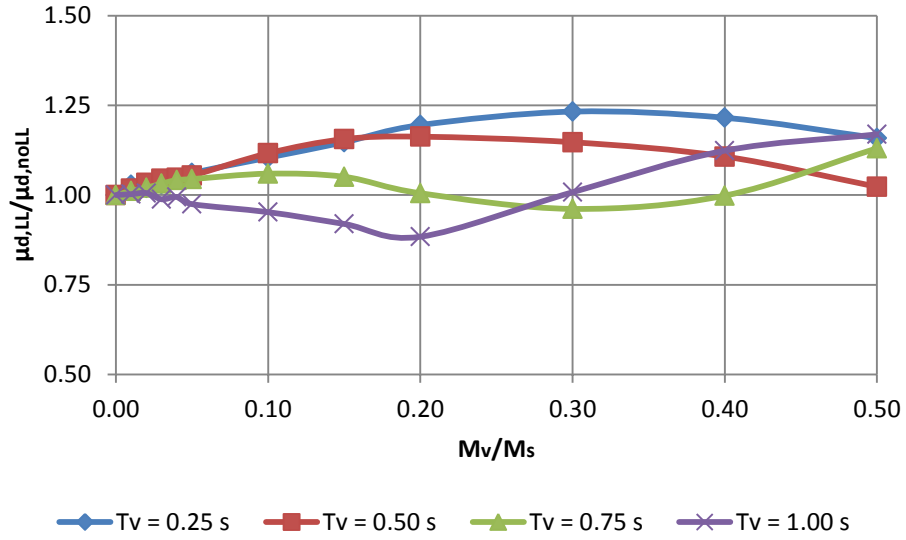
## **7.6. Summary**

Results from of preliminary parameter study on the factors influencing the effect of live load on seismic response have been presented in this chapter. Parameters studied

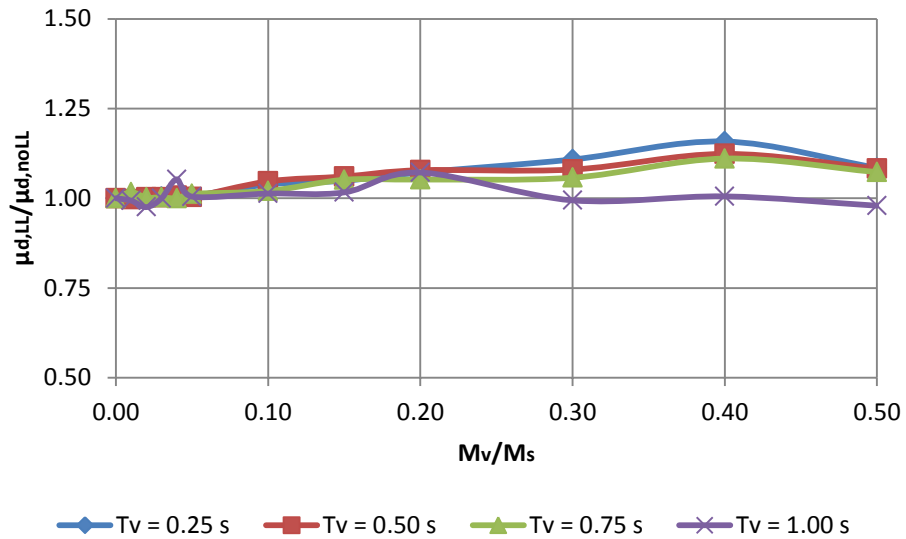
included live-load-to-bridge mass ratio, vehicle period and damping, earthquake level and type, number and placement of vehicles on the bridge. Confidence in the results of this study was obtained by showing consistency with the experimental observations in Chapter 5.

**Table 7.4.1. Maximum Displacements for Different Vehicle Configurations**

Truck(s)	Mass Ratio	Maximum Displacement (in)		Displacement Ratio	
		North Bent	South Bent	North Bent	South Bent
3	0.031	1.842	2.127	0.976	1.007
4		1.853	2.135	0.982	1.011
3,4	0.063	1.957	2.245	1.037	1.063
4,6		1.833	2.112	0.972	1.000
1,3,5	0.094	1.873	2.088	0.993	0.988
2,4,6		2.021	2.263	1.071	1.071
1,2,5,6	0.125	1.754	1.929	1.930	0.913
3,4,5,6		1.907	2.200	1.011	1.041
1,2,3,5,6	0.157	1.842	2.038	0.976	0.965
1,2,3,4,5		1.939	2.158	1.028	1.021
1,2,3,4,5,6	0.188	1.887	2.112	1.000	1.000

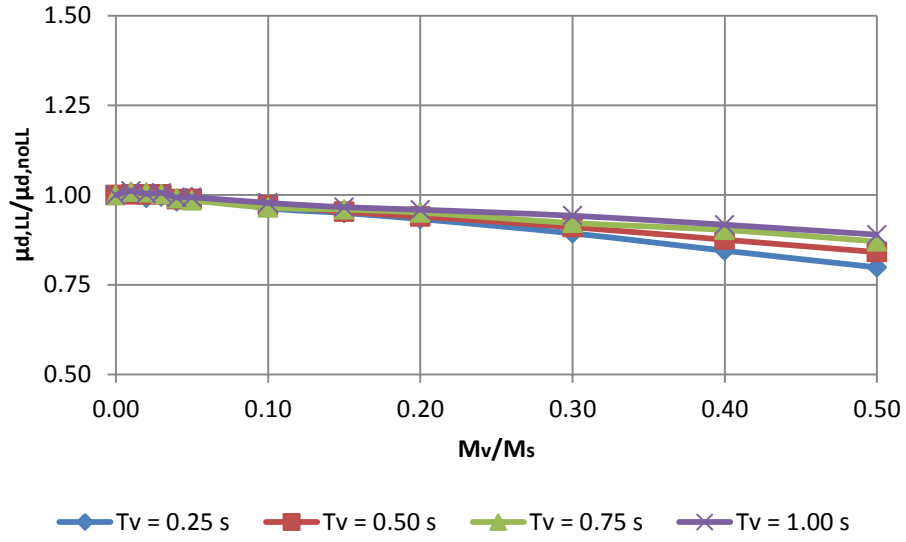


(a)

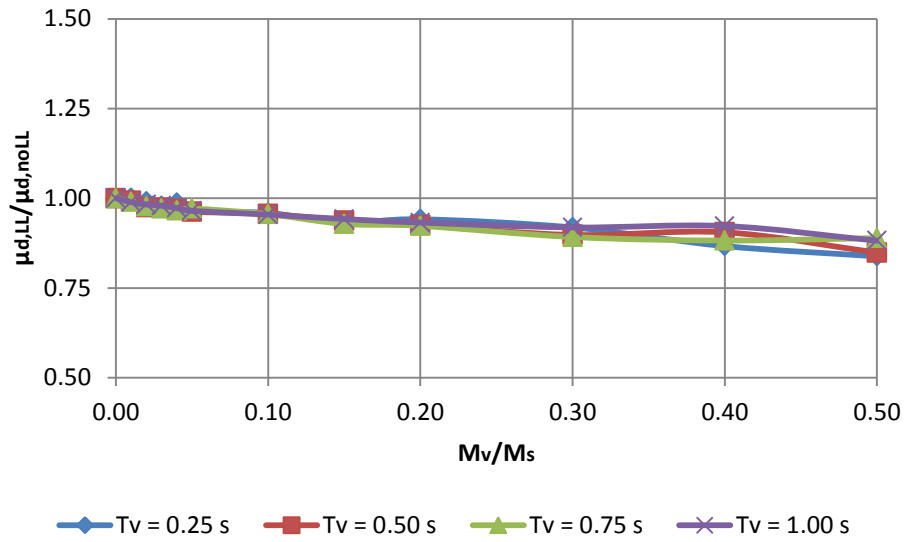


(b)

**Figure 7.4.1. Ductility Demand Ratios for (a) 100% and (b) 300% DE Cases with Sylmar Record Considering 0% Damping in the Live Load Using Stick Model**

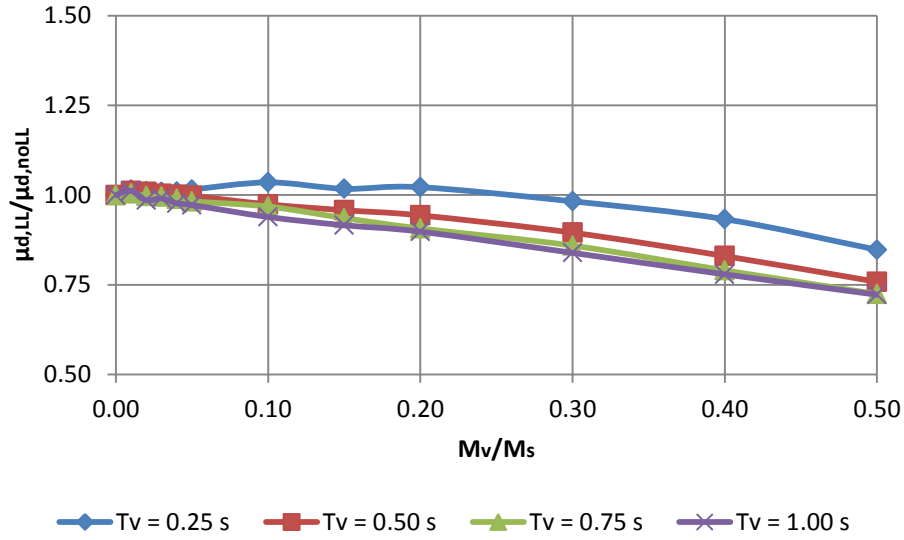


(a)

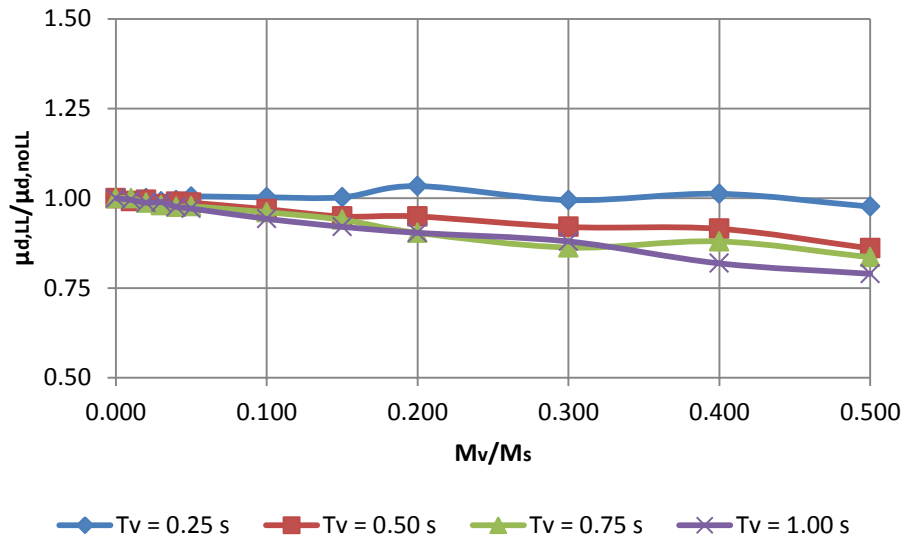


(b)

**Figure 7.4.2. Ductility Demand Ratios for (a) 100% and (b) 300% DE Cases with Sylmar Record Considering 5% Damping in the Live Load Using Stick Model**

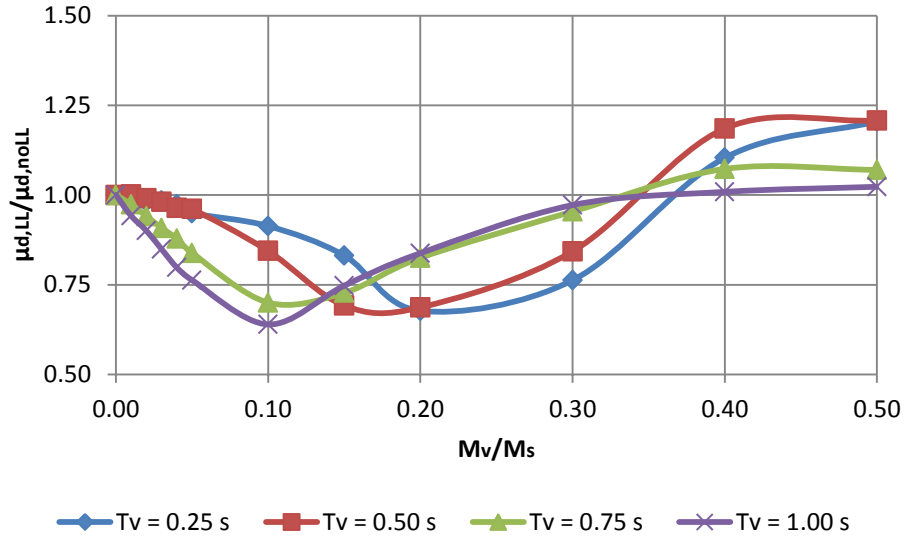


(a)

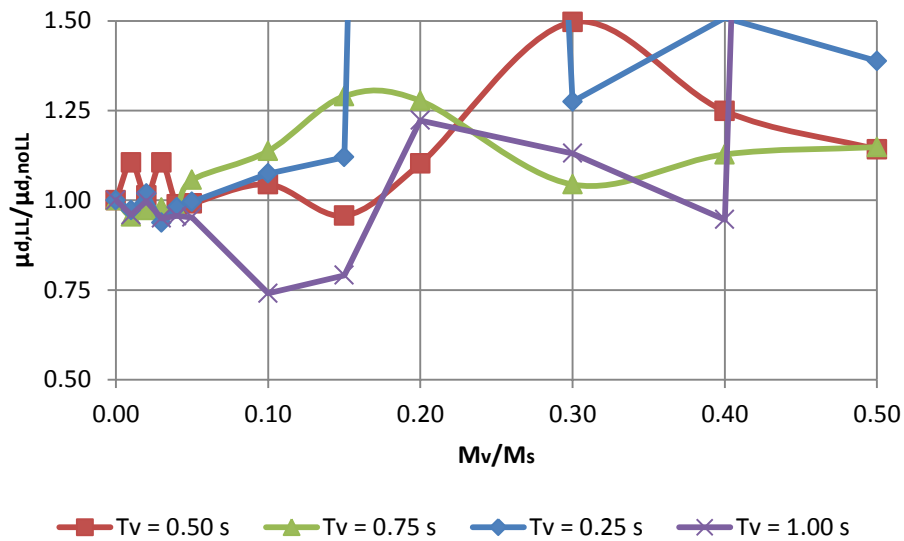


(b)

**Figure 7.4.3. Ductility Demand Ratios for (a) 100% and (b) 300% DE Cases with Sylmar Record Considering 25% Damping in the Live Load Using Stick Model**

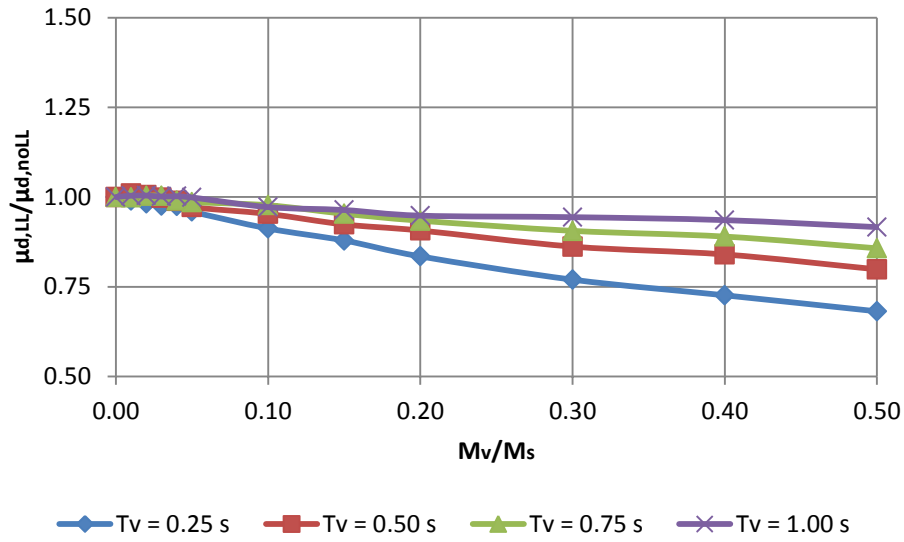


(a)

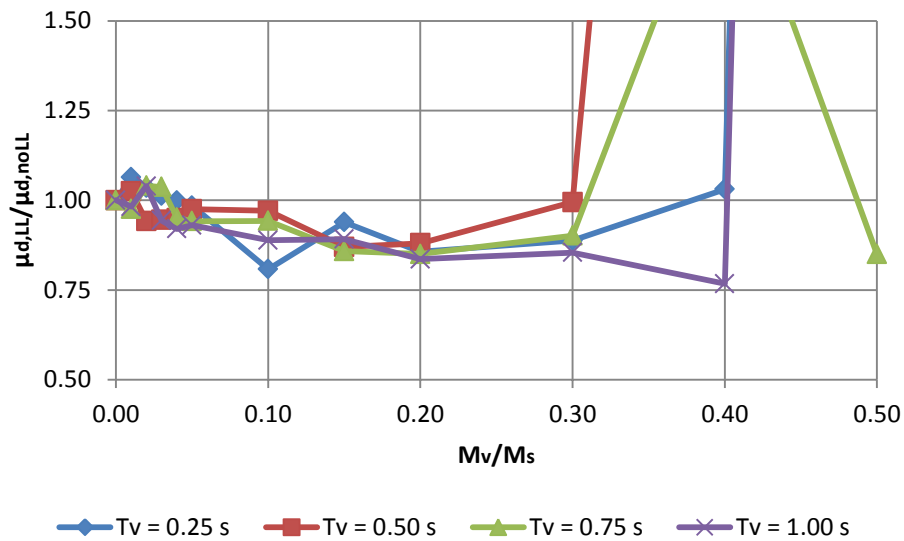


(b)

**Figure 7.4.4. Ductility Demand Ratio for (a) 100% and (b) 300% DE Cases with El Centro Record Considering 0% Damping in the Live Load Using Stick Model**

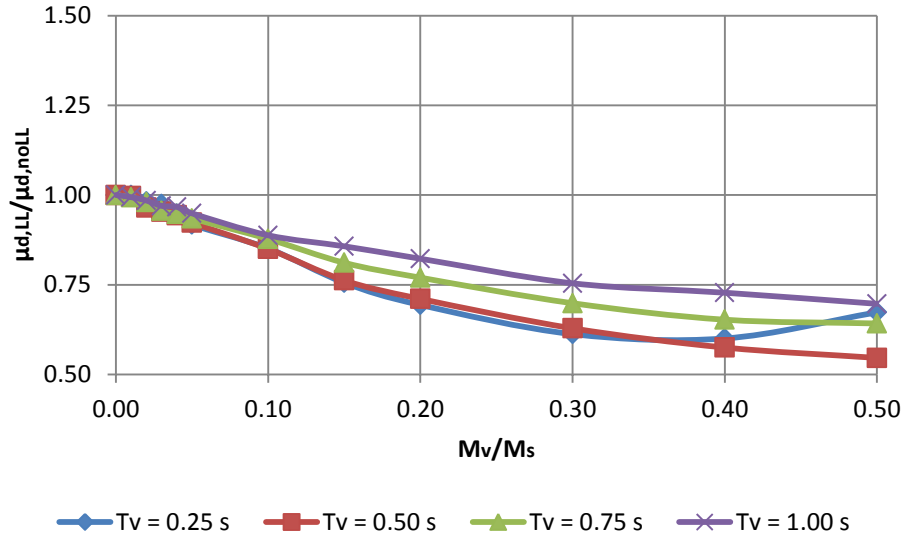


(a)

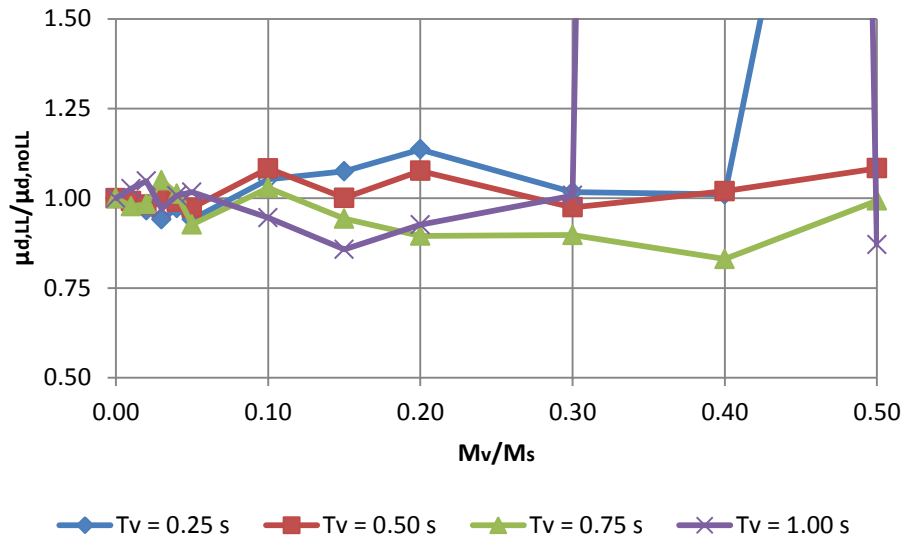


(b)

**Figure 7.4.5. Ductility Demand Ratios for (a) 100% and (b) 300% DE Cases with El Centro Record Considering 5% Damping in the Live Load Using Stick Model**

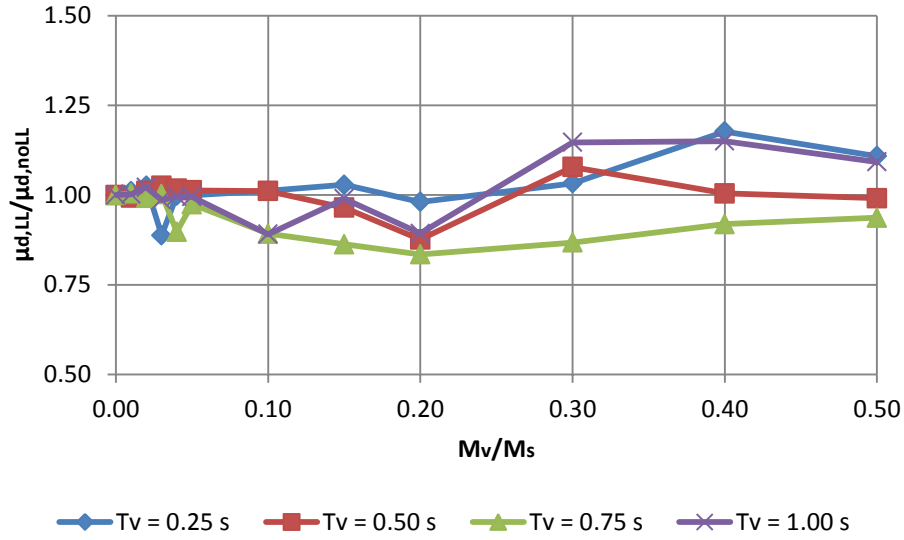


(a)

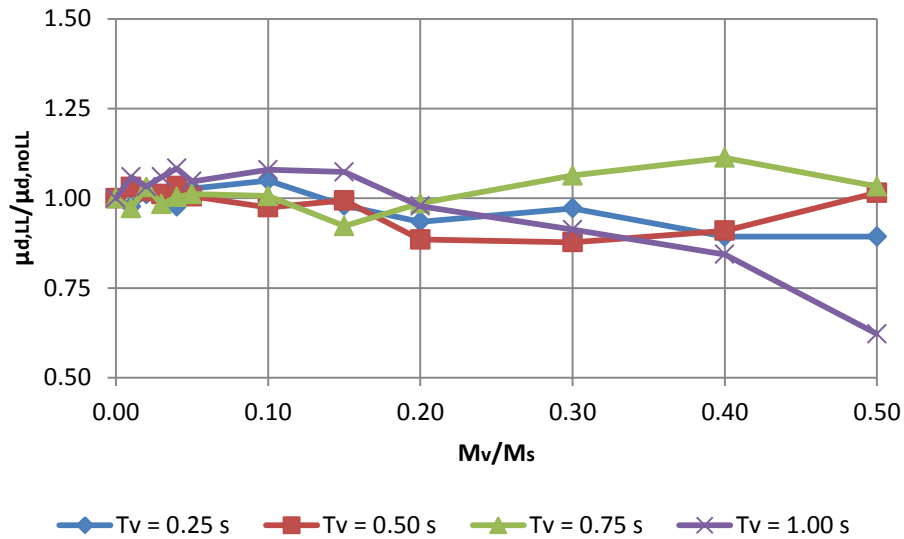


(b)

**Figure 7.4.6. Ductility Demand Ratios for (a) 100% and (b) 300% DE Cases with El Centro Record Considering 25% Damping in the Live Load Using Stick Model**

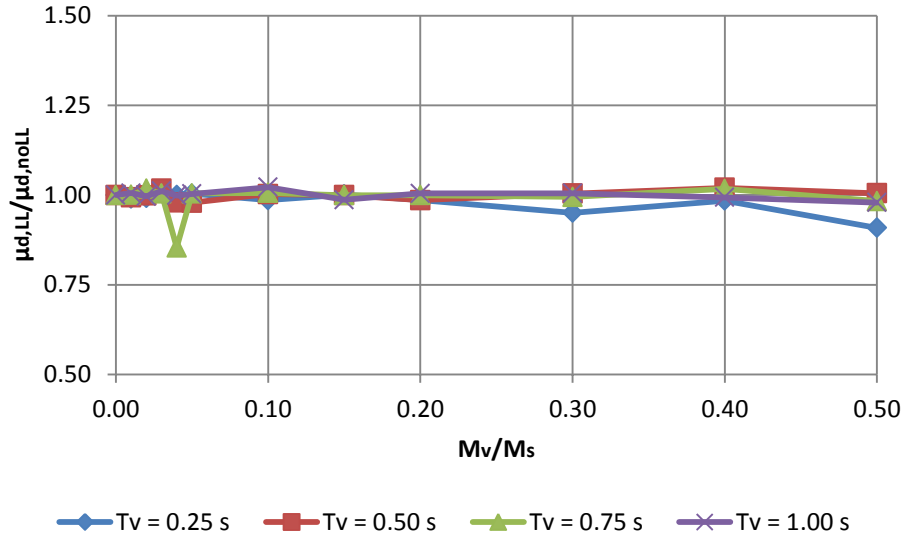


(a)

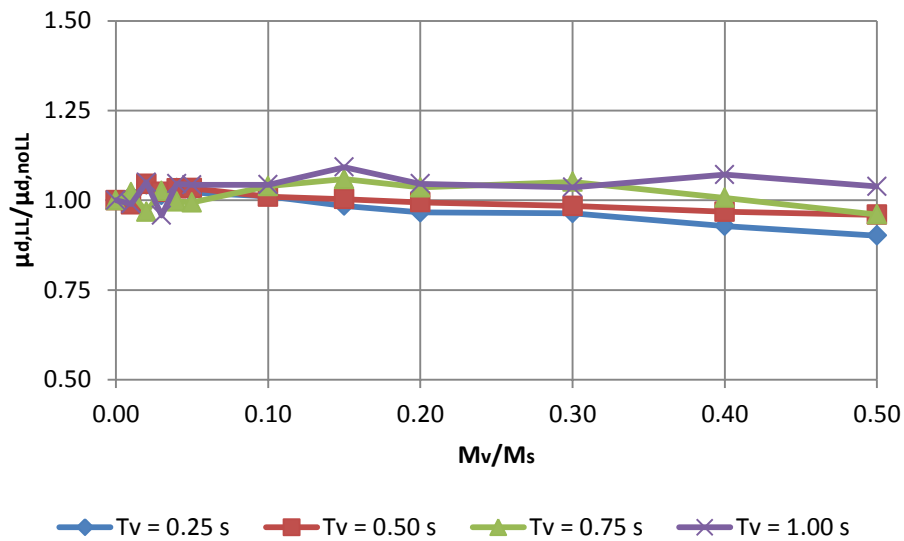


(b)

**Figure 7.4.7. Ductility Demand Ratios for (a) 100% and (b) 300% DE Cases with Takatori Record Considering 0% Damping in the Live Load Using Stick Model**

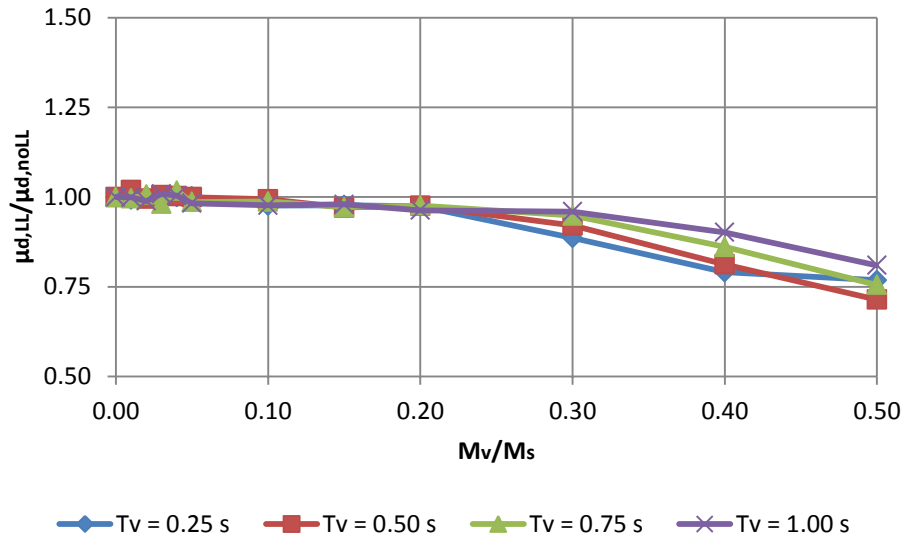


(a)

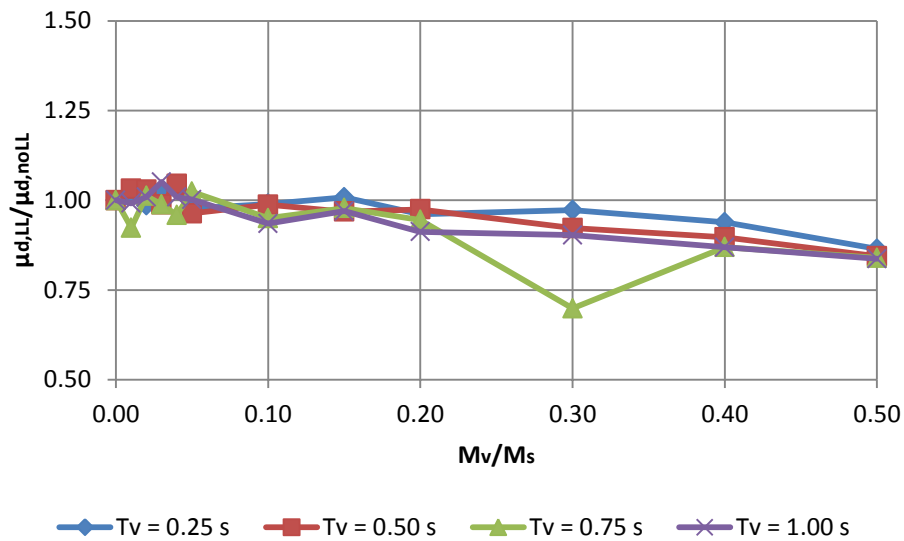


(b)

**Figure 7.4.8. Ductility Demand Ratios for (a) 100% and (b) 300% DE Cases with Takatori Record Considering 5% Damping in the Live Load Using Stick Model**

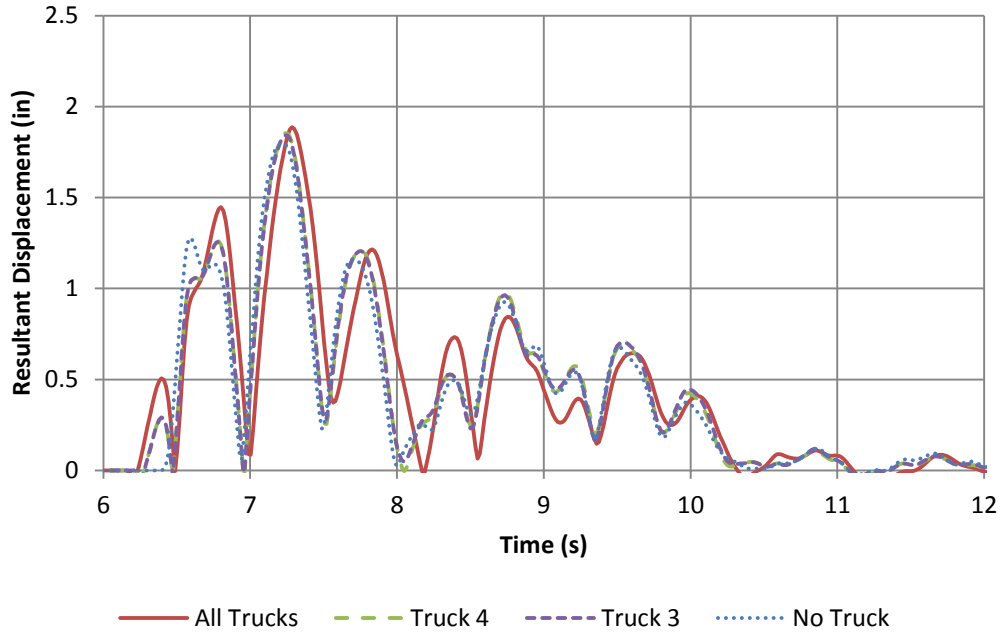


(a)

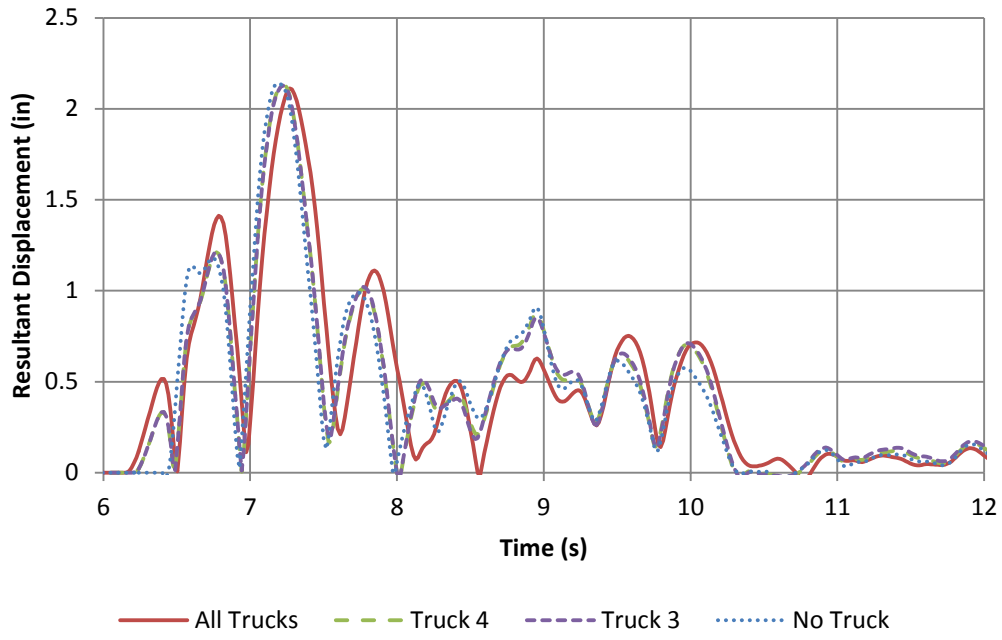


(b)

**Figure 7.4.9. Ductility Demand Ratios for (a) 100% and (b) 300% DE Cases with Takatori Record Considering 25% Damping in the Live Load Using Stick Model**

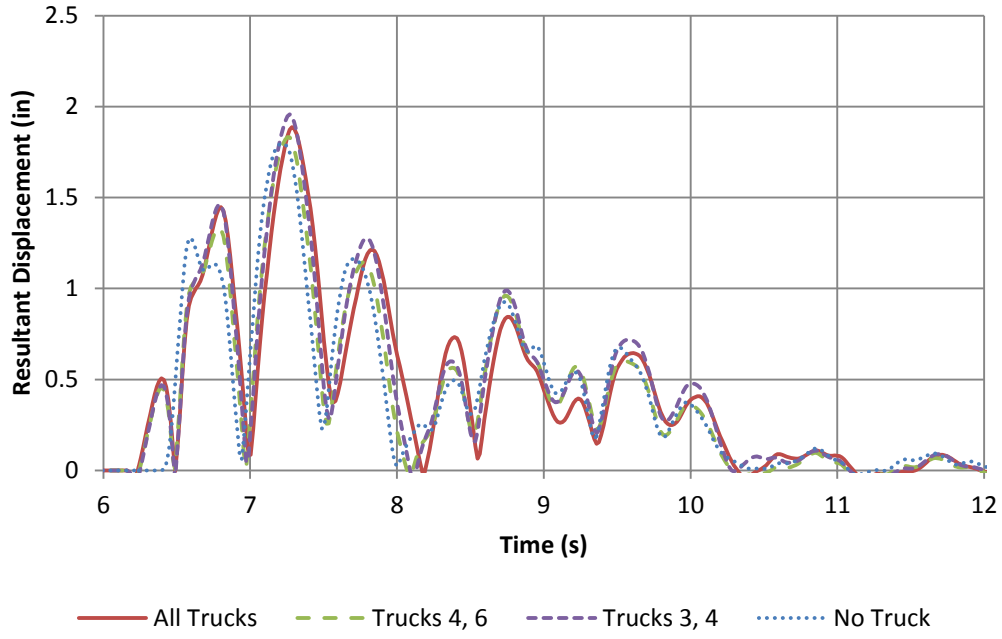


(a)

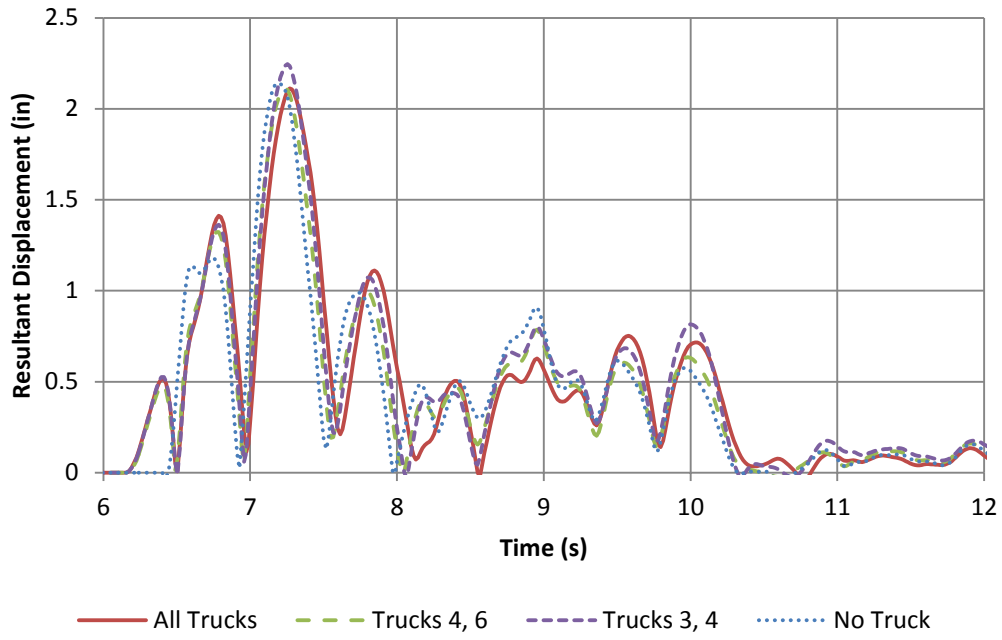


(b)

**Figure 7.4.10. (a) North and (b) South Column Resultant Displacement Histories for Single-Vehicle Case**

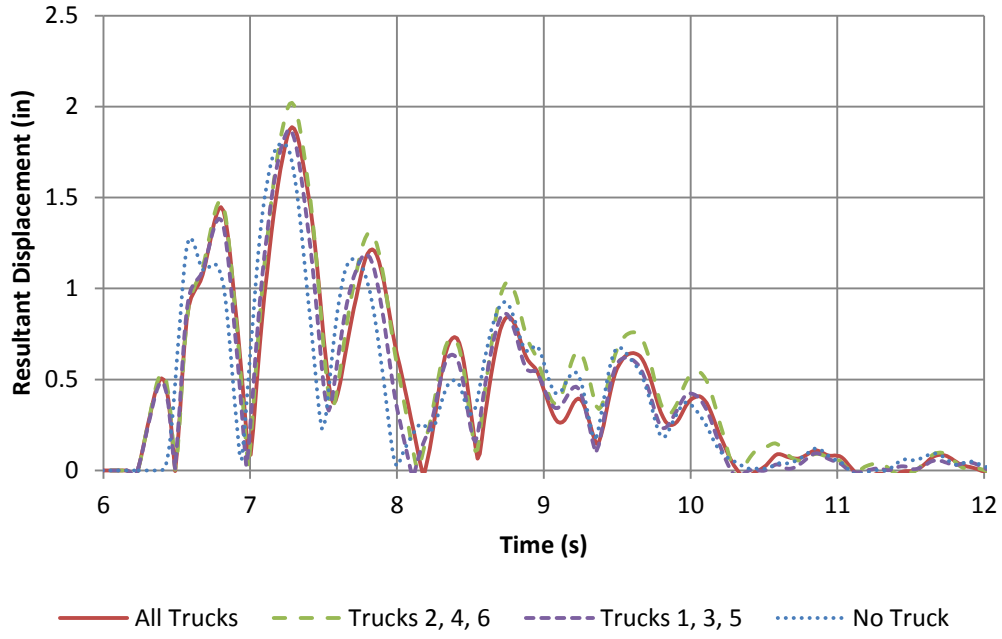


(a)

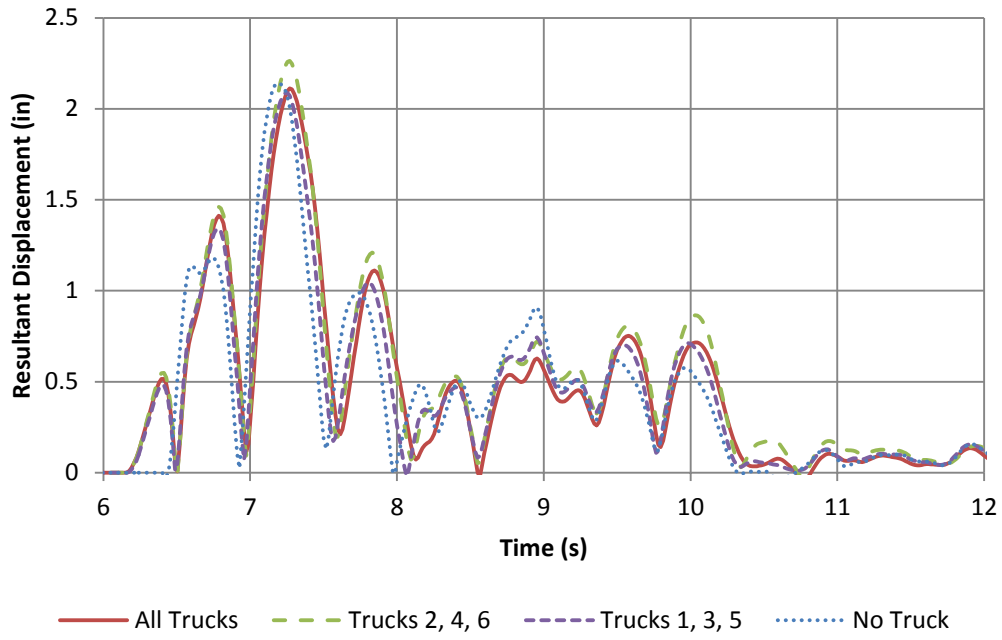


(b)

**Figure 7.4.11. (a) North and (b) South Column Resultant Displacement Histories for Two-Vehicle Case**

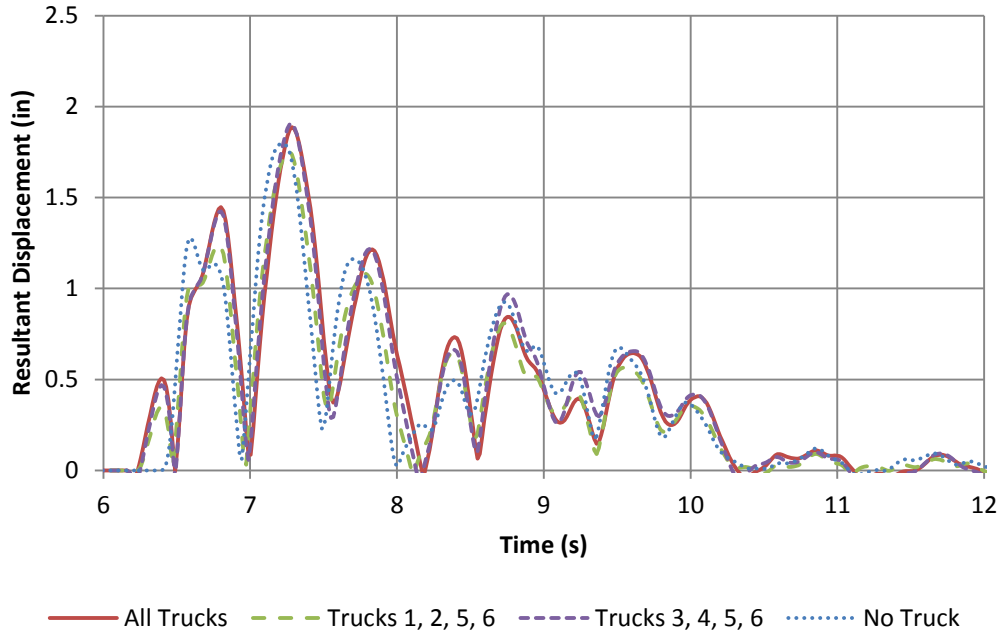


(a)

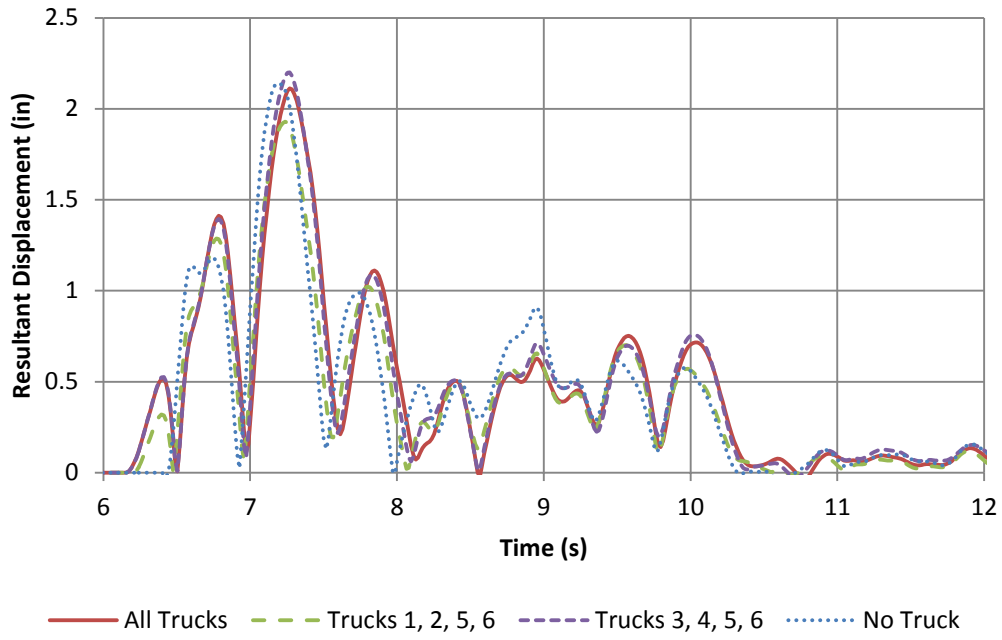


(b)

Figure 7.4.12. (a) North and (b) South Column Resultant Displacement Histories for Three-Vehicle Case

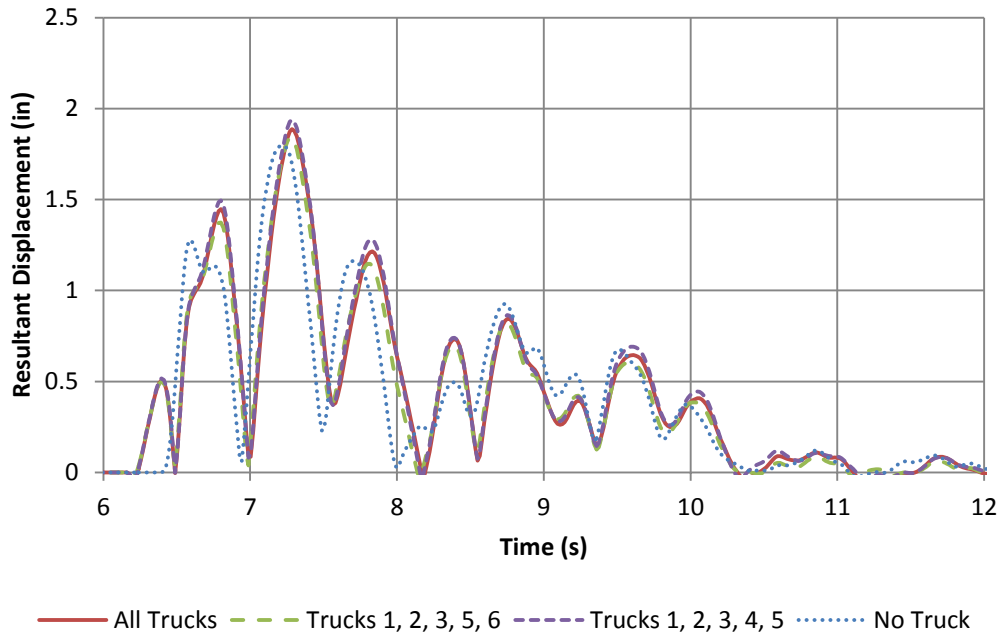


(a)

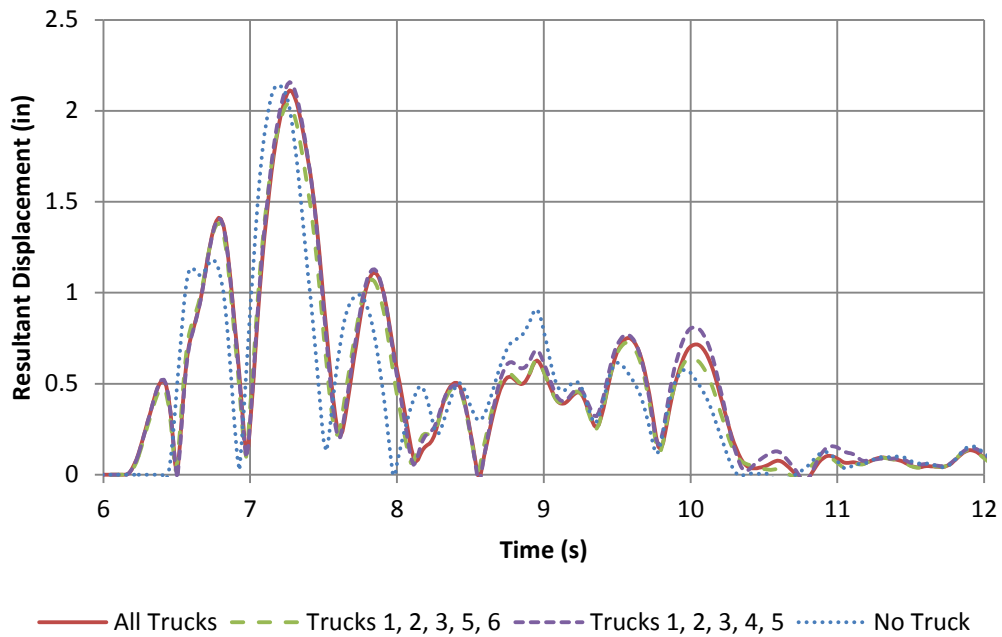


(b)

**Figure 7.4.13. (a) North and (b) South Column Resultant Displacement Histories for Four-Vehicle Case**



(a)



(b)

**Figure 7.4.14. (a) North and (b) South Column Resultant Displacement Histories for Five-Vehicle Case**

## CHAPTER 8. OBSERVATIONS AND RECOMMENDATIONS

### 8.1. Observations

This report describes a study on the effect of live load on the seismic response of ordinary bridges. This study involved a literature review, a large-scale experiment using multiple shake tables, development of a nonlinear finite element model for bridge-vehicle interaction, and a preliminary parameter study.

It is shown that for the bridge tested, a 2/5-scale model of a 3-span continuous curved bridge carrying six trucks, the effect of live load was beneficial. It reduced the demand in the structure, as evidenced by a decrease in displacements, accelerations, and internal forces. It also delayed the formation of cracks and concrete spalling in the columns and reduced column damage for the same level of earthquake excitation. Girder uplift at the abutments and degradation of column torsional stiffness was less with live load on the bridge.

The 3D finite element model for bridge-vehicle interaction, developed using a commercial finite element package, was able to replicate this behavior particularly with respect to peak values of displacement and force. Although this model could be refined to further improve accuracy, it is believed to be sufficiently accurate for use in parameter studies on live load effects.

The results of a preliminary parameter study showed that live load can give both beneficial and adverse effects on the seismic response of bridges. Factors affecting this response include vehicle-to-bridge mass ratio, vehicle period and damping, and earthquake ground motion (type and level). In general undamped vehicles give beneficial effects at mass ratios less than 10% and adverse effects at higher ratios for all vehicle periods and earthquake levels. However, a modest amount of vehicle damping (5% of critical) can give favorable results for all mass ratios and vehicle periods particularly for the design level earthquake. When adverse effects have been found for damped vehicles they are generally within 10% of the no-live load case.

These results are consistent with the experimental results reported above for a system with bridge-vehicle mass ratio of 19%, truck period of 0.8 s and truck damping of 10-15%, subject to two levels of the Sylmar ground motion.

Although the literature on this topic is very limited, the above results are also consistent with the findings that have been published by others such as Kameda *et al.* (1992, 1999) and Kawatani *et al.* (2007).

One of the reasons for the beneficial effect is likely to be explained by the so-called “tuned mass damper effect”. These devices are known to be very effective at controlling response to wind and traffic loads (particularly if there is more than one acting together), but their effectiveness for earthquake loads is not so clear. However,

recent work on nonlinear energy sinks, which are essentially multiple nonlinear tuned mass dampers, have shown attractive results for controlling the seismic response of buildings. It is very possible that multiple trucks on a bridge, each with moderately damped nonlinear rear suspensions, are acting as a set on nonlinear energy sinks, with the same favorable results. Validation of this explanation is outside the scope of this report. Another possible reason for the beneficial effect is related to the period elongation and additional damping provided by the live load, which moves the bridge to a more favorable part of the acceleration spectrum.

## **8.2. Recommendations / Future Work**

Based on the results and discussions summarized above, the following recommendations are made:

1. More detailed parameter studies should be carried out to confirm the above findings, that live load has a beneficial effect on seismic response for moderately damped trucks over a wide range of bridge-vehicle mass ratios, vehicle periods, and earthquake ground motions.
2. Rigorous analyses using 3D finite element models should be undertaken on a wide range of structures (e.g. long span box-girder, short span PC-girder bridges, and bridges with seismic isolation devices) and truck types (e.g. 3- and 4- axle tractor-trailer rigs) to extend the database beyond the bridge and vehicle type used in the above study. These analyses will require detailed truck data to be available which may require a special effort to obtain.
3. The mechanics of bridge-vehicle interaction should be explored in greater detail than possible in this study to understand the observed phenomena. The theory for multiple nonlinear tuned mass dampers appears to be a good place to start.

## REFERENCES

- Abé, M. and Fujino, Y. (1994). Dynamic Characterization of Multiple Tuned Mass Dampers and Some Design Formulas. *Earthquake Engineering and Structural Dynamics*, 23 (8), pp. 813-835.
- Acosta, J. G. A. (2011). *Seismic Performance of Circular and Interlocking Spirals RC Bridge Columns under Bidirectional Shake Table Loading*. Ph.D. Dissertation, Department of Civil and Environmental Engineering, University of Nevada, Reno.
- American Association of State Highway and Transportation Officials, AASHTO. (2007). *AASHTO LRFD Bridge Design Specifications, Customary U.S. Units, 4<sup>th</sup> Edition with 2008 and 2009 Interim Revisions*. Washington, DC: AASHTO.
- American Association of State Highway and Transportation Officials, AASHTO. (2009). *AASHTO Guide Specifications for LRFD Seismic Bridge Design, 1<sup>st</sup> Edition*. Washington, DC: AASHTO.
- American Association of State Highway and Transportation Officials, AASHTO. (2012). *AASHTO LRFD Bridge Design Specifications, Customary U.S. Units, 6<sup>th</sup> Edition with 2013 Interim Revisions*. Washington, DC: AASHTO.
- Au, F. T. K., Cheng, Y. S., and Cheung, Y. K. (2001). Vibration Analysis of Bridges under Moving Vehicles and Trains: An Overview. *Progress in Structural Engineering and Materials*, 3 (3), pp. 299-304.
- Aviram, A., Mackie, K. R., and Stojadinović, B. (2008). *Guidelines for Nonlinear Analysis of Bridge Structures in California, Report PEER 2008/03*. Berkeley: Pacific Earthquake Engineering Research Center.
- Ayoub, M. I. M. (2010). *Behavior of Pile Extension Connections to Slab Bridges under Cyclic Loading Effect*. Ph.D. Dissertation, Department of Civil and Environmental Engineering, University of Nevada, Reno.
- Ayre, R. S., Ford, G., and Jacobsen, L. S. (1950). Transverse Vibration of a Two-Span Beam under Action of a Moving Constant Force. *Journal of Applied Mechanics ASME*, 17 (1), pp. 1-12.
- Ayre, R. S. and Jacobsen, L. S. (1950). Transverse Vibration of a Two-Span Beam under the Action of a Moving Alternating Force. *Journal of Applied Mechanics ASME*, 17 (3), pp. 283-290.
- Ayre, R. S., Jacobsen, L. S., and Hsu, C. S. (1952). Transverse Vibration of One- and of Two-Span Beams under the Action of Moving Mass Load. *Proceedings of the First National Congress on Applied Mechanics*, Chicago, IL, June 11-16, pp. 81-90.
- Baumgaertner, W. (1998). Bridge-Truck Interaction: Simulation, Measurements and Load Identification. *Proceedings of the 5<sup>th</sup> International Symposium on Heavy*

- Vehicle Weights and Dimensions*, Maroochydore, Australia, March 29-April 2, pp. 114-131.
- Bojanowski, C. and Kulak, R. F. (2011). Seismic and Traffic Load Modeling on Cable Stayed Bridge. *Proceedings of Transportation Research Board 90<sup>th</sup> Annual Meeting*, Washington, DC, January 23-27, 13 pp.
- Brady, S. P., Gonzalez, A., Znidaric, A., and O'Brien, E. J. (2002). Impact Factors on Medium Span Bridges due to Multiple Vehicle Presence. *Proceedings of 7<sup>th</sup> International Symposium on Heavy Vehicle Weights & Dimensions*, Delft, Netherlands, June 16-20, 10 pp.
- Bruni, S., Boccione, M., and Baretta, S. (2003). Simulation of Bridge-Heavy Road Vehicle Interaction and Assessment of Structure Durability. *Heavy Vehicle Systems*, 10 (1/2), pp. 70-85.
- Bryja, D. and Śniady, P. (1998). Stochastic Non-Linear Vibrations of Highway Suspension Bridge under Inertial Sprung Moving Load. *Journal of Sound and Vibration*, 216 (3), pp. 507-519.
- California Department of Transportation, Caltrans. (2011). *California Amendments to the AASHTO LRFD Bridge Design Specifications (Fourth Edition)*. Sacramento: Caltrans.
- Carvalho, E. C. (1998). Seismic Testing of Structures. *Proceedings of the Eleventh European Conference on Earthquake Engineering*, Paris, France, 6-11 September, pp. 53-64.
- Chatterjee, P. K., Datta, T. K., and Surana, C. S. (1994). Vibration of Continuous Bridges under Moving Vehicles. *Journal of Sound and Vibration*, 169 (5), pp. 619-632.
- Chen, G. and Wu, J. (2001). Optimal Placement of Multiple Tune Mass Dampers for Seismic Structures. *Journal of Structural Engineering ASCE*, 127 (9), pp. 1054-1062.
- Christiano, P. P. and Culver, C. G. (1969). Horizontally Curved Bridges Subject to Moving Load. *Journal of the Structural Division ASCE*, 95 (ST8), pp. 1615-1643.
- Cifuentes, A. O. (1989). Dynamic Response of a Beam Excited by a Moving Mass. *Finite Elements in Analysis and Design*, 5 (3), pp. 237-246.
- Clark, A. J. (1988). Multiple Passive Tuned Mass Dampers for Reducing Earthquake Induced Building Motion. *Proceedings of Ninth World Conference on Earthquake Engineering*, Volume V, Tokyo-Kyoto, Japan, August 2-9, pp. 779-784.
- Clarke, C. B. (1966). Testing of a Model Curved Steel Girder Bridge. *Engineering Journal AISC*, 3 (3), pp. 106-112.
- Computers and Structures, Inc, CSI. (2011). SAP2000 (Version 15.1.0) [Computer Software]. Berkeley: CSI.

- Connor, J. J. (2003). *Introduction to Structural Motion Control*. Upper Saddle River: Prentice Hall.
- Culver, C. G. and Christiano, P. P. (1969). Static Model Tests of Curved Girder Bridge. *Journal of the Structural Division ASCE*, 95 (ST8), pp. 1599-1614.
- Fafard, M., Bennur M., and Savard, M. (1997). A General Multi-Axle Vehicle Model to Study the Bridge-Vehicle Interaction. *Engineering Computations*, 14 (5), pp. 491-508.
- Fancher, P. S., Ervin, R. D., Winkler, C. B., and Gillespie, T. D. (1986). *A Factbook of the Mechanical Properties of the Components for Single-Unit and Articulated Heavy Trucks, Report UMTRI-86-12*. Ann Arbor: The University of Michigan Transportation Research Institute.
- Federal Highway Administration (FHWA). (1996). *Seismic Design of Bridges: Design Example No. 6 – Three Span Continuous CIP Concrete Box Girder, Publication No. FHWA-SA-97-011*. Washington, D.C.: Federal Highway Administration.
- Fřyba, L. and Yau, J. –D. (2009). Suspended Bridges Subjected to Moving Loads and Support Motions due to Earthquake. *Journal of Sound and Vibration*, 319 (1-2), pp. 218-227.
- Garinei, A. (2006). Vibrations of Simple Beam-like Modelled Bridge under Harmonic Moving Loads. *International Journal of Engineering Science*, 44 (11-12), pp. 778-787.
- Gesund, H. and Young, D. (1961). Dynamic Response of Beams to Moving Loads. *International Association for Bridge and Structural Engineering Publication*, 21, pp. 95-110.
- Ghosn, M., Moses, F., and Wang, J. (2003). *Design of Highway for Extreme Events, NCHRP Report 489*. Washington, DC: Transportation Research Board.
- Gong, L. and Cheung, M. S. (2008). Computer Simulation of Dynamic Interactions between Vehicle and Long Span Box Girder Bridges. *Tsinghua Science and Technology*, 13 (S1), pp. 71-77.
- Green, M. F. and Cebon, D. (1994). Dynamic Response of Highway Bridges to Heavy Vehicle Loads: Theory and Experimental Validation. *Journal of Sound and Vibration*, 170 (1), pp. 51-78.
- Green, M. F. and Cebon, D. (1997). Dynamic Interaction between Heavy Vehicles and Highway Bridges. *Computers and Structures*, 62 (2), pp. 253-264.
- Gu, M, Chen S. R., and Chang, C. C. (2001). Parametric Study on Multiple Tuned Mass Dampers for Buffeting Control of Yangpu Bridge. *Journal of Wind Engineering and Industrial Aerodynamics*, 89 (11-12), pp. 987-1000.

- Gupta, R. K. and Traill-Nash, R. W. (1980). Bridge Dynamic Loading due to Road Surface Irregularities and Braking of Vehicle. *Earthquake Engineering and Structural Dynamics*, 8 (2), pp. 83-96.
- Gutenbrunner, G., Savov, K., and Wenzel, H. (2007). Sensitivity Studies on Damping Estimation. *Proceedings of Experimental Vibration Analysis for Civil Engineering Structures 2007*, Porto, Portugal, 9 pp.
- Han, Y., Xia, H., Guo, W., and Zhang, N. (2003). Dynamic Analysis of Cable-Stayed Bridge Subjected to Running Trains and Earthquakes. *Environmental Vibration*, Chen Y. and Takemiya, H. (eds.), pp. 242-251.
- Harris, H. G. and Sabnis, G. M. (1999). *Structural Modeling and Experimental Techniques*, 2<sup>nd</sup> Ed. Boca Raton: CRC Press.
- Harrison, N. W. (2011). *Pre-Experimental Analysis and Design of Reinforced Concrete Bridge Columns for Seismic Testing of a Bridge System with Horizontal Curvature*. M.S. Thesis, Department of Civil and Environmental Engineering, University of Nevada, Reno.
- Hawk, H. and Ghali, A. (1981). Dynamic Response of Bridges to Multiple Truck Loading. *Canadian Journal of Civil Engineering*, 8 (3), pp. 392-401.
- He, X., Kawatani, M., Hayashikawa, T., and Matsumoto, T. (2011). Numerical Analysis on Seismic Response of Shinkansen Bridge-Train Interaction System under Moderate Earthquakes. *Earthquake Engineering and Engineering Vibration*, 10 (1), pp. 85-97.
- Huang, D. (2008). Dynamic Loading of Curved Steel Box Girder Bridges due to Moving Vehicles. *Structural Engineering International*, 18 (4), pp. 365-372.
- Huang, D., Wang, T. -L., and Shahawy, M. (1998). Vibration of Horizontally Curved Girder Bridges due to Vehicles. *Computers and Structures*, 68 (4), pp. 513-528.
- Humar, J. L. and Kashif, A. M. (1993). Dynamic Response of Bridges under Travelling Loads. *Canadian Journal of Civil Engineering*, 20 (2), pp. 287-298.
- Ibrahim, I. M. (2004). A Generally Applicable 3D Truck Ride Simulation with Coupled Rigid Bodies and Finite Element Models. *Heavy Vehicle Systems*, 11 (1), pp. 67-85.
- Jangid, R. S. (1995). Dynamic Characteristics of Structures with Multiple Tuned Mass Dampers. *Structural Engineering and Mechanics*, 3 (5), pp. 497-509.
- Kameda, H., Murono, Y., Maekawa, Y., and Sasaki, N. (1992). Dynamic Structure-Vehicle Interaction for Seismic Load Evaluation of Highway Bridges. *Proceedings of the Tenth World Conference on Earthquake Engineering*, Madrid, Spain, July 19-24, pp. 4861-4866.
- Kameda, H., Murono, Y., Nanjou, A., and Sasaki, N. (1999). Earthquake Response of Highway Bridges under Bridge-Vehicle System. *Journal of Structural Mechanics*

and *Earthquake Engineering JSCE (Doboku Gakkai Ronbushuu A)*, 626 (I-48), pp. 93-106. (In Japanese)

- Kareem, A. and Kline, S. (1995). Performance of Multiple Mass Dampers under Random Loading. *Journal of Structural Engineering ASCE*, 121 (2), pp. 348-361.
- Kawashima, K. and Penzien, J. (1979). Theoretical and Experimental Dynamic Behaviour of a Curved Model Bridge Structure. *Earthquake Engineering and Structural Dynamics*, 7 (2), pp. 129-145.
- Kawashima, K., Unjoh, S., and Mukai, H. (1994). Research on Live Load Effect to Earthquake Response of Bridges (Part 1). *PWRI Research Report No. 3316*, 59 pp. (In Japanese)
- Kawashima, K., Sasaki, T., Kajiwara, K., Ukon, H., Unjoh, S., Sakai, J., Takahashi, Y., Kosa, K., and Yabe, M. (2009). Seismic Performance of a Flexural Failure Type Reinforced Bridge Column Based on E-Defense Excitation. *Journal of Structural Mechanics and Earthquake Engineering JSCE (Doboku Gakkai Ronbushuu A)*, 65 (2), pp. 267-285.
- Kawatani, M., Kim, C. W., and Yasui, K. (2007). Seismic Response of a Highway Bridge under Traffic Loadings. *Proceedings of Pacific Structural Steel Conference 2007: Steel Structures in Natural Hazards*, Wairakei, New Zealand, March 13-16, pp. 183-188.
- Kim, C. W. and Kawatani, M. (2001). A Comparative Study on Dynamic Wheel Loads of Multi-Axle Vehicle and Bridge Responses. *Proceedings of ASME 2001 Design Engineering Technical Conference and Computers and Information in Engineering Conference*, Pittsburg, PA, September 9-12, pp. 1909-1917.
- Kim, C. W., Kawatani, M., and Kim, K. B. (2005). Three-Dimensional Dynamic Analysis for Bridge-Vehicle Interaction with Roadway Roughness. *Computers and Structures*, 83 (19-20), pp. 1627-1645.
- Kim, C. -W. and Kawatani, M. (2006). Effect of Train Dynamics on Seismic Response of Steel Monorail Bridges under Moderate Ground Motion. *Earthquake Engineering and Structural Dynamics*, 35 (10), pp. 1225-1245.
- Kim, C. W., Kawatani, M., Konaka, S., and Kitaura, R. (2011). Seismic Responses of a Highway Viaduct Considering Vehicles of Design Live Load as Dynamic System during Moderate Earthquakes. *Structure and Infrastructure Engineering*, 7 (7-8), pp. 523-534.
- Klasztorny, M. and Langer, J. (1990). Dynamic Response of Single-Span Beam Bridges to a Series of Moving Loads. *Earthquake Engineering and Structural Dynamics*, 19 (8), pp. 1107-1124.

- Kožar, I. (2009). Security Aspects of Vertical Actions on Bridge Structure: Comparison of Earthquake and Vehicle Induced Dynamical Forces. *Engineering Computations*, 26 (1/2), pp. 145-165.
- Kwasniewski, L., Li, H., Wekezer, J., Malachowski, J. (2006a). Finite Element Analysis of Vehicle-Bridge Interaction. *Finite Elements in Analysis and Design*, 42 (11), pp. 950-959.
- Kwasniewski, L., Wekezer, J., Roufa, G., Li, H., Ducher, J., and Malachowski, J. (2006b). Experimental Evaluation of Dynamic Effects for a Selected Highway Bridge. *Journal of Performance of Constructed Facilities*, 20 (3), pp. 253-260.
- Law, S. S. and Zhu X. Q. (2004). Dynamic Behavior of Damaged Concrete Bridge Structures under Moving Vehicular Loads. *Engineering Structures*, 26 (9), pp. 1279-1293.
- Lee, C. S., Goda, K., and Hong, H. P. (2012). Effectiveness of Using Tuned-Mass Dampers in Reducing Seismic Risk. *Structure and Infrastructure Engineering*, 8 (2), pp. 141-156.
- Levi, M. J. (2011). *Seismic Response of Columns in Horizontally Curved Bridges*. M.S. Thesis, Department of Civil and Environmental Engineering, University of Nevada, Reno.
- Lewandowski, R. and Grzymilawska, J. (2009). Dynamic Analysis of Structures with Multiple Tuned Mass Dampers. *Journal of Civil Engineering and Management*, 15 (1), pp. 77-86.
- Li, C. and Liu, Y. (2002). Further Characteristics for Multiple Tuned Mass Dampers. *Journal of Structural Engineering ASCE*, 128 (10), pp. 1362-1365.
- Li, C. and Qu, W. (2006). Optimum Properties of Multiple Tuned Mass Dampers for Reduction of Translational and Torsional Response of Structures Subject to Ground Acceleration. *Engineering Structures*, 28 (4), pp. 472-494.
- Licari, J. S. and Wilson, E. N. (1962). Dynamic Response of a Beam Subjected to a Moving Forcing System. *Proceedings of the Fourth U.S. National Congress of Applied Mechanics*, Berkeley, CA, June 18-21, pp. 419-425.
- Lin, J. –H. (2012). Dynamic Responses of a Simply Supported Bridge to Moving Vehicle Loads. *Applied Mechanics and Materials*, 117-119, pp. 231-235.
- Liu, K., De Roeck, G., and Lombaert, G. (2009). The Effect of Dynamic Train-Bridge Interaction on the Bridge Response during a Train Passage. *Journal of Sound and Vibration*, 325 (1-2), pp. 240-251.
- Liu, M. –F., Chang, T. –P., and Zeng, D. –Y. (2011). The Interactive Vibration Behavior in a Suspension Bridge System under Moving Vehicle Loads and Vertical Seismic Excitations. *Applied Mathematical Modelling*, 35 (1), pp. 398-411.

- Lou, P. (2005). A Vehicle-Track-Bridge Interaction Element Considering Vehicle's Pitching Effect. *Finite Elements in Analysis and Design*, 41 (4), pp. 397-427.
- Majka, M. and Hartnett, M. (2008). Effects of Speed, Load and Damping on the Dynamic Response of Railway Bridges and Vehicles. *Computers and Structures*, 86 (6), pp. 556-572.
- Mander, J. B., Priestley, M. J. N., and Park, R. (1988). Theoretical Stress-Strain Model for Confined Concrete, *Journal of Structural Engineering ASCE*, 114 (8), pp. 1804-1826.
- Mermetas, V. (1998). Dynamic Interaction between the Vehicle and Simply Supported Curved Bridge Deck. *Computer Methods in Applied Mechanics and Engineering*, 162 (1-4), pp. 125-131.
- Miao, T. J. and Chan, T. H. T. (2002). Bridge Live Load Models from WIM Data. *Engineering Structures*, 24 (8), pp. 1071-1084.
- Monzon, E. V. (2013). *Seismic Performance of Curved Steel Plate Girder Bridges with Seismic Isolation*. Ph.D. Dissertation, Department of Civil and Environmental Engineering, University of Nevada, Reno.
- Mulcahy, N. L. (1983). Bridge Response with Tractor-Trailer Vehicle Loading. *Earthquake Engineering and Structural Dynamics*, 11 (5), pp. 649-665.
- Nassif, H. H. and Liu, M. (2004). Analytical Modeling of Bridge-Road-Vehicle Dynamic Interaction System. *Journal of Vibration and Control*, 10 (2), pp. 215-241.
- Neves, S. G. M., Azevedo, A. F. M., and Calçada, R. (2012). A Direct Method for Analyzing the Vertical Vehicle-Structure Interaction. *Engineering Structures*, 34 (1), pp. 414-420.
- Nowak, A. S. (1993). Live Load Model for Highway Bridges. *Structural Safety*, 13 (1-2), pp. 53-66.
- Nowak, A. S. and Ferrand, D. M. (2004). Truck Load Models for Bridges. *Proceedings of the 2004 Structures Conference: Building on the Past Securing the Future*, Nashville, TN, May 22-26, 10 pp.
- Nowak, A. S. and Hong, Y. -K. (1991). Bridge Live-Load Models. *Journal of Structural Engineering ASCE*, 117 (9), pp. 2757-2767.
- Ngo, L. D. (1978). *Three-Dimensional Dynamic Analysis of Bridge-Vehicle Systems*. Ph.D. Dissertation, Department of Civil Engineering, University of Auckland, New Zealand.
- Otsuka, H., Unjoh, S., and Mukai, H. (1999). Research on Live Load Effect to Earthquake Response of Bridges (Part 2). *PWRI Research Report No. 3355*, 40 pp. (In Japanese)

- Palamas, J., Coussy, O., and Bamberger, Y. (1985). Effects of Surface Irregularities upon the Dynamic Response of Bridges under Suspended Moving Loads. *Journal of Sound and Vibration*, 99 (2), pp. 235-245.
- Pan, T. -C. and Li, J. (2002). Dynamic Vehicle Element Method for Transient Response of Coupled Vehicle-Structure Systems. *Journal of Structural Engineering ASCE*, 128 (2), pp. 214-223.
- Park, J. and Reed, D. (2001). Analysis of Uniformly and Linearly Distributed Mass Dampers under Harmonic and Earthquake Excitation. *Engineering Structures*, 23 (7), pp. 802-814.
- Rajapakse, N. I. and Happawana, G. S. (2004). A Nonlinear Six Degree-of-Freedom Axle and Body Combination Roll Model for Heavy Trucks' Directional Stability. *Proceedings of 2004 ASME International Mechanical Engineering Congress and Exposition*, Anaheim, CA, November 13-20, pp. 287-296.
- Rana, R. (1996). Response Control of Structures by Tuned Mass Dampers and Their Generalizations. *Proceedings of Eleventh World Conference on Earthquake Engineering*, Paper No. 498, 8 pp.
- Robinson, M. J. and Kosmatka, J. B. (2011). Experimental Dynamic Response of a Short-Span Composite Bridge to Military Vehicles. *Journal of Bridge Engineering ASCE*, 16 (1), pp. 166-170.
- Rösler, M. (1994). Dynamic Interaction between Bridge and Vehicle. *Transportation Research Record*, 1460, pp. 81-86.
- Sanford, D. M. (2013). *Preliminary Experimental Study on the Effect of Live Load on the Seismic Response of Highway Bridges*. M.S. Thesis, Department of Civil and Environmental Engineering, University of Nevada, Reno.
- Scott, M. H. (2010). *Combined Seismic Plus Live Load Analysis of Highway Bridges, Report OTREC-RR-09-261*. Portland: Oregon Transportation Research and Education Consortium.
- Sen, D., Bhattacharya, B., and Manohar, C. S. (2012). Reliability of Bridge Deck Subject to Random Vehicular and Seismic Loads through Subset Simulation. *Proceedings of 6<sup>th</sup> International Conference on Bridge Maintenance, Safety and Management (IABMAS 2012)*, Stresa, Italy, July 8-12, pp. 668-675.
- Senthilvasan, J., Brameld, G. H., and Thambiratnam, D. P. (1997). Bridge-Vehicle Interaction in Curved Box Girder Bridges. *Microcomputers in Civil Engineering*, 12 (3), pp. 171-182.
- Senthilvasan, J., Thambiratnam, D. P., and Brameld, G. H. (2002). Dynamic Response of a Curved Bridge under Moving Truck Load. *Engineering Structures*, 24 (10), pp. 1283-1293.

- Shi, X. M. and Cai, C. S. (2009). Simulation of Dynamic Effects of Vehicles on Pavement Using a 3D Interaction Model. *Journal of Transportation Engineering ASCE*, 135 (10), pp. 736-744.
- Shooshtari, M. and Mortezaie, H. (2012). Performance Improvement of Tall Reinforced Concrete Structures with Multiple Tuned Mass Dampers (MTMD). *Proceedings of 15<sup>th</sup> World Conference on Earthquake Engineering*, Lisbon, Portugal, September 24-28, 7 pp.
- Simeon, B., Grupp, F., Führer, C., and Rentrop, P. (1994). A Nonlinear Truck Model and Its Treatment as a Multibody System. *Journal of Computational and Applied Mathematics*, 50 (1-3), pp. 523-532.
- Sridharan, N. and Mallik, A. K. (1979). Numerical Analysis of Vibration of Beams Subjected to Moving Loads. *Journal of Sound and Vibration*, 65 (1), pp. 147-150.
- Sugiyama, I., Kameda, H., Sasaki, N., and Kawakita, S. (1990). Dynamic Structure-Vehicle Interaction of Highway Bridges and Its Implication to Seismic Design. *Proceedings of the 6<sup>th</sup> U.S.-Japan Bridge Engineering Workshop*, Lake Tahoe, NV, May 7-8, pp. 379-392.
- Sungil, K. and Jongwon, K. (2012). Bridge/Train Interaction Analysis of a Suspension Bridge Subjected to Seismic Loads. *Proceedings of 6<sup>th</sup> International Conference on Bridge Maintenance, Safety and Management (IABMAS 2012)*, Stresa, Italy, July 8-12, pp. 1733-1740.
- Szőke, D. and Györgyi, J. (2002). Road Vehicle-Bridge Interaction. *Proceedings of the 8<sup>th</sup> Mini Conference on Vehicle System Dynamics, Identification and Anomalies*, Budapest, Hungary, November 11-13, pp. 665-672.
- Szurgott, P., Wekezer, J., Kwasniewski, L., Siervogel, J., and Ansley M. (2011). Experimental Assessment of Dynamic Responses Induced in Concrete Bridges by Permit Vehicles. *Journal of Bridge Engineering*, 16 (1), pp. 108-116.
- Tan, C. P. and Shore, S. (1968a). Dynamic Response of a Horizontally Curved Bridge. *Journal of the Structural Division ASCE*, 94 (ST3), pp. 761-781.
- Tan, C. P. and Shore, S. (1968b). Response of Horizontally Curved Bridge to Moving Load. *Journal of the Structural Division ASCE*, 94 (ST9), pp. 2135-2151.
- Tan, G. H., Brameld, G. H., and Thambiratnam, D. P. (1998). Development of an Analytical Model for Treating Bridge-Vehicle Interaction. *Engineering Structures*, 20 (1-2), pp. 54-61.
- Terzic, V. and Stojadinović, B. (2010). *Post-Earthquake Traffic Capacity of Modern Bridges in California, Report PEER 2010/103*. Berkeley: Pacific Earthquake Engineering Research Center.

- Tokunaga, M. and Sogabe, M. (2012). Effect of Dynamic Interaction between Train Vehicle and Structure on Seismic Response of Structure. *Proceedings of 15<sup>th</sup> World Conference on Earthquake Engineering*, Lisbon, Portugal, September 24-28, 10 pp.
- Valášek, M., Stejskal, V., Šika, Z., Vaculín, O., and Kovanda, J. (1998). Dynamic Model of Truck for Suspension Control. *Vehicle System Dynamics*, 28 (SUPPL), pp. 496-505.
- Valášek, M., Kejval, J., Máca, J., and Šmilauer, V. (2004). Bridge-Friendly Truck Suspension. *Vehicle System Dynamics*, 41 (SUPPL), pp. 13-22.
- Wakui, H., Tanabe, M., and Matsumoto, N. (1994). A Study on Dynamic Interaction Analysis for Railway Vehicles and Structures – Mechanical Model and Practical Analysis Method. *Quarterly Report of Railway Technical Research Institute*, 35 (2), pp. 96-104.
- Wang, T. L., Shahawy, M., and Huang, D. Z. (1993). Dynamic Response of Highway Trucks due to Road Surface Roughness. *Computers and Structures*, 49 (6), pp. 1055-1067.
- Wierschem, N. E., Spencer, Jr., B. F., Bergman, L. A., and Valakis, A. F. (2011). Numerical Study of Nonlinear Energy Sinks for Seismic Response Reduction. *Proceedings of the 6<sup>th</sup> International Workshop on Advanced Smart Materials and Smart Structures Technology (ANCRiSST 2011)*, Dalian, China, July 25-26, 9 pp.
- Wierschem, N. E., Quinn, D. D., Hubbard, S. A., Al-Shudeifat, M. A., McFarland, D. M., Luo, J., Fahnestock, L. A., Spencer, Jr., B. F., Vakakis, A. F., and Bergman, L. A. (2012). Passive Damping Enhancement of a Two-Degree-of-Freedom System through a Strongly Nonlinear Two-Degree-of-Freedom Attachment. *Journal of Sound and Vibration*, 331 (25), pp. 5393-5407.
- Williams, D. and Godden, W. (1979). Seismic Response of Long Curved Bridge Structures: Experimental Model Studies. *Earthquake Engineering and Structural Dynamics*, 7 (2), pp. 107-128.
- Wu, J. S. and Dai, C. W. (1987). Dynamic Response of Multispan Nonuniform Beam due to Moving Loads. *Journal of Structural Engineering ASCE*, 113 (3), pp. 458-474.
- Wyss, J. -C., Su, D., and Fujino, Y. (2011). Prediction of Vehicle-Induced Local Responses and Application to a Skewed Girder Bridge. *Engineering Structures*, 33 (4), pp. 1088-1097.
- Xia, H., Han, Y., Zhang, N., and Guo, W. (2006). Dynamic Analysis of Train-Bridge System Subjected to Non-Uniform Seismic Excitations. *Earthquake Engineering and Structural Dynamics*, 35 (12), pp. 1563-1579.
- Xiang, T. and Zhao, R. (2005). Dynamic Interaction Analysis of Vehicle-Bridge System using Transfer Matrix Method. *Structural Engineering and Mechanics*, 20 (1), pp. 111-121.

- Xu, K. and Igusa, T. (1992). Dynamic Characteristics of Multiple Substructures with Closely Spaced Frequencies. *Earthquake Engineering and Structural Dynamics*, 21 (12), pp. 1059-1070.
- Yamaguchi, H. and Harnpornchai, N. (1993). Fundamental Characteristics of Multiple Tuned Mass Dampers for Suppressing Harmonically Forced Oscillations. *Earthquake Engineering and Structural Dynamics*, 22 (1), pp. 51-62.
- Yang, F. and Fonder, G. A. (1996). An Iterative Solution Method for Dynamic Response of Bridge-Vehicles Systems. *Earthquake Engineering and Structural Dynamics*, 25 (2), pp. 195-215.
- Yang, Y. -B. and Lin, B. -H. (1995). Vehicle-Bridge Interaction Analysis by Dynamic Condensation Method. *Journal of Structural Engineering ASCE*, 121 (11), pp. 1636-1643.
- Yang, Y. -B., Liao, S. -S, and Lin, B. -H. (1995). Impact Formulas for Vehicles Moving over Simple and Continuous Beams. *Journal of Structural Engineering ASCE*, 121 (11), pp. 1644-1650.
- Yang, Y. -B. and Yau, J. -D. (1997). Vehicle-Bridge Interaction Element for Dynamic Analysis. *Journal of Structural Engineering ASCE*, 123 (11), pp. 1512-1518.
- Yang, Y. -B., Chang, C. -H., and Yau, J. -D. (1999). An Element for Analysing Vehicle-Bridge Systems Considering Vehicle's Pitching Effect. *International Journal for Numerical Methods in Engineering*, 46 (7), pp. 1031-1047.
- Yau, J. D. (2009). Dynamic Response Analysis of Suspended Beams Subjected to Moving Vehicles and Multiple Support Excitations. *Journal of Sound and Vibration*, 325 (4-5), pp. 907-922.
- Yau, J. -D., Wu, Y. -S., and Yang, Y. -B. (2001). Impact Response of Bridges with Elastic Bearings to Moving Loads. *Journal of Sound and Vibration*, 248 (1), pp. 9-30.
- Yau, J. D. and Frýba, L. (2007). Response of Suspended Beams due to Moving Loads and Vertical Seismic Ground Excitations. *Engineering Structures*, 29 (12), pp. 3255-3262.
- Yener, M. and Chompooming, K. (1994). Numerical Method of Lines for Analysis of Vehicle-Bridge Dynamic Interaction. *Computers and Structures*, 53 (3), pp. 709-726.
- Zeng, H. and Bert, C. W. (2001). Bridge/Vehicle Interaction Analysis by a Semi-Analytical Method. *Proceedings of International Modal Analysis Conference XIX: A Conference on Structural Dynamics*, Kissimmee, FL, February 5-8, pp. 1675-1681.
- Zhang, Z. C., Lin, J. H., Zhang, Y. H., Zhao, Y., Howson, W. P., and Williams, F. W. (2010). Non-Stationary Random Vibration Analysis for Train-Bridge Systems

Subjected to Horizontal Earthquakes. *Engineering Structures*, 32 (11), pp. 3571-3582.

Zhao, J. and Sritharan, S. (2007). Modeling of Strain Penetration Effects in Fiber-Based Analysis of Reinforced Concrete Structures. *ACI Structural Journal*, 104 (2), pp. 131-141.

Zuo, L. (2009). Effective and Robust Vibration Control Using Series Multiple Tuned-Mass Dampers. *Journal of Vibration and Acoustics ASME*, 131 (3), 11 pp.

# APPENDIX A. BASIC THEORY FOR TUNED MASS DAMPER AND MULTIPLE TUNED MASS DAMPERS

## A.1. General

In this appendix, the theory of a tuned mass damper (TMD) is given for the following cases:

1. Undamped single degree-of-freedom (SDOF) structure and undamped tuned mass damper (TMD)
2. Undamped SDOF structure and damped TMD
3. Damped SDOF structure and damped TMD, and
4. Damped multi-degree-of-freedom (MDOF) structure and damped TMD.

This material is followed by the basic theory for a damped, multiple tuned mass damper (MTMD) system installed on a damped MDOF structure.

The theory in this Appendix is taken from Connor (2003) and Xu and Igusa (1992).

## A.2. Undamped Structure and Undamped Tuned Mass Damper

For a SDOF structure, the simplest case of a structure with TMD is an undamped structure and undamped TMD, as shown in Figure A.1. For this system subjected to ground motion or excitation, the equations of motion for the TMD and the structure can be written as follows:

$$m_d(\ddot{u}_d + \ddot{u}) + k_d u_d = -m_d \ddot{u}_g \quad (\text{A.1})$$

$$m\ddot{u} + ku - k_d u_d = -m\ddot{u}_g \quad (\text{A.2})$$

where:

- $m$  = mass of the structure
- $m_d$  = mass of the TMD
- $k$  = stiffness of the structure
- $k_d$  = stiffness of the TMD
- $u$  = displacement of the structure
- $u_d$  = displacement of the TMD
- $\ddot{u}$  = acceleration of the structure

$\ddot{u}_d$  = acceleration of the TMD

$\ddot{u}_g$  = acceleration of the ground

If, for simplicity of discussion, we let the ground acceleration be a periodic function, or mathematically written as:

$$\ddot{u}_g = \hat{u}_g \sin(\Omega t) \quad (\text{A.3})$$

where:

$\hat{u}_g$  = maximum acceleration of the ground

$\Omega$  = angular frequency of the ground acceleration

$t$  = time

Then the displacement responses can be written as a function of the periodic function as follows:

$$u = \hat{u} \sin(\Omega t) \quad (\text{A.4})$$

$$u_d = \hat{u}_d \sin(\Omega t) \quad (\text{A.5})$$

The parameters  $\hat{u}$  and  $\hat{u}_d$  are defined as:

$$\hat{u} = -\frac{m\hat{u}_g}{k} \left( \frac{1 + \bar{m} - \rho_d^2}{D_1} \right) \quad (\text{A.6})$$

= amplitude of the displacement of the structure

$$\hat{u}_d = -\frac{m\hat{u}_g}{k_d} \left( \frac{\bar{m}}{D_1} \right) \quad (\text{A.7})$$

= amplitude of the displacement of the TMD

in which

$$D_1 = (1 - \rho^2)(1 - \rho_d^2) - \bar{m}\rho^2 \quad (\text{A.8})$$

where:

$$\bar{m} = \frac{m_d}{m} \quad (\text{A.9})$$

= mass ratio

$$\rho = \frac{\Omega}{\omega} \quad (\text{A.10})$$

= ground motion's frequency to structure's frequency ratio

$$\rho_d = \frac{\Omega}{\omega_d} \quad (\text{A.11})$$

= ground motion's frequency to TMD's frequency ratio

### A.3. Undamped Structure and Damped Tuned Mass Damper

A more common case for TMD is the device with damping. The damping is assumed to be viscous, i.e., proportional to the velocity. For this system of undamped structure and damped TMD, as shown in Figure A.2, the equations of motion become:

$$m_d \ddot{u}_d + c_d \dot{u}_d + k_d u_d + m_d \ddot{u} = -m_d \ddot{u}_g \quad (\text{A.12})$$

$$m \ddot{u} + k u - c_d \dot{u}_d - k_d u_d = -m \ddot{u}_g \quad (\text{A.13})$$

where:

$$c_d = \text{damping coefficient of the TMD}$$

$$\dot{u}_d = \text{velocity of the TMD}$$

Because of the inclusion of damping terms in the equation of motion, there is a phase shift between the periodic ground excitation and the response. Therefore, it is more convenient to express the ground acceleration as a complex function as follows:

$$\ddot{u}_g = \hat{u}_g e^{i\Omega t} \quad (\text{A.14})$$

The term  $\hat{u}_g$  is a real quantity. Then the displacement responses can also be written as complex functions as follows:

$$u = \tilde{u} e^{i\Omega t} \quad (\text{A.15})$$

$$u_d = \tilde{u}_d e^{i\Omega t} \quad (\text{A.16})$$

The parameters  $\tilde{u}$  and  $\tilde{u}_d$ , which are the structure's and TMD's displacement amplitudes, are complex quantities. Moreover, the real and imaginary parts of  $\ddot{u}_g$  correspond to the cosine and sinusoidal inputs, respectively. The corresponding solution, therefore, is given by either the real or imaginary part of  $u$  and  $u_d$ . The parameters  $\tilde{u}$  and  $\tilde{u}_d$  can now be defined as:

$$\tilde{u} = -\frac{\hat{u}_g m}{k D_2} \left[ (1 + \bar{m}) f^2 - \rho^2 + i 2 \xi_d \rho f (1 + \bar{m}) \right] \quad (\text{A.17})$$

$$\tilde{u}_d = -\frac{\hat{u}_g m}{k D_2} \quad (\text{A.18})$$

in which

$$D_2 = (1 - \rho^2)(f^2 - \rho^2) - \bar{m} \rho^2 f^2 + i 2 \xi_d \rho f [1 - \rho^2 (1 + \bar{m})] \quad (\text{A.19})$$

where:

$$f = \frac{\omega_d}{\omega} \quad (\text{A.20})$$

= TMD's frequency to structure's frequency ratio

$$\xi_d = \frac{c_d}{2 \omega_d m_d} \quad (\text{A.21})$$

= damping ratio of the TMD

These solutions can also be written in polar form as follows:

$$\tilde{u} = -\frac{\hat{u}_g m}{k} H_2 e^{i \delta_2} \quad (\text{A.22})$$

$$\tilde{u}_d = -\frac{\hat{u}_g m}{k} H_4 e^{-i \delta_3} \quad (\text{A.23})$$

where:

$$H_2 = \frac{\sqrt{\left[ (1 + \bar{m}) f^2 - \rho^2 \right]^2 + \left[ 2 \xi_d \rho f (1 + \bar{m}) \right]^2}}{|D_2|} \quad (\text{A.24})$$

$$H_4 = \frac{1}{|D_2|} \quad (\text{A.25})$$

$$|D_2| = \sqrt{\left\{ (1 - \rho^2)(f^2 - \rho^2) - \bar{m} \rho^2 f^2 \right\}^2 + \left\{ 2 \xi_d \rho f [1 - \rho^2 (1 + \bar{m})] \right\}^2} \quad (\text{A.26})$$

$$\delta_2 = \alpha_2 - \delta_3 \quad (\text{A.27})$$

$$\tan \delta_3 = \frac{2\xi_d \rho f [1 - \rho^2 (1 + \bar{m})]}{(1 - \rho^2)(f^2 - \rho^2) - \bar{m} \rho^2 f^2} \quad (\text{A.28})$$

$$\tan \alpha_2 = \frac{2\xi_d \rho f (1 + \bar{m})}{(1 + \bar{m}) f^2 - \rho^2} \quad (\text{A.29})$$

Figure A.3 shows the deformation response factor or dynamic amplification factor ( $H_2$ ) for the case of an undamped structure with a 5%, 10%, and 25% damped TMD. The effective frequency range for the TMD is when the response of the structure with the TMD is less than the response of the structure without the TMD. From Figure A.3 this occurs when  $0.8 < \Omega/\omega < 1.2$  (approx.) which is a slightly larger range than for an undamped TMD.

#### A.4. Damped Structure and Damped Tuned Mass Damper

The system can be expanded to also have damping in the structure, as shown in Figure A.4. For such system, the equations of motion can be written as follows:

$$m_d \ddot{u}_d + c_d \dot{u}_d + k_d u_d + m_d \ddot{u} = -m_d \ddot{u}_g \quad (\text{A.30})$$

$$m \ddot{u} + c \dot{u} + k u - c_d \dot{u}_d - k_d u_d = -m \ddot{u}_g \quad (\text{A.31})$$

where:

$c$  = damping coefficient of the structure

$\dot{u}$  = velocity of the structure

Following the previous discussion, the solutions of these equations of motion can be expressed in polar form as follows:

$$\tilde{u} = -\frac{\hat{u}_g m}{k} H_6 e^{i\delta_6} \quad (\text{A.32})$$

$$\tilde{u}_d = -\frac{\hat{u}_g m}{k} H_8 e^{i\delta_8} \quad (\text{A.33})$$

where:

$$H_6 = \frac{\sqrt{[(1 + \bar{m}) f^2 - \rho^2]^2 + [2\xi_d \rho f (1 + \bar{m})]^2}}{|D_3|} \quad (\text{A.34})$$

$$H_8 = \frac{\sqrt{1 + [2\xi\rho]^2}}{|D_3|} \quad (\text{A.35})$$

$$|D_3| = \left\{ \begin{aligned} & \left[ -f^2 \rho^2 \bar{m} + (1 - \rho^2)(f^2 - \rho^2) - 4\xi\xi_d f \rho^2 \right]^2 + \dots \\ & \dots + 4 \left[ \xi\rho(f^2 - \rho^2) + \xi_d f \rho(1 - \rho^2(1 + \bar{m})) \right]^2 \end{aligned} \right\} \quad (\text{A.36})$$

$$\delta_6 = \alpha_2 - \delta_7 \quad (\text{A.37})$$

$$\delta_8 = \alpha_3 - \delta_7 \quad (\text{A.38})$$

$$\tan \delta_7 = 2 \frac{\xi\rho(f^2 - \rho^2) + \xi_d f \rho [1 - \rho^2(1 + \bar{m})]}{-f^2 \rho^2 \bar{m} + (1 - \rho^2)(f^2 - \rho^2) - 4\xi\xi_d f \rho^2} \quad (\text{A.39})$$

$$\tan \alpha_3 = 2\xi\rho \quad (\text{A.40})$$

$$\xi = \frac{c}{2\omega m} \quad (\text{A.41})$$

= damping ratio of the structure

Figure A.5 shows the deformation response factor or dynamic amplification factor ( $H_6$ ) for the case of a 5% damped structure with a 0%, 5%, and 25% damped TMD. As with the previous case (Figure A.3), the effective frequency range for the TMD is when the response of a structure with the TMD is less than the response of the structure without the TMD. From Figure A.5 this occurs for  $\Omega/\omega >$  about 0.9, which is a considerably larger range than for an undamped structure (Figure A.3).

## A.5. Multiple Degree-of-Freedom System with Tuned Mass Damper

One can further develop the theory for MDOF system with TMD, as shown in Figure A.6 for a two degree-of-freedom (2DOF) structure with TMD. The equations of motion for this system can be formulated as follows:

$$m_d \ddot{u}_d + c_d \dot{u}_d + k_d u_d = -m_d (\ddot{u}_2 + \ddot{u}_g) \quad (\text{A.42})$$

$$m_2 \ddot{u}_2 + c_2 (\dot{u}_2 - \dot{u}_1) + k_2 (u_2 - u_1) - c_d \dot{u}_d - k_d u_d = -m_2 \ddot{u}_g \quad (\text{A.43})$$

$$m_1 \ddot{u}_1 + c_1 \dot{u}_1 + k_1 u_1 - c_2 (\dot{u}_2 - \dot{u}_1) - k_2 (u_2 - u_1) = -m_1 \ddot{u}_g \quad (\text{A.44})$$

Equations (A.42) and (A.43) can also be written in matrix form as follows:

$$\mathbf{M}\ddot{\mathbf{U}}+\mathbf{C}\dot{\mathbf{U}}+\mathbf{K}\mathbf{U}=\begin{bmatrix} -m_1\ddot{u}_g \\ -m_1\ddot{u}_g \end{bmatrix}+\begin{bmatrix} 0 \\ k_d u_d + c_d \dot{u}_d \end{bmatrix} \quad (\text{A.45})$$

where:

$$\mathbf{M}=\begin{bmatrix} m_1 & 0 \\ 0 & m_2 \end{bmatrix} \quad (\text{A.46})$$

$$\mathbf{C}=\begin{bmatrix} c_1+c_2 & -c_2 \\ -c_2 & c_2 \end{bmatrix} \quad (\text{A.47})$$

$$\mathbf{K}=\begin{bmatrix} k_1+k_2 & -k_2 \\ -k_2 & k_2 \end{bmatrix} \quad (\text{A.48})$$

$$\mathbf{U}=\begin{bmatrix} u_1 \\ u_2 \end{bmatrix} \quad (\text{A.49})$$

The displacement matrix  $\mathbf{U}$  can be transformed into modal coordinate and written as:

$$\mathbf{U}=\Phi_1 q_1+\Phi_2 q_2 \quad (\text{A.50})$$

Note that the modal vectors satisfy the following orthogonality relations:

$$\Phi_j^T \mathbf{K} \Phi_i = \delta_{ij} \omega_j^2 \Phi_j^T \mathbf{M} \Phi_i \quad (\text{A.51})$$

Therefore, modal mass, damping, and stiffness terms can be written as:

$$m_j^* = \Phi_j^T \mathbf{M} \Phi_j \quad (\text{A.52})$$

$$c_j^* = \Phi_j^T \mathbf{C} \Phi_j \quad (\text{A.53})$$

$$k_j^* = \Phi_j^T \mathbf{K} \Phi_j = \omega_j^2 m_j^* \quad (\text{A.54})$$

in which

$$\Phi_j = \begin{bmatrix} \Phi_{j1} \\ \Phi_{j2} \end{bmatrix} \quad (\text{A.55})$$

For simplicity of the discussion, the damping term can be assumed to be Rayleigh damping, i.e., the damping matrix is proportional to the mass and stiffness matrices

$$\mathbf{C}=\alpha \mathbf{M}+\beta \mathbf{K} \quad (\text{A.56})$$

In modal coordinates, the equations of motion uncoupled and become:

$$m_j^* \ddot{q}_j + c_j^* \dot{q}_j + k_j^* q_j = \Phi_{j1} (-m_1 \ddot{u}_g) + \Phi_{j2} (-m_2 \ddot{u}_g + k_d u_d + c_d \dot{u}_d) \quad (\text{A.57})$$

where  $j = 1, 2$  for a 2DOF system and the modal damping ratio is formulated as:

$$\xi_j = \frac{c_j^*}{2\omega_j m_j^*} \quad (\text{A.58})$$

Equation (A.56) is a set of two equations, each of them for DOFs 1 and 2 for a 2DOF system, with mass, damping, and stiffness terms associated with the particular DOF. TMD is only effective for a narrow range of operational frequency. Therefore, one has to make a decision on which modal resonant frequency is to be controlled with the TMD. After this has been selected, one can proceed to calculate the response of the system. Suppose that the first mode is selected, Equation (A.56) yields to:

$$m_1^* \ddot{q}_1 + c_1^* \dot{q}_1 + k_1^* q_1 = -(m_1 \Phi_{11} + m_2 \Phi_{12}) \ddot{u}_g + \Phi_{12} (k_d u_d + c_d \dot{u}_d) \quad (\text{A.59})$$

The term  $u_2$  can be obtained by superposing the modal contributions from each mode as follows:

$$u_2 = \Phi_{12} q_1 + \Phi_{22} q_2 \quad (\text{A.60})$$

However, since the exciting frequency is close to the first modal frequency  $\omega_1$ , the first modal response will dominate. Hence, the term  $u_2$  can be approximated by:

$$u_2 \cong \Phi_{12} q_1 \quad (\text{A.61})$$

Then one can conveniently solve for  $q_1$  by inversion:

$$q_1 = \left[ \frac{1}{\Phi_{12}} \right] u_2 \quad (\text{A.62})$$

Substituting this back in Equation (A.58) gives:

$$m_{1,eq}^* \ddot{u}_2 + c_{1,eq}^* \dot{u}_2 + k_{1,eq}^* u_2 = c_d \dot{u}_d + k_d u_d - \Gamma_{1,eq} m_{1,eq}^* \ddot{u}_g \quad (\text{A.63})$$

where the terms  $m_{1,eq}^*$ ,  $c_{1,eq}^*$ ,  $k_{1,eq}^*$ , and  $\Gamma_{1,eq}$  represent the equivalent SDOF parameters that are defined as:

$$m_{1,eq}^* = \left[ \frac{1}{\Phi_{12}^2} \right] m_1^* \quad (\text{A.64})$$

$$k_{1,eq}^* = \left[ \frac{1}{\Phi_{12}^2} \right] k_1^* \quad (\text{A.65})$$

$$c_{1,eq}^* = \alpha m_{1,eq}^* + \beta k_{1,eq}^* \quad (A.66)$$

$$\Gamma_{1,eq} = \frac{\Phi_{12}}{m_1^*} (m_1 \Phi_{11} + m_2 \Phi_{22}) \quad (A.67)$$

If one lets  $m_{1,eq}^* \equiv m$ ,  $c_{1,eq}^* \equiv c$ ,  $k_{1,eq}^* \equiv k$ ,  $\Gamma_{1,eq} \equiv \Gamma$ , and  $u_2 \equiv u$ , Equation (A.62) becomes:

$$m\ddot{u} + c\dot{u} + ku = c_d \dot{u}_d + k_d u_d - \Gamma m \ddot{u}_g \quad (A.68)$$

This equation differs from the SDOF equation discussed previously on the exciting force term by a factor  $\Gamma$ . Therefore, the solutions developed previously can still be utilized after modifying to account for this factor as follows:

$$H_6 = \frac{\sqrt{[(\Gamma + \bar{m})f^2 - \Gamma\rho^2]^2 + [2\xi_d \rho f(\Gamma + \bar{m})]^2}}{|D_3|} \quad (A.69)$$

$$H_8 = \frac{\sqrt{[1 + \rho^2(\Gamma - 1)]^2 + [2\xi\rho]^2}}{|D_3|} \quad (A.70)$$

$$\delta_6 = a_2 - \delta_7 \quad (A.71)$$

$$\delta_8 = a_3 - \delta_7 \quad (A.72)$$

$$\tan a_2 = \frac{2\xi_d f \rho (\Gamma + \bar{m})}{f^2 (\Gamma + \bar{m}) - \Gamma \rho^2} \quad (A.73)$$

$$\tan a_3 = \frac{2\xi\rho}{1 + (\Gamma - 1)\rho^2} \quad (A.74)$$

The mass ratio for this case is slightly modified as:

$$\bar{m} = \frac{m_d}{m_{1,eq}^*} \quad (A.75)$$

Then one can proceed to obtain the solution as described for the damped SDOF with damped TMD case. If the system is tuned for the  $i^{\text{th}}$  mode instead of the first mode as shown previously, one can derive the solution by changing:

$$q_i \cong \left[ \frac{1}{\Phi_{i2}} \right] u_2 \quad (A.76)$$

and follow the same procedure.

## A.6. System with Multiple Tuned Mass Dampers

Consider now a system with multiple tuned mass dampers (MTMD). The system consists of a main oscillator and  $n$  sub-oscillators as depicted in Figure A.7. The sub-oscillators are usually tuned to the main oscillator. Therefore, such system is identical to a 2DOF vibration problem. The exact response of the main oscillator with respect to the base when subjected to periodic ground motion excitation of frequency  $\Omega$  can be formulated as:

$$u_0 = \frac{1 - (i\Omega m_0)^{-1} Z}{\omega_0^2 - 2i\Omega\omega_0\xi_0 - \Omega^2 - i\Omega m_0^{-1} Z} \quad (\text{A.77})$$

where:

$$Z = -i\Omega \sum_{j=1}^n \frac{m_j (\omega_j^2 - 2i\Omega\omega_j\xi_j)}{\omega_j^2 - 2i\Omega\omega_j\xi_j - \Omega^2} \quad (\text{A.78})$$

The term  $Z$ , which is a frequency function, has an important physical interpretation. Figure A.8 shows the series of sub-oscillators on the ground without the main oscillators. If the base is subjected to a unit harmonic velocity then  $Z$  is the amplitude of the harmonic force required to produce the base excitation. Thus, the term  $Z$  can be seen as the impedance of the sub-oscillators.

A special case for the system is when the sub-oscillators are identical, i.e., have the same damping ratio and frequency or mathematically  $\xi_1 = \xi_2 = \dots = \xi_n = \xi_s$  and  $\omega_1 = \omega_2 = \dots = \omega_n = \omega_s$ . For this case, it can be shown that the response amplitude of the main oscillator is equal to that of an equivalent 2DOF system. In this equivalent 2DOF system, the main oscillator is that of the original system and the sub-oscillator has the damping ratio  $\xi_s$ , natural frequency  $\omega_s$ , and mass  $m_s = m_1 + m_2 + \dots + m_n$ .

## A.7. Summary

The theory for both damped and undamped tuned mass dampers has been summarized in this Appendix. This theory may help explain the dynamic effect of live load on a bridge, wherein each vehicle may be viewed as a tuned mass damper. Since multiple vehicles may be on a bridge at any point in time, the theory for multiple mass dampers is of interest and hence its inclusion in this Appendix.

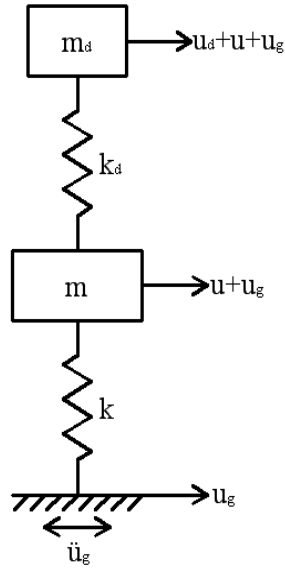


**Figure A.1. Undamped SDOF Structure and Undamped TMD**

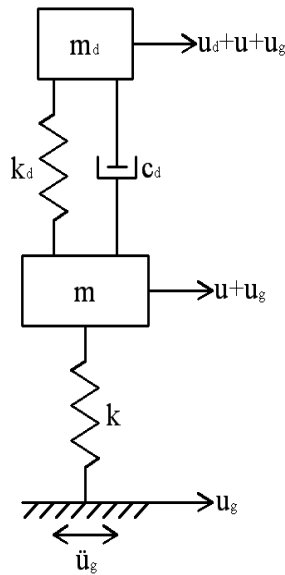


**Figure A.2. Undamped SDOF Structure and Damped TMD**

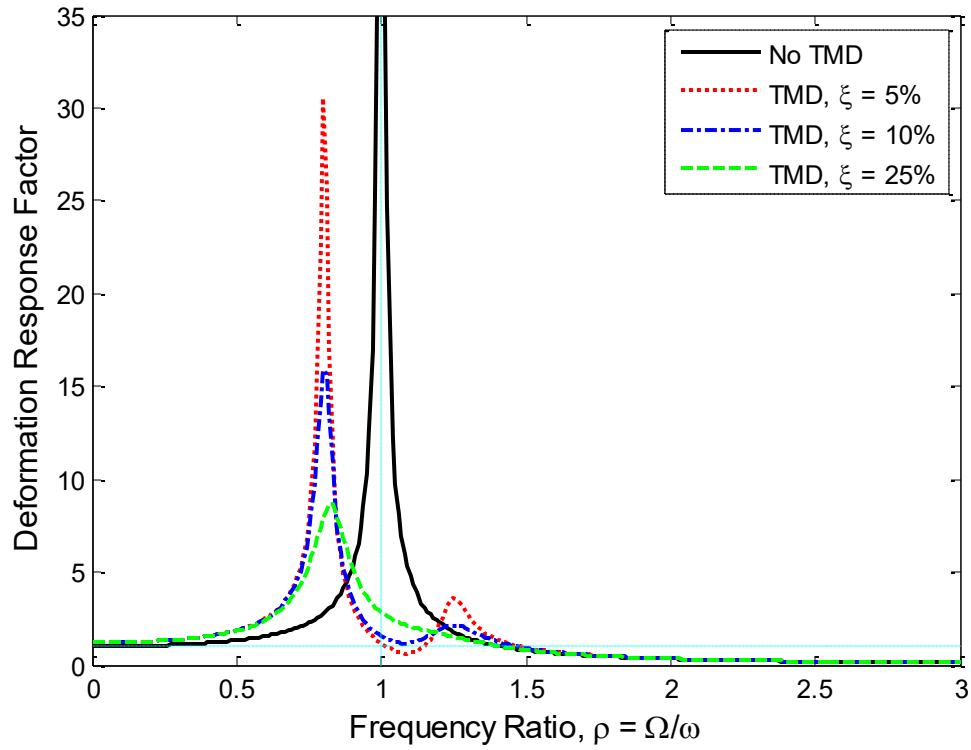


**Figure A.3. Deformation Response Factor for Undamped Structure and Damped TMD,  $m_d/m=0.2$ ,  $\omega_d/\omega=1.0$  (Connor 2003)**

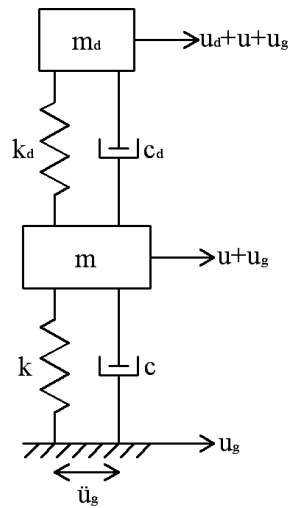


**Figure A.4. Damped SDOF Structure and Damped TMD**

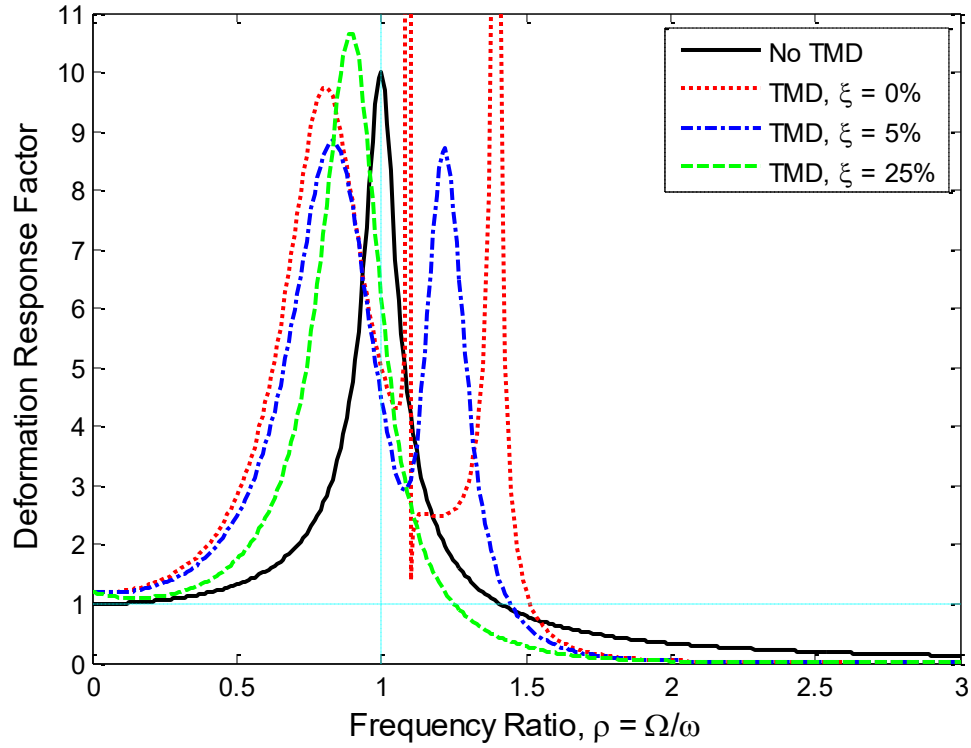


Figure A.5. Deformation Response Factor for 5% Damped Structure and Damped TMD,  $m_d/m=0.2$ ,  $\omega_d/\omega=1.0$  (Connor 2003)

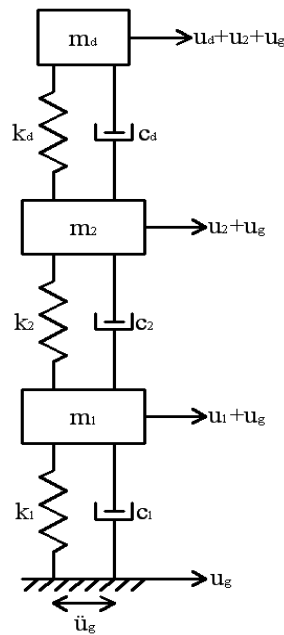


Figure A.6. Damped MDOF Structure and Damped TMD

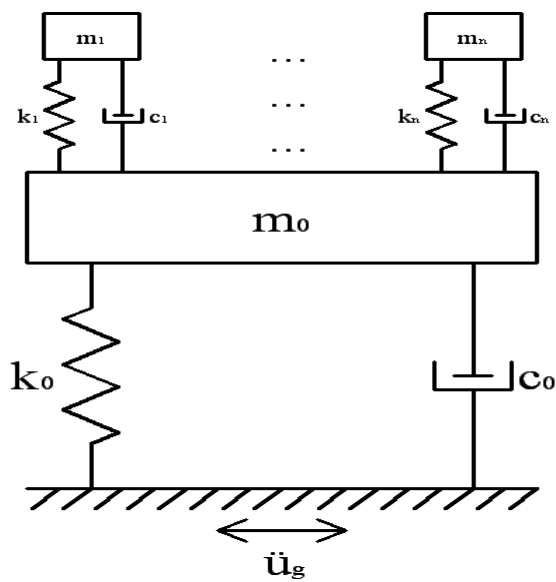


Figure A.7. Damped SDOF Structure and Damped MTMD

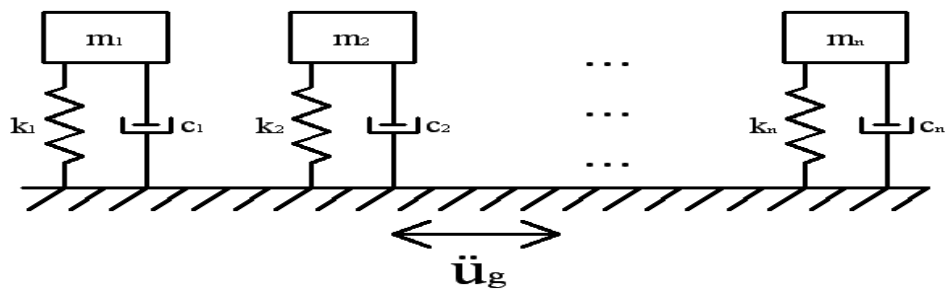


Figure A.8. Sub-oscillators on the Ground